CHARACTERIZATION OF HALVED UNDERSQUINTED SCARF JOINT AND STOP-SPLAYED UNDERSQUINTED & TABLED SCARF JOINT WITH KEY (JUPITER JOINT)

Dissertation

submitted to and approved by the

Department of Architecture, Civil Engineering and Environmental Sciences

University of Braunschweig – Institute of Technology

and the

Department of Civil and Environmental Engineering

University of Florence

in candidacy for the degree of a

Doktor-Ingenieur (Dr.-Ing.) /

Dottore di Ricerca in Civil and Environmental Engineering[*)]

by

Elena Perria

born 13/10/1985

from Pontedera (Pisa), Italy

Submitted on	01/09/2016
Oral examination on	09/11/2016
Professorial advisors	Prof. Michele Paradiso
	Prof. Martin Kessel

2017

*) Either the German or the Italian form of the title may be used.

[…] Ad intaglio a zigzag cuneiforme in testa. (Questo intaglio chiamasi anche a tratto di Giove per la sua rassomiglianza coi fulmini che gli artisti pongono nelle mani del dio tonante) […].

Mazzocchi Luigi, *Trattato sulle costruzioni in legno*,
Antonio Vallardi, Milano 1871, pag. 212.

Acknowledgements

I would like to thank my supervisors, Prof. Michele Paradiso, Prof. Martin Kessel for the support and the copious and diversified possibilities they gave me. I have been learning a lot. Many thanks also to Mike (*editor's note*: Sieder, he allowed us to call him per name!) for his steady support, suggestions and opinions.

I thank the CNR IVALSA institute for the identification conducted on the wooden species imported from the other part of the Ocean.

The iBHolz Institut für Baukonstruktion und Holzbau of the Technische Universität Braunschweig for the personal and material financial support is gratefully acknowledged. Moreover, the collaboration and advices of Ralf Augustin and the Team of the LHT Labor für Holztechnik in the HAWK Hildesheim, "my" jointer/carpenters Sören, Jan, Andreas.

The colleagues of the iBHolz for their nice converses during the *Frühstück Pause* and the help with the structural model, physical model, CAD model of the dome and miscellaneous.

After the official acknowledgements, I would like to thanks all the possibilities and the people that gave me the possibilities, the opportunities, the support, their fleeting, constant, periodic presence along my way. I would like to acknowledge people and places full of meanings; more, something that was in the backstage of the work: the poetry (that sometimes was more but a drama). I'll acknowledge all of them in order of temporal apparition, and not of importance, because it would be so much difficult for me.

My parents, Giovanna, Fabio, my family. The lunch-break-long opportunity to do a Phd. Thanks to the first Braunschweig, the APM, and the people that were there with me. The rave and the falling asleep. The coming back to Italy, the Feeling of having salt in the hairs jumping in the see, the House in Firenze and my flatmates, the Friends that where there and the Summer. Torino, Tolouse and Bucaramanga with all my Friends. My Students that made me crazy, Dieguito and his Rayuela, the Trip to Tayrona and the Company, the Weekends, the Music, the Salsa. Zapatoca, la Cueva, the Silence of Guane and the melting Sensation in Barranquilla. Bogotà, the Salt Cathedral and the Tears to come back. The week in Italy. The second Braunschweig, the opportunity to know a New Face of the same person, the Hardwork, the Decision to remain. Susanna to be my Friend, Psychologist and for sharing with me such crazy Moments and Chats. The Learning possibilities given by the EU. The first Snow and the first feeling to be *Zuhouse*. Hildesheim, HAWK and the first Lab staff to making me feel Home. The feeling to have the possibility to do a good work and feel Home. The Tools in on and for the Wood. The Wood. The few Hot Days with the mud-bathing-girls, many thanks to follow me. The Bells in a bright Morning with Clouds. Again my parents to support me. The coming back and the marvellous Christmas time in Germany. The Joy and the Tears. My new Collegues. The rainy Weekends of Germany. The Music. The Sensation to feel free. The second lab staff. The last

crazy Summer. All the people, buds and flowers that were surrounding me in these years. The Help, and the last sunny days. The amount of sad sensations in any moment, and approaching the end of the Phd.

Again all the People that helped me, in any manner.

I cannot explain with normal words how I felt and what his experience meant for me; thus, I can only thanks and that is why I acknowledge this international experience. Thanks to it I've learned how to survive my own feelings.

English Abstract

Thesis title: “Characterization of the *halved undersquinted scarf* joint and *stop-splayed and tabled scarf with key* joint (*Jupiter joint*)”.

Historical timber frame structures are diffused all around the world and constitute a huge part of the cultural heritage. The preservation of such structures and buildings requires a good understanding of both the original constructional methods and of the load-bearing principles of the structure. The carpentry connections are crucial for the behaviour of the structures, and a good understanding of them is of basic importance to lead a correct structural analysis. Rational rules and standardization for the description of the load-bearing capacity and failure of carpentry joints, as well as strengthening rules, are missing in the international standards.

The present work introduces the basic load-bearing principles of the *stop-splayed and tabled scarf joint with key* (*Jupiter joint*) and the *halved undersquinted joint*; two among the basic types of lengthening joints used in traditional *half-timbered* and *frame structures*. The *halved joint* was used as a reference for developing an overview on the general structural behaviour. Therefore, the problem was examined in depth with the experimental and numerical analysis of the *halved undersquinted scarf*. Basic analytical linear-elastic models were developed. Tests were conducted under static loads in order to describe the maximum load, failure mechanisms, position of the forces along the loading process, rotational stiffness, friction mechanisms and the influence of the geometry on the load-bearing behaviour. The analytical model, based on the initial assumptions was calibrated on the experimental results. The influence and function of both the sloped surfaces and the wedge is investigated through some intermediate geometries. Finally, in order to give general remarks about the behaviour of the *splayed and tabled scarf with key joint* (*Jupiter joint*) along the strong and weak axis, a small series of specimens were tested, in order to describe the interaction between normal force (N) and bending moment (M) in a N-M interaction diagram and to record the failure modes along the strong and weak axis.

In order to verify the reliability of the analytical model and the experimental results, the experimental outputs were compared with the numerical results obtained from the structural analysis of the dome of Santiago de Cuba’s cathedral. The case study was chosen because the inner timber framed structure of the building demonstrated reliability against earthquakes and hurricane along the centuries. Among the carpentry connections employed in the dome, the most diffused and effective was the *Jupiter joint*, that elongates the dome’s main ribs.

The description of such carpentry connection through a static model is of importance in the scientific field for the knowledge of the mechanical behaviour of old constructional systems. It can be the basis for many applications in the structural analysis with the aim of reinforce and restoration of old timber structures.

Italian Abstract

Titolo della tesi: “Caratterizzazione del giunto a *mezzo legno con teste inclinate* e *dardo di Giove con biette*”.

Le strutture a telaio in legno sono diffuse in tutto il mondo e formano parte del patrimonio storico culturale mondiale. Con il fine della conservazione di tali strutture si richiede sia una buona conoscenza dei metodi costruttivi originali, che una buona comprensione dei principi portanti delle strutture in legno. Le connessioni di falegnameria sono cruciali nel comportamento delle strutture e una buona comprensione dei loro principi di funzionamento è di importanza basica per una corretta analisi strutturale. Nelle norme internazionali vi è carenza, sia di regole razionali e standardizzate per la descrizione della capacità portante e i meccanismi di collasso delle connessioni di carpenteria, che di norme che indichino modalità di consolidamento e rinforzo.

La presente tesi vuole introdurre i principi di base sulla capacità portante del giunto a *dardo di Giove* e del giunto semplificato *a mezzo legno con dente inclinato*, due tra le principali tipologie di connessioni longitudinali utilizzate nelle tradizionali strutture a graticcio e a telaio. Il giunto a *mezzo legno*, è stato utilizzato come riferimento per elaborare un quadro generale del comportamento strutturale, dopodichè il problema è stato esaminato in profondità con l'analisi sperimentale e numerica del giunto *a mezzo legno con dente inclinato*. Inizialmente sono stati sviluppati modelli analitici basati su un comportamento lineare-elastico del giunto, in un secondo momento, prove sperimentali sotto carichi statici sono state condotte per descrivere il carico massimo, i meccanismi di rottura, la posizione delle forze durante il processo di carico, la rigidezza rotazionale del giunto, i meccanismi di attrito e l’influenza della geometria sul comportamento generale del nodo. L’iniziale modello analitico è stato poi calibrato sui risultati sperimentali ottenuti. L'influenza e la funzione sia delle superfici inclinate che della bietta sono stati valutati attraverso test sperimentali su alcune geometrie intermedie. Infine, con l’obiettivo di divulgare osservazioni generali sul comportamento dei giunti *a mezzo legno con dente inclinato* e a *dardo di Giove* sia lungo l’asse principale che secondario. Una piccola serie di campioni è stata testata per poter disegnare il corrispondente diagramma di interazione N-M per entrambe le geometrie.

Con il fine di verificare la veridicità del modello analitico e i risultati sperimentali, questi sono stati confrontati con i risultati dell’analisi numerica del modello strutturale della cupola della cattedrale di Santiago de Cuba. Il caso studio è stato scelto perché l’affidabilità della struttura a telaio in legno contro i terremoti e uragani nei secoli. Tra le connessioni carpenteria impiegate nella cupola, la più diffusa ed efficace è appunto il *dardo di Giove*, che unisce le nervature principali della cupola nel senso longitudinale.

La descrizione di tale connessioni di carpenteria attraverso un modello statico è di fondamentale importanza in campo scientifico per una conoscenza più approfondita del comportamento meccanico dei sistemi costruttivi tradizionali in legno. Il presente lavoro può costituire inoltre la base per applicazioni nella analisi strutturale allo scopo di ripristinare e/o rinforzare strutture in legno appartenenti al patrimonio storico costruito.

Table of Contents

List of Figures

List of Tables

List of Diagrams

Notations

The following symbols are used in this work.

A	Accidental action
A_k	Cross section area of the *snap joint* (physical model)
A_s	Cross section area of the *scarf joint* (physical model)
A_1	Area of the surface 1
A_2	Area of the surface 2
A_3	Area of the surface 3
$\overline{AB}$	Surface 1
$\overline{BC}$	Surface 2
C_{p0}	External pressure coefficient (wind)
$\overline{CD}$	Surface 3CO Load Combination
E	Young's modulus of elasticity
E_d	Design values of the effect
$E_{d,dst}$	Design value of effect of destabilising actions
$E_{d,stb}$	Design value of effect of stabilising actions
E_{mean}	Mean value of modulus of elasticity
F	External applied force
$F_{applied}$	Applied external force (universal testing machine)
$F_{c,max}$	Maximum applicable compression force (universal testing machine)
F_d	Friction force due to the contribution of the static friction μ_d
F_f	F action that is necessary to start the propagation of the crack (characteristic resistance value for the specimen).
$F_{f,B}$	see $F_{f,2}$
$F_{f,C}$	see $F_{f,3}$
$F_{f,2}$	F action that is necessary to start the propagation of the crack in the fiber in B
$F_{f,3}$	F action that is necessary to start the propagation of the crack in the fiber in C
$F_{i,\perp}$	Resultant force of the meant distributed load, perpendicular to the surface i
$F_{i,\perp,0}$	Component of the force $F_{i,\perp}$ parallel to the grain
$F_{i,\perp,90}$	Component of the force $F_{i,\perp}$ perpendicular to the grain

$F_{i,//}$	Resultant force parallel to the surface i
$F_{i,//,0}$	Component of the force $F_{i,//}$ parallel to the grain
$F_{i,//,90}$	Component of the force $F_{i,//}$ perpendicular to the grain
$F_{max,dynamic}$	Maximum force reachable with the coefficient of dynamic friction
$F_{max,static}$	Maximum force reachable with the coefficient of static friction
F_{pc}	Pre - compression force.
$F_{pc,0}$	Component of the pre - compression force F_{pc} parallel to the grains
$F_{pc,90}$	Component of the pre - compression force F_{pc} perpendicular to the grains
F_s	Friction force due to the contribution of the static friction μ_s ,
F_{target}	Pre-selected value of applied force F_I (universal testing machine)
$F_{t,max}$	Maximum applicable tension force (universal testing machine)
F_u	Ultimate value of the F action (failure value)
F_x	Forces along the x axis
F_y	Forces along the y axis
$F_{B'C'',\perp}$	Resultant force on the $\overline{B'C''}$ surface due to the external load, perpendicular to the surface.
$F_{C'B'',\perp}$	Resultant force on the $\overline{C'B''}$ surface due to the external load, perpendicular to the surface.
$F_{T2,\perp}$	Resultant force on the table 2 (T2 = surface $\overline{C'B''}$) of the joint, perpendicular to the surface.
$F_{T3,\perp}$	Resultant force on the table 3 (T3 = surface $\overline{B'C''}$) of the joint.
$F_{T3,\perp,0}$	Component of the resultant force on the table 3 $F_{T3,\perp}$ parallel to the grains.
$F_{2,\perp}$	Resultant force on the face $\overline{AB}$ due to the external applied load.
$F_{3,\perp}$	Resultant force on the face $\overline{DC}$ due to the external applied load.
F_I	Force applied by the Piston I
$F_{I,passive}$	Passive response on the piston I (universal testing machine)
F_{II}	Force applied by the Piston II
$F_{II,passive}$	Passive response on the piston II (universal testing machine)
$F_{II,u}$	Value of the applied force F_{II} (of the piston P_{II}) at the failure
$F_{v,2}$	Shear force on the shear plane $\overline{C'H}$
$F_{v,3}$	Shear force on the shear plane $\overline{B'K}$
FC(i)1	First Force boundary Condition, model (i)
FM I	Failure mode I
FM II	Failure mode II
FM III	Failure mode III
FM IV	Failure mode IV
FM V	Failure mode V
G	Shear Modulus
G_f	External work of fracture
$G_{f,tot}$	Critical value of work of fracture

G_{mean}	Mean value of shear modulus
GC(i)1	First Geometric boundary Condition, model (i).
I	Moment of inertia
J	Moment of inertia of the cantilever
K	Bulk modulus
LC	Load Case
LC(i)	Limit case (first)
LS2(i)	Limit State, model (i)
M	External applied bending moment
$M_{\exp}$	Experimental bending action
$M_{stb/dst}$	(De) stabilizing moment
M_u	Value of the moment M at the failure
My,k,max	Maximum characteristic Moment in the plane *yz*
Mz,k,max	Maximum characteristic Moment in the plane *xy*
MT,k,max	Maximum characteristic torsional Moment (plane *yz*)
N	Normal force (also, force F applied on the neutral axis of the beam)
$N_{\exp}$	Experimental normal action
$N_{stb/dst}$	(de) stabilizing normal force
N_u	Value of the load F at the failure
P0	Procedure 0
P1	Procedure 1
P2	Procedure 2
R	Resistance
R_c	Compression load-carrying capacity
R_d	Design value of a load-carrying capacity
R_k	Characteristic value of a load-carrying capacity
$R_{ax,\theta_{CD},k}$	Characteristics load-carrying capacity at an angle $\theta = \frac{\pi}{2} - \alpha$ (α = inclination of the surface 3)
R_v	Shear resistance
S	Surface
S0	Specimen S0
S1	Specimen S1
S2	Specimen S2
T	Kinetic energy
V_F	Criteria of advancement of the piston, stress control mode [Load / Time]
V_w	Criteria of advancement of the piston, displacement control mode [Path / Time]

(K) *Snap Joint* model

(S) *Scarf Joint* model

(i) equilibrium configuration correspondent to (I)

(ii) equilibrium configuration inclusive of (II),(III) and (IV)

(iii) equilibrium configuration (III), particular case of (II)

(vii) equilibrium configuration inclusive of (V), (VI) and (VII)

(I) equilibrium configuration (I)

(II) equilibrium configuration (II)

(III) equilibrium configuration (III)

(IV) equilibrium configuration (IV)

(V) equilibrium configuration (V)

(VI) equilibrium configuration (VI)

(VII) equilibrium configuration (VII)

a Lever arm

a, *b* Length of the semi-axis of the ellipse (physical model)

a_d Relevant geometric factors

a_1 Distance from the $F_{f,1}$ and the end of the cantilever of the surface 1

a_2 Distance from the $F_{f,2}$ and the end of the cantilever of the surface 2

b Base of the cross section

blow Lower bay size of the rib

bup Upper bay size of the rib

d Diameter of the stick (physical model)

d_l Lower diameter of the dome

d_u Upper diameter of the dome

dA Area of extension of the crack

dG_f Potential energy

e distance between the support and the application of the load (eccentricity)

e_F Distance of the force F respect to the 0 position (axially)

$e_{P,1}$ Lever arm of the force $F_{1,\perp}$ to the point P

$e_{P,2}$ Lever arm of the force $F_{2,\perp}$ to the point P

$e_{P,3}$ Lever arm of the force $F_{3,\perp}$ to the point P

e_1 Distance of the force $F_{1,\perp}$ respect to the 0 position

e_2 Distance of the force $F_{2,\perp}$ respect to the 0 position

f Height of the dome, linear value

$f_{c,0,d}$ Design compressive strength parallel to the grain;

$f_{c,90,d}$	Design compressive strength perpendicular to the grain;
$f_{c,0,k}$	Characteristic strength for compression
$f_{c,90,k}$	Characteristic strength for compression perpendicular
$f_{m,k}$	Characteristic strength for bending
$f_{t,0,k}$	Characteristic strength for tension
$f_{t,90,k}$	Characteristic strength for tension perpendicular
$f_{v,k}$	Characteristic shear strength
h	Height of the cross-section
h_{eff}	Effective height of the cross section
$h_{eff,2}$	Effective height of the cross section determined by the vertical projection of the segment $\overline{AB}$ (surface 2)
$h_{eff,3}$	Effective height of the cross section determined by the vertical projection of the segment $\overline{CD}$ (surface 3)
h_{AB}	Height of the segment $\overline{AB}$ (vertical projection)
h_{BC}	Height of the segment $\overline{BC}$ (vertical projection)
h_{DC}	Height of the segment $\overline{DC}$ (vertical projection)
k	Rotational stiffness
$k_{c,90}$	factor taking into account the load configuration, possibility of splitting and degree of compressive deformation.
k_{mod}	Modification factor for duration of load and moisture content
k_{φ}	rotational stiffness of the joint.
kϕx	Rotational stiffness in the plane *yz*
kϕy	Rotational stiffness in the plane *xz*
kϕz	Rotational stiffness in the plane *xy*
l	Length
$l_b/2$	distance between the support and the center of the joint (hinge)
l_j	Total length of the joint, horizontal projection of the segment $\overline{BC}$;
l_{AB}	Lenght of the segment $\overline{AB}$
l_{BC}	Lenght of the segment $\overline{BC}$
l_{DC}	Lenght of the segment $\overline{DC}$
l_v	Length of the shear segment
m_b	mass of the bolt
m_c	mass of the metallic cube
q_i	Linear uniform distributed load on the *i* element
q_{ref}	Wind pressure of reference
s	Thickness
u	Displacements

u_{top}	Applied displacement at the top of the rib
u_x	Displacements along *x*
u_y	Displacements along *y*
u_z	Displacements along *z*
$u_{PII}(M_u)$	Displacement of the piston P_{II} at the failure
v_{ref}	Wind reference velocity
w_e	Value of wind load (linear)
$w_{e,low}$	Value of wind load (linear) on the bottom of the rib
$w_{e,up}$	Value of wind load (linear) on the top of the rib
w_I	Displacement of the piston I (universal testing machine)
w_{II}	Displacement of the piston II (universal testing machine)
α	Angle formed by the lower (upper) squint with the lower face of the joint
β	Angle formed by the splayed surface with the beam's axis
γ	Specific weight
γ_m	Partial factor for material properties, also accounting for model uncertainties and dimensional variations.
$\gamma_{x,max}$	Rotation at the base of the rib in the *yz* plane
$\gamma_{y,max}$	Rotation at the base of the rib in the *xz* plane
$\gamma_{z,max}$	Rotation at the base of the rib in the *xy* plane
ε_1	Parameter that defines the position of the force $F_{1,\perp}$ along the surface 1
ε_2	Parameter that defines the position of the force $F_{2,\perp}$ along the surface 2
ε_3	Parameter that defines the position of the force $F_{3,\perp}$ along the surface 3
ε_F	Parameter that defines the position of the applied force *F* along the height of the cross section
θ	Angle of rotation at the support respect to the applied bending action M
$\theta_{[\deg]}$	angle of rotation of the beam at the failure, in degrees
$\theta_{[rad]}$	angle of rotation of the beam at the failure, in radiant
μ_d	Coefficient of dynamic friction
μ_s	Coefficient of static friction
μ_α	Coefficient of static friction referred to the surface with angle *α*
μ_β	Coefficient of static friction referred to the surface with angle *α*
ν	Poisson's ratio
π	Pi
ρ	Density
$\sigma_{c-s,k}$	Characteristic stress in the cross-section
$\sigma_{c-s,k,\max}$	Maximum characteristic stress in the cross-section

$\sigma_{jj,k}$	Characteristic stress in the *Jupiter joint* (jj)
$\sigma_{jj,k,eff}$	Characteristic stress in the cross-section with reduced effective height
$\sigma_{jj,\max}$	Maximum characteristic stress in the *Jupiter joint* (jj)
$\sigma_{c,\theta,d}$	Design compressive stress in the contact area at an angle θ to the grain
$\sigma_{c,\theta_{CD},k}$	Characteristics compressive stress in the contact area at an angle $\theta = \frac{\pi}{2} - \alpha$ (α = inclination of the surface 3)
$\tau_{jj,k}$	Characteristic shear stress in the *Jupiter joint*
$\tau_{jj,k,\max}$	Maximum characteristic shear stress in the *Jupiter joint* (*jj*)
φ_0	Pre- imposed rotation at the base of the rib
$\psi_{\lambda\alpha}$	Slenderness factor
ϕ	Elastic strain energy

Chapter 1 INTRODUCTION

1.1 General framework

Timber structures have been used all-over the world in any times. They are diffused in historical buildings in the European, Asiatic and American areas with significant regional differences. The carpentry structures and the joinery techniques are the result of a long-term process of evolution along the centuries, developed in the practice of the use, with a process of continuous try and error. The fashioning of structure and joints depends on not only the geographic area, but also historical period and carpenter that created them. More than 600 different geometries of carpentry joints are known, and there are so many constructive techniques than cultures. The shape of the joint does not have, time to time, only a specific function to conduct, and is not self-evident which use or position any of the connections has to carry out (Graubner, 2004).

It is thus very difficult to systematize the calculation of those structures. Once more, not only because of the variety of the structures but also because of the anisotropic nature of material wood, the variety of geometries and static indetermination of the structures. First, the stiffness and strength of the joints depends on the material orthotropic properties and on the loading. The static indetermination of that structures brings to the possibility that the internal loads follow different pathways. Considering different pathways, means assign to the structural elements and joints that manage the transfer of forces between the connected structural elements, different and unknown stiffness values. Finally, the old carpentry connections base the transfer of forces on the contact friction. Necessary and fundamental is that independently on the outer load on the element, the adjacent surfaces work only in compression. According to the kind of load combination that such pair of element or group of elements have to bear and their position in the frame, the combination of the surfaces is fashioned every time in a specific way. For all these reasons, understanding the purpose and behaviour of the joints is very important during the study of a structure, because the behaviour of joints normally governs the stress capacity of the whole structure.

The complexity of the forms and the difficulty to calculate these traditional timber-frame structures according to the rules of the science of materials brought to the progressive desertion of these structures during the last century. In the last years, the attention towards the material wood has been increasing, due to the convenient properties of these old timber-framed structures, among them the seismic reliability and timber attributes in general, like the sustainability, thermal, acoustic, electrical, mechanical, aesthetic suitable properties, recyclability and possibility of prefabrication of the elements. The old timber structures were re-evaluated and recognised as very effective load-carrying structures. The necessity of structural

interventions due to the abandon or improper maintenance of the different stylistic and technic languages developed in the period before the XVIII century, brought to the necessity of understand these systems.
The generalized presence of wooden frame buildings in the world, and the relatively numerous developed investigations, have no specific counterpart in the European or American codes and regulations for what concerns a big variety of wood-wood connections. The lack of good rational methods in design practice with respect to risk for perpendicular to grain fracture (Blass, Aune et alii, 2005) brings to a generalized presence of errors in phase of strengthening or design e.g. overlapping of unsuitable techniques during the remodelling of existing structures, or over-dimensioning of structures in case of new structures. Therefore, is important the understanding of the principles under which the connection is used, and how, depending on the geometry of the one, the forces are transmitted within the structural joint.
The present work started some years ago with a study on the structural behaviour and reinforcement of Santiago de Cuba's cathedral, wonderful proponent of the *Colonial* system in Cuba. The structure has been able to resist the frequent hurricanes and earthquakes along the centuries, thanks to the inner load-carrying timber framed structure. The employed structural connections in the dome and church's structure are numerous; here, the *Jupiter joint* is the most spread and it is used to connect longitudinally the dome's ribs and some of the main structure's beams.

1.2 Objectives

The *fil rouge* of the present work is the understanding of the working mechanisms of the carpentry connections Jupiter joint and the simplified version called *halved and undersquinted scarf* joint. These two geometries were widely diffused in many of the timber structural systems of the past. Woodworking joinery is a very wide and varied topic to be completed in only one thesis; therefore, the aim of this work is the description of the basic working principles and mechanical properties of the joints. The load-carrying mechanisms, the failure modes, for the quantification of the ultimate load of both the connection and the structure under combined compressive and bending action are investigated. Key-point is the influence of the geometric parameters on the structural performance.
In points, the most important goals are:

- Evaluation of the load-carrying capacity of the *halved undersquinted scarf*, the *stop-splayed and undersquinted scarf*, the *halved undersquinted and tabled with key scarf*, and the *stop-splayed undersquinted and tabled with key scarf* joint (*Jupiter joint*) under combined compressive and bending action with experimental tests. The representation of the experimental load-carrying capacity of the above mentioned joints in a N-M interaction diagram (diagram that describes the interaction between normal force N and bending moment M).
- Evaluation of the in-plane and out-of-plane behaviour of the *Jupiter joint* under combined compressive and bending action based on experimental tests.
- Evaluation of the most important parameters that influence the behaviour of the *halved undersquinted scarf* joint, friction mechanisms and geometric factors.
- Evaluation of the failure modes for all the geometries in both the in-plane and out-of plane load directions.

- Definition of structural models that describe the limit states and failure modes of the *halved and undersquinted scarf* to be used for the lecture of the experimental results.
- The final goal is to give a quantification of the rotational stiffness's values for the connections, that would be used in structural analysis and structural analysis simulation.

The reliability of the work is pursued through the case study Santiago de Cuba Cathedral's dome. The case study is necessary to do a comparison between the reality and the simplifications in the geometric and static models adopted for the investigation. The dome is analysed through a physical model, CAD model and structural frame models:

- the physical model of the case-study is for the qualitative evaluation of the contribution of the geometric factor to the stiffness;
- the CAD model is used for the simplification of the real imperfect geometry into a perfect theoretic one;
- the structural frame model permits the comparison between the resistance design values R_d obtained from the tests with the numerical design values of the effect E_d of the specific case study.

This knowledge is of fundamental importance in sight of a further development in the modern restoration techniques for the old timber-framed structures. This work may be preparatory for the developing of some regulations on the wood-wood connections in existing structures. In general, the final goal is to provide useful information on the behaviour of the analysed carpentry connections for practical purposes.

1.3 Methodology

1.3.1 Approach to the problem

Since was found that the shape of the joint plays an important role in the behaviour of the joint, the approach to the understanding of the properties of the connections occurs through a step-by-step process. From the simplest joint with less surfaces to the most complicated scarf form, with multiple surfaces and a wedge. The first analysed geometry is the (*half-timber*) *halved* joint where the squints are perpendicular to the grains and the cut is horizontal in correspondence with the half of the height of the cross section and the *halved undersquinted,* where the squints are inclined of an angle *α* to the grains. The intermediate geometries are the *stop-splayed and undersquinted, and halved undersquinted and tabled with key* joints; here, the central surface is sloping in the first, and a wedge is inserted in the central cut in correspondence of the *table*. The final geometry is the *stop-splayed undersquinted & tabled scarf* joint (*Jupiter joint*) where both the squints and the central surface are sloping, and the wedge is also present. This method integrates progressive complexities in the geometries of the object of research and permit to understand the meaning of the different cuts and elements that compound the joints.

1.3.2 Scientific method

The adopted methodology is the scientific method. It consists of developed theories, systematic tests, measurement, observation, and modification of the initially adopted hypotheses. The approach of the thesis to the problem is experimental – analytical – numerical.

The work consists of a first part of formulation of a structural model for the connection based on the static equilibrium principles. Afterwards, the experimental evidence showed the connection has a non–linear

geometric behaviour under external actions. In order to formulate a reliable *first order linear-geometric* analytic model some “equilibrium configurations” were developed. This static model describes the sequence of loading instants, the equilibrium configurations, under the hypothesis of small displacements and small deformations adopting suitable geometric and material variables. The continuous comparison among the analytical models with the experimental measurements guarantees the feasibility of the proposed model.

1.3.3 Structural analysis

The structural analysis follows with the verification of the equilibrium limit state; the material failure and failure for excessive deformations (the buckling failure, even present, is not analysed in the present work). All the calculations and the tests are performed referring to the Eurocode 0 regulations.

1. The loss of equilibrium verification consist of (EC0)

$$E_{d,dst} \leq E_{d,stb} \qquad 1\text{-}1$$

Where:

$E_{d,dst}$ = destabilizing actions

$E_{d,stb}$ = stabilizing actions

In the analysis, the equilibrium limit state is present for modest external actions. The addiction of the additional term of static friction μ_s was found a determinant stabilizing factor. Therefore:

$$E_{stb} = \{a_d, \mu_s, M_{stb}, N_{stb}\} \qquad 1\text{-}2$$

$$E_{dst} = \{a_d, M_{dst}, N_{dst}\} \qquad 1\text{-}3$$

Where:

a_d = relevant geometric factors

μ_s = static friction coefficient

$M_{stb/dst}$ = (de) stabilizing moment

$N_{stb/dst}$ = (de) stabilizing normal force

2. The material failure / excessive deformations verification consist of (EC 0)

$$E_d \leq R_d \qquad 1\text{-}4$$

Where:

$$E_d = \{M_{Ed}, N_{Ed}\} \qquad 1\text{-}5$$

$$R_d = \{a_d, M_{Rd}, N_{Rd}\} \qquad 1\text{-}6$$

1.3.4 Failure prediction

The failure prediction is developed both according to the state-of-the art on the timber structures (in Section 3.7) and the static models proposed in the work (in Chapter 4).

The failure prediction of the *halved and undersquinted scarf* joint was not possible through the limit states (LS) developed in the static models; nevertheless, once obtained the experimental results was possible to characterised the local resistance F_f. Thanks to the proposed models and the combination of the external experimental actions $N_{\exp}, M_{\exp}$ with geometric variables a, b the resistance value of the connection is described as

$$R_k = a \cdot N_{\exp} \oplus b \cdot M_{\exp} \qquad 1\text{-}7$$

To conclude, the research does not pretend to be exhaustive in terms of anticipation of joints' behaviour or development of regulations for the strengthening of historical wooden buildings, but to give a description of the mechanical properties of the *halved and undersquinted scarf* and *Jupiter joint* as basis for possible future developments in terms of general regulations on carpentry structures.

1.4 Outline of the thesis

The thesis is divided in 10 main chapters and 6 annexes.

The present Chapter 1 gives an introduction of the work explaining the framework, objectives and adopted methodologies.

In the Chapter 2 a short literature review on the *timber frame* and *half-timber* techniques and the employed woodworking joints is given. A further detailed description of the most important "families" of carpentry joints and a detailed description of the main features of the *halved undersquinted*, *stop splayed*, and *stop-splayed undersquinted and tabled with key scarf* joint (*Jupiter joint*) is done. Finally a literature review of the past treatises and present papers on the main topic is given.

In the Chapter 3 considerations and design requirements for the *halved-undersquinted scarf* are done. Basic hypothesis, relevant parameters, background of the failure mode calculations basing on the international codes, and description of the relevant imperfections in the structural analysis are introduced.
In the Chapter 4 the analytical characterization of the *halved undersquinted scarf* is given. For any of the developed models (equilibrium configurations) the entity and distribution of the internal forces, the main parameters, boundary conditions and failure modes are described.

In the Chapter 5 the materials and methods adopted for the experimental campaign are given. The wood used for the specimen is characterized. The different assets and devices for the used Universal Testing Machine (UTM) are presented. For the methods of testing, the adopted procedures are mainly two: the stress and displacement control modes. The main features and reason for the use of one or the other methods here is explained.

In the Chapter 6 the results of the experimental pre-campaign are presented. In this chapter the significance of the most important parameters and the reliability of the analytic model(s) are demonstrated through experimental tests. First, the evaluation of the friction coefficients μ_α and μ_β, and the importance of the geometric features, like the angle *α* of the squint is done; second, the verification of the geometric and forces boundary conditions and equilibrium limit state for the model(s) is performed.

In the Chapter 7 the results of the experimental campaign performed for the *halved and undersquinted*, *stop-splayed and undersquinted scarf*, *halved undersquinted and tabled scarf with key* joint and the *Jupiter joint* are given. The N-M interaction diagrams for in-plane combined compressive and bending stress for the specimen under static tests are proposed. For the *Jupiter joint,* also the out-of-plane behaviour is proposed. The failure modes are classified for main areas for any of the proposed geometries. Finally, for the *halved undersquinted scarf* joint, the lecture of the experimental results through the developed analytic model is done.

In the Chapter 8 the case-study is introduced. A brief geometric description of the geometry of Santiago de Cuba Cathedral's dome is done. The case study is analysed through a physical model and a CAD model. The results of the in-scale experimental campaign on a physical model of the dome permit to develop of the first hypothesis on the importance of the "scarf" geometry. The structural 3D framework model permits the simplification of the geometric main features for the following steps.

In the Chapter 9 is performed the structural analysis simulation of the case-study. The main geometric, material and stiffness properties are described. The numerical analysis on *dead loads*, *imperfections* and *wind loads* load cases and load combinations is performed. Finally, the comparison among the scaled-specimens results and the numerical responses is done.

The Chapter 10 presents a summary of the research carried out. The main conclusions about the properties of the analysed geometries are presented. Some recommendations and outlooks for future research are given.

Chapter 2 LITERATURE REVIEW

2.1 Introduction

The present chapter gives an overview about the historical use and diffusion of timber structures and carpentry connections, passing through a short explanation of the different geometries of the scarf connections and the actual state-of-the art on the structural analysis of connection.

Timber has been one of the oldest construction material in most region of the world. In association with stone, bricks, clay or earth, solid timber is a material used to shape a big variety of structural forms as beams, columns, rafters and grids. Wood has been easily available in the forests with a thousand of different species. Over the centuries, the original forest was replaced with secondary-growth forest, and the available trees supplied with shorter and younger timbers respect to the previously commonly used. Therefore, the consolidated tradition of the timber buildings faced the lack of the primary construction material.

In the XVI century, the lack of wood, in conjunction with the progressive increasing of structures' dimensions and the necessity of standardization of the constructional techniques brought to the evolution of new systems and technologic solutions to connect together shorter structural elements.

The *wooden* techniques work under the principle of the cage: the structural elements are linked together in order to form a structural organism. The *half-timbered* structures are all the buildings whose frame is intended to be left exposed, while the *frame buildings* are generally all the buildings whose frame is covered with the *weatherboards.* The connections play an important role for all of the developed systems. Depending on the entity of the stress in the elements to join, each of the connection type consider the use of the different geometric solutions. All the structural elements can be joined and the systems adopted got different names: *bearing joints* for connections between horizontal with vertical elements, *lengthening joint* for coplanar elements, *corner joints* for corner elements or *shoulder joints* for oblique elements. The main distinction is between the traditional *carpentry joints* and the *mechanical joints*. The first are realized with grooves, notches and sloping surfaces, which basic mechanism is the transmission of forces through the interaction among contact surfaces, and the seconds, connect the members by steel plates or mechanical fasteners that work mechanically. The *carpentry joinery* was the technique used and developed in the early wooden structures, replaced during the centuries by the second one.

2.2 Timber frame buildings: their use and dissemination

The first vernacular wooden structures date back to the primeval man age, where the first shelters with circular plant where built. The first timber framed-houses known as longhouses where erected in the

4500 BC. Around the 600 BC the first roman timber bridges appeared,and developed along the whole roman empire era. The first known timber-framed house system was found in Herculaneum (Naples) before the 79 BC; the system called *Opus Graticium* was developed by Vitruvius. The structural system combines a timber frame with masonry infill. During the Roman time were also introduced more elaborated techniques, like the joinery techniques called *mortise and tennon*, and triangulated roof structures. The half-timber constructions became widespread near the end of the Middle Ages. At this time, many forests in central Europe and the British islands were becoming depleted. Therefore, the frame construction, which requires much less wood than the horizontal-log construction, was implemented and diffused.

Half–timbered structures spread throughout Europe, in Portugal (*edificios Pombalinos*), in Italy (*Casa Baraccata*), in Germany (*Fachwerk*), in Greece (Lefkas island's Technique), in France (*Colombage*), Scandinavia (*Bindingverk*), United Kingdom (*Half-timber*) and Spain (*entramado Mudejar*). After the colonial expansion, Spain, UK, and France, exported this technique in the world. The integration of the *western* techniques together with the indigenous ones, brought to the implementation of the European systems. Different stylistic and constructive characteristics were developed in the "new worlds". From the Iberian tradition the *Colonial system* developed in southern America and Caribbean areas; original from the English tradition, the *Gingerbread houses* were adapted in Haiti to the American environment; finally, the *Colombage pierroté* construction, derived from the French culture, acquired proportions, morphologic characters and construction materials that suit with the new location in Haiti. The wooden frame structures diffused also in India (*Dhajji-dewari*) and Turkey (*hımış* construction). Furthermore, the Germanic tradition was exported in Pennsylvania, North Carolina, Texas, Missouri and Wisconsin. The *Fachwerk* structures were not intended to be built as the German constructional "aesthetical" finishing but under the same constructional concept. The half-timber framework was employed for the construction of economic buildings until the first half of the XIX century in most of the continental European regions, America and UK.

2.2.1 Asiatic and European examples

In India and Kashmir, the traditional timber-brick masonry (*dhajji-dewari*) construction is a brick-nogged timber frame construction that consists of burnt clay bricks filling in a framework of timber to create a patchwork of masonry, which is confined in small panels by the surrounding timber elements. (Lagenbach, 2013).

In Turkey the typical timber-framed construction is called *hımış* (Figure 2-1 and Figure 2-2). The technique is very similar to the Indian one, because this constructional method was diffused during the Ottoman Empire. The first floor consists in a masonry wall normally without any wooden element (the variant with horizontal wooden laces was called *hatil*), on which a complete timber frame with the insertion of masonry in between the columns beams and studs is located. The infill masonry is either brick or rubble stone. Depending on the availability of the wood on the territory, for example in the Bosporus area around Istanbul, the masonry infill is replaced by short rough pieces of wood plastered from the inner and outer side, in order to form a solid wall. This technique is called *Bagdadi* (Figure 2-3 and Figure 2-4).

The adoption of timber as a structural material in Portugal became common after the destruction of Lisbon due to the strong earthquake in the year 1755. The *Gaiola Pombalina* technique consists in a three-dimensional braced timber structure (Figure 2-5 and Figure 2-6). The *gaiola* (cage, in Portuguese) consists

of horizontal, vertical and diagonal bracing members, the St. Andrew's crosses. The timber frame is a self-bearing structure filled with either rubble or brick masonry, or even mud and hay (Poletti, 2013).

The *Casa Baraccata* (Figure 2-7) is a structural system born in the XIV century in the central Italy. It is the first anti-seismic system who entered in the "national" regulations of the Bourbon state. After the earthquake of the 1783 in Calabria and in the city of Messina, was in fact compulsory to re-built the new buildings and restore the old ones with this anti-seismic technique. It is not a proper timber frame, but a timber skeleton placed inside the load-carrying masonry walls. The timbers are installed both along the corners of the walls in a vertical orientation, and along the two diagonals of each wall to bear the lateral loads (Ruggieri, 2013).

On the Greek island Lefkas the buildings were built according to a special technique present since the time of the Knossos Palace on Crete and Santorini (Figure 2-8). The house is erected on a stone podium, on which the timber frame is located. The geometry of the timber-framed walls usually consisted of main vertical elements on horizontal connecting elements, and some sparse diagonals (Vintzileou et al., 2007; Makarios and Demosthenous, 2006). The half-timbered structure is laying onto the masonry walls of the ground floor and on timber columns beside the perimeter of the walls. The timber beams of the floor are connected to the walls through metal ties. Corner connections were usually strengthened with additional diagonal timber elements.

Figure 2-1 – *hımış* construction in Gölcük, Turkey (© Langenbach)

Figure 2-2 - *hımış*, traditional Turkish construction (© Langenbach)

Figure 2-3 – *Bagdadi* Construction in Instanbul (© Langenbach)

Figure 2-4 – *Bagdadi*, traditional Turkish construction (© Langenbach)

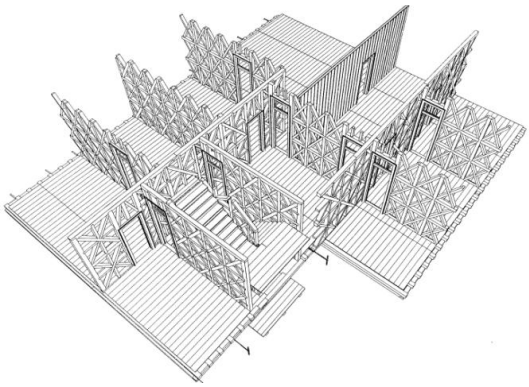

Figure 2-5 - Example of the disposition of the internal walls in the *Pombalino* system (from Cóias, 2007, in Poletti 2013)

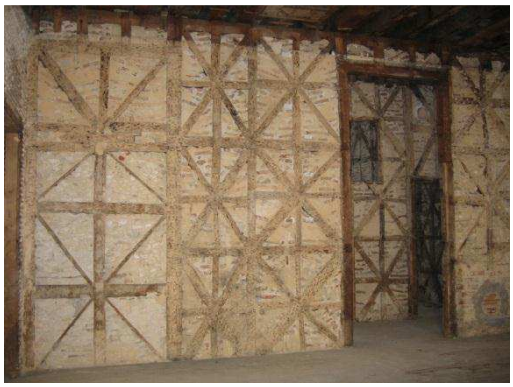

Figure 2-6 - Example of frontal wall in a Pombalino building in Lisbon (from MONUMENTA http://monumenta.pt/ in Poletti 2013)

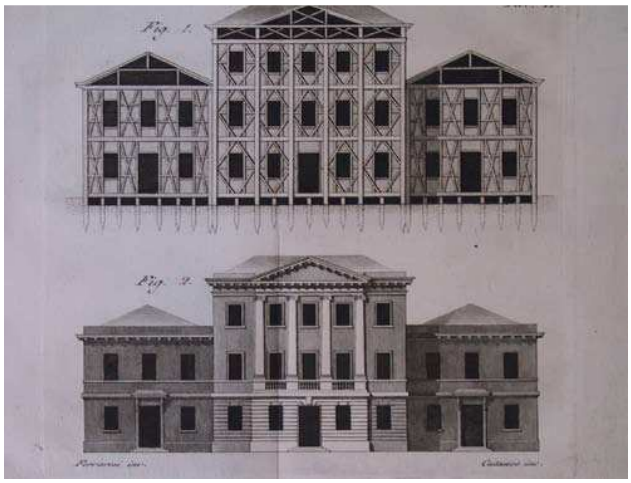

Figure 2-7 – Example of the *Casa Baraccata* (Ruggieri, 2013)

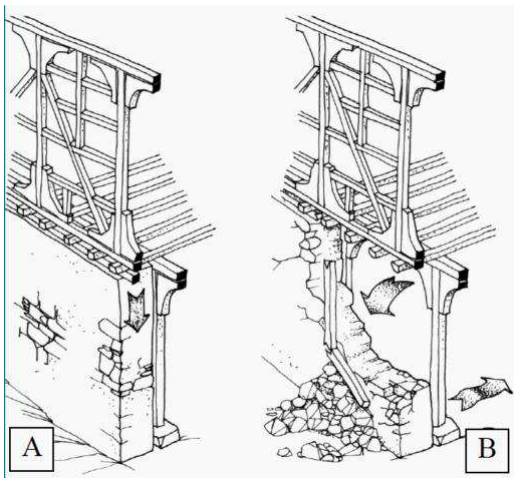

Figure 2-8 – Greek structure on Lefka island (Touliatos, 2004; in Poletti, 2013)

In Denmark, England, Germany and parts of France and Spain, in localities where timber was in good supply, the timber constructions diffused with different names and regional changes. There is not one unique constructional technique that can describe the multiple regional techniques; nevertheless, the European Continental and English traditions have very similar general characters that can be summarized as the main typologies of *timber-frame* and *half-timbered* structures. The techniques evolved along the centuries and locations, from the first *aisled construction* and the *Cruck construction* to the improved *box frame* (Figure 2-9). The most mature and effective forms, are the *post-and-truss* structure, called *Geschossbauweise in Germany* (Figure 2-10) and the *storey framing* called *Stockwerksbauweise* in Germany or *Wealded frame* in Kent and Sussex, England (Figure 2-11).

In the *post-and-truss* framing, the *wall-frames*, *cross frames* and *purlin roof* are combined in an integrated structure. In the earliest half-timber structures, the posts were set into the ground, then, positioned onto stone pads in the ground or wooden logs that distanced the framework from the ground, and in the final evolution, on a basement. The passage to the *post-and-truss* technique happened when the posts were joined into a cill beam, which was raised above the damp ground on a plinth wall. In order to improve the load-carrying behavior and solve the stability problems, the supporting framework, initially still *post and lintel* framing, was immediately provided with *wall frames*. The structural system reached a high level of sophistication in the connections between the timbers. The load-carrying structure consists of a series of

parallel *wall frames*. In the *wall frames*, the posts connect with the *wall plate* in the upper part and to the *sill-beam* in the lower part; the first employed joining technique is the *extended mortise and tennon*, that later on was replaced by the simple *mortise and tennon* (Figure 2-20 and Figure 2-21). The vertical supplementary elements that compose the wall are called *studs* and the horizontal ones are called *nogging pieces*. The transversal walls incorporate diagonal braces. The *diagonal bracing* in correspondence of the right-angle connections between post and beam in the wall is installed to prevent the racking or movement of the structure. The used joinery technique was earlier the *halved dovetailed* joint and later *mortise and tennon*. The opposing *wall-frames*, are connected by transversal *cross-frames* at regular intervals, stiffened with horizontal *rails* and *diagonal braces*. The structure is above closed by a *purlin roof*. In a *purlin roof* the *rafters* are supported on horizontal timbers, the *purlins*, which transmitted the roof load to *trusses* or *cross-frames*. To resist the tendency of the roof structure to rack, wind braces are usually (but not always) incorporated between the *purlin* and *trusses*. The frame building consists of a wooden skeleton with exterior surfaces made weather tight in various way. On the Continent, the opening in between the frame were generally filled with *rubble and plaster*, with *brick* or with *wattle-and-daub*. The framework was left exposed to form a pattern between the plastered or brick panels. In England, were the lumber was abundant, the wood-frame had a wood sheeting called *weatherboards*.

The *storey-framing* construction presents similar characteristics to the *post-and-truss* construction, but has a characteristic second-storey overhang. The frame of *sleepers*, *posts* and *wall-plate* system elevates for only one level. The multiple levels are overlapped one over the other and are self-standing structures. Each further floor is in fact supported on the horizontal cantilever beam, the *jetty bressummer* (*Schwelle*) of the lower level that bears the weight of the upper new storey. Structurally speaking, each of the storeys is an independent box, conceived with its proper posts and bracing to avoid horizontal deformation of the frame. The main advantage of the cantilever is structural: the cantilevers at the ends of the beams partially counterbalance the load carried by their spanning portions. A very important role is played by the *joists*. The *ceiling joist* (*Deckenbalken*) of the upper level lays on the *wall-plate* (*Rähmholz*) of the lower level without any complex connection with the posts. In very narrow small ground areas, the *ceiling joist* of each floor are installed perpendicular to the long axis of the house; then, the projection gains a small amount of space on the upper levels. On the girder beams, the studs are installed through a *mortise and tennon* connection. On the corners the structure is reinforced by tension braces. For very wide houses, also horizontal elements that got the name of *noggin pieces* were added. The upper floor is closed with a wall plate, where the roof, mainly collar roof, lays.

2.2.2 Expansion to the Americas

During the colonization of the Americas, the European constructive methods were exported over the Ocean. In North America, examples of *half-timbered* structures are in New Orleans, while the French *Colombage* was exported to Mississippi (Poletti, 2013) and in Haiti, where the architectural elements of the *Gingerbread* houses were adapted to the tropical climate. In Central America, the timber frame structures were also exported from the French and Spanish crowns during the establishment of representatives buildings in the new towns. The *Colombage* (Figure 2-12) is a timber-frame filled with brick and diagonals at the angles. The wood, with carved shapes, adorns façades and roof banks, high ceilings and large openings onto vast porches.

Figure 2-9 - A XVI century *box frame*, town house in east Kent, UK

Figure 2-10 – *Geschossbauweise*, Oldenburg, Germany

Figure 2-11 – *Stockwerksbauweise,* from (Gerner, 1983)*;* photo of the Author, Quedlinburg, Germany

Figure 2-12 - *Colombage* structure in France (Langenbach, 2015)

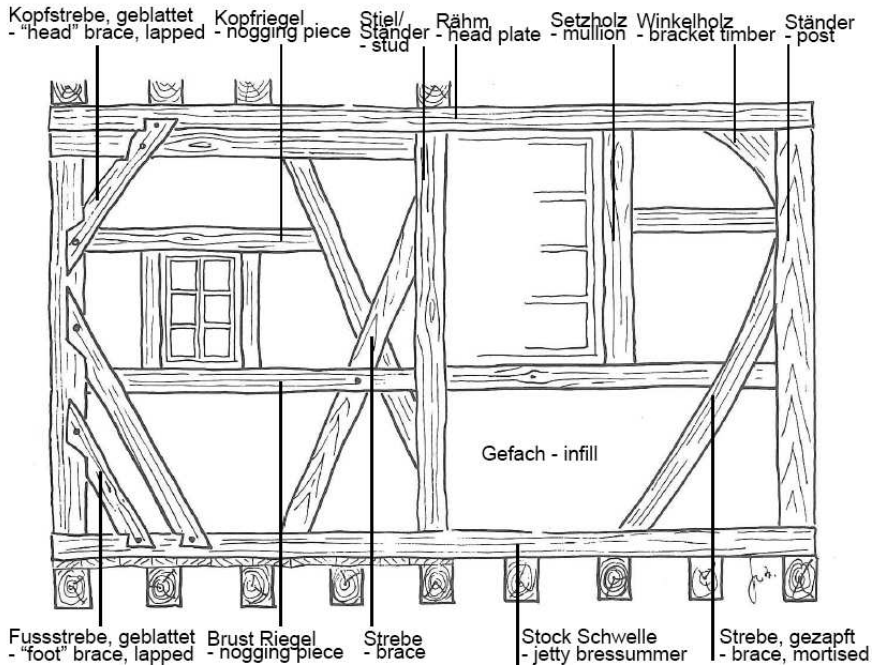

Figure 2-13 – *Storey-framing* evolution. From the *lapped joint* to the *mortise-an-tennon* (Gerner, 1983, adaptation)

The second version of the houses is the braced timber-frame clad with horizontal lapped-wood siding on the exterior, also known as *shiplap siding*. The *Gingerbread* houses are designed to take advantage of ventilation and shade, and exclude moisture. Large windows and doors allow for cross breezes. Tall ceilings and large attics with ventilators allow hot air to rise, collect, and be expelled. Deep porches that extend from the front façade to the side walls provide shading for the windows and allow the living space to extend outside the walls of the house (Avrami, 2010).

In the Spanish Caribbean area and south America, the most diffused technique before the IV Century was the *Bahareque* technique. The *Bahareque* construction (Figure 2-15 (c)) is a *post and lintel* system, composed of vertical and horizontal wooden elements combined with specific type of unions to form a collaborative frame with tightening function. The filling materials are intertwined branches (wood fibers, bamboo or coconut fibers) covered with fragmented stone material and bonded with lime mortar and plaster, the *cuje* walls. When the Spanish imported their European know-how, the native technique a new constructional system was implemented: the *Colonial* system.

The *Colonial* architecture (Figure 2-15 (a), (b), Figure 2-18 and Figure 2-19) was the commingling of the imported Spanish-Arabic *Mudéjar* architecture, common in the southern part of the Iberian peninsula, and the the *Bahareque*, the local autochthonous constructional technique. The *Colonial* system is also a *post and lintel* system. The *horcónes,* the load-bearing pile foundations, are individual poles or groups of wooden poles (depending from the dimension of the structure) that from the ground rise up to the upper edge beams of the roof. They have squared cross-section or also a raw form with variable and irregular circular section. This self-bearing timber structure is culminated with the typically colonial roof *cubierta de par y nudillo* structure. Inspired by the *Mudéjar* system and the naval engineering, it has a reverse boat frame shaped form (Figure 2-14). The horizontal and vertical elements are connected with carpentry wood-wood connections from the European tradition (Figure 2-16 and Figure 2-17). The wooden structure is drown into masonry or brick walls.

Figure 2-14 – Typical Colonial Roof structure. Cathedral of Santiago de Cuba, Santiago, Cuba.

(Photo of the Author).

(a)

(b)

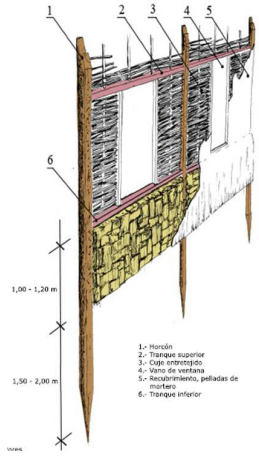

(c)

Figure 2-15 – (a) (b) particulars of the *Colonial arquitecture* in Cuba. (c) *Bahareque* Constructional technique (Orozco Melgar, 2004)

Figure 2-16 – Timber elements of the wooden dome of Santiago de Cuba's Cathedral, Cuba

Figure 2-17 – *Jupiter joint* of the wooden dome of Santiago de Cuba's Cathedral, Cuba

Figure 2-18 – Typical Colonial building. Calle S Jeronimo, Santiago de Cuba, Santiago, Cuba

Figure 2-19 – Typical Colonial building. La Casona, Santiago de Cuba, Santiago, Cuba

2.2.3 The treatises

One of the first theoretical and practical treatise on constructional techniques dates back to the end of the XVI century. This moment signed the beginning of a change of paradigm in the way of doing and building arts and crafts. This treatise was *L'architecture* de Philibert de l'Orme, printed at Paris by Frederic Morel in 1567. The author brought together into the architect's hands not only the general design, but the equally complicated and infinitely more technical and practical matter of how buildings were put together. The treatise contained also an annex that was a milestone in the history of wood, as the first theorization of *Wood*

Roof Covering and Vaults technique. Here, he described the technique that allowed the construction of ribs to support spans of up to 30 m by lapping and pinning together short timbers. The same planks, typically 250 x 120 mm, were previously used for smaller spans. In the following centuries, further theorization of the wooden technique and carpentry where published. Among them, in Germany, *Zimmermann Kunst* by Johann Jacob Schübler published in 1731; then, in the year 1781 *Principi di architettura civile* was written by Francesco Milizia. Mazzocchi wrote in the 1871 the *Trattato su le costruzioni in legno*. In the XIX century was published in London the Manual of carpentry and joinery in the year 1905, and in Spain (1899) *Carpinteria de armar* by Luis Gaztelu and (1912) *Carpinteria de lo blanco* by Lopez de Arenas. One of the last treatise was the American *Woodwork joints* in the 1917, and others. The most in-deepened study of traditional carpentry joints was pioneered by Cecil Hewett in the 1960s.

2.2.4 Modern literature

In modern times, the study of the carpentry connections is related to different aspects. On one side, it is connected to the interest in restauration of old buildings that need interventions due to structural problems, change of use or exceptional actions; on the other side, glean the knowledge of old constructional techniques and methods, as a base for the developing of new constructional systems in the field of timber structures. The knowledge on the carpentry joints was mainly based on the praxis and know-how of expert carpenters. In the last two decades wood-wood connections has been studied from a scientific point of view and important steps has been done. The performances of the *mortise and tennon* joint, take into account the different geometries and the influence of the moisture content, were studied by Schelling and Hinkes (1985); Kessel and Augustin (1990) studied the tensile load-carrying capacity for the *mortise and tennon with pegs* and proposed appropriate design values. As they were the most diffused joints, the *mortise and tennon* and also the *notched joints*, are represented in some Spanish and German standards. The *lap joints* and the *scarf joints* are also very diffused in old structures and used for the reparation of modern structures. Nevertheless, the few research campaign have been conducted are not sufficient to develop some design or reparation rules. The few research on the *scarf* family focuses on the tensile resistance of the *splayed and tabled scarf with key*, also called *Jupiter joint* (Sangree, 2009) and the *halved and table tennoned scarf*, from Aira and alii. (2015). About the bending resistance, the study carried out by TRADA (Yeomans, 2008) suggests that the limiting moment capacity for the *scarf joint* is only equal to one third of the strength of the correspondent unjointed beam. More, an analysis about the bending capacity of various types of scarf and the reinforcing effect of wooden pegs was done by Hirst et al. (2008). The last the outcomes of the COST FP1101 action, which focused on the carpentry connections, published by Branco and Descamps (2015), affirm that the approach to the shear resistance of old carpentry joints that refers to standard shear tests for contemporary structures may be not suitable for old structures. For this reason, a good understanding of how the joints work and how the forces are balanced is required, in order to develop design and reinforcement specification for joints.

2.3 The carpentry connections

Carpentry connections are structural elements result of a long evolutionary process along the centuries. They are fashioned by able craftsmans, that were able to perfect the shape and the specific geometry correspondent to the necessary load--carrying capacity of each of the structural elements. The most majority

of the old buildings show a very high level of sophistication and ingenuity. Carpentry joints are able to transmit any kind of stress: compression, tension, shear or torsion. In dependence on the role they have to fulfil, different kind of "families" of carpentry connections are defined.

- *Lengthening Joint*: for the lengthening of beams and other timbers. Among them are the *lapped, halved, fished, scarfed and tabled*. Every category differs from the others according to the stresses they are to be subjected.
- *Widening Joint*: These joints are used for extending the width of boards and planks. Are also called *Side Joints. Butt, dovetailed* joint, *rebated* joint, *rebated and filleted* joint, *ploughed and tonguered* joint, *tongued and grooved* joint, *rebated, tongued and grooved* joint*, splayed* joint, *dowelled joint, matched and beaded, matched and V*-joint.
- *Bearing joints* are provided when two members meet at right angles, to give the sufficient strength to the functions. Bearing joints are *halved* joint, (*angle halved* joint, *bevel halved* joint, *dovetailed halved* joint, *longitudinal halved* joint, *tee halved* joint), *notched* joint (*single notched, double notched*), *cogged* joint, *housed* joint, *mortise and tennon*.
- *Framing Joints* are similar to the *bearing joints*, but they are not supposing to bear stresses of the entity of the bearing ones. They are used not for carpentry, but for frames or doors, windows, etc.…
- *Angle* or *Corner Joint* are used to join a corner or an angular edge of a frame. Among them are the *butt* joint, *grooved & tongued, plain mitred, mitred & feathered, shoulder and housed, dovetailed and housed, housed tongue & groove & mitred*.
- *Oblique shouldered Joint* are used when members has to be joined meet at acute or obtuse angle. Among them is the *briddle* joint, *mitred* joints, *dovetailed and halved* joint, *birdsmouth* joint, *oblique tennon* joint.

The basic mechanism of load transmission is the contact pressure and friction on the notches and contact surfaces. The entire joint's categories are traditionally assembled without any kind of mechanical fasteners, but also with mechanical fasteners like wedges or pins. The most common mechanical fasteners are the *pegs; they* are wooden elements usually slight tapered, typically 18-22 mm in section and roughly polygonal. Using a system called *draw-boring* the hole for the peg in the side of the mortise was slightly off-set on the tennon so that when the peg was finally driven through, the whole joint tightened up. Pegs are used in joints that have to resist withdrawal. In Europe, pegs were most made of hardwood like oak, even when the frame elements are in softwood. The key is formed by two V-shaped blocks (wedges) that are forced into the space between the two pieces (*tabling*), and have the role to pre-compress the joint.

The basic types of joints used in traditional h*alf-timbered* and *frame* structures carpentry are the *half lap*, *mortise and tennon* and *scarf joints*. The *mortise and tennon* (Figure 2-20 and Figure 2-21) is one of the most diffused and presents in a big variety of forms, used to connect mainly perpendicular but also diagonal timbers in the wall frames. *Scarf joints* are used to elongate beams, plate and purlins. Various forms of scarf were developed to suit the directions of forces acting on them. In the tie beam, the combination *lap-dovetail joint*, *mortise and tennon* joint were succeeding one after the other during the evolution if the truss-framed buildings from the XIII century onwards.

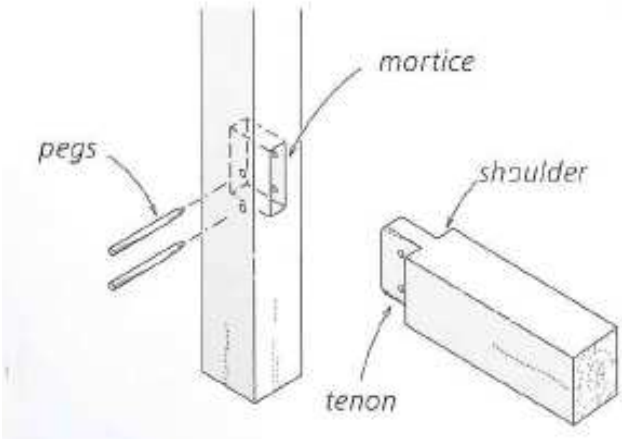

Figure 2-20 – Typical *mortise and tennon*

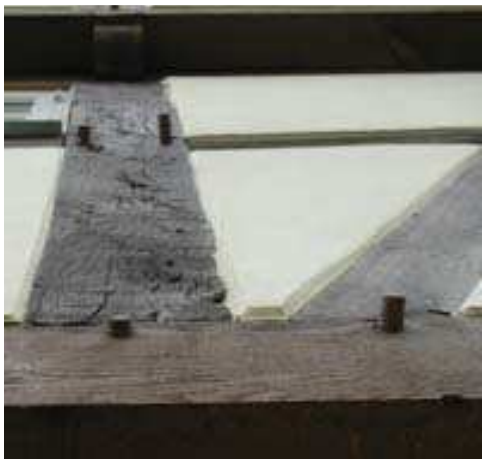

Figure 2-21 –Application of the *mortise and tennon*

(a)

(b)

(c)

(d)

Figure 2-22 – Diverse *fachwerk* structures, Quedlinburg, Germany. Photos of the Author. (a) Detail of a *halved and undersquinted scarf* and wooden pegs; (b) Detail of a *stop splayed and undersquinted with table scarf* joint; (c) Detail of a *halved scarf* joint; (d) Detail of a *dovetail* through *mortise-and-tenon* joint

2.3.1 The wood-wood connections: the *Scarf Joints*

Among the lengthening joints, the “scarfing” method can be further divided in three classes of *scarf*: *halved*, *splayed*, and *bridled*. A *halved scarf* is a lap whose surfaces are parallel with the timbers. A *splayed scarf* is a *halved scarf* with sloping lapped surfaces. A *bridled scarf* takes the form of a *tongue-and-fork* or *open mortise-and-tenon*. *Scarfs* can easily bear compression stresses, but with the presence of one or more pegs,

they can be also suitable to bear tensile stresses. The shear resistance it is of relevance in presence of notched beams. The shear stress is always present in concomitance with bending, torsion, tension and/or compression stresses. Some *scarf joints* can resist tensile stresses; the *Jupiter joint* is one of them. This tension resistance depends, apart the essence of the wood, on a number of geometric factors, as the presence of the table. The torsion resistance is very few in the *scarf joints*. For some of them, some surfaces which main purpose is to bear other kind of stresses along the strong axis, confer indirectly some minimal resistance along the torsional axis. Finally the bending resistance. Bending is the most difficult force for a scarf to resist. In literature is reported that the *scarf* connections are non-resistant to bending and in the classical engineering analysis is usually described as *hinge*; therefore, they are able to transfer axial load but without any bending load-carrying capacity. This because was needed an approximation of the real behaviour for lack of a deeper knowledge about this kind of carpentry connection. Even though, it is evident that some of the scarf joint are also able to resist bending load. The *Jupiter joint* is one of them.
The load-carrying capacity of four main typologies of *scarf* connection, is the main topic of this work. It follows a short description of the geometry and properties according to the current literature.

The *halved and undersquinted* scarf joint

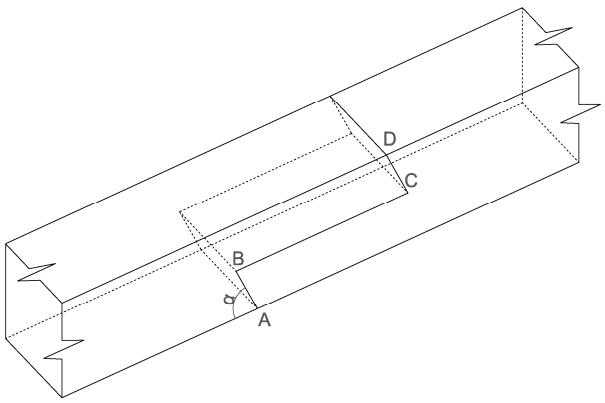

Figure 2-23 – *Halved and undersquinted scarf* joint.

The *halved and undersquinted scarf joint*, together with the simplest version called *halved scarf* (α = 90°) is one of the most common among the lengthening joint, and more specifically among the *scarf joints*.
A basic *halved scarf*, also called *half-wood* or *half-lap* is probably the simplest to fashion and thus the most abundant to find in structures all over the world. It was usually used in large span structures, in order to enlarge length of beams, tie beams, or protract high columns. It consists in one piece projecting and fitting into the recessed portion of the other. The lap surfaces are parallel with the timbers' and the abutments are shaped with a right angle (α = 90°). It performs well in axial compression but has moderate shear strength and no bending or tensile strength.
A considerable improvement of the basic *halved scarf* joint is the *halved and undersquinted scarf*. *Halved* refers to the cut of the horizontal surface, that is in correspondence of the half of the timber cross section. *Undersquinted* refers to the angle for the *abutments*, or *squints*. The angle of the lower squint is not necessarily the same as the angle of the upper one; nevertheless, in the present work, the two angles are considered equal and equal to an angle α. The joint is able to resist is axial compression and is not resistant to tension and torsion, it has moderate shear strength and bending capacity depending on the angle of the abutment. The inclination of the angle confers the connection different load-carrying behaviour: the shallower is the angle the easier the notch is subjected to the shear/tension failure; for bigger angles, the same failure

mode is reached with a higher level of load. This joint is a considerable improvement to the simple *halved* one, because the *undersquinted* end improves bending strength and resistance to seasoning twist of the joint (Sobon, 2002).

The pieces can be assembled together with modern mechanical fasteners (screw, bolts), or traditionally with wooden pegs to improve torsion resistance and resist to tension loads. The present study disregard the effectiveness of the *half splayed scarf* depending on this elements, considered as reinforcement. It is in fact demonstrated (Hirst, 2008) that the effectiveness of the wooden pegs improve the general performances of the joint, but is not necessary for the effectiveness of the specimen.

The *stop-splayed and undersquinted scarf* joint

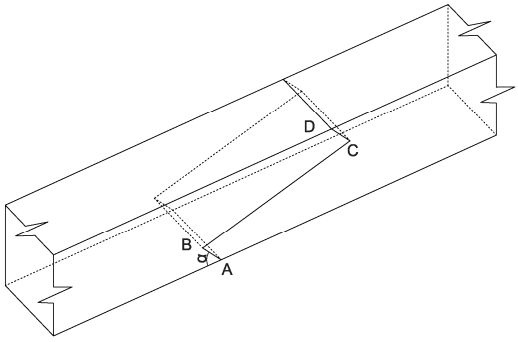

Figure 2-24 – The *stop-splayed and undersquinted scarf* joint

The *stop-splayed and undersquinted scarf* joint consists of a pair of complementary straight sloping cuts. The sloped, lapped, portion is stopped by *undersquinted* butts (Figure 2-24). Compared with the *half-lap*, the shear strength is highly improved by the sloped surface. It works well in compression and shear. The undersquinting of the abutments confers the joint some resistance to twisting respect to the *stop-splayed with square butts*. It has no tensile resistance.

The *stop-splayed, undersquinted and tabled scarf* joint with key (*Jupiter joint*)

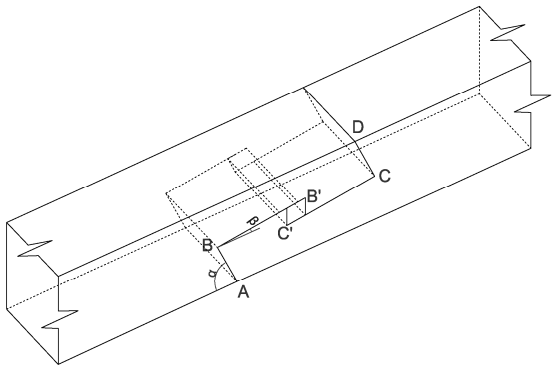

Figure 2-25 - The *stop-splayed, undersquinted and tabled scarf joint with key* (*Jupiter joint*)

Among the longitudinal joints there is also the *stop-splayed, undersquinted and tabled scarf joint with key* (*Jupiter joint*). In literature, this kind of joint is also called *splayed and tabled scarf joint with key*, *scarf bolt of-lightening joint*, *tabled hooked scarf joint with wedge*, *splayed indent scarf*, *stop-splayed scarf joint with key*. The geometry cannot be univocally described; in fact, the adjectives contained in the name give a general geometric idea of the joint. In general, the *Jupiter joint* can be described as a slanting Z-shaped cut in the end of both timbers to fit each other. It was used in large span structures, in order to enlarge the length of

beams, tie beams, or protract high columns. It has been used mainly to bear tension forces in the lower tie-beams of king post trusses, or lower chord (tie-beam) in trusses.
As defined in the Encyclopédie des métiers:

> ***Trait de Jupiter**, n. m. Assemblage de charpente servant à réunir deux pièces de bois bout à bout, et capable de résister à des efforts de traction ; il doit son nom au fait de que sa forme rappelle celle d'un éclair, et que Jupiter était le dieu de la foudre. (Le glossaire : du charpentier, p. 17-86)*

The terms *splayed* refers to the inclination of the lap surface (BB' and C'C). The sloped, lapped portion is stopped (*stop-splayed*) with a blunt end of the sloped portion. Compared with the half-lap, the shear strength is improved by the sloped surface. The abutments can have various inclination, but not necessary the same in the upper (CD) and lower squint (AB). In this work the two ones are considered with the same inclination equal to an angle α. The height of the abutment is comprised between 1/5 and 1/6 of the height of the cross-section. Both parts of the joint have a space in the central part of the splayed-ends (*tabling*) that is prepared for the introduction of two folded wedges. The two wedges are driven inside the empty space until it is filled, forced at the same time from the two opposite surfaces. The two shoring elements have a special wedge form that avoid the lateral movements and any disjunction along the vertical direction, or the inflection of the connected beam. The folding wedges pre-stress the joint, and the tensile capacity, torsion, and bending strength along the main and weak axes are greatly increased respect to the *stop-splayed undersquinted*, where the table of the two pieces are directly in contact. The total length of the joint is very important. If we refer to a tension load, the ideal length of the *Jupiter joint* is between three and five times the height of the cross-section. Below this size the shear planes surfaces (the sloping surfaces) that take up the loads is insufficient. It is nevertheless common a total length of scarf about from two to four times the depth of beam for compressed timber. It is important to remark that all these dimensions refer to the praxis of the timber joinery, and not to specific studies.
The version with squared abutments (α = 90°) has the maximum resistance to the axial compression. The more the abutment inclines, the earlier is the splitting of the fibers in compression. The version with inclined abutment has medium resistance in bending in all directions. Both versions are not very reliable on lateral displacements.

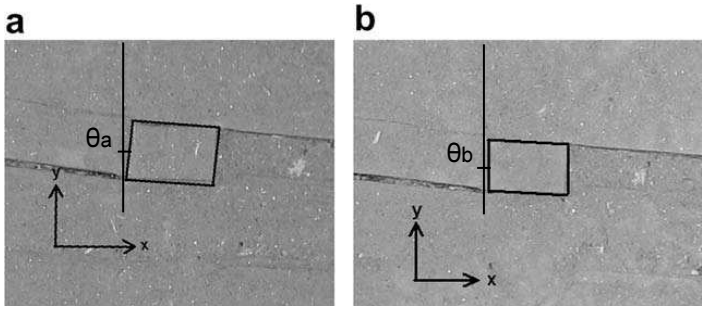

Figure 2-26 - (a) Square-cut key geometry and (b) oblique-cut key geometry. Note: x is the direction of loading. (In: Sangree and Schafer, 2009)

Sangree and Schafer (2009) analysed the *stop-splayed, undersquinted and tabled scarf joint with key* in tension, and determined that the key has the most influence on scarf joint behaviour. The orientation of the key causes the joint to be loaded in compression perpendicular to grain. The positioning of the key can vary from *square-cut* to *oblique-cut* (Figure 2-26), and its orientation influences the joint axial stiffness. In the

square-cut geometry the angle between the fibers and the key is not equal to zero ($\theta_a \neq 0$); while, in the oblique cut the angle of the wedge respect to the fibers is $\theta_b = 0$.

Some of these joints are provided with pins, nails or screws. The present study disregard the effectiveness of the *Jupiter joint* depending on this elements, considered as reinforcement. Nevertheless, experimental tests (Sangree and Schafer, 2009.) also revealed the importance of clamping bolts. Results of the first tests without clamping bolts, revealed that a combination of the scarf joints' splayed geometry and the presence of the key create additional eccentricity that caused a limit state of "key rolling". The lateral clamping force avoid the eccentric load path.

2.4 Structural analysis and carpentry connections

The description of such carpentry connections through a static model is of importance in a scientific field for the knowledge of the mechanical behaviour of old constructional systems and many applications in the structural analysis with the aim of reinforce and restoration of old timber structures.

The analysis of structures shall be carried out using static models which consider to an acceptable level of accuracy the behaviour of the structure and of the supports (EC5, section 5.4.1).

To properly understand the behaviour of old timber frames, the understanding of the influence of the connections is of importance. The main factors to be taken into account for the study of the mechanical behaviour of the carpentry joints are:

- the stiffness and strength of the joints depend on the material orthotropic properties and on the loading conditions;
- the static indetermination of the old timber structures. The loads can in fact follow different pathways and that means, solve additional equations to express the relative stiffness of all those pathways;
- the non-linearity of the geometry during the loading process;
- Imperfection of both the structure and the joint s that bring to a irregular and eccentric distribution of forces (see Chapter 3.6);
- The transferring of forces among the members happen via contact pressure and/or friction of the facing surfaces (Branco & Descamps, 2015).

The mechanical properties and behaviour of the connections have to be taken into account, on order to model the right kind of internal restraint. One of the basic assumptions of conventional structural analysis is that joints are either perfectly rigid or perfectly hinged. In static analysis, there is a substantial variation in the distribution of bending moment for a beam with hinged, semi-rigid, and fixed joints.

In the classical engineering analysis, this kind of *scarf* connections are usually described as perfect hinges, able to transfer axial load but without any bending load-carrying capacity. They are calculated as pure tensile/ compressive stressed, as the member they belong to. From the observation and analysis of different geometries of the family of the *scarf joints* in existing structures, it is clear that due to the shrinkage of the wood, wrong assembly or imperfections in the structure, the connection is usually in the condition to bear eccentric forces. According to the EC5, the *fictitious beam elements and spring elements may be used to model eccentric connections. The orientation of fictitious beam elements and the location of the spring elements should coincide as closely as possible with the actual joint configuration.* The joints that consider the presence of rotational springs along one, two or three directions which separates a member from it is

surrounding environment are defined as semi-rigid connections (McGuire John, 2009). Both the axial and rotational stiffness are parameters that have to be considered for the evaluation of the joint to achieve a more accurate structural analysis.

The rotational spring (Figure 2-27, (a)) is characterized by the *rotational stiffness of the spring* k, defined as the ratio between the moment M and the correspondent rotation θ as in the eq. 2-1. The rotational stiffness of the joint is characterized by the slope of the moment-rotation curve (Figure 2-27, (b)).

$$k = \frac{M}{\theta} \qquad \left[\frac{kN \cdot m}{rad}\right] \tag{2-1}$$

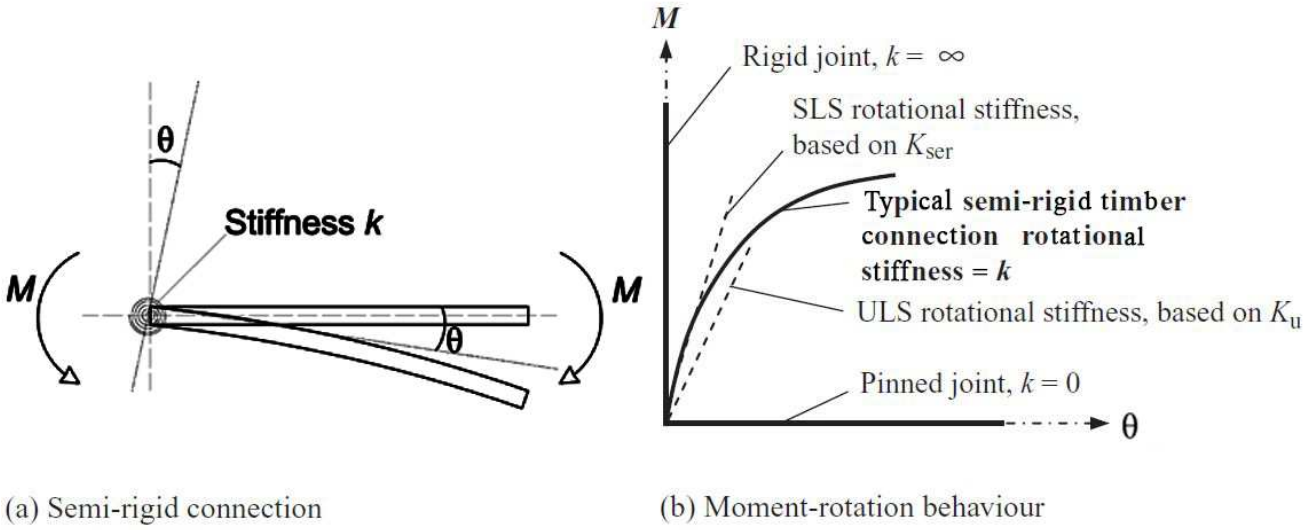

Figure 2-27 – Different types of rotational stiffness k, in a timber connection (in Porteous, 2013)

According to the EC5 recommendations the value of *k*, the *rotational stiffness of the joint*, is the topic value that has to be defined for a correct structural analysis of carpentry structures.

The present work estimate the value rotational stiffness of the *Jupiter joint* and the simplified version *halved undersquinted scarf* joint. In order to pursue the goal, the geometric parameters of the joint, the loading conditions, the resulting internal forces, and all the factors that influence the joint's behaviour will be evaluated through laboratory tests, analytical analysis and numerical modelling of a case-study.

Chapter 3 ANALYSIS CONSIDERATIONS AND DESIGN REQUIREMENTS FOR THE *HALVED AND UNDERSQUINTED SCARF* JOINT

3.1 Introduction

The aim of the work is the characterization of the *Jupiter joint*. The first step to reach the aim is the analysis of the *halved and undersquinted* joint, that is to describe in a simplified form the behaviour of the *Jupiter joint*. In the present chapter some pre-consideration about the *halved and undersquinted joint* are done. During the experimental pre-campaign (Chapter 6) the behaviour of the joint has been observed and taken into account for the statement of the basic hypothesis, relevant parameters and the formulation of equilibrium configurations.

3.2 Basic hypothesis

The load-carrying capacity of a structure depends both on the load-bearing mechanisms of the structure and the material. The main load-bearing mechanisms of the connection are influenced by the connection and their geometry. The load-carrying capacity of the connection bases on:

- The transmission of forces from one member to another by compression in the contact area;
- The transmission of forces from one member to another is accompanied by friction;
- The imperfections of the surfaces/assembled members may generate an irregular loading path of the forces in the joint.

For practicality in the handling of the calculation, the joint is considered as perfect. The three basic hypothesis under which the structural analysis of the *joints* is performed are:

HP. 1: Presence of compressive force in the contact surfaces

HP. 2: Absence/presence of friction in the contact surfaces (with respect to the selected model);

HP. 3: The perfect matching of the contact areas of the two facing surfaces (no gaps or imperfections).

3.3 Static scheme and loading conditions

The structure consist of two quasi-rigid bodies simply supported at one of the extremities and jointed together in correspondence of the other far end. In the model, the joint is represented as a *hinge* and the body is externally loaded in combined compressive and bending force at the two extremities as represented in Figure 3-1.

In the work, the symbols used for the external actions in the *beam structure* are represented in the schematic version like in the *static scheme*.

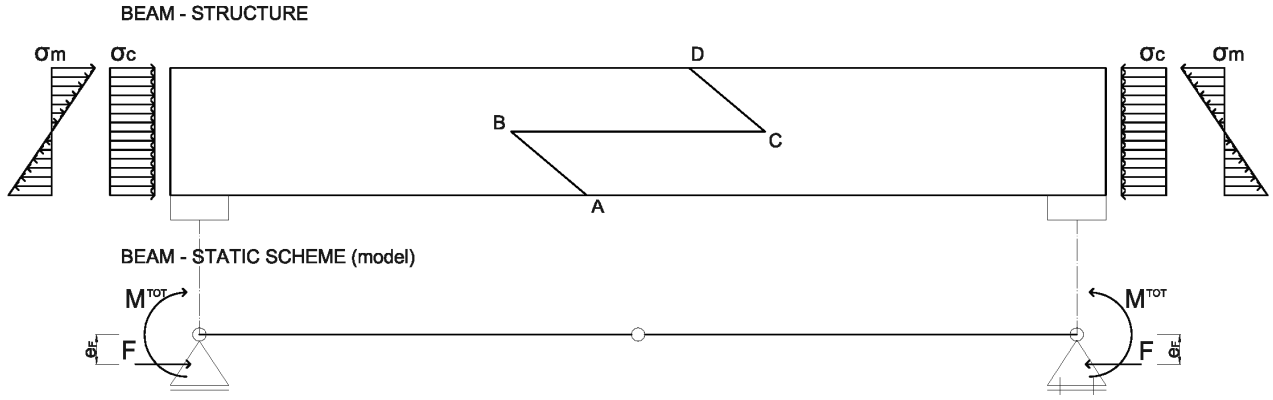

$F, M^{TOT} \geq 0\,; \quad e_F \geq 0\,; \quad N \geq 0$

Figure 3-1 – Beam static scheme and loading conditions.

Where F is the external applied action with eccentricity e_F respect to the neutral axis of the beam; the M^{TOT} is the total external moment, and for the definition of the normal force N see the following paragraph 3.4.2.

3.4 Basic geometry and parameters for the definition of the static models

3.4.1 Basic geometry

The general geometry of the *splayed and undersquinted scarf* joint is following described in the Figure 3-2.

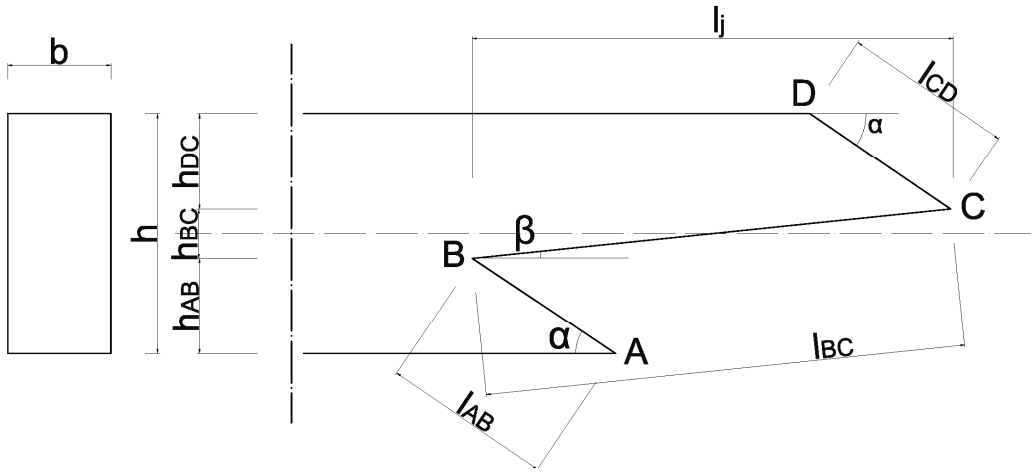

Figure 3-2 – Geometric parameters of the general *half splayed and undersquinted scarf*

Beam parameters:

b = depth of the cross section;

h = height of the cross section.

Joint parameters

l_j = total length of the joint, horizontal projection of the segment $\overline{BC}$;

α = angle of the abutment $\overline{AB} = \overline{CD}$ with the lower and upper horizontal face of the beam respectively;

β = angle of the abutment $\overline{BC}$ with a segment parallel to the horizontal lower face of the beam;

$$l_{BC} \cdot \cos\beta = l_j \qquad 3\text{-}1$$

$$l_{BC} = \frac{l_j}{\cos\beta} \quad \text{(length of the segment } \overline{BC} \text{ of the joint)} \qquad 3\text{-}2$$

$$l_{AB} = \frac{h - l_{BC} \cdot \sin\beta}{2 \cdot \sin\alpha} \qquad 3\text{-}3$$

$$l_{AB} = l_{CD} = \frac{h - l_j \cdot \tan\beta}{2 \cdot \sin\alpha} \quad \text{(length of the segment } \overline{AB} = \overline{CD} \text{ of the joint)} \qquad 3\text{-}4$$

For the *halved and undersquinted* scarf, the geometry of the joint is further simplified (Figure 3-3). The parameters acquire the values contained in the eq. 3-5 - 3-9.

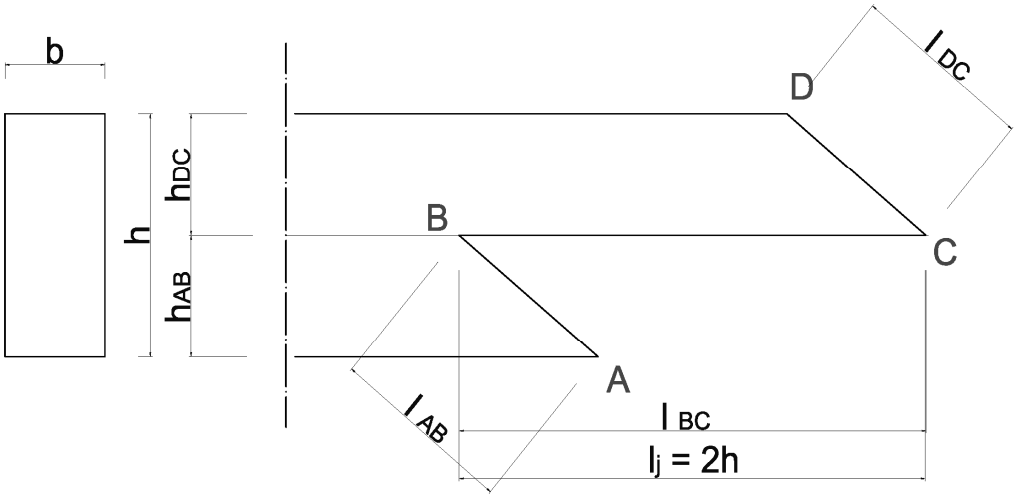

Figure 3-3 – Geometry of the *halved and undersquinted* scarf.

$$l_{BC} = l_j = 2 \cdot h \qquad 3\text{-}5$$

$$l_{AB} = l_{CD} = \frac{h}{2 \cdot \sin\alpha} \qquad 3\text{-}6$$

$\overline{AB}$ = surface 2 3-7

$\overline{BC}$ = surface 1 3-8

$\overline{CD}$ = surface 3 3-9

3.4.2 The parameters ε_1, ε_2, ε_3 and ε_F

According to the hypothesis HP.1 once the beam is loaded with an external action, the transmission of the forces through the joint happens only via compression on the *contact-surfaces.* The *contact-surface* is defined as a surface (Eq. 3-7 – Eq. 3-9) that have length equal to the front segments $\overline{AB}$, $\overline{BC}$ and $\overline{CD}$ and interest the whole depth *b* of the beam.

The internal resultant load on the surfaces has a trapezoidal/triangular distribution, and the shape of the distribution changes during the loading process. The force $F_{surface,\perp}$ is defined as the resultant force of the meant distributed load. The resultant forces $F_{1,\perp}$, $F_{2,\perp}$ and $F_{3,\perp}$ are defined in the Figure 3-4.

During the loading process, the entity of the *contact-surface* changes; therefore, during the loading process is registered a variation of the position of the internal resultant forces $F_{\perp,surface}$. The parameter for the

definition of the variable position of the resultant forces $F_{\perp,surface}$ is the coefficient $\varepsilon_{surface}$. According to the definition of the surfaces, the parameters are ε_1, ε_2, ε_3 respectively for the force $F_{1,\perp}$, $F_{2,\perp}$ and $F_{3,\perp}$.

ε_1 defines the position of the resultant force $F_{1,\perp}$.

$$e_1 = \varepsilon_1 \cdot l_{BC} \qquad 3\text{-}10$$

$$0 \le \varepsilon_1 \le 1 \qquad 3\text{-}11$$

ε_2 defines the position of the resultant force $F_{2,\perp}$:

$$e_2 = \varepsilon_2 \cdot l_{AB} \qquad 3\text{-}12$$

$$1 \le \varepsilon_2 < 0 \qquad 3\text{-}13$$

ε_3 defines the position of the resultant force $F_{3,\perp}$:

$$e_3 = \varepsilon_3 \cdot l_{AB} \qquad 3\text{-}14$$

$$0 < \varepsilon_3 \le 1 \qquad 3\text{-}15$$

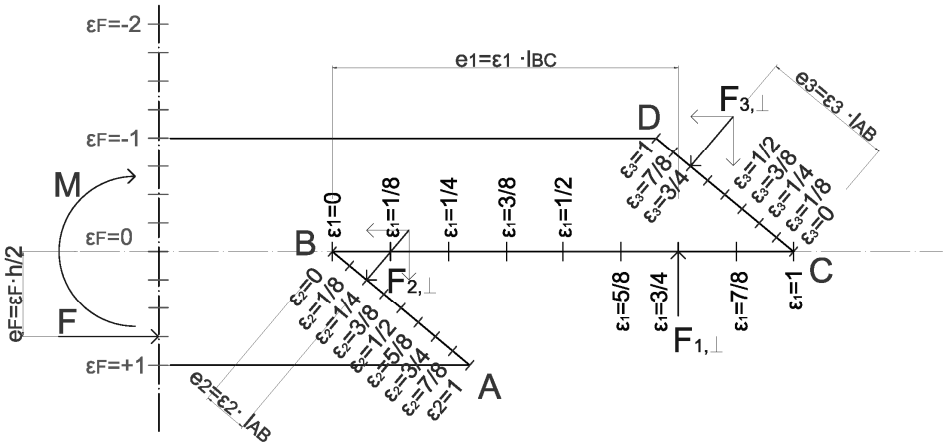

Figure 3-4 – Definition of the parameters ε_1, ε_2, ε_3

More, the coefficient ε_F defines the position of the applied force *F* (Figure 3-4). That parameter refers to the height of the cross section and it is defined as follows:

$$e_F = \varepsilon_F \frac{h}{2} \qquad 3\text{-}16$$

$$-\infty < \varepsilon_F < +\infty \qquad 3\text{-}17$$

When the force F is applied in correspondence with the axis of the beam the value of the coefficient e_F is null. In the present work, is considered:

$$e_F = \varepsilon_F = 0 \qquad 3\text{-}18$$

$$M^{TOT} \equiv M^F + M = F \cdot e_F + M = M \qquad 3\text{-}19$$

Where:

$M^F = F \cdot e_F$ moment caused by the eccentric position of the force F

M applied external load

It results that:

$M^{TOT} = M$

$F \equiv N$

Therefore: N, M independent; $N, M \ge 0$

3.4.3 The coefficient of static friction μ_α

According to the HP.2 the contact surfaces are characterized by the coefficient of static friction μ_s. The coefficient of static friction μ_s is significant for the load-bearing behaviour of the joint; however, it is not possible to determine a priori the exact value for it; in fact, this value depends on the finishing of the surface and the angle of contact (see Chapter 6.4). Friction is the force exerted by the surface that makes an effort to move across it. The friction force μ_s is connected with the level of $F_{\perp,surface}$ and $F_{//,surface}$; the maximum amount that a surface can exert is (eq. 3-20):

$$\mu_s = \frac{F_{surface,//}}{F_{surface,\perp}} \qquad 3\text{-}20$$

In the present work is considered only the static friction on the facing surfaces $\overline{AB}$, and μ_α and it is defined as in the eq. 3-21.

$$\mu_\alpha = \frac{F_{2,//}}{F_{2,\perp}} \qquad 3\text{-}21$$

3.4.4 More parameters for the definition of the static models

With the definition of the static models, some more parameters for the definition of the reciprocal position of the internal resultant forces has to be defined.

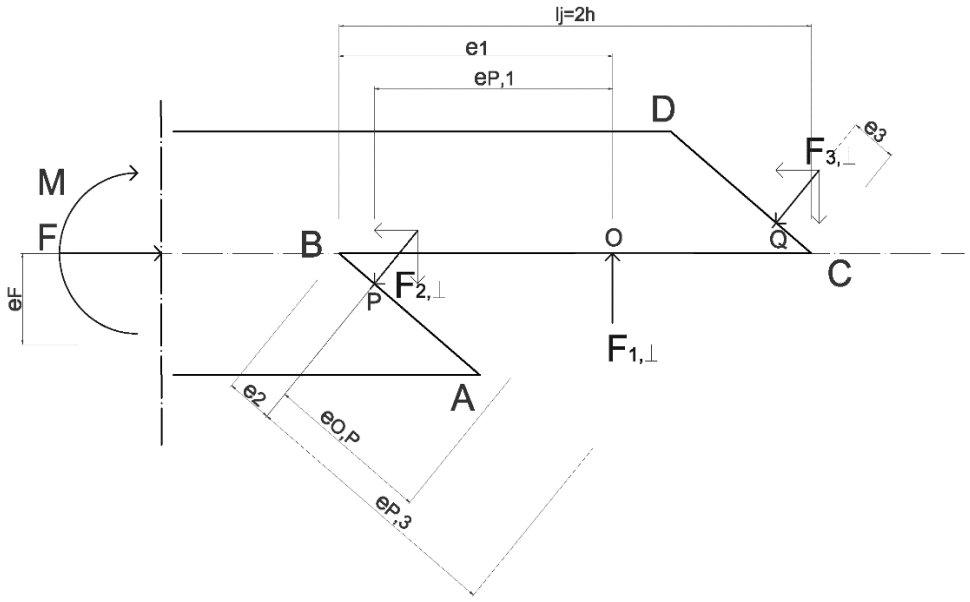

Figure 3-5 – more parameters in the static model

$e_{P,1}$:

$$e_{P,1} = e_1 - e_2 \cdot \cos\alpha$$

$$e_{P,1} = \varepsilon_1 \cdot l_{BC} - \varepsilon_2 \cdot l_{AB} \cdot \cos\alpha$$

$$e_{P,1} = \varepsilon_1 \cdot 2 \cdot h - \varepsilon_2 \cdot \frac{h}{2\sin\alpha} \cdot \cos\alpha$$

$$e_{P,1} = \varepsilon_1 \cdot 2 \cdot h - \varepsilon_2 \cdot \frac{h}{2\sin\alpha} \cdot \cos\alpha$$

$$e_{P,1} = 2 \cdot h \cdot \left(\varepsilon_1 - \frac{\varepsilon_2}{4 \cdot \tan \alpha} \right) \quad 3\text{-}22$$

$e_{P,3}$:

$$e_{P,3} = l_{BC} \cdot \cos \alpha - e_2 - e_3$$

$$e_{P,3} = l_{BC} \cdot \cos \alpha - l_{AB} \cdot (\varepsilon_2 + \varepsilon_3)$$

$$e_{P,3} = 2 \cdot h \cdot \cos \alpha - \frac{h}{2 \cdot \sin \alpha} \cdot (\varepsilon_2 + \varepsilon_3)$$

$$e_{P,3} = 2 \cdot h \cdot \left(\cos \alpha - \frac{\varepsilon_2 + \varepsilon_3}{4 \cdot \sin \alpha} \right) \quad 3\text{-}23$$

$e_{O,P}$:

$$e_{O,P} = e_1 \cdot \cos \alpha - e_2$$

$$e_{O,P} = \varepsilon_1 \cdot l_{BC} \cdot \cos \alpha - \varepsilon_2 \cdot l_{AB}$$

$$e_{O,P} = 2 \cdot h \cdot \left(\varepsilon_1 \cdot \cos \alpha - \varepsilon_2 \cdot \frac{1}{4 \cdot \sin \alpha} \right) \quad 3\text{-}24$$

$$e_{P,F} = \varepsilon_F \cdot \frac{h}{2} - \varepsilon_2 \cdot \frac{h}{2} = \frac{h}{2} \cdot (\varepsilon_F - \varepsilon_2) \quad 3\text{-}25$$

3.5 Equilibrium configurations

The external loading conditions are described by the bending force *M* and the compressive force *F*. Along the loading process a rotation of the pieces that compose the connection was observed. The internal rotation of the connection is influent; therefore, the passage from the *zero* load to the ultimate-load would be described by means of a *second order non-linear* model. In order to formulate an analytic model to describe the *non-linear* geometric behaviour of the joint, different *first- order linear-elastic* models (equilibrium configurations) were developed.

The configurations consider the limit state of the beam, as the behaviour of the joint were linear, i.e. without taking into account the real deflections. In fact, the equilibrium configurations describe the instant position of the internal forces along the loading process. Therefore, the deflections are described in every configuration by specific parameters ($\varepsilon_{surface}$).

The description of the equilibrium configurations (Figure 3-6) with the evaluation of the entity/position and the general relations among the parameters follows.

(I) The connection is loaded in pure bending *M*. The friction coefficient μ_α acquires the maximum value. The value of the friction force is $F_{2,//} = F_{2,\perp} \cdot \mu_\alpha$

(II) The connection is loaded in combined compressive and bending force *F* + *M*. Here positive value of friction μ_α reduces.

(III) The connection is loaded in combined compressive and bending force *F* + *M*. In this configuration the value of the friction coefficient μ_α is null.

(IV) The connection is loaded in combined compressive and bending force *F* + *M*. The value of μ_α acquire negative values.

(V), (VI) The connection is loaded in combined compressive and bending force $F+\Delta F$ + *M*. The increasing of the normal force $F+\Delta F$ brings first to the appearance of the contact on the surface CD, expressed by the resultant $F_{3,\perp}$, and the consequent friction force $F_{3,//} = F_{3,\perp} \cdot \mu_\alpha$

(VII) The connection is loaded in combined compressive and bending force $F+\Delta F$ + *M*, and pure compression F. The friction force μ_α is negligible because the very high values of compressive force *F*.

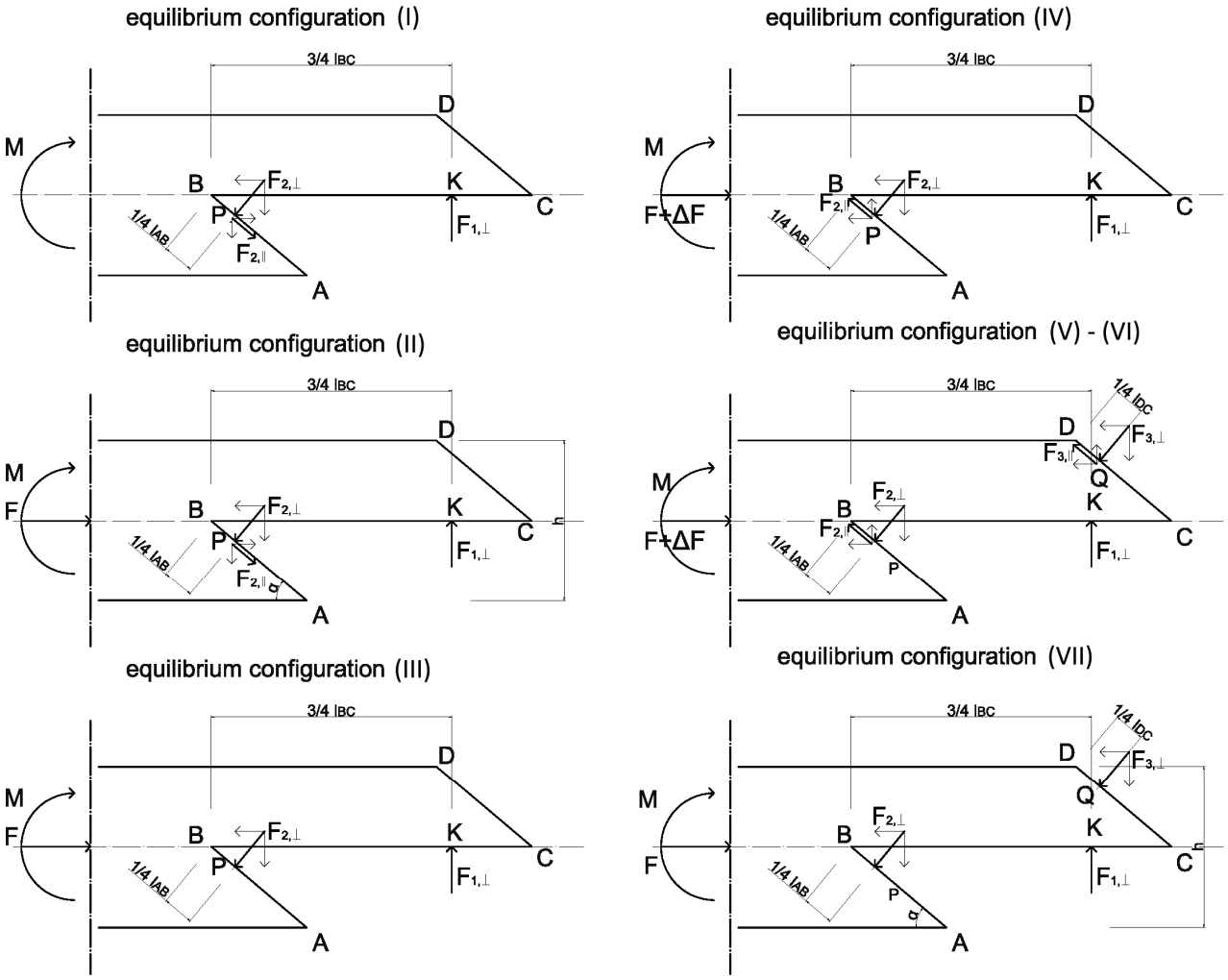

Figure 3-6 – equilibrium configurations of the sub-substructures, summary

The description of the non-linear *N-M* curve is approached with a sequence of linear-elastic static models (I) (II) (III), (IV), (V) – (VI), (VII). Due to changes in the stress, the changes of the position of the forces $F_{1,\perp}$, $F_{2,\perp}$ and $F_{3,\perp}$ is accompanied by deflections. The models describe the sequence of loading instants under the hypothesis of small displacements and small deformations (Figure 3-6). The range of validity of each model defines the loading-instants where the position of the internal resultant forces is described through proper parameters called ε_1, ε_2 and ε_3.

The present work limits the description of the beam's behaviour in the first-order linear-elastic field. For what concern the model (VII), that describes the upper branch of the diagram, the result of the loading process is a larger deflection under a static load; indeed, it is not precise to write the equilibrium of the deformed

configuration as to the one of the non-deformed one. The characterization of the upper branch on the diagram is therefore not thorough.

3.5.1 Conclusions

The description of the non-linear *N-M* curve through the analytic models is further simplified (Figure 3-7) considering the following observations.

1) The models (II) ≡ (III) ≡ (IV) are equivalent (and describe the changing of verse of the force $F_{2,//}$). They will be described as an inclusive model (ii):

   (ii) The connection is loaded in combined compressive and bending force *F* + *M*. The value of μ_α goes from the maximum value $F_{2,//} = F_{2,\perp} \cdot \mu_\alpha$ to zero (in the single-configuration-model (iii)) and then acquires negative values. For the specific value of μ_α see Chapter 4.

2) The model (VII) gives a description of the external loading conditions and the internal forces neglecting the friction force μ_α. It is possible to do it because of the very high values of compressive force *F*. Therefore, the models (V), (VI) and (VII) are fully described by the inclusive model (vii). Therefore:

   (vii) The connection is loaded in combined compressive and bending force $F + \Delta F$ + *M*, and pure compression F. The friction force μ_α is negligible because very high values of F.

As a conclusion, the adopted static models are the models (i), (ii), (iii) and (vii) (Figure 3-7) and are the ones further described in the Chapter 4. The model (iii) is a unique configuration, particular case of the model (II).

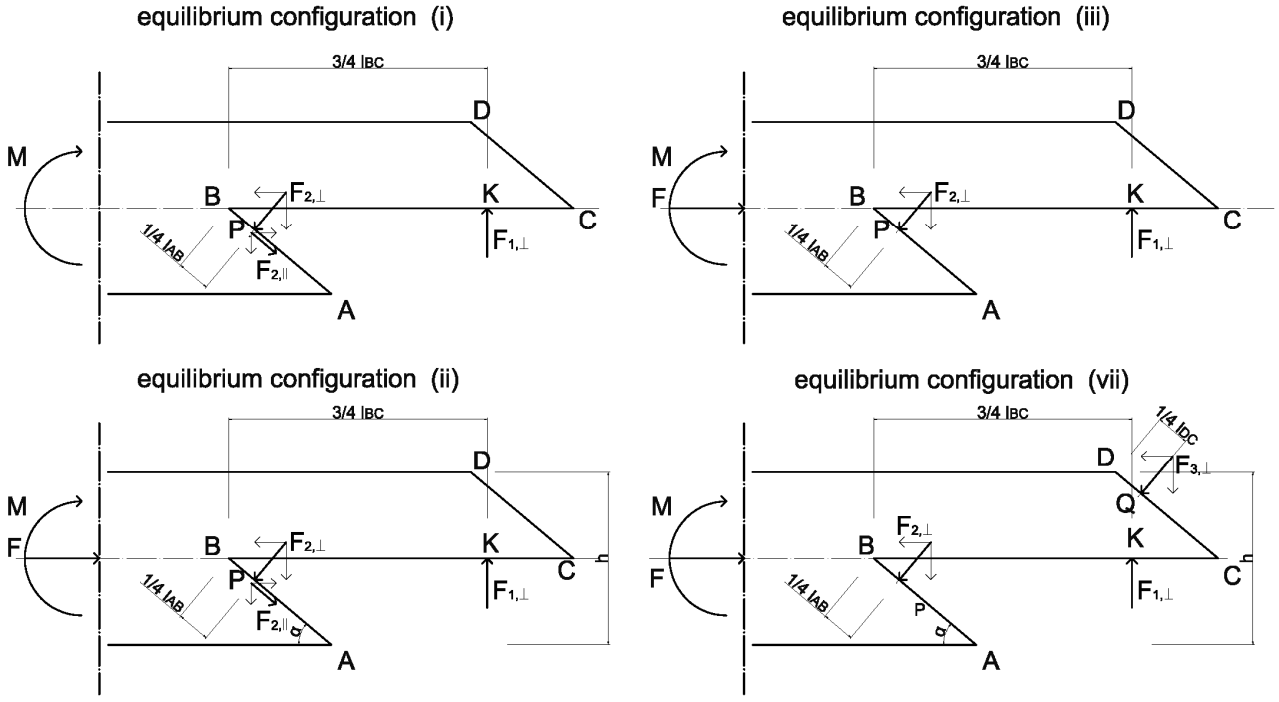

Figure 3-7 - Final equilibrium configurations of the sub-substructures

The following considerations on the coefficients are done:

$$\varepsilon_F = 0 \qquad \text{3-26}$$

In the present work, is considered *F* as applied in correspondence with the neutral axis of the element's cross section (eq. 3-26); therefore, the force *F* is defined as *N*.

3) The basic configuration, correspondent to the zero-load has to be generally considered the configuration

$$\varepsilon_1 = \varepsilon_2 = \varepsilon_3 = 0.5 \quad \text{3-27}$$

With the increasing of the load, the three coefficients tend to the configuration:

$$\varepsilon_1 = \varepsilon_3 \to 1 \quad \text{3-28}$$

$$\varepsilon_2 \to 0 \quad \text{3-29}$$

4) In the proposed models, the value of the coefficient that define the position of the resultant forces in the failure configuration is:

$$\varepsilon_1 = \frac{3}{4},\ \varepsilon_2 = \frac{1}{4}, \text{ and } \varepsilon_3 = \frac{3}{4} \quad \text{3-30}$$

These are values are chosen to err on the side of safety, in order to describe the ultimate configuration that anticipate the failure.

5) The relation among the coefficients ε_2 and ε_F is described by the following three cases:

5.I.) $e_F > e_2$ 3-31

$$\varepsilon_F \cdot \frac{h}{2} > \varepsilon_2 \cdot \frac{h}{2} \quad \text{3-32}$$

$$\varepsilon_F > \varepsilon_2 \quad \text{3-33}$$

The contribution of the normal force F is against the moment force (considering the center of rotation in P), and it constitutes a kind of "reinforcement" for the connection.

5.II.) $e_F < e_2$. 3-34

$$\varepsilon_F < \varepsilon_2 \quad \text{3-35}$$

The force F contributes to weaken the connection, because (considering the center of rotation in P) the moment due to F is concordant with the direction of rotation of the moment M. The unique "reinforcement" for the connection is constituted by $F_{1,\perp}$.

5.III.) $e_F = e_2$. 3-36

$$\varepsilon_F = \varepsilon_2 . \quad \text{3-37}$$

In this last case, always considering the center of rotation in P, the connection have no external contribution of the force F aiming to the equilibrium to the rotation.

3.6 Imperfections

According to the HP.3 the imperfections of the wood members/specimen/test installation may generate an irregular loading path/response of the forces in the joint. The imperfections can significantly influence the joint's behaviour, and the possible effects have to be taken into account. The imperfections govern the behaviour of the joint in the a) timber specimen b) manufacture of the specimen c) installation of the specimen in the test machine (Figure 3-8 and Figure 3-9).

a) In first instance, the timber is very variable material, and every specimen has different specific strength and stiffness properties. For the general grading (probabilistic) of the timber would be necessary to test a consistent value of specimen with the same procedure and from there extrapolate the 5th percentile value

(Classification EN 14081). The classification procedure to extrapolate the elasticity modulus *E* of some of the specimen has been done according to EN 14081 and DIN 26891. In the present work, the statistic of the wooden properties is not performed. The timber is visually graded in order to register significant grains deviations, knots, growing or environmental-caused imperfections (Figure 3-9 a)) of the specimens.

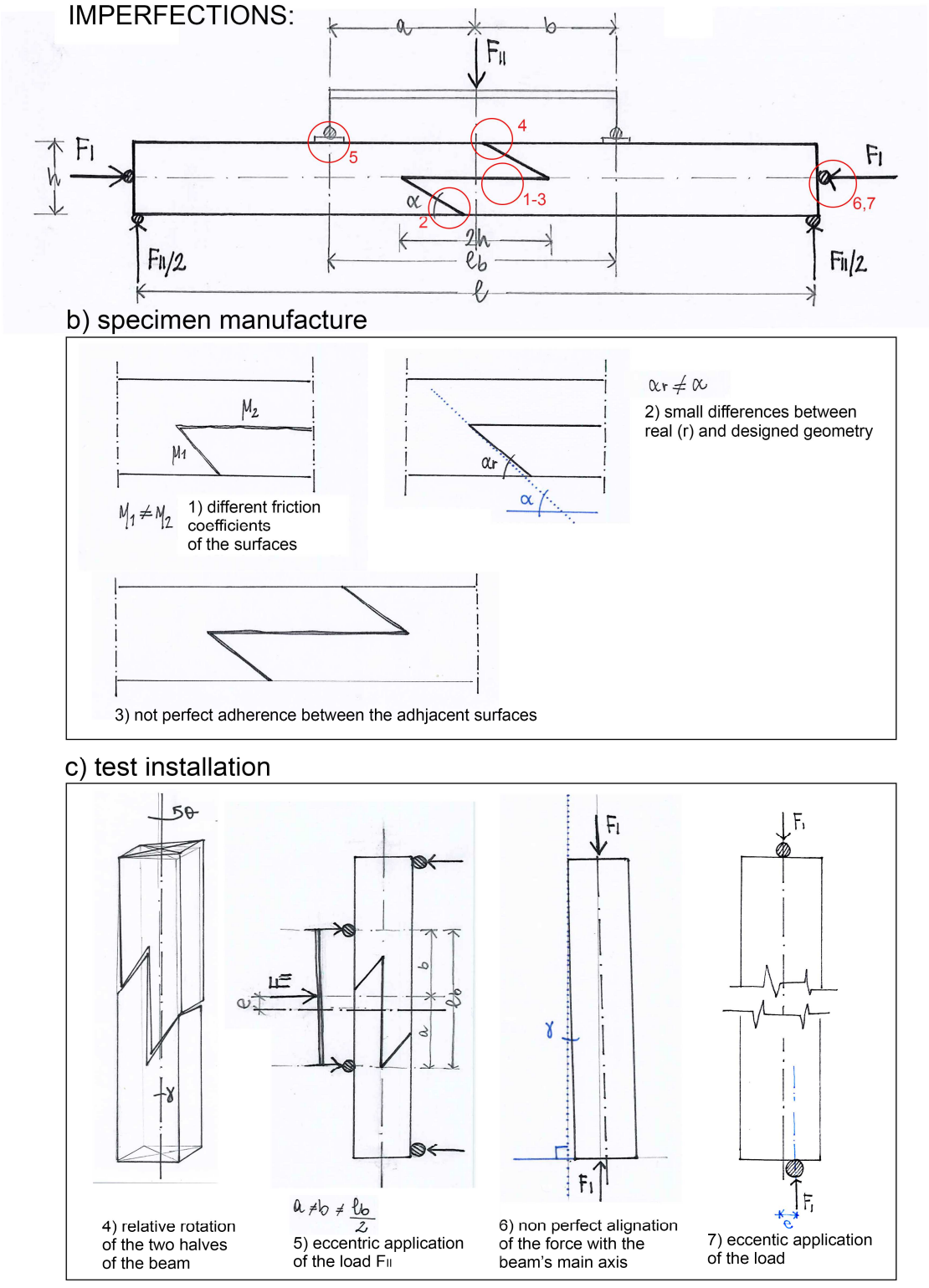

Figure 3-8 – Imperfection in the timber manufacturing or the test installation: on the top, summary; b) specimen manufacture; c) test installation.

a) WOODEN IMPERFECTIONS

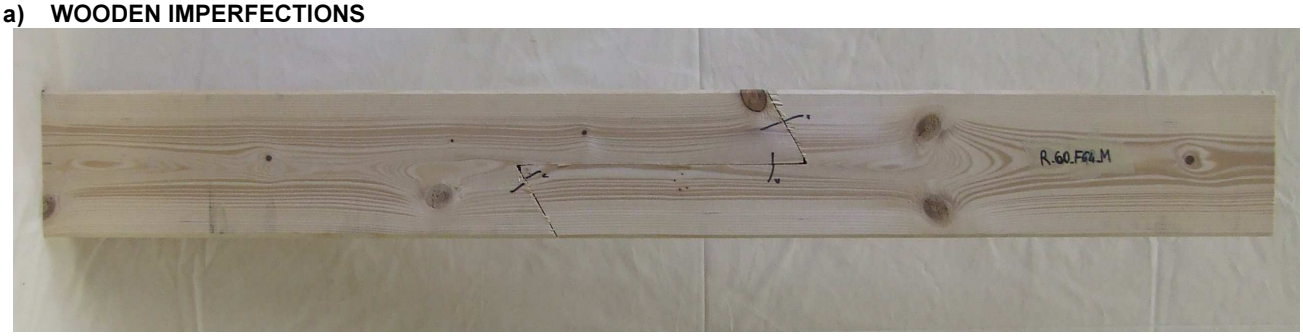

grains deviations and knots in a specimen

b) MANUFACTURING OF THE CONNECTION

1) Different friction on the adjacent surfaces

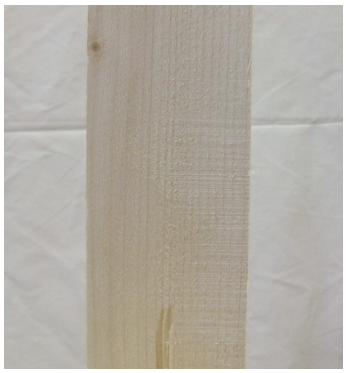

surface cut with the circular saw

two surfaces cut with the band saw

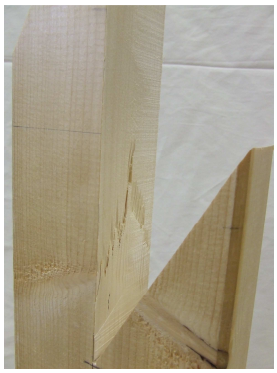

variation of the roughness of the surface

cracked cross - section

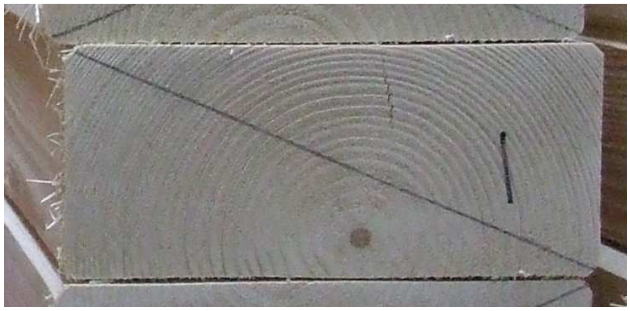

wooden hearth in the cross - section

2) Small differences between real and designed geometry

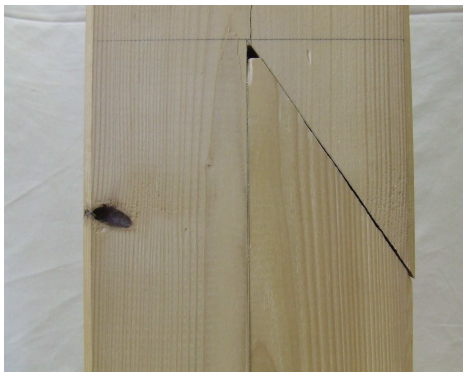

$\alpha_r \neq \alpha$

torsion of the length of the specimen

non verticality of the specimen

3) Non-perfect match of two facing surfaces

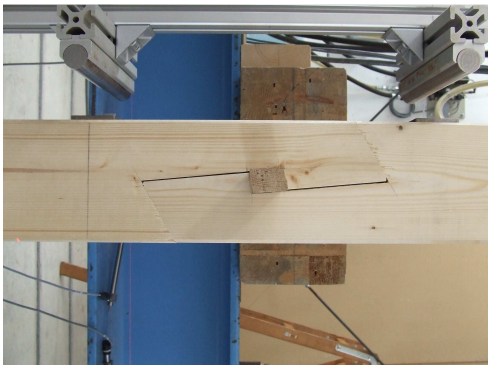

Space between the two halves

Presence of small growing imperfection

c) TESTS INSTALLATION

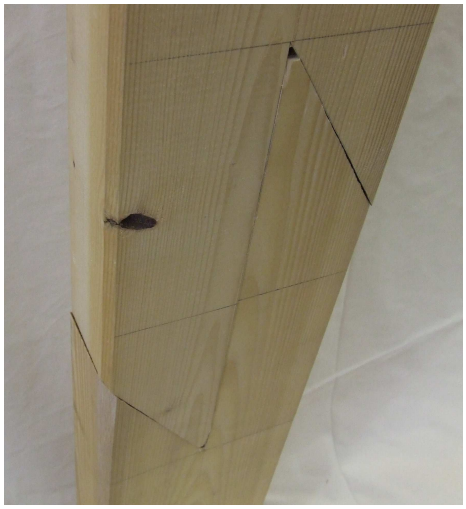

relative rotation of the two halves of the beam

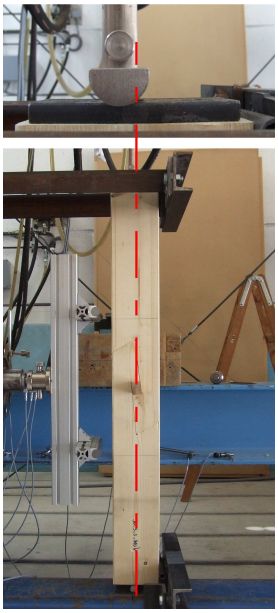

not perfect alignment of the specimen's axis with the vertical load

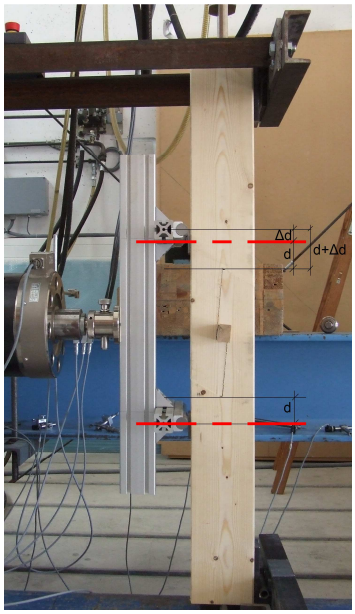

not perfect installation of the piece symmetrically with the pure bending

Figure 3-9 – Imperfections in the timber manufacturing or the test installation – examples from the experimental campaigns. (a) wooden imperfections; (b) manufacturing of the connection; (c) tests installation.

b) In second instance, during the manufacturing of the connection, the specimen can be subjected to different fashion procedures. Depending on the saw-machine or cutting methods, the timber/joint friction properties or others parameters like the perfect match of two facing surfaces are influenced (Figure 3-9 b)). During the assembly of the two pieces may not fit perfectly one into the other; indeed, internal eccentricities that brings to a slightly amount of internal bending force on both the weak and strong axis is produced. Last, the presence of a minimal additional amount of bending force in the tests is also caused by c).

c) Both the not perfect alignment of the specimen's axis with the vertical load, because of the not perfect verticality of the specimen, or the not perfect installation of the piece symmetrically with the pure bending load causes a further eccentricity of the load (Figure 3-8 – (c), Figure 3-9 – (c)).

3.7 Failure modes and verification

For the development of the analytic models three main failure modes (FM) were considered:

I. FM I - compression perpendicular to the grain in the segment CD;
II. FM II - Shear/tension perpendicular to the grain failure in the point B.
III. FM III - Shear/tension perpendicular to the grain failure in the point B and C.

For the calculation of the limit state of the connection, the Eurocode 5 version EC 1995-1-1:2012 was considered. The calculations of the FM I were performed according to EC5 section 6.2.2 - Compression stresses at an angle to the grain; while, for the FM II and FM III the Gustafsson formula (Gustafsson, 2003) for the evaluation of the load for the propagation of a crack in a bending-loaded beam is re-elaborated.

3.7.1 Compression inclined to the grain verification

As well known, due to the orthotropic nature of wood, the design compressive stress applied at generic angle α to the grain is varying. For the calculation of the maximum external applied force F_{max}, the UNI – EN1995 1 / CNR DT 206:2007 / Eurocode 5, session 6.2.2 has been used. For the strength classes the EN 338_Structural timber - Strength classes has been used.

The Hankinson formula (Hankinson, 1921) used in the Eurocode for the strength under compression load at the generic angle α between the applied force and the direction of the grains, is used in the present work.

Respect to the Eurocode nomenclature, the generic angle between the applied force and the direction of the grains is called θ, that is defined in the following eq. 3-38.

$$\pi = \theta + \alpha + \frac{\pi}{2}$$

$$\theta + \alpha = \frac{\pi}{2} \qquad \text{3-38}$$

$$\theta = \frac{\pi}{2} - \alpha$$

Where α is the angle that defines the inclination of the joint. The design compressive stress at an angle θ to the grain is thus defined as:

$$\sigma_{c,\theta,d} = \frac{f_{c,0,d}}{\left(\frac{f_{c,0,d}}{k_{c,90} f_{c,90,d}}\right)\sin^2\theta + \cos^2\theta} \qquad \text{3-39}$$

In order to verify the connection:

$$\sigma_{c,\theta_{CD},k} \cdot A_3 = R_{ax,\theta_{CD},k} \quad [N] \qquad \text{3-40}$$

Characteristics load-carrying capacity at an angle $\theta = \frac{\pi}{2} - \alpha$

3.7.2 Shear/tensile stress perpendicular to the grain verification

Follows the evaluation of the load-carrying capacity of a connection from the EC5 to the Gustaffson one.

Introduction: short background on the EC5 formula

The equation contained in the EC5 for the calculation of the shear/tension perpendicular to the grain stresses in notched beams origins from a study developed by Gustafsson in the year 1988 on the evaluation of the load for the propagation of a crack in a bending-loaded beam. In the following years was confirmed the analogy with the strength of bending-loaded beam with end-notches (Gustafsson, 1988 and Riberholt, 1991); thus, a further step for the formulation of the present formula was done, adapting the original equation for a nineteen-degrees cut notch. Before the development of the EC5 equation, other simplifications were made. Larsen (Larsen, 1992), thanks to the results of some laboratory tests, approximated some parameters from the original formula, some others were avoided; finally, thanks to a further adaptation (Riberholt et al., 1991), the parameters for the presence of a taper in the notch were also included in the EC5 formula.

In the wood-wood connections, the slanting cuts that compound the joint can be approximated both to a notched connection or an ending-crack. The EC5 formula for the calculation of the FM I for the notched joints or beams with holes, as shortly described above, is a further approximation of the Gustafsson formula (Gustafsson, 1988) developed for the ending-cracked beam. The results for the F_u in case of FM I calculated from the EC5 for this application were not satisfying the values registrated in the experimental part of the work.

The similarities between the Gustafsson beam and the connection are also relevant. The Gustafsson beam is a simply supported cantilever beam, which cross-section is cracked at the middle of the height; more, the external applied forces are null and the internal resulting force is the reaction of the unique support. The scarf connection, despite the inclination of the surfaces, can be approximated in a simply supported cantilever, divided into two cantilevers (determinate by $h_{eff,1}$ and $h_{eff,2}$) by the surface 1; more, the internal resultant force $F_{2,\perp}$ is the only loading force in each of the two cantilevers, in two opposite senses respectively in the $h_{eff,1}$ cross section and $h_{eff,2}$ cross-section. The external applied forces are null.

For all this reason, in the present work the calculation of the FM I is conducted taking into account the Gustafsson formula.

The shear/tensile stress perpendicular to the grain stress in the connection

The initiation of a crack growth is, in case of a notched or holed beam, is due to the perpendicular to the grain tensile stress or shear stress or a combination of the two. According to linear elastic classic stress analysis, the stress at the tip of the notch approaches the infinity. Due to the limited strength of the material, the stress of the tip, in reality, does not approach the infinity. This meaningless result derives from the classic linear elastic approach and the stress criterion for the determination of the load-carrying capacity in a beam with notch, bring to the necessity to approach differently to the problem. For the present work, the calculation of a shear force in a notch was done taking into account the original Gustafsson formula that was taking into account the analysis within the framework of the linear elastic fracture mechanics (LEFM). A solid body responds to extreme loading undergoing large fractures, the calculation of the magnitude of that load that causes fracture is the most important. The LEFM can be used for calculating the loads that gives propagation of an pre-existing crack or, in our case, a sharp notch, having “infinite stress” at the tip of the

crack or notch. The fracture of the material is in fact governed by its stiffness and the fracture energy (Gustafsson, 2003). The fracture energy can be directly determined by work of fracture, giving the parameter that is denoted as G_f.

The parameter G_f, that defines the energy dissipating ability of the material, is density-dependent, and has a very large variance. For the European softwoods it is roughly in the order of $G_f = 150 - 600 J/m^2$. That variance is also depending on the inclination of the application of the force is considered (Boström, 1992). For the definition of the value of G_f some tests were conducted (Gustafsson, 1992 and Wernesson. 1992) and demonstrated that the peak tensile and shear stresses do not occur at the same time. For this reason the mean curves for the tensile stress and normal deformation and shear stress vs shear deformation, where conducted for different mixed mode, that correspond to different angles respect to the wood fibers. The mixed mode fracture properties (Wernesson. 1994) are illustrated in the following table. The different angles represent the different inclination of the stroke displacement vector.

Mixed mode angle	σ MPa	τ MPa	$G_{f,\sigma}$ J/m^2	$G_{f,\tau}$ J/m^2	$G_{f,\text{tot}}$ J/m^2
0°	4.8	0.9	475	0	475
45°	3.3	8.1	146	481	627
51°	2.7	9.4	75	552	627
90°	0.2	10.9	0	1120	1120

Table 3-1 – Mixed mode fracture properties. From (Wernesson, 1994)

For what concerns the present work, the fracture criterion is the one in eq. 3-41; here, the value considered is the one contained in the eq. 3-42.

$$G_f = G_{f,tot} \qquad 3\text{-}41$$

$$G_c = 1100\, J/m^2 = 0.0011\, \frac{N}{mm}. \qquad 3\text{-}42$$

Verification method (energy release analysis).

A beam with an end-crack as in the following picture is considered.

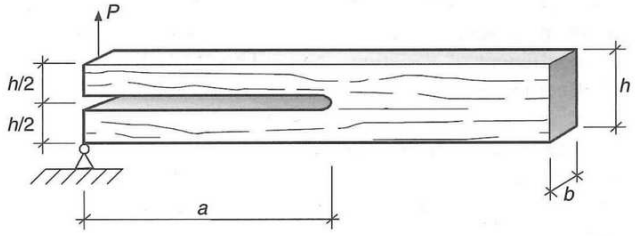

Figure 3-10 - Scheme of the beam with end-crack.

The energy balance during the extension of the cracked area by dA is (Gustafsson, 1988):

$$G_f = W - \frac{dT}{dA} - \frac{d\phi}{dA} \qquad 3\text{-}43$$

Where G_f is the external work of fracture, T the kinetic energy and ϕ is the elastic strain energy (Hellan, 1985)

In the hypothesis of:

a) quasi-static situation
b) linear elastic solid
c) small displacements

The resulting formula is:

$$G_f = \frac{1}{2}\left(\frac{{F_f}^2}{b}\right)\left(\frac{dC(a)}{da}\right) \quad \text{3-44}$$

Where

$$b = \frac{dA}{ds} \quad \text{3-45}$$

is the width of the fracture area, da is the elongation of the fracture during the loading, F_f is the load that is necessary to start the propagation of the crack.

The calculation of the ultimate load F_u is done considering the Gustaffson (1988) theory on the energy release connected with the fracture of a cracked beam and Griffith (1920). According to the elementary beam theory, the displacement of the cantilever beam (for two cantilevers, in the example proposed by Gustafsson) is

$$C = \frac{1}{K} = \frac{\delta}{P} = 2 \cdot \left(\frac{a^3 \cdot P}{3 \cdot E_0 \cdot J}\right)\frac{1}{P} = \frac{2}{3} \cdot \left(\frac{a^3}{E_0 \cdot J}\right) \quad \text{3-46}$$

That correspond to two times the elongation of half of the beam cross section (two cantilevers of $h = h_{eff}$).

Where E_0 is the modulus of elasticity of the beam and J is the moment of inertia of the cantilever where the load is applied to

$$J = \frac{b \cdot h_{eff}^3}{12} \quad \text{3-47}$$

During the increasing of the loading, the potential energy, dG_f, during a propagation, da, of the crack, is then obtained by derivation

$$dG_f = \left(\frac{{F_f}^2 a^2}{b \cdot E_0 \cdot J}\right) \quad \text{3-48}$$

Where $\frac{dC(a)}{da} = \frac{2a^2}{E_0 \cdot J}$ 3-49

This decrease of the potential energy corresponds to a positive energy release. When the load is so large that the crack starts to propagate, then, G_f has reached its critical value $G_{f,tot}$ (see above for the values). Thus, the fracture criteria is (Larsen and Gustafsson, 1990) $G_f = G_{f,tot}$

The final formula, for the calculation of the F_u is the eq. 3-50 to eq. 3-52.

$$F_f = \sqrt{G_f \cdot b \cdot \frac{E_0 \cdot J}{a^2}} \quad \text{3-50}$$

$$F_f = \sqrt{G_f \cdot b \cdot \frac{E_0 \cdot \frac{b \cdot h_{eff}^3}{12}}{a^2}} \quad \text{3-51}$$

$$F_f = b \cdot h_{eff} \sqrt{h_{eff}} \sqrt{\frac{G_f \cdot E_0}{12 \cdot a^2}} \qquad 3\text{-}52$$

Applying the general Gustafsson formula to the particular case of the *halved and undersquinted* scarf for the fracture in B and C the following equations, that refers to the Figure 3-11, are considered.

In general, the cracking force $F_{f,i}$ is according to eq. 3-50.

For the failure in B, FM III it is:

$$F_{f,2}(a_2): \qquad a_2 = e_2 \cdot \cos\alpha = \varepsilon_2 \cdot l_{AB} \cdot \cos\alpha = \varepsilon_2 \cdot \frac{h}{2 \cdot \sin\alpha} \cdot \cos\alpha = \varepsilon_2 \cdot \frac{h}{2 \cdot \tan\alpha} \qquad 3\text{-}53$$

$$F_{f,2} = \sqrt{G_f \cdot b \cdot \frac{E_0 \cdot \frac{b \cdot h_{eff,2}^3}{12}}{{a_2}^2}} \qquad 3\text{-}54$$

For the failure in C, FM III it is:

$$F_{f,3}(a_3): \qquad a_3 = e_3 \cdot \cos\alpha = \varepsilon_3 \cdot l_{CD} \cdot \cos\alpha = \varepsilon_3 \cdot \frac{h}{2 \cdot \sin\alpha} \cdot \cos\alpha = \varepsilon_3 \cdot \frac{h}{2 \cdot \tan\alpha} \qquad 3\text{-}55$$

$$F_{f,3} = \sqrt{G_f \cdot b \cdot \frac{E_0 \cdot \frac{b \cdot h_{eff,3}^3}{12}}{{a_3}^2}} \qquad 3\text{-}56$$

Where

$h_{eff} = \frac{1}{2} \cdot h$ effective height of the cross-section, in this case, the half.

$G_f = 0.0012$ value extrapolated from the Table 3-1

a as in the eq. 3-53, eq. 3-55, or see Figure 3-11.

In general, the failure criteria is:

FRACTURE IN B

$$F_{2,\perp} \cdot \cos\alpha \le F_{f,2} = F_{f,B} \qquad 3\text{-}57$$

FRACTURE IN C (with inversion of the value of M for $F_{3,\perp}$)

$$F_{3,\perp} \cdot \cos\alpha \le F_{f,3} = F_{f,C} \qquad 3\text{-}58$$

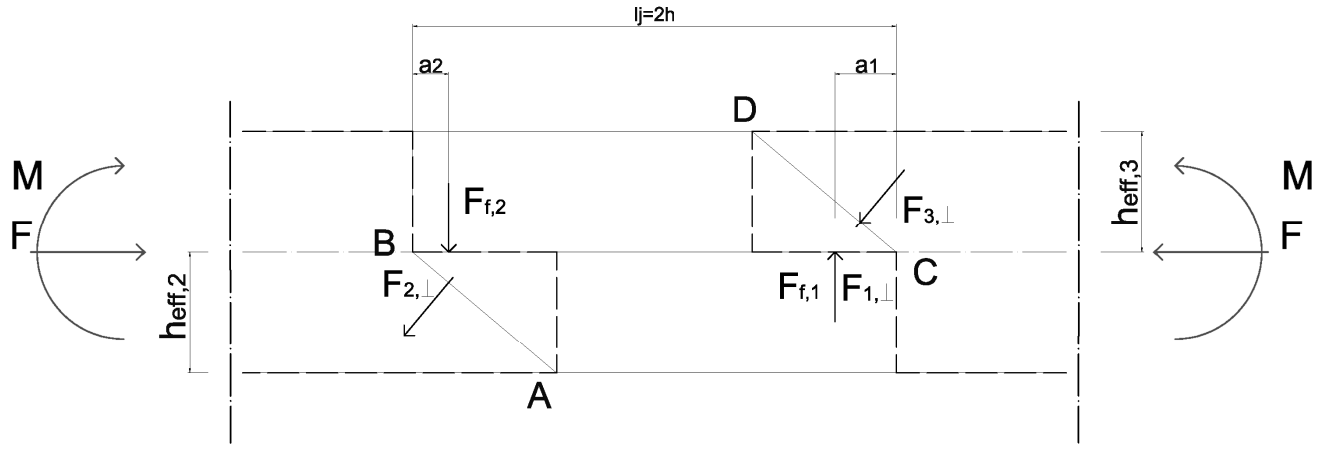

Figure 3-11 – Failure mode parameters. Schematization.

Chapter 4 ANALYTICAL CHARACTERIZATION OF THE *HALVED AND UNDERSQUINTED SCARF* JOINT

4.1 Introduction

In the present chapter, the analytical characterization of the *halved and undersquinted scarf* joint is proposed. In order to define the resistance of the joint, the generic geometry with $\alpha \neq 0$ and the particular case $\alpha = 0$ (*halved joint*) are approached. The *halved* joint is proposed as a simplification of the problem. For the *halved and undersquinted scarf* joint, the equilibrium configurations contained in the Figure 3.8 are analysed in detail.

4.2 Analytic characterization of the halved joint.

The *halved* joint represents the particular case of the *halved and undersquinted scarf* joint where $\alpha = 0$. The analysis of this particular case is in order to clarify in simple terms the resistance of the joint, considering a connection that belongs to a quasi-rigid body, without friction on the surfaces, and under the independent external actions F and moment M. The F is applied in correspondence of the neutral axis ($F \equiv N$), i.e $\varepsilon_F = 0$. Referring to the EC0, both the loss of equilibrium failure (ref. eq. 1-1) and the material failure (ref eq. 1-4) are considered. The first condition is represented by the *forces boundary conditions* and the second by the *limit states*.

$$quasi-rigid: \begin{cases} INFINITE\ \_stiffness \\ FINITE\ \_strength \end{cases}; \qquad \mu_\alpha = 0; \qquad F \equiv N \text{ independent from M}$$

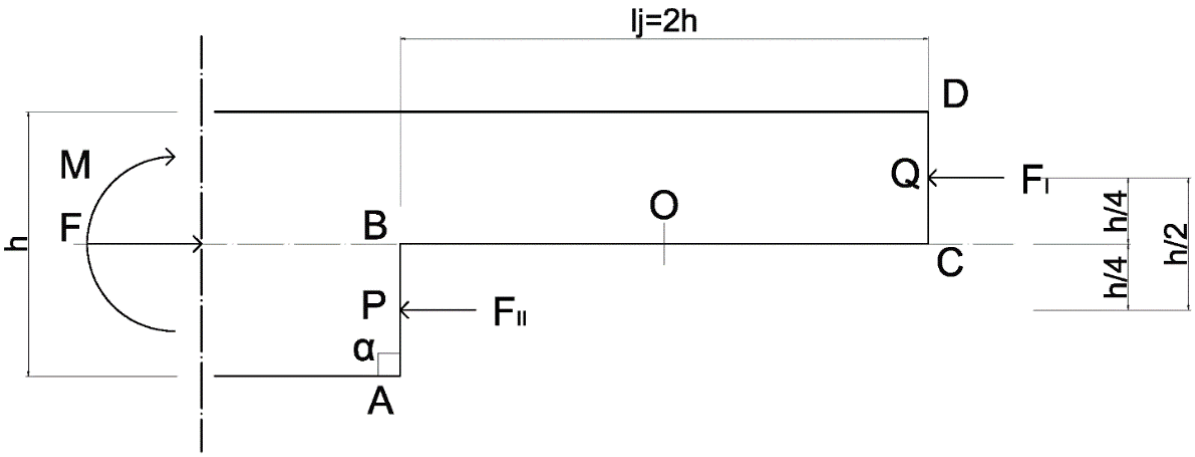

Figure 4-1– Equilibrium Configuration (*α = 90°*)

4.2.1 Resultant forces

HP

The model (α = 90°) is valid for the following external loading condition; where F is independent from M.

$$M > 0; \qquad F > 0 \tag{4-1}$$

Internal resultant forces:

$$F_I > 0; \qquad F_{II} > 0; \qquad \mu_\alpha = 0 \tag{4-2}$$

Equilibrium Eq.:

$$\sum F_x = 0 \tag{4-3}$$

$$F_I + F_{II} = F \tag{4-4}$$

$$F_I = F - F_{II} \tag{4-5}$$

$$\sum F_y = 0 \tag{4-6}$$

$$\sum M_P = 0 \tag{4-7}$$

$$F_{II} \cdot \frac{h}{4} - F_I \cdot \frac{h}{4} + M = 0$$

$$F_{II} \cdot \frac{h}{4} - \left(F - F_{II}\right) \cdot \frac{h}{4} + M = 0$$

$$F_{II} \cdot \frac{h}{2} - F \cdot \frac{h}{4} + M = 0$$

$$F_{II} = \frac{F}{2} - \frac{2M}{h} \tag{4-8}$$

Inserting the eq. 4-8 in the eq. 4-5 , it follows:

$$F_I = \frac{F}{2} + \frac{2M}{h} \tag{4-9}$$

Summary of the value of the resultant forces

$$F_I = \frac{F}{2} + \frac{2M}{h} \tag{4-10}$$

$$F_{II} = \frac{F}{2} - \frac{2M}{h} \tag{4-11}$$

4.2.2 Boundary conditions

Forces boundary conditions FC(i)

According to HP.1, it has to verify the conditions:

$$F_I \geq 0 \quad \cap \quad F_{II} \geq 0 \tag{4-12}$$

FC(90°)1: $F_{1,\perp} \geq 0$

Always.

FC(90°)2: $F_{2,\perp} \geq 0$

$$F_{II} = \frac{F}{2} - \frac{2M}{h} \geq 0 \tag{4-13}$$

$$\frac{F}{2} \geq \frac{2M}{h} \qquad 4\text{-}14$$

4.2.3 Limit states.

The model (α = 90°) provides one forces limit state, compression parallel to the grain resistance, associated with the equilibrium failure in the eq. 4-14.

$$\begin{matrix} I : LS(90)1 \\ II : FC(90)2 \end{matrix} \begin{cases} \frac{F}{2} + \frac{2 \cdot M}{h} \leq R_c \\ \frac{F}{2} - \frac{2 \cdot M}{h} > 0 \end{cases} \qquad 4\text{-}15$$

$$\begin{matrix} I : LS(90)1 \\ II : FC(90)2 \end{matrix} \begin{cases} F \leq 2 \cdot R_c - \frac{4 \cdot M}{h} \\ F > \frac{4 \cdot M}{h} \end{cases} \qquad 4\text{-}16$$

In the Diagram 4-1, the limit state for the *halved* joint (eq. 4-16) is represented. The two conditions represented in the N-M diagram describe the maximum resistance of the connection. The condition **I** is the material limit state, and the condition **II** the equilibrium limit state. The light blue-area inside the diagram represents the possible combinations of N, M in which the joint ist stable and there is no material failure for the *halved joint*.

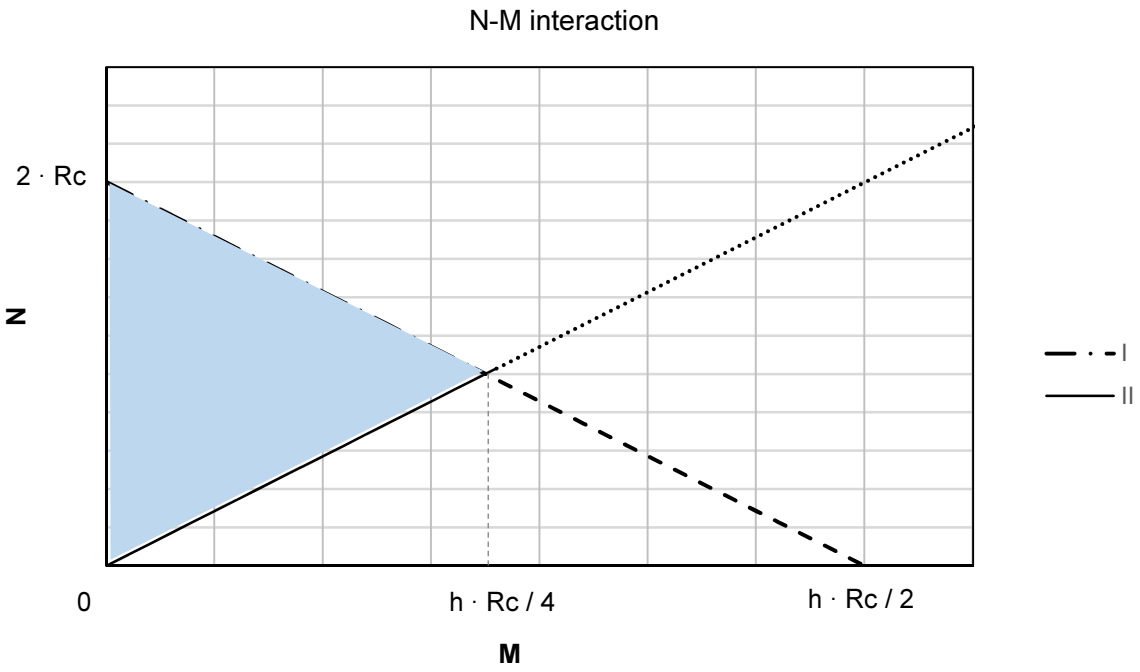

Diagram 4-1– N-M interaction for the *halved joint*. Limit state diagram for the connection with α = *90°*.

4.3 Equilibrium configuration (i): M>0 F=0

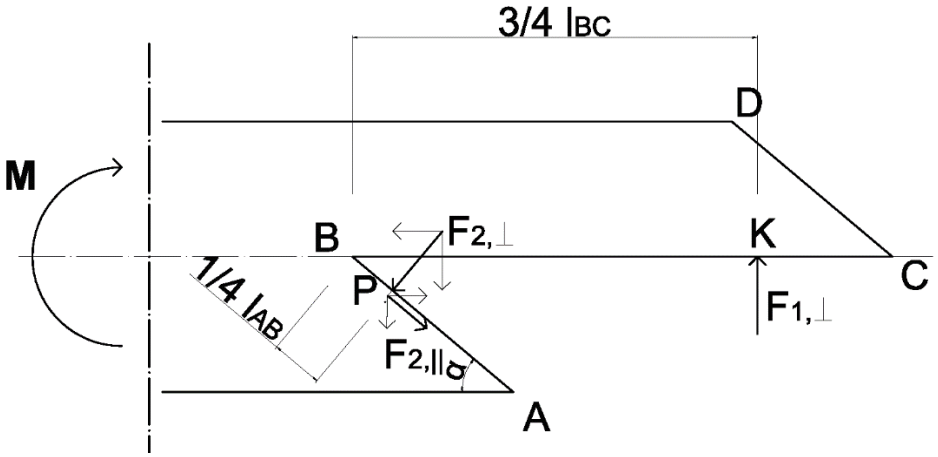

Figure 4-2 – EquilibriumConfiguration (i)

4.3.1 Resultant forces

HP

The model (i) is valid for external loading condition pure compression:

$$M > 0; \qquad F = 0 \tag{4-17}$$

And internal resultant forces:

$$F_{2,//} > 0; \qquad F_{2,\perp} > 0; \qquad F_{1,\perp} > 0; \qquad F_{1,//} = 0; \qquad F_{3,\perp} = 0; \qquad F_{3,//} = 0 \tag{4-18}$$

Equilibrium Eq.:

$$\sum F_x = 0 \tag{4-19}$$

$$F_{2,//,0} = F_{2,\perp,0}$$

$$F_{2,//} \cos\alpha = F_{2,\perp} \cdot \sin\alpha$$

$$F_{2,//} = F_{2,\perp} \cdot \tan\alpha$$

$$\mu_\alpha = \frac{F_{2,//}}{F_{2,\perp}} = \tan\alpha \tag{4-20}$$

$$\sum F_y = 0 \tag{4-21}$$

$$F_{1,\perp} = F_{2,//,90} + F_{2,\perp,90}$$

$$F_{1,\perp} = F_{2,//} \cdot \sin\alpha + F_{2,\perp} \cdot \cos\alpha$$

$$F_{1,\perp} = F_{2,\perp} \cdot \left(\tan\alpha \cdot \sin\alpha + \cos\alpha\right) \tag{4-22}$$

$$\sum M_P = 0 \tag{4-23}$$

$$F_{1,\perp} \cdot e_{P,1} = M$$

$$F_{1,\perp}\left[2 \cdot h \cdot \left(\varepsilon_1 - \frac{\varepsilon_2}{4 \cdot \tan\alpha}\right)\right] = M$$

$$F_{1,\perp} = \frac{M}{\left[2 \cdot h \cdot \left(\varepsilon_1 - \frac{\varepsilon_2}{4 \cdot \tan\alpha}\right)\right]} \tag{4-24}$$

Inserting the previous eq. 4-24 in the eq. 4-22 , it follows:

$$F_{2,\perp} = \frac{\frac{M}{h}}{2 \cdot \left(\varepsilon_1 - \frac{\varepsilon_2}{4 \cdot \tan \alpha} \right) \cdot \left(\cos \alpha + \tan \alpha \cdot \sin \alpha \right)} \qquad 4\text{-}25$$

$$F_{2,\perp} = \frac{\frac{M}{h}}{2 \cdot \left(\varepsilon_1 - \frac{\varepsilon_2}{4 \cdot \tan \alpha} \right) \cdot \left[\frac{1}{\cos \alpha} \cdot \left(\cos^2 \alpha + \sin^2 \alpha \right) \right]}$$

$$F_{2,\perp} = \frac{M}{h} \cdot \frac{\cos \alpha}{2 \cdot \left(\varepsilon_1 - \frac{\varepsilon_2}{4 \cdot \tan \alpha} \right)} \qquad 4\text{-}26$$

Observation on the resultant forces

Limit Case (i) = (ii)

The model (i) is the particular case of the model (ii) in which the applied force F = 0 (Figure 4-1).

Analysis of the μ_α

The eq. 4-20 gives a very important result for the definition of the friction value μ_α on the segment $\overline{AB}$ in case of pure bending. The effectiveness of the definition is demonstrated in the Chapter 6.4.2.3, TEST 8.

The eq. 4-20 is furthermore verified when:

$$\begin{cases} F_{2,//} = \dfrac{M \cdot \cos \alpha}{2 \cdot h \cdot \left(\varepsilon_1 - \dfrac{\varepsilon_2}{4 \cdot \tan \alpha} \right)} \cdot \mu_\alpha \geq 0 \\ F_{2,\perp} = \dfrac{M \cdot \cos \alpha}{2 \cdot h \cdot \left(\varepsilon_1 - \dfrac{\varepsilon_2}{4 \cdot \tan \alpha} \right)} > 0 \end{cases} \qquad 4\text{-}27$$

$$\begin{cases} \mu_\alpha \geq 0 \\ M > 0 \\ \alpha > 0 \\ \varepsilon_1 - \dfrac{\varepsilon_2}{4 \cdot \tan \alpha} > 0 \qquad GC(ii)1 \end{cases} \qquad 4\text{-}28$$

4.3.2 Boundary conditions

Geometry boundary conditions GC(i)

GC(i)1

The condition GC(i)1 is the same as the GC(ii)1 descripted in the eq. 4-55 and eq. 4-56.

Forces boundary conditions FC(i)

According to HP.1, it has to verify the conditions:

$$F_{1,\perp} \geq 0 \quad \cap \quad F_{2,\perp} \geq 0 \qquad 4\text{-}29$$

FC(i)1: $F_{1,\perp} \geq 0$

The general FC(i)1 condition is in accordance with the FC(ii)1.1 described in the eq. 4-62 for the FC(i)2.

FC(i)2: $F_{2,\perp} \geq 0$

The general condition, is in accordance with the eq. 4-69 and eq. 4-70 for the FC(ii)2.

4.3.3 Limit states

The model (i) provides the limit state LS2, associated with the FM II shear/tension perpendicular to the grain in the point B, valid for the eq. 4-31.

LS2(i):

$$F_{1,\perp} \leq F_f \qquad \text{4-30}$$

$$M \leq F_f \cdot 2 \cdot h \cdot \left(\varepsilon_1 - \frac{\varepsilon_2}{4 \cdot \tan \alpha} \right) \qquad \text{4-31}$$

4.4 Equilibrium configuration (ii): M>0 F>0

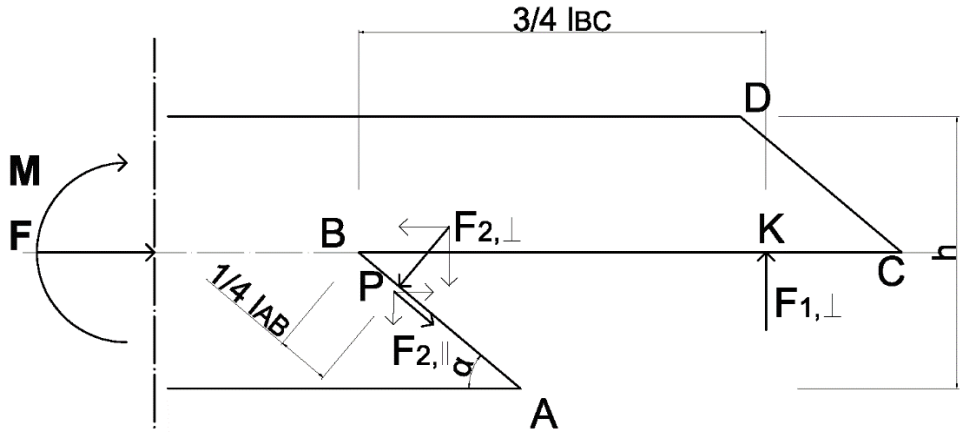

Figure 4-3 – Equilibrium Configuration (ii)

4.4.1 Resultant forces

HP

The model (ii) is valid for the external loading condition combined compressive and bending force:

$$M > 0; \qquad F > 0 \qquad \text{4-32}$$

And internal resultant forces:

$$F_{2,//} > 0; \qquad F_{2,\perp} > 0; \qquad F_{1,\perp} > 0; \qquad F_{1,//} = 0; \qquad F_{3,\perp} = 0; \qquad F_{3,//} = 0 \qquad \text{4-33}$$

Equilibrium Eq.:

$$\sum F_x = 0 \qquad \text{4-34}$$

$$F + F_{2,//,0} = F_{2,\perp,0}$$

$$F + F_{2,//} \cdot \cos\alpha = F_{2,\perp} \cdot \sin\alpha$$

$$F_{2,//} = F_{2,\perp} \cdot \frac{\sin\alpha}{\cos\alpha} - \frac{F}{\cos\alpha} \qquad \text{4-35}$$

$$\sum F_y = 0 \qquad \text{4-36}$$

$$F_{1,\perp} = F_{2,//,90} + F_{2,\perp,90}$$

$$F_{1,\perp} = F_{2,//} \cdot \sin\alpha + F_{2,\perp} \cdot \cos\alpha$$

$$F_{2,//} = \frac{F_{1,\perp}}{\sin\alpha} - F_{2,\perp} \cdot \frac{\cos\alpha}{\sin\alpha} \qquad \text{4-37}$$

From the equivalence of the eq. 4-35 and eq. 4-37 , it follows:

$$\frac{F_{1,\perp}}{\sin\alpha} - F_{2,\perp}\cdot\frac{\cos\alpha}{\sin\alpha} = F_{2,\perp}\cdot\frac{\sin\alpha}{\cos\alpha} - \frac{F}{\cos\alpha}$$

$$\frac{F_{1,\perp}}{\sin\alpha} + \frac{F}{\cos\alpha} = F_{2,\perp}\left(\frac{\sin^2\alpha + \cos^2\alpha}{\cos\alpha\cdot\sin\alpha}\right)$$

$$\frac{F_{1,\perp}}{\sin\alpha} + \frac{F}{\cos\alpha} = F_{2,\perp}\cdot\left(\frac{1}{\cos\alpha\cdot\sin\alpha}\right)$$

$$F_{2,\perp} = F_{1,\perp}\cdot\cos\alpha + F\cdot\sin\alpha \qquad \text{4-38}$$

$$F_{2,//} = \left(F_{1,\perp}\cdot\cos\alpha + F\cdot\sin\alpha\right)\cdot\frac{\sin\alpha}{\cos\alpha} - \frac{F}{\cos\alpha}$$

$$F_{2,//} = F_{1,\perp}\cdot\sin\alpha + F\cdot\left(\frac{\sin^2\alpha - 1}{\cos\alpha}\right)$$

$$F_{2,//} = F_{1,\perp}\cdot\sin\alpha - F\cdot\cos\alpha \qquad \text{4-39}$$

$$\sum M_P = 0 \qquad \text{4-40}$$

$$F_{1,\perp}\cdot e_{P,1} - M - F\cdot e_{P,F} = 0$$

Using the eq. 3-20 and eq. 3-23.

$$F_{1,\perp}\cdot\left[2\cdot h\cdot\left(\varepsilon_1 - \frac{\varepsilon_2}{4\cdot\tan\alpha}\right)\right] - M - F\cdot\left[\frac{h}{2}\cdot\left(\varepsilon_F - \varepsilon_2\right)\right] = 0$$

$$F_{1,\perp} = \frac{M + F\cdot\left[\frac{h}{2}\cdot\left(\varepsilon_F - \varepsilon_2\right)\right]}{\left[2\cdot h\cdot\left(\varepsilon_1 - \frac{\varepsilon_2}{4\cdot\tan\alpha}\right)\right]} \qquad \text{4-41}$$

Inserting the eq. 4-41 in the eq. 4-38, it follows:

$$F_{2,\perp} = \frac{M + F\cdot\left[\frac{h}{2}\cdot\left(\varepsilon_F - \varepsilon_2\right)\right]}{\left[2\cdot h\cdot\left(\varepsilon_1 - \frac{\varepsilon_2}{4\cdot\tan\alpha}\right)\right]}\cdot\cos\alpha + F\cdot\sin\alpha$$

$$F_{2,\perp} = \frac{M}{2\cdot h\cdot\left(\varepsilon_1 - \frac{\varepsilon_2}{4\cdot\tan\alpha}\right)}\cdot\cos\alpha + F\cdot\frac{\left[\frac{h}{2}\cdot\left(\varepsilon_F - \varepsilon_2\right)\right]}{2\cdot h\cdot\left(\varepsilon_1 - \frac{\varepsilon_2}{4\cdot\tan\alpha}\right)}\cdot\cos\alpha + F\cdot\sin\alpha$$

$$F_{2,\perp} = \frac{1}{2\cdot h\cdot\left(\varepsilon_1 - \frac{\varepsilon_2}{4\cdot\tan\alpha}\right)}\left\{M\cdot\cos\alpha + F\cdot\left[\frac{h}{2}\cdot\left(\varepsilon_F - \varepsilon_2\right)\cdot\cos\alpha + \sin\alpha\cdot 2\cdot h\cdot\left(\varepsilon_1 - \frac{\varepsilon_2}{4\cdot\tan\alpha}\right)\right]\right\}$$

$$F_{2,\perp} = \frac{\cos\alpha}{2\cdot\left(\varepsilon_1 - \frac{\varepsilon_2}{4\cdot\tan\alpha}\right)}\cdot\left\{\frac{M}{h} + 2\cdot F\cdot\left[\tan\alpha\cdot\left(\varepsilon_1 - \frac{\varepsilon_2}{4\cdot\tan\alpha}\right) + \frac{\left(\varepsilon_F - \varepsilon_2\right)}{4}\right]\right\} \qquad \text{4-42}$$

Considering

$$\mu_\alpha = \frac{F_{2,//}}{F_{2,\perp}} \qquad \text{4-43}$$

From the eq. 4-39 and eq. 4-38 , it follows the definition of μ_α:

$$\frac{F_{1,\perp}\cdot\sin\alpha - F\cdot\cos\alpha}{F_{1,\perp}\cdot\cos\alpha + F\cdot\sin\alpha} = \mu_\alpha \qquad 4\text{-}44$$

and a second definition of the internal force $F_{1,\perp}$:

$$F_{1,\perp} = F\cdot\frac{\cos\alpha + \mu_\alpha\cdot\sin\alpha}{\sin\alpha - \mu_\alpha\cdot\cos\alpha} \qquad 4\text{-}45$$

Observations on the resultant forces

Limit Case $F_{2,//} = 0$

The case $F_{2,//} = 0$ means the passage from positive values of μ_α , defined according to eq. 4-44 , to the case of null friction coefficient $\mu_\alpha = 0$ (unique configuration defined in the model (iii)).

$$F_{2,//} = F_{1,\perp}\cdot\sin\alpha - F\cdot\cos\alpha = 0 \qquad 4\text{-}46$$

$$\frac{M}{h} = 2\cdot F\cdot\left[\frac{1}{\tan\alpha}\cdot\left(\varepsilon_1 - \frac{\varepsilon_2}{4\cdot\tan\alpha}\right) - \frac{(\varepsilon_F - \varepsilon_2)}{4}\right] \qquad 4\text{-}47$$

The eq. 4-47 gives a further equilibrium condition for specimen with $\mu_\alpha = 0$.

Analysis of the μ_α

Considering the eq. 4-48 also for the model (ii) the μ_α is verified when the denominator is different from zero.

$$F_{2,\perp} \neq 0 \qquad 4\text{-}48$$

$$\frac{M}{h} \neq -2\cdot F\cdot\left[\tan\alpha\cdot\left(\varepsilon_1 - \frac{\varepsilon_2}{4\cdot\tan\alpha}\right) - \frac{(\varepsilon_F - \varepsilon_2)}{4}\right] \qquad 4\text{-}49$$

The eq. 4-49 is in accordance with the FC(ii)2 ($F_{2,\perp} \neq 0$), and demonstrates the (Hp. 1).

If the nominator is null, then $\mu_\alpha = 0$ (Limit case $F_{2,//} = 0$).

$$F_{2,//} = \frac{M}{h} + 2\cdot F\cdot\left[\frac{(\varepsilon_F - \varepsilon_2)}{4} + \frac{1}{\tan\alpha}\cdot\left(\varepsilon_1 - \frac{\varepsilon_2}{4\cdot\tan\alpha}\right)\right] = 0 \qquad 4\text{-}50$$

it follows:

$$F_{2,//} = 0 \Rightarrow \mu_\alpha = 0$$

The eq. 4-50 is in accordance with the LIMIT CASE $F_{2,//} = 0$ and demonstrate the continuity between positive and negative values of μ_α (Hp. 2).

Equilibrium condition on the (ii)*:*

Both the eq. 4-41 and eq. 4-45 give a definition of $F_{1,\perp}$. From the equivalence of both, the equilibrium condition is obtained:

$$F_{1,\perp} = F\cdot\frac{\cos\alpha + \mu_\alpha\cdot\sin\alpha}{\sin\alpha - \mu_\alpha\cdot\cos\alpha} = \frac{M + F\cdot\left[\frac{h}{2}\cdot(\varepsilon_F - \varepsilon_2)\right]}{\left[2\cdot h\cdot\left(\varepsilon_1 - \frac{\varepsilon_2}{4\cdot\tan\alpha}\right)\right]} \qquad 4\text{-}51$$

$$F \cdot \left[\frac{\cos\alpha + \mu_\alpha \cdot \sin\alpha}{\sin\alpha - \mu_\alpha \cdot \cos\alpha} - \frac{\frac{h}{2} \cdot \left(\varepsilon_F - \varepsilon_2\right)}{2 \cdot h \cdot \left(\varepsilon_1 - \frac{\varepsilon_2}{4 \cdot \tan\alpha}\right)} \right] = \frac{M}{2 \cdot h \cdot \left(\varepsilon_1 - \frac{\varepsilon_2}{4 \cdot \tan\alpha}\right)}$$

$$F = \frac{M}{2 \cdot h \cdot \left(\varepsilon_1 - \frac{\varepsilon_2}{4 \cdot \tan\alpha}\right)} \cdot \frac{1}{\left[\frac{\cos\alpha + \mu_\alpha \cdot \sin\alpha}{\sin\alpha - \mu_\alpha \cdot \cos\alpha} - \frac{\frac{h}{2} \cdot \left(\varepsilon_F - \varepsilon_2\right)}{2 \cdot h \cdot \left(\varepsilon_1 - \frac{\varepsilon_2}{4 \cdot \tan\alpha}\right)} \right]}$$

$$F = \frac{\frac{M}{h}}{\left[2 \cdot \left(\varepsilon_1 - \frac{\varepsilon_2}{4 \cdot \tan\alpha}\right) \cdot \left(\frac{\cos\alpha + \mu_\alpha \cdot \sin\alpha}{\sin\alpha - \mu_\alpha \cdot \cos\alpha} \right) - \frac{\left(\varepsilon_F - \varepsilon_2\right)}{2} \right]} \qquad 4\text{-}52$$

The equilibrium equation eq. 4-52 LS1(ii): $f\left(\mu_\alpha;\varepsilon_1;\varepsilon_2;\varepsilon_3;\varepsilon_{F,}N;M\right)$ describes the equilibrium path followed by the specimen along the loading process until failure (demonstration with the Chapter 6.7 TEST 13).

4.4.2 Boundary conditions:

Geometric boundary conditions GC(ii)

GC(ii)1

The eq. 4-53 represents the configuration in which the direction of the vector-resultant-force $F_{1,\perp}$ is tangent to P, point of application of the resultant force $F_{2,\perp}$, which is considered as point of rotation for the equilibrium to the moment.

$$e_{P,1} = 0 \qquad 4\text{-}53$$

$$2 \cdot h \cdot \left(\varepsilon_1 - \frac{\varepsilon_2}{4 \cdot \tan\alpha}\right) = 0$$

$$\left(\varepsilon_1 - \frac{\varepsilon_2}{4 \cdot \tan\alpha}\right) = 0$$

$$\varepsilon_1 = \frac{\varepsilon_2}{4 \cdot \tan\alpha} \qquad 4\text{-}54$$

The condition expressed in the eq. 4-54 is represented in the Diagram 4-2 for angles $0° \le \alpha \le 90°$. The function on the diagram represents the geometric configuration where the alignment of the line of force of $F_{1,\perp}$ with the point P, confers the connection no internal resultant moment (demonstrate in the Chapter 6.3.3 TEST 3).

Thus, the condition GC(ii)1 for the effectiveness of the joint is given by eq. 4-55 and eq. 4-56.

$$e_{P,1} > 0 \qquad 4\text{-}55$$

$$\varepsilon_1 > \frac{\varepsilon_2}{4 \cdot \tan\alpha} \qquad 4\text{-}56$$

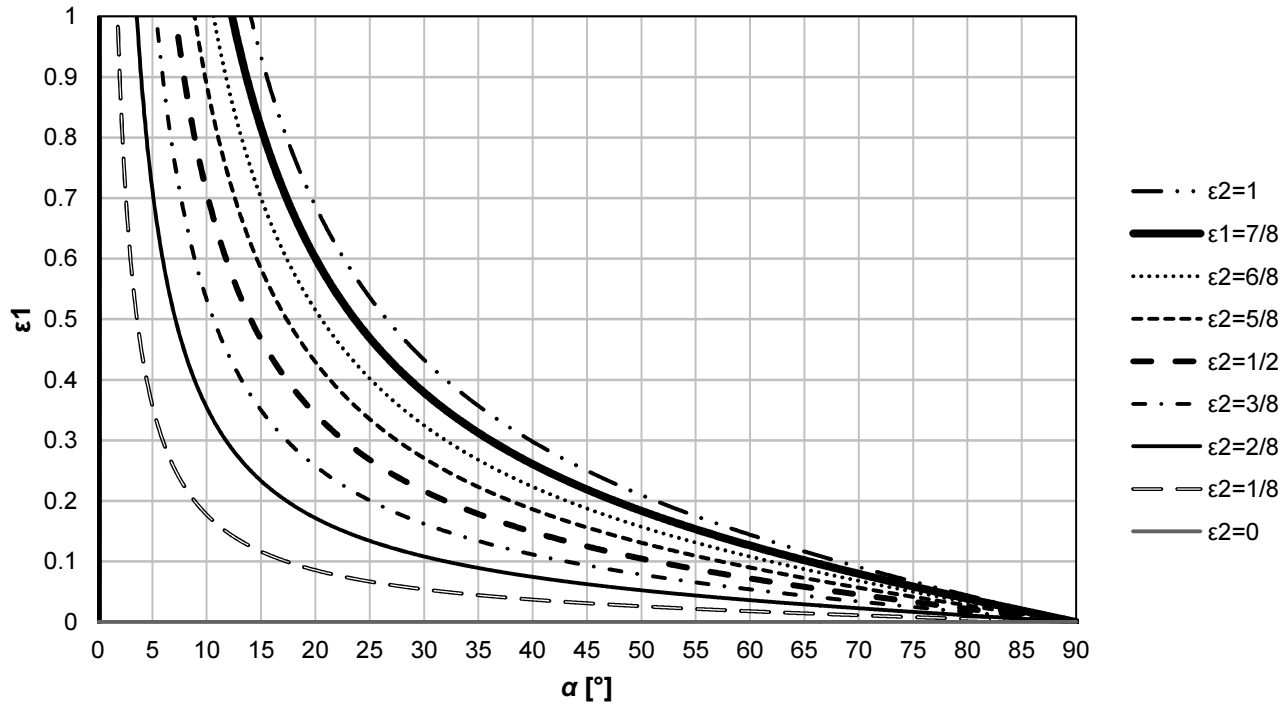

Diagram 4-2 – GC(ii)1 Alignment configuration.

Loss of load-bearing resistance for angles $0 \le \alpha \le 90$. $f(\varepsilon_2, \alpha): \varepsilon_1 = \frac{\varepsilon_2}{(4 \cdot \tan\alpha)}$.

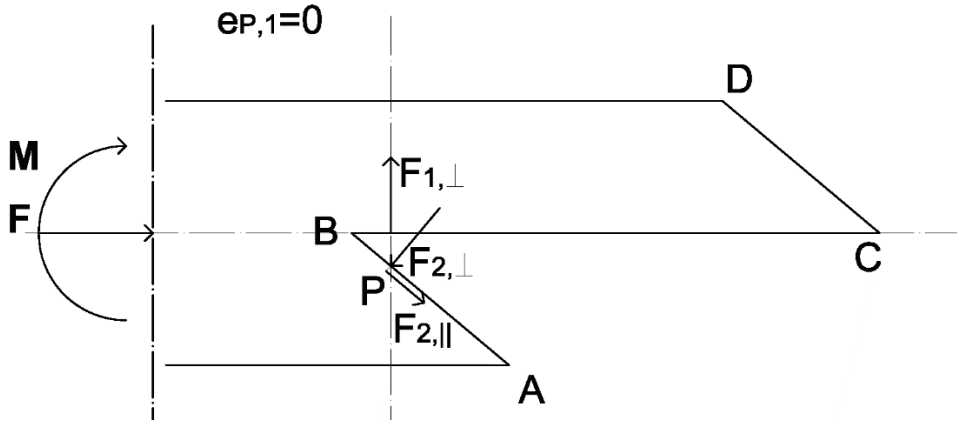

Figure 4-4 - GC(ii)1 Loss of load-bearing resistance. Position of the parameter $e_{P,1} = 0$

Forces boundary conditions FC(ii)

According to Hp.1 it has to verify the conditions:

$$F_{1,\perp} \ge 0 \quad \cap \quad F_{2,\perp} \ge 0 \qquad \text{4-57}$$

FC(ii)1.1: $F_{1,\perp} \ge 0$

The inequality eq. 4-58 describes the limit of validity of the static model according to the basic hypothesis of compression on the joint's surfaces for the first definition of the force $F_{1,\perp}$**:**

$$\frac{M - F \cdot \left[\frac{h}{2} \cdot (\varepsilon_F - \varepsilon_2)\right]}{2 \cdot h \cdot \left(\varepsilon_1 - \frac{\varepsilon_2}{4 \cdot \tan\alpha}\right)} \ge 0 \qquad \text{4-58}$$

In accordance with the geometric condition GC(ii)1 , the denominator is always bigger than zero (eq. 4-55 and eq. 4-56); therefore, the FC(ii)1.1 is determined by:

$$M - F \cdot \left[\frac{h}{2} \cdot \left(\varepsilon_F - \varepsilon_2 \right) \right] \geq 0 \qquad 4\text{-}59$$

The value of the parameters is following defined:

$$\varepsilon_F = 0 \qquad 4\text{-}60$$

$$0 < \varepsilon_2 \leq 1 \qquad 4\text{-}61$$

results:

$$F \geq -\frac{2 \cdot M}{h \cdot \varepsilon_2} \qquad 4\text{-}62$$

The value of the force F has to be always a positive value.

FC(ii)1.2: $F_{1,\perp} \geq 0$

The inequality eq. 4-63 describes the limit of validity of the static model according to the basic hypothesis of compression on the joint's surfaces for the second definition of the force $F_{1,\perp}$ (eq. 4-45):

$$\frac{\cos \alpha + \mu_\alpha \cdot \sin \alpha}{\sin \alpha - \mu_\alpha \cdot \cos \alpha} \geq 0 \qquad 4\text{-}63$$

Two solutions S1 and S2 follow.

The first solution is:

$$\text{S1: } \begin{cases} \cos\alpha + \mu_\alpha \cdot \sin\alpha \geq 0 \\ \sin\alpha - \mu_\alpha \cdot \cos\alpha > 0 \end{cases} \qquad 4\text{-}64$$

$$\text{S1: } \begin{cases} -\dfrac{1}{\tan\alpha} \leq \mu_\alpha \\ \tan\alpha > \mu_\alpha \end{cases}$$

$$\text{S1: } -\frac{1}{\tan\alpha} \leq \mu_\alpha < \tan\alpha \qquad 4\text{-}65$$

The second solution is:

$$\text{S2: } \begin{cases} \cos\alpha + \mu_\alpha \cdot \sin\alpha \leq 0 \\ \sin\alpha - \mu_\alpha \cdot \cos\alpha < 0 \end{cases} \qquad 4\text{-}66$$

$$\text{S2: } \begin{cases} -\dfrac{1}{\tan\alpha} \geq \mu_\alpha \\ \tan\alpha < \mu_\alpha \end{cases}$$

$$\text{S2: } \mu_\alpha \leq -\frac{1}{\tan\alpha} \cup \mu_\alpha > \tan\alpha \qquad 4\text{-}67$$

This condition expressed by the FC(ii)1.2 is very important for the definition of the limit of validity of the model in connection with the values of friction μ_α on the surface 2. The eq. 4-65 and eq. 4-67 define the variation of the static friction μ_α along the loading process. The variation for the single connection with the specific inclination of α is plotted in the Diagram 4-3 and Diagram 4-4.

The variation of the friction values along the loading and in dependence of the angle is demonstrated in the Chapter 6.4.2.2 TEST 7).

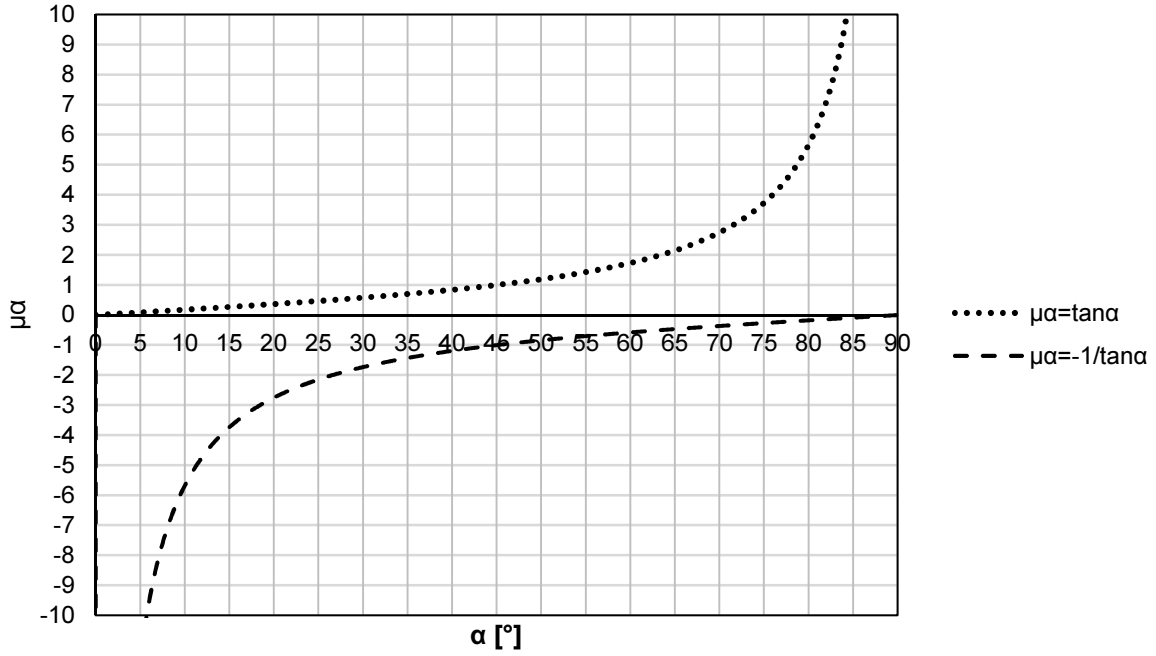

Diagram 4-3 – FC(ii)1.2. Variation of μ_α for angles 0° ≤ *α* ≤ 90°

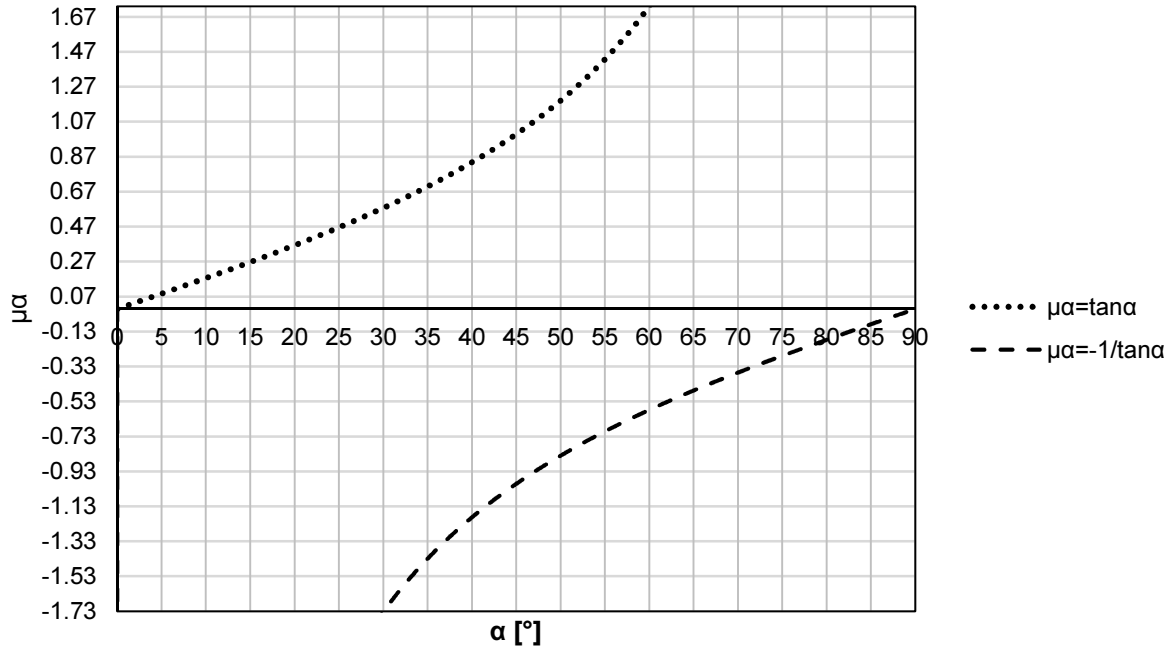

Diagram 4-4 - FC1.2 variation of μ_α for angles 0°≤ *α* ≤90° - zoom

FC(ii)2: $F_{2,\perp} \geq 0$

The inequality eq. 4-68 describes the limit of validity of the static model according to the basic hypothesis of compression on the joint's surfaces for the first definition of the force $F_{2,\perp}$:

$$F_{2,\perp} = \frac{\cos\alpha}{2\cdot\left(\varepsilon_1 - \frac{\varepsilon_2}{4\cdot\tan\alpha}\right)}\cdot\left\{\frac{M}{h} + 2\cdot F\cdot\left[\tan\alpha\cdot\left(\varepsilon_1 - \frac{\varepsilon_2}{4\cdot\tan\alpha}\right) + \frac{(\varepsilon_F - \varepsilon_2)}{4}\right]\right\} \geq 0 \qquad 4\text{-}68$$

$$\text{S1:}\begin{cases} \varepsilon_1 - \dfrac{\varepsilon_2}{4\cdot\tan\alpha} > 0 \\ \cos\alpha > 0 \\ \dfrac{M}{h} + 2\cdot F\cdot\left[\tan\alpha\cdot\left(\varepsilon_1 - \dfrac{\varepsilon_2}{4\cdot\tan\alpha}\right) + \dfrac{(\varepsilon_F - \varepsilon_2)}{4}\right] \geq 0 \end{cases} \qquad 4\text{-}69$$

$\varepsilon_1 - \frac{\varepsilon_2}{4\cdot\tan\alpha} > 0$ is verified by the eq. 4-56, GC(ii)1.

$\cos\alpha \geq 0$ is always positive.

$$\frac{M}{h} + 2\cdot F\cdot\left[\tan\alpha\cdot\left(\varepsilon_1 - \frac{\varepsilon_2}{4\cdot\tan\alpha}\right) + \frac{(\varepsilon_F - \varepsilon_2)}{4}\right] \geq 0 \qquad 4\text{-}70$$

When the eq. 4-70 is equal to zero, the equilibrium equation for the model (ii) and (iii) ($F_{2,//} = 0$) expressed in the eq. 4-47, is verified.

4.4.3 Limit states

The static model provides three limit states (LS):

- LS1: it is described by the equilibrium equation described by the equilibrium eq. 4-71. Critical parameters that bring to the failure are geometric parameters.
- LS2 and LS3: are the equilibrium states associated with the failure mode II (FM II) shear/tension perpendicular to the grain in B, and failure mode III (FM III) shear/tension perpendicular to the grain in point B and C, valid for the eq. 4-73 and eq. 4-75. The critical parameters that bring to the failure are the strength and stiffness of the material and geometric parameters. The Gustaffson ultimate values F_f associated with that failure modes are the $F_{f,B}$ and the $F_{f,C}$ (see Chapter 3.7.2 eq. 3-55 and eq. 3-56).

LS1(ii):

From the eq. 4-52 the limit state (or equilibrium state) LS1 is described in the equivalent eq. 4-71. This equilibrium equation describes the loading path of the specimen demonstrated in the Chapter 6.7 TEST 13, according to values of μ_α in the eq. 4-44.

$$\text{LS1(ii):}\quad F = \frac{\frac{M}{h}}{\left[2\cdot\left(\varepsilon_1 - \frac{\varepsilon_2}{4\cdot\tan\alpha}\right)\cdot\left(\frac{\cos\alpha + \mu_\alpha\cdot\sin\alpha}{\sin\alpha - \mu_\alpha\cdot\cos\alpha}\right) - \frac{(\varepsilon_F - \varepsilon_2)}{2}\right]} \qquad 4\text{-}71$$

LS2(ii):

From the eq. 4-51:

$$F_{1,\perp} = \frac{M + F\cdot\left[\frac{h}{2}\cdot(\varepsilon_F - \varepsilon_2)\right]}{\left[2\cdot h\cdot\left(\varepsilon_1 - \frac{\varepsilon_2}{4\cdot\tan\alpha}\right)\right]} \leq F_f \qquad 4\text{-}72$$

LS2(ii): $F \le \frac{2}{(\varepsilon_F - \varepsilon_2)} \cdot \left[2 \cdot F_f \cdot \left(\varepsilon_1 - \frac{\varepsilon_2}{4 \cdot \tan\alpha} \right) - \frac{M}{h} \right]$ 4-73

In the LS2, it is contained the information about the position of the point of application of the resultant forces $F_{1,\perp}$ and $F_{2,\perp}$. It is clear how the position of these two forces are of basic importance for the description of the load-carrying capacity of the connection. With the changing of position of the parameter ε_1 or ε_2, the load-carrying capacity of the joint increases (the increasing of the load-carrying capacity of the joint in function of the positioning of the internal forces is demonstrated in the TESTS 1, 2, 3 contained in the Chapter 6.3).

LS3(ii):

In the LS3 (from the eq. 4-51) the basic information is the value of static friction μ_α and the amount of applied external force *F* are contained.

$$F_{1,\perp} = F \cdot \frac{\cos\alpha + \mu_\alpha \cdot \sin\alpha}{\sin\alpha - \mu_\alpha \cdot \cos\alpha} \le F_f \qquad 4\text{-}74$$

LS3(ii): $F \cdot \frac{\cos\alpha + \mu_\alpha \cdot \sin\alpha}{\sin\alpha - \mu_\alpha \cdot \cos\alpha} \le F_f$ 4-75

In this case the load-bearing behaviour is determined by the inclination of the squint and the consequent friction coefficient.

The condition to satisfy the condition $F \le F_f$ is:

$$\frac{\sin\alpha - \mu_\alpha \cdot \cos\alpha}{\cos\alpha + \mu_\alpha \cdot \sin\alpha} \ge 0 \qquad 4\text{-}76$$

The solution of the eq. 4-76 is a condition that is described in the eq. 4-65 of the FC(ii)1.2. In the Diagram 4-3 and Diagram 4-4, the inner area between the two function is the area of admissible values for μ_α in the model (ii). The variation of the friction values along the loading and in dependence of the angle is demonstrated in the Chapter 6.4.2.2 TEST 7.

4.5 Equilibrium configuration (iii): M>0 F>0

The model (iii) correspond to the single configuration $\mu_\alpha = 0$ for the model (ii).

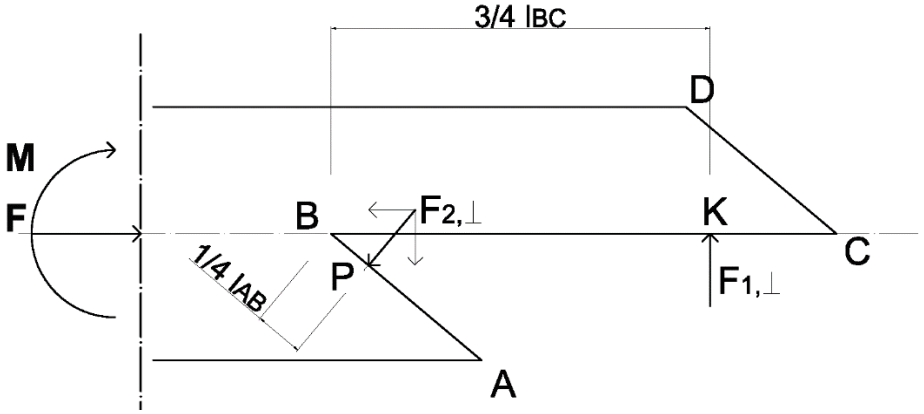

Figure-4-5 – Equilibrium Configuration (iii)

Observation on the resultant forces

The model (iii) is the particular case of the model (ii), the unique configuration $\mu_\alpha = 0$ ($F_{2,//} = 0$) represented in the Figure-4-5.

4.6 Equilibrium configuration (vii): M>0 F>0

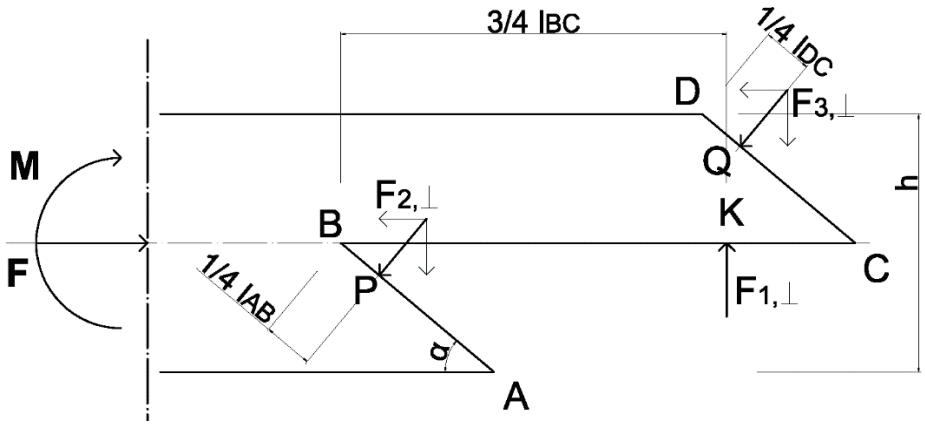

Figure-4-6 – Equilibrium Configuration (vii)

4.6.1 Resultant forces

HP

The model (vii) is valid for external loading conditions combined bending and compressive force, and pure compression:

$$M > 0; \qquad F > 0 \tag{4-77}$$

And internal resultant forces:

$$F_{2,//} = 0; \qquad F_{2,\perp} > 0; \qquad F_{1,\perp} > 0; \qquad F_{1,//} = 0; \qquad F_{3,\perp} > 0; \qquad F_{3,//} = 0 \tag{4-78}$$

Equilibrium Eq.:

$$\sum F_x = 0 \tag{4-79}$$

$$F = F_{2,\perp,0} + F_{3,\perp,0}$$

$$F = F_{2,\perp} \cdot \sin\alpha + F_{3,\perp} \qquad F_{2,\perp} = \frac{F}{\sin\alpha} - F_{3,\perp} \tag{4-80}$$

$$F_{2,\perp} = \left(F - F_{3,\perp} \cdot \sin\alpha\right) \cdot \frac{1}{\sin\alpha}$$

$$\sum M_P = 0 \tag{4-81}$$

$$M + F_{3,\perp} \cdot e_{P,3} + F \cdot \left(\varepsilon_F \cdot \frac{h}{2} - \varepsilon_2 \cdot \frac{h}{2}\right) = F_{1,\perp} \cdot e_{P,1}$$

$$M + F_{3,\perp} \cdot 2 \cdot h \cdot \left(\cos\alpha - \frac{\varepsilon_2 + \varepsilon_3}{4 \cdot \sin\alpha}\right) + F \cdot \frac{h}{2} \cdot \left(\varepsilon_F - \varepsilon_2\right) = F_{1,\perp} \cdot 2 \cdot h \cdot \left(\varepsilon_1 - \frac{\varepsilon_2}{4 \cdot \tan\alpha}\right)$$

$$F_{3,\perp} = \left[-F \cdot \frac{h}{2} \cdot \left(\varepsilon_F - \varepsilon_2\right) + F_{1,\perp} \cdot 2 \cdot h \cdot \left(\varepsilon_1 - \frac{\varepsilon_2}{4 \cdot \tan\alpha}\right) - M\right] \cdot \frac{1}{2 \cdot h \cdot \left(\cos\alpha - \frac{\varepsilon_2 + \varepsilon_3}{4 \cdot \sin\alpha}\right)} \tag{4-82}$$

$$\sum F_y = 0 \tag{4-83}$$

$$F_{1,\perp} = F_{2,\perp,90} + F_{3,\perp,90}$$

$$F_{1,\perp} = F_{2,\perp} \cdot \cos\alpha + F_{3,\perp} \cdot \cos\alpha$$

$$F_{1,\perp} = \left(\frac{F}{\sin\alpha} - F_{3,\perp}\right) \cdot \cos\alpha + F_{3,\perp} \cdot \cos\alpha$$

$$F_{1,\perp} = \frac{F}{\tan\alpha} \qquad \text{4-84}$$

Completing the eq. 4-82 with the eq. 4-84:

$$F_{3,\perp} = \left[-F \cdot \frac{h}{2} \cdot (\varepsilon_F - \varepsilon_2) + \frac{F \cdot 2 \cdot h}{\tan\alpha} \cdot \left(\varepsilon_1 - \frac{\varepsilon_2}{4 \cdot \tan\alpha} \right) - M \right] \cdot \frac{1}{2 \cdot h \cdot \left(\cos\alpha - \frac{\varepsilon_2 + \varepsilon_3}{4 \cdot \sin\alpha} \right)} \qquad \text{4-85}$$

$$F_{3,\perp} = \left[-\frac{F}{4} \cdot (\varepsilon_F - \varepsilon_2) + \frac{F}{\tan\alpha} \cdot \left(\varepsilon_1 - \frac{\varepsilon_2}{4 \cdot \tan\alpha} \right) - \frac{M}{2 \cdot h} \right] \cdot \frac{1}{\left(\cos\alpha - \frac{\varepsilon_2 + \varepsilon_3}{4 \cdot \sin\alpha} \right)}$$

$$F_{3,\perp} = \left\{ F \cdot \left[-\frac{(\varepsilon_F - \varepsilon_2)}{4} + \frac{1}{\tan\alpha} \cdot \left(\varepsilon_1 - \frac{\varepsilon_2}{4 \cdot \tan\alpha} \right) \right] - \frac{M}{2 \cdot h} \right\} \cdot \frac{1}{\left(\cos\alpha - \frac{\varepsilon_2 + \varepsilon_3}{4 \cdot \sin\alpha} \right)} \qquad \text{4-86}$$

And inserting the eq. 4-86 in the eq. 4-80:

$$F_{2,\perp} = \frac{F}{\sin\alpha} - \left\{ F \cdot \left[-\frac{(\varepsilon_F - \varepsilon_2)}{4} + \frac{1}{\tan\alpha} \cdot \left(\varepsilon_1 - \frac{\varepsilon_2}{4 \cdot \tan\alpha} \right) \right] - \frac{M}{2 \cdot h} \right\} \cdot \frac{1}{\left(\cos\alpha - \frac{\varepsilon_2 + \varepsilon_3}{4 \cdot \sin\alpha} \right)} \qquad \text{4-87}$$

$$F_{2,\perp} = F \cdot \left\{ \frac{1}{\sin\alpha} - \frac{\left[\frac{(\varepsilon_2 - \varepsilon_F)}{4} + \frac{1}{\tan\alpha} \cdot \left(\varepsilon_1 - \frac{\varepsilon_2}{4 \cdot \tan\alpha} \right) \right]}{\left(\cos\alpha - \frac{\varepsilon_2 + \varepsilon_3}{4 \cdot \sin\alpha} \right)} \right\} + \frac{\frac{M}{2 \cdot h}}{\left(\cos\alpha - \frac{\varepsilon_2 + \varepsilon_3}{4 \cdot \sin\alpha} \right)} \qquad \text{4-88}$$

Observation to the resultant forces

Limit Case (vii) = (iii) $F_{3,\perp} = 0$

The case expressed in the eq. 4-89 represents the passage from this model to the model (ii) where (Hp. 2) the presence of a friction force $F_{2,//}$ is considered on the surface $\overline{AB}$.

$$F_{3,\perp} = 0 \qquad \text{4-89}$$

$$F_{3,\perp} = \left\{ F \cdot \left[-\frac{(\varepsilon_F - \varepsilon_2)}{4} + \frac{1}{\tan\alpha} \cdot \left(\varepsilon_1 - \frac{\varepsilon_2}{4 \cdot \tan\alpha} \right) \right] - \frac{M}{2 \cdot h} \right\} \cdot \frac{1}{\left(\cos\alpha - \frac{\varepsilon_2 + \varepsilon_3}{4 \cdot \sin\alpha} \right)} = 0$$

$$\left\{ F \cdot \left[-\frac{(\varepsilon_F - \varepsilon_2)}{4} + \frac{1}{\tan\alpha} \cdot \left(\varepsilon_1 - \frac{\varepsilon_2}{4 \cdot \tan\alpha} \right) \right] \right\} = \frac{M}{2 \cdot h}$$

$$\frac{M}{h} = 2 \cdot F \cdot \left[-\frac{(\varepsilon_F - \varepsilon_2)}{4} + \frac{1}{\tan\alpha} \cdot \left(\varepsilon_1 - \frac{\varepsilon_2}{4 \cdot \tan\alpha} \right) \right] \qquad \text{4-90}$$

The present eq. 4-89 confirms the equilibrium condition LS1 in the (ii) when $\mu_\alpha = 0$ (see eq. 4-47).

4.6.2 Boundary conditions

Geometry boundary conditions GC(vii)

GC(vii)1

The geometry boundary condition GC(vii)1:

$$e_{P,1} > 0 \qquad \text{4-91}$$

is demonstrated under the same conditions demonstrated in the GC(ii)1. This condition is described in eq. 4-55 and eq. 4-56.

GC(vii)2

The parameter $e_{P,3}$ describes the lever arm between the forces $F_{3,\perp}$ and the internal rotation point considered in P (eq. 4-92).

$$e_{P,3} = 2 \cdot h \cdot \left(\cos \alpha - \frac{\varepsilon_2 + \varepsilon_3}{4 \cdot \sin \alpha} \right) \qquad \text{4-92}$$

$$e_{P,3} = 2 \cdot h \cdot \left(\cos \alpha - \frac{\varepsilon_2 + \varepsilon_3}{4 \cdot \sin \alpha} \right) = 0 \qquad \text{4-93}$$

$$4 \cdot \sin \alpha \cdot \cos \alpha = \varepsilon_2 + \varepsilon_3$$

$$2 \cdot \sin(2\alpha) = \varepsilon_2 + \varepsilon_3 \qquad \text{4-94}$$

The eq. 4-94 is represented in the following Diagram 4-5. Furthermore, different load-carrying capacity is shown in the configurations described in the following three cases:

a) $e_{P,3} > 0$ the $F_{3,\perp}$ sum up with the external moment M

b) $e_{P,3} = 0$, the force $F_{3,\perp}$ doesn't influence the external applied moment M

c) $e_{P,3} < 0$ the $F_{3,\perp}$ subtract the external moment M (for big *α*) and it contributes reducing the rotation of the connection caused by M.

To improve the load-carrying capacity the joint has to satisfy the condition following expressed in the case a). Thus, the GC(vii)2 is the one of the following eq. 4-95:

$$2 \cdot \sin(2\alpha) > \varepsilon_2 + \varepsilon_3 \qquad \text{4-95}$$

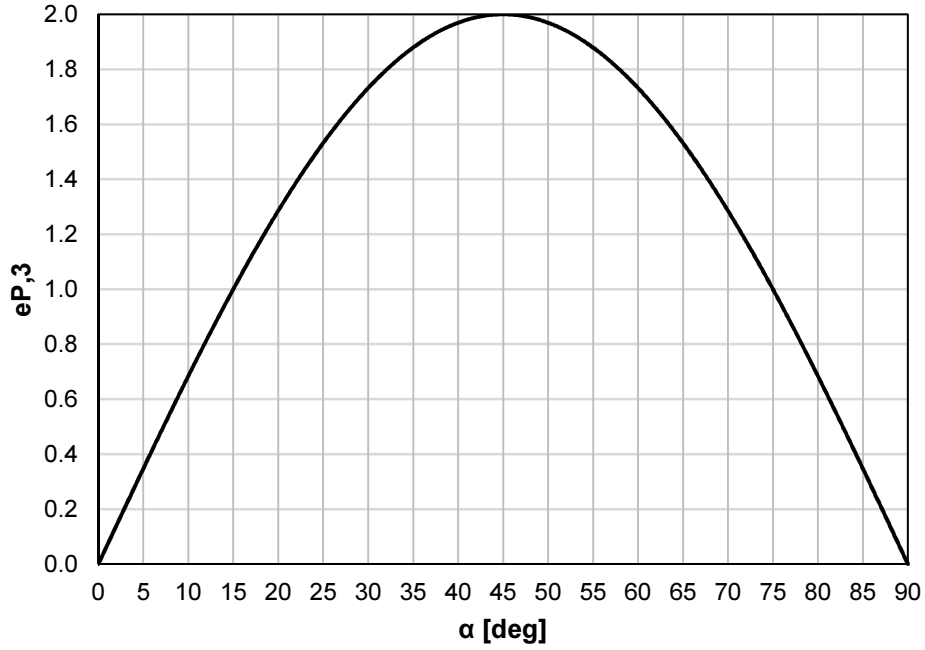

Diagram 4-5 - GC(vii)2 = GC(vii)3. Loss of load-carrying capacity of the joint for squint 0° ≤ *α* ≤ 90° described by the $f(\alpha): 2 \cdot \sin(2\alpha) = \varepsilon_2 + \varepsilon_3$

GC(vii)3

Furthermore, in case of alignment of the forces $F_{1,\perp}$ - $F_{2,\perp}$ - $F_{3,\perp}$, the load-carrying capacity of the connection is null, independently on the load-bearing conditions (this assertion is demonstrated in Chapter 6.3.4, TEST 4).

The alignment is verified when:

$$\begin{cases} e_{O,P} = 0 \\ e_{P,3} = 0 \end{cases} \qquad \text{4-96}$$

$$\begin{cases} e_{O,P} = 2 \cdot h \cdot \left(\varepsilon_1 \cdot \cos\alpha - \varepsilon_2 \cdot \dfrac{1}{4 \cdot \sin\alpha} \right) = 0 \\ e_{P,3} = 2 \cdot h \cdot \left(\cos\alpha - \dfrac{\varepsilon_2 + \varepsilon_3}{4 \cdot \sin\alpha} \right) = 0 \end{cases}$$

$$\begin{cases} \varepsilon_2 = 4 \cdot \varepsilon_1 \cdot \cos\alpha \cdot \sin\alpha \\ 4 \cdot \cos\alpha \cdot \sin\alpha = \varepsilon_2 + \varepsilon_3 \end{cases}$$

$$\begin{cases} \varepsilon_2 = 4 \cdot \varepsilon_1 \cdot \cos\alpha \cdot \sin\alpha \\ 4 \cdot \cos\alpha \cdot \sin\alpha = 4 \cdot \varepsilon_1 \cdot \cos\alpha \cdot \sin\alpha + \varepsilon_3 \end{cases}$$

$$\text{S1 U S2} \begin{cases} \varepsilon_3 = 2 \cdot (1 - \varepsilon_1) \cdot \sin(2\alpha) \\ 2 \cdot \sin(2\alpha) = \varepsilon_2 + \varepsilon_3 \end{cases} \qquad \text{4-97}$$

The S1 represents the alternative condition under which the alignment is possible. The S2 is the condition under the GC(vii)2.

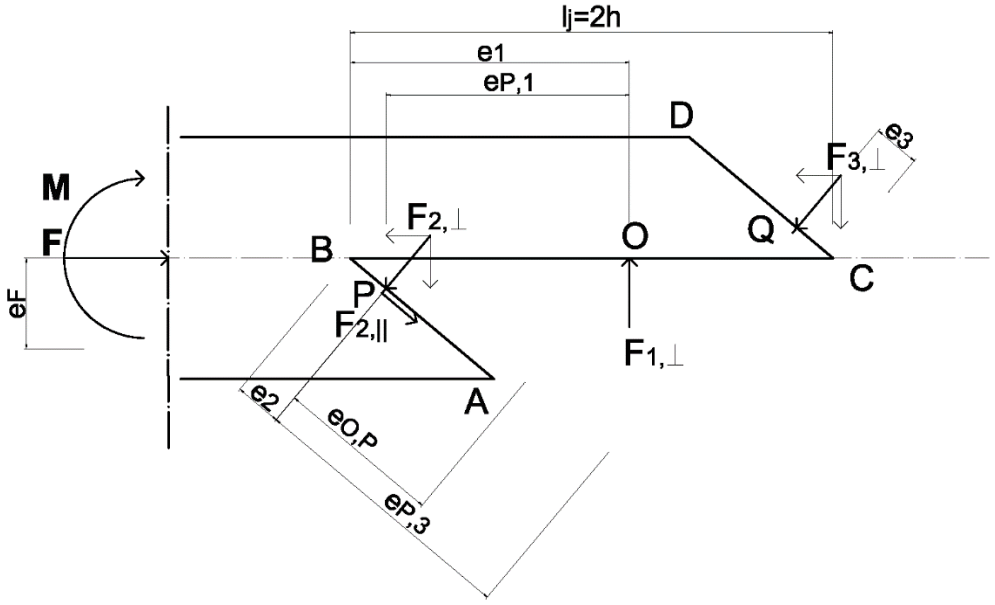

Figure 4-7 – GC(vii)3. Loss of load-bearing resistance of the joint.
Position of the parameters $e_{O,P}$ *and* $e_{P,3}$.

Forces boundary conditions FC(vii):

It has to verify the conditions:

$$F_{1,\perp} \geq 0 \quad \cap \quad F_{2,\perp} \geq 0 \quad \cap \quad F_{3,\perp} \geq 0 \qquad \text{4-98}$$

FC(vii)1:

$$F_{1,\perp} \geq 0 \qquad \text{4-99}$$

$$F \geq 0 \quad for \quad 0° \leq \alpha < 90° \qquad \text{4-100}$$

FC(vii) 2:

$$F_{2,\perp} \geq 0 \qquad \text{4-101}$$

$$F \cdot \left(\cos\alpha - \frac{\varepsilon_2 + \varepsilon_3}{4 \cdot \sin\alpha} \right) \cdot \left\{ \frac{1}{\sin\alpha} - \frac{\left[\frac{(\varepsilon_2 - \varepsilon_F)}{4} + \frac{1}{\tan\alpha} \cdot \left(\varepsilon_1 - \frac{\varepsilon_2}{4 \cdot \tan\alpha} \right) \right]}{\left(\cos\alpha - \frac{\varepsilon_2 + \varepsilon_3}{4 \cdot \sin\alpha} \right)} \right\} \geq -\frac{M}{2 \cdot h} \qquad \text{4-102}$$

In the inequality:

$\left(\cos\alpha - \frac{\varepsilon_2 + \varepsilon_3}{4 \cdot \sin\alpha} \right) > 0$, always according to eq. 4-95

$M>0,\ F>0$ always according to eq. 4-77

It follows that the condition eq. 4-101 is satisfied.

FC(vii)3:

$$F_{3,\perp} \geq 0 \qquad \text{4-103}$$

$$F \cdot \left[-\frac{(\varepsilon_F - \varepsilon_2)}{4} + \frac{1}{\tan\alpha} \cdot \left(\varepsilon_1 - \frac{\varepsilon_2}{4 \cdot \tan\alpha} \right) \right] \geq \frac{M}{2 \cdot h} \qquad \text{4-104}$$

In the inequality:

$\left(\cos\alpha - \frac{\varepsilon_2 + \varepsilon_3}{4 \cdot \sin\alpha} \right) > 0$, always according to eq. 4-95

$M>0,\ F>0$ always according to eq. 4-77

It follows that the condition in the eq. 4-103 is satisfied.

The case $F_{3,\perp} \geq 0$ is further confirmed by the eq. 4-105 that is equal to the eq. 4-90.

$$\frac{M}{h} = F \cdot 2 \cdot \left[\frac{(\varepsilon_F - \varepsilon_2)}{4} + \frac{1}{\tan\alpha} \cdot \left(\varepsilon_1 - \frac{\varepsilon_2}{4 \cdot \tan\alpha} \right) \right] \qquad \text{4-105}$$

4.6.3 Limit states

LS4(vii): Failure mode: Shear/Tension perpendicular to the grain in the points B and C

In general, the failure criteria is:

$$\begin{cases} F_{2,\perp} \cdot \cos\alpha \leq F_{f,B} \\ F_{3,\perp} \cdot \cos\alpha \leq F_{f,C} \end{cases} \qquad \text{4-106}$$

FRACTURE IN B:

$$F_{2,\perp} \cdot \cos\ \alpha\ \leq F_{f,\mathbf{B}} \qquad \text{4-107}$$

$$F \cdot \cos\alpha \cdot \left\{ \frac{1}{\sin\alpha} - \frac{\left[\frac{(\varepsilon_2 - \varepsilon_F)}{4} + \frac{1}{\tan\alpha} \cdot \left(\varepsilon_1 - \frac{\varepsilon_2}{4 \cdot \tan\alpha} \right) \right]}{\left(\cos\alpha - \frac{\varepsilon_2 + \varepsilon_3}{4 \cdot \sin\alpha} \right)} \right\} + \frac{M}{2 \cdot h} \cdot \frac{\cos\alpha}{\left(\cos\alpha - \frac{\varepsilon_2 + \varepsilon_3}{4 \cdot \sin\alpha} \right)} \leq F_{f,B} \qquad \text{4-108}$$

$$F \le \left\{ F_{f,B} - \frac{M}{2\cdot h}\cdot\frac{\cos\alpha}{\left(\cos\alpha - \frac{\varepsilon_2+\varepsilon_3}{4\cdot\sin\alpha}\right)} \right\} \cdot \frac{1}{\left\{ \frac{1}{\tan\alpha} - \cos\alpha \cdot \frac{\left[\frac{(\varepsilon_2-\varepsilon_F)}{4} + \frac{1}{\tan\alpha}\cdot\left(\varepsilon_1 - \frac{\varepsilon_2}{4\cdot\tan\alpha}\right)\right]}{\left(\cos\alpha - \frac{\varepsilon_2+\varepsilon_3}{4\cdot\sin\alpha}\right)} \right\}} \qquad \text{4-109}$$

FRACTURE IN C:

$$F_{3,\perp}\cdot\cos\alpha \le F_{f,C} \qquad \text{4-110}$$

$$\left\{ F\cdot\left[-\frac{(\varepsilon_F-\varepsilon_2)}{4} + \frac{1}{\tan\alpha}\cdot\left(\varepsilon_1 - \frac{\varepsilon_2}{4\cdot\tan\alpha}\right)\right] - \frac{(-M)}{2\cdot h}\right\}\cdot\frac{\cos\alpha}{\left(\cos\alpha - \frac{\varepsilon_2+\varepsilon_3}{4\cdot\sin\alpha}\right)} \le F_{f,C} \qquad \text{4-111}$$

$$F \le \left\{ F_{f,C} + \frac{(-M)}{2\cdot h}\frac{\cos\alpha}{\left(\cos\alpha - \frac{\varepsilon_2+\varepsilon_3}{4\cdot\sin\alpha}\right)} \right\} \cdot \frac{\left(\cos\alpha - \frac{\varepsilon_2+\varepsilon_3}{4\cdot\sin\alpha}\right)}{\cos\alpha\cdot\left[\frac{(\varepsilon_2-\varepsilon_F)}{4} + \frac{1}{\tan\alpha}\cdot\left(\varepsilon_1 - \frac{\varepsilon_2}{4\cdot\tan\alpha}\right)\right]} \qquad \text{4-112}$$

Where the $F_{f,B}$ and $F_{f,C}$ are respectively from the eq. 3-54 and eq. 3-55. The failure mode FM III fracture in the point C is evaluated inverting the direction of the bending moment M because the fibers in C belongs to the left half of the specimen.

The following formula (eq. 4-113) is for the evaluation of the generic F_f from the eq. 3-54.

$$F\left\{ \frac{1}{\tan\alpha} - \cos\alpha\cdot\frac{\left[\frac{(\varepsilon_2-\varepsilon_F)}{4} + \frac{1}{\tan\alpha}\cdot\left(\varepsilon_1 - \frac{\varepsilon_2}{4\cdot\tan\alpha}\right)\right]}{\left(\cos\alpha - \frac{\varepsilon_2+\varepsilon_3}{4\cdot\sin\alpha}\right)} \right\} + M\left[\frac{1}{2\cdot h}\cdot\frac{\cos\alpha}{\left(\cos\alpha - \frac{\varepsilon_2+\varepsilon_3}{4\cdot\sin\alpha}\right)} \right] \le F_f \qquad \text{4-113}$$

LS5(vii) – Compression inclined to the fibers in the surface 3 (not verified)

$$\sigma_{c,\theta,d} = \frac{f_{c,0,d}}{\left(\frac{f_{c,0,d}}{k_{c,90}\cdot f_{c,90,d}}\right)\cdot\sin^2\theta + \cos^2\theta} \qquad \text{4-114}$$

In order to verify the connection:

$\sigma_{c,\theta CD,k}\cdot A_3 = R_{ax,\theta CD,k}$ $[N]$ Characteristics load-carrying capacity at an angle $\theta = \frac{\pi}{2} - \alpha$

$$F_{3,\perp} \le R_{ax,\theta CD,k} \quad [N] \qquad \text{4-115}$$

$$\left\{ F\cdot\left[-\frac{(\varepsilon_F-\varepsilon_2)}{4} + \frac{1}{\tan\alpha}\cdot\left(\varepsilon_1 - \frac{\varepsilon_2}{4\cdot\tan\alpha}\right)\right] - \frac{M}{2\cdot h}\right\}\cdot\frac{1}{\left(\cos\alpha - \frac{\varepsilon_2+\varepsilon_3}{4\cdot\sin\alpha}\right)} \le R_{ax,\theta CD,k} \qquad \text{4-116}$$

$$F \le \left\{ R_{ax,\theta CD,k} + \frac{M}{2\cdot h}\cdot\frac{1}{\left(\cos\alpha - \frac{\varepsilon_2+\varepsilon_3}{4\cdot\sin\alpha}\right)} \right\} \cdot \frac{\left(\cos\alpha - \frac{\varepsilon_2+\varepsilon_3}{4\cdot\sin\alpha}\right)}{\left[\frac{(\varepsilon_2-\varepsilon_F)}{4} + \frac{1}{\tan\alpha}\cdot\left(\varepsilon_1 - \frac{\varepsilon_2}{4\cdot\tan\alpha}\right)\right]} \qquad \text{4-117}$$

4.7 SUMMARY

4.7.1 Model (i)

Summary of resultant forces

$$F_{1,\perp} = \frac{M}{\left[2 \cdot h \cdot \left(\varepsilon_1 - \frac{\varepsilon_2}{4 \cdot \tan \alpha}\right)\right]}$$

$$F_{2,\perp} = \frac{M}{h} \cdot \frac{\cos \alpha}{2 \cdot \left(\varepsilon_1 - \frac{\varepsilon_2}{4 \cdot \tan \alpha}\right)}$$

$$\mu_\alpha = \frac{F_{2,//}}{F_{2,\perp}} = \tan \alpha$$

Boundary conditions

GC(i)1: $$\varepsilon_1 > \frac{\varepsilon_2}{4 \cdot \tan \alpha}$$

Limit state

LS2(i), FM II: $$M \le F_f \cdot 2 \cdot h \cdot \left(\varepsilon_1 - \frac{\varepsilon_2}{4 \cdot \tan \alpha}\right)$$

4.7.2 Model (ii)

Summary of resultant forces

$$F_{1,\perp} = \frac{M}{2 \cdot h \cdot \left(\varepsilon_1 - \frac{\varepsilon_2}{4 \cdot \tan \alpha}\right)}$$

$$F_{1,\perp} = F \cdot \frac{\cos \alpha + \mu_\alpha \cdot \sin \alpha}{\sin \alpha - \mu_\alpha \cdot \cos \alpha}$$

$$F_{2,\perp} = \frac{\cos \alpha}{2 \cdot \left(\varepsilon_1 - \frac{\varepsilon_2}{4 \cdot \tan \alpha}\right)} \cdot \left\{\frac{M}{h} + 2 \cdot F \cdot \left[\tan \alpha \cdot \left(\varepsilon_1 - \frac{\varepsilon_2}{4 \cdot \tan \alpha}\right) + \frac{\left(\varepsilon_F - \varepsilon_2\right)}{4}\right]\right\}$$

$$\mu_\alpha = \frac{F_{1,\perp} \cdot \sin\alpha - F \cdot \cos\alpha}{F_{1,\perp} \cdot \cos\alpha + F \cdot \sin\alpha}$$

Boundary conditions

GC(ii)1: $$\varepsilon_1 > \frac{\varepsilon_2}{4 \cdot \tan \alpha}$$

FC(ii)1.1: $$M - F \cdot \left[\frac{h}{2} \cdot \left(\varepsilon_F - \varepsilon_2\right)\right] \ge 0$$

FC(ii)1.2: $$-\frac{1}{\tan \alpha} \le \mu_\alpha < \tan \alpha$$

FC(ii)1.2: $$\varepsilon_1 > \frac{\varepsilon_2}{4 \cdot \tan \alpha}$$

Limit state

LS1(ii) – equilibrium state:
$$F = \frac{\frac{M}{h}}{\left[2\cdot\left(\varepsilon_1 - \frac{\varepsilon_2}{4\cdot\tan\alpha}\right)\cdot\left(\frac{\cos\alpha + \mu_\alpha\cdot\sin\alpha}{\sin\alpha - \mu_\alpha\cdot\cos\alpha}\right) - \frac{(\varepsilon_F - \varepsilon_2)}{2}\right]}$$

LS2(ii) – FM II:
$$F_{1,\perp} = \frac{M + F\cdot\left[\frac{h}{2}\cdot(\varepsilon_F - \varepsilon_2)\right]}{\left[2\cdot h\cdot\left(\varepsilon_1 - \frac{\varepsilon_2}{4\cdot\tan\alpha}\right)\right]} \le F_f$$

LS3(ii) - Fu:
$$F\cdot\frac{\cos\alpha + \mu_\alpha\cdot\sin\alpha}{\sin\alpha - \mu_\alpha\cdot\cos\alpha} \le F_f$$

with α according to Diagram 4-4

4.7.3 Model (vii)

Summary of resultant forces

$$F_{1,\perp} = \frac{F}{\tan\alpha}\quad F_{2,\perp} = F\cdot\left\{\frac{1}{\sin\alpha} - \frac{\left[\frac{(\varepsilon_2 - \varepsilon_F)}{4} + \frac{1}{\tan\alpha}\cdot\left(\varepsilon_1 - \frac{\varepsilon_2}{4\cdot\tan\alpha}\right)\right]}{\left(\cos\alpha - \frac{\varepsilon_2 + \varepsilon_3}{4\cdot\sin\alpha}\right)}\right\} + \frac{\frac{M}{2\cdot h}}{\left(\cos\alpha - \frac{\varepsilon_2 + \varepsilon_3}{4\cdot\sin\alpha}\right)}$$

$$F_{3,\perp} = \left\{F\cdot\left[-\frac{(\varepsilon_F - \varepsilon_2)}{4} + \frac{1}{\tan\alpha}\cdot\left(\varepsilon_1 - \frac{\varepsilon_2}{4\cdot\tan\alpha}\right)\right] - \frac{M}{2\cdot h}\right\}\cdot\frac{1}{\left(\cos\alpha - \frac{\varepsilon_2 + \varepsilon_3}{4\cdot\sin\alpha}\right)}$$

Boundary conditions

GC(vii)2:
$$2\cdot\sin(2\alpha) > \varepsilon_2 + \varepsilon_3$$

According to the Diagram 4-5

GC(vii)2: S1 U S2:
$$\begin{cases}\varepsilon_3 = 2\cdot(1 - \varepsilon_1)\cdot\sin(2\alpha)\\ 2\cdot\sin(2\alpha) = \varepsilon_2 + \varepsilon_3\end{cases}$$

Limit state

LS4 (vii) – FMIII:

FRACTURE IN B:
$$F \le \left\{F_{f,B} - \frac{M}{2\cdot h}\cdot\frac{\cos\alpha}{\left(\cos\alpha - \frac{\varepsilon_2 + \varepsilon_3}{4\cdot\sin\alpha}\right)}\right\}\cdot\frac{1}{\left\{\frac{1}{\tan\alpha} - \cos\alpha\cdot\frac{\left[\frac{(\varepsilon_2 - \varepsilon_F)}{4} + \frac{1}{\tan\alpha}\cdot\left(\varepsilon_1 - \frac{\varepsilon_2}{4\cdot\tan\alpha}\right)\right]}{\left(\cos\alpha - \frac{\varepsilon_2 + \varepsilon_3}{4\cdot\sin\alpha}\right)}\right\}}$$

FRACTURE IN C: $$F \le \left\{ F_{f,C} + \frac{(-M)}{2 \cdot h} \frac{\cos\alpha}{\left(\cos\alpha - \frac{\varepsilon_2 + \varepsilon_3}{4 \cdot \sin\alpha}\right)} \right\} \cdot \frac{\left(\cos\alpha - \frac{\varepsilon_2 + \varepsilon_3}{4 \cdot \sin\alpha}\right)}{\cos\alpha \cdot \left[\frac{(\varepsilon_2 - \varepsilon_F)}{4} + \frac{1}{\tan\alpha} \cdot \left(\varepsilon_1 - \frac{\varepsilon_2}{4 \cdot \tan\alpha} \right) \right]}$$

Where $F_{f,B}$ and $F_{f,C}$ are respectively from the eq. 3-54 and eq. 3-55.

The following formula is for the evaluation of the F_f from experimental values from the eq. 3-54

$$F \left\{ \frac{1}{\tan\alpha} - \cos\alpha \cdot \frac{\left[\frac{(\varepsilon_2 - \varepsilon_F)}{4} + \frac{1}{\tan\alpha} \cdot \left(\varepsilon_1 - \frac{\varepsilon_2}{4 \cdot \tan\alpha} \right) \right]}{\left(\cos\alpha - \frac{\varepsilon_2 + \varepsilon_3}{4 \cdot \sin\alpha} \right)} \right\} + M \left[\frac{1}{2 \cdot h} \cdot \frac{\cos\alpha}{\left(\cos\alpha - \frac{\varepsilon_2 + \varepsilon_3}{4 \cdot \sin\alpha} \right)} \right] \le F_f$$

The equation for the FRACTURE IN B is not verified, while the equation for the FRACTURE IN C can be used for the anticipation of the load-carrying capacity of the joint in pure compression; here, the value of $F_{f,C}$ is the one contained in the eq. 3-53.

LS5(vii), FM I (not verified): $$F \le \left\{ R_{ax,\theta_{CD},k} + \frac{M}{2 \cdot h} \cdot \frac{1}{\left(\cos\alpha - \frac{\varepsilon_2 + \varepsilon_3}{4 \cdot \sin\alpha} \right)} \right\} \cdot \frac{\left(\cos\alpha - \frac{\varepsilon_2 + \varepsilon_3}{4 \cdot \sin\alpha} \right)}{\left[\frac{(\varepsilon_2 - \varepsilon_F)}{4} + \frac{1}{\tan\alpha} \cdot \left(\varepsilon_1 - \frac{\varepsilon_2}{4 \cdot \tan\alpha} \right) \right]}$$

Chapter 5 MATERIALS AND METHODS

5.1 Introduction

In the present chapter, the material and methods used in the experimental campaigns are explained. The aim to adopt different procedures, performed with different universal proof machines, is to clarify different aspects of the main topic: the material characterization, the verification of the analytical model for the *halved undersquinted scarf* joint, and finally the test to design the N–M interaction curves for different joint geometries.

5.2 Materials characterization

The specimens are prepared from artificially dried solid timber beams of length 650 cm with a cross-section of b = 60 mm, h = 140 mm. The wood specie is spruce (*Picea abies*), timber strength class C24. The specimens are stored at a temperature of 20° C with relative humidity of 65%. The moisture content was measured using a wood moisture analyser (Fa. Gann, Hydrometer M2050). After completion of the first series of tests (specimen 0), the measurement of the raw density was done in accordance with the DIN EN 408_I.7. Moreover, the average ring width was determined and documented in accordance with the DIN 4074-1. The following table summarizes some of the samples with the respective properties (Otten, 2015).

Table 5-1 – moisture content, density and average ring width of the specimen (from Otten, 2015)

Geometry	Specimen name	Moisture content [%]	Density [kg/m³]	Average ring width [mm]
Joint α = 45°	0415_01	16.5	422.4	2.4
Joint α = 30°	0416_01	17.1	512.3	1.9

The experimental characterization of the specimen's mechanical properties (local and global modulus of elasticity in tension, compression, shear and shear, parallel and perpendicular to the grain) in accordance with the DIN 26-891 and EN 338:2002 was performed only for a limited number of specimens. The properties used for the analytic calculations are the ones contained in the eq. 5-1, 5-2 and 5-3 (according to EN 338:2002 and EN 1912:2004 for the strength class C24). For further specification on the used properties, see Chapter 9.2, Table 9-1 and Table 9-2. Strength Properties:

$$f_{m,k} = 24{,}0 N/mm^2$$

$$f_{c,0,k} = 21{,}0 N/mm^2 \qquad \text{5-1}$$

$$f_{t,0,k} = 14{,}0 N/mm^2$$

Stiffness Properties:

$$E_{mean} = 11.0 kN / mm^2$$
$$G_{mean} = 0.69 kN / mm^2$$ 5-2

Further properties (from Gustafsson, 1988, see above Chapter 4.6.2)

$$G_f = 600 \frac{J}{m^2} = 0.0006 \frac{J}{mm^2}$$ 5-3

5.3 Equipment

Testing machine 1

The first used machinery is a universal tensile strength testing machine TIRAtest 2850 (force range up to 50 kN) manufactured by TIRA GmbH with data recording and controlling software TIRAsoft. The double-column electromechanical table-top testing machine controls the force ($F_{applied}$ = F) through an hydraulic jack; the force is exerted on the test specimen by means of movable cross heads. The piston moves vertically up and down in a linear guide. In dependence on the performed test, the heads of the pistons are provided with different accessorize for the transmission of the load to the specimen (Figure 5-1).

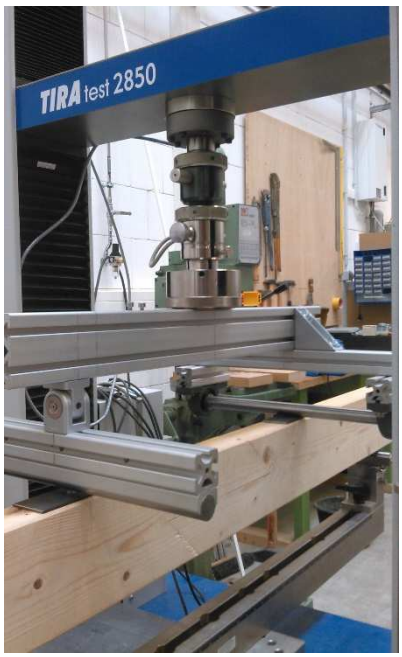

Figure 5-1 - Test machine 1 (bending test)

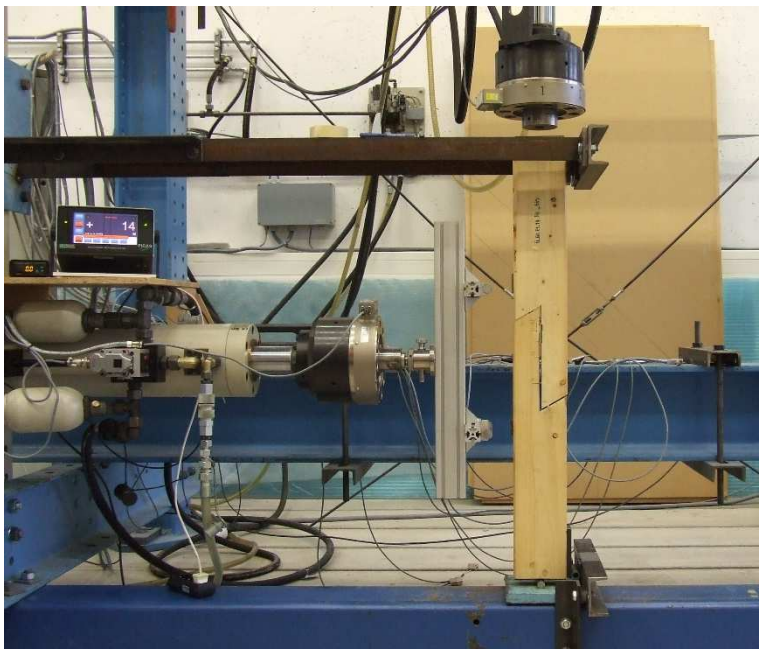

Figure 5-2 - Test machine 2

Testing machine 2

The second used machinery is a Walter+Bai ag. machine (for forces up to $F_{c,max}$ = 250 kN and $F_{t,max}$ = 160 kN) controlled by a desktop computer with software Proteus. It consists in the combination of two subsystems, two hydraulic jacks, one for vertical loads and the other for the horizontal loads. The pistons move respectively vertically up and down (F_I) and left-right (F_{II}) in a linear guide. The Piston I is used for the application of axial forces ($F_{applied}$ = F_I) and the Piston II for the application of bending moment ($F_{applied}$ = F_{II}). The force is exerted on the test specimen by means of movable cross-heads fixed to the fixed frame. The head of the Piston II is provided with a head for the application of bending moment to the specimen (Figure 5-2).

5.4 Unity system

The data-sheet for the diagrams contains pieces of information about *F*, applied force by the correspondent piston stated in [kN], and displacements *u* of the piston expressed in [mm]. No linear transducers LVDT are used; therefore, any information about the specimen's displacement/rotation/deformation is collected.

5.5 Methods

In sight of the achievement of the N-M characteristic diagram for *the half splayed and undersquinted scarf* joint, for all the test the adopted criteria is the one explained in the Table 5-2. First, a pure bending test (a) and a pure compression test (b) are performed; once obtained the value Fu for compression, the tests are decided on the base of the values (c), (d), (e), (f) for the achievement of intermediate values on the N–M curve.

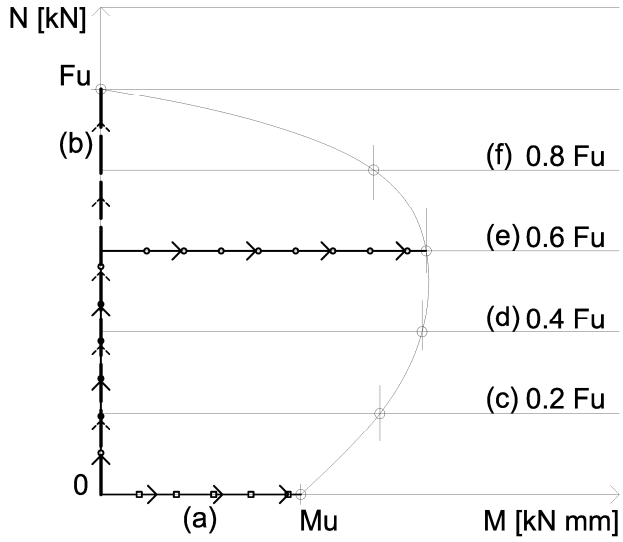

Table 5-2 – Criteria for the building of the N-M interaction curve:

a) 0 · Fu (pure bending)
b) Fu (Pure compression)
c) 0.2 Fu
d) 0.4 Fu
e) 0.6 Fu
f) 0.8 Fu

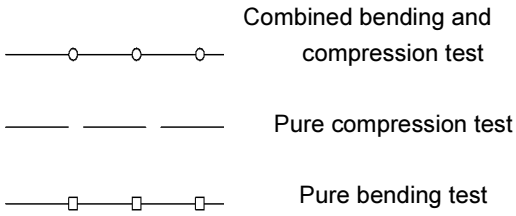

5.6 Procedures

All the operated procedures follow a static load test method. The tests with procedure 0 (P0) are performed with the test machine 1 (Figure 5-3). The procedure 1 (P1) and procedure 2 (P2) are performed with the testing machine 2.

PROCEDURE 0 (P0)

The tests performed with P0 follow a displacement-control mode procedure with a medium velocity of v = 0,6 mm / min in the testing machine 1. The performed test are mainly three.

P0 + a. Pure bending test (Figure 5-3-(a)). Flexural bend standard test methods according to EN 408:2003. The specimen rests in horizontal position on two free supports L, M (Figure 5-4) equipped with rotating rollers. The loading members are symmetrically placed relative to the central length point; the test specimen is loaded in the point F and G. The relationship between the applied force (F) and the bending action (M) and the normal force (N) are:

$$M = \frac{F}{2} \cdot 390 \qquad [kN \cdot mm] \qquad 5\text{-}4$$

$$N = F \qquad [kN]$$

P0 + b. **Pure compression test** (Figure 5-3-(b)). Standard test method according to EN 408:2003. The specimen is installed in a vertical position, and the main axis of the beam is aligned with respect to the hydraulic jack's axis. The load on the specimen is applied in H and I (Figure 5-5; here, two rollers are located in correspondence of the two far ends. The relationship between the applied force (F) and the bending action (M) and the normal force (N) are:

$$M = 0 \qquad [kN \cdot mm]$$
$$N = F \qquad [kN] \qquad \text{5-5}$$

P0 + c. **Combined compressive and bending stress test** (Figure 5-3 (c)). The specimen rests in a vertical position, and the main axis of the beam is not aligned with respect to the hydraulic jack's axis. The distance between the main beam's axis and the point of application of the load (F) is called eccentricity *a* and it is variable. The load on the beam is applied in E, G (Figure 5-6). In dependence of the entity of *a*, different installations are provided: in the Figure 5-6 is represented the test setup of the specimen whose eccentricity is contained in the beam's cross action (0 mm < *a* < 70 mm). For eccentricities larger than the beam's cross section (*a* ≥ 70 mm), the devices represented in the Figure 5-7 – are installed in correspondence with both of the far ends. The relationship between the applied force (F) and the bending action (M) and the normal force (N) are:

$$M = a \cdot F \qquad [kN \cdot mm]$$
$$N = F \qquad [kN] \qquad \text{5-6}$$

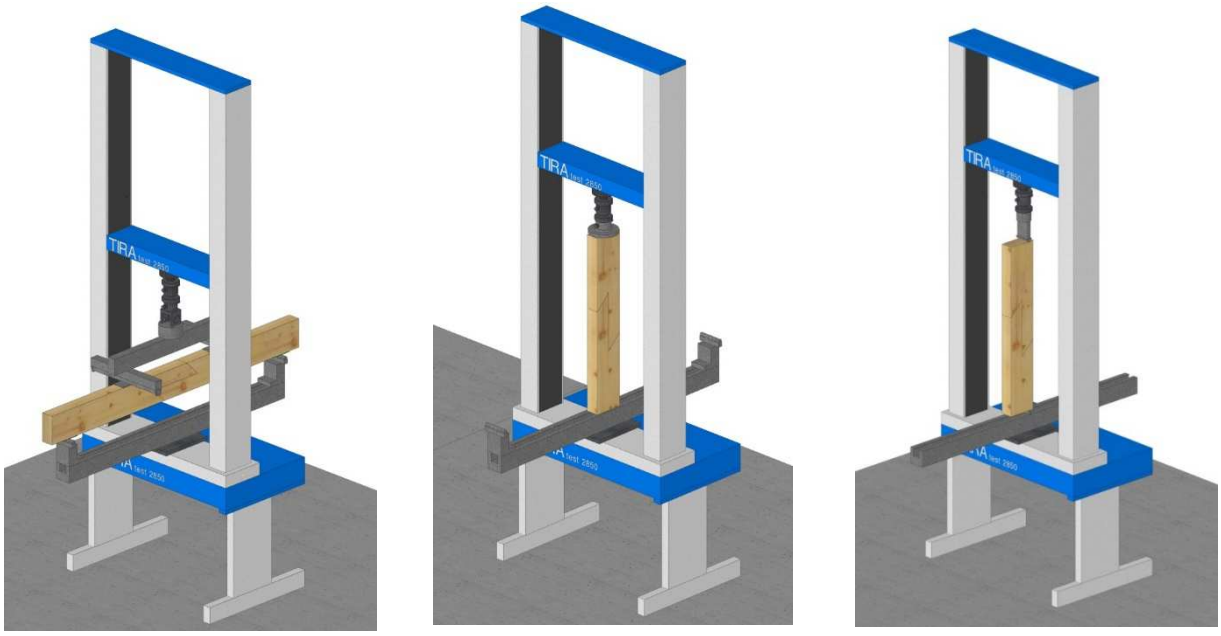

(a) (b) (c)

Figure 5-3 – (a) P0 + a. procedure's test machine and scheme of the installation; (b) P0 + b. procedure's test machine and scheme of the installation; (c) P0 + c. procedure's test machine and scheme of the installation.

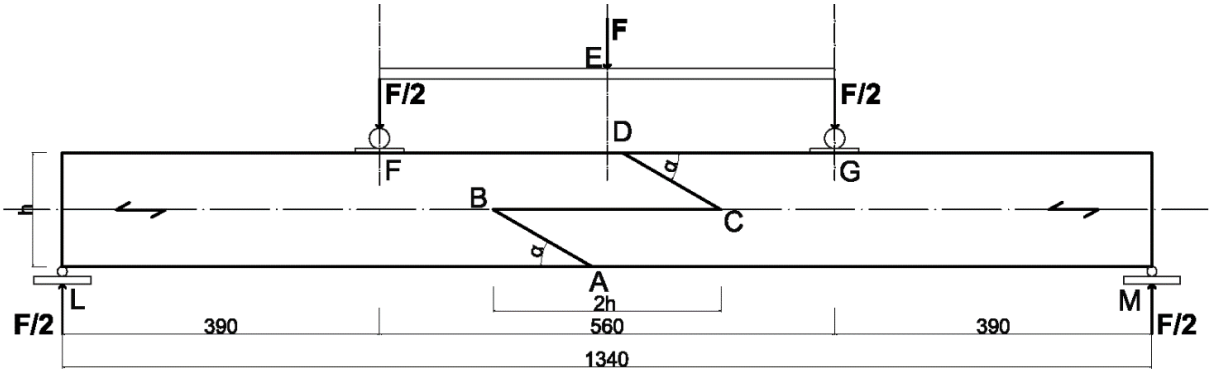

Figure 5-4 – Procedure P0 + a. All the dimensions are in [mm].

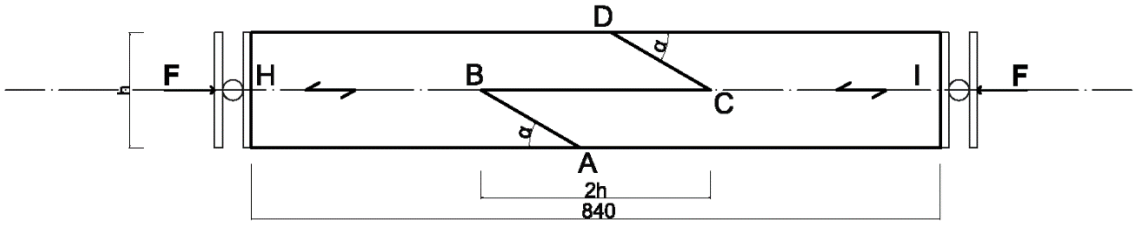

Figure 5-5 – Procedure P0 + b. All the dimensions are in [mm].

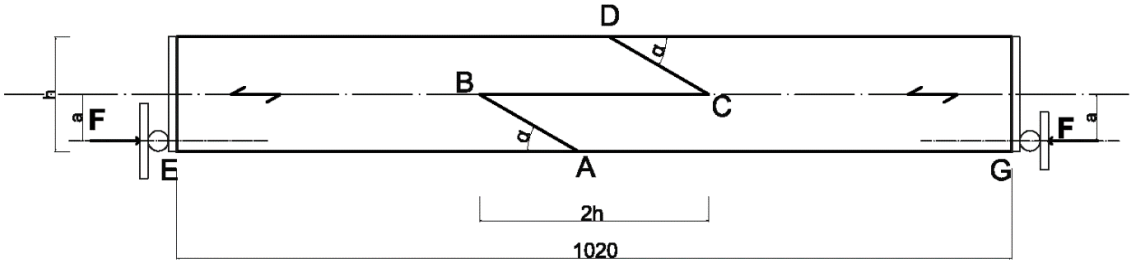

Figure 5-6 – Procedure P0 + c for 0 mm < *a* < 70 mm. All the dimensions are in [mm].

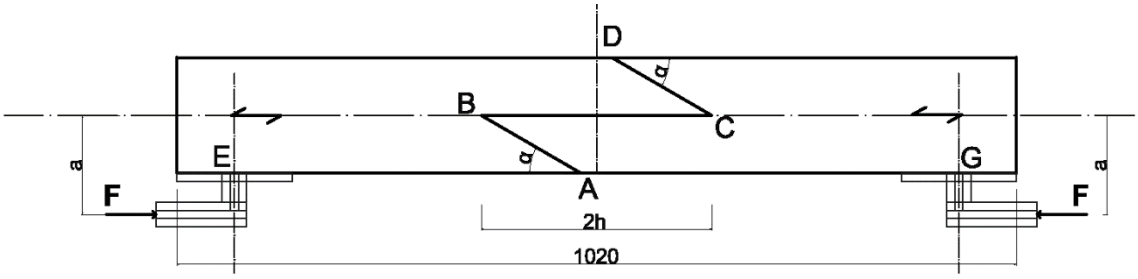

Figure 5-7 – Procedure P0 + c for *a* ≥ 70 mm. All the dimensions are in [mm].

Figure 5-8 – Procedure P0 + c for 0 mm< *a* < 70 mm lever arm device.

Figure 5-9 – Procedure P0 + c for 70 mm ≤*a* < 180 mm lever arm device.

Figure 5-10 – Procedure P0 + c for *a* ≥ 180 mm lever arm device.

In the tests, the simulation of the different lever arms is done using special devices. For the Procedure P0 + c, 0 mm< *a* < 70 mm lever arm, the load is applied via load transfer fins; to avoid additional deformations due to the application of a concentrated load, a steel plate of thickness s = 10 mm is screwed on the upper cross-section (Figure 5-). For the Procedure P0 + c., 70 mm ≤ *a* < 180 mm lever arm, the load is applied with a rectangular-shaped device; the lever arm on the specimen is produced by mean of a screwed-on steel plate on the side of the beam (Figure 5-9). For the Procedure P0 + c., *a* ≥ 180 mm lever arm, the loading is applied via screwed-on steel plates on the beam's lower face welded with a nut to connect the specimen with the machinery, by means of a threaded bolt (Figure 5-10).

PROCEDURE 1 (P1)

The application of the load according to the procedure P1 is described by the separate and consecutive loading of specimens by the Piston I (Figure 5-22 – (a)) and Piston II (Figure 5-22 – (b)). The force F_I corresponds to the application of normal compressive force through the Piston I, while the force F_{II} corresponds to the application of bending force on the specimen by means of the Piston II. Both pistons work with load or stress-controlled mode; here, the force is increased at a given rate V_F (V_F = Load / Time), constant for the duration of the test. During the failure phase, the test cylinder accelerates to maintain the V_F constant. During the loading the forces F_I and F_{II} and the correspondent pistons' displacements w_I and w_{II} are measured. The relation among the applied F_{II} force and the bending moment (M) is defined by the following eq. 5-8. The one among F_I and the normal force (N) by the eq. 5-7.

In the P1, an interesting phenomenon described as *passive response* on the Piston II and Piston I was registered. The *passive response* consists in the presence of a *passive* force F recorded on the inactive piston.

a) The activation of the force F_{II} causes the passive response $F_{I,passive}$ ($F_{I,passive}$ = F_I) on the Piston I. Referring to the Figure 5-11, the specimen is restrained along the axial direction at the extremities H and I. During the application of the load F_{II}, the joint rotates; therefore, because of its geometry, the two connected elements separate one from the other, and both the far ends displace along the direction of the beam's axis. This deformation provokes the compression load passive response $F_{I,passive}$ on the Piston I. The behaviour depends on the chosen angle of the squint *α*.

b) Similarly, the activation of the force F_I on the Piston I causes the passive response $F_{II,passive}$ ($F_{II,passive}$ = F_{II}) on the Piston II. Referring to the Figure 5-12, the specimen is restrained because of the presence of the Piston II. During the application of the load F_I, because of its geometry, the joint rotates; the central part of the connected elements bent in the direction of the Piston II and activate the passive $F_{II,passive}$ compression.

PROCEDURE 2 (P2)

The P2 tests follow a mixed force-controlled and displacement-controlled mode procedure. The P2 is described by the separate and consecutive loading of specimens by the Piston I and Piston II. The load F_I increases with force-controlled mode up to the chosen value of F_{target}; afterwards, the F_{II} with displacement-controlled mode is applied until the specimen's failure. With displacement-controlled mode, the loading piston F_I increases at given rate V_w (V_w = Path / Time), constant for the duration of the test; furthermore, the hydraulic jack test constantly adjusts the specific ultimate target F (F_{target}). During the failure phase the test cylinder does not accelerates, but maintains the same rate. During the loading the forces F_I and F_{II} and the correspondent pistons displacements w_I and w_{II} are measured. As well as in P1, the force F_I corresponds to the application of normal compressive force through the Piston I, while the force F_{II} corresponds to the application of bending force on

the specimen by means of the Piston II. The relation among the applied F_{II} force and the bending moment (M) is defined by the following eq. 5 8. The one among F_I force and the normal force (N) by the eq. 5 7.

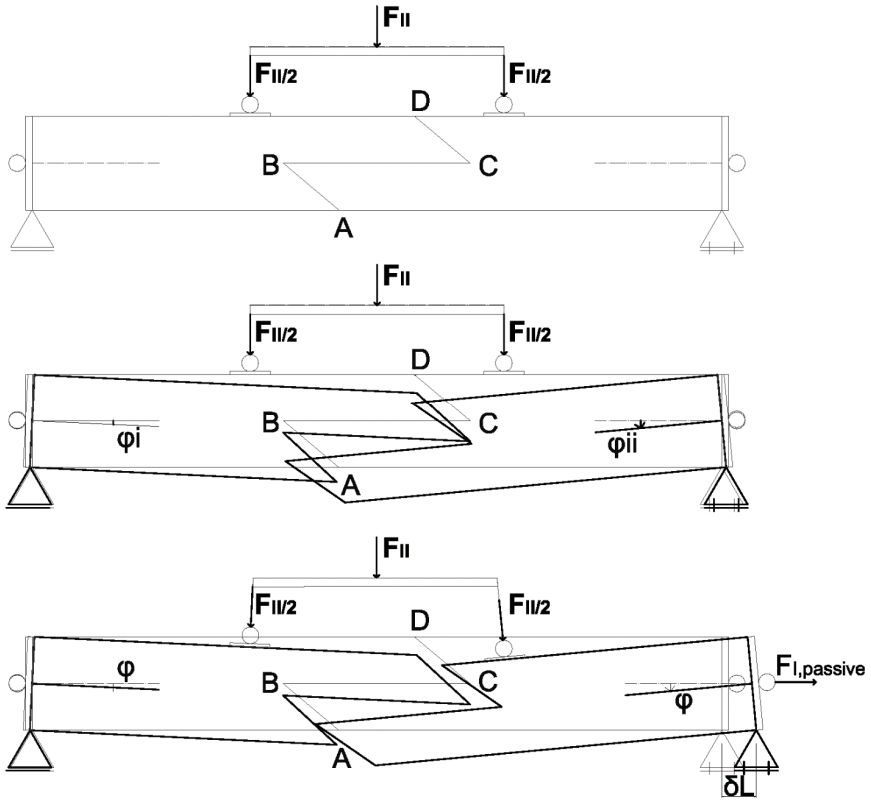

Figure 5-11 – Passive response of the Piston I

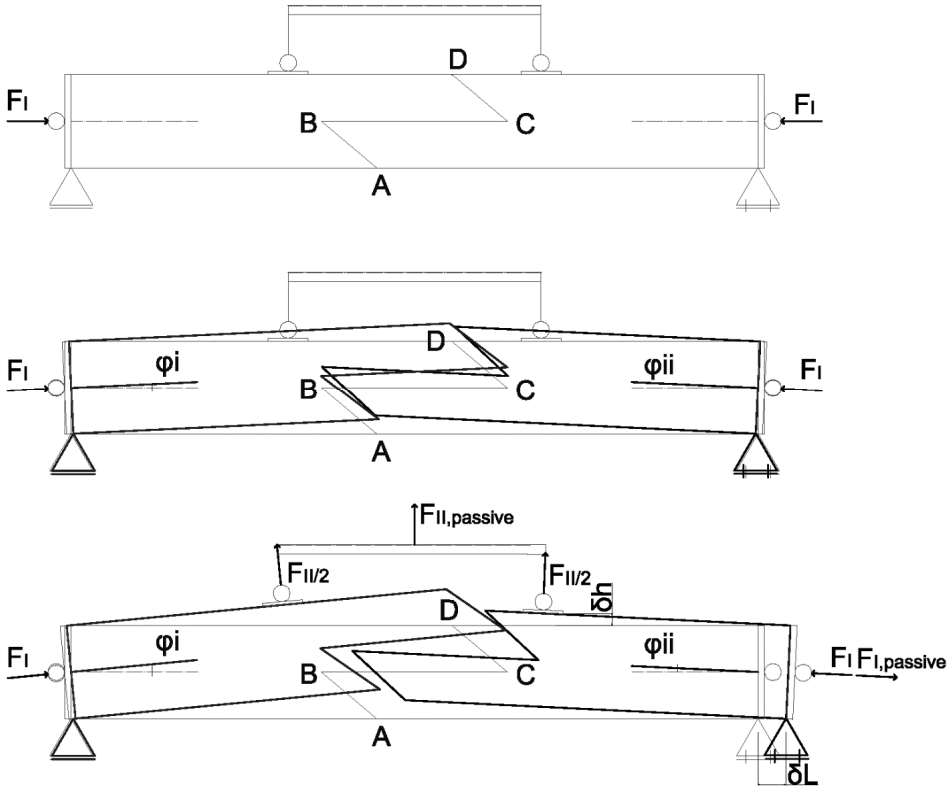

Figure 5-12 – Passive response of the Piston II

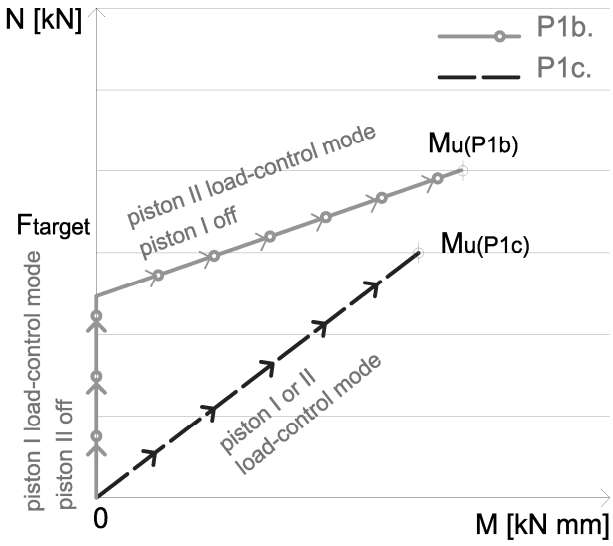

Figure 5-13 – P1 – scheme of the loading

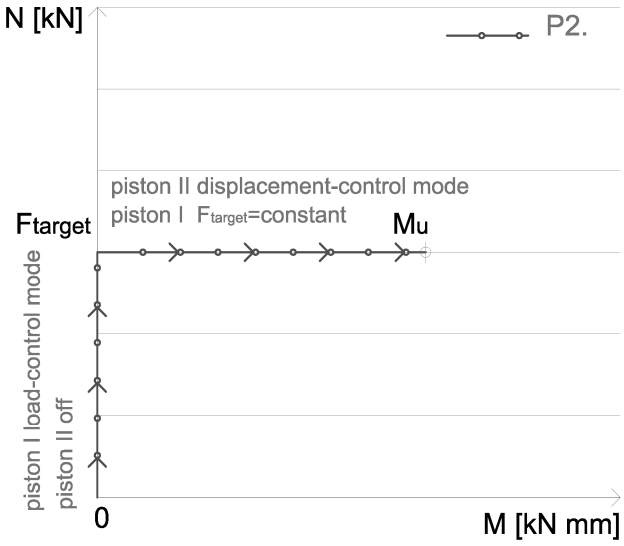

Figure 5-14 – P2 + c – scheme of the loading

Table 5-3 – Test procedures and loading conditions

Procedure	Control Mode	v [m/s]	Test Machine	Test direction	Loading			
					M	M (+ N)	N	N + M
P0 + a	displacement c.m.	0.6	1	strong axis	a			
P0 + b	displacement c.m.	0.6	1	strong axis			b	
P0 + c	displacement c.m.	0.6	1	strong axis				c
P1 + a	stress c.m.	var.	2	strong axis	a			
P1 + b	stress c.m.	var.	2	strong axis			b	
P1 + c	stress c.m.	var.	2	strong axis				c
P1 + d	stress c.m.	var.	2	strong axis		d		
P2 + a	stress + displacement c.m.	var.	2	strong axis	a			
P2 + b	stress + displacement c.m.	var.	2	strong axis			b	
P2 + c	stress + displacement c.m.	var.	2	strong axis				c
P2 + d	stress + displacement c.m.	var.	2	strong axis		d		
P3 + a	stress + displacement c.m.	var.	2	weak axis	a			
P3 +b	stress + displacement c.m.	var.	2	weak axis			b	
P3 + c	stress + displacement c.m.	var.	2	weak axis				c

$$N = F_I \qquad [kN] \tag{5-7}$$

$$M = \frac{F_{II}}{2} \cdot a \qquad [kN \cdot mm] \tag{5-8}$$

Where:

$$a = 405\,mm \quad for \quad P1, P2$$
$$a = 390\,mm \quad for \quad P3 \tag{5-9}$$

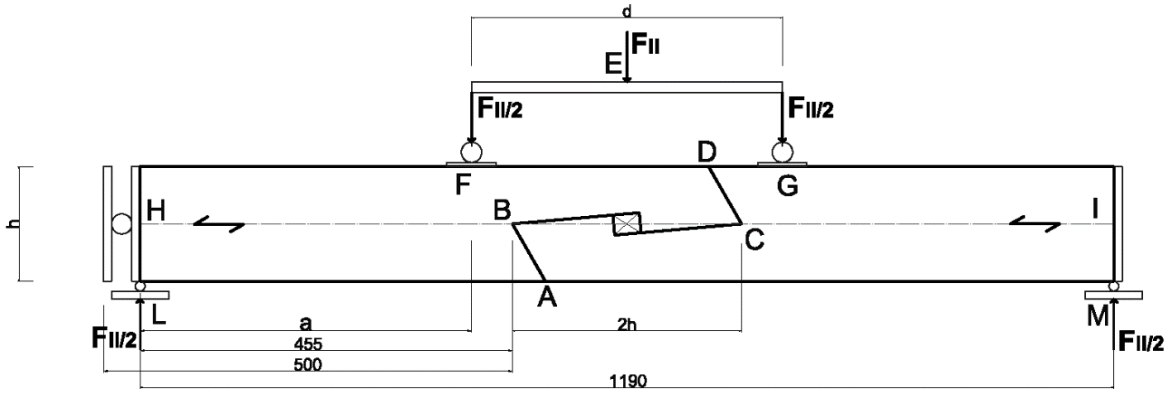

Figure 5-15 – P1 – P2 + a. All the dimensions are in [mm].

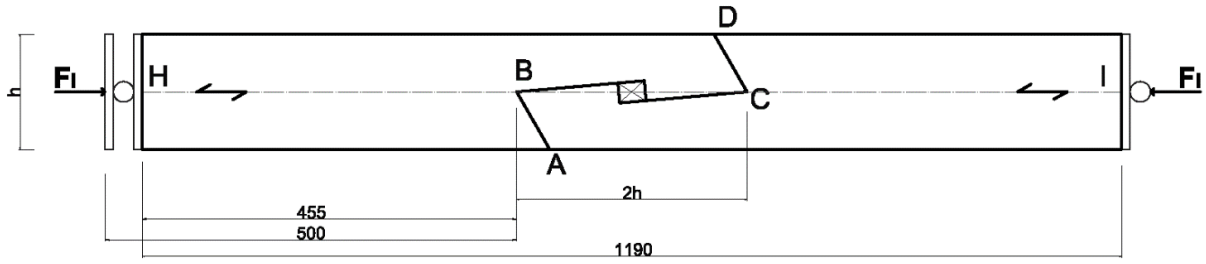

Figure 5-16 – P1 – P2 + b. All the dimensions are in [mm].

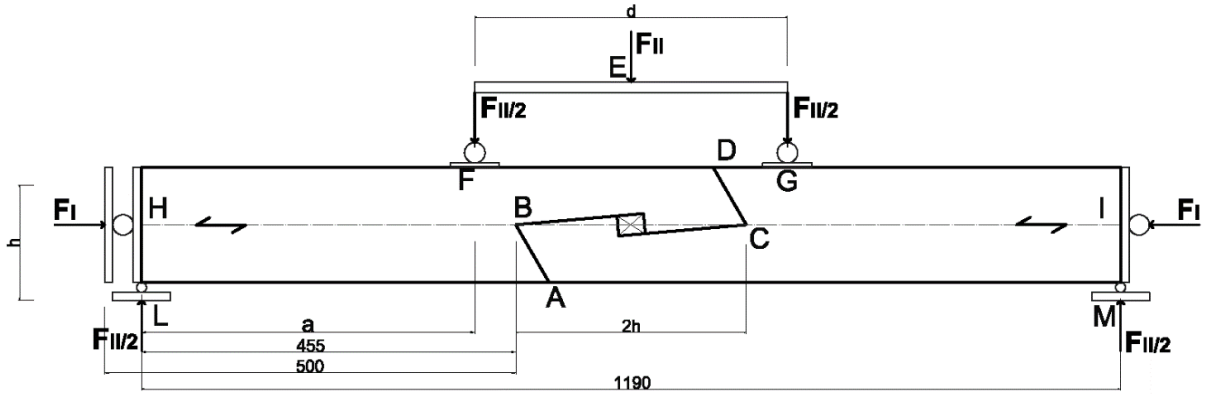

Figure 5-17 – P1 – P2 + c. All the dimensions are in [mm].

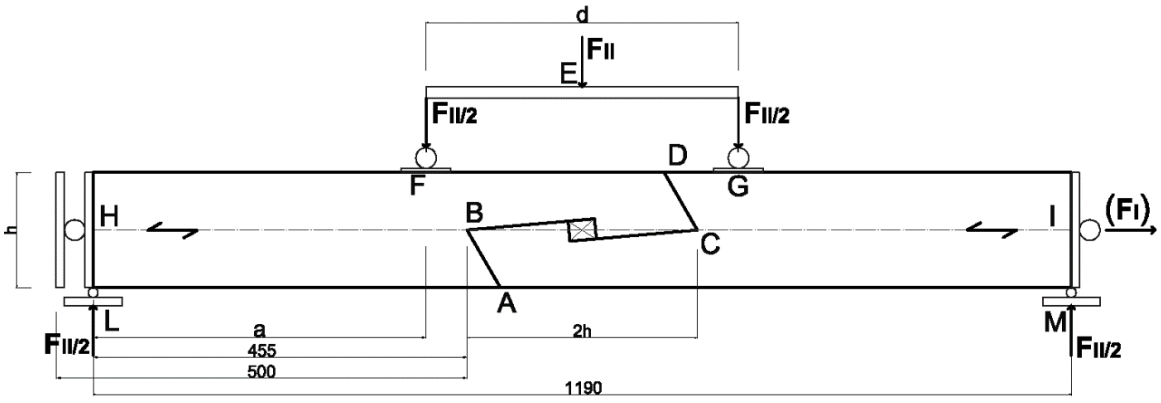

Figure 5-18 – P1 + d. All the dimensions are in [mm].

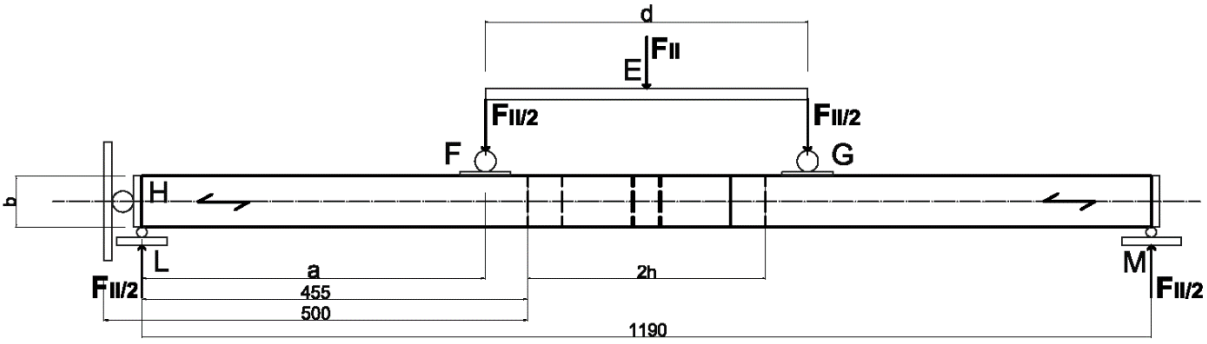

Figure 5-19 – P3 + a. All the dimensions are in [mm].

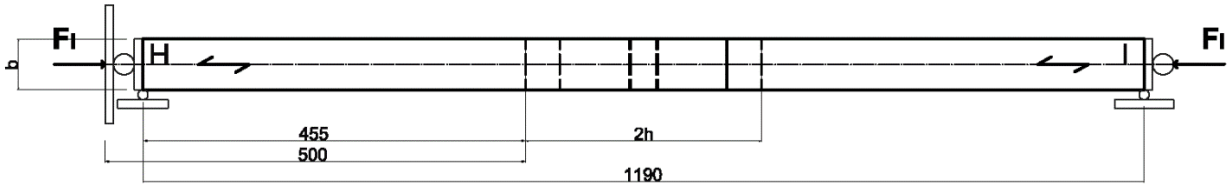

Figure 5-20 – P3 + b. All the dimensions are in [mm].

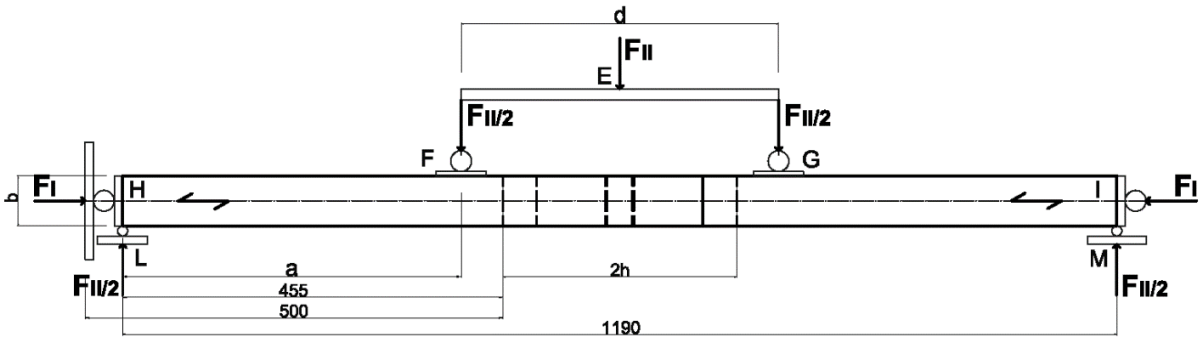

Figure 5-21 – P3 + c. All the dimensions are in [mm].

(a) (b)

Figure 5-22 – For the Procedures P2 and P3 the (a) Compression device, (b) Bending device

PROCEDURE 3 (P3)

The P3 tests follow a mixed force-controlled and displacement-controlled mode procedure. The P3 is correspondent to the Procedure 2, but the specimen is turned 90° and tested along the weak axis. The relation among the applied F_{II} force and the bending moment (M) is defined by the following eq. 5-8. The one among F_I force and the normal force (N) by the eq. 5-7.

The following a), b), c), d), e) procedures are the specification to the general Procedure P1, P2, P3 (Table 5-3). According to the aim, the tests follow different procedures:

a. Pure bending test. Application of F_{II}. The specimen is free to displace in the axial direction.

b. Pure compression test. Application of F_I through the Piston I. The specimen is free to displace in the horizontal direction.

c. Mixed compression and bending test. Application of F_I until the $F_I = F_{target.}$ It follows the application of F_{II}.

d. Mixed compression and bending test with respectively inducted bending and compression actions. Application of F_I until the $F_I = F_{target}$ and passive response $F_{II,passive}$; afterwards, the application of F_{II} and passive response $F_{I,passive}$.

e. Bending test with inducted axial compression. Application of F_{II} and *passive response* of $F_{I,passive}$.

5.6.1 Conclusion

The data derived from two different test procedure, the P1 and the P2, are not comparable the one respect to the other; in fact, the kind of information that each of the procedure is able to produce is different.

The P1 shows the following advantages:

a) the forces can be conveniently applied or removed when a different type of load along the loading process, in order to have a direct control on forces applied to the specimen;

b) this procedure permits the lecture of the specimen's equilibrium path along the loading process;

c) the force-controlled mode simulates the behaviour of a beam under real conditions. In fact, as well as an in-situ beam, it is bending-loaded with live and dead loads (by means of F_{II}); therefore, the deformation δL along the axial direction, that causes the axially pure compression on the Piston 1, is the response of the structure, which the two connected beams are part.

On the other side, the disadvantage identified in the performing of the P1 is d) the extreme variability of the test results for different specimens. This problematic derives from the difficulty of reproduction of the same load conditions in the procedure to come to comparable results.

The P2 showed the following advantages:

a) the displacement-controlled mode procedure avoids the *passive response* on the non-active piston; therefore, the specimen are loaded only along the chosen direction and load condition;

b) it is used to get more accurate responses for the mixed compression and bending tests, because of the extreme reliability of the test results for different specimens.

The P2, and more specifically the displacement controlled mode tests, are more suitable to get a reproducible result, and present only the disadvantage the beam is not simulating a behaviour like under real conditions.

Chapter 6 EXPERIMENTAL PRE-CAMPAIGN FOR THE *HALVED UNDERSQUINTED SCARF* JOINT CHARACTERIZATION

6.1 Introduction

In the present chapter, the experimental pre–campaign is presented. The chapter offers a general description of the parameters that affect the load-carrying capacity of the *halved undersquinted scarf*. The aims are:

- calibration of the analytical model;
- tests for the definition of the general behaviour of the joint;
- description of the importance of the inclination of the angle *α* of the squint;
- evaluation of the friction parameters μ_α and μ_β;
- description of the significance of the parameters ε_1, ε_2 and ε_3;
- demonstration of the reliability of the analytical models (limit states, boundary conditions).

The tests were carried out in the LHT Labor für Holztechnik of the Fakultät Bauen und Erhalten in the HAWK (University of applied sciences) Hildesheim, Germany during the period April 2015 - July 2015. Static in-plane and out-of-plane tests on scaled timber beams were performed.

6.2 Specimen preparation

Three different montages of the specimen were prepared. In dependence of the required inclination and roughness of the surface, the specimen's surfaces are cut either with circular saw or with band saw.

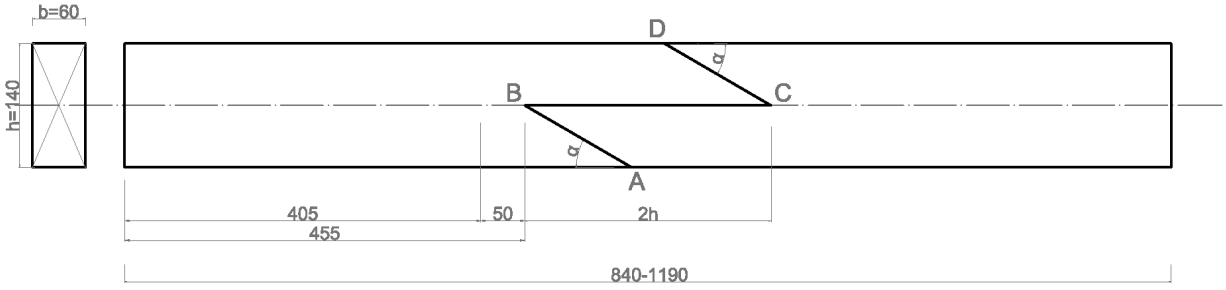

Figure 6-1 – SPECIMEN 1. All the dimensions are in [mm].

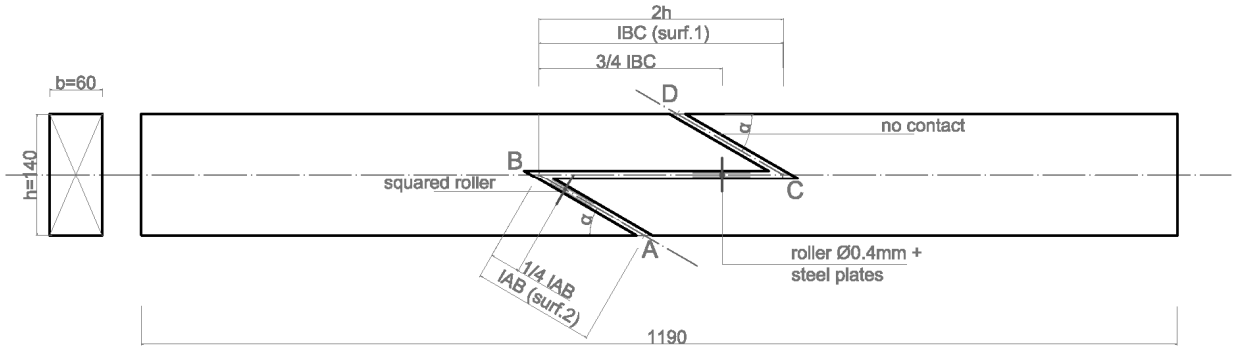

Figure 6-2 – SPECIMEN 2. Model (ii). All the dimensions are in [mm].

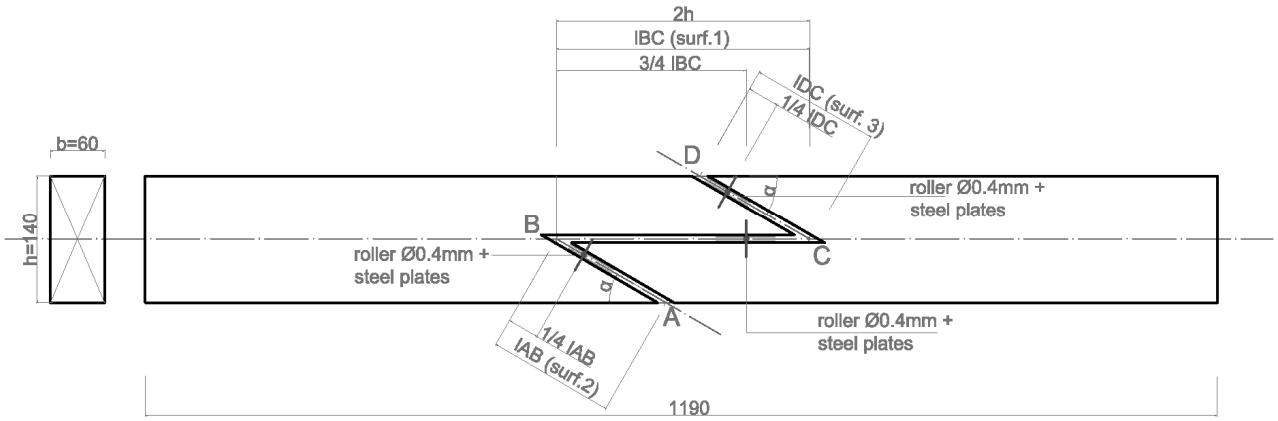

Figure 6-3 – SPECIMEN 2. Model (vii). All the dimensions are in [mm].

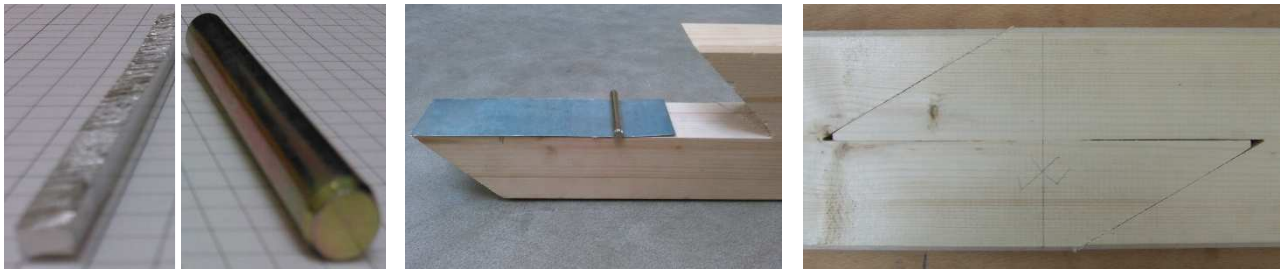

(a) (b) (c) (d)

Figure 6-4 – (a) *rsquared* (friction) (b) *rround* and (c) *rround* on steel plate (no friction) (d) cut-off of the peaks B & C.

SPECIMEN 0 (S0)

The Specimen 0 is used to observe the general behaviour of the joint. The specific assemblage of the specimen is from time to time described in the tests.

SPECIMEN 1 (S1)

The Specimen 1 is used with the main purpose of understand the general behaviour of the *halved undersquinted scarf joint* and the most significant parameters that manage it. Preparation: the Figure 6-1 represents the specimen. The facing adjacent surfaces are in contact. The peaks in correspondence with points B and C are cut-away to avoid the split-effect that can anticipate the failure (Figure 6-4 - d).

SPECIMEN 2 (S2)

The Specimen 2 is used for the verification of the analytic model. Preparation: the joint's cut is provided with a distance between adjacent surfaces, where some rollers are located. The rollers are devices used to force the

position of the resultant force into the desired position ε_i. This is chosen in dependence on the analysed model. The rollers are of two different kind, the squared "roller" (*rsquared*) (Figure 6-4_a) and the circular roller (*rround*) (Figure 6-4 - b). In order to eliminate any friction to the facing surfaces, the *rround* is used in between two steel plates, glued on the wood (Figure 6-4 - c); on the other side, the *rsquared* lays directly on the surface, in order to confer some amount of friction component. For the models (i) (ii) (iii) (iv) was used a *rsquared* on the surface $\overline{AB}$ and a *rround* on the surface $\overline{BC}$ (Figure 6-2). For the models (vii) was employed the *rround* both on the surfaces $\overline{AB}$, $\overline{BC}$ and $\overline{CD}$ (Figure 6-3).

6.3 Parameters ε_1, ε_2, ε_3

From the observation of experimental pre-tests, has been concluded that the connection shows a *non-linear* behaviour from *zero* to the ultimate-load. In fact, the length of the segments $\overline{AB}$, $\overline{BC}$ and $\overline{CD}$ (contact segment and correspondent contact surface) reduces in dependence of the increasing compression/bending load (Figure 6-5). The analytical models in the Chapter 4 describe the joint's *linear behaviour* through the variation of the parameters ε_1, ε_2 and ε_3. (position of the internal forces). In the present paragraph the amount of load-carrying capacity in dependence of the position of the parameters ε_1 and ε_2 is tested. The influence of the parameter ε_3 is neglected.

TEST 1. The position for the parameters ε_i in the models (ii), (vii) correspondent to the joint's failure are represented in Table 6-1.

(ii)	(vii)
$\begin{cases} \varepsilon_1 = \frac{3}{4} \\ \varepsilon_2 = \frac{1}{4} \end{cases}$	$\begin{cases} \varepsilon_1 = \frac{1}{2} \\ \varepsilon_2 = \frac{1}{2} \\ \varepsilon_3 = \frac{1}{2} \end{cases}$

Table 6-1 – Value of the parameters ε_i at the failure

TEST 2.

The load-carrying capacity of the connection depends on the position of the resultant forces $F_{1,\perp}$ and $F_{2,\perp}$.

- the load-carrying capacity of the connection increases when the value of ε_1 increases;
- the load-carrying capacity of the connection increases when the value of ε_2 decreases.

TEST 3.

- In the idealized connection, the load-carrying capacity of the connection is null when the *geometric condition* GC1 (i) expressed in the eq. 6-2 occurs. Under this peculiar geometric condition, the load-carrying capacity is independent from the external load conditions.
- Taking into account the mass of the system and the applied load, in case $\varepsilon_F \neq 0 = a$; $\mu_\alpha = 0$ and $\mu_\alpha = 0$ for the configurations in the equation eq. 6-1, the system is in equilibrium.

$$\frac{a}{h} = \frac{1}{\tan\alpha}\left[2 \cdot \varepsilon_1 - \varepsilon_2\left(\frac{\tan\alpha}{2} + \frac{1}{2 \cdot \tan\alpha}\right)\right] \qquad 6\text{-}1$$

TEST 4.

- The load-carrying capacity of the connection is null when the *geometric condition* GC(vii) expressed in the eq. 6-5 occurs. Under this peculiar geometric condition, the load-carrying capacity is independent from the external load conditions.

6.3.1 TEST 1: Linearization of the *N-M* interaction curve

Hypothesis

The position of the parameters ε_1, ε_2, ε_3 describes the loading instants in the equilibrium configurations, and the F_u in the analytical models of the *half splayed and undersquinted scarf* joint.

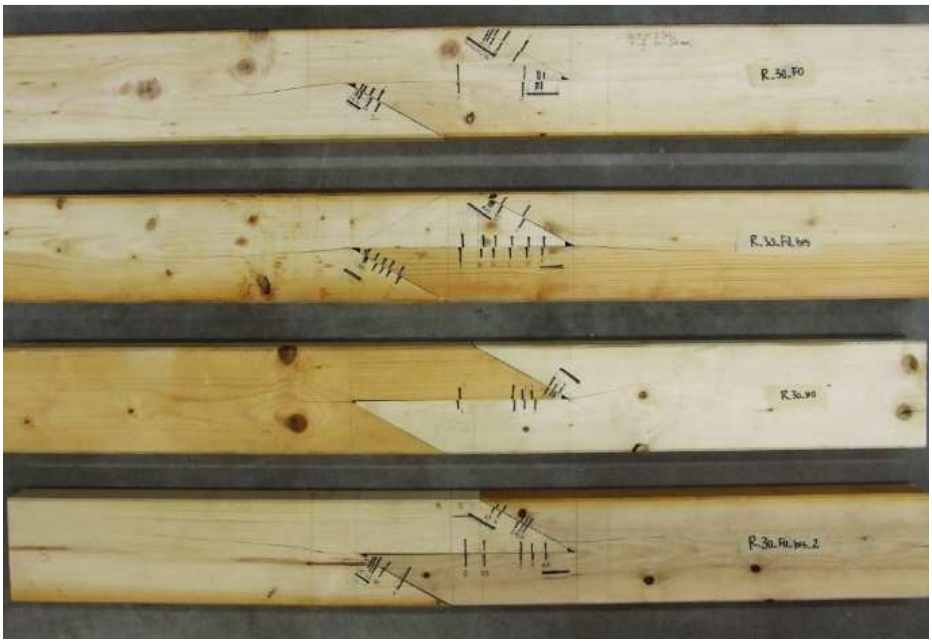

Figure 6-5 – Change in the position of the internal resultant forces due to the increasing load. Tests α = *30°*, various loading conditions.

Test description

Date: 20/01/2016 and 01/02/2016; Specimen: S1; Testing machine 2. Procedure: various.

To describe the change of position of the resultant forces $F_{1,\perp}$, $F_{2,\perp}$ and $F_{3,\perp}$ along the loading process, consecutive configurations for the parameters ε_1, ε_2 and ε_3 are defined. The medium values for the parameters ε_1, ε_2 and ε_3 are defined in the following Table 6-2 and Table 6-3.

Table 6-2 – Medium values for the parameters ε_1, ε_2 and ε_3 in the tests R30_F0_bis_2 (Pure bending, procedure P1 - e) and α = 30° specimen R30_M0 (Pure compression, procedure P1 - b)

α = 30°						
	Models (i) (ii)			**Model (vii)**		
F_u values	***ε1***	***ε2***	***ε3***	***ε1***	***ε2***	***ε3***
0Fu	1/2	1/2	1/2	1/2	3/4	1/4
0.2Fu	3/4	3/16	5/8	1/2	3/4	1/4
0.4Fu	13/16	3/16	13/16	5/8	1/2	3/16
0.6Fu	7/8	1/8	7/8	3/4	1/2	3/16
0.8Fu	7/8	1/8	7/8	7/8	1/2	1/8
F_u	15/16	1/8	7/8	7/8	1/2	1/8

Table 6-3 – Medium values for the parameters ε_1, ε_2 and ε_3 in the tests *α = 60°* specimen R60_F0 (Pure bending, procedure P2 + a) and R60_F16_M (Combined compressive and bending force, procedure P2 + c: F_{target} *= 16 kN +* M_u)

***α* = 60°**						
	Models (i) (ii)			**Model (vii)**		
F_u values	***ε1***	***ε2***	***ε3***	***ε1***	***ε2***	***ε3***
0Fu	7/8	1/2	1/2	1/2	1/2	1/2
0.2Fu	7/8	1/2	1/2	1/2	1/2	1/2
0.4Fu	7/8	3/8	5/8	1/2	1/2	1/2
0.6Fu	15/16	3/8	5/8	1/2	1/2	1/2
0.8Fu	15/16	1/4	6/8	1/2	1/2	1/2
F_u	15/16	1/4	13/16	(Fue)1/2	(Fue)1/2	(Fue)1/2

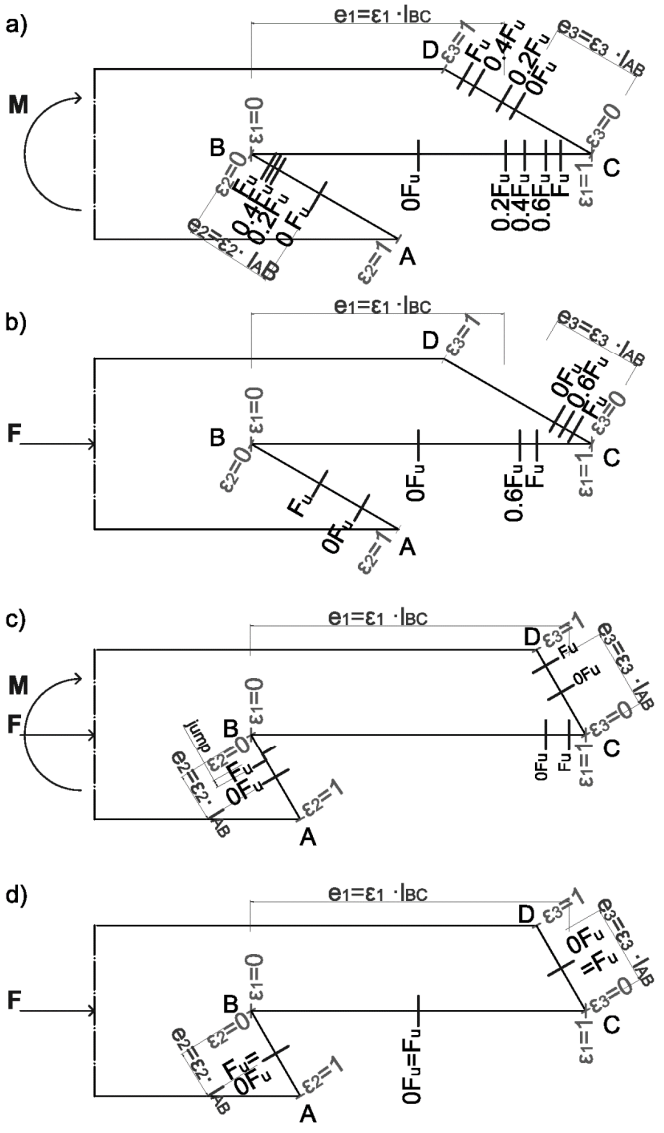

Figure 6-6 a) Specimen R30_F0_bis_2 (*α = 30°*; F_{II}). Positioning of the resultant force along the loading process; b) Specimen R30_M0 (*α = 30°*; pure compression). Positioning of the resultant force along the loading process; c) R60_F16_M (*α = 60°*; F_I (=16kN)+ F_{II}); d) Specimen R60_F0 (*α = 60°*; pure bending). Positioning of the resultant force along the loading process.

Conclusions

The specimens with *α = 30°* and *α = 60°* behave differently.

On one hand, the $\alpha = 30°$ shows very evident changes in the resultant forces' positions along the loading process, with big displacements (reciprocal rotation) of the two joint's left and right pieces. On the other hand, the $\alpha = 60°$ specimens show small changes in the resultant forces' positions between the zero load configuration and the F_u configuration. Nevertheless, in the case of $\alpha = 60°$ and low F_l values (in the order of $F_l = 0.6 \cdot Fu$) and presence of bending load, the adjacent surfaces of the segment $\overline{AB}$ slip one on the other (buckling failure, FM IV – see Chapter 7.2.4). The final setup of the failure for buckling in correspondence of a load stress equal to F_u is represented in the Figure 6-6 - c) ("jump" of the right piece on the left piece).

More, the specimen $\alpha = 60°$ in case of pure compression shows that:

- the adjacent surfaces maintain until F_{ue} a perfect adherence;
- the resultant forces are centred on all the surfaces from a value of loaf equal to $F_u = 0$ until $Fu = F_{ue}$.

6.3.2 TEST 2: Variation of the parameter ε_1

Test description

Date: 21/07/2015; Specimen: S0; Procedure: none. $F_{2,\perp}$, $F_{1,\perp}$ constrained on various ε_2 and ε_1 specified time to time in Table 6-4.

In the test, the position of both the parameters ε_1 and ε_2 is modified according to the variation described in paragraph 3.4.2. The tests are proposed for the external load conditions both in self-weight (M), and self-weight + additional weight of metallic cube (m_c = 1386g) (Load conditions: M + number of cubes).

Table 6-4 – Test results 21/07/2015 – influence of the ε1 parameter on the connection's load-carrying capacity.

	α [°]	**Fixed ε2**	**e1** [mm]	**ε1**	**l_{AB}** [mm]	**l_{BC}** [mm]	**Load condi-tions**	**Descri-ption**	**Photo**
a	35	0.5	55	0.196	120	280F	M	(conf 1) equilibrium	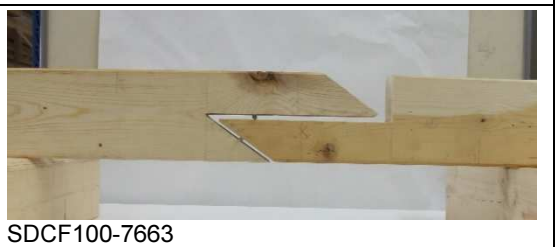 SDCF100-7663
b	35	0.5	55	0.196	120	280F	M (+ 1 x cube)	(conf 1) kinematic	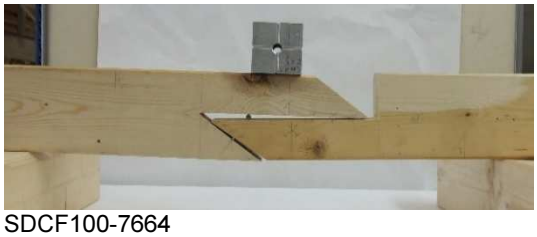 SDCF100-7664
c	35	0.5	90	0.321	120	280	M	(conf 2) equilibrium	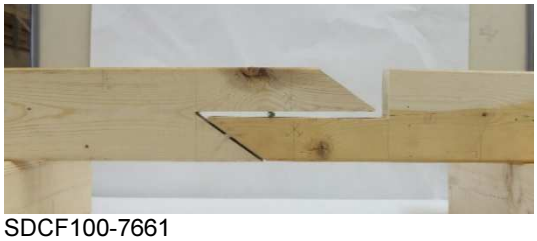 SDCF100-7661

d	35	0.5	90	0.321	120	280	M (+ 1 x cube)	(conf 2) equilibrium	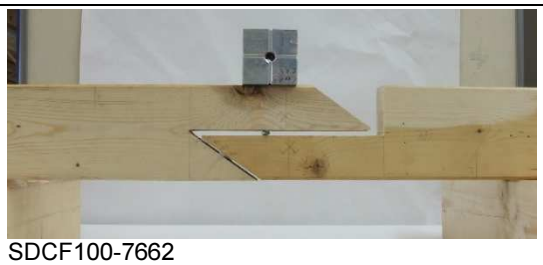 SDCF100-7662
e	35	0.5	230	0.821	120	280	M (+ 2 x cube)	(conf 3) equilibrium	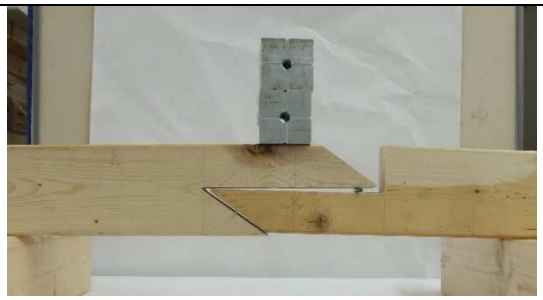 SDCF100-7666
f	35	0.375	230	0.821			M (+ 3x cube)	(conf 3) equilibrium	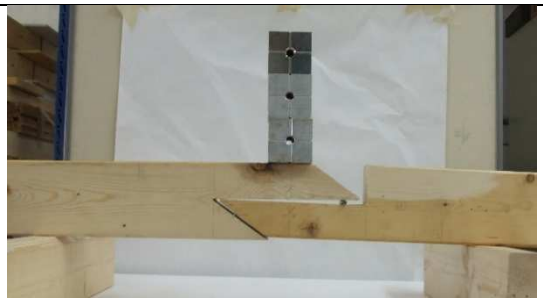 SDCF100-7673
g	35	0.625	55	0.196	120	280	M	equilibrium	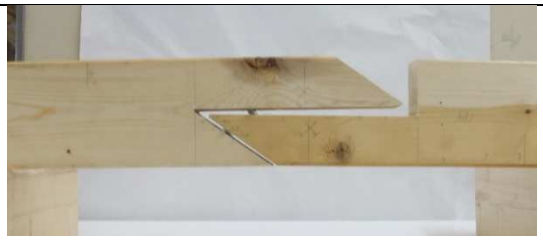 SDCF100-7670
h	35	0.375	55	0.196	201	280	M (+ 1 x cube)	equilibrium	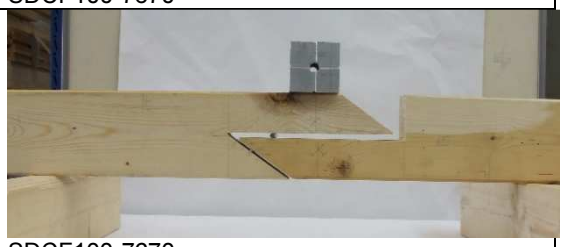 SDCF100-7670

Conclusions

Considering the changing of position of ε_1 and ε_2:

- the load-carrying capacity of the connection increases when the value of ε_1 increases. In *a* (Table 6-4), the connection is able to bear the connection's self-weight but, as shown in *b*, not the weight of the cube. Changing the point of application from $\varepsilon_1 = 0.2$ to $\varepsilon_1 = 0.3$, the connection is not only able to bear the self-weight (*c*), but also the cube's weight (*d*). A further increasing of ε_1 (*e*) up to the value of $\varepsilon_1 = 0.8$ demonstrates that the connection is able to bear also the weight of two cubes (m_c = 2772g).
- The load-carrying capacity of the connection increases when the value of ε_2 decreases. Comparing the cases *a*, *b*, with the cases *g*, *h*, the value of ε_1 is maintained fixed, but the value of ε_2 is changed from

$\varepsilon_2 = 0.5$ to $\varepsilon_2 = 0.37$ (*h*); in contrast with *b*, where the connection is kinematic, in *h* the configuration is not only able to bear the self weight, but also the cube's weight (m_c = 1386g).

6.3.3 TEST 3: Alignment of ε_1 and ε_2 (Significance of the boundary condition GC1 (i))

Hypothesis

The load-carrying capacity of the connection is null when the condition GC1 expressed in the eq. 6-2 is verified. The GC1 is a *geometric boundary condition*; therefore, the load-carrying capacity is independent from the external load conditions.

GC1	$e_{P,1} = 0$ (internal torque of equilibrium forces)	$\varepsilon_1 = \frac{\varepsilon_2}{4 \cdot \tan\alpha}$	6-2

Test description

Date: 21/07/2015; Specimen: S0; Procedure: none. $F_{2,\perp}$, $F_{1,\perp}$ constrained time to time various to ε_2 and ε_1.

The connection properties are following described:

$l_{BC} = l_j = 2h$

$l_{AB} = 120mm$

$\alpha = 35°$

The test setup Specimen 2, provides the conditions described in the eq. 6-3. According to the eq. 6-2, once fixed the value ε_2, the values of alignment with ε_1 are the ones in Table 6-5.

$$\begin{cases} F_{1,\perp} > 0 \\ F_{1,//} \neq 0 \\ F_{2,\perp} > 0 \\ F_{2,//} > 0 \end{cases} \qquad 6\text{-}3$$

The distance *a* of the point of application of the force $F_{1,\perp}$ respect to the edge B is calculated with eq. 6-4

$$e_1 = \varepsilon_1 \cdot l_{BC} = \frac{\varepsilon_2}{4\tan\alpha} \cdot l_{BC} \qquad 6\text{-}4$$

Table 6-5 – values of alignment of the parameters ε_1 and ε_2, for the connection *α = 35°*

α **[°]**	ε_2	$\varepsilon_1 = \frac{\varepsilon_2}{4\tan\alpha}$
35	0	0.000
35	0.125	0.045
35	0.25	0.089
35	0.375	0.134
35	0.5	0.179
35	0.625	0.223
35	0.75	0.268
35	0.875	0.312
35	1	0.357

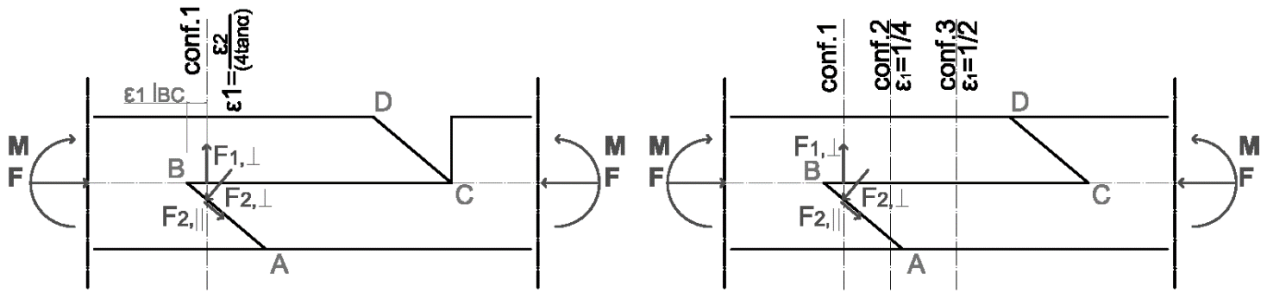

(a) (b)

Figure 6-7 - (a) test setup of the alignment configuration. (b) test setup of the different ε_1 and ε_2 configs.

The geometric configuration in which the direction of the vector force $F_{1,\perp}$ is aligned (Figure 6-7) with the point P, point of application of the resultant force $F_{2,\perp}$, is proposed for the external load conditions in self-weight (M), self-weight + additional weight of a bolt (m_b = 115g) (M + n° bolt), and self-weight + axial manual-compression (F+M), as in the following Table 6-6.

Table 6-6 – Tests 21/07/2015

	α [°]	**Fixed ε2**	**e1** [mm]	**ε1**	**l_{AB}** [mm]	**l_{BC}** [mm]	**Load condi-tions**	**Descri-ption**	**photo**
a	35	0.5	50	0.179	120	280	M	(Conf 1) precarious equilibrium	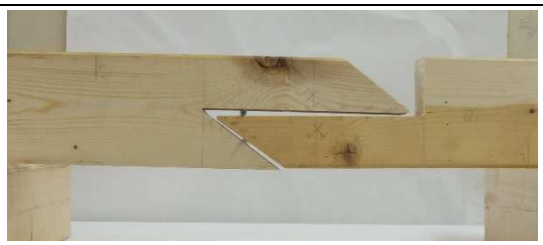 SDCF100-7657
b	35	0.5	50	0.179	120	280	M (+ 1 x bolt)	(Conf 1) kinematic	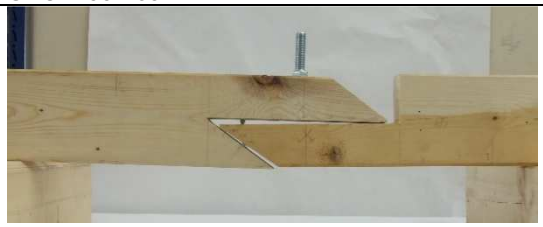 SDCF100-7658
c	35	0.375	37.5	0.134	120	280	M	(Conf 1) precarious equilibrium	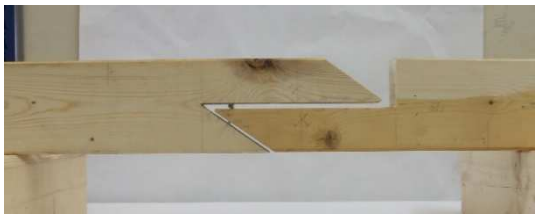 SDCF100-7659
d	35	0.375	37.5	0.134	120	280	M (+ 1 x bolt) + F	(Conf 1) kinematic	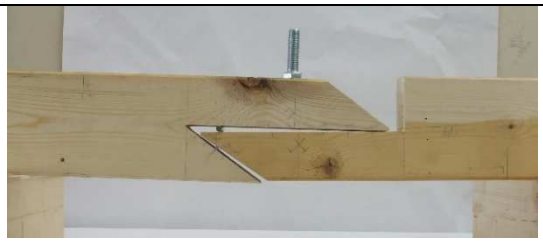 SDCF100-7660

e	35	0.5	50	0.179	120	280	M+F	(Conf 1) precarious equilibrium	 SDCF100-7674
f	35	0.5	50	0.179	120	280	M (+ 1 x bolt) + F	(Conf 1) kinematic	 SDCF100-7675

Conclusions

- Considering the cases *a*, *c* in the Table 6-5, differently to what is expressed in the eq. 6-2, the connection is not kinematic, but in "precarious equilibrium". In fact, the connection can bear the self-weight due to the non-perfect *null* value of friction μ_β on the surface 1, and imperfections in the alignment of rollers.
- In order to confirm the hypothesis expressed in eq. 6-2 the tests *b*, *d* are considered. The proposed configurations are equivalent to the configurations contained in the cases *a*, *c*, respectively; here, an additional weight (bolt) is applied. The connections does not show any load-carrying capacity.
- The alignment-configuration is also proposed for the loading condition combined bending and normal force (*e*, *f*). Here, the scenario repeats what already observed for the loading condition self-weight (*a*, *c*). In *e* the connection loaded with self-weight is in precarious equilibrium. In *f* the connection loaded with the additional weight (bolt), shows a kinematic behaviour.
- The proposed alignment-configuration is a boundary condition for the equilibrium configurations (i), (ii) and (iii), and it defines a kinematic configuration for the connection. This *geometric boundary condition* is independent from the external load conditions.
- Despite the previous points, for the case $\mu_\alpha = 0$ and some specific configurations, the connection load-carrying capacity is, in contrast, independent from the applied load.

6.3.4 TEST 4: Alignment of the ε_1, ε_2 and ε_3 (boundary condition GC2 (vii))

Hypothesis

The load-carrying capacity of the connection is *null* when the condition expressed in the eq. 6-5 is verified. The GC(vii)2 is a *geometric boundary condition*; therefore, the load-carrying capacity is independent from the external load conditions.

GC(vii)2	$\begin{cases} e_{O,P} = 0 \\ e_{P,3} = 0 \end{cases}$ (alignments of the centers)	$\begin{cases} \varepsilon_3 = 2 \cdot (1 - \varepsilon_1) \cdot \sin(2\alpha) \\ 2 \cdot \sin(2\alpha) = \varepsilon_2 + \varepsilon_3 \end{cases}$	6-5

Test description

Date: 21/07/2015; Specimen: S0; Procedure: none. $F_{2,\perp}$, $F_{3,\perp}$ constraint on $\varepsilon_2 = 0.5$ and $\varepsilon_3 = 0.5$.

Connection properties:

$$\varepsilon_1 = 0.5 \quad \varepsilon_2 = 0.5 \quad \varepsilon_3 = 0.5 \tag{6-6}$$

$$l_{BC} = l_j = 2h \quad \alpha = 75° \tag{6-7}$$

External loading conditions: F+M

According to the Figure 6-9, the test setup provide the conditions

$$\begin{cases} F_{1,\perp} > 0 \\ F_{1,//} \neq 0 \\ F_{2,\perp} > 0 \\ F_{2,//} = 0 \\ F_{3,\perp} = 0 \\ F_{3,//} = 0 \end{cases} \tag{6-8}$$

According to the eq. 6-5, for $\alpha = 15° \wedge \alpha = 75°$ and values of $e_{P,3} = 0$, the alignment of the forces $F_{1,\perp}$ - $F_{2,\perp}$ - $F_{3,\perp}$ is verified. In the Figure 6-9 is represented a scheme of this alignment configuration. In the Figure 6-8 the demonstration of the hypothesis is done.

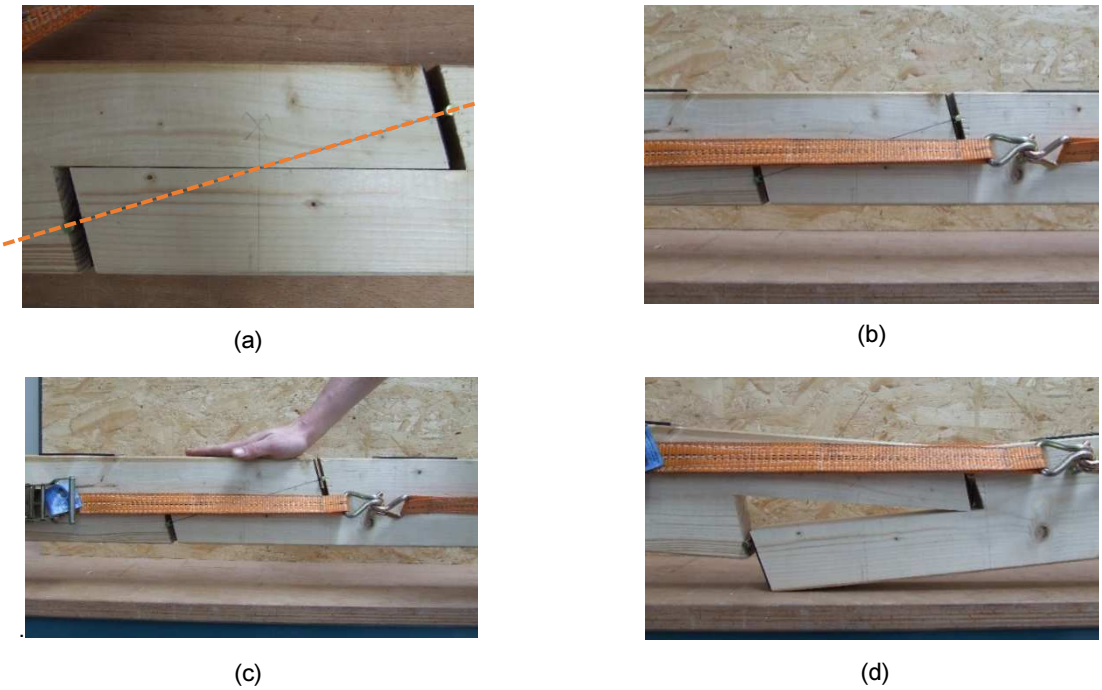

(a) (b) (c) (d)

Figure 6-8 - Demonstration: *α = 75°* Alignment of the center of rotation and no bending resistance. Test performed on 24/04/2015. (a) Alignment of the centers ; (b) Application of a normal force through a strip in correspondence of the neutral axis; (c) application of small amount of bending force; (d) failure.

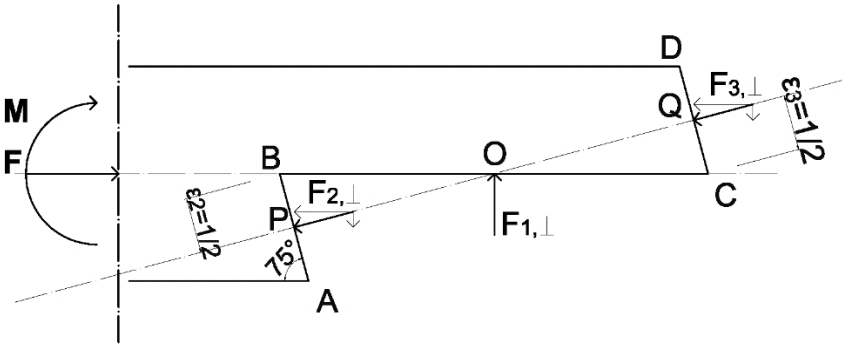

Figure 6-9 – Alignment configuration: scheme of the $e_{P,3} = 0$, for $\alpha = 75°$.

Conclusions

According to the eq. 6-9 and eq. 6-10 the lever arm between the forces $F_{3,\perp}$ and $F_{1,\perp}$ the internal rotation point located in P, point of application of $F_{2,\perp}$, is null; therefore, the load-carrying capacity of the connection is also *null*, independently on the external loading conditions.

$$\text{S1: } \varepsilon_3 = 2 \cdot (1 - \varepsilon_1) \cdot \sin(2\alpha) \qquad \text{6-9}$$

$$\text{S2: } 2 \cdot \sin(2\alpha) = \varepsilon_2 + \varepsilon_3 \qquad \text{6-10}$$

For joints with a squint's angle equal to $\alpha = 75°$ the alignment of $F_{1,\perp}$ - $F_{2,\perp}$ - $F_{3,\perp}$ is for $\varepsilon_1 = \varepsilon_2 = \varepsilon_3 = 0.5$.

6.4 Qualitative evaluation of the friction coefficient

The static friction μ_s is a difficult parameters to describe; nevertheless, it plays an important role in the load-carrying capacity of the specimen. The contribution and significance of the μ_s on the load-carrying capacity of the *halved undersquinted scarf* joint is following explained.

According to the Hp. 2, the transmission of the forces between adjacent surfaces occurs by friction. The entity of the friction is unknown, but significant parameters are:

- Angle α of the specimen.
- The roughness of the surfaces influences the load-carrying capacity and stiffness of the specimen (TEST 5).
- The increasing of the bending load-carrying capacity with the decreasing of the angle α (TEST 6).
- The value of μ_α corresponds, in the respective models (i) and (ii) to (TEST 7):

$$\begin{cases} \mu_\alpha = \tan\alpha & F_1 = 0 \quad for\,(i) \\ \tan\alpha < \mu_\alpha - \dfrac{1}{\tan\alpha} & F_1 > 0 \quad for\,(ii) \end{cases} \qquad \text{6-11}$$

- The friction coefficient μ_α decreases with the increasing of the angle α of the specimen (TEST 9).
- The maximum value for the static friction μ_α that permits to maintain in equilibrium the connection under self-weight is for (TEST 7 and TEST 8):

$$\mu_\alpha = \tan\alpha < 0.7 \quad \text{for model (i)} \qquad \text{6-12}$$

$$0.7 < \mu_\alpha < 1 \quad \text{for model (ii)} \qquad \text{6-13}$$

- The contribution of the friction force μ_β on the surface 1 increases furthermore the load-carrying capacity of the connection (TEST 9 and TEST 10). According to the level of the present research, the information about this parameter is only qualitative.
- The surface 3 is not relevant for the load-bearing behaviour of the connection loaded in pure bending and relative (to the parameter *α*) low values of combined compressive and bending force (TEST 9).
- For the elaboration of the equilibrium configurations, the parameter μ_β (in case $\beta = 0$), is not considered; in fact, the influence of this parameter on the global stiffness of the connection is minimal (TEST 10).

6.4.1 TEST 5: The friction coefficient μ_s and μ_d influenced by the roughness of the surface

Hypothesis

$$F_s = \mu_s \cdot F \qquad 6\text{-}14$$

$$F_d = \mu_d \cdot F$$

$$F_s > F_d \qquad 6\text{-}15$$

where F_s is the friction force due to the contribution of the static friction μ_s, and F_d is the friction force due to the contribution of the static friction μ_d.

The friction offered by different surface's roughness is different.

The roughness of the specimen's surfaces influences the load-carrying capacity of the specimen.

Test description

Date: 16/05/2015; Specimen: S1; Procedure: none.

The surface's roughness is in the present test artificially influenced. The different "fiber contact" is following described. The key for the lecture of the tests is contained in Figure 6-10 (a). In the Figure 6-10 (b) are represented the two different *fiber contact*.

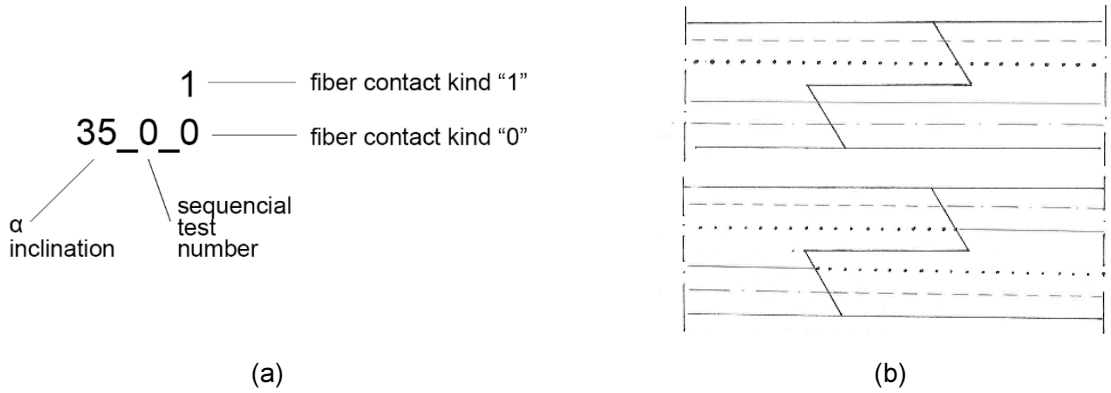

Figure 6-10 –lecture-key of the test results and (b) scheme: above, *fiber contact* "0"; under, *fiber contact* "1"

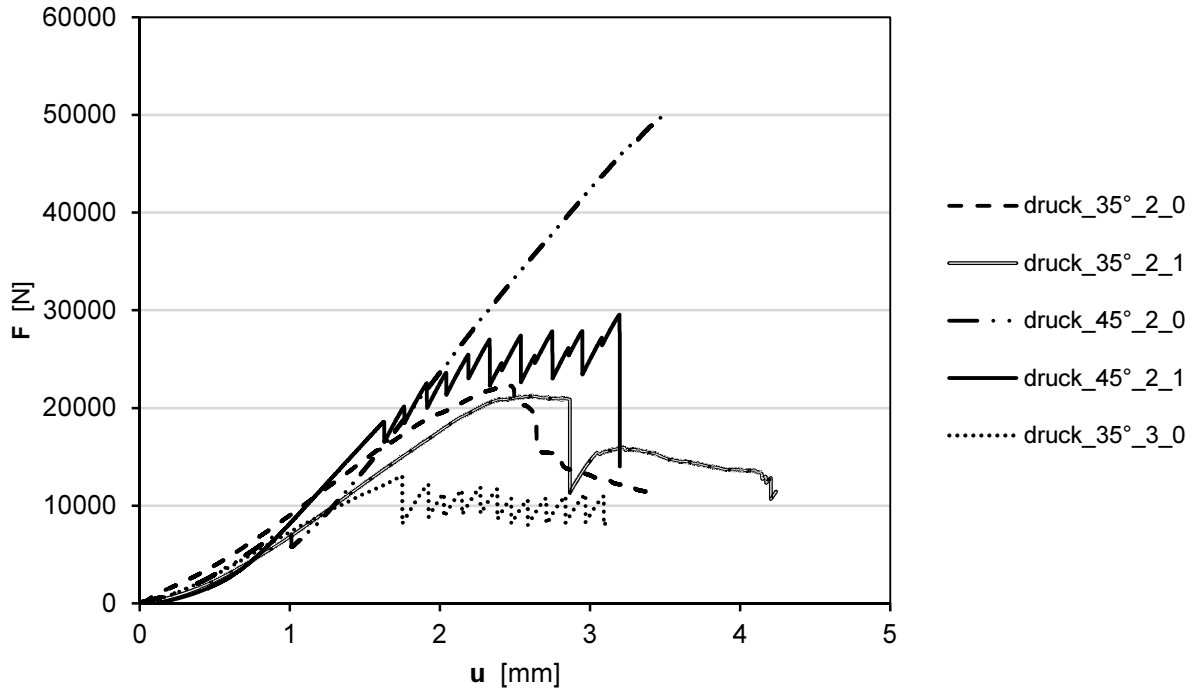

Diagram 6-1 – Test results on the different roughness of the surface2

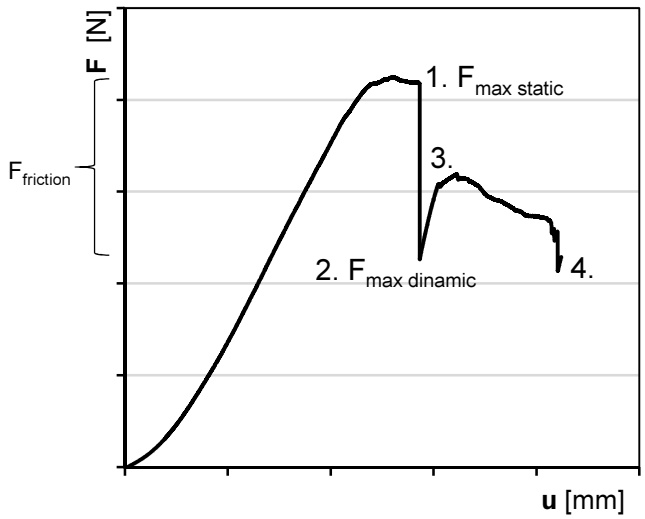

Diagram 6-2 – Schematization of the loading process for the specimen 35_2_1

The *fiber contact 0* describes specimens which joint is shaped from the same piece; here, the grains in the two pieces are continuous and facing. The *fiber contact 1* describes specimens which joint is from two different timber pieces, or from the same overturned piece; here, the grains are not consecutive from one to the other joint's part.

In the Diagram 6-1 the performed tests are represented. In the tests is observed that the F_u for specimens with same geometry but different roughness of surfaces 2 and 3 is different. In particular:

a) the behaviour of the specimen *fiber contact 1* and *fiber contact 0* is different;

b) the specimen *fiber contact 0* are stiffer than the ones with *fiber contact 1*;

c) the specimen druck_35_3_0 represents an exception to the observation b);

d) specimens with bigger *α* angle are stiffer.

What is of interest is also the "jump" observed for most of the specimens. In particular, for the specimen druck_35_2_1 the oscillating result has been explained in dependence on the passage from the $F_{max,static}$ (due to the static friction coefficient μ_s) to the $F_{max,dynamic}$ (due to the coefficient of dynamic friction μ_d). Referring to the Diagram 6-2, a lecture of the points' number is following done:

1. = limit of the μ_s;

2. = reaching of the equilibrium. The connection reaches the equilibrium and keeps behaving in a static manner;

2-3 = the load is again increasing from 2 to 3. The load is increasing with static trend. This is due to the slipping of the homogenous surface between the two annual rings;

3-4 = in 3 the maximum load is reached with the contribution of the static friction μ_s; then, the surface starts again behaving in a constant way, this time with the contribution of the dynamic friction μ_d, until the status 4 is reached;

The process continue with such behaviour's sequence, up to the failure.

Conclusions

For specimens loaded in pure compression, with same geometry but different surfaces' roughness, due to the different kind of *fiber contact*, the F_u and the stiffness are different. Therefore, the roughness influences the joint's behavior.

As demonstrated in the present tests, the roughness of the specimen can be influenced at the time of the fabrication through the kind of saw machine and pieces used for the joint's fashioning.

6.4.2 Contribution of μ_α

6.4.2.1 TEST 6: influence of the angle on the load – bearing capacity of the surface $\overline{AB}$

Date: 16/04/2015; Specimen: S1; Procedure: P0 - a.

Table 6-7 – Medium values

Specimen	*α* [°]	Distance to the support [mm]	Fmax [kN]	Mu [kN mm]	Failure mode
0415_01	45	400	2.71	542	Shear/tension grain in B
0415_02	60	400	0	0	-
0415_03	30	400	F = $F_{u,e}$ = 3.5 kN	700	Shear/tension grain in B

Hypothesis

The load-carrying capacity in bending increases with the decreasing of the angle *α*.

Conclusions

The specimens demontrates the increasing of the bending load-carrying capacity with the decreasing of the angle *α*. The specimen *α = 60°* doesn't have any bending resistance, while the specimen *α = 30°* demonstrates

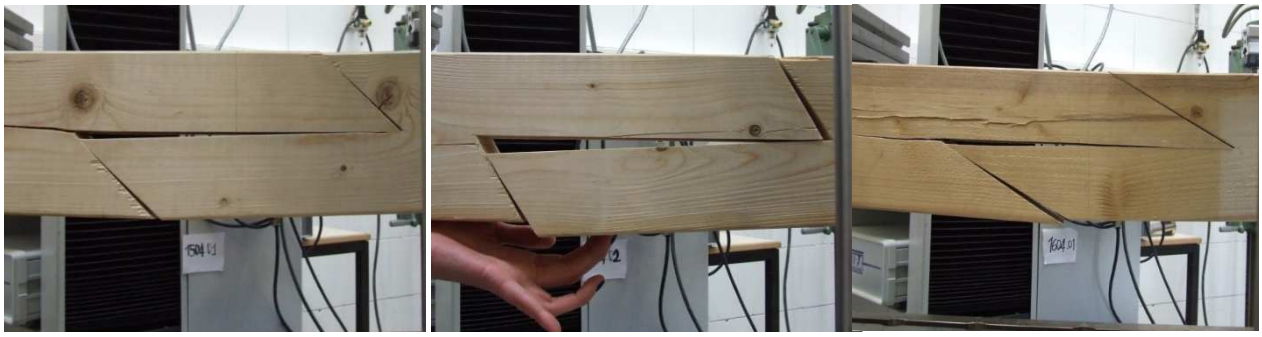

(a) (b) (c)

Figure 6-11 – Failure of (a) $\alpha = 45°$ specim. 0415_01; (b) $\alpha = 60°$ specim. 0415_02; (c) $\alpha = 30°$ specim. 0415_03.

the maximum load-carrying capacity. The present test demonstrate the limit state of static equilibrium (EQU) for the *halved undersquinted* half joint (see EN 1990:2002 Eurocode - Basis of structural design – section 6.4 a)).

Considering the *halved undersquinted and tabled* scarf joint, the presence of the table, confers further load-carrying capacity to the connection with squint $\alpha = 60°$. For more details see the Annex A.

6.4.2.2 TEST 7: Significance of the μ_α value, according to the static models (ii).

Hypothesis

The models (i), (ii) give the description of the equilibrium path followed from the test specimen according to eq. 6-11.

Test description

Date: 20/01/2016; Specimen: S1; Procedure: P1 - d.

The data showed in the Table 6-8 are data registered along the loading process (*test results*), and their analytical elaboration (*analytic test results*) is calculated according to the model (ii). In the field *analytic test results*, the values of ε_1, ε_2 and ε_3 are chosen according to the Table 6-2, and the friction coefficient μ_α is quantified as in eq. 6-16.

Table 6-8 – Data test specimen R30_F0_bis and analytical elaboration according to (ii). PI = Piston I; P II = Piston II

								test results				analytic results model (ii)				
									P II		P I					
		α [°]	**h** [mm]	**ε1**	**ε2**	**ε3**	**ε F**	**lever arm** [mm]	**F_{II}** [kN]	**M** [kN mm]	**F_I=N** [kN]	**F2,⊥** [kN]	**F2,//** [kN]	**F1,⊥** [kN]	**F3,⊥** [kN]	**μα**
R_30_F0_bis	a	30	140	0.5	0.5	-	0	405	0.040	8.10	0.01	0.090	0.040	0.098	-	0.448
	b	30	140	0.5	0.5	-	0	405	0.060	12.50	0.018	0.135	0.057	0.145	-	0.423
	c	30	140	0.5	0.25	-	0	405	0.093	18.83	0.056	0.212	0.058	0.213	-	0.272
	d	30	140	0.5	0.25	-	0	405	0.134	27.14	0.09	0.247	0.039	0.233	-	0.156
	e	30	140	0.5	0.25	-	0	405	0.274	55.49	0.208	0.624	0.042	0.424	-	0.067
	f	30	140	0.5	0.25	-	0	405	0.52	105.30	0.312	1.070	0.188	0.855	-	0.175
	g	30	140	0.5	0.25	-	0	405	0.813	164.63	0.515	1.486	0.263	1.419	-	0.177
	j	30	140	0.5	0.25	-	0	405	1.078	218.30	0.66	1.962	0.371	1.885	-	0.189
	k	30	140	0.75	0.25	-	0	405	1.146	232.07	0.707	1.412	-0.001	1.223	-	-0.001
	l	30	140	0.75	0.25	-	0	405	1.633	330.68	1.009	2.013	-0.003	1.742	-	-0.001
	m	30	140	0.81	0.19	-	0	405	2.897	586.64	2.05	3.392	-0.409	2.734	-	-0.120
	n	30	140	0.88	0.13	-	0	405	4.332	877.23	4.057	5.200	-1.682	3.662	-	-0.324
	o	30	140	0.94	0.13	-	0	405	6.375	1290.90	6.04	7.355	-2.728	5.006	-	-0.371
	p	30	140	0.94	0.13	-	0	405	6.646	1345.80	6.417	7.724	-2.950	5.214	-	-0.382

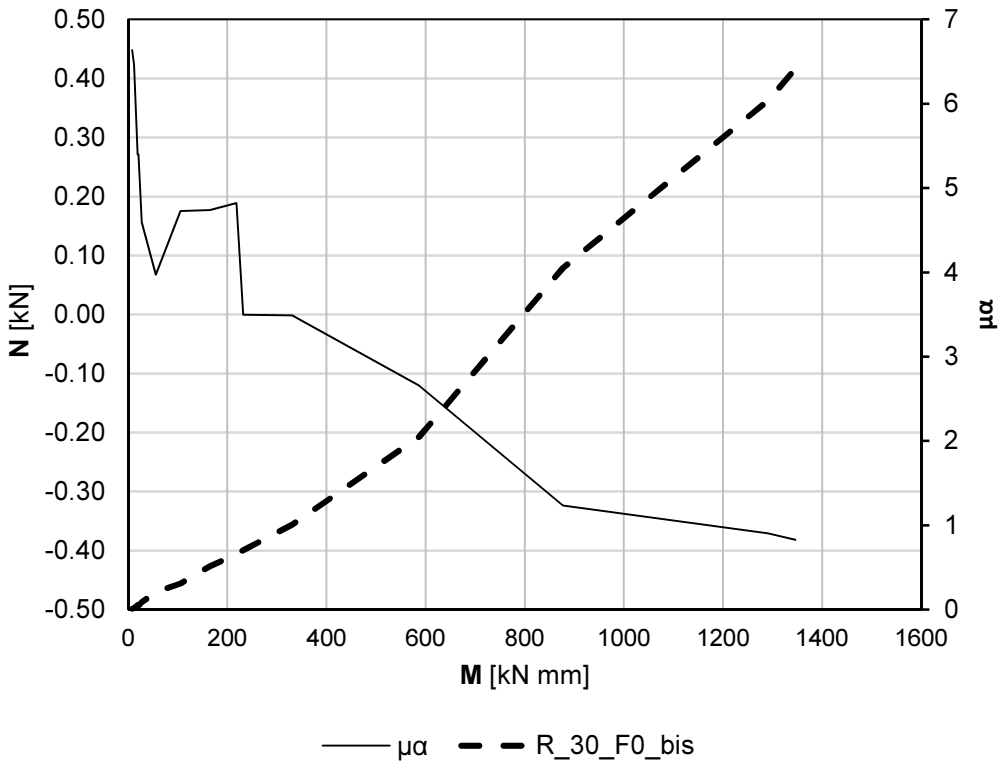

Diagram 6-3 – N-M interaction curve of the test specimen R30_F0_bis with *μα* values calculated according to eq. 6-16 model (ii).

$$\mu_\alpha = \frac{F_{1,\perp} \sin \alpha - F \cos \alpha}{F \sin \alpha + F_{1,\perp} \cos \alpha} \qquad 6\text{-}16$$

For any of the pair of forces recorded in different loading instants, the value of the resultant forces and friction are described according to the analytical model (ii).

In the N-M interaction Diagram 6-3 the equilibrium path of the specimen R30_F0_bis is described, and correspond to the equilibrium path described by LS1 of the model (ii).

The model R30_F0_bis cannot verify the model (i), because the field of validity of the model (ii) is F > 0; nevertheless, the smaller the amount of stress in the specimen, the bigger the value of μ_α.

The specimen verifies the models for the following values of μ_α:

Model (i):

$$\lim_{N \to 0} \mu_\alpha = \tan(\alpha) \qquad 6\text{-}17$$

for

$$0.534 \leq \mu_\alpha < 0 \qquad 6\text{-}18$$

Model (ii):

$$\begin{cases} 0kN < F < 0.707kN \\ 0kN \cdot mm \leq M \leq 232.07kN \cdot mm \end{cases} \qquad 6\text{-}19$$

for

$$0.534 \leq \mu_\alpha < 0 \qquad 6\text{-}20$$

Model (iii) :

$$\begin{cases} F = 0.707kN \\ M = 232.07kN \end{cases} \quad \text{6-21}$$

for

$$\mu_\alpha = 0 \quad \text{6-22}$$

Finally, the specimen verifies the condition LS1 for the model (ii)

$$\begin{cases} F > 0.707kN \\ M > 232.07kN \end{cases} \quad \text{6-23}$$

for

$$0 < \mu_\alpha \leq -0.382 \quad \text{6-24}$$

Conclusions

- Along the loading process, the connection follows the values of μ_α expected in the model (ii) eq. 6-11.
- It is important to remark that the values of friction described in the Table 6-8 that verify the model (ii) are not describing the expected methodically behaviour described in the eq. 6-11. While the value of μ_α for the pair of forces *l*, *m*, *n*, *o*, *p*, *q* is methodically increasing, the values of μ_α for the pair of forces *a* to *i* (to be verified in accordance with (ii)) are not methodically decreasing with the increasing of the loading. To further confirm the validity of the model (ii) the analysis of the specimens Mod2_30_E1_F0_3/4 follows in the TEST 8.
- The model (i) cannot be verified for F = 0 and M = 0; therefore, a further demonstration of the validity of the model (i) is also given in the TEST 8.

6.4.2.3 TEST 8: increasing value of friction during the loading process, according to (i) and (ii).

Hypothesis

The models (i) and (ii) give the description of the equilibrium path followed from the test specimen according to eq. 6-11. Since the values of μ_α in the model (ii) have already been demonstrated in the TEST 7, the parameter μ_α for (i) should assume the values in the eq. 4-20.

Test description

Date: 26/11/2015; Specimen: S2; Procedure: P1 - e. $F_{1,\perp}$, $F_{2,\perp}$ constrained on $\varepsilon_1 = 3/4$ and $\varepsilon_2 = 1/4$.
The data in Table 6-9 describe the specimen Mod2_30_e1_3/4_F0 along the loading process (*test results*) and their analytical elaboration (*analytic test results*) according to the model (ii). The specimen is loaded in pure bending with the Piston 2. The Diagram 6-4 represent the data elaborated in the Table 6-9.

- The specimen has no deformation along the vertical axes until the value of $M = 140kN \cdot mm$. Afterwards, is triggered a deformation along the longitudinal direction, that causes the *passive response* on the Piston 1.

Table 6-9 – Date description of the tests (a) Mod2_30_E1_F0_3/4

		α [°]	h [mm]	ε1	ε2	ε3	ε F	test results				analytic results model (ii)				
								II piston			I piston	F2,⊥ [kN]	F2,// [kN]	F1,⊥ [kN]	F3,⊥ [kN]	μα
								lever arm [mm]	FII [kN]	M [kN mm]	FI=N [kN]					
Mod2_30_e1_3/4_F0	a	30	140	0.75	0.25	-	0	405	0.599	121.3	0	0.585	0.338	0.675	-	0.577
	b	30	140	0.75	0.25	-	0	405	0.6	121.5	0	0.586	0.338	0.676	-	0.577
	c	30	140	0.75	0.25	-	0	405	0.669	135.47	0	0.653	0.377	0.754	-	0.577
	d	30	140	0.75	0.25	-	0	405	0.853	172.73	0.1	0.874	0.389	0.952	-	0.445
	e	30	140	0.75	0.25	-	0	405	1.218	246.65	0.3	1.313	0.412	1.343	-	0.314
	f	30	140	0.75	0.25	-	0	405	1.56	315.9	0.4	1.689	0.513	1.719	-	0.304
	g	30	140	0.75	0.25	-	0	405	1.66	336.15	0.5	1.828	0.478	1.822	-	0.262

- In the first part of the loading, corresponding to pure bending loading, from the lines a, b, c of the Table 4-6 - a, and according to the model (i) is confirmed that:

$$\mu_\alpha = \tan\alpha = \tan(30) = 0.577 \qquad 6\text{-}25$$

- In the second part of the loading, the value of the parameter μ_α decreases along the loading process according to the model (ii).

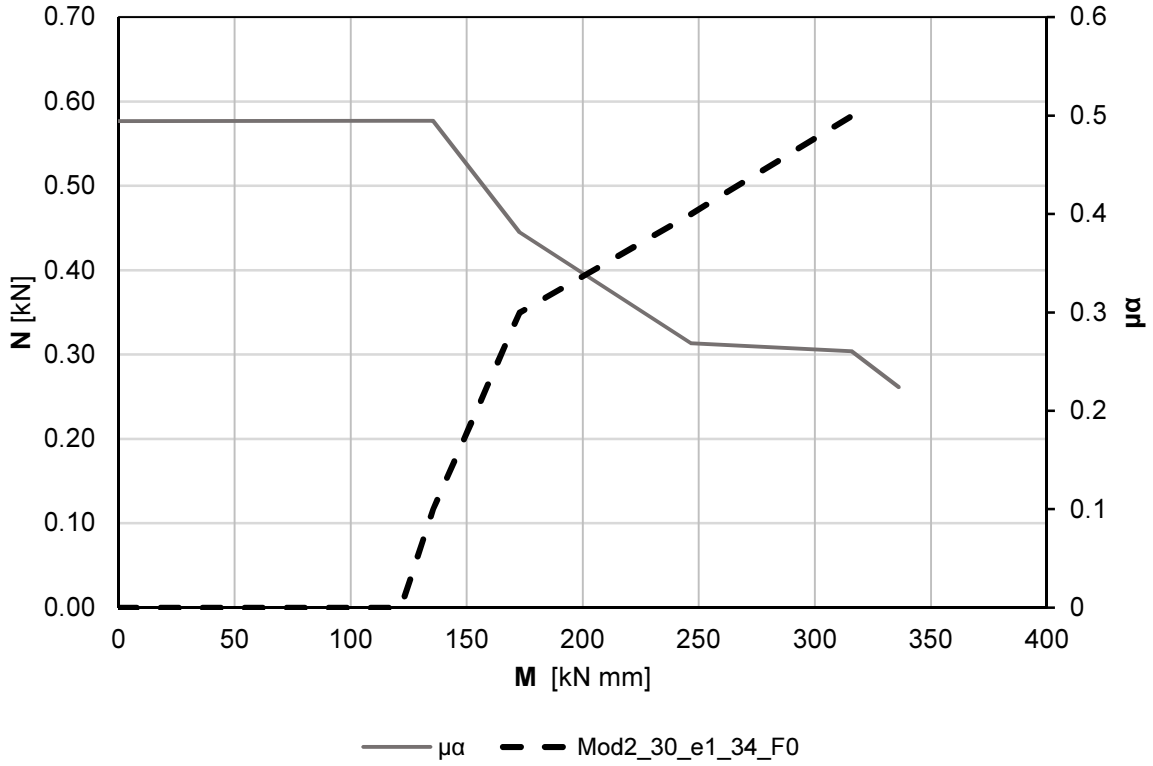

Diagram 6-4 – Mod2_30_E1_F0_3/4. N-M diagram with μ_α values according to (ii)

Conclusions

It is demonstrated that along the loading process, the connection follows the values of μ_α expected in the eq. 4-20 and eq. 6-11.

6.4.3 Contribution of μ_β

6.4.3.1 TEST 9: Contribution of μ_β

Date: 28/04/2015; Specimen: S0. Procedure: none. Configuration 1 (no constraint); Configuration 2 ($F_{1,\perp}$ constraint at approx. $\varepsilon_1 = 3/4$).

The test specimens have different entity of parameter α, and are stressed with different external loading conditions, as the configurations represented in the Figure 6-12 (a) and (b), and contained in Table 6-10.

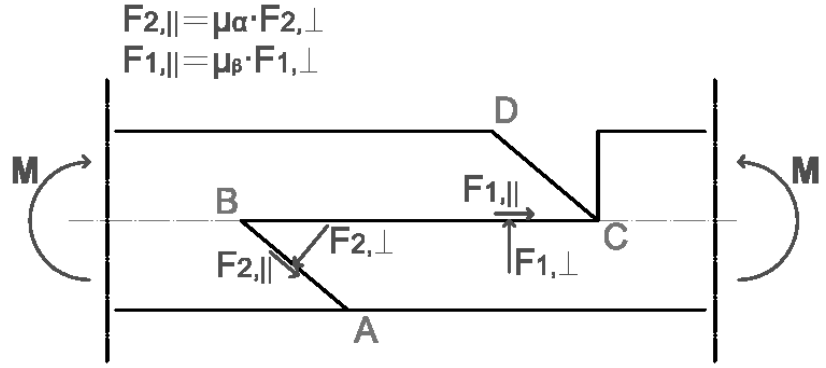

(a)

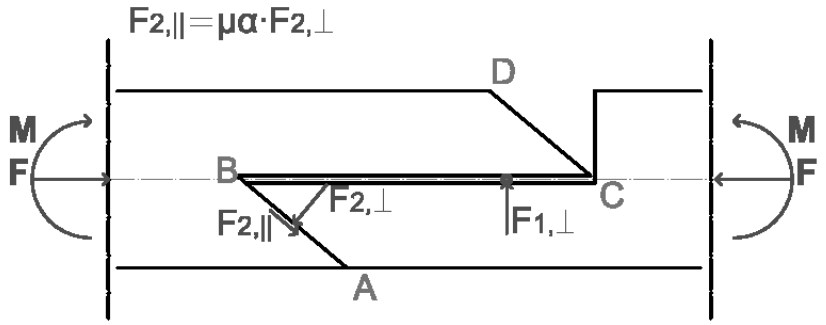

(b)

Figure 6-12 – (a) Configuration 1 (contact on both the surfaces 1 and 2); (b) configuration 2 (contact on the surface 2 and roller on the surface 1)

According to the Figure 6-12, in the configuration (1) the forces $F_{1,\perp}$ and $F_{2,\perp}$ on the surfaces 1 and 2 are associated with the friction force, respectively μ_β and μ_α. In the configuration (2), the contribution of the surface 1 is limited to the transmission of the force $F_{1,\perp}$ that is constrained at approx. $\varepsilon_1 = 3/4$ (with the *rround* roller device), and no friction component; while, along the surface 2 the force $F_{2,\perp}$ is associated with the friction force equal to μ_α. The loading conditions are LC1: only self-weight (pure bending M) and LC2: self-weight (M) combined with axial manual-compression (F). In the Table 6-10, the tests are described.

Conclusions

- The maximum value for the static friction μ_α that permits to maintain in equilibrium the connection under self-weight is for a value of α in between $\alpha = 30°$ and $\alpha = 35°$. In fact, in conf. 2 the connection $\alpha = 30°$ bears the self-weight, while the connection $\alpha = 35°$ and $\alpha = 45°$ have no load-carrying capacity. According to the correspondent calculations contained in (i), the value of friction considered is the one in eq. 6-26.

$$\mu_\alpha = \tan\alpha < 0.7 \qquad 6\text{-}26$$

- In conf. 2, the connection $\alpha = 45°$ has no load-carrying capacity. According to (i), the friction value for such connection is $\mu_\alpha = \tan\alpha = 1$. → According to (i) the amount of friction on the surface 2 is:

$$0.7 < \mu_\alpha < 1 \qquad 6\text{-}27$$

- While for the models with $\alpha = 30°$ the contribution of the friction in the surface 1 is negligible respect to the one of the surface 2, for the load-carrying capacity of specimens $\alpha > 30°$ the contribution of the friction on the surface 1 is of significance. In fact, the confs. 1 are always in equilibrium and the confs. 2 are not.
- The surface 3 ($\overline{CD}$) is not relevant for the load-bearing behaviour of the connection loaded in pure bending and relative low values of combined compressive and bending force → the model (ii) is developed basing on this statement.

Table 6-10 – Tests: influence of the parameters μ_α and μ_β without the contribution of the surface $\overline{CD}$

α [°]	**LC1: Self-weight (M) (configuration 1)**	**LC1: Self-weight (M) (configuration 2)**	**LC2: Self-weight +axial manual-compression (M+F) (configuration 2)**
30	100-7015 - equilibrium 	100-7017 - equilibrium 	
35	100-7022 - equilibrium 	100-7023 - kinematic 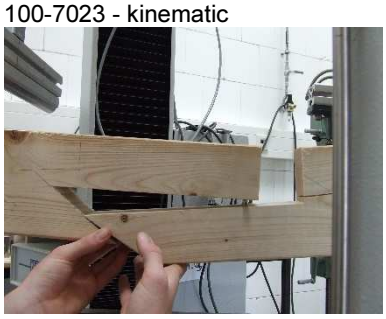	100-7024 - kinematic 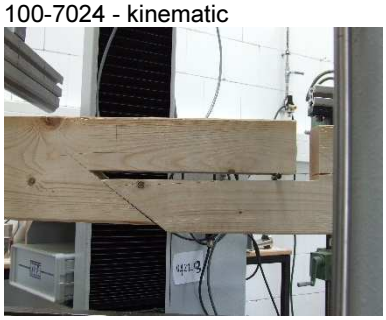
45	100-7008 - equilibrium 	100-7009- kinematic 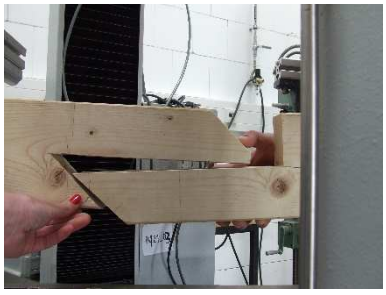	100-7010- kinematic 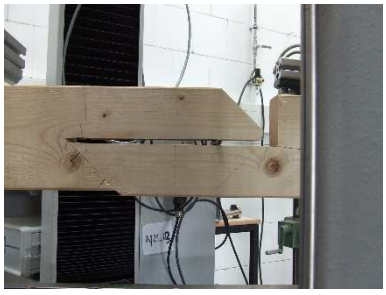

6.4.3.2 TEST 10: Qualitative evaluation of the parameter μ_β (LC: pure compression)

Date: 04-11/05/2015; Specimen: S0. Procedure: P1 - b. Various constraints.

In the following Table 6-11 and in the Figure 6-13 are represented the performed tests. The test refers to the static model (vii).

Table 6-11 – Description of the tests performed on the 04-11/05/2015

Test	Specimen	Loading conditions	Procedure	Comments
Druck_01	S1	Pure compression	P0b	
Druck_02	S1 with steel plates and rollers on the surfaces 2 and 3	Pure compression	P0b	no friction in 2 and 3
Druck 03	S1 with gap between the facing surfaces1	Pure compression	P0b	no friction in 1

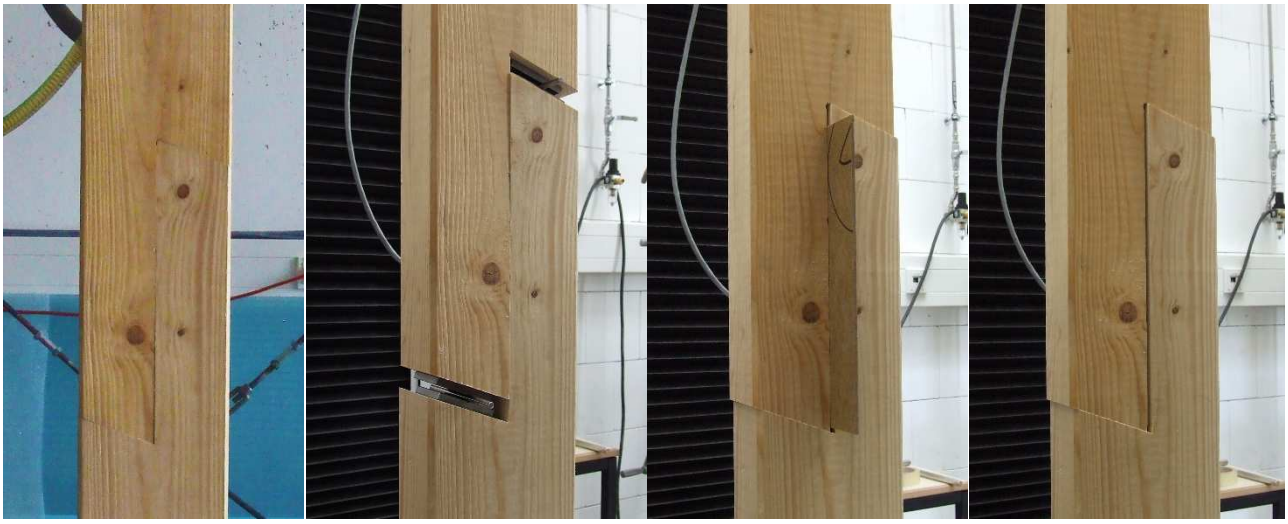

(a) (b) (c) (d)

Figure 6-13 – (a) Druck_01; (b) Druck_02; (c) Druck_03 – preparation of the gap; (d) Druck 03 test

The Diagram 6-5 illustrates the test results for three different test specimens. The specimen Druck_01 shows the highest value of stiffness, while the test Druck_02 the lowest one. The specimen Druck_03 an intermediate value of stiffness between the Druck_01 and Druck_02. Two different friction coefficients supply to the stiffness and the ultimate value of the two specimen. On one side, the specimen Druck_02 can count on the contribution of the friction coefficient of the surface 1; here, the friction of the surface 2, and surface 3 is null. On the other side, the specimen Druck_03 cannot count on the friction of the surface 1, but of surfaces 2 and 3.
From the observation of the diagram is thus evident that under pure compression stress, the stiffness contribution of the surface 1 is smaller than the contribution of the surface 2 (and surface3).

Conclusions

From the tests is concluded that the parameter μ_β, in case $\beta = 0$, has a minimum influence on the stiffness of the connection. Therefore, for the elaboration of the equilibrium consideration, it can be considered as null.

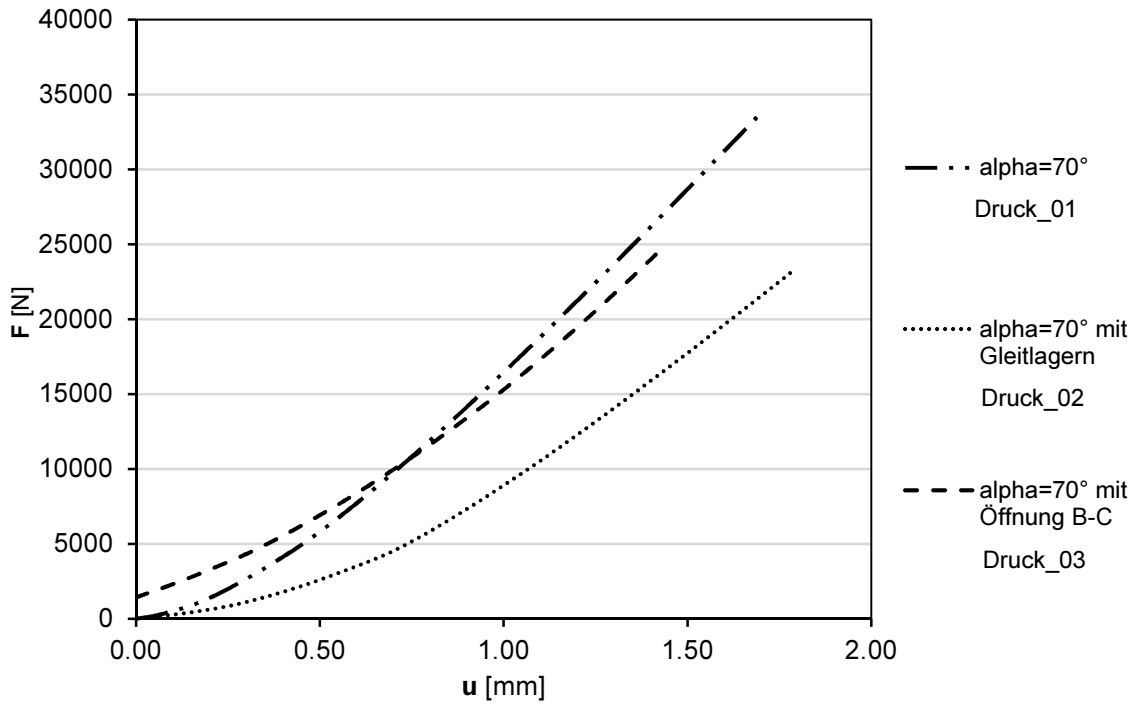

Diagram 6-5 - Contribution of the friction force on the surface1

6.5 TEST 11: Influence of the pre–compression in the halved undersquinted joint

The following TEST 11 gives a demonstration of the independence of the loading path from the value of the initial pre-compression.

TEST DESCRIPTION

Date: 20/01/2016; Specimen: S1. Procedure: P2 - d.

In the Diagram 6-6 are represented the N–M the curves for the tests R30_F_M_2; R30_F_M_3 and R30_F_M_4. The three specimen are the same timber specimen (re-used). This was possible because in each of the tests the specimen was not loaded until failure, but the tests were stopped when the loading path was superposing with the one of the other specimens. Furthermore, the fourth specimen R_30_F_M was selected as visually graded as with similar characteristics with the specimen R30_F_M_2. This is loaded up to a value of $F_{I,target}$ = 2 kN and then up to failure.

- As first step, each specimen was pre-compressed with the Piston I with an amount of pure compression equal to $F_{I,target}$ different for each specimen, as described in the Table 6-12.
- In the first part of the loading ($F_{I,target}$), where the pre–compression is applied, the specimens cover different paths.
- In the second part (F_{II}) of pure bending loading, the specimens align their loading path.
- On the other side, it is also evident that the first part of the pure compression loading, approximately a linear path, has for the three specimen equivalent inclination.

Conclusions

During the loading process, the specimen follows a specific load path that is not dependent on the value of the applied pre-compression. → The equilibrium path of the specimen is independent from the initial pre-compression.

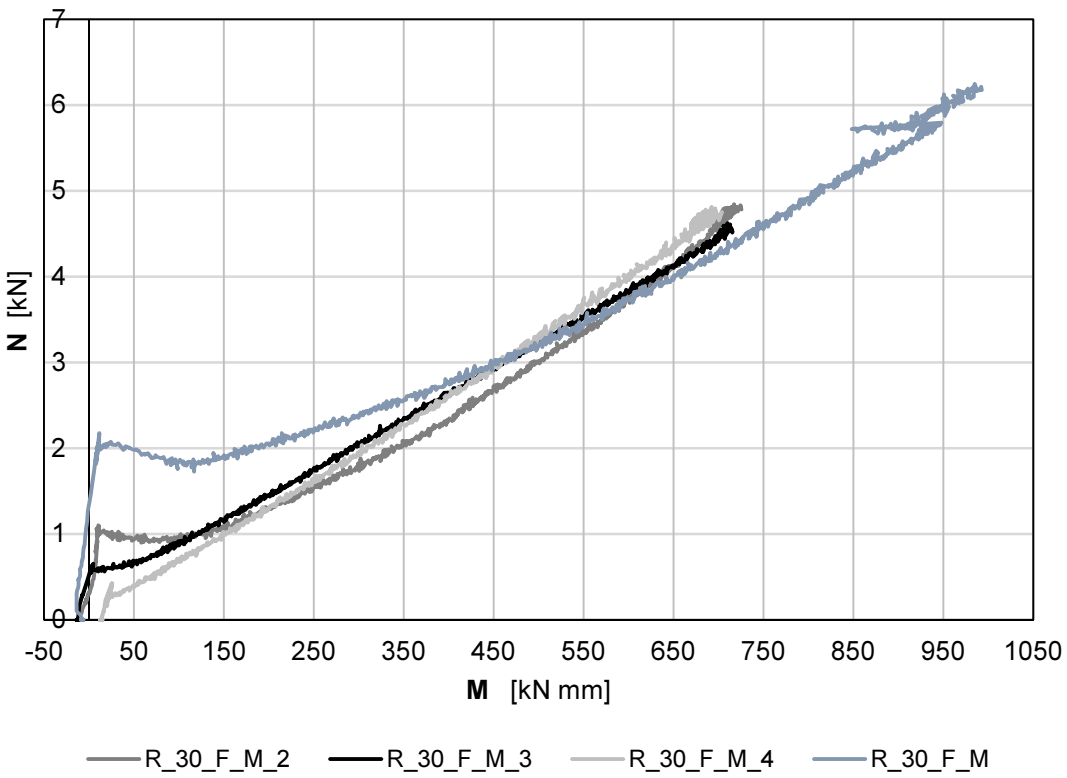

Diagram 6-6 – The equilibrium path of the specimen is independent from the initial pre-compression

Table 6-12 – Description of the pre – compression influence tests

Specimen	F_{target} F_{II} [kN]	Proce-dure	F_{II} [kN]	F_I [kN]	Dist. support [mm]	M [kN mm]	N [kN]	Observations
R30_F_M	2	P2 - d	4.90	6.20	405	1984.5	6.20	(s)
R30_F_M_2	1	P2 - d	3.49	4.78	405	1413.45	4.78	(s)
R30_F_M_3	0.5	P2 - d	3.40	4.66	405	1377	4.66	(s) Same specimen R30_F_M_2
R30_F_M_4	0.25	P2 - d	3.23	4.67	405	1308.15	4.67	(s) Same specimen R30_F_M_3.

(s) Stopped test (not up to break)

6.6 TEST 12: The function of the surface 1 ($\overline{BC}$)

Test description

Date: 07/06/2015; Specimen: S1. Procedure: P0 - c for 0 mm < *a* < 70 mm lever arm (lever arm *a = 58.3 mm)*. The Specimen Cb75_0_1 is represented in the Figure 6-14 – a) and b).

The specimen is loaded in combined compressive and bending stress. During the loading process, a gap (a jump between the facing surfaces 2) appeared at F = 5 kN. F_u = *21 kN*, FM IV: instability/buckling.

Date: 07/06/2015; Specimen: S1. Procedure P0 - c for 0 mm < *a* < 70 mm lever arm (lever arm *a = 58.3 mm)* + spacing. The Specimen Cb75_0_3 is represented in Figure 6-14 – c) and d). A space in correspondence of the adjacent surfaces 1 (wooden sheets with a thickness of s = 3 mm) is created before the starting the tests. Nevertheless, the specimen had to be pre-compressed in order to maintain it in the initial fixed equilibrium

situation; in fact, the space tends to close after removing the wooden sheets. The pre-compression did not altered the final result (see TEST 6.).

The specimen is loaded in combined compressive and bending stress. Since the very beginning, the connection shows gaps (jumps between the facing surfaces 2). F_u = *17 kN*, FM IV: instability/buckling.

(a) (b) (c) (d)

Figure 6-14 – Tests performed on 07/06/2015. (a) cb75_0_1 *a = 58.3mm*; (b) Cb75_0_3 *a = 58.3 mm* + spacing: positioning of the distanciators; (c) Cb75_0_3 *a = 58.3 mm* test; (d) Failure mode of the specimen

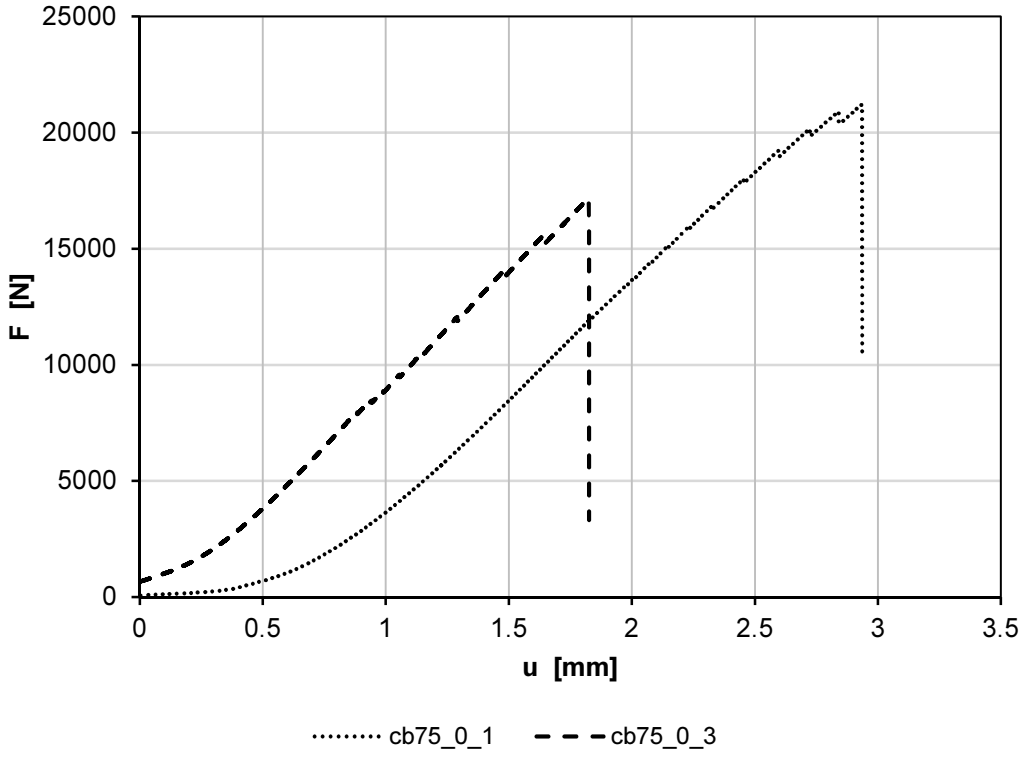

Diagram 6-7 – Results for the cb75_0_1 and cb75_0_3 loaded in pure compression.

Conclusions

Considering the specimen with *a = 58.3mm*. The specimen cb75_0_1 (without the spacing between the adjacent surfaces achieved a higher value of F_u respect to the specimen cb75_0_3. Therefore, the surface 1 increases the load-carrying capacity of the connection.

6.7 TEST 13: Verification of the equilibrium condition LS1

Hypothesis

Considering the equilibrium equation LS1 for the models (ii)

$$F = \frac{\frac{M}{h}}{\left[2\left(\varepsilon_1 - \frac{\varepsilon_2}{4\tan\alpha}\right)\left(\frac{\cos\alpha + \mu_\alpha \sin\alpha}{\sin\alpha - \mu_\alpha \cos\alpha}\right) - \frac{(\varepsilon_F - \varepsilon_2)}{2}\right]} \qquad 6\text{-}28$$

And the equilibrium equation LS1 for the model (iii)

$$F = \frac{\frac{M}{h}}{\left[\frac{2}{\tan\alpha}\left(\varepsilon_1 - \frac{\varepsilon_2}{4\tan\alpha}\right) - \frac{(\varepsilon_F - \varepsilon_2)}{2}\right]} \qquad 6\text{-}29$$

The equilibrium condition LS1 of the models (ii) (iii) describes the equilibrium path of the specimens along the loading process, for values of F equal to $0 < F \le F_u$.

Test description

Referring to the Table 6-8 (Model R30_F0_bis) and the Diagram 6-3 for the selected pair of forces c), j), l), p), the verification of the equilibrium condition LS1(ii) i.e. (iv) follows:

c) $M = 18.833\,;\ N = 0.056;\ \mu_\alpha = 0.232\ ;\ \varepsilon_1 = 0.5\ ;\ \varepsilon_2 = 0.25$

$$0.056 = \frac{\frac{18.833}{140}}{\left[2\left(0.5 - \frac{0.25}{4\cdot\tan(30)}\right)\left(\frac{\cos(30) + (0.272)\cdot\sin(30)}{\sin(30) - (0.272)\cdot\cos(30)}\right) - \frac{(0 - 0.25)}{2}\right]} \cong 0.048$$

j) $M = 218.3\,;\ N = 0.66\,;\ \mu_\alpha = 0.189\ ;\ \varepsilon_1 = 0.5\ ;\ \varepsilon_2 = 0.25$

$$0.66 = \frac{\frac{218.3}{140}}{\left[2\left(0.5 - \frac{0.25}{4\cdot\tan(30)}\right)\left(\frac{\cos(30) + (0.189)\sin(30)}{\sin(30) - (0.189)\cdot\cos(30)}\right) - \frac{(0 - 0.25)}{2}\right]} \cong 0.6599 \qquad 6\text{-}30$$

l) $M = 330.68\,;\ N = 1.00\,;\ \mu_\alpha = -0.001\ ;\ \varepsilon_1 = 0.75\ ;\ \varepsilon_2 = 0.25$

$$1.009 = \frac{\frac{330.68}{140}}{\left[2\left(0.75 - \frac{0.25}{4\cdot\tan(30)}\right)\left(\frac{\cos(30) + (-0.001)\sin(30)}{\sin(30) - (-0.001)\cdot\cos(30)}\right) - \frac{(0 - 0.25)}{2}\right]} \cong 1.008 \qquad 6\text{-}31$$

p) $M = 1345.8\,;\ N = 6.417\ ;\ \mu_\alpha = -0.232\ ;\ \varepsilon_1 = 0.937\,;\ \varepsilon_2 = 0.125$

$$6.417 = \frac{\frac{1345.8}{140}}{\left[2\left(0.937 - \frac{0.125}{4\cdot\tan(30)}\right)\left(\frac{\cos(30) + (-0.382)\sin(30)}{\sin(30) - (-0.382)\cdot\cos(30)}\right) - \frac{(0 - 0.125)}{2}\right]} \cong 6.417 \qquad 6\text{-}32$$

As already observed, the value of friction is variating along the loading process. More, the special value of friction $\mu_\alpha = 0$ is univocally described by the model (iii). A further verification according to the LS1 (iii) for the case k), follows.

k) $M = 232.07$; $N = 0.707$; $\mu_\alpha = -0.001 \cong 0$; $\varepsilon_1 = 0.75$; $\varepsilon_2 = 0.25$

$$232.07 = \left[\frac{2}{\tan(30)} \left(0.75 - \frac{0.25}{4 \cdot \tan(30)} \right) - \frac{0 - 0.25}{2} \right] \cdot 0.707 \cdot 140 \cong 232.523 \qquad \text{6-33}$$

Conclusions

The test results confirmed that the equilibrium path is well described through the equilibrium equations LS1 for LS1(ii) i.e. (iv) and the LS1 (iii) of the developed analytical model.

Chapter 7 EXPERIMENTAL CAMPAIGNS

7.1 Introduction

In the present chapter, a little experimental information is given on the behaviour of some of the most diffused elongation wood-wood connections. The aim is to obtain N-M interaction diagrams for the *halved undersquinted scarf, the Jupiter joint*, and intermediate geometries like the *halved joint*, *the stop-splayed and undersquinted* scarf and the *halved undersquinted and tabled scarf with key* scarf joint. Static in-plane and out-of-plane tests on scaled timber beams were performed.
The tests were carried out in the LHT Labor für Holztechnik of the Fakultät Bauen und Erhalten in the HAWK (University of applied sciences) Hildesheim, Germany, during the period April 2015 - July 2016.

7.2 Experimental campaign: halved and undersquinted scarf joint

7.2.1 Specimen preparation

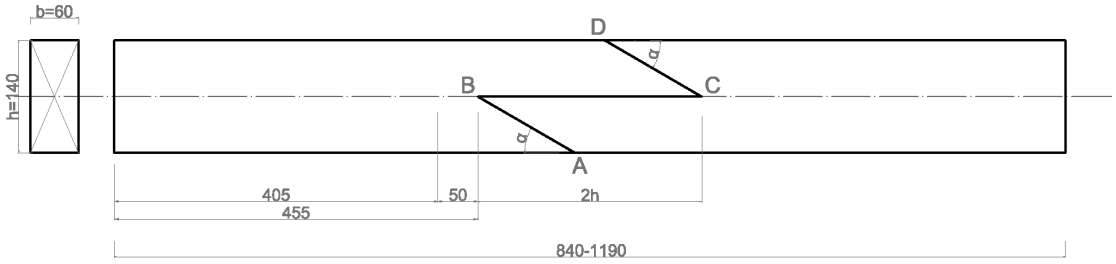

Figure 7-1 – SPECIMENS 1 and 3. All the dimensions are in [mm].

SPECIMEN 1&3 (S1&S3)

The Figure 7-1 represents the specimens S1 & S3. Preparation: the adjacent facing surfaces are in contact. The peaks in correspondence with points B and C are cut-away to avoid the split-effect (Figure 6-4 - d).

7.2.2 TESTS: *halved undersquinted scarf* joint

In the following Diagram 7-1 the N-M interaction curves for the *halved undersquinted scarf* with squint *α = 30°* (orange) and *α = 60°* (green) are given. The curves are not the interpolation, but the interpretation of the test results (contained in the diagram's key) connected through a spline. Referring to the specimen R60_M0_2 (*α = 60°*), loaded the in pure compression, the point on the diagram is not representing the failure point but an intermediate phase of the loading; in fact, the test was stopped for safety reasons. The single test results

specified in the diagram's key are reported in detail in the Annex B, respectively in the Diagram B-1 for the *α = 30°* and Diagram B-2 for *α = 60°*. The Table B-1 contains the description of the test results of the mentioned diagrams, performed both with procedures P1 and P2, and their failure modes; here, the tests performed with comparable procedures are highlighted.

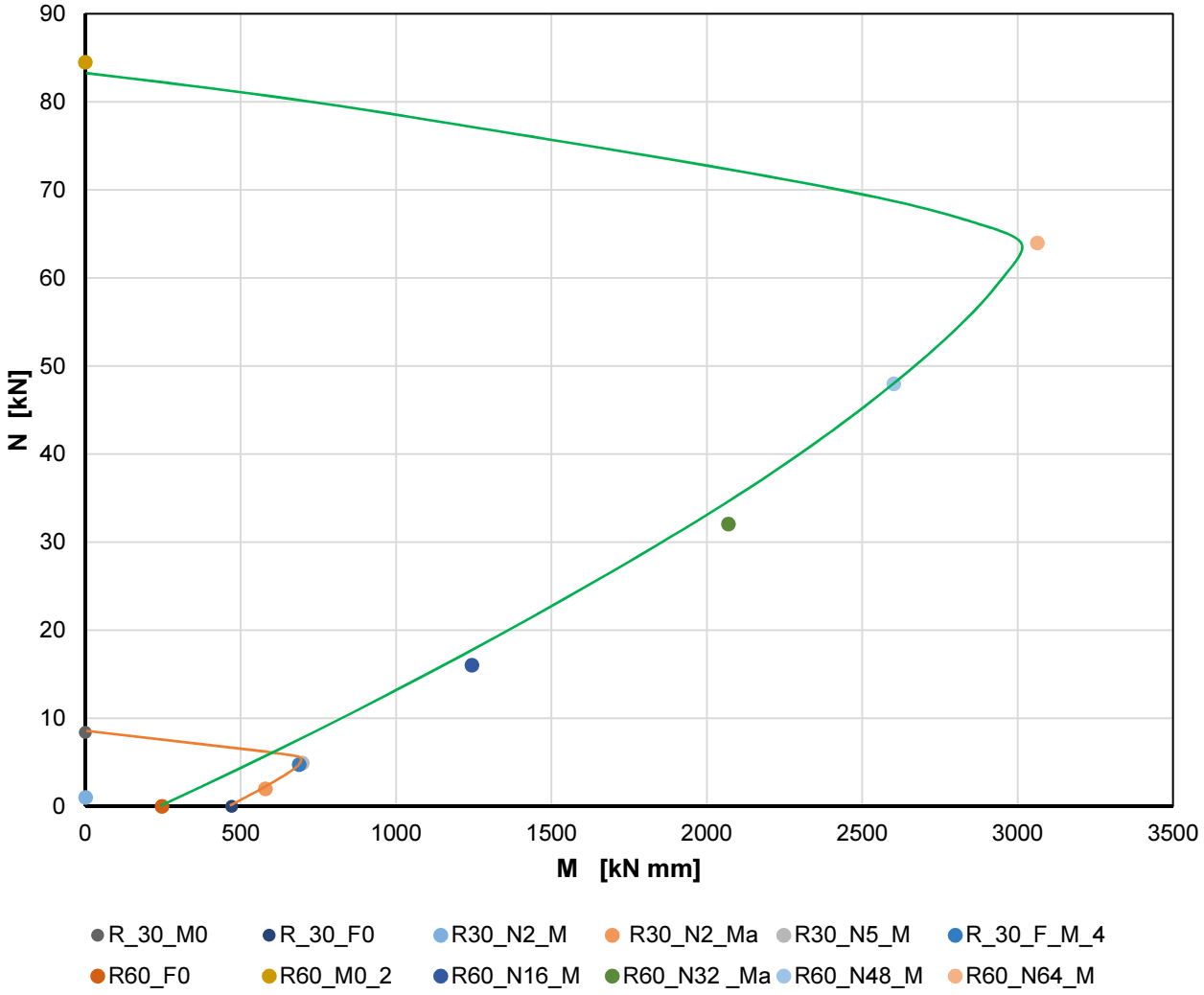

Diagram 7-1 – M-N interaction curve for *α = 30°* (orange) and *α = 60°* (green). Tests performed with P1 and P2 procedures (See Table B-1 for a better legibility)

7.2.3 Conclusions

OBSERVATIONS ON THE *HALVED UNDERSQUINTED SCARF* WITH SQUINT *α = 30°*:

The test results showed in the Diagram B-1 for the *α = 30°* seem to be scattered on the N-M diagram. The irregular distribution is because the pieces of information that are shown in that diagram come from partially comparable procedures (P1 and P2). In fact, the results obtained according to the procedure P1 are valid for the verification of the analytic model developed for the *halved undersquinted* connection (see Annex B) but are difficult to be reproduced in duplicates. Nevertheless, if we observe the results for *α = 30°* reported in the Diagram 7-1, the diagram's points acquire a more logical order; in fact, these tests are from comparable results, the ones marked with the grey field in the Diagram B-2.

Therefore, for the understanding of the general load-bearing behaviour of the *halved undersquinted*, we refer to the interaction curve in Diagram 7-1, where only comparable results are reported.

The behaviour ($\sigma - \varepsilon$) during the loading process relative to the main tests is showed in the Annex C.1.

Pure bending area:

1. The specimens $\alpha = 30°$ show a relevant pure bending load-carrying capacity. The ultimate value of bending registered in the tests, after which the specimens failed, is around M_u = 700 kN · mm.
2. The failure in pure bending is relatively ductile. Referring to the specimens R30_F0 (Table 7-1 – (a)) and R30_F0_2 (Table 7-2 – (e)), they recover after the first or the second break, if we refer to the case of R30_F0.

Pure compression area:

3. The specimens reaches the ultimate value at F_u = 8 kN, and the failure is also relatively ductile.
4. The equilibrium path of the specimens is independent from the initial pre-compression. That is demonstrated for the specimens R30_F_M_2; R30_F_M_3; and R30_F_M_4 in the Chapter 6.5, TEST 11.

OBSERVATION ON THE *HALVED UNDERSQUINTED SCARF* WITH SQUINT $\alpha = 60°$:

The single results obtained for the joint with $\alpha = 60°$ are reported in the Annex B, section B.2.2.

The general behaviour during the loading process, relative to the main tests, is showed in the Annex C.2.

Pure bending area:

1. The tests were performed with the specimens in vertical position. Therefore, the pure bending tests are not a perfect pure bending test because the vertical self-weight on the axis of the beam influences the results. Nevertheless, the test results are admissible.
2. The failure of the specimens in pure bending is *instability failure*; In fact, the upper part of the connection jumps out on the lower part (Figure 7-3- e).

Pure compression area:

3. The test $\alpha = 60°$ in pure compression R60_M0 was stopped before the achievement of the F_u up to the value $F_{u,e}$ = 85 kN. In fact, the high value of the load, summed up with the imperfections described in Chapter 3.6 brings to the instability of the specimens in the test setup. Therefore, the value F_u is hypothesized in the Figure 7-2.
4. The instability problems recorded during the compression tests are mainly related with imperfections (see above Chapter 3.6).
5. More, during the tests R60_N16_M; R60_N32_M; R60_N48_M and pure bending R60_F0 (equal to: $F_I = 0.2 \cdot F_u$; $F_I = 0.4 \cdot F_u$; $F_I = 0.6 \cdot F_u$ and the pure bending test $F_I = 0$), the specimens needed to be pre-compressed up to a value of 16 N. This minimal amount of pre-compression was needed in order to maintain the vertical position and not fail for instability with $F_I = 0$. The pre-compression stabilized the specimens but not influence the results, as demonstrated in the TEST 11, Chapter 6.5.

GENERAL COMMENTS ON THE TEST RESULTS

From the observation of the experimental Diagram 7-1 for both the angles $\alpha = 30°$ and $\alpha = 60°$, some observations are done.

1. The pure bending resistance for small angles ($\alpha = 30°$) is the double than the one for big angles ($\alpha = 60°$).

2. The pure compression resistance for *α = 60°* is more than 10 times bigger respect to the one of *α = 30°*. Nevertheless, as already mentioned, the specimen R60_M0_2 for *α = 60°* loaded in pure compression is not representing the ultimate value in pure compression for the angle *α = 60°*; in fact, the test has to be stopped for security problems in the test configuration. The approximation of the general behaviour for the *halved undersquinted scarf* joint *α = 60°* is given in the Figure 10-1.

3. The general results are more reliable in the "intermediate area" of the diagram; here, the specimens are loaded with medium values of both bending and compression force. In fact, both the pure bending and pure compression areas are characterized by the *instability effect* of the specimens that can sensibly alter the test results. The entity of the *instability effect* is very dependent on the entity of the angle *α* and the imperfections.

4. As already commented in the Chapter 5.6, for all the test specimens tested with the P1 procedure, the increasing of the F_{II} load causes an inducted force on the F_I piston. In the Diagram 7-1 this situation is represented by the specimens R_30_F0_bis; R_30_F0_bis2; R30_F_M_2; R30_F_M_3; R30_F_M_4.
The passive response phenomena is not very evident with the vice versa application of the compressive load (F_I as active load), but the application of normal force is in any case barely influent on the F_{II} value. In the Diagram 7-1 this situation is represented by the specimen R60_M0; R60_M02.

5. Sufficient results were obtained to understand the *halved undersquinted* joint's load-carrying capacity and mechanical behaviour both for the inclination of the squints *α = 30°* and *α = 60°*. Nevertheless, the N-M interaction diagram of the joint (Figure 7-2) contains only min values and it is a qualitative diagram for different "small" and "big" squint's angles. The approximation of the general behaviour for the *halved undersquinted scarf* joint is given in the Figure 10-1. A significant improvement on the knowledge is possible only with a higher number of specimens. In the present work no further tests were performed.

6. Considering the general behaviour of the *halved undersquinted* joint, is not possible to do a general description of the joint's behaviour only dependent on the F/M ratio. In fact, the differences in the behaviour of the joint, from the loading response to the failure modes, are remarkable in dependence of the joint's geometry (entity of the angle *α*).

Some general observations follows in eq. 7-1 and eq. 7-2. The Figure 7-2 contains a general schematization about the qualitative behaviour of the joint with squint *α = 30°* compared with the one with squint *α = 60°*, according to the experimental results and the expected ones.

$$M_{\max,\exp erimental(\alpha=60°)} = \frac{1}{3} M_{u(\alpha=30°)} \qquad 7\text{-}1$$

$$F_{u,\exp erimental(\alpha=60°)} = 10 \cdot F_{u(\alpha=30°)} \qquad 7\text{-}2$$

7.2.4 Failure modes

The failure modes observed during the tests are mainly three and are following described as:

II. FM II. Shear/tension perpendicular to the grain failure in the point B

III. FM III. Combined shear/tension perpendicular to the grain failure in the points B and C

IV. FM IV. Buckling

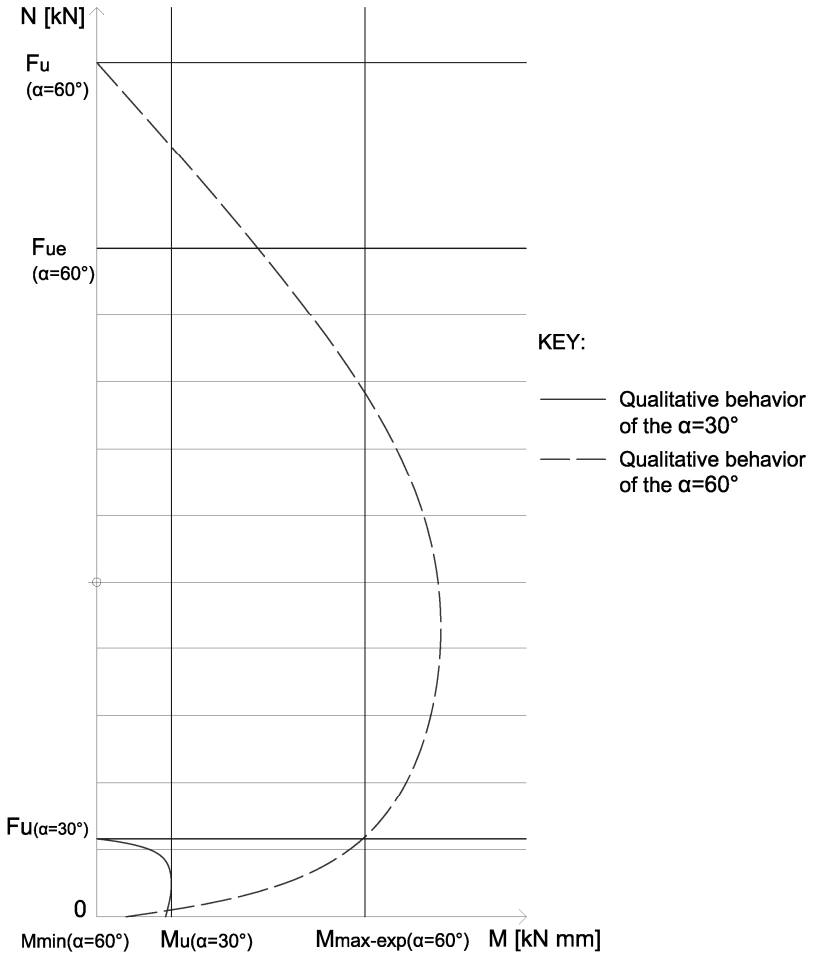

Figure 7-2 – Qualitative scheme of the specimens' behaviour

FM I	FM II		FM III	FM IV	
(…)	 (a)	 (b)	 (c)	 (d)	 (e)

Figure 7-3 – Failure mode of specimens of *halved undersquinted scarf* joint. (a): Specimen R30_F0 *α = 30°* 20/01/2016 pure bending. FM II; (b): Specimen R60_F64_M *α = 60°* 01/02/2016 bending + compression. FM II; (c): Specimen R30_M0 *α = 30°* 20/01/2016 - pure compression. FM III; (d): Specimen *α = 75°* compression + bending a = 58.3 05/06/2015. FM IV; (e): Specimen R60_F0 *α = 60* pure bending. FM IV.

In Figure 7-3 some example of failed specimens with different failure modes are given. The FM II is recorded for small (a) and big angles (b); the FM III is only registered for small angles (c), and the FM IV is registered for only big angles (d), (e). For what concerns the failure mode FM I (Compression perpendicular to the grain in the segment $\overline{CD}$ as described in the Chapter 3.7.1), it was not observed during the experimental campaign. Therefore, a hypothesis to be verified in future research, is that the FM I may occurs on surfaces $\overline{AB}$ and $\overline{CD}$ of connections with "big *α*" (*α > 45°*) loaded very high values of pure compression. In fact, in the present experimental campaign was not possible to reach such high values of loading for instability problems.

Conclusion on the failure modes

1. For the specimens with small and big angles, represented respectively by the performed tests with *α = 30°* and *α = 60°*, the failure modes are described in details in Figure 7-3.
2. The smaller is the angle *α* of the considered geometry, the earlier is the failure for tension perpendicular to the grain in B (and C). In fact, according to the first failure hypothesis, the smaller is the angle *α*, the bigger is the $F_{2,\perp}$ vertical component ($F_{2,\perp,90}$):

$$V_2 = F_{1,\perp}\cos\alpha + F_{2,\perp}\cos\alpha$$

$$V_{cr} \geq V_2 \rightarrow failure$$

where the V_2 is the force that brings the connection to the failure perpendicular to the grains in B.

3. Is observed that the three failure modes observed during the tests, can be grouped in the N-M diagram in *failure areas* as in Figure 7-4. These three big *failure areas* have "shifting boundaries" depending first, on the geometry of the joint (squint's inclination *α*), second, on the loading conditions (pure or mixed external action), and third, on the positioning of the external forces respect to the correspondent geometry.
4. Referring to the Figure 7-4:
   - The failure modes registered for the specimens depends on the level of compression and geometric parameters $f\{a_d, N_d\}$
   - Small angles (*α = 30°*). The main failure mode in compression (registered for the 80% of the compression resistance) is the shear / tension perpendicular to the grains in B (FM II). In pure bending, the main failure mode is shear / tension perpendicular to the grains in the points B and C (FM III).
   - Big angles (*α = 60°*). It is to remark that the evaluation of the ultimate load F_u for *α = 60°* in pure compression was experimentally not possible; therefore, the value of ultimate load we refer is the experimental value $F_u = F_{u,e} = 80kN$. In the lower diagram area, correspondent to the pure bending up to a 20% of the ultimate load ($F_u = 0.2 \cdot F_{u,e}$) the failure is for buckling (FM IV). From the 20% to the 100% (experimental) of the ultimate load ($F_u = (0.2 \div 1) \cdot F_{u,e}$), correspondent to pure bending and combined bending and compressive force loading, the shear/tension perpendicular to the grains in B (FM II). The ultimate load F_u in pure compression for the *halved undersquinted α = 60°* is estimated as $F_u = F_{u,e} + 20\% \cdot F_{u,e}$. The expected failure mode for values of force $F_{u,e} \leq F < F_u$ is hypothesized the FM III, while for pure compression the expected failure mode is the FM IV.

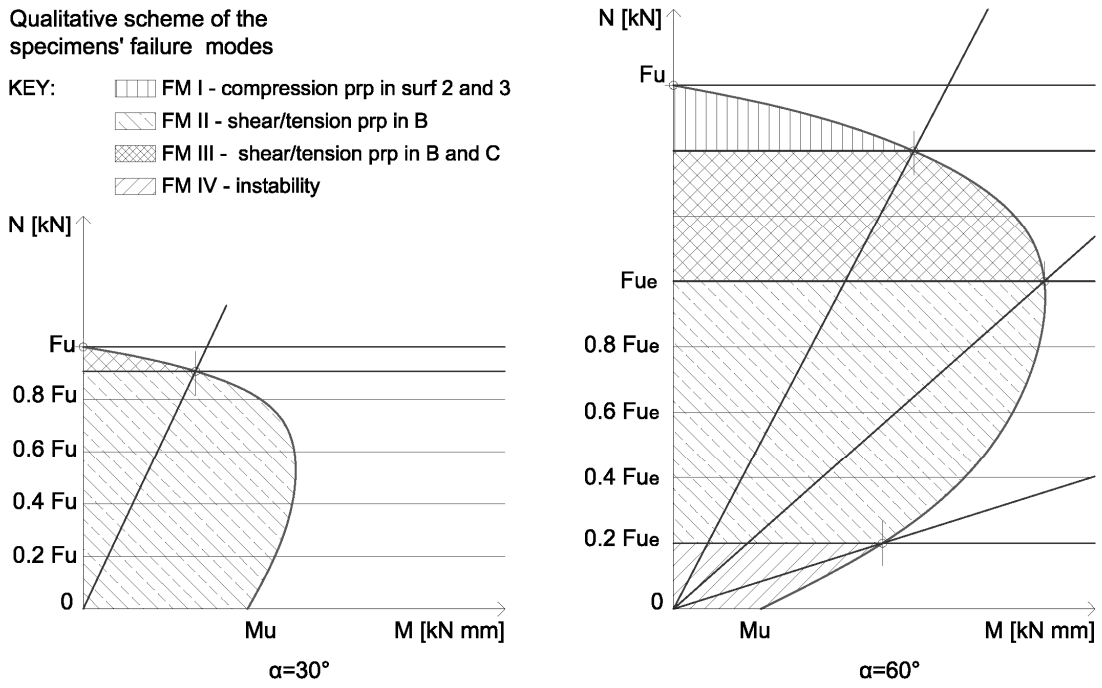

Figure 7-4 – Qualitative schema of the specimens' failure mode for *α = 30°* and *α = 60°* (The scale of the two diagrams is purely qualitative. The values on the diagrams are not comparable).

7.3 Comparison between the analytical and experimental results for the halved undersquinted scarf joint

For both the inclination of the squints *α = 30°* and *α = 60°* the evaluation of the experimental results on the *halved undersquinted scarf* joint through the analytical model of the Chapter 4 is performed in the Annex B. Therefore, the analytical model is verified.

7.3.1 General conclusions

Referring to the Annex B (and the Diagram B-7 as an example) the following conclusions are resumed. From the observation of the superposition of the experimental diagram with the experimental model for the *halved undersquinted scarf joint*, a critical lecture is done:

1. the LS1 for the models (i), (ii), and (iii) describes the value of μ_α for the single specimen; the value of μ_α derives from the failure values F_u and M_u.
2. The LS1 defines the equilibrium path of the specimens during the loading (see above Chapter 6.4.2.2, TESTS 7 and TEST 8).
3. The ultimate value $F_{f,i}$ is not linear but changes with the changing of the loading conditions; therefore, it cannot be evaluated as a constant. It is not possible to evaluate the F_f in specimens loaded in combined compression and bending action. The evaluation is *a posteriori* from the test results.
4. The FM III is described by the LS4 (vii). It is possible to evaluate the load-carrying capacity of the *halved undersquinted scarf* joint $\alpha = 30°$ in case of external pure compression action. The evaluation is done according to the eq. 4-117 with value of $F_{f,C}$ contained in the eq. 3-40. For the evaluation of the *halved undersquinted scarf* joint $\alpha = 60°$ the value of crack energy, correspondent to $F_{f,C}$ has to be evaluated with more tests. The verification is still possible with the eq. 4-117.

5. The FM II is described by the models (i) (ii) (iii) the description of $F_{f,\exp}$ it is experimentally possible, through the LS2 (ii) and respective value of μ_α for the single specimen.

6. from $LS1 \cap LS2 = LS3$ the $F_{f,\exp}$ for each specimen is determined in the N-M diagram by the intersection of the LS1 with the LS2 straight line.

from $LS1 \cap LS3 = LS2$ (to define LS3 we need the value of friction, to define LS1 also the value of friction).

7.4 Experimental campaign: stop splayed & undersquinted scarf joint, and halved undersquinted and tabled scarf with key

The aim of this two intermediate geometries is the one to demonstrate the improvements conferred to the connection by the splayed $\overline{BC}$ surface and the key.

7.4.1 Specimen preparation

The specimens preparation consists of two different montages according to the below described procedures.

SPECIMEN 4 (S4)

Stop - splayed & undersquinted scarf joint. Test the contribution of the inclined overlap in terms of in-plane behaviour. Check the contribution that the inclination of the overlap gives in terms of stabilization to the in-plane instability (specimens *α = 60°* , *β = 10°*).

SPECIMEN 5 (S5)

Halved undersquinted and tabled scarf with key. Test the contribution of the key in terms of stabilization to the in-plane behaviour (for specimens *α = 60°*). See specimen R60_F0 for the instability failure and R60_N16_M for the jump instability failure in Figure 7-3 – e and Annex D.2.2.

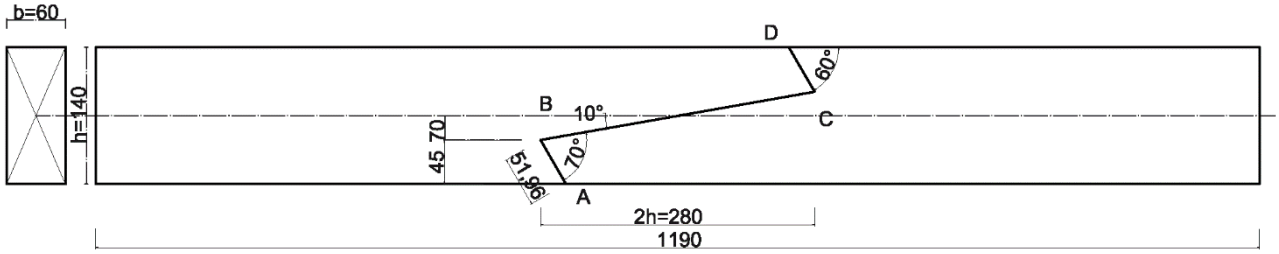

Figure 7-5 – SPECIMEN 4 - *Stop - splayed & undersquinted scarf* joint. All the dimensions are in [mm].

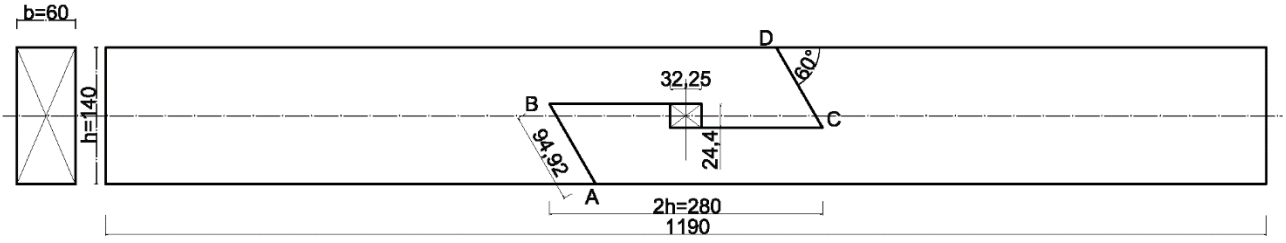

Figure 7-6 – SPECIMEN 5 - *Halved undersquinted and tabled scarf with key* joint. All the dimensions are in [mm].

7.4.2 TESTS: *stop splayed and undersquinted* joint

In the following Diagram 7-14 the N-M interaction curve for the *halved splayed scarf* with squint $\alpha = 60°$ and $\beta = 10°$ tested on the strong axis is given. The curve is the interpretation of the test results reported in the Diagram's key and in the Table 7-3. All the tests were performed on the 20/07/16 with specimen S4 and procedure P2.

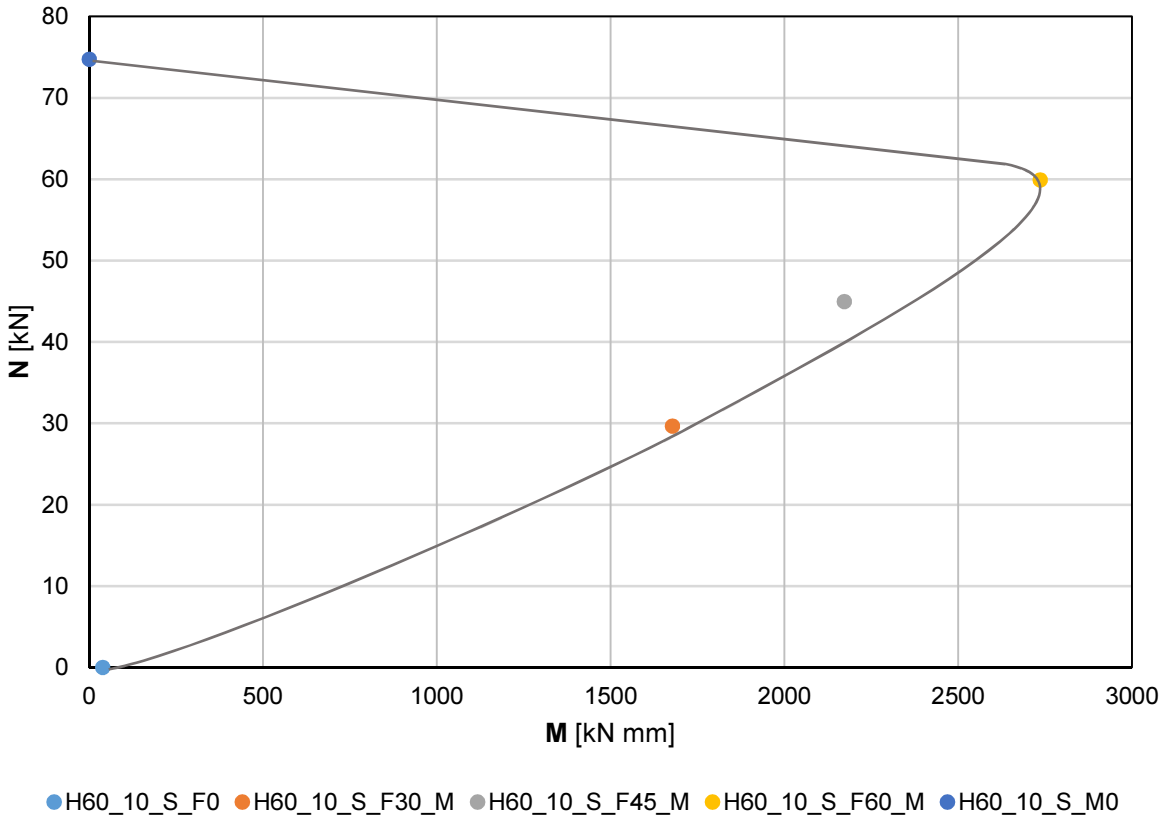

Diagram 7-2 – N-M interaction curve for the *stop - splayed and undersquinted* joint (H60_10_s)

7.4.3 Failure modes

The failure mode observed during the tests are mainly two and are following described as:

II. FM II. Shear/tension perpendicular to the grain failure in the point B

IV. FM IV. Buckling

In Figure 7-7 some example of failed specimens with different failure modes are schematized. In Table 7-3 are presented the test results.

Table 7-3 – Results for the J60_10_s

specimen	$F_{target\ FII}$ [kN]	proce-dure	F_{II} [kN]	F_I [kN]	dist. support [mm]	M [kN mm]	N [kN]	FM	observations
H60_10_S_F0	-	P2 - a	0.20	0.00	390.00	39.20	0.00	FM IV	
H60_10_S_F30_M	30	P2 - c	8.61	29.67	390.00	1678.17	29.67	FM II	
H60_10_S_F45_M	45	P2 - c	11.14	44.96	390.00	2172.11	44.96	FM II	
H60_10_S_F60_M	60	P2 - c	14.03	59.93	390.00	2735.46	59.93	FM II	Same specimen H60_10_S_F0.
H60_10_S_M0	-	P2 - b	0.00	74.76	390.00	0.00	74.76(s)	-	Same specimen H60_10_S_F0. Stopped. Can bear up to $F_I \approx$ 80-90kN

(s) Stopped test (not up to break)

FM I	FM II	FM III	FM IV
(...)	 *(a)*	*(...)*	 *(b)*

Figure 7-7 - Failure mode of specimens of *stop splayed undersquinted scarf* joint. (a): Specimen H60_10_s_F45_M *α = 60° β = 10°* 20/07/2016 compression + bending. FM II; (b): Specimen H60_10_s_F0 *α = 60° β = 10°* 20/07/2016 pure bending FM IV;

7.4.4 Conclusions

1. Pure compression area. The test in pure compression of the specimen H60_10_s_M0 was stopped before the achievement of the F_u because of problems encountered in loading with high values of normal forces. In fact, the high value of the load summed up with the imperfections make the system not stabile. Nevertheless, it is experimentally evaluated that $F_{u,e} = F_I = 75kN$, and it is estimated that the ultimate load of the *stop splayed undersquinted scarf* joint can reach approximatively up to $F_u = F_I \cong 80 \div 90kN$.

2. Pure bending area. The specimen H60_10_s_F0 loaded in pure bending shows almost zero bending-resistance.

3. The failure modes are the same for the general *halved undersquinted* and represented in Figure 7-7.

COMPARISON:

The pure bending load-carrying capacity of the *stop – splayed & undersquinted* joint (*α = 60°*) is only 1/5 of the one of the *halved undersquinted* (*α = 60°*). The disadvantage of the *stop – splayed & undersquinted* joint lays in the smaller dimension of the squint. In fact, the smaller surface of the squint confers less friction, therefore less stability to the joint. The recorded failure modes are similar to the one registered for the *halved underquinted* (*α = 60°*).

The exact load-carrying capacity in compression of the *stop – splayed & undersquinted* joint (*α = 60°*) and the *halved undersquinted* (*α = 60°*) is not comparable because in both cases the pure compression tests were stopped for unstable test setup. Observing the tendency of both the N-M interaction curves, the tendencies of the tests, and observing the behaviour of a *half-timber* joint, we can suppose that the *halved undersquinted* joint (*α = 60°*) has more load-carrying capacity in compression than the other.

7.4.5 TESTS: *halved undersquinted and tabled scarf* joint *with key*

In the following Diagram 7-15 the N-M interaction curve for the *halved splayed scarf* with squint $\alpha = 60°$ and $\beta = 10°$ tested on the strong axis is given. The curve is the interpretation of the test results reported in the diagram's key and the Table 7-4.

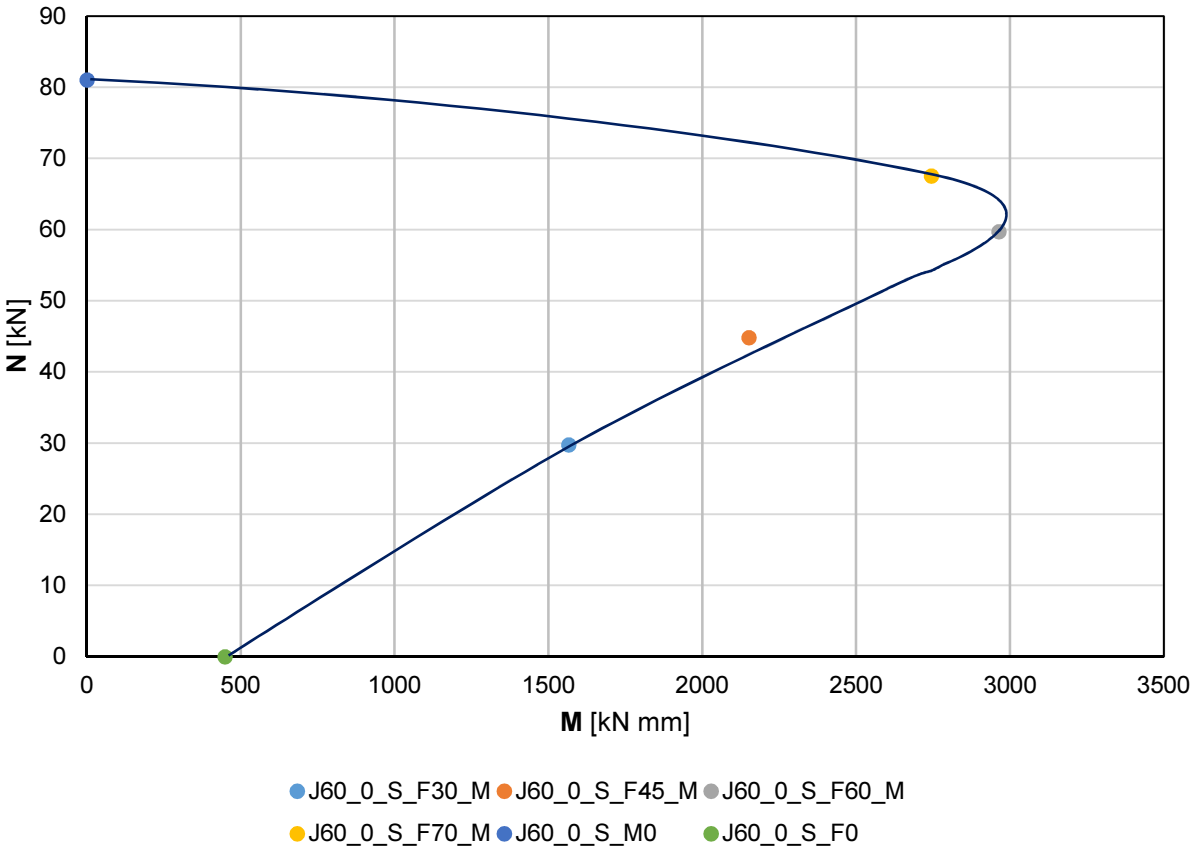

Diagram 7-3 – N-M interaction curve for the *Halved undersquinted and tabled scarf* joint *with key* (J60_10_s).

7.4.6 Failure modes

The failure mode observed during the tests are mainly three and are following described as:

II. FM II. Shear/tension perpendicular to the grain failure in the point B

IV. FM IV. Buckling

V. FM V. Shear failure in the KBB''C'KBB''C' prism.

In the following Table 7-4 are listed the tests data and the respective failure for specimens. In Figure 7-8 some example of failed specimens with different failure modes are schematized.

7.4.7 Conclusions

1. Pure compression area. The specimen J60_0_S_M0 is stopped at a level of compression load equal to $F_I = F_{u,e} = 80$ kN. In fact, the high value of applied force summed up with the imperfections made the system not stabile. Therefore, the test in pure compression was stopped before the achievement of the *Fu*.

2. Pure bending area. The specimen J60_0_s_F0 loaded in pure bending shows a good level of bending-resistance.

3. A new failure mode appears in the global panorama of the connections: the shear failure. The shear failure in the *halved undersquinted and tabled scarf* joint *with key* regards the failure of the "block" KBB''C'KBB''C' that is the *table* volume. The failure happens because of the pre-compression given by the wedges, in opposition with the compression force on the squints' surfaces.

Table 7-4 – Results for the J60_10_s

specimen	**date**	**F_{II}** [kN]	**F_I** [kN]	**dist. support** [mm]	**M** [kN·mm]	**N** [kN]	**FM**	**observations**
J60_0_S_F30_M	20/07/16	8.03	29.78	390.00	1564.88 (s)	29.78	FM II + FM V	Stopped first crack B'. Same specimen upper J60_0_S_M0.
J60_0_S_F45_M	20/07/16	11.03	44.83	390.00	2150.66 (s)	44.83	FM II + FM V	Stopped first crack B'. Same specimen upper J60_0_S_M0.
J60_0_S_F60_M	19/07/16	15.20	59.73	390.00	2963.61 (s)	59.73	FM II	Stopped first crack B. Same specimen upper J60_0_S_M0.
J60_0_S_F70_M	20/07/16	14.07	67.54	390.00	2744.04 (s)	67.54	FM II + FM V	Stopped first crack B'. Same specimen upper J60_0_S_M0.
J60_0_S_M0	19/07/16	0.00	81.03	390.00	0.00	81.03 (s)	FM II	Stopped. It can bear more and more N.
J60_0_S_F0	19/07/16	2.30	0.00	390.00	448.11	0.00	FM V	

(s) Stopped test (not up to break)

FM I	FM II	FM III	FM IV	FM II + FM IV
(...)	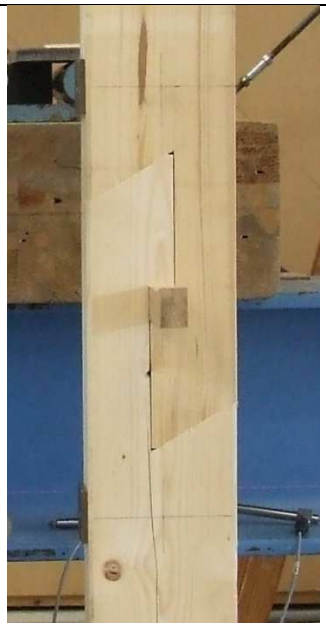 *(a)*	*(...)*	*(...)*	 *(b)*

Figure 7-8 - Failure mode of specimens of *halved undersquinted and tabled scarf* joint *with key*. (a): Specimen J60_0_S_M0 *α = 60°, β = 0°* 19/07/2016 pure compression. FM II; (b): Specimen J60_0_S_F0 *α = 60°, β = 0°* 19/07/2016 pure bending.

COMPARISON:

The load-carrying capacity of the *halved undersquinted and tabled scarf* joint *with key* (*α = 60°*) in bending is almost the double of the correspondent in the *halved undersquinted* (*α = 60°*). The improved load-carrying capacity of the *halved undersquinted and tabled scarf* joint *with key* joint, lays first of all in the pre-compression

of the wedge, that avoid the instability failure registered for both the *halved undersquinted* (*α = 60°*) and the *stop-splayed & undersquinted* (*α = 60°*). The disadvantage for that kind of joint is the shear failure of the prism KBB''C'KBB''C', due to the non-sufficient length of the $\overline{CC'}$ segment.

The load-carrying capacity in compression of the *stop–splayed & undersquinted* joint, the *halved undersquinted* (*α = 60°*) and the *halved undersquinted and tabled scarf with key* is again not comparable because in all three cases the compression tests were stopped for unstable test setup. Observing the tendency of all the N-M interaction curves, the tendencies of the tests, and observing the behaviour of a *half-timber* joint, we can suppose that the *halved undersquinted* (*α = 60°*) joint has more compression load-carrying capacity than the *stop-splayed and undersquinted*, but less than the *halved undersquinted* (*α = 60°*). The reason lays in the presence of both the *key* and the *table*. On one side, the insertion of the *key* influences the pre-compression that increases the load-carrying capacity; on the other side, the presence of the *table*, without an adequate length of the joint's segment $\overline{CC'}$, causes the failure for shear (FM V).

7.5 Experimental campaign: Jupiter joint (stop-splayed undersquinted & tabled with key scarf joint)

7.5.1 Specimen preparation

The specimen preparation consists on the montage as described below.

SPECIMEN 6 (S6)

Specimens prepared for the analysis of the *Jupiter joint* along the strong and weak axis are represented in Figure 7-9. The specimens' surfaces are inclined of *α = 60°* and *β = 5°*. The preparation of the specimens for the installation in the testing machine is in Figures 5-15 to Figure 5-18 for what concern the installation for the in-plane behaviour, and Figures 5-19 to Figure 5-21 for the out-of-plane behaviour.

Preparation: the peaks in correspondence with points B and C are cut-away to avoid the split-effect that can anticipate the failure (Figure 6-24 - d). The two halves of the joint are first arranged in contact; then, the *key* is installed. The joint is provided with a *square-cut* key (see Annex E). That means that the key is squared, and the walls of the key are perpendicular to the one of the splayed area defined by the segments $\overline{BB'}$ and $\overline{CC'}$, i.e. they are inclined to the grains. The key is compounded by two wedges that are hammered in the empty quadrilateral $\overline{B''B'C''C'}$. The pre-compression of the specimens is time to time different, according to the force of installation of the *wedges*. In order to guarantee a similar pre-compression, important features are both in the production and installation of the wedges. Some information follows.

Production of the wedges:

- all the wedges have the same direction of the grain;
- all the wedges have the same inclination of the grain;
- all the wedges have the smallest imperfection as possible.

The pre- compression capacity of the key depends on the key's angle. (see Annex E) The adopted key has is in scale 1:1 with the same angle present in the original case study's beams. The ratio between the length and the height of the key is 1:6 (Figure 7-11).

Installation of the wedges:

- insert both the wedges from the opposite sides of the connection;
- hammer them at the same time to the center of the beam.

Problems related with the non perfect centrality of the key and relative appearance of gaps (imperfections) during the installation are also explained in the Annex E.

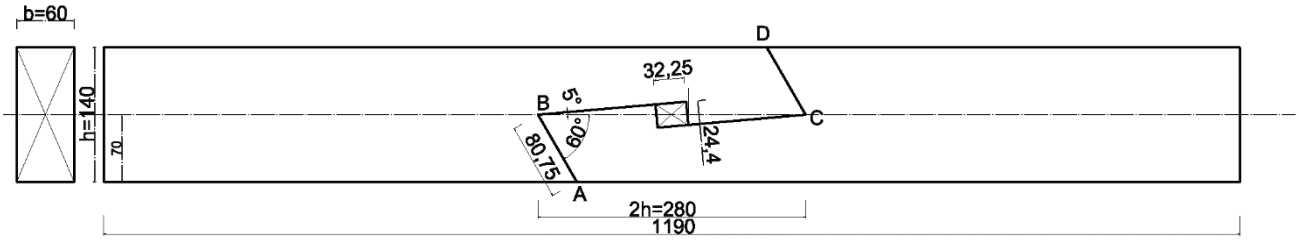

Figure 7-9 – SPECIMEN 6. *Jupiter joint*. All the dimensions are in [mm].

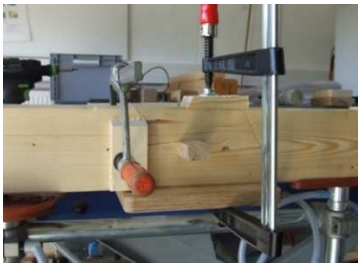

Figure 7-10 – Montage of the wedges in the *Jupiter joint*

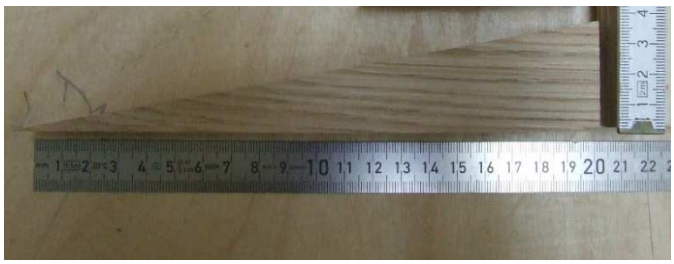

Figure 7-11 –Wedges in the *Jupiter joint*

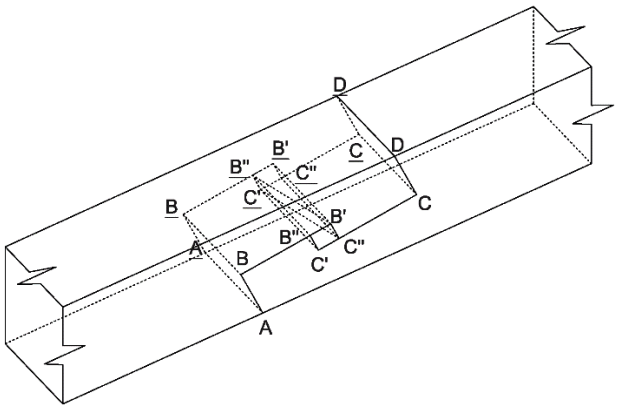

Figure 7-12 – Reference points for the *Jupiter joint*'s analysis (the underlined points X are on the tension side)

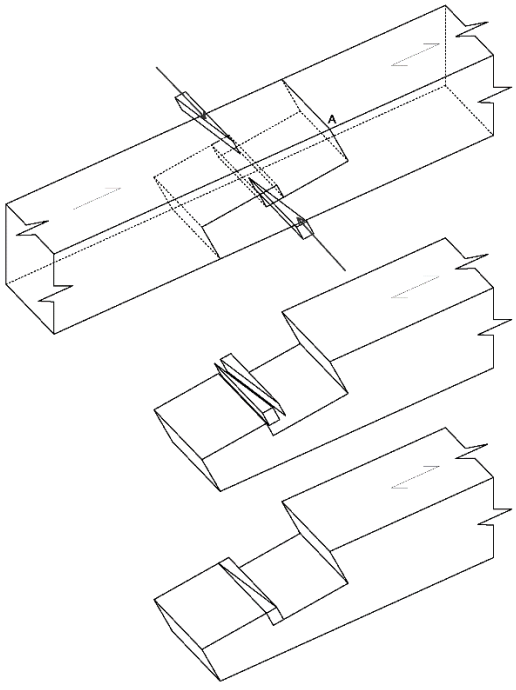

Figure 7-13 – Montage of the wedges in the *Jupiter joint*, procedure

7.5.2 STRONG AXIS TESTS

In following Diagram 7-4 are given the N-M interaction curves for the *stop-splayed undersquinted and tabled with key scarf* joint with squints $\alpha = 60°$ and splayed surface $\beta = 5°$, for the in-plane and out-of-plane behaviour.

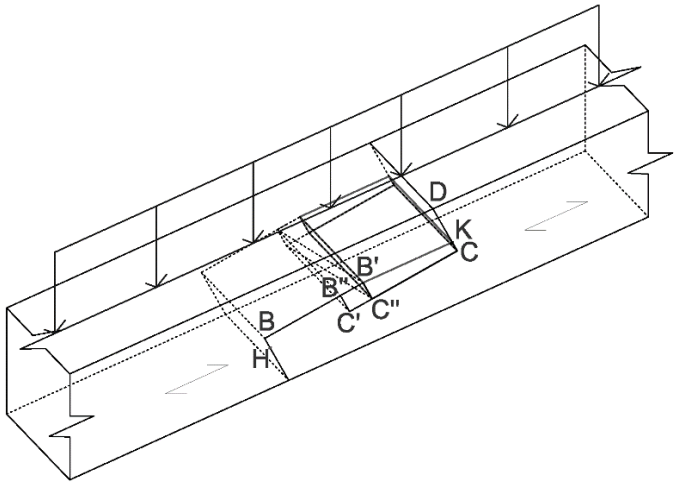

Figure 7-14 – Specimen loaded on the strong axis

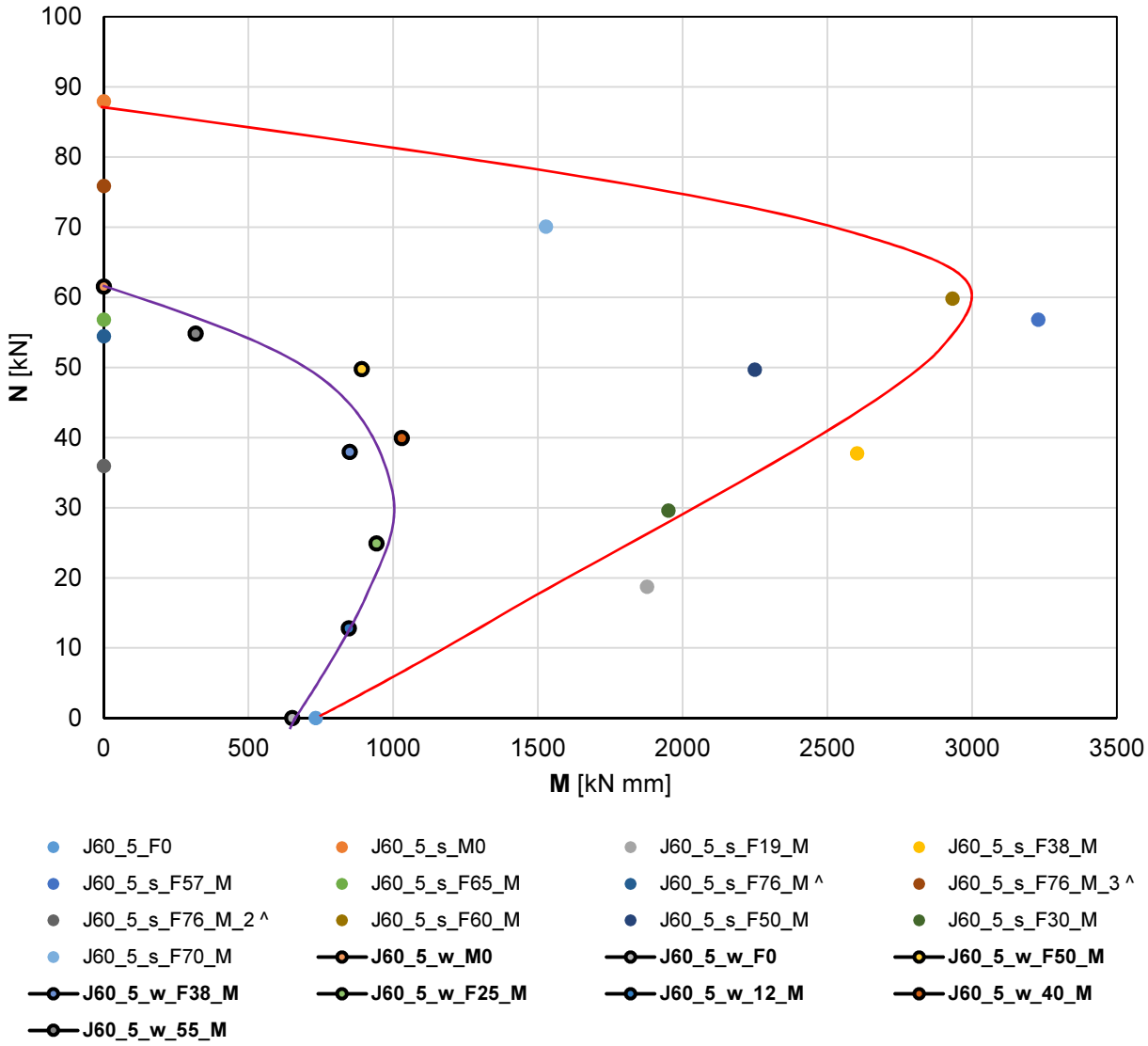

Diagram 7-4 – N-M interaction diagram for the *Jupiter joint* along the strong and weak axis (J60_5_s+w).

Table 7-5 – Results for the J60_5_s

specimen (procedure)	date	F_{target} [kN]	FII [kN]	FI [kN]	dist. support [mm]	M [kN·mm]	N [kN]	FM	observations
J60_5_F0 (P2 – a)	18/07/16	-	3.75	0.00	390.00	731.25	0.00	FM V	
J60_5_s_M0 (P2 – b)	18/07/16	-	0.00	87.95	390.00	0.00	87.95 (s)	-	Stopped.
J60_5_s_F19_M (P2 –c)	19/07/16	19	9.62	18.73	390.00	1876.10	18.73	FM II + FM V	
J60_5_s_F38_M (P2 –c)	19/07/16	38	13.34	37.77	390.00	2601.30	37.77	FM II + FM V	
J60_5_s_F57_M (P2 –c)	19/07/16	57	16.55	56.80	390.00	3226.86	56.80	FM II + FM V	
J60_5_s_F65_M (P2 –c)	19/07/16	65	0.00	54.30	390.00	0.00	54.30	FM II + FM III	brittle failure, loaded in only pure compression Fi
J60_5_s_F76_M (P2 –c) ^	19/07/16	76	0.00	54.47	390.00	0.00	54.47	FM II	loaded in only pure compression Fi
J60_5_s_F76_M_2 ^(P2 –c)	19/07/16	76	0.00	35.94	390.00	0.00	35.94	FM II + FM III	brittle failure, loaded in only pure compression Fi
J60_5_s_F76_M_3 ^(P2 –c)	19/07/16	76	0.00	75.87	390.00	0.00	75.87	FM II + FM III	brittle failure, loaded in only pure compression Fi
J60_5_s_F60_M (P2 –c)	20/07/16	60	15.03	59.84	390.00	2931.05	59.84	FM II	
J60_5_s_F50_M (P2 –c)	20/07/16	50	11.53	49.71	390.00	2248.55	49.71	FM II	
J60_5_s_F30_M (P2 –c)	20/07/16	30	10.00	29.60	390.00	1950.00	29.60	FM II	
J60_5_s_F70_M (P2 –c)	20/07/16	70	7.83	70.09	390.00	1527.24	70.09	FM II	brittle failure

(s) Stopped test (not up to break)

Referring to the Diagram 7-4, in red is represented the N-M interaction curve of the *Jupiter joint* loaded along the strong axis, and in violet is described the curve for the specimens loaded along the weak axis. The curves are the interpretation of the test results reported in the diagram's key.

The points in bolt, linked with the violet line are the test results of the specimens loaded along the weak axis, which results are reported in detail in the Table 7-6. Tests performed on the 20/07/16. All the tests specimens are S6, and performed with P3. The points not in bolt, linked by the red line are the test results of the specimens loaded along the strong axis, which results are reported in detail in the Table 7-5. The tests were performed from the 19/07/16 to the 20/07/2016. The specimens are S6, performed with P2.

7.5.3 Failure modes

The failure modes FM observed in the weak axis tests are mainly three and are following described as:

II. FM II. Shear/tension perpendicular to the grain failure in the point B

III. FM III Combined shear/tension perpendicular to the grain failure in the points B and C

V. FM V. Shear failure in the BB''C'H prism.

In the following Table 7-4, the loading data and the failure of the specimens are listed. In Figure 7-8 some example of failed specimens with different failure modes the are schematized.

For all the specimens loaded along the strong axis the main failure modes are the FM II and the combination of FM II and FM V.

Referring to Figure 7-14 the failure mode FM V (the shear failure) is recorded in the lower timber piece's BB''C'H prism, while the failure mode FM II happens along the fibres in correspondence of the lower timber piece's point B.

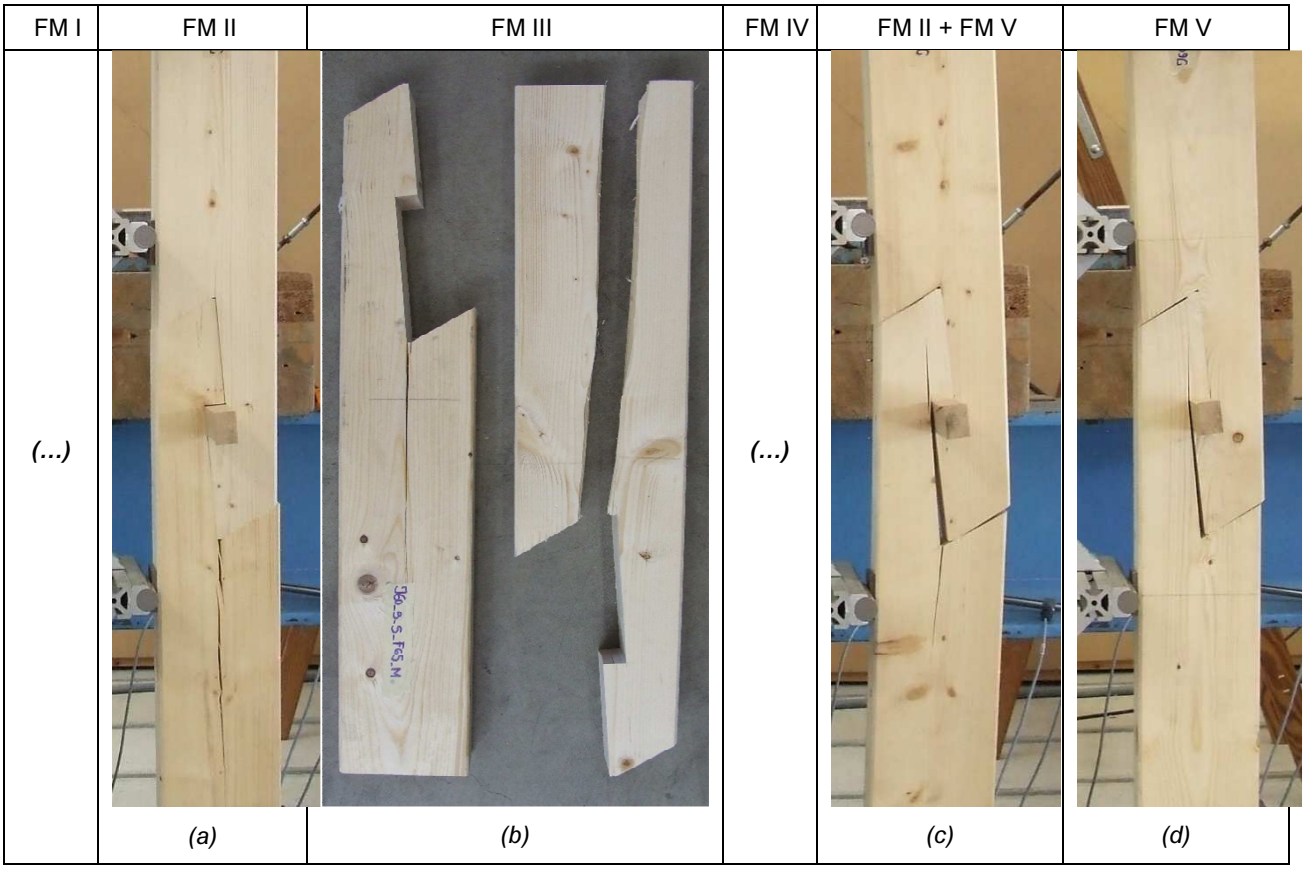

Figure 7-15 - Failure mode of specimens of *Jupiter joint*, in-plane testing: (a): Specimen J60_5_S_F76_M $\alpha = 60°$ $\beta = 5°$ 19/07/2016 compression force. (b): Specimen J60_5_S_F65_M $\alpha = 60°$ $\beta = 5°$ 19/07/2016 compression force. (c): Specimen J60_5_S_F19_M $\alpha = 60°$ $\beta = 5°$ 19/07/2016 compression and bending force. (d): Specimen J60_5_S_F0 $\alpha = 60°$ $\beta = 5°$ 18/07/2016 pure bending.

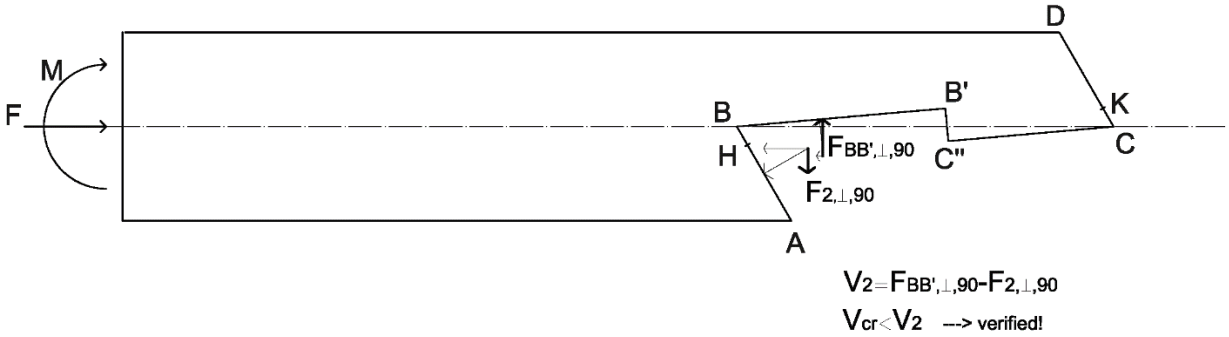

Figure 7-16 – FM II. Shear/ tension perpendicular to the grains failure.

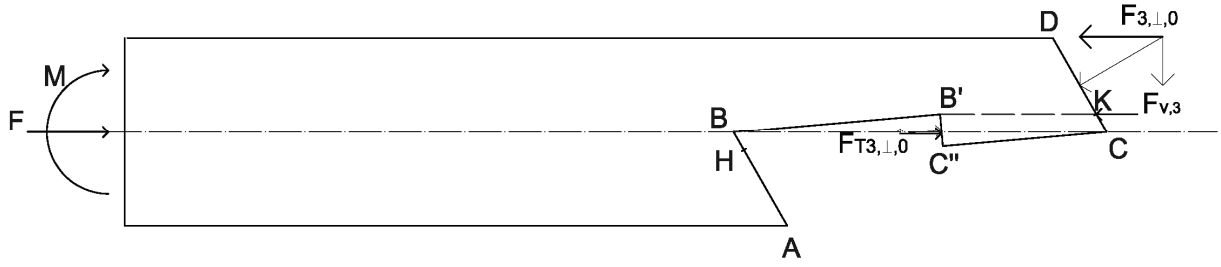

Figure 7-17 – FM V Shear failure.

FM II

The plain mechanism of fracture FM II on the compression and tension side is explained in Figure 7-16 and Figure 7-20. The failure, according to the first failure hypothesis valid also for the *halved undersquinted scarf* joint, is due to the contemporary action of the forces

$$V_2 = F_{BB',\perp,90} - F_{2,\perp,90}$$

$$V_{cr} \geq V_2 \rightarrow failure \qquad 7\text{-}3$$

FM V

The shear failure is present both on the compressed side. The shear mechanism develop on the $\overline{B'K}$ shear plane. According to the Figure 7-17, the shear force $F_{v,3}$ is dependent on the $F_{T3,0}$ and the $F_{3,\perp,0}$.

$$F_{T3,\perp,0} = F_{B'C'',\perp,0} + F_{pc,0} \qquad 7\text{-}4$$

The shear force acting on the shear plane $\overline{B'K}$ is:

$$F_{v,3} = F_{3,\perp,0} - F_{T3,\perp,0} \qquad 7\text{-}5$$

The section is verified when:

$$\frac{F_{v,3}}{b \cdot \overline{B'K}} \leq R_v \qquad 7\text{-}6$$

Where :

F_{pc}	Pre - compression force.
$F_{B'C'',\perp}$	Resultant force on the $\overline{B'C''}$ surface due to the external load, perpendicular to the surface.
$F_{T3,\perp}$	Resultant force on the table 3 (T3 = surface $\overline{B'C''}$) of the joint, perpendicular to the surface.
$F_{3,\perp}$	Resultant force on the face $\overline{DC}$ due to the external applied load, perpendicular to the surface.

7.5.4 WEAK AXIS TESTS

The N-M interaction curve for the *stop-splayed undersquinted and tabled with key scarf* joint with squints *α = 60°* and splayed surface *β = 5°* loaded along the weak axis is represented by the violet curve in the Diagram 7-4.

7.5.5 Failure modes

According to the Figure 7-21, the compression side is characterized by points A, H, B, B', B'', C', C'', C, K, D; while the tension side is characterized by the points A, H, B, B', B'', C', C'', C, D.

The observed failure modes FM in the weak axis's loading are mainly three and are following described as:

II. FM II. Shear/tension perpendicular to the grain failure in the point B

III. FM III. Combined shear/tension perpendicular to the grain failure in the points B and C

V. FM V. Shear failure in the BB''C'HBB''C'H prism.

In the following Table 7-6, the loading data and the failure of the specimens are listed. The failure modes for both the compression and the tension side are schematized respectively in the Figure 7-18 and Figure 7-19. For all the specimens loaded along the weak axis the prevalent failure mode is the FM II, followed by the FM IV. Referring to the Figure 7-21, the failure mode FM V is the shear failure in the lower timber piece's prism called BB''C'HBB''C'H prism. The failure mode FM II happens in the upper timber piece's point B.

Table 7-6 – Results for the J60_5_w

specimen (procedure)	$F_{I,target}$ [kN]	F_{II} [kN]	F_I [kN]	dist. suppor [mm]	M [kN·mm]	N [kN]	FM		observations
							compr-ession	Ten-sion	
J60_5_w_M0 (P2 – b)	-	0	61.53	390	0	61.53	C, C', B	B	
J60_5_w_F0 (P2 – a)	-	3.34	0	390	650.91	0		-	
J60_5_w_F50_M (P2 – c)	50	4.57	49.75	390	891.15	49.75	B	B	
J60_5_w_F38_M (P2 – c)	38	4.36	37.97	390	850.00	37.97	B, C', C	B, B', C', C	
J60_5_w_F25_M (P2 – c)	25	4.83	24.89	390	941.85	24.89	-	C', B	the specimen has knots in the center of the cross-section, on both compressed and tensile sides.
J60_5_w_12_M (P2 – c)	12	4.34	12.77	390	846.69	12.771	H, B	K, C, B', B	the specimen is bent respect to the vertical. Once loaded with FII, the lower contact with the external support happened in a second moment respect to the upper one.
J60_5_w_40_M (P2 – c)	40	5.28	39.91	390	1029.80	39.91	B, C'	B	
J60_5_w_55_M (P2 – c)	55	1.63	54.85	390	317.85	54.85	B, C	B, C	brittle failure. Used specimen. Upper part in good conditions from w_F50_M, lower part from s_F60_M with some cracks.

FM I	FM II	FM III	FM IV	FM II + FM V	FM V
(...)	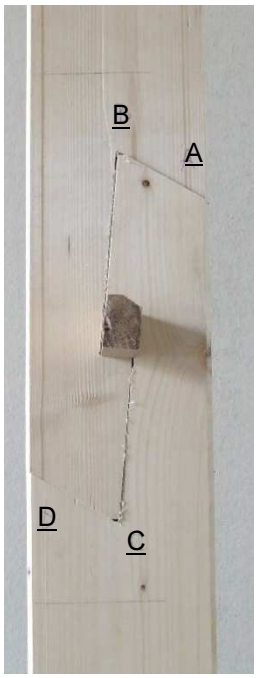 (a)	 (b)	(…)	 (c)	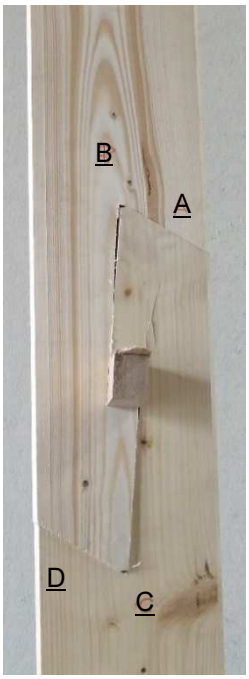 (d)

Figure 7-18 – Failure mode on the tension side of specimens of *Jupiter joint*; out-of-plane tests: (a): Specimen J60_5_w_F50_M *α = 60° β = 5°* 21/07/2016 compression and tension stress. (b): Specimen J60_5_w_F55_M *α = 60° β = 5°* 21/07/2016 compression and tension stress. (c): Specimen J60_5_w_F12_M *α = 60° β = 5°* 21/07/2016, compression and tension stress. (d): Specimen J60_5_w_F25_M *α = 60° β = 5°* 21/07/2016 compression and tension stress.

FM I	FM II	FM III	FM IV	FM II + FM IV	FM V
(…)	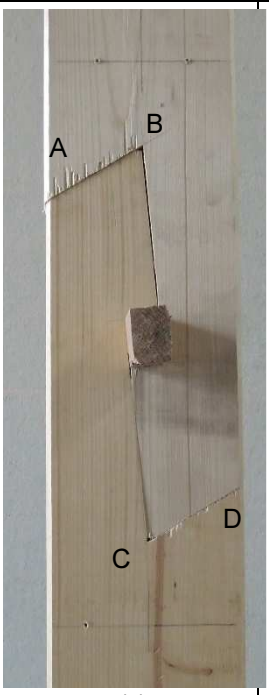 (a)	 (b)	(…)	 (c)	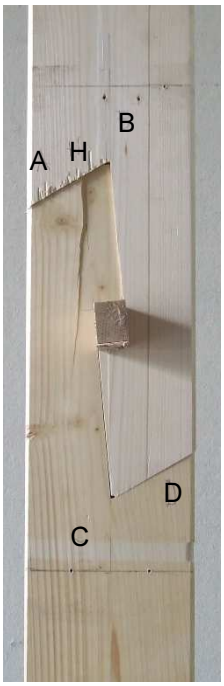 (d)

Figure 7-19 – Failure modes on the compression side of specimens of *Jupiter joint*; out-of-plane tests: (a): Specimen J60_5_w_F50_M $\alpha = 60°$ $\beta = 5°$ 21/07/2016 compression and tension stress. (b): Specimen J60_5_w_F55_M $\alpha = 60°$ $\beta = 5°$ 21/07/2016 compression and tension stress. (c) Specimen J60_5_w_F38_M $\alpha = 60°$ $\beta = 5°$ 21/07/2016, compression and tension stress. (d): Specimen J60_5_w_F12_M $\alpha = 60°$ $\beta = 5°$ 21/07/2016 compression and tension stress

Conclusions on the failure modes

In the following paragraph, the failure modes are interpreted, basing on the results and some basic equilibrium rules. The problem of the failure is very complicated because it implies some internal kinematic mechanisms that causes the FM II and FM V. Such mechanisms are explained in the Figure 7-20 and Figure 7-21. The FM III is considered a failure of secondary importance due to the presence of imperfections in the wood.

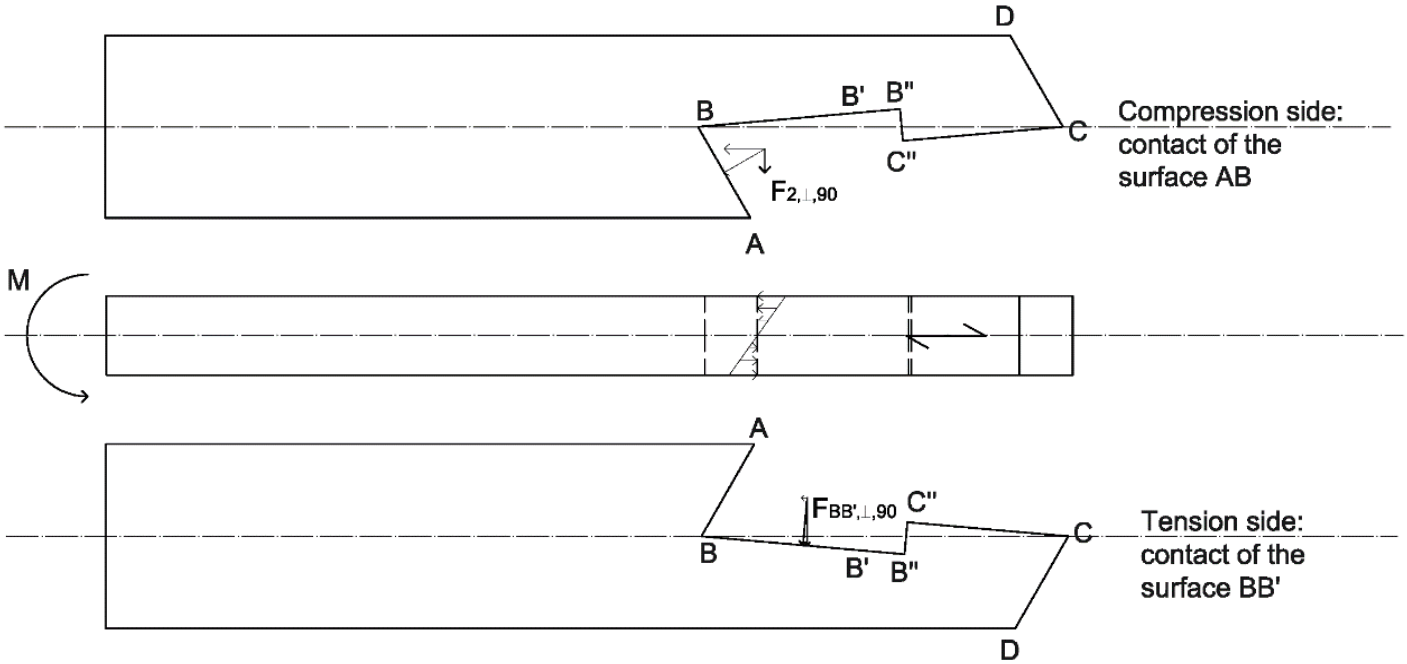

Figure 7-20 – FM II: Failure tension/shear perpendicular to the grains in B

FM II

The plain mechanism of fracture FM II on the compression and tension side is explained in the Figure 7-20. Furthermore, referring to the Figure 7-21 and Figure 7-23, the FM II is explained through some three dimensional diagrams that consider the variation of the forces in the cross–section and the relative developed kinematic mechanisms.

a) Because of $F_{T2,\perp,90}$ force, the grains in B are tensile-stressed in the upward direction;

b) Because of $F_{2,\perp,90}$ on the tension side, the fibers in B are tensile-stressed in the downward direction;

c) Because of $F_{T2,\perp,90}$ and $F_{2,\perp,90}$ forces, the clockwise torque $M_{BHC'B''}$ forms along the longitudinal direction of the compression side. The torque brings to the additional compression of the facing $\overline{AB}$ and $\overline{BB''}$ surfaces on the compressed side;

d) The force $F_{2,\perp,90}$ on the tension side, together with the $F_{2,\perp,90}$ on the compression side brings to the formation of the anticlockwise torque M_{BHBH}. The torque brings to the torsion of the specimen along the neutral axis that causes a non-homogeneous distribution of the compression force in the squint ABAB (Figure 7-23). Because of the kinematic mechanisms above descripted in a), b), c), d), the FM II develops both in B on the compression side and B on the tension side.

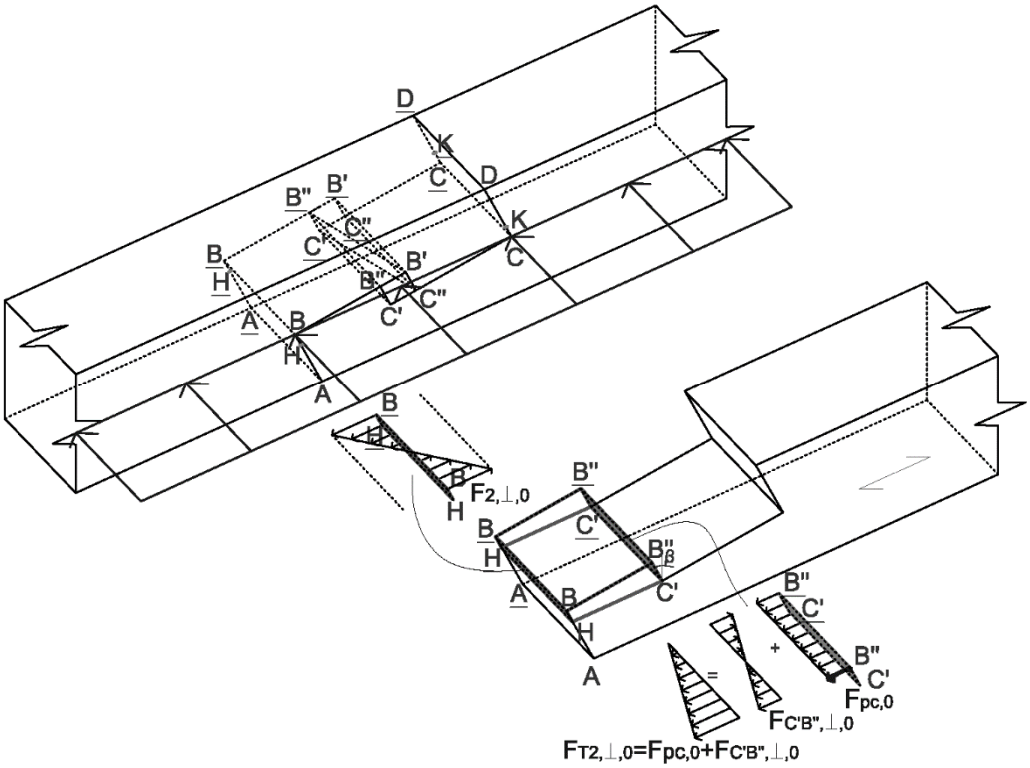

Figure 7-21 – Complex mechanisms of transmission of the forces in the BB''C'HBB''C'H prism

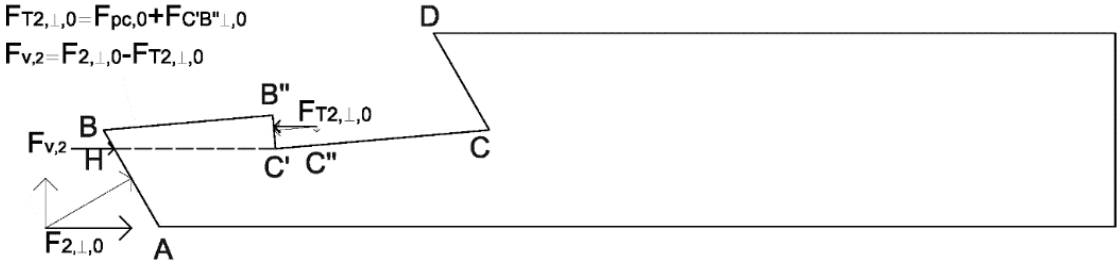

Figure 7-22 – FM V: Failure for shear on the prism BB''C'H – shear plane HC'

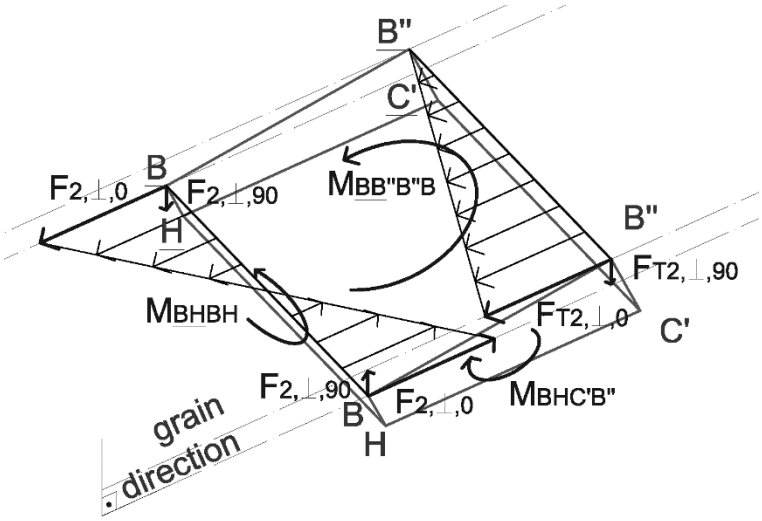

Figure 7-23 – Detail of the forces in the BB''C'HBB''C'H prism and relative developed kinematic mechanisms

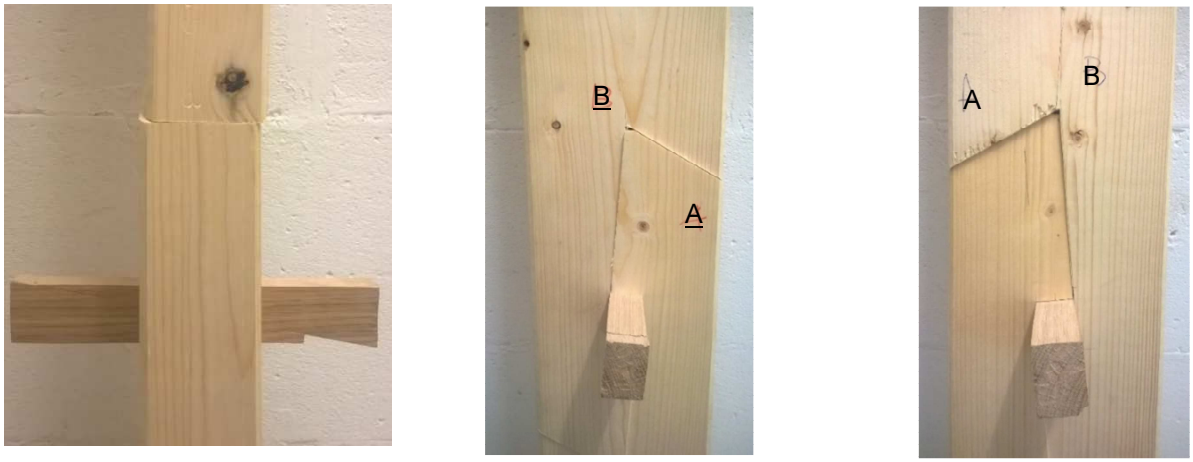

(a) (b) (c)

Figure 7-24 – FM II on the specimen J60_5_w_F0 (a) Rotation of the upper to le lover side. The right part is compressed, the left is tensile-stressed. (b) Tension side. The segment BB' is further compressed. (c) Compression side. The segment BA is further compressed.

FM V

The shear failure is present both on the compression and the tension side. The shear mechanism develops even though on different shear planes.

Compression side. Shear plane: $\overline{HC'}$. A first planar approach on the shear failure in $\overline{HC'}$ is given in the Figure 7-22. The shear force acting on the shear plane $\overline{C'H}$ is eq. 7-8 and depends on eq. 7-7.

$$F_{T2,\perp,0} = F_{pc,0} + F_{B''C',\perp,0} \quad 7\text{-}7$$

$$F_{v,2} = F_{2,\perp,0} - F_{T2,\perp,0} \quad 7\text{-}8$$

Where :

$F_{C'B'',\perp}$ Resultant force on the $\overline{C'B''}$ surface due to the external load, perpendicular to the surface.

$F_{T2,\perp}$ Resultant force on the table 2 (T2 = surface $\overline{C'B''}$) of the joint, perpendicular to the surface.

$F_{2,\perp}$ Resultant force on the face $\overline{AB}$ due to the external applied load.

The section is verified when:

$$\frac{F_{v,2}}{b \cdot \overline{C'H}} \leq R_v \quad 7\text{-}9$$

Referring to the Figure 7-23 the problem is further completed with some observations about the kinematic mechanisms in the third dimension. Because of both different resultant forces at the two compression and tension side, the anticlockwise torque $M_{B''B'\underline{BB}''}$ forms on the shear plane (transversal direction).

As an example that demonstrates the failure mechanisms in the beam, some images from the tests of the failure of the specimen J60_5_w_F0 are proposed in the Figure 7-24:

(a) The upper timber part is rotated respect to the lower timber part due to the torque $M_{BH\underline{BH}}$ that creates a torsion along the beam's axis.

(b) The internal kinematic mechanisms (torque $M_{BHC'B''}$) causes a rotation that brings to the further compression of the segment $\overline{BB'}$ on the tension side and (c) the segment $\overline{AB}$ on the compression side. The key is a further fixed point that establish a horizontal rotation axis that causes the torsion of the upper respect to the lower part.

<u>Tension side</u>. Shear plane $\overline{\mathrm{B'K}}$. The shear failure can also verify on the tension side, on the fibers in $\overline{\mathrm{B'K}}$, because of the compression on $\overline{CD}$ (see specimen J60_5_w_F12, Figure 7-18- c).

7.5.6 General conclusions on the *Jupiter joint*

LOAD-CARRYING CAPACITY.

From a first comparison on the load-carrying capacity of the *Jupiter joint* lead to the followings conclusions.

1. The load-carrying capacity of the *Jupiter joint* in pure bending is the same for both the strong and weak axis.
2. In pure compression, the test specimen loaded on the weak axis (J60_5_w_F0) showed a smaller F_u respect to the one loaded on the strong axis (J60_5_s_F0). The reason of this difference in the load-carrying capacity of the specimens lies in specimens manufacturing, the timber's specific lower properties and finally in the test setup. This last imperfection is in fact more significant for the specimens loaded on the weak axis, where the minimum imperfection can really affect the test results.

FAILURE MODES.

The FM II, shear/tension perpendicular to the grain failure in the point B, is always recurrent in the weak and strong axis' tests. The basic reason of the failure is the same concluded and calculated for the *halved undersquinted* scarf joint; nevertheless the problem is in the *Jupiter joint* is more complex, because of the presence of more factors:

- the presence of imperfections (that affect the weak axis more than the strong axis);
- the variability of the pre-compression F_{pc} of the key;
- the entity of both the angle α of the squint and β of the splayed surface;
- the internal friction (not considered in the present section of the work);

Furthermore, the FM V is dependent on the length of the shear segment $\overline{C'H}$. The bigger is the surface of the shear plane (longer shear segment) the bigger is the load-carrying capacity of the specimen.

7.6 Evaluation of the rotational stiffness

Referring to the Figure 7-25, the calculation of the rotational stiffness (eq. 7-15) is done according to the ultimate values of applied load and the displacements of the correspondent piston P_{II}. The calculation is performed as follows.

$$e = 0.405\,m \tag{7-10}$$

$$M_u = \frac{F_{II,u}}{2} \cdot e \tag{7-11}$$

$$u_{PII}\left(M_u\right) \tag{7-12}$$

$$\theta_{[\deg]} = arctg\left(\frac{u_{P2}}{l_b/2}\right) \tag{7-13}$$

$$\theta_{[rad]} = \frac{\theta_{[\deg]} \cdot \pi}{180°} \tag{7-14}$$

$$k_\varphi = \frac{M_u}{\theta_{[rad]}} \tag{7-15}$$

Where

e	distance between the support and the application of the load
$l_b/2$	distance between the support and the center of the joint (hinge).
$F_{II,u}$	Value of the applied force F_{II} (of the piston P_{II}) at the failure
M_u	Value of the moment M at the failure
$u_{PII}\left(M_u\right)$	displacement of the piston P_{II} at the failure
$\theta_{[\deg]}$	angle of rotation of the beam at the failure, in degrees
$\theta_{[rad]}$	angle of rotation of the beam at the failure, in radiant
k_φ	rotational stiffness of the joint.

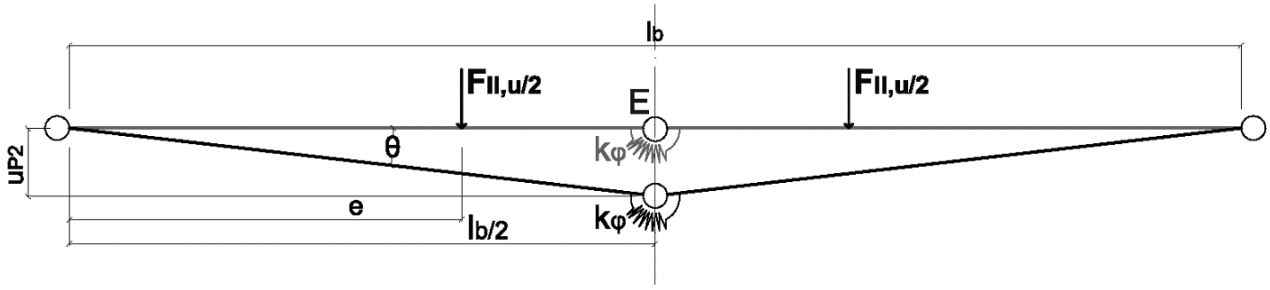

Figure 7-25 – Scheme of the rotational stiffness of the hinge

7.6.1 Stiffness in the *halved undersquinted scarf* joint (in-plane)

According to the performed tests, the rotational stiffness along the strong axis for the *halved undersquinted scarf* joint is evaluated for both for the squint inclinations $\alpha = 30°$ and $\alpha = 60°$, respectively in the Table 7-7 and Table 7-8. The considered value of rotational stiffness in pure bending is, for both the inclinations, the smaller among the experimental values. In short, the eq. 7-16 and eq. 7-17 give a resume of the rotational stiffness in the *halved undersquinted* according to the experimental tests.

Table 7-7 – Values of rotational stiffness in the *halved undersquinted scarf α = 30°*

TESTS R30_s α = 30°	**u**P2 [m]	**FII** [kN]	**uP1** [m]	**FI** [kN]	**lb/2** [m]	**e** [mm]	**Mu** [kN m]	**Fu** [kN]	**θ[rad]**	**kφy** [kN m / rad]
R_30_F0	0.0104	2.329	0.0000	0.000	5.95	0.405	0.472	0.000	0.0017	**271**
R_30_M0	0.0000	0.000	0.0061	8.402	5.95	0.405	0.000	8.402	0.0000	0
R_30_F0_bis	0.0155	6.481	0.0000	6.333	5.95	0.405	1.312	6.333	0.0026	505
R_30_F0_bis2	0.0160	4.343	0.0000	7.873	5.95	0.405	0.879	7.873	0.0027	327
R_30_F0_2	0.0103	3.354	0.0000	0.000	5.95	0.405	0.679	0.000	0.0017	392
R_30_F_M	0.0094	4.902	0.0019	6.177	5.95	0.405	0.993	6.177	0.0016	631
R_30_F_M_2	0.0135	5.712	0.0018	7.939	5.95	0.405	1.157	7.939	0.0023	510
R_30_F_M_3	0.0072	3.533	0.0003	4.515	5.95	0.405	0.715	4.515	0.0012	593
R_30_F_M_4	0.0067	3.402	0.0001	4.718	5.95	0.405	0.689	4.718	0.0011	615

Table 7-8 –Values of rotational stiffness in the *halved undersquinted scarf α = 60°*

TESTS R60_s α = 60°	**u**P2 [m]	**FII** [kN]	**uP1** [m]	**FI** [kN]	**lb/2** [m]	**e** [mm]	**Mu** [kN m]	**Fu** [kN]	**θ[rad]**	**kφy** [kN m / rad]
R60_F0	0.0038	1.223	0.0000	0	5.95	0.405	0.2477	0.0000	0.00065	**383**
R60_M0	-0.0671	0.000	0.0057	41.665	5.95	0.405	0.0000	41.6650	-0.01128	0
R60_M0_2	0.0000	0.000	0.0108	84.516	5.95	0.405	0.0000	84.5160	0.00000	0
R60_N16_M	0.0068	6.144	0.0015	16.008	5.95	0.405	1.2442	16.0080	0.00114	1095
R60_N32 _Ma	0.0115	10.219	0.0015	32.069	5.95	0.405	2.0693	32.0690	0.00193	1072
R60_N48_M	0.0121	12.848	0.0030	47.967	5.95	0.405	2.6017	47.9670	0.00204	1276
R60_N64_M	0.0120	15.130	0.0049	63.979	5.95	0.405	3.0638	63.9790	0.00202	1515

$k\varphi y_{\exp} = 271$ (*α = 30°; strong axis*) 7-16

$k\varphi y_{\exp} = 383$ (*α = 60°; strong axis*) 7-17

In contradiction with the demonstration in Chapter 6.4.2.1, TEST 6, in the eq. 7-16 and eq. 7-17, the value of rotational stiffness for *α = 60°* is bigger than the one for the *α = 30°*. In fact, in the TEST 6 is demonstrated that the specimen *α = 60°* has not load-carrying capacity. Therefore, the vertical positioning of the specimen in the machine 2 influences the test results in pure bending, because of the self-weight, and is able to resist a minimum amount of pure bending action. As a conclusion, the orientation of the specimen in the structure, influence also the load-carrying behaviour of the connection.

The values of rotational stiffness of the specific joint's geometry to be considered for practical purposes, are reported in Table 7-10.

7.6.2 Stiffness in the *Jupiter joint*

Referring to Figure 7-25, the calculation of the rotational stiffness k_φ is done according to the ultimate values of applied load and the displacements of the correspondent piston P_{II}.

In the Table 7-9 are reported the values of rotational stiffness for the *Jupiter jo*int, respectively (a) for the strong and (b) for the weak axis' evaluation. In this latter case, the test of reference are the one performed in vertical position with the testing machine 2.

The following eq. 7-18 gives a resume of the experimental value of rotational stiffness in the *Jupiter joint.*

$k\varphi y_{\exp} = 663$

$k\varphi z_{\exp} = 262$ 7-18

Table 7-9 – Results for the J60_5_s (a) and J60_5_w (b)

TESTS JJ60_5_s α = 60°; β = 5°	uP2 [m]	FII [kN]	uP1 [m]	FI [kN]	lb/2 [m]	e [mm]	Mu [kN m]	Fu [kN]	θ[rad]	kφy [kN m / rad]
J60_5_F0	0.0066	3.75	0.0000	0.00	5.95	0.39	0.7313	0.0000	0.00110	**663**
J60_5_s_M0	0.0000	0.00	0.0078	87.95	5.95	0.39	0.0000	87.9460	0.00000	#DIV/0!
J60_5_s_F19_M	0.0171	9.62	0.0020	18.73	5.95	0.39	1.8761	18.7340	0.00288	652
J60_5_s_F38_M	0.0177	13.34	0.0033	37.77	5.95	0.39	2.6013	37.7650	0.00298	874
J60_5_s_F57_M	0.0171	16.55	0.0047	56.80	5.95	0.39	3.2269	56.8010	0.00288	1120
J60_5_s_F65_M	0.0000	0.00	0.0053	54.30	5.95	0.39	0.0000	54.3000	0.00000	#DIV/0!
J60_5_s_F76_M ^	0.0000	0.00	0.0065	54.47	5.95	0.39	0.0000	54.4700	0.00000	#DIV/0!
J60_5_s_F76_M_2 ^	0.0000	0.00	0.0037	35.94	5.95	0.39	0.0000	35.9440	0.00000	#DIV/0!
J60_5_s_F76_M_3 ^	0.0000	0.00	0.0074	75.87	5.95	0.39	0.0000	75.8700	0.00000	#DIV/0!
J60_5_s_F60_M	0.0095	15.03	0.0052	59.84	5.95	0.39	2.9310	59.8380	0.00159	1843
J60_5_s_F50_M	0.0080	11.53	0.0042	49.71	5.95	0.39	2.2485	49.7080	0.00134	1680
J60_5_s_F30_M	0.0107	10.00	0.0023	29.60	5.95	0.39	1.9500	29.5960	0.00180	1084
J60_5_s_F70_M	0.0000	7.83	0.0066	70.09	5.95	0.39	1.5272	70.0870	0.00000	#DIV/0!
					(a)					
TESTS JJ60_5_w α = 60°; β = 5°	**uP2** [m]	**FII** [kN]	**uP1** [m]	**FI** [kN]	**lb/2 [m]**	**e** [mm]	**Mu** [kN m]	**Fu** [kN]	**θ[rad]**	**kφz** [kN m / rad]
J60_5_w_F0	0.0148	3.34	0.0000	0.00	5.95	0.39	0.6509	0.0000	0.00248	**262**
J60_5_w_M0	0.0000	0.00	0.0061	61.53	5.95	0.39	0.0000	61.5250	0.00000	#DIV/0!
J60_5_w_F50_M	0.0160	4.57	0.0042	49.75	5.95	0.39	0.8912	49.7500	0.00269	331
J60_5_w_F38_M	0.0137	4.36	0.0038	37.97	5.95	0.39	0.8500	37.9680	0.00229	370
J60_5_w_F25_M	0.0132	4.83	0.0028	24.89	5.95	0.39	0.9419	24.8900	0.00222	424
J60_5_w_12_M	0.0177	4.34	0.0013	12.77	5.95	0.39	0.8467	12.7710	0.00298	284
J60_5_w_40_M	0.0154	5.28	0.0036	39.91	5.95	0.39	1.0298	39.9140	0.00260	397
J60_5_w_55_M	0.0068	1.63	0.0050	54.85	5.95	0.39	0.3179	54.8450	0.00115	277
					(b)					

7.6.3 CONCLUSIONS

As a conclusion, the Table 7-10 gives a resume of the rotational stiffness for all the performed tests.

Table 7-10 – Resume of the value of rotational stiffness kφ for all the connections' geometries. pure bending action.

in-plane pure bending tests						
	α [°]	**β** [°]	**HORIZONTAL POSITION**		**VERTICAL POSITION**	
			TEST	$k\varphi y_{exp}$	**TEST**	$k\varphi y_{exp}$
halved undersquinted scarf	30	0	0415_03	363	R30_F0	271
	45	0	0415_01	344	-	-
	> 45	0	desum.	0	-	-
	60	0	0415_02	0	R60_F0	383
halved undersquinted and tabled scarf	45	0	0421_02	434	-	-
	60	0	0421_01	490	-	-
stop splayed and undersquinted	60	10	manual	0	H60_10_s_F0	174
halved undersquinted and tabled with key	60	0	-	-	J60_5_s_F0	323
Jupiter joint	60	5	-	-	J60_0_s_F0	663
out-of-plane pure bending tests						
	α [°]	**β** [°]	**HORIZONTAL POSITION**		**VERTICAL POSITION**	
			TEST	$k\varphi z_{exp}$	**TEST**	$k\varphi z_{exp}$
halved undersquinted scarf	30	0	-	-	manual	0
Jupiter joint	60	5	-	-	J60_0_w_F0	262

Chapter 8 THE CASE STUDY

8.1 Introduction

In order to understand and give a clear description of the behaviour of the *Jupiter joint*, the case study of Santiago de Cuba's cathedral has been investigated. The case study is necessary to do a comparison between the real behaviour and the geometric and static simplifications adopted for the structural analysis. With that purpose, the work is divided into three sections: real geometry, physical model, CAD model, and structural model. In any of these sections, specific aspects are investigated.

In this chapter is first given a brief description of the dome and the structural elements that compose it. Then, a physical model that extremely simplifies the real geometry, and uses some "devices" to simulate the real behaviour is described. This was the first step to approach the problem about the *Jupiter joint's* properties. Finally, a CAD model is used to simplify the imperfect real geometry into a perfect ideal one, to be afterward modelled in the structural analysis program.

In this chapter, have been done the most important pre-assumptions about the importance of the joint's geometry. Thanks to this conclusions the analytical models and experimental tests were approached.

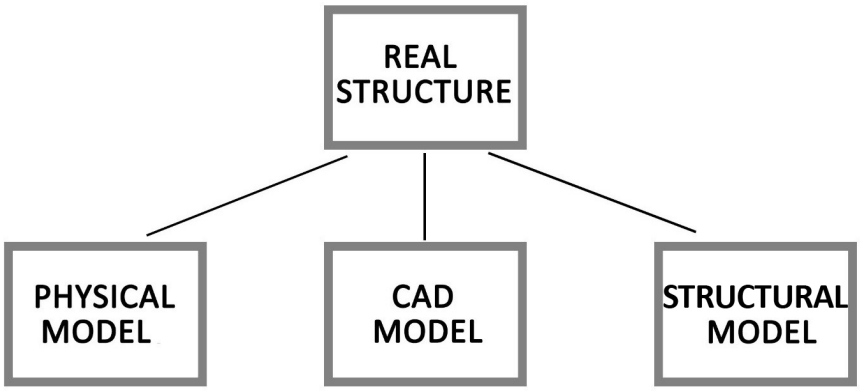

Figure 8-1 - Real structure ↔ Erection ↔ CAD model ↔ RFEM model ⇒ load-bearing behavior of the structure.

8.2 Geometric description

The next description of the dome has his counterpart in the CAD models of the Figure 8-28 to Figure 8-31.

DOME

The structure of the dome lays on four masonry arches and abutment. The rectangular volume generated by the pillars is approximatively 8.4 meters long, 7.2 meters wide and 24.2 meters high (10 x 8.5 x 25 Spanish

arms). The two west-oriented abutments measure approximatively 300 x 200 cm, and the ones that are east–oriented 200 x 200 cm and all four contain wooden *horcones* inside. The structure of the dome is made by cedar wooden elements that form a continuous system with the horizontal squared masonry surface of abutments were it lays. The '*media naranja'* (half orange) covers a span of about 9 metres, is 7 metres high and it is concluded with a clerestory 3.5 metres high. For the first 130 cm it is enclosed inside the masonry wall on which it lays. The wooden structure is formed by 40 main arches and two chains, one on the top and one on the bottom of such ribs. The cross-section of the arches is 18 x 20 ÷ 23 cm^2 with a developing surface in height of 755.8 cm. The ribs are formed by 2 or 3 curved pieces; each piece is linked to the consecutive with an elongation carpentry joint called *Jupiter joint*. The position of the discontinuity is discussed in the Table 8-1. In the lower part, the ribs are linked with a wooden circular chain (Figure 8-8). The ribs are connected to the chain with *mortise and tennon* joint (Figure 8-10). Each of the curved pieces that form the lower chain is aprox. 260 cm long and with a cross-section of 20 x 20 cm^2. The pieces are linked together by *mortise and tennon* joint (*quijera joint*). The chain on the upper side is formed by three chains (Figure 8-11). The first (1) and second (2) from the bottom are circular and have a diameter of 370 cm; the third (3) one is octagonal inscribed in the circumference (it is proper to the clerestory). The cross-section of the chains are respectively 27 x 27 cm^2, 17 x 17 cm^2 and 14 x 14 cm^2. The connection between the upper structure and the ribs is by the use of a nail. The geometry of the elements in correspondence of the contact surfaces is unknown because of the bad conservation of the structure. We assume two possible scenery (Figure 8-14): the first assumption (hp. 1) is that the rib's head are inclined of 30° respect to the vertical, then, the first upper chain were not squared, but "wedge-shaped"; therefore, the geometry of this element was used to block the head of the ribs, as a "key" of an arch. The second assumption (hp. 2) is that the ribs' heads were straight, and also the upper circumference have a regular squared section; here, the ribs are juxtapose with the upper chain and connected with a nail. The most probably scenery is the second one.

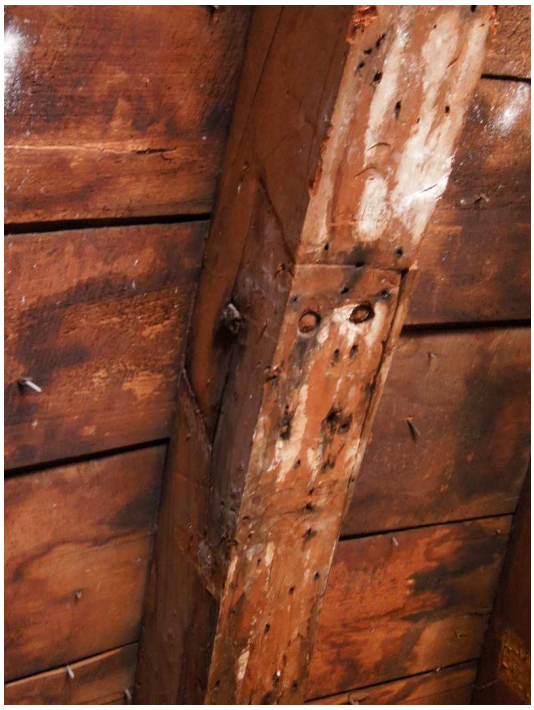

Figure 8-2 - *Jupiter joint* in the cathedral's dome

Figure 8-3 – Wooden basket

Figure 8-4 – one side of the *Jupiter joint and quijera joint*

Figure 8-5 - Upper steel chain

Rib n°	Constituent parts
1	2
2	3
3	2
4	3
5	3
6	2
7	2
8	2
9	2
10	3
11	3
12	3
13	2
14	3
15	2
16	2
17	2
18	2
19	3
20	3
21	2
22	3
23	2
24	3
25	2
26	3
27	3
28	2
29	2
30	-
31	2
32	2
33	2
34	2
35	3
36	2
37	3
38	2
39	3
40	2

Table 8-1 - Detailed description of the ribs

Figure 8-7– *Mortise and tennon* joint (*quijera joint*)

Figure 8-8 - Foot of the rib – the lower ring

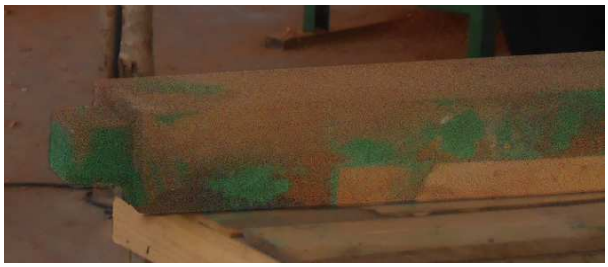

Figure 8-9 – *Mortise and tennon* joint (*tennon* at the rib's foot)

Figure 8-6 – Ribs: *Mortise and tennon* and *Jupiter joint*

Figure 8-10 - *Mortise & tennon* joint (*mortise* in the lower ring)

Figure 8-11 Upper rings, head of the ribs

Figure 8-12 - Upper ring-rib connection, second assumption

Figure 8-13 - Outer planking and inner parallels

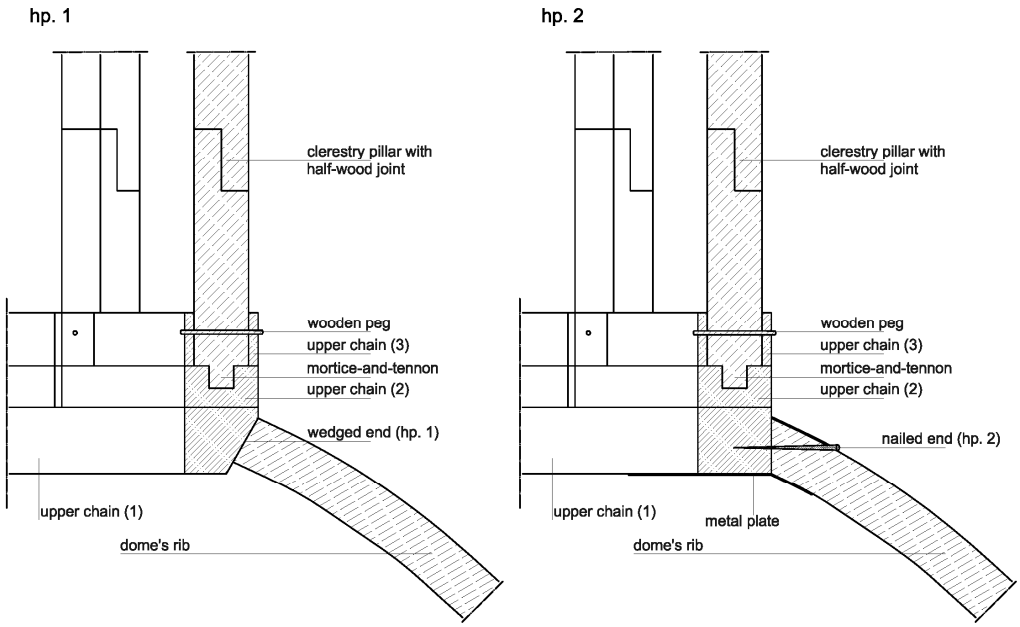

Figure 8-14 - Upper ring-rib connection, first assumption

The head of the ribs is also braced with a metallic chain. The aims of this metallic element, settled presumably in XX century, is to collect the ribs' head and connect them with the main ring and with the half XX century concrete overlapping layer. The ribs are originally linked each other in their left and right faces, with a system of parallel circular tie beams (Figure 8-12). The elements are perpendicular to the main ribs' axes, and the aim is to fix the distance between the ribs. The cross-section of such elements is 3 cm in height and 2 cm in width; the element are separated 18 cm one to the next one. In the outer part, a wooden planking layer of boards (Figure 8-13) measuring 3 x 12 (variable) x 35 cm each is spiked to the main ribs. There are 21 planks approx. distributed in the height of each rib, forming a system of parallels that give stiffness to the main system.

CLERESTORY

The main structure of the lantern is in wood too. The clerestory dome is based on an octagonal chain, that lays on the main dome's upper chains. The clerestory covers 330 cm of diameter and 360 cm of height. The main structure is formed by 8 pillars in correspondence with the edges of the octagonal base, and morticed in the ring (Figure 8-17). The cross-section of the pillars is 16 x 16 cm^2 and cover a height of 290 cm. The main structure of little dome is formed by 8 wooden arches with section of 11 x 8.5 cm^2 (Figure 8-18). Each beam is formed by 2 pieces connected each other with *half timber* (*half-lap*) joint (Figure 8-16). In the extrados of the ribs, wooden planks are nailed to the main beams in order to stiff the structure. A central pole with octagonal section of 20 cm diameter links the main arches in their upper part. This pole pass 60 cm through the head of the dome, and supports externally the cross. A ventral transversal tie beam with section of 17 x 17 cm^2 tights the base of the clerestory.

The clerestory (clerestory weight = 18 kN) loads the lower chain in correspondence of each of the 40 ribs with 18 kN. Considering the number of nails that connect the dome, that corresponds to 40 ≈ 0.5 kN per nail.

Figure 8-15 – Exploded view of the clerestory

Figure 8-16 – View of the clerestory' s dome

Figure 8-17 – *Mortise and tennon* joint at the base of the main ribs of the clerestory

Figure 8-18 – H*alf timber* connection in the ribs' structure

Figure 8-19 - *Cuje* underlay

Figure 8-20 - Inner gypsum decorations

NON-LOAD-BEARING COMPONENTS

On the wooden frame is spiked a lead shell 1 mm thick. The external covering of the dome is a 5 cm thick cast concrete and waterproofed mesh layer finishes the dome externally.

Inside, the infill 8 internal wooden ribs is made by *cuje* (Figure 8-19) fixed by rivets on the parallels and ribs of the main structure. The technique consists of intertwined branches of plant fibres, covered with fragmented stone material bonded with lime mortar. This underlay supports a decorative chalk (Figure 8-20).

MATERIALS

In the Table 8-2 the results of the investigation conducted by the IVALSA institute in Sesto Fiorentino on the wooden specimen from the wooden structure of the Cathedral (see Annex F). At the time of the investigation, the structure of the dome was not already visible, thus in the year 2012, when it was open for the first time from the construction, some specimen were already collected. From a visual and macroscopic investigation of the new specimen, was concluded that the Cedar is the construction material of the dome. In the Table 8-3 are represented the mechanical characteristics desumed from the work (Monica, 2010) of the Prof.ssa Maira Monica, academic of the Wooden Structure course at the Universidad de Oriente di Santiago de Cuba.

Table 8-2 – Wooden species according to the IVALSA investigation

SPECIMEN				RESULTS	
Name			description	WOOD NAME	
Origin	n°	year		scientific	vulgar
S	1	2010	clear specimen on horcon amb. 1	*Cedrela* Sp.	Cedro
S	2	2010	clear specimen on horcon amb.1	*Calophyllum* cfr. brasiliense	St. Mary
S	3	2010	clear specimen on viga amb.1	*Millettia* sp.	Wengé
S	4	2010	clear specimen on horcon amb.3	*Calophyllum* cfr. brasiliense	St. Mary
S	5	2010	clear specimen on horcon amb.4	*Millettia* sp.	Wengé

Table 8-3 – Wooden properties of the Cedar (Monica, 2010)

Cedar			
Young's Modulus	E	8220	[N/mm²]
Shear Modulus	G	2874	[MPa]
Poissons Ratio	v	0.43	
Specific weight	γ	4.5	[kN/m^3]
Bulk modulus	K	1.96E+04	[N/mm²]
Lame's Constant	λ	1.77E+04	[N/mm²]
Density	ρ	450	[kg/m^3]
Characteristics strength for bending	$f_{m,k}$	80	[N/mm²]
Characteristics strength for tension	$f_{t,0,k}$	69	[N/mm²]
Characteristics strength for tension perpendicular	$f_{t,90,k}$	0.5	[N/mm²]
Characeristics strength for compression	$f_{c,0,k}$	52.7	[N/mm²]
Characteristics strength for compression perpendicular	$f_{c,90,k}$	11.5	[N/mm²]

8.3 Physical model

Two simplified models are presented. The models have a relatively simple 3D approximation of the structure, that simulate the behaviour of the structure with diverse *restraint-conditions* between the sticks. The two variations are the *Scarf joint* (S) model and "*Snap" joint* (K).

8.3.1 Geometry of the models

RIBS. The main load-bearing structure is composed by 8 ribs. The ribs are created through wooden sticks. The thin elements were chosen because their cross section is negligible compared to its lengths, low load-bearing capacity, no tensile strength, and eventual quick failure for buckling of the element. The ribs are clamped-in, for a deep of 2÷3 mm in a carton, the base of the model. In their upper part, the ribs are also clamped in the upper ring through a hole.

The rib is divided along its length into 2 or 3 sections. The 3-pieces ribs and the 2-pieces ribs alternate in the structure. The sections are connected by two different geometric interfaces and linked together by means of a gummy cylinder. The geometric interfaces are the *scarf joint* interface (S) and the *snap joint* interface (K).

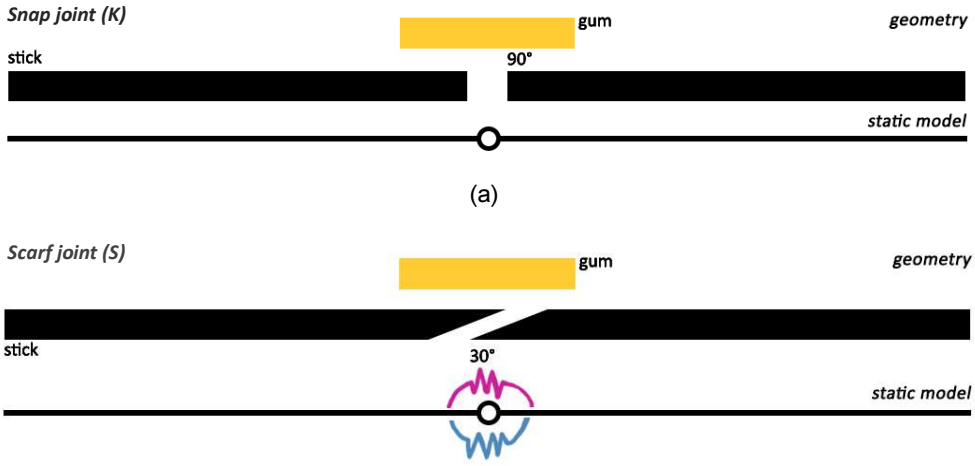

Figure 8-21 – The *Snap joint (K) model* (a); the *Scarf Joint* (S) model.

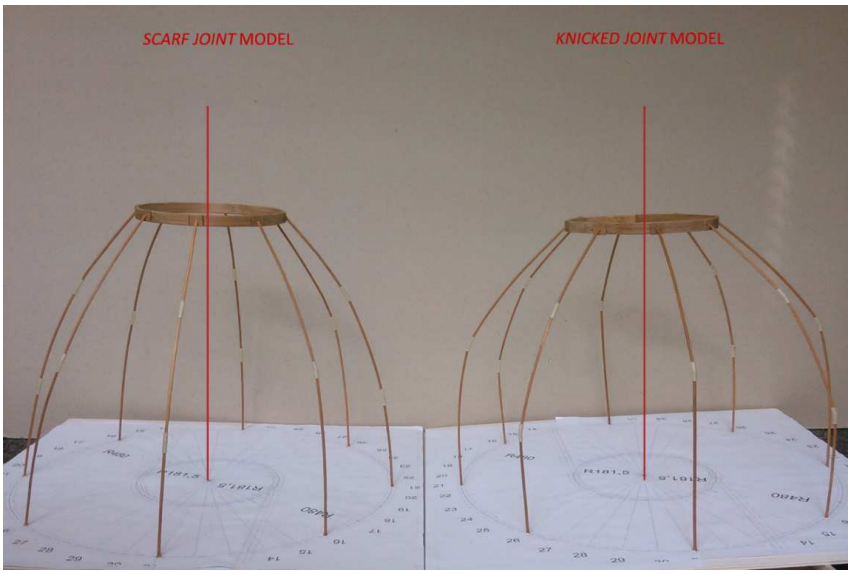

Figure 8-22 – Case 0, dead load. Models *(S) joint* to the left and *(K) joint* to the right.

(K) In the *Snap Joint* model, the plane interface is plane and forms a 90° angle with the element' s axis, that corresponds to the stick cross-section in eq. 8-1.

$$A_k = \pi \cdot r^2 = \pi \cdot \left(\frac{d}{2}\right)^2 = \pi \cdot \frac{d^2}{4} \quad 8\text{-}1$$

Where:

A_k cross section area

d diameter of the stick.

(S) In the *Scarf Joint* model, the facing interface is a slanting surface. This sloping surface is with an angle aprox. 30° of inclination respect to the plane cross-section, and it is called *scarf* interface. The scarf interface's the area is the area of the ellipse derived from a cut of 30° in the cross section (eq. 8-2).

$$A_s = \pi \cdot a \cdot b \quad 8\text{-}2$$

$$S = \frac{d}{\sin 30} = 2 \cdot d \quad 8\text{-}3$$

$$a = \frac{d}{2}; b = S = \frac{2d}{2} = d \quad 8\text{-}4$$

$$A_s = \pi \cdot \frac{d}{2} \cdot d = \pi \cdot \frac{d^2}{2} \quad 8\text{-}5$$

Where:

a and *b* the semi-axis of the ellipse.

d diameter of the stick and also one of the two axis of the sloping surface

As a conclusion, the contact area of facing surfaces, is doubled in *scarf joint* in deference to *snap joint*.

$$A_s = 2 \cdot A_k \quad 8\text{-}6$$

BOARDS. Another feature in the dome is the presence of the external boards. In the real structure the boards are nailed to the main structure. This real structure's component is schematized with a *ring*. The ring is a thin and continuous element, correspondent with a complete circumference around the dome. The geometry of this element resumes the main real mechanical feature of the nailed table; nevertheless, in the model, as a difference with the reality, the single ring does not offer a big amount of compression resistance and also does not guarantees space between the ribs.

8.3.2 Static models

The *rotational stiffness* of a joint is defined as *the moment required to produce an unitary rotation*

$k = M / \theta$

Where:

k rotational stiffness;

M the applied force;

θ the resulting rotation from the applied force [rad].

The *static model (S)* represented in Figure 8-23 is the static model of the *(S) model*, while, the static model represented in Figure 8-24 represents the *(K) model*.

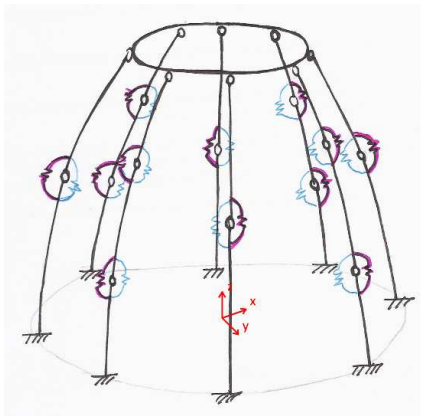

Figure 8-23 - static model of the (S) joint model

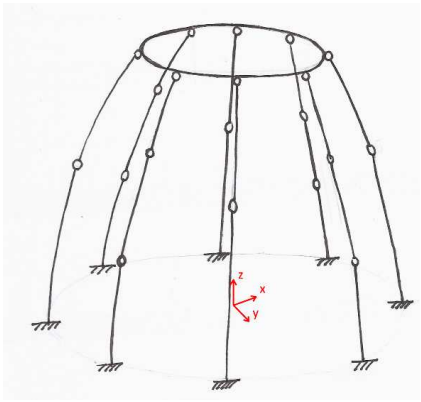

Figure 8-24 - static model of the (K) joint model

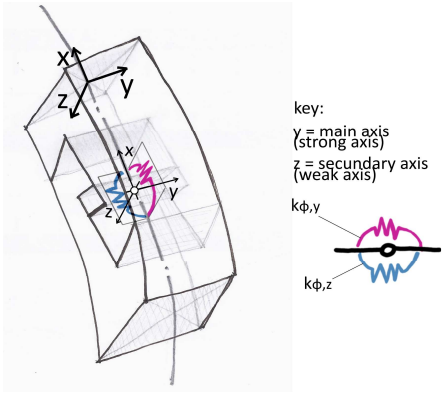

Figure 8-25 - key for the spring element.

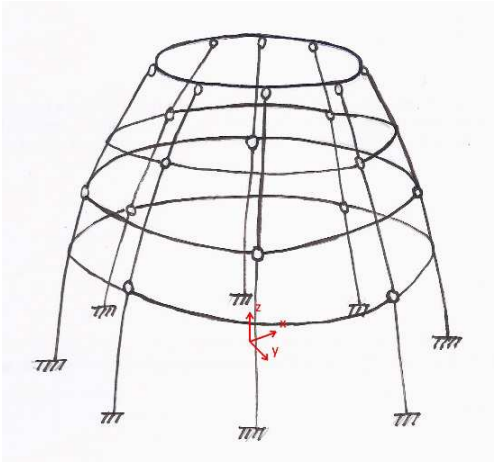

Figure 8-26 - static model of *(K) – (3) model*

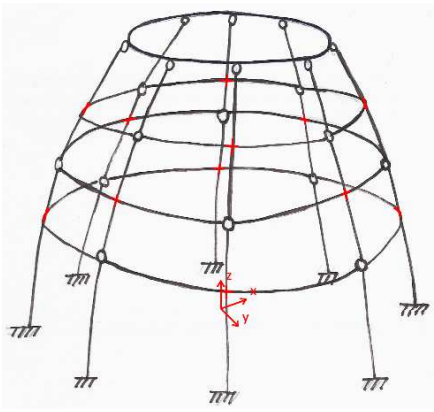

Figure 8-27 - static model of *(K) – (3fix) model*.

(K) The connections are represented by a fully hinge. In the fully hinge the values of spring stiffness are the one expressed in the Table 8-4.

(S) The hinges are characterized by the presence of rotational springs in two assigned directions. The rotational springs confers some quantity of rotational stiffness to the hinge (Table 8-4 and Figure 8-25).

Table 8-4 – key of the stiffnesses in (K) and (S).

(K)				(S)			
kϕ		**u**		**kϕ**		**u**	
kϕx	= 0	ux	= 0	kϕx	= 0	ux	= 0
kϕy	= 0	uy	= 0	kϕy	≠ 0	uy	= 0
kϕz	= 0	uz	= 0	kϕz	≠ 0	uz	= 0

In the Figure 8-25 the two springs along the main and weak axis of the model (S) are schematized. The pink spring corresponds to the rotational stiffness $k_{\varphi,y}$ along the strong axis *y*, while the blue spring corresponds to the rotational stiffness $k_{\varphi,z}$ along the weak axis *z*.

8.3.3 Load conditions

FIRST VARIABLE. The loads. Precision weights by the amount of 100 g or 200 g. are used

SECOND VARIABLE. Position of the weight. Centred or eccentric, respect to the central rotational axis of the dome.

8.3.4 Tests

FIRST STEP

In the first step, the stiffness of the local connection in the structure has been investigated. The models (S) and (K) are loaded with same loading conditions as in the Table 8-5 and the results are reported in the Table 8-8.

Table 8-5 – FIRST STEP case studies

Geometry		**Load conditions**		**Case number**
Kind of joint	**External Rings**	**Position of load**	**Amount of load** [g]	
Scarf	No	**-**	Self-weight	0 (S)
Snap	No	-	Self-weight	0 (K)
Scarf Joint (S)	No	centered	100	1
	No	centered	200	2
	No	eccentric	100	3
	no	eccentric	200	4
Snap Joint (K)	No	centered	100	9
	No	centered	200	10
	No	eccentric	100	11
	no	eccentric	200	12 (not performed)

SECOND STEP

In the second step, the stiffness of the global structure has been investigated. The model (K) was provided with one (1) or three (3) external rings and loaded with different loading conditions as in the Table 8-6. In the first version, the rings are connected to the ribs in correspondence of the couplings (Figure 8-26); in the second version, the rings are connected in correspondence of the intersected ribs, with a fixed restraint (Figure 8-27).

Table 8-6 – SECOND STEP case studies

Geometry		Load conditions		Case number
Kind of joint	External Rings	Position of load	Amount of load [g]	
Snap Joint (K)	(1)	Centered	100	5
	(1)	Centered	200	6
	(1)	eccentric	100	7
	(1)	eccentric	200	8
	(3)	Centered	100	13
	(3)	Centered	200	14
	(3) fix	Centered	100	17
	(3) fix	Centered	200	18

8.3.5 Results

In the present paragraph the results of the tests on the scale model are done. In the following Table 8-7 the key of the Table 8-8 is done.

Table 8-7 – Key of the Table 8-8:

STRUCTURE	reference axis system of the structure 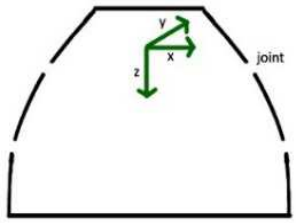						
	LOAD						
LOAD	Entity of the load		Position of the load				
	+	++			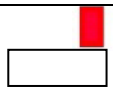		
	= 100 g	= 200 g	eccentric left	central	eccentric right		
	RESPONSE						
RESPONSE	Entity of the deformation		Intensity of the response				
			+	++	+++	++++	∞
	displace-ment	rotation	low	medium	medium/ high	high	very high

Table 8-8 – Comparison of loading case - results

Case n°	RESPONSE				RESULTS		
	Vertical displace-ment	Lateral displace-ment	Bending main axis	Bending weak axis	Scheme of behavior	Photo	
						Front	Top
0 (S)					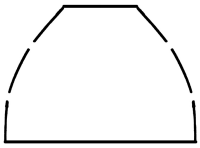	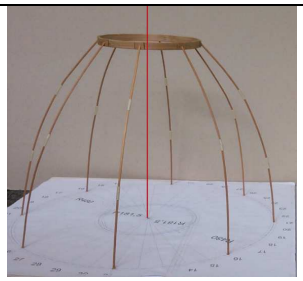	
	RESPONSE: The structure is in equilibrium.						
0 (K)	+				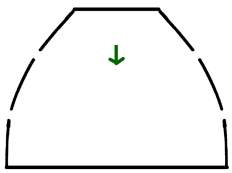	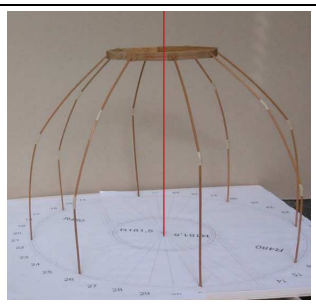	
	RESPONSE: Minimum symmetric displacement in *z*.						

	RESPONSE					Photo	
	Vertical displace-ment	Lateral displace-ment	Bending main axis	Bending weak axis	Scheme of the behaviour	Front	Top
1 (S)	+	+	+	+	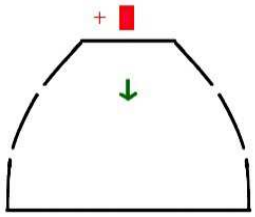	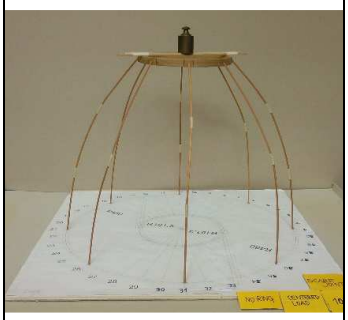	
	Minimum symmetric displacement in *z*. Because of constructive imperfection (S) is loaded in both weak and strong axis (lateral buckling)						
2 (S)	++	+	++	++	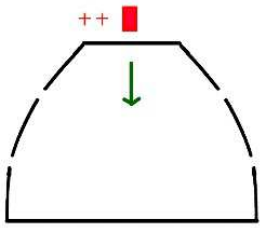	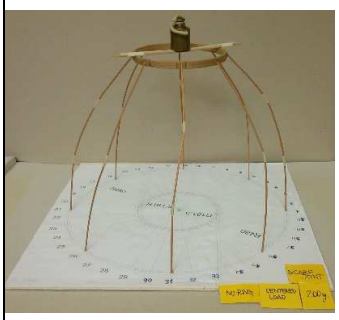	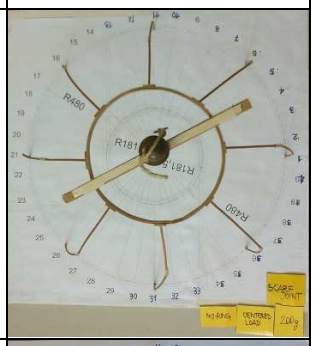
	Symmetric displacement in *z*. Because of constructive imperfection (s) is loaded in both weak and strong axis (lateral buckling).						
3 (S)	+	++	+	S	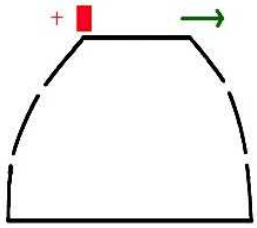	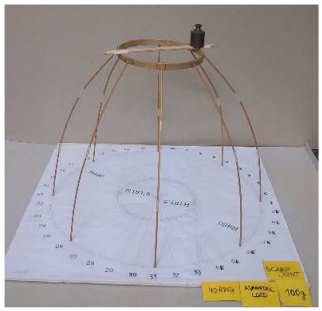	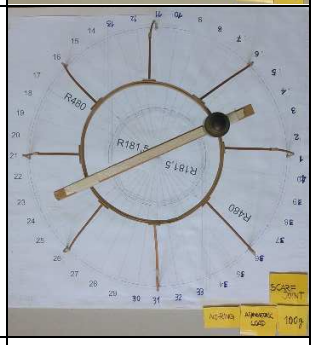
	RESPONSE: Asymmetric displacements in *zx* .						
4 (S)	+	++	+	+	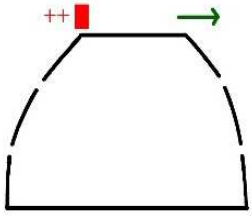	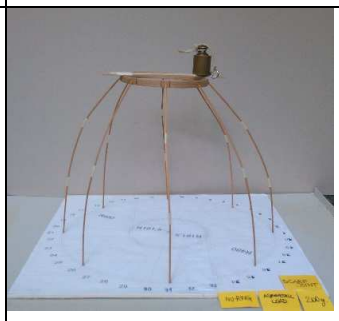	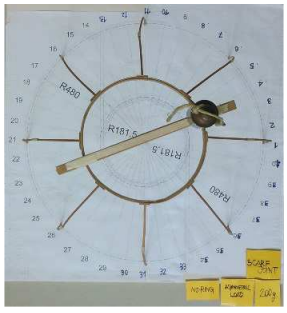
	RESPONSE: Asymmetric displacements in *zx* . jj is loaded in both weak and strong axis (lateral buckling).						
9 (K)	++	++	++	++	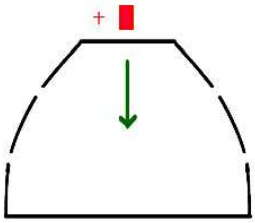	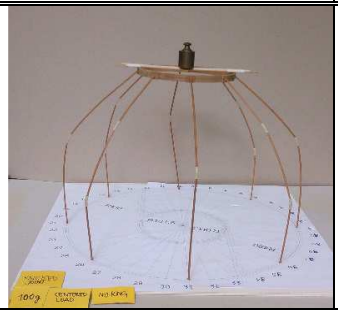	
	RESPONSE: kinematic						

	RESPONSE					Photo	
	Vertical displace-ment	Lateral displace-ment	Bending main axis	Bending weak axis	Scheme of the behaviour	Front	Top
10 (K)	++++	8	++++	++++	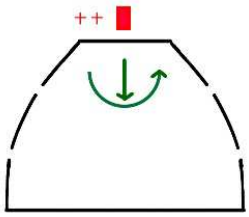	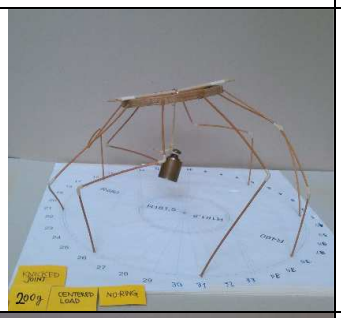	
	RESPONSE: Kinematic						
11 (K)	++++	8	++++	++++	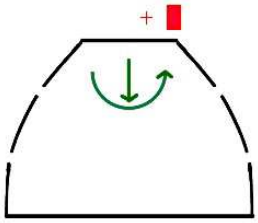	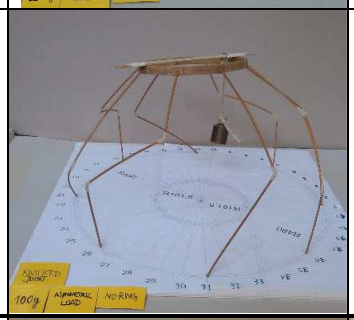	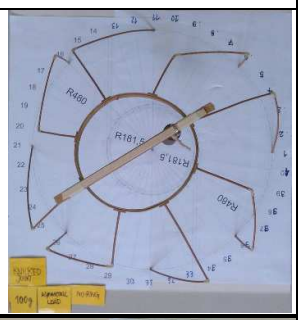
	RESPONSE: Kinematic						
5 (K)	++	++	+	+	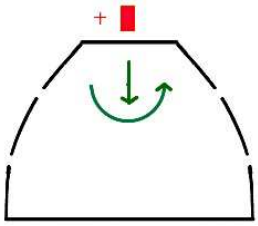	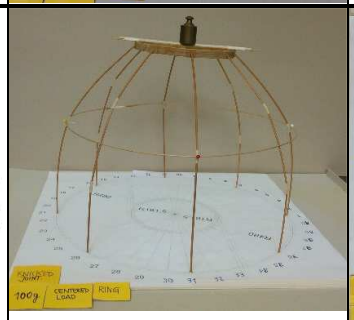	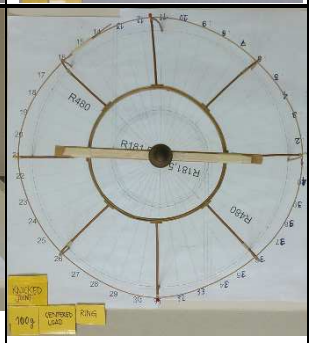
	RESPONSE: Asymmetric displacements in *zx*. Because of constructive imperfection, (K) is loaded in both weak and strong axis (lateral buckling).						
7 (K)	+	+++	+	+	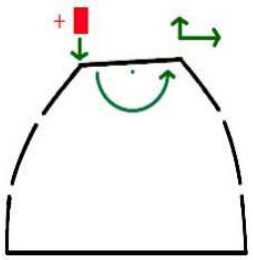	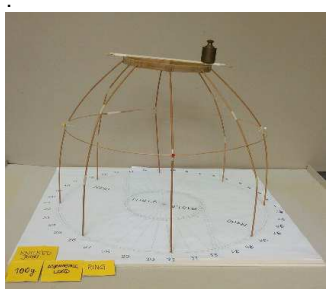	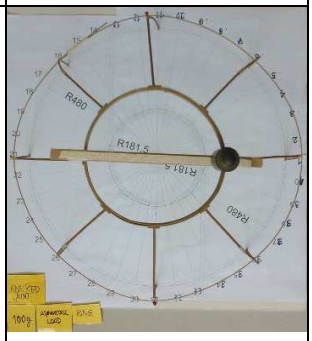
	RESPONSE: Asymmetric displacements in *zx*. Because of the very marked rotation in *xy* plane, model can be considered kinematic.						
6 (K)	+++	++	++	++	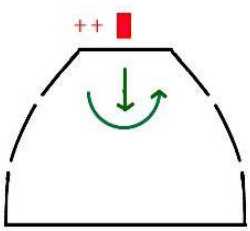	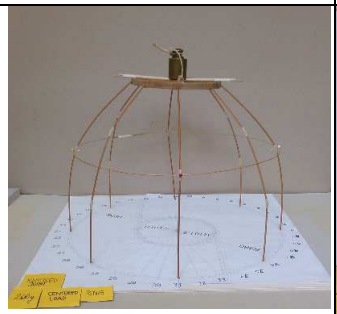	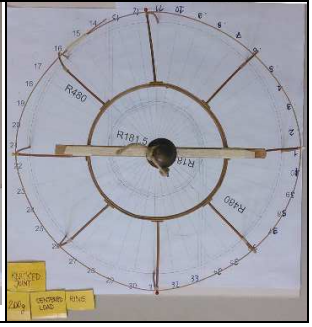
	RESPONSE: Asymmetric displacements in *zx*. Because of constructive imperfection, (K) is loaded in both weak and strong axis (lateral buckling).						

	RESPONSE					Photo	
	Vertical displace-ment	Lateral displace-ment	Bending main axis	Bending weak axis	Scheme of the behaviour	Front	Top
8 (K)	+	+++	++	++	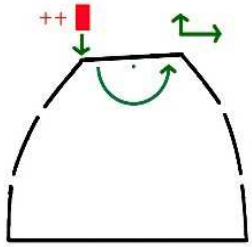	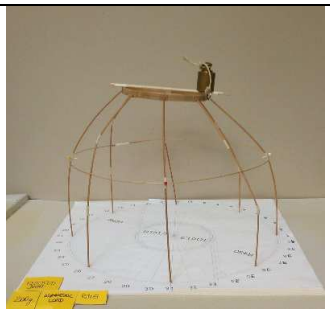	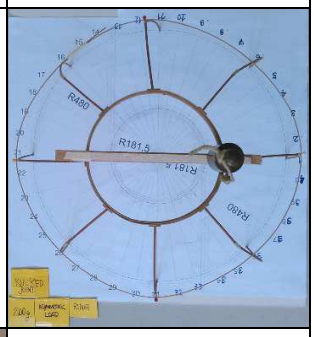
	RESPONSE: Asymmetric displacements in *zx* . Because of the very marked rotation in *xy* plane, model can be considered kinematic.						
13 (K)	++	++	++	++	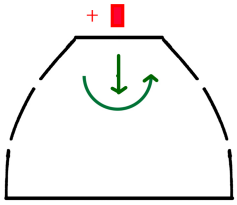	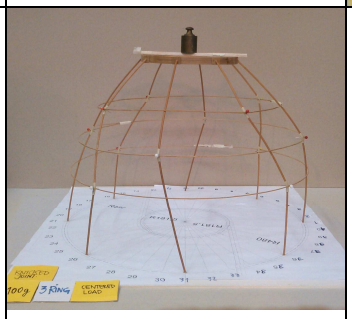	
	RESPONSE: Symmetric displacement in *z*. Because of constructive imperfections, lateral buckling of the connection.						
14 (K)	++	++	++	++	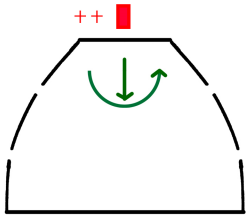	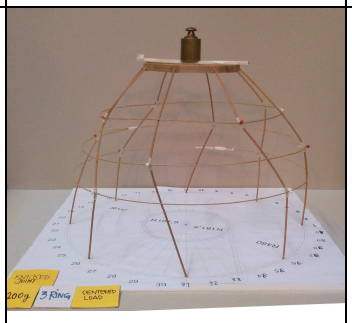	
	RESPONSE: Symmetric displacement in *z*. Because of constructive imperfections, lateral buckling of the connection.						
17 (K)	+	++	+	+	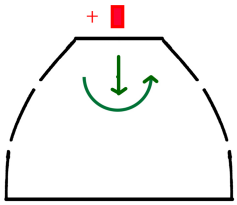	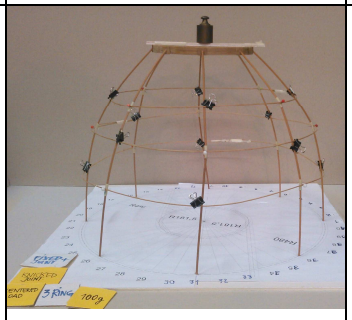	
	RESPONSE: Symmetric displacement in *z*. Small rotation of the structure because of imperfections.						
18 (K)	+	++	+	+	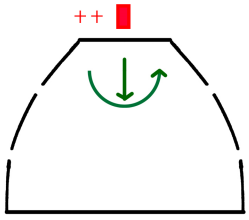	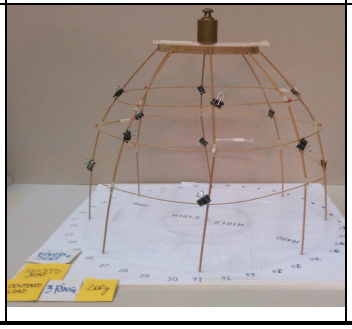	
	RESPONSE: Symmetric displacement in *z*. Small rotation of the structure because of imperfections.						

8.3.6 Conclusions on the physical model tests

Case 0 (S), 0 (K), self-weight

The *(S) model* shows more load-carrying capacity respect to the *(K) model*.

➔ The *scarf joint* shows more load-carrying capacity respect to the *snap joint*.

Case 2 (S), 10 (K), 200g, without ring

The (K) shows bigger deformations respect to the (S). Under same load conditions the (K) is in fact kinematic and the (S) is isostatic.

➔ The *scarf joint* (S) model is stiffer respect to the *snap joint* (K).

➔ The described behavior demonstrates that the effectiveness of the connection depends only on the geometry of the interface of the connection elements. Some quantity of stiffness is generated only by the *scarf* cut.

Case 5 (K)

Reproduces the same loading conditions of the case 2 (S), 1 (K), but the structure 5 (K) is provided with a ring. The behaviour of the 5 (K) is similar to the one shown by the 2 (S)

➔ The external ring generates some quantity of stiffness.

Case 10 (K)

The load is applied centrally and the structure is axially symmetric; therefore, the deformations are expected symmetrical respect to the main dome's axis. Nevertheless, the resulting configuration shows lateral buckling of the beams.

➔ The physical model, as well as the real structure are characterized by imperfections both in the geometry of the elements and in the joints.

Case 3 (S), 11 (K)

In case of asymmetric load (or deformations by the imperfections), a certain amount of lateral buckling is observed along both the models. The 3 (S) is stiffer than the 11 (K). To reach the same performances of the 3 (S), the introduction of a ring is necessary, as in the model 7 (K).

➔ The *scarf joint* model shows certain amount of rotational stiffness along both the strong and weak axis. The alternative for the stiffening of the structure is the introduction of the ring (planking).

Case 6 (K), 18 (K)

In the 6 (K) the single ring assigns certain amount of stiffness to the structure (respect to the equivalent without rings), but the structure can still rotate around its main axis. In order to avoid this rotation, more stiffness is needed. Certain amount of stiffness is due to the combination of rings 18 (K). The structure behaves as a shell structure. It acquires more amount of stiffness and strength, respect to the single-ring element. This is because of the shear interaction forces among the planks, which assign more stiffness to the structure, and avoid rotation around central axis of structure.

8.4 General conclusions

- The global stiffness is increased by the positioning *spring restraints* in correspondence with the rib.

The *spring element* represented in the model as circular closed ring, is in the real structure the nailed planking.

- The local stiffness is increased by positioning rotational spring in correspondence with the hinge. The rotational stiffness is given by the geometry of the joint.

8.5 CAD model

In the following images, the structure of the dome is modelled in a CAD model. Thanks to the CAD model, the geometry of the structure is simplified for the structural model, and more understandable for the reader.

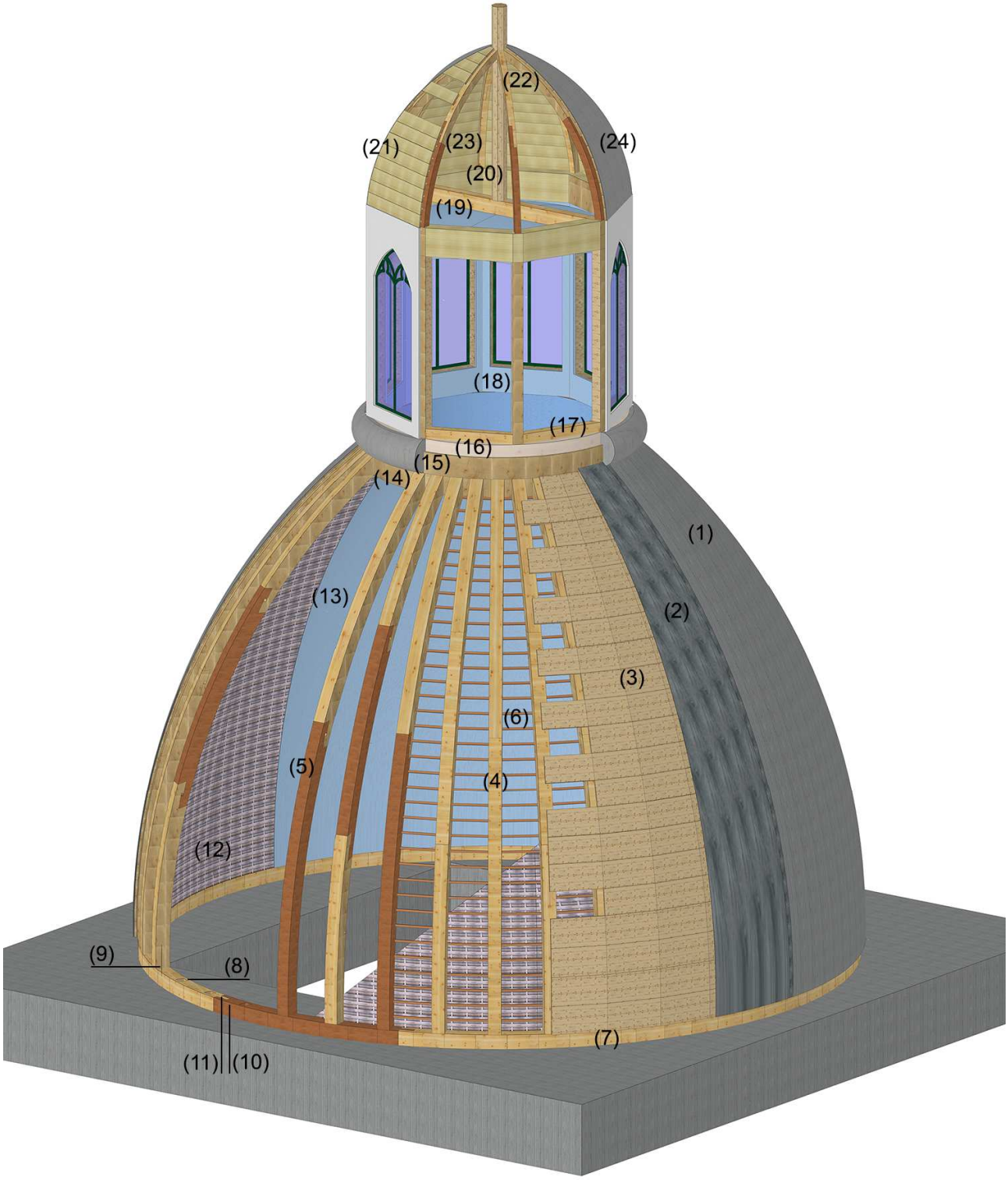

Figure 8-28 – Materic view of the dome. The components are: (1) cement layer; (2) load layer; (3) nailed planking; (4) wooden ribs; (5) *Jupiter joint*; (6) inner parallels; (7) lower ring; (8) mortise (mortise and tennon joint); (9) tennon (mortise and tennon joint); (10) mortise (extended mortise and tennon joint); (11) extended tennon (extended mortise and tennon joint); (12) *cuje* layer; (13) gypsum layer; (14) upper chain (1); (15) upper chain (2); (16) upper chain (3); (17) clerestory's octagonal base; (18) clerestory's pillars; (19) tie beam; (20) central octagonal pole; (21) clerestory's planking; (22) clerestory's arched beams; (23) half-timber joint; (24) cover layer.

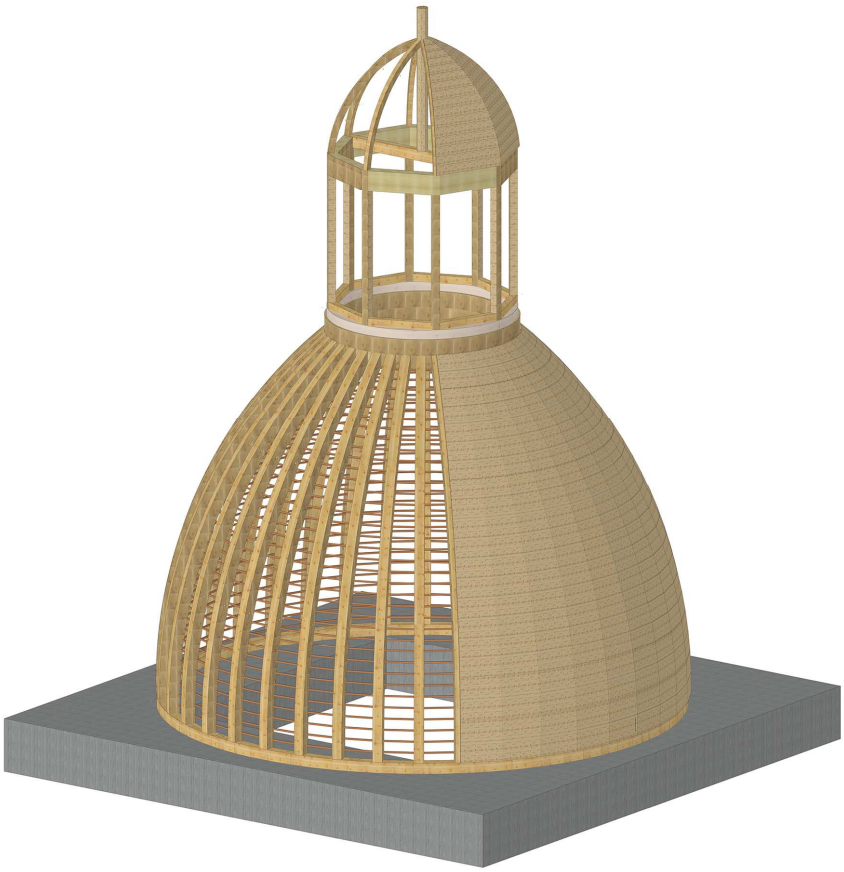

Figure 8-29 – General view of the dome's wooden skeleton

Figure 8-30 – General view of the dome

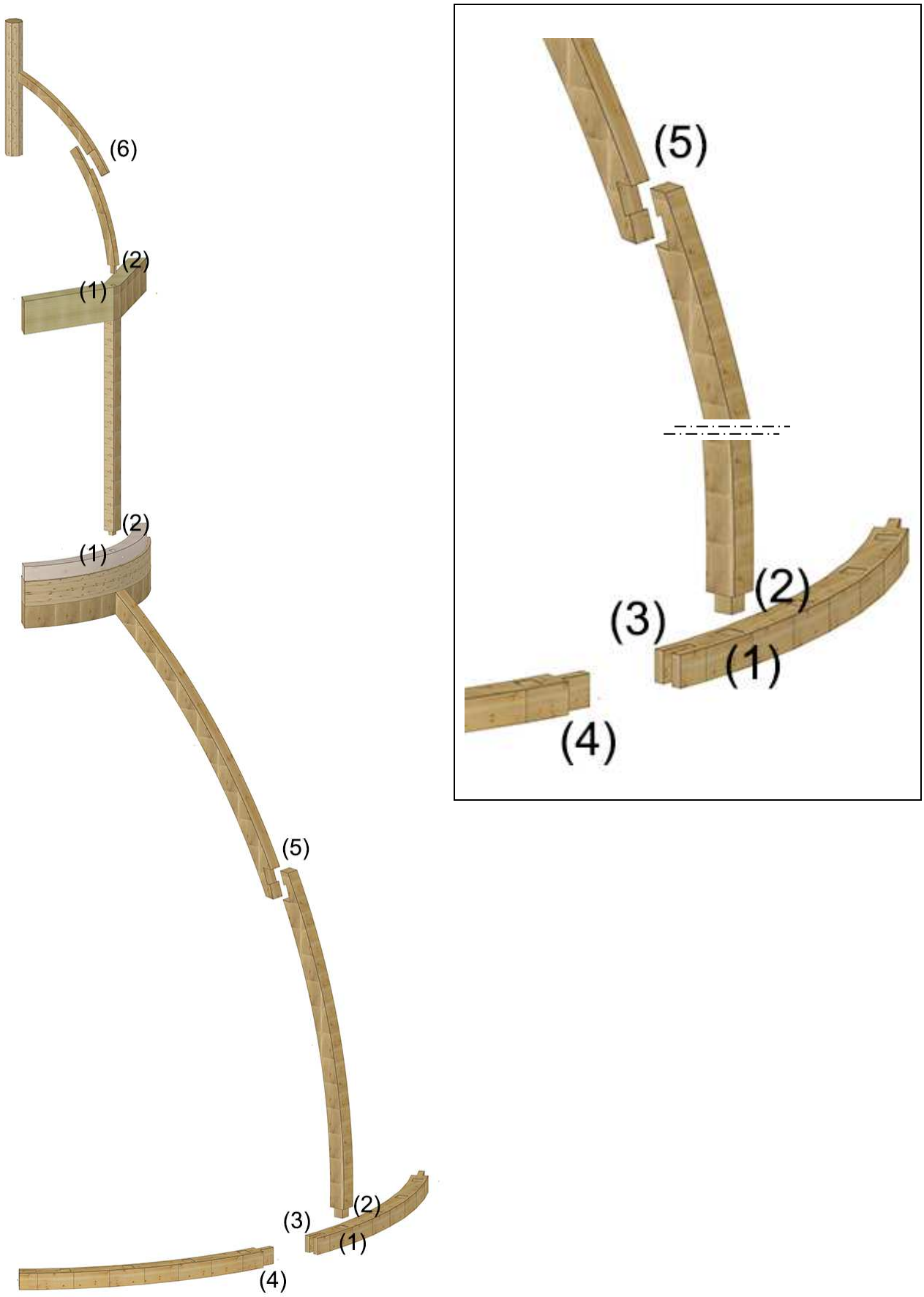

Figure 8-31 – Left: exploded view of a dome's rib from the top to the bottom. (1) mortise (mortise and tennon joint); (2) tennon (mortise and tennon joint); (3) mortise (extended mortise and tennon joint); (4) extended tennon (extended mortise and tennon joint); (5) *Jupiter joint*; (6) half-timber joint. Right: zoom of the left image.

8.6 Why the Jupiter joint?

The approach to the problem has been done making some first assumptions about the reason of the use of the *Jupiter joint* from the carpenters for the erection of the dome. Some assumptions of geometric, material and constructive nature are following listed.

8.6.1 Geometry factors

The geometry of the structure is a very important factor to take into account. The dome has a circular lower ring and the ribs are arcs of circumference. The shape is determinant because of the following reasons.

1. Under the assumption of perfect axial-symmetry of the structure, the load-carrying capacity of a curved beam is in compression higher (for shape) than one formed by linear elements. At the same time, the imperfect structure has to be taken into account. Under the assumption of imperfect structure, the imperfections as well as eccentricities of the load, are much more influent in a curved beam than in a linear one. Therefore, in the choice of the connection the behaviour out-of-plane of the same has to be taken into account (see mechanical properties).
2. The circular shape is a fundamental fact in the choice of the joint. In case of external horizontal action (i.e. wind), the constructional elements are positioned along the radiant direction with centre on the rotational axis of the dome. With respect to the joint's axis, the load comes from different angles in dependence of the position of the beam; therefore, a "three dimensional" behaviour is necessary. The joint is required to have a minimum amount of rotational stiffness along both the weak and strong axis (see mechanical properties).
3. The harvesting and the fashioning of the (curved) beam have also a very big influence on the load-carrying capacity of the beam and the connection. In fact, a different fashioning of the beam means different angle of action of the force with respect to the inclination of the grain; therefore, a different load-carrying capacity of the beam (it follows in material factors).

8.6.2 Material factors

Another reason why we need a wood-wood connection is a material factor. Both because of the supply of wood in the environment and the fashioning are factors that can influence the choice of the wooden connection.

1. In the nature, the timbers can reach only restricted lengths. Because of the artefact to build, the total length of the beams has to reach approx. 700 cm. The span of each piece is approx. 200–300 cm and the two pieces have to be linked according to the rules of good practice, in order to transmit the stresses from one to the other side of the timber elements.
2. Depending on the fibers's direction the performances of the *Jupiter joint* (or woodworking joints in general) are changing. The wood is in fact a orthotropic material, and the direction of the cut from the tree for the fashioning of the timber is an important factor to be taken into account. Here follow two different hypothesis for the cut. In the Hp. (a) a smaller waste of material is expected in comparison with the Hp. (b). Here the ribs' cross section is 20 cm. In order to get a one-piece rib, each of the trunks you need would have the useable cross-section of approximately 300 cm diameter; then, dividing the whole length in 2-3 pieces, the needed cross-section (also net of the cuttings) would be only 100-150 cm. The Hp. (a) is therefore the more probable for economy reasons.

3. The different angle between the axis and the wood grains between the hypothesis (a) and (b) causes a different behaviour of the connection respect to the shear, moment and compression actions.

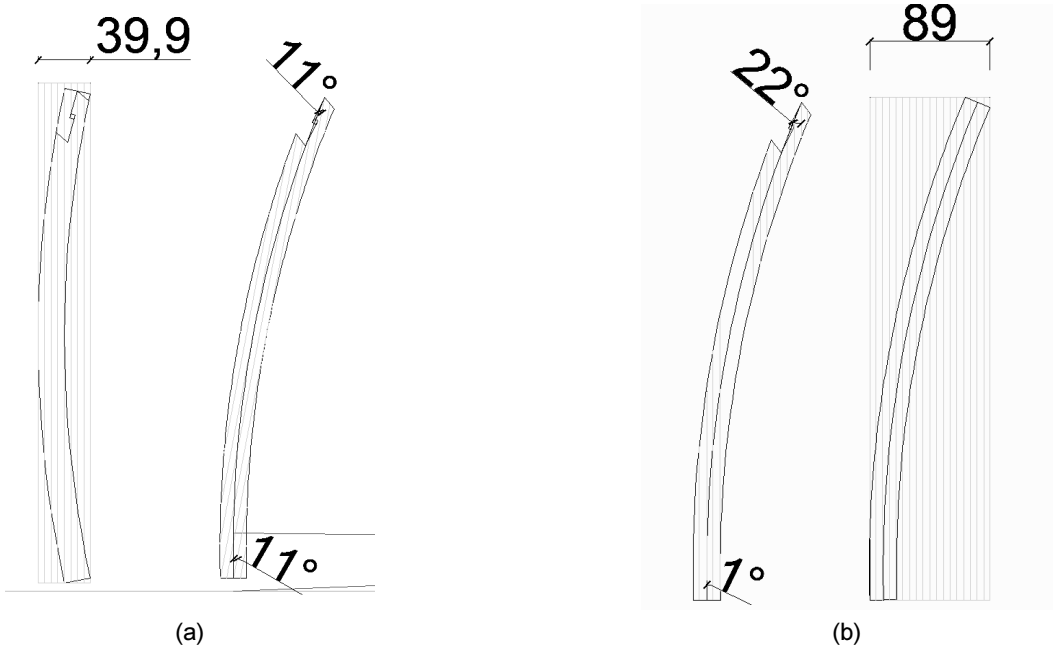

Figure 8-32 – Hypothesis of fashioning of the beam from the timber. (a) Hp. 1 (b) Hp. 2.

8.6.3 Mechanical properties

The mechanical properties of the *Jupiter joint* were for sure one of the main reason of the choice. The practical experience demonstrated the reliability of the connection in compression and tension; therefore, the masters of the opera decided to use it for the realization of the dome.

8.6.4 Montage reasons

Finally, the reason of the choice of the *Jupiter joint* because of constructive reasons.

Some assumptions on dome's construction follow.

Hp (1) of construction of the dome (Figure 8-33)

1. Lower circle assembly
2. Construction of whole ribs with stencil
3. Building of scaffold with platforms
4. Upper circle positioning
5. Erection of 5 ribs: 4 main + 1 diagonal
6. Connection of ribs with upper ring with the nail
7. Erection of left ribs
8. Disassembling of the scaffold
9. Planking positioning
10. Construction of circular wall (h=150cm from circular lower ring)

Hp (2) of construction of the dome (Figure 8-34)

1. Erection of circular wall (h=50cm from circular lower ring)
2. Lower circle assembly

3. Building of scaffold with platforms
4. Positioning of ach of 40 ribs' first piece in lower circle
5. Positioning of first circular planking levels (stiff the structure)
6. Assembling of second piece of ribs. Assembling of *Jupiter joints* on site
7. Positioning of second circular planking levels (stiff the structure)
8. Upper circle positioning
9. Connection upper ring + ribs that already reach the top, with nail
10. Assembling of third pieces of left ribs. Connection upper ring + ribs that are left, with nail
11. Positioning of left circular planking levels
12. Erection of circular wall (h=150cm from circular lower ring)

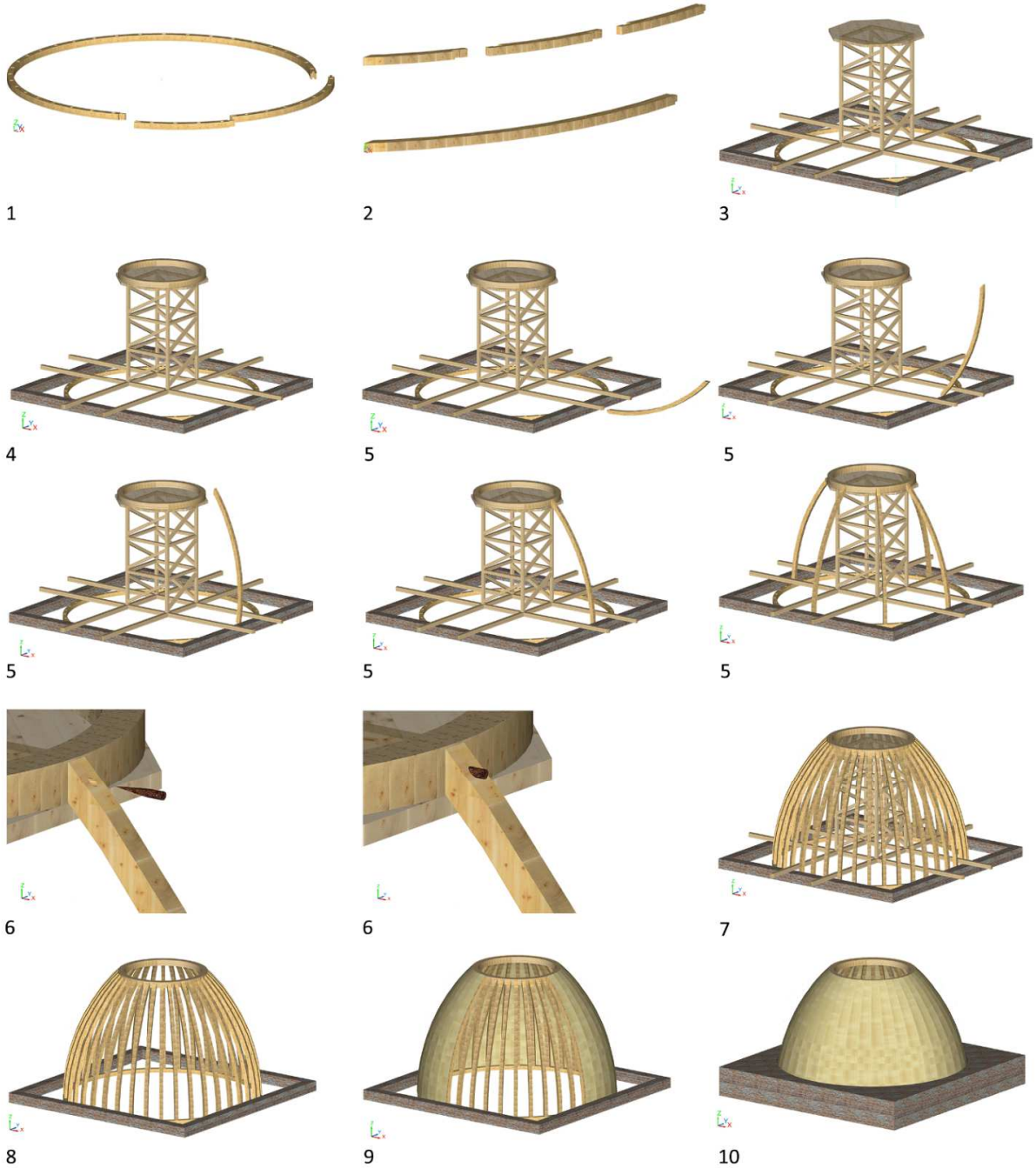

Figure 8-33 – Hp. 1. of construction of the dome

Hp (3) of construction of the dome (Figure 8-35)

1. Lower circle assembly
2. Construction of whole ribs with stencil
3. Building of scaffold with platforms
4. Upper ring positioning
5. Erection of first section + planking
6. Erection of second section + planking
7. Erection of third section + planking
8. Erection of fourth section + planking
9. Disassembling of the scaffold
10. Construction of circular wall (h = 150cm from circular lower ring).

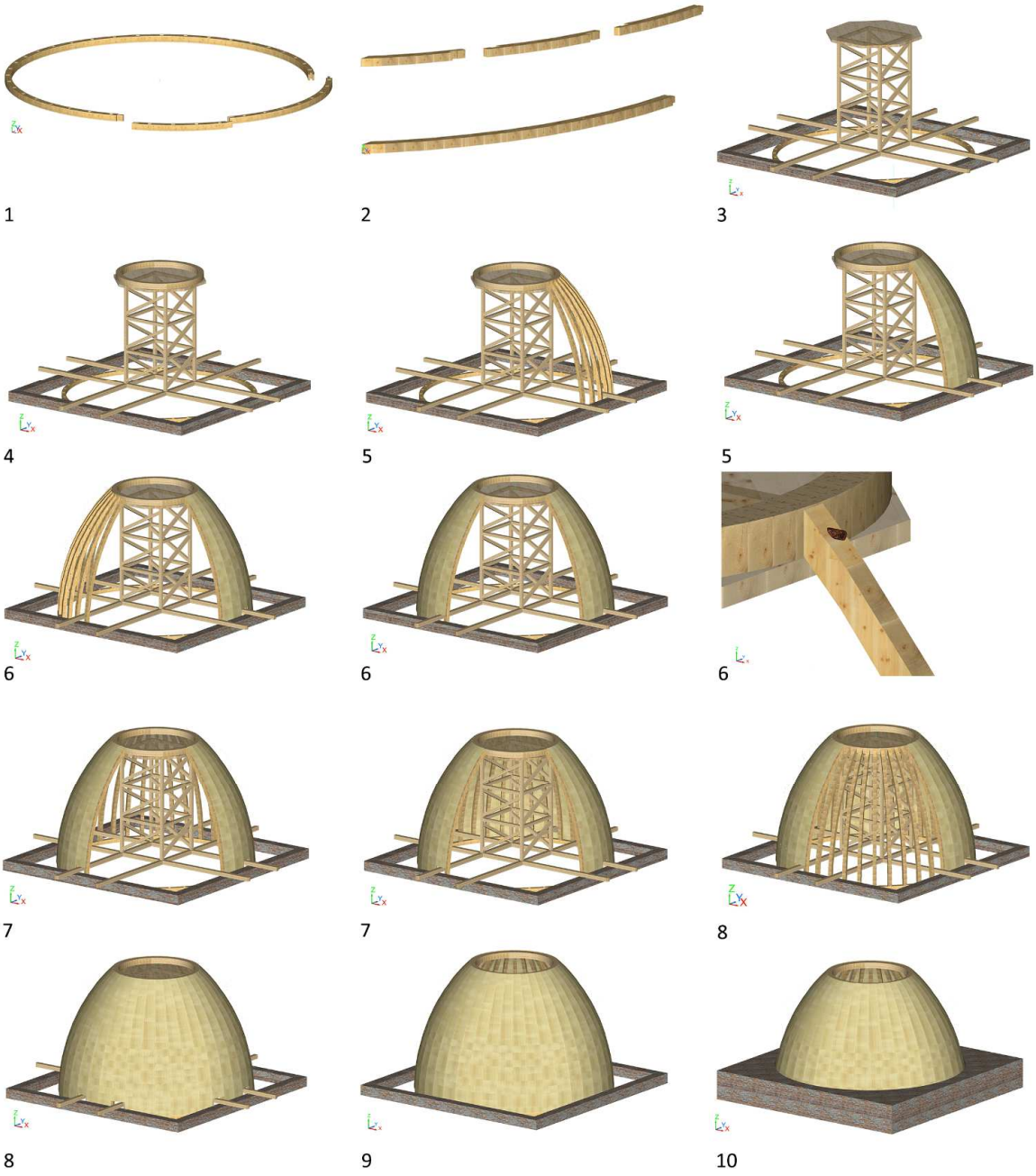

Figure 8-34 – Hp. 2. of construction of the dome

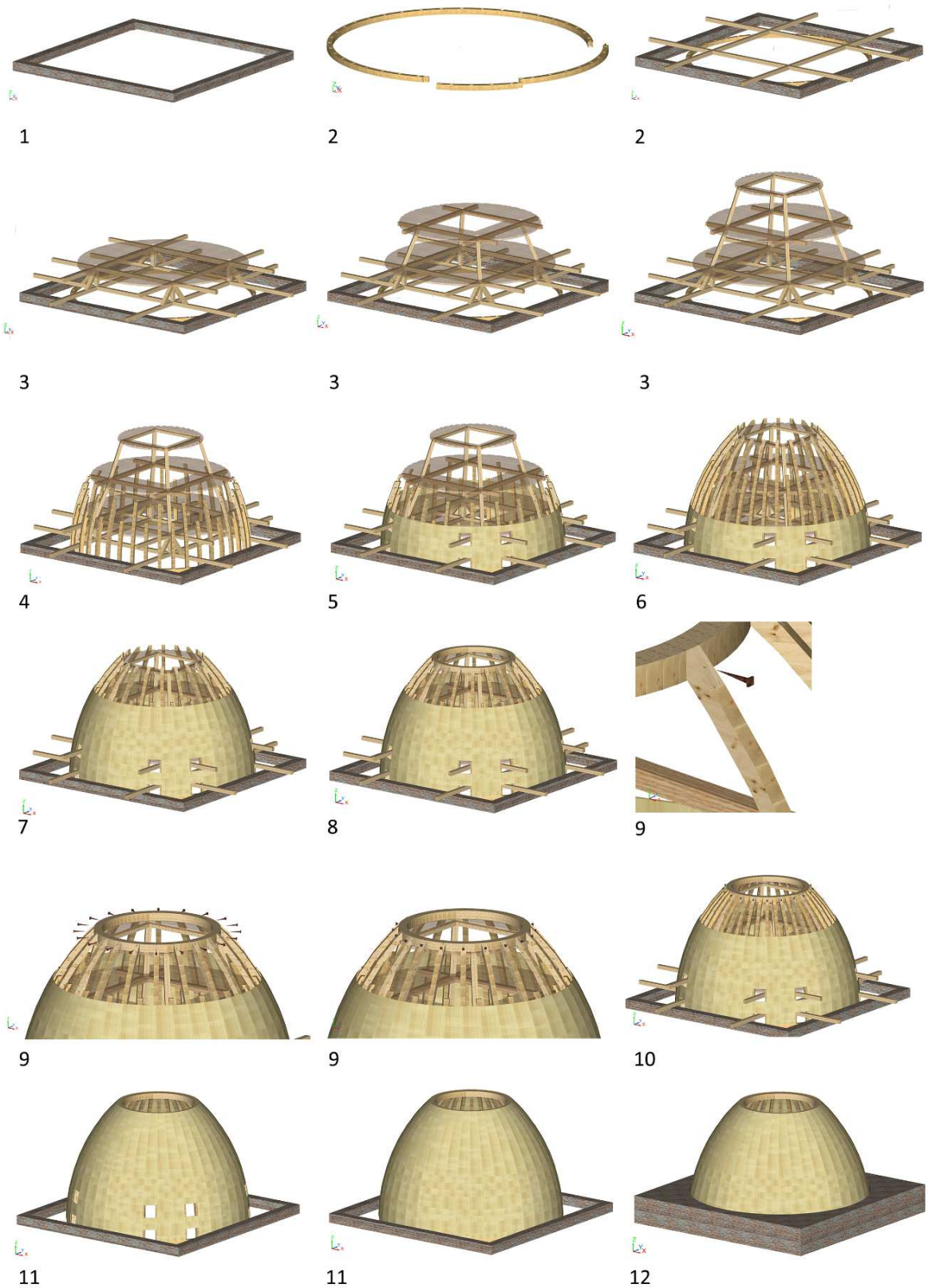

Figure 8-35 – Hp. 3. of construction of the dome

Chapter 9 NUMERICAL SIMULATIONS OF THE CASE STUDY

9.1 Introduction

In the present chapter, the study of the numerical model of the case study is presented. According to the dome's description in the Chapter 8, the geometry of the dome was reproduced in a structural model. The modelling is performed with the software of structural analysis RFEM Dlubal.

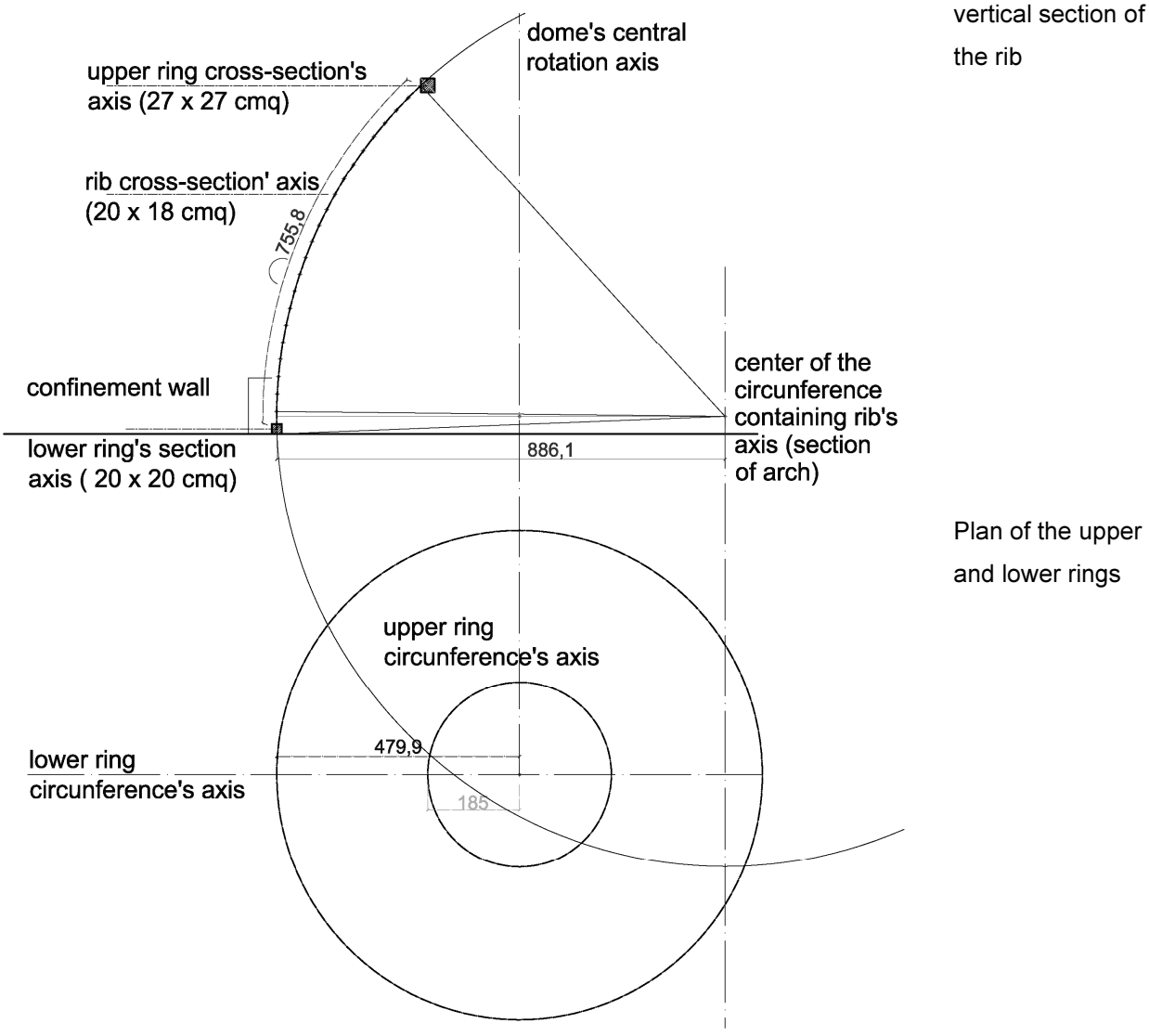

Figure 9-1 – Homogenization of the irregular geometry of the beam.

9.2 Structural model analysis considerations and design requirements

Geometry

The structural model's geometry is a simplification of the real geometry. The non-regular segmentation of the 2-pieces and 3-pieces main beams of the dome is regularized with a homogeneous distribution of the ones. The simplified geometry is represented in the Figure 9-1, while the CAD reconstruction of the real structure is represented in the Figures 8-28 to Figure 8-31.

Material properties

In the model, the dome's ribs, upper and lower rings, are considered as if they were a "new" structure. Therefore, the mechanical characteristics chosen for the wooden ribs and rings are the one in the Table 9-1. On the other side, for the planking's wood is chosen a reduced amount of Young's modulus (E) in order to simulate a decrease of mechanical capability of the nail-board-nail system. The process of selection of the planking's material properties and stiffness is explained in the Annex E. The properties chosen for the boards' wood are contained in Table 9-2.

Table 9-1 – *Cedar - Hardwood Timber D35* mechanical properties

Cedar - Hardwood Timber			
Young's Modulus	E	8000	[N/mm^2]
Shear Modulus	G	2758	[N/mm^2]
Poisson's Ratio	v	0.45	
Specific weight	γ	4.5	[kN/m^3]
Coefficient of thermal expansion	α	5.00E-06	[1/°C]
Partial safety factor	γ_M	1.30E+00	
Isotropic linear elastic material			

Table 9-2 – Cedar (planking) reduced mechanical properties

Cedar (planking)			
Young's Modulus	E	400	[N/mm^2]
Shear Modulus	G	137.931	[N/mm^2]
Poisson's Ratio	v	0.45	
Specific weight	γ	4.5	[kN/m^3]
Coefficient of thermal expansion	α	5.00E-06	[1/°C]
Partial safety factor	γ_M	1.30E+00	
Isotropic linear elastic material			

Static system

In the Figure 9-2 is represented the two-dimensional static model. The *Jupiter joints* are represented through hinges provided with *rotational springs*, to which values of rotational stiffness $k\phi x$, $k\phi y$, $k\phi z$ are assigned. More, the structure is provided with *horizontal springs*, structural modelling device to represent the planking. The spring elements have different stiffness levels, managed with correspondent *member end releases*, represented in the Table 9-3. The value of the rotational stiffness k for the hinge (*Jupiter Joint*) and of the planking are unknown. In order to assign the proper stiffness to the elements in the system, the calculation of the load-bearing behaviour of the dome is conducted through a step-by-step process contained in the ANNEX F.

Strength and stiffness parameters

The stiffness properties for the *Jupiter joint*, the planking, and other wood-wood connections calibrated in the ANNEX F are reported in the Table 9-3. In the Table 9-4 the geometry of the elements is described. A more detailed description of the stiffness and geometric characteristics of the structural elements follows.

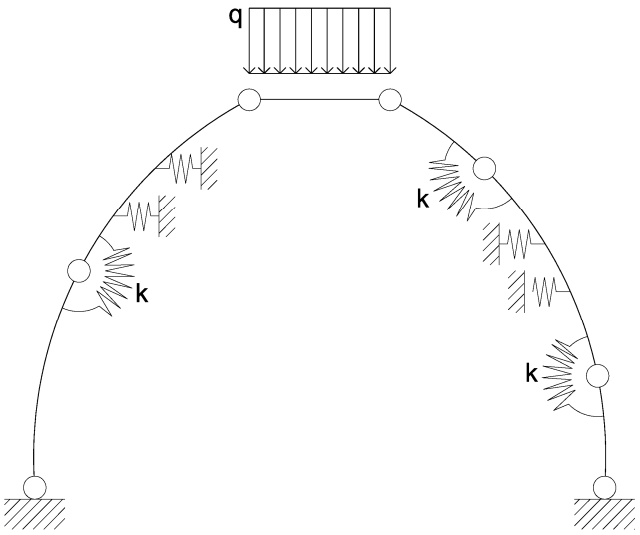

Figure 9-2 - Static system assigned to the structure (2D scheme)

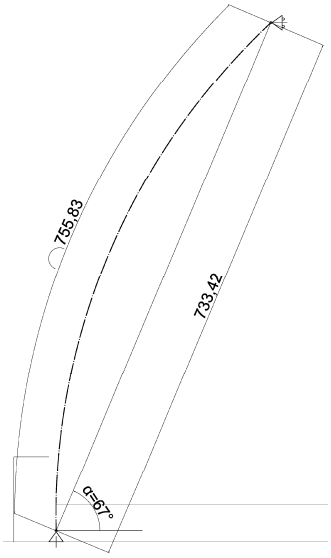

Figure 9-3 - Scheme of the rib

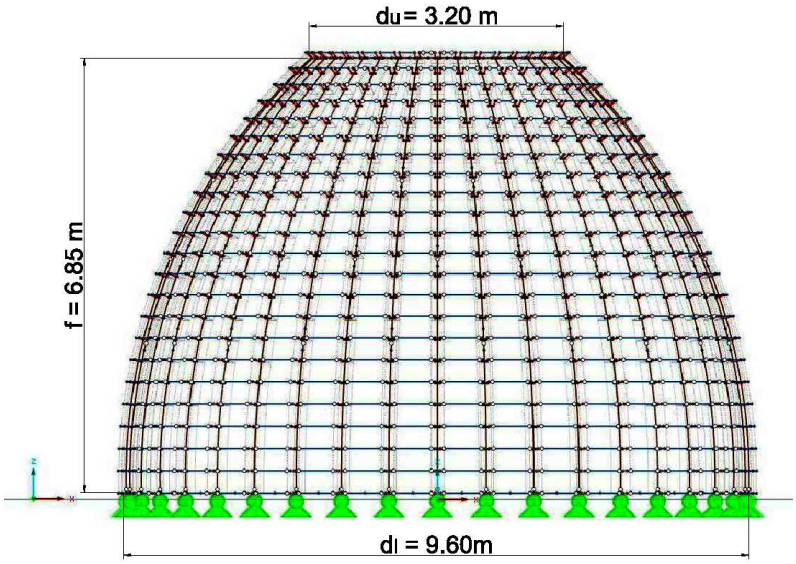

Figure 9-4 - Static system assigned to the structure (3D scheme)

Table 9-3 – End-releases of the elements

	PLANKING			rib with upper ring	rib with lower ring	rib inner connection	upper - lower ring
	n° 10 (start)	n°5 (end)	Eboards	n° 13	n° 6	n° 11	n° 9
ux	0	0	k6 = 400 MPa (see Table 9-2)	0	0	0	0
uy	0	0		0	0	0	0
uz	0	0		0	0	0	0
kϕx [kN m / rad]	0	∞		0	0	0	∞
kϕy [kN m / rad]	0	0		0	0	100	∞
kϕz [kN m / rad]	13	13		0	10	0	∞

Table 9-4 – Geometry of the elements

	material		Cross-section		
	definition	**E** [Mpa]	**definition**	**dimention** [cm]	**element length** [cm]
PLANKING	Wood CEDRO (Table 9-1)	E_{boards}	T - rectangle	34.8 x 3	(variable)
NAILS (planking)	-	-	dummy rigid	5 + 10	15.5
UPPER RING	Hardwood D35 CEDRO (Table 9-1)	8000	T - rectangle	27 x 27	185 radius
LOWER RING	Hardwood D35 CEDRO (Table 9-1)	8000	T - rectangle	20 x 20	479.9 radius
RIB	Hardwood D35 CEDRO (Table 9-1)	8000	T - rectangle	18 x 20	755.83
INNER RING	-	-	-	-	-

Rib

The main ribs are 40. Each rib is an arch of circumference which total length is l = 755.83 cm; the circumference's radius is 886.1 cm. In the *xz* plane, the ribs cover an angle of aprox. 47°. The center of the circumference is not on the dome's central rotation axis (Figure 9-1). Referring to the Figure 9-6, each rib is divided into 11 segments (beams), for a total number of 23 nodes and 22 beams (start, middle, and end node of each segment). The rib's cross-section is *T rectangle 18 x 20 cm* in Cedar wood. The model simplifies the real structure with a regular distribution of the joints in the ribs; starting from rib 1, there is alternation of *two-pieces* and *3-pieces* ribs. The *two-pieces-ribs* are 22. The hinge that represent the *joint* is assigned in correspondence with the node 12. The (start) far end of the beam 11 is released with the m*ember end release n° 11*, as described in the Table 9-4. The *three-pieces-ribs* are 22. The hinges that represent the *Jupiter joint* is assigned in correspondence with node 8 and 16. The (start) far end of the beam 8 and 16 are released with the m*ember end release n° 11*, as described in the Table 9-3.

Lower ring

The lower ring has 479.9 cm of radius, divided into 40 curved beams that link the node n° 23 of the main ribs. The cross-section is *T rectangle 20 x 20 cm* in Cedar wood. The ring is divided in 10 curved wooden pieces, by groups of four beams each. The connection between each group is the one assigned for the *member end release n° 9*.

Upper ring

In the structural model only the upper ring (1) is modelled. The left rings are calculated, together with the clerestory, as external uniform applied load (see paragraph 9.3, LC1 DEAD LOADS). The upper ring has radius of 185 cm, and is formed by 40 curved beams. The cross-section is *T rectangle 27 x 27 cm* in Cedar wood. The ring is subdivided in 6 curved wooden pieces, by groups of 6 or 7 beams each. The connection between each group is the one assigned for the *member end release n° 9*.

Connection between the rib and the upper (1) ring

The connection of the upper ring (1) connection with the rib is not a carpentry connection but a metal-ring connected to the rib's head with a nail. The metallic chain is not considered in the model. The connection is a *dummy rigid* element that connect horizontally the rib's node n° 1 and the upper ring main axis. The m*ember end release n° 13* is assigned to the *dummy rigid* elements.

Connection between the rib and the lower ring

The rib are connected with the lower ring through mortise and tennon connection. The far end of the node n° 23 of the rib is connected with lower ring main axis; the *member end release n° 6* is assigned to it.

Planking

Cross-section *T rectangle 34.8 x 3 cm* in Cedar wood. The planking is represented by a system of beams connected in the outer part of ribs; each plank lays in a plane tangent to the axes of the beam. The planks are distributed along 23 circles, in correspondence with the 23 rib's nodes. Each of the beam has a different rotation respect to the horizontal plane. A more precise description is in the Table 9-5. The angle calculated in the Table 9-5 was found by 90°- {[46,66° (total angle from node 1 to 22) /21 parts] x n} 0,63° (angle left from 22O22 to horizontal).

The connection between the beams (planking) and the rib's nodes is through *dummy rigid L-shaped* elements; these elements shift 4 cm horizontally and 11.5 cm parallel to the correspondent starting rib's node. For the planking beams, the *member end release n° 10* is assigned to far end A (start), while the *member end release n° 5* is assigned *to* far end B (end).

Inner parallels

The inner parallels are not modelled because of their low contribution to the stiffness of the structure.

Table 9-5 - rotation assigned to the planking elements

Knot correspondance nr.		Cross section number		Member rotation	
	Member type	start	end	Type	Angle
1	Beam	7	7	&Angle	43.97
2	Beam	7	7	&Angle	46.19
3	Beam	7	7	&Angle	48.41
4	Beam	7	7	&Angle	50.64
5	Beam	7	7	&Angle	52.86
6	Beam	7	7	&Angle	55.08
7	Beam	7	7	&Angle	57.30
8	Beam	7	7	&Angle	59.52
9	Beam	7	7	&Angle	61.75
10	Beam	7	7	&Angle	63.97
11	Beam	7	7	&Angle	66.19
12	Beam	7	7	&Angle	68.41
13	Beam	7	7	&Angle	70.63
14	Beam	7	7	&Angle	72.85
15	Beam	7	7	&Angle	75.08
16	Beam	7	7	&Angle	77.30
17	Beam	7	7	&Angle	79.52
18	Beam	7	7	&Angle	81.74
19	Beam	7	7	&Angle	83.96
20	Beam	7	7	&Angle	86.19
21	Beam	7	7	&Angle	88.41
22	Beam	7	7	&Angle	90.00
23	Beam	7	7	&Angle	90.00

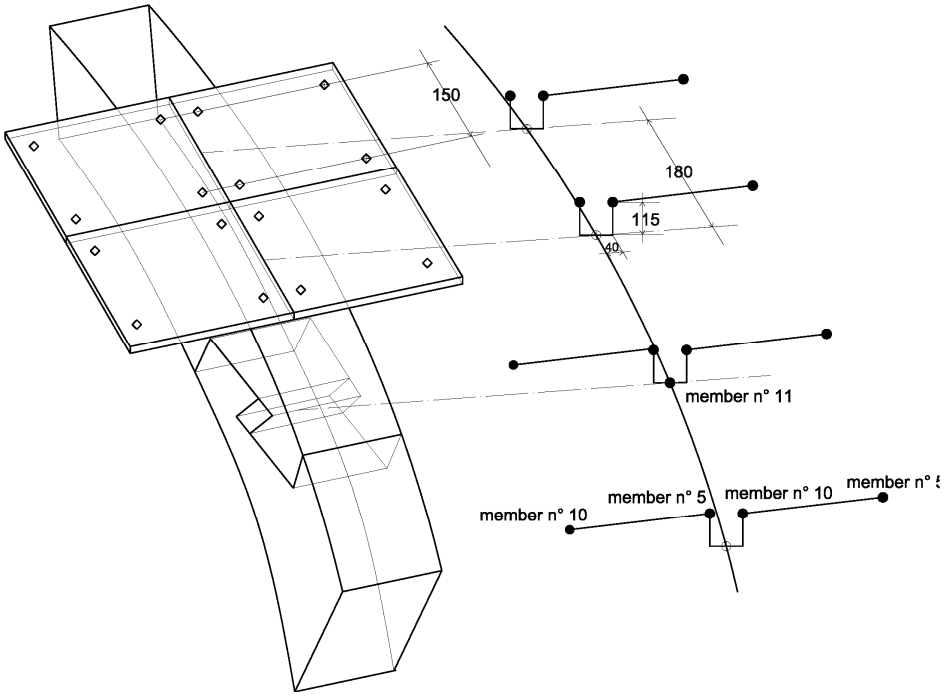

Figure 9-5 – Scheme of the ribs + planking: *Jupiter joint* & nailed connection

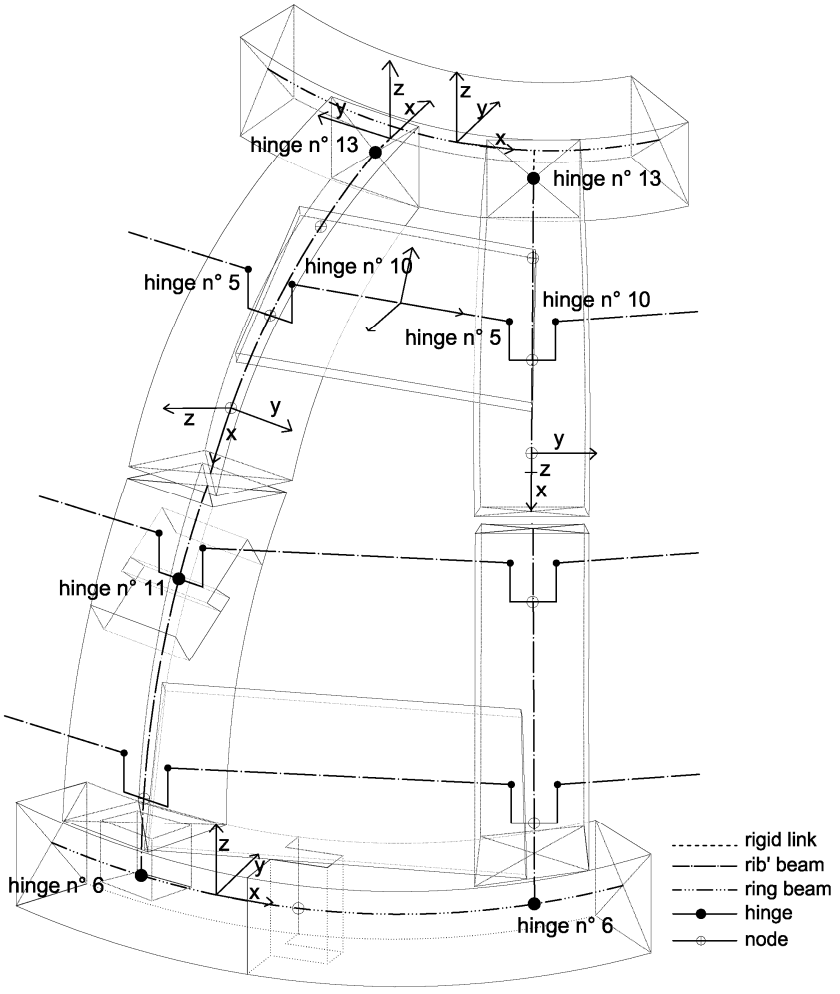

Figure 9-7 - Resume of the assigned end releases

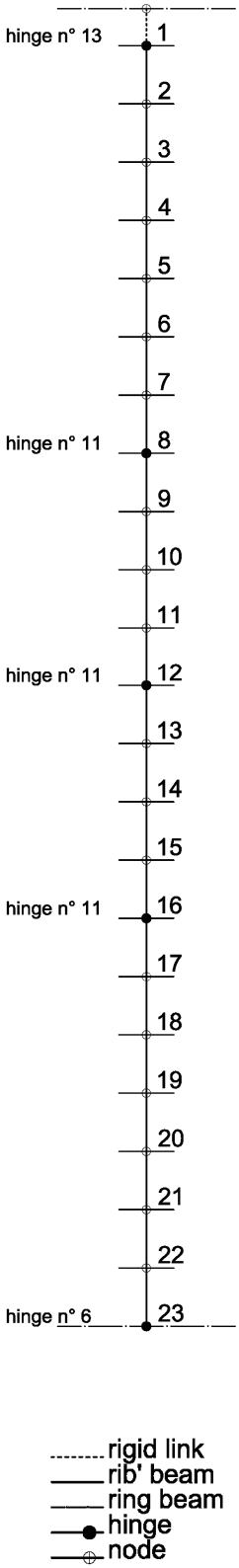

Figure 9-6 – scheme of the ribs with the upper and lower connection to the upper and lower ring.

9.3 Load cases and load combinations

The calculated load cases (LC) are listed in the Table 9-6, while the Table 9-7 contains the load combinations (CO). Both for the deformation analysis and the stress analysis, the results are expressed in characteristics values f_k .

Table 9-6 – Load cases.

LC1	DEAD loads	Self weight + clerestory + cement cover + lead cover weight
LC2	Wind +x	WIND loads wind velocity v_{ref} = 250 km/h level IV Saffir – Simpson Hurrican scale.
LC3	Imperfection 1	Initial sinusoidal curvature between the nodes of the structure corresponding to a maximum eccentricity *e* of the beam's axis. (EN 1995-1-1:2010 – Section 5.4.4).
LC4	Imperfection 0	Deformation which is found by applying an angle φ of inclination (EN 1995-1-1:2010 – Section 5.4.4).

Table 9-7 – Combinations used for the deformation analysis (characteristics values).

CO1	Self weight + Imperfection 0	1.00 LC1 + 1.00 LC4
CO2	Self weight + Imperfection 1	1.00 LC1 + 1.00 LC3
CO3	Self weight + Imperfection 0 + Imperfection 1	1.00 LC1 + 1.00 LC3 + 1.00 LC4
CO4	Self weight + Wind	1.00 LC1 + 1.00 LC2
CO5	Self weight + Imperfection 0 + Wind	1.00 LC1 + 1.00 LC2 + 1.00 LC4
CO6	Self weight + Imperfection 1 + Wind	1.00 LC1 + 1.00 LC2 + 1.00 LC3
CO7	Self weight + Imperfection 0 + Imperfection 1 + Wind	1.00 LC1 + 1.00 LC2 + 1.00 LC3 + 1.00 LC4

Table 9-8 – Combinations used for the stress analysis (design values).

CO8	Self weight + Imperfection 0	1.35 LC1 + 1.00 LC4
CO9	Self weight + Imperfection 1	1.35 LC1 + 1.00 LC3
CO10	Self weight + Imperfection 0 + Imperfection 1	1.35 LC1 + 1.00 LC3 + 1.00 LC4
CO11	Self weight + Wind	1.35 LC1 + 1.50 LC2
CO12	Self weight + Imperfection 0 + Wind	1.35 LC1 + 1.50 LC2 + 1.00 LC4
CO13	Self weight + Imperfection 1 + Wind	1.35 LC1 + 1.50 LC2 + 1.00 LC3
CO14	Self weight + Imperfection 0 + Imperfection 1 + Wind	1.35 LC1 + 1.50 LC2 + 1.00 LC3 + 1.00 LC4

LC1 DEAD LOADS

CLERESTORY. The clerestory is applied as linear uniform distributed load in the direction global system, related to the true member length ZL of the upper ring members (b) as in 9-1.

$$q_{clerestory} = -1.5\,\frac{kN}{m} \qquad 9\text{-}1$$

In the Table 9-10 the amount of the single materials, specific loads and volumes is specified.

COVER. On the planking the load of the concrete and lead cover are applied. The weight per square meter on the planking is detailed in the Table 9-9. The load is uniformly applied on the planking elements (beam elements section *T-rectangle 34.8 x 3 cm² from* Table 9-4) in the direction global system, related to the true member length ZL of the members (a) and it is equal to:

$$q_{plank} = 1.36\,\frac{kN}{m^2} \cdot 0.348m = 0.473\,\frac{kN}{m} \qquad 9\text{-}2$$

Table 9-9 – Concrete + lead cover load

material	specific weight [kN/m³]	dimension			weight [kN/m²]
		s [m]	**l** [m]	**h** [m]	
Concrete	25	0.05	dome surface		1.25
Lead	113.4	0.01	dome surface		0.11
Total weight per square meter					**1.36**

Table 9-10 – Clerestory upper load

Clerestory weight:							
Material	**Specific weight [kN/m³]**	**object**	**number**	**Dimension [m]**			**Volume [m³]**
				S	**s**	**h**	
cedar	4,5	Ring	1	0,17	0,17	11,43	0,33
cedar	4,5	Ring	1	0,17	0,17	11,43	0,33
cedar	4,5	columns	8	0,16	0,16	3,05	0,62
cedar	4,5	horizontal pole	1	0,15	0,15	1,80	0,04
cedar	4,5	vertical pole	1	0,15	0,15	3,00	0,07
cedar	4,5	ribs	8	0,11	0,09	2,84	0,22
	TOTAL cedar VOLUME [m³]						1,62
	TOTAL cedar WEIGHT [kN]						7,28
glass	25	windows	8	1,50	3,20	0,00	0,08
	TOTAL glass VOLUME [m³]						0,08
	TOTAL glass WEIGHT [kN]						1,92
iron	78	windows frames	8	3,20	0,05	0,05	0,06
iron	78	cross	1	-	-	-	0,00
	TOTAL iron VOLUME [m³]						0,06
	TOTAL iron WEIGHT [kN]						4,99
lead	114	lead cover	1	0,001	16,20	1,00	0,02
	TOTAL lead VOLUME [m³]						0,02
	TOTAL lead WEIGHT [kN]						1,85
		total clerestory weight [kgf]					16,04
		total clerestory weight APROX [kN]					17,00

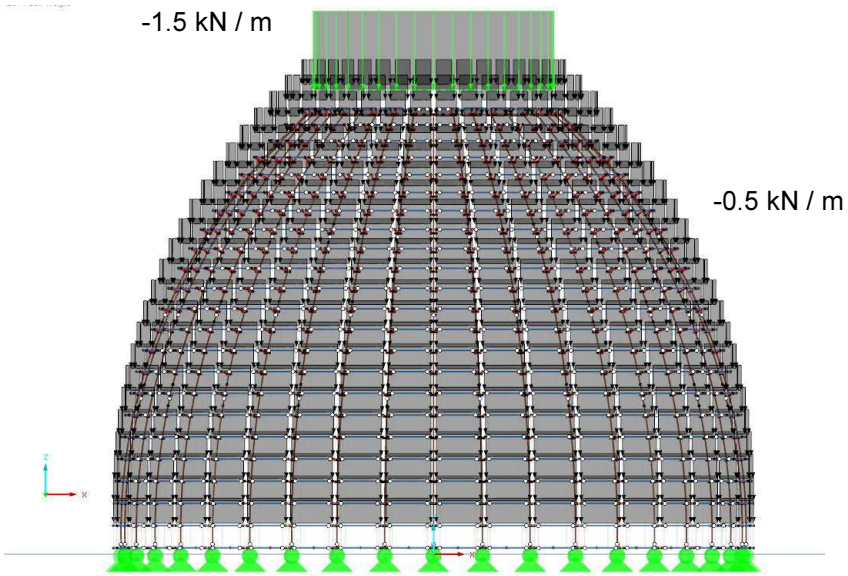

Figure 9-8 – LC1: Dead loads

LC2 WIND LOADS

The calculation of the wind pressure is according to the value of wind pressure IV on the Saffir – Simpson Hurricane scale (quantity given in the Cuban Standard). The calculation according to the Eurocode 1 for the LC2 has been adapted for such high values of wind reference pressure q_{ref} .

$$v_{ref} = 69.4 m/s \cong 250 km/h \quad \text{9-3}$$

$$q_{ref} = \frac{v_{ref}{}^2}{1600} = \frac{69.4^2}{1600} = 3.00 kN/m^2 \quad \text{9-4}$$

$h < 25m$ → Simplification with constant pressure coefficient q_{ref} along the height of the structure.

According to the EC0 definition, since the hurricane is an hazard, the *LC2 wind loads* is considered an accidental action (*A*) with short duration.

Calculation of the wind pressure according two possibilities:

1. DIN EN 1991 – 1 – 4: 2010 - 12 Section 7.2.8. Gekrümmte Dächer und Kuppeln
2. DIN EN 1991 – 1 – 4: 2010 – 12 Section 7.9 Kreiszylinder

1. Calculation according to DIN EN 1991-1-4:2010-12. Section 7.2.8. *Gekrümmte Dächer und Kuppeln*.

By extrapolation the dimension ratio *f / dl* for the dome (Figure 9-4) is beyond the acceptable ratio for this case; therefore, the calculation will be performed according to 2.

$$c_p \approx 1.0 \quad \text{9-5}$$

2. Calculation of the wind pressure according to DIN EN 1991–1–4:2010–12. Section 7.9 *Kreiszylinder*.

(1) The pressure coefficient of the section depends on the Reynolds numbers *Re* defined in the eq. 9-6

$$\mathrm{Re} = \frac{b \cdot v(z_e)}{\nu} \quad \text{9-6}$$

Where $b = d_i$ (Figure 9-4)

For the upper diameter (d_u)

$$\mathrm{Re}_{du} = \frac{d_u \cdot v(z_e)}{\nu} = \frac{9.60 \cdot 69.4\, m/s}{15 \cdot 10^{-6}\, m^2/s} = 4.4 \cdot 10^7 \quad \text{9-7}$$

For the lower diameter (d_l)

$$\mathrm{Re}_{dl} = \frac{d_l \cdot v(z_e)}{\nu} = \frac{3.70 \cdot 69.4\, m/s}{15 \cdot 10^{-6}\, m^2/s} = 1.7 \cdot 10^7 \quad \text{9-8}$$

According to the diagram to the right in the Figure 9-9 the Reynold number is in the 10^7 area. The external pressure coefficient C_{p0} is given for various Reynolds numbers as a function of the sectors. The slenderness factor $\psi_{\lambda\alpha}$ is determined time by time in dependence of the sector (EC 1 Eq. 7.17).

Sector 1 (0°) 9-9

$$\psi_{\lambda,1} = 1.0$$

$$C_{p0} = 1.0$$

Sector 2 (90°) 9-10

$$\psi_{\lambda,2} = 1.0$$

$$C_{p0} = -1.5$$

Sector 3 (180°) 9-11

$\lambda = \frac{l}{b}$ or $\psi_{\lambda,3} = 70$

$\lambda = \frac{6.85}{9.60} = 0.70$ (lower $\psi_{\lambda,3,l}$)

$\lambda = \frac{6.85}{3.70} = 1.85$ (upper $\psi_{\lambda,3,l}$)

$\varphi = \frac{A}{Ac}$ (EC1, Figure 7.36)

$\Rightarrow \psi_{\lambda,3,l} = 0.6$

$C_{p0} = -0.8$

Referring to the Figure 9-10 for each sector the maximum value of C_{p0}, divided for sectors 1, 2, 3. Are extrapolated from the diagram on the right in the Figure 9-9.

Sector 1 – maximum value in correspondence with $\alpha = 0°$ 9-12

$C_{pe} = 1.0 \cdot 1.0 = 1.0$

$w_e = 1.0 \cdot 3.00 = 3.00\, kN/m^2$

Sector 2 – maximum value in correspondence with $\alpha = 0°$ 9-13

$C_{pe} = -0.8 \cdot 0.6 = -0.48$

$w_e = -0.48 \cdot 3.00 = 1.44\, kN/m^2$

Sector 3 – constant value 9-14

$C_{pe} = -1.5 \cdot 1.0 = -1.5$

$w_e = -1.5 \cdot 3.00 = -4.50\, kN/m^2$

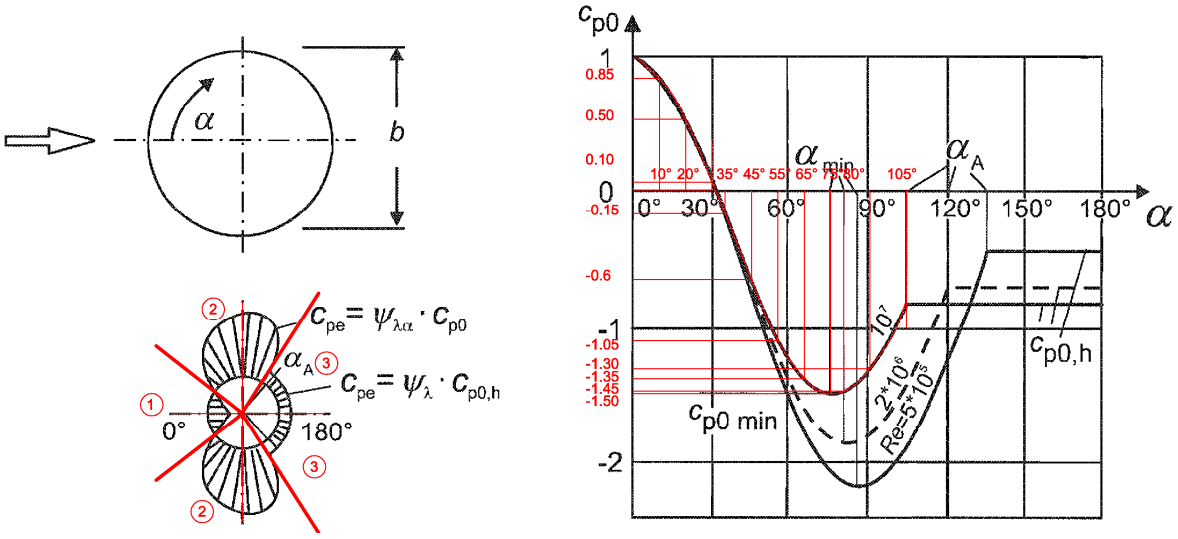

Figure 9-9 – Extrapolation of the intermediate values of $C_{p,0}$ from DIN EN 1991 – 1 – 4: 2010 – 12, Section 7.9

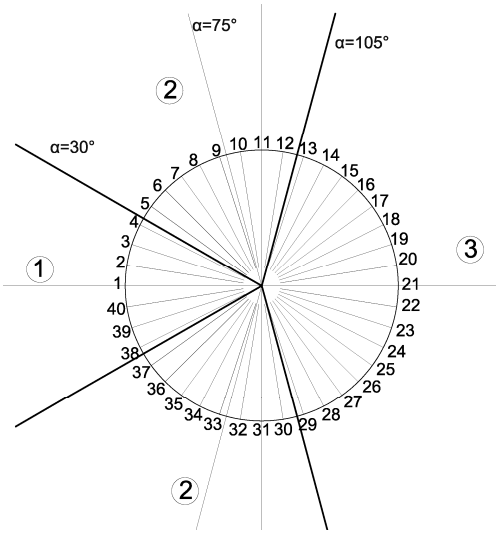

Figure 9-10 - Sections of the dome, according to (a).

Table 9-11 – Local value of the C_{p0} in the sections.

set of member	***α*** [°]	**C_{p0}**	**w_e** [kN/m²]	**$w_{e,low}$** [kN/mL]	**$w_{e,up}$** [kN/mL]	**b_{low}** [m]	**b_{up}** [m]
1	0	1.00	3.00	2.25	0.90	0.75	0.3
2	10	0.85	2.55	1.91	0.77	0.75	0.3
3	20	0.50	1.50	1.13	0.45	0.75	0.3
4	30	0.10	0.30	0.23	0.09	0.75	0.3
5	35	-0.15	-0.45	-0.34	-0.14	0.75	0.3
6	45	-0.60	-1.80	-1.35	-0.54	0.75	0.3
7	55	-1.05	-3.15	-2.36	-0.95	0.75	0.3
8	65	-1.30	-3.90	-2.93	-1.17	0.75	0.3
9	75	-1.50	-4.50	-3.38	-1.35	0.75	0.3
10	80	-1.45	-4.35	-3.26	-1.31	0.75	0.3
11	90	-1.35	-4.05	-3.04	-1.22	0.75	0.3
12	100	-1.00	-3.00	-2.25	-0.90	0.75	0.3
13	100-180	-0.80	1.44	1.08	0.43	0.75	0.30
14							
15							
16							
17							
18							
19							
20							

The Table 9-11 contains the intermediate linear values of the wind pressure to apply on each rib. The correspondent angle *α* for the beam is founded according to the dome's geometry represented in (b).

The wind pressure is applied as linear trapezoidal load on the beams (set of members) as represented in the Figure 9-12. The value of the wind pressure is variable along the length of the beam. The reference dimension for the lower bay of the rib is b_{low} and the reference upper bay size of the rib is b_{up}. The actions on the bottom part and upper part are respectively $w_{e,low}$ and $w_{e,up}$.

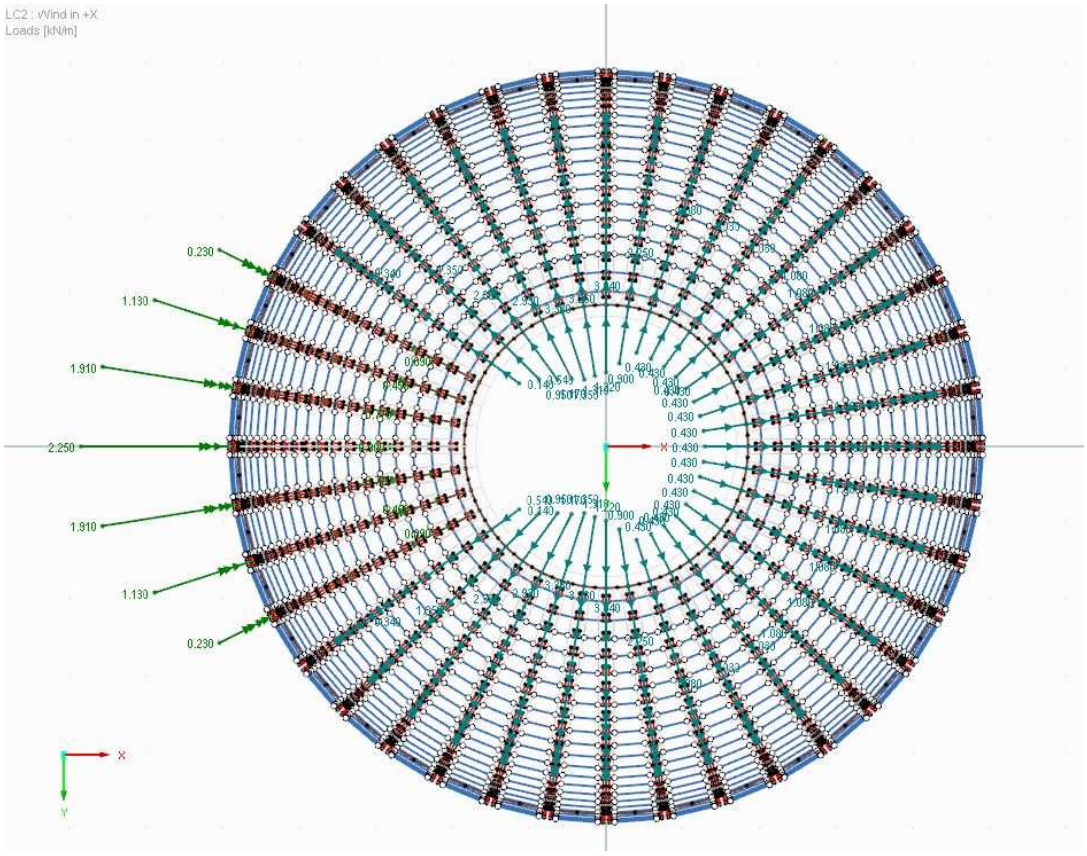

Figure 9-11 – wind loads +x. View from the z direction

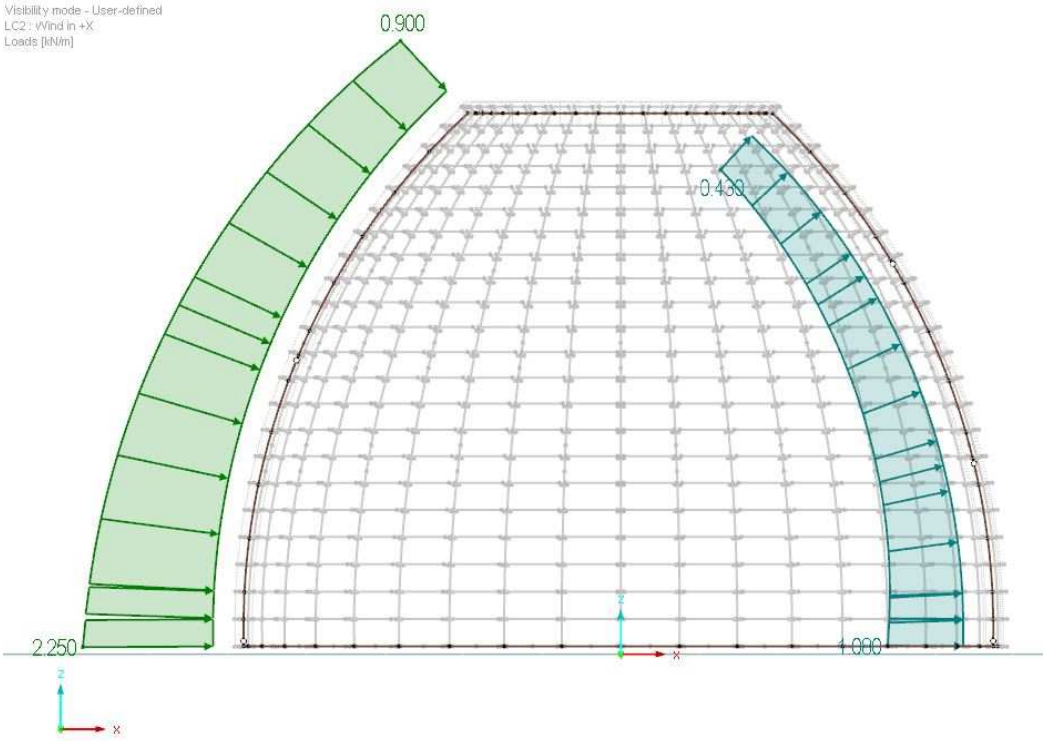

Figure 9-12 – Wind load +x. View from the y direction

9.3.1 Imperfections

The nature and entity of the imperfections has been already commented in the Chapter 3.6. The imperfection may rise for lack of evenness of the surfaces, cyclic loads along the centuries, or structural failures. The

EC 5 specifies the prescribed relevant geometric imperfections to be considered for common design cases. The prescription is regarding the wooden frame structure, but no specific rules are given for the joints. In the present work the imperfection assigned to the structural model are considered as in the EC5 section 5.4.4. The imperfections are assumed to correspond to an initial deformation which is found by applying an angle φ of inclination at the base of the ribs (member hinge n° 6), together with an initial sinusoidal curvature between the top (member hinge n° 13) and the bottom (member hinge n° 6) of the rib corresponding to a maximum eccentricity *e*.

Being an historical hint, the amount of the considered imperfection is increased of a further 20% on the safe side.

LC3 Imperfection 1

The imperfection 1 is considered as a bending of the central part of the main beams.

$e_{0,EC5} = l \cdot 0.0025$ (bending of the beam according to EC 5) 9-15

$e_0 = 0.0025 + 0.005 = 0.003 = 1/333$ (amount of pre-bending increased +20%) 9-16

$733.42 / 380 = 1.930cm = 19.3mm$ 9-17

With this purpose, the elements that compound the beam are grouped in set of members to assign the imperfection as in the eq. 9-17.

LC4 Imperfection 0

The imperfection 0 is applied in form of displacement of the upper part of the beam (set of members) of an amount equal to the one in the eq. 9-21.

$\varphi_0 = 0.005\sqrt{5/h}$ for $h > 5m$ 9-18

$\varphi_0 = 0.005\sqrt{5/6.85} = 4.27 \cdot 10^{-3} rad = 0.00427rad$ (rotation at the base of the rib, EC5) 9-19

$u_{top,EC5} = \frac{7334}{234} = 31.34mm$ (displacement at the top of the rib according to EC5) 9-20

$u_{top} = 31.34mm + 6.268 \cong 37mm$ (displacement at the top of the rib increased +20%) 9-21

The imperfection is applied through a rotational moment at the top of the dome.

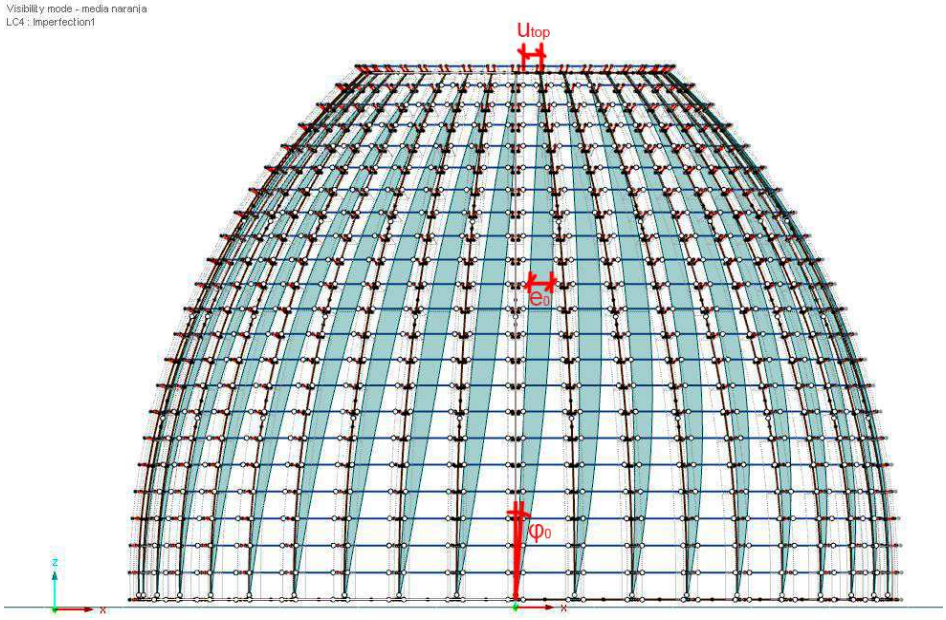

Figure 9-13 – imperfection 0 and imperfection 1

9.4 Structural analysis

For the comparison of the non-deformed with the deformed structure, some reference values have been chosen. The procedure for the deformation analysis is described in the 9.4.2.

The procedure followed for the stress analysis is described in the 9.4.1. The properties of the Cedar wood (*Cedrela sp.*) contained in the Table 8-3 are not classifiable in any of the strength classes described by the European codes; therefore, the stress analysis is considered the value of the wooden class D24 contained in the DIN EN 1912:2012-06. The timber contained in the mentioned wood class has poorer properties respect to the properties listed in the Table 8-3; therefore, the verification is done on the safe side.

Table 9-12 – Wooden properties of the Strength class D24 (Structural timber - strength classes UNI EN 338)

Density	ρ	450	[kg/m^3]
Characteristics strength for bending	$\boldsymbol{f_{m,k}}$	**24**	**[N/mm²]**
Characteristics strength for tension parellel	$f_{t,0,k}$	14	[N/mm²]
Characteristics strength for tension perpendicular	$f_{t,90,k}$	0.6	[N/mm²]
Characeristics strength for compression parallel	$\boldsymbol{f_{c,0,k}}$	**21**	**[N/mm²]**
Characteristics strength for compression perpendicular	$f_{c,90,k}$	7.8	[N/mm²]
shear	$f_{v,k}$	4	[N/mm²]

9.4.1 Stress analysis

The verifications of the most stressed cross section has been done as in the eq. 9-22 and eq. 9.23

$$\left(\frac{\sigma_{c,o,d}}{f_{c,0,d}}\right)^2 + \frac{\sigma_{m,y,d}}{f_{m,y,d}} + k_m \cdot \frac{\sigma_{m,z,d}}{f_{m,z,d}} \leq 1 \qquad 9\text{-}22$$

$$\left(\frac{\sigma_{c,o,d}}{f_{c,0,d}}\right)^2 + k_m \cdot \frac{\sigma_{m,y,d}}{f_{m,y,d}} + \frac{\sigma_{m,z,d}}{f_{m,z,d}} \leq 1 \qquad 9\text{-}23$$

Where the characteristic values are the one contained in the Table 9-11 and modified for different kind of loads in design values according to the Table 9-13. The stresses are considered as follows:

$$\sigma_{c,0,d} = \frac{N}{A} = \frac{N}{b \cdot h} \qquad 9\text{-}24$$

$$\sigma_{m,y,d} = \frac{My \cdot z}{I_y} = \frac{My \cdot 6}{b \cdot h^2} \qquad 9\text{-}25$$

$$\sigma_{m,z,d} = \frac{Mz \cdot y}{I_z} = \frac{Mz \cdot 6}{h \cdot b^2} \qquad 9\text{-}26$$

Table 9-13 – Modification factors and design values applied in the structural analysis

	D24							
	fc,0,k [N/mm²]	**fm,k** [N/mm²]	**γm**	**k**mod	**fc,0,d** [N/mm²]	**fm,y,d** [N/mm²]	**fm,z,d** [N/mm²]	**km**
Perma-nent loads	21	24	1.3	0.6	9.69	11.08	11.08	0.7
short-term loads (wind)	21	24	1.3	0.9	14.54	16.62	16.62	0.7

The level of stress σ is verified on the area of influence $A = b \cdot h$. The full cross section's verification considers $h = h_b$; while in the *Jupiter joint* is considered the half of the cross section's height $h = h_{eff} = h/2$ on the safe side.

9.4.2 Deformation analysis

The verification of the displacements in the beam has been performed with values that refers to some reference values in the "imperfect" structure as defined in the EC 5 section 5.4.4.

ROTATIONS:

The rotations at the base of the rib are compared with the value of imposed imperfection γ_0 from eq. 9-19.

DISPLACEMENTS:

The displacements at the top of the rib are compared with the value in the eq. 9-27.

$$\frac{u_{top}[mm]}{h_{dome}[mm]} = \frac{31}{6750} = 0.0046 \qquad 9\text{-}27$$

where

u_{top} from the eq. 9-20, displacement at the top of the beam;

h_{dome} height of the dome, linear quote.

9.4.3 Nails verification

For what concerns the load-carrying capacity of the nails that connect the boards with the ribs, the maximum value of normal force in the boards along the height is chosen according to the eq. 9-28.

$$N_{boards,\max} = \begin{cases} \left|N_{\max,c,d}\right| \\ \left|N_{\max,t,d}\right| \end{cases} \qquad 9\text{-}28$$

$$N_{\max,d} = \left|N_{board,\max}\right| / 2 \quad \text{(Normal force on the single nail)} \qquad 9\text{-}29$$

The characteristic load-carrying capacity for nails in single shear (Eurocode 5 – Section 8.2.2) is:

$$F_{v,Rk} = 1.15 \cdot \sqrt{\frac{2\cdot\beta}{1+\beta}} \cdot \sqrt{2 \cdot M_{y,Rk} \cdot f_{h,1,k} \cdot d} = 1.15 \cdot 1 \cdot \sqrt{2 \cdot 17729 \cdot 22.76 \cdot 5} = 2.3kN \qquad 9\text{-}30$$

Where

$$\beta = \frac{f_{h,1,k}}{f_{h,2,k}} = 1$$

$$d = 5mm$$

$$f_{h,i,k} = 0.082 \cdot \rho_k \cdot d^{-0.3} = 0.082 \cdot 450 \cdot 5^{-0.3} = 22.76 \frac{N}{mm^2} \qquad 9\text{-}31$$

$$M_{y,Rk} = 0.45 \cdot f_u \cdot d^{2.6} = 0.45 \cdot 600 \cdot 5^{2.6} = 17729N \qquad 9\text{-}32$$

The design values for the verification are considered as follows:

$$F_{v,d,p} = F_{v,Rk} \cdot \frac{K_{\mathrm{mod},p}}{\gamma_m} = \frac{2.3}{1.3} \cdot 0.6 = 1.06kN \quad \text{(for permanent load combinations)} \qquad 9\text{-}33$$

$$F_{v,d,s} = F_{v,Rk} \cdot \frac{K_{\mathrm{mod},s}}{\gamma_m} = \frac{2.3}{1.3} \cdot 0.9 = 1.59kN \quad \text{(for short-term load combinations)} \qquad 9\text{-}34$$

where

$K_{\mathrm{mod},p} = 0.6$ (for permanent load combinations)

$K_{\mathrm{mod},s} = 0.9$ (for short-term load combinations)

For the final verification, it done according to the following eq. 9-35.

$$N_{\max,d} < F_{v,d} \qquad 9\text{-}35$$

9.5 Calculations

The calculations are divided in three parts. The first one is concerning the calibration of the stiffness properties of the *Jupiter joint* and the structure (reported in the Annex F), the second part concerns the calculation of the perfect structure, than, third, the calculation of the imperfect structure.

The results of the structural analysis simulation are contained in the Table 9-14. The results are divided in global and local stresses/deformations in the *Jupiter joint* at the two-pieces rib (2p) and the three-pieces rib (3p-1, upper joint, 3p-2, lower joint). The results are expressed in service limit state (SLS) with characteristic values for the deformation analysis and in ultimate limit states (ULS) with design values for the stress analysis.

9.5.1 Perfect structure

The perfect structure is the one calculated in the loading cases LC1, CO15 (dead loads) and CO4, CO11 (dead loads and wind load). The printouts in the next pages refers to the *perfect structure* and represent the global deformations *u* in the structure (Figure 9-14), local deformations in direction u_z (Figure 9-15), normal force N (Figure 9-16) and moment My (Figure 9-17).

Table 9-14 – Elaboration of the structural analysis' results

PERFECT STRUCTURE

		Assigned stiffness values				Results														
						deformations SLS										internal resultant forces ULS				
			jupiter joint			displacements							rotation at the base			Moment			Normal force	members
						global		global, top of the rib			local in *jupiter joint*			local, base of the rib						
		E_{boards} [MPa]	$k_{\phi,x}$ [kN·m/rad]	$k_{\phi,y}$ [kN·m/rad]	$k_{\phi,z}$ [kN·m/rad]	u_{max} [mm]	$u_{top,max}$ [mm]	$u_{top,x,max}$ [mm]	$u_{top,y,max}$ [mm]	$u_{top,z,max}$ [mm]	$u_{x,max}$ [mm]	$u_{y,max}$ [mm]	$u_{z,max}$ [mm]	$\gamma_{x,max}$ [mrad]	$\gamma_{y,max}$ [mrad]	$\gamma_{z,max}$ [mrad]	$M_{T,max,d}$ [kN·m]	$M_{y,max,d}$ [kN·m]	$M_{z,max,d}$ [kN·m]	$N_{max,d}$ [kN]	
dead loads	LC1-CO15	400.00	0.00	100.00	0.00	1.28	0.53	0.19	0.00	**-0.49**	0.34	0.00	-0.98	0.00	**0.79**	0.00	0.00	0.16	0.00	-3.77	3p-1 (m. 3298)
											0.27	0.00	1.25				0.00	-0.20	0.00	-7.16	3p-2 (m. 2793)
											0.22	0.00	0.09	0.00	0.49	0.00	0.00	-0.03	0.00	-5.49	2p (m. 1086)
																	0.00	-0.50	0.00	-9.57	c-s (m. 1082)

		Assigned stiffness values				Results														
						deformations SLS										internal resultant forces ULS				
			jupiter joint			displacements							rotation at the base			Moment			Normal force	members
						global		global, top of the rib			local in *jupiter joint*			local, base of the rib						
		E_{boards} [MPa]	$k_{\phi,x}$ [kN·m/rad]	$k_{\phi,y}$ [kN·m/rad]	$k_{\phi,z}$ [kN·m/rad]	u_{max} [mm]	$u_{top,max}$ [mm]	$u_{top,x,max}$ [mm]	$u_{top,y,max}$ [mm]	$u_{top,z,max}$ [mm]	$u_{x,max}$ [mm]	$u_{y,max}$ [mm]	$u_{z,max}$ [mm]	$\gamma_{x,max}$ [mrad]	$\gamma_{y,max}$ [mrad]	$\gamma_{z,max}$ [mrad]	$M_{T,max,d}$ [kN·m]	$M_{y,max,d}$ [kN·m]	$M_{z,max,d}$ [kN·m]	$N_{max,d}$ [kN]	
dead loads wind	CO4-CO11	400.00	0.00	100.00	0.00	107.07	95.15	-59.98	**81.21**	-76.02	20.00	9.10	57.15	**-34.48**	0.72	0.60	0.03	-0.22	-0.13	-5.84	3p-1 (m. 2798)
											5.36	4.81	35.47				0.02	-0.71	-0.09	-8.52	3p-2 (m. 2793)
											-24.63	-0.05	-104.66	0.04	**-32.83**	0.00	0.00	3.60	0.00	-28.87	2p (m. 1086)
																	0.00	3.79	0.00	-28.45	c-s (m. 1085)

IMPERFECT STRUCTURE

		Assigned stiffness values				Results														
						deformations SLS										internal resultant forces ULS				
			jupiter joint			displacements							rotation			Moment			Normal force	members
						global		global, top of the rib			local in *jupiter joint*			local, base of the rib						
		E_{boards} [MPa]	$k_{\phi,x}$ [kN·m/rad]	$k_{\phi,y}$ [kN·m/rad]	$k_{\phi,z}$ [kN·m/rad]	u_{max} [mm]	$u_{top,max}$ [mm]	$u_{top,x,max}$ [mm]	$u_{top,y,max}$ [mm]	$u_{top,z,max}$ [mm]	$u_{x,max}$ [mm]	$u_{y,max}$ [mm]	$u_{z,max}$ [mm]	$\gamma_{x,max}$ [mrad]	$\gamma_{y,max}$ [mrad]	$\gamma_{z,max}$ [mrad]	$M_{T,max,d}$ [kN·m]	$M_{y,max,d}$ [kN·m]	$M_{z,max,d}$ [kN·m]	$N_{max,d}$ [kN]	
dead loads imp 0	CO1-CO8	400.00	0.00	100.00	0.00	36.43	36.40	0.25	**-36.39**	-0.62	0.43	-30.69	-1.16	-1.14	0.99	6.93	-0.11	0.14	0.24	-3.77	3p-1 (m. 2798)
											0.34	-16.54	1.52				-0.09	-0.20	0.21	-7.16	3p-2 (m. 2793)
											0.30	-24.65	0.12	-1.20	0.66	6.95	-0.10	-0.03	0.21	-5.48	2p (m. 1086)
																	-0.01	-0.50	0.00	-9.56	c-s (m.1082)
dead loads imp 1	CO2-CO9	400.00	0.00	100.00	0.00	1.56	0.47	0.25	-0.24	**-0.62**	0.43	-0.22	-1.07	-1.38	0.99	-0.05	-0.01	0.14	-0.01	-3.77	3p-1 (m. 2798)
											0.34	-0.14	1.52				-0.03	-0.20	0.00	-7.16	3p-2 (m. 2793)
											0.30	-0.27	0.12	-1.36	0.66	-0.05	-0.03	-0.03	0.00	-5.49	2p (m. 1086)
																	-0.03	-0.50	0.00	9.57	c-s (m. 1082)
dead loads imp 0 imp 1	CO3-CO10	400.00	0.00	100.00	0.00	36.68	36.60	0.25	**-36.60**	-6.23	0.43	-30.89	-1.16	-2.52	0.99	6.88	-0.12	0.14	0.23	-3.76	3p-1 (m. 2798)
											0.34	-16.67	1.52				-0.12	-0.20	0.21	-7.15	3p-2 (m. 2793)
											0.30	-24.90	0.13	-2.57	0.62	6.89	-0.12	-0.03	0.21	-5.48	2p (m. 1086)
																	-0.03	-0.50	-0.26	9.56	c-s (m. 1082)

IMPERFECT + wind

dead loads imp 0 wind	CO5-CO12	400.00	0.00	100.00	0.00	115.74	117.59	-59.97	**-116.47**	-76.00	20.03	-20.09	57.21	1.37	15.84	4.51	-0.06	-0.22	0.11	-5.94	3p-1 (m. 2798)
											5.37	-11.01	35.52				-0.06	-0.71	0.10	-8.65	3p-2 (m. 2793)
											-24.63	-23.51	-104.65	-1.38	-32.83	6.56	-0.11	3.59	0.20	-27.87	2p (m. 1086)
																	0.08	3.73	-0.16	-28.49	c-s (m. 1085)
dead loads imp 1 wind	CO6-CO13	400.00	0.00	100.00	0.00	107.08	95.15	-59.98	**-81.46**	-76.20	20.01	8.88	57.16	-1.67	15.94	-2.15	0.02	-0.22	-0.14	-5.84	3p-1 (m. 2798)
											5.36	4.64	35.48				-0.02	-0.71	-0.09	-8.66	3p-2 (m. 2793)
											-24.63	-0.65	-104.66	-3.02	-32.83	0.06	-0.07	3.60	0.02	-27.86	2p (m. 1086)
																	0.02	3.79	-0.21	-28.35	c-s (m. 1085)
dead loads imp 0+imp 1 wind	CO7-CO14	400.00	0.00	100.00	0.00	115.94	116.72	-59.97	**-116.72**	76.01	20.03	-20.70	57.21	-2.94	15.95	4.46	-0.10	-0.22	0.10	-5.85	3p-1 (m. 2798)
											5.37	-11.17	35.52				-0.10	-0.72	0.10	-8.66	3p-2 (m. 2793)
											-24.63	-24.14	-104.64	-4.40	-32.83	6.62	-0.17	3.59	0.27	-27.85	2p (m. 1086)
																	0.10	3.79	-0.67	-28.48	c-s (m. 1082)

DEAD LOADS (LC1 and CO15)

According to the Table 9-14 in the LC1 rotations and displacement in the structure are very low, and smaller than the reference values respectively contained in eq. 9-19 and eq. 9-27.

The Table 9-15 contains the calculation of the stress levels for both the *Jupiter joint* and the most stressed cross section that are generally very low and occupy as maximum the 6% of the load-capability (verification 1); therefore, the LC1 is verified.

Table 9-15 – Results of the stresses in the CO15

		PERFECT STRUCTURE (permanent load)																
		Results				Analysis												members
		Moment			Normal force	geometry		max. stresses in the cross section			verification 1			verification 2				
		$\|M_{T,max,d}\|$ [N·mm]	$\|M_{y,max,d}\|$ [N·mm]	$\|M_{z,max,d}\|$ [N·mm]	$\|N_{max,d}\|$ [N]	b [mm]	h [mm]	$\sigma_{c,0,d}$ [N/mm²]	$\sigma_{m,y,d}$ [N/mm²]	$\sigma_{m,z,d}$ [N/mm²]							
dead loads	CO15	0	159300	0	3768.9	180	100	0.21	0.53	0.00	0.05	≤	1	0.03	≤	1	3p-1
		0	201400	0	7157.1	180	100	0.40	0.67	0.00	0.06	≤	1	0.04	≤	1	3p-2
		0	28100	0	5486	180	100	0.30	0.09	0.00	0.01	≤	1	0.01	≤	1	2p
		0	504200	0	9565.6	180	200	0.27	0.42	0.00	0.04	≤	1	0.03	≤	1	c-s

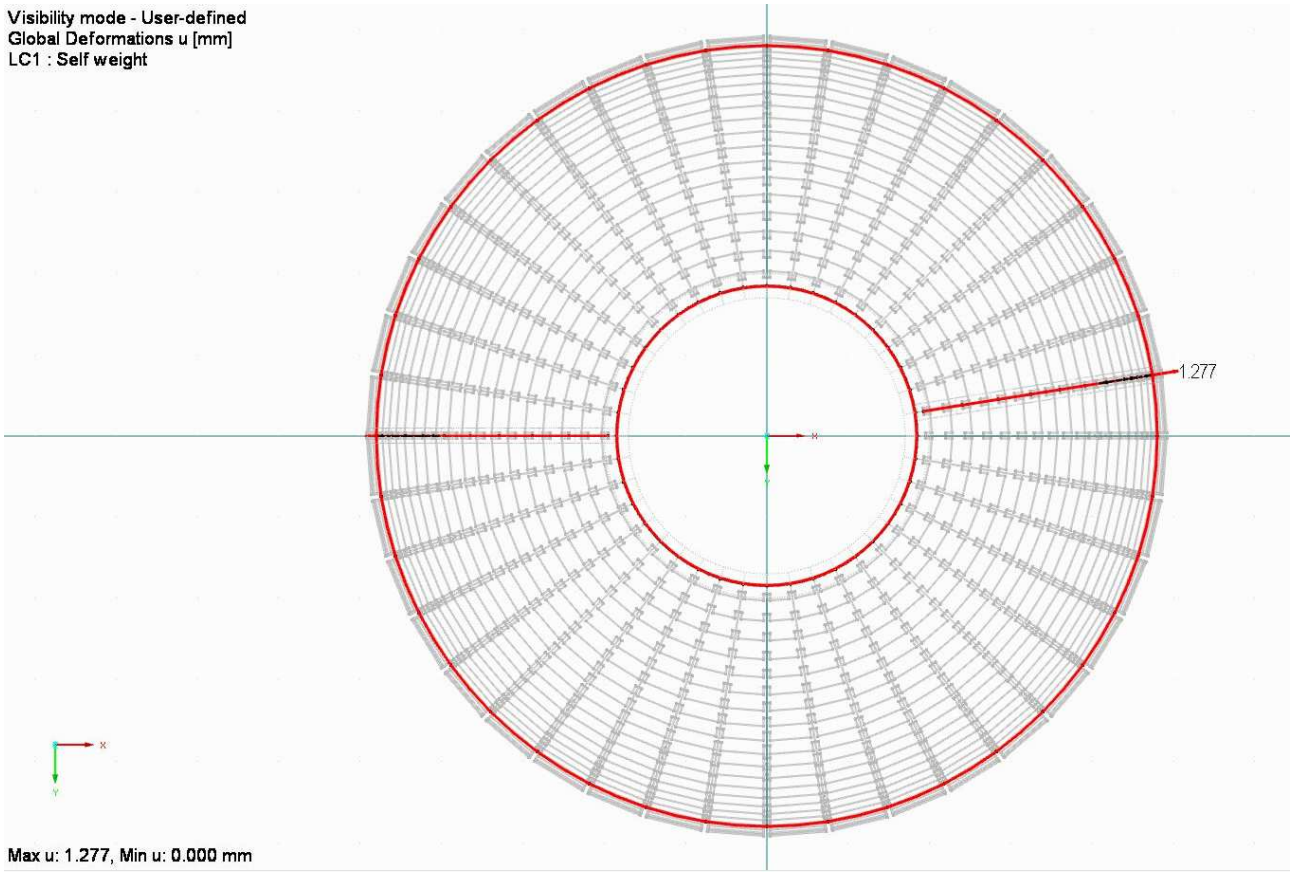

Figure 9-14 – 1.00 · LC1.
Global deformations *u* [mm] (top)

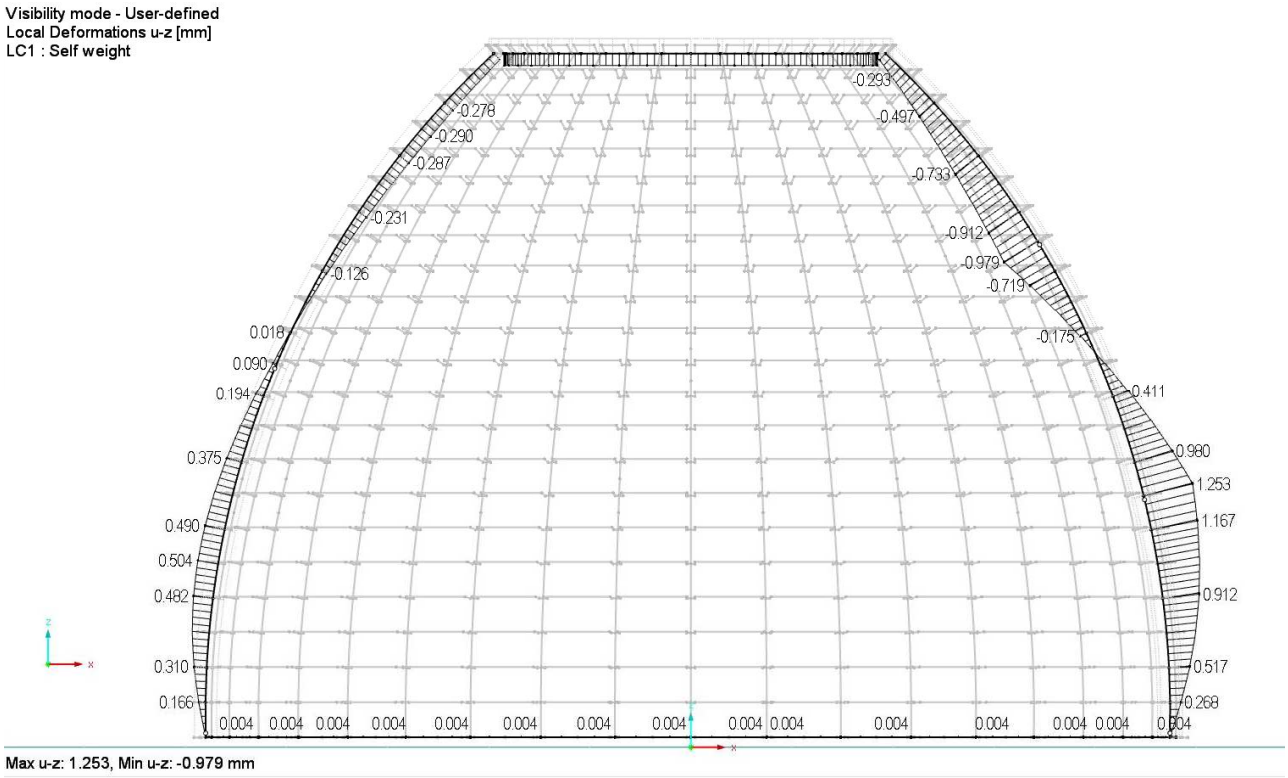

Figure 9-15 – 1.00 · LC1.

Local deformations u_z [mm] in the 2p (left) and 3-piece ribs (right).

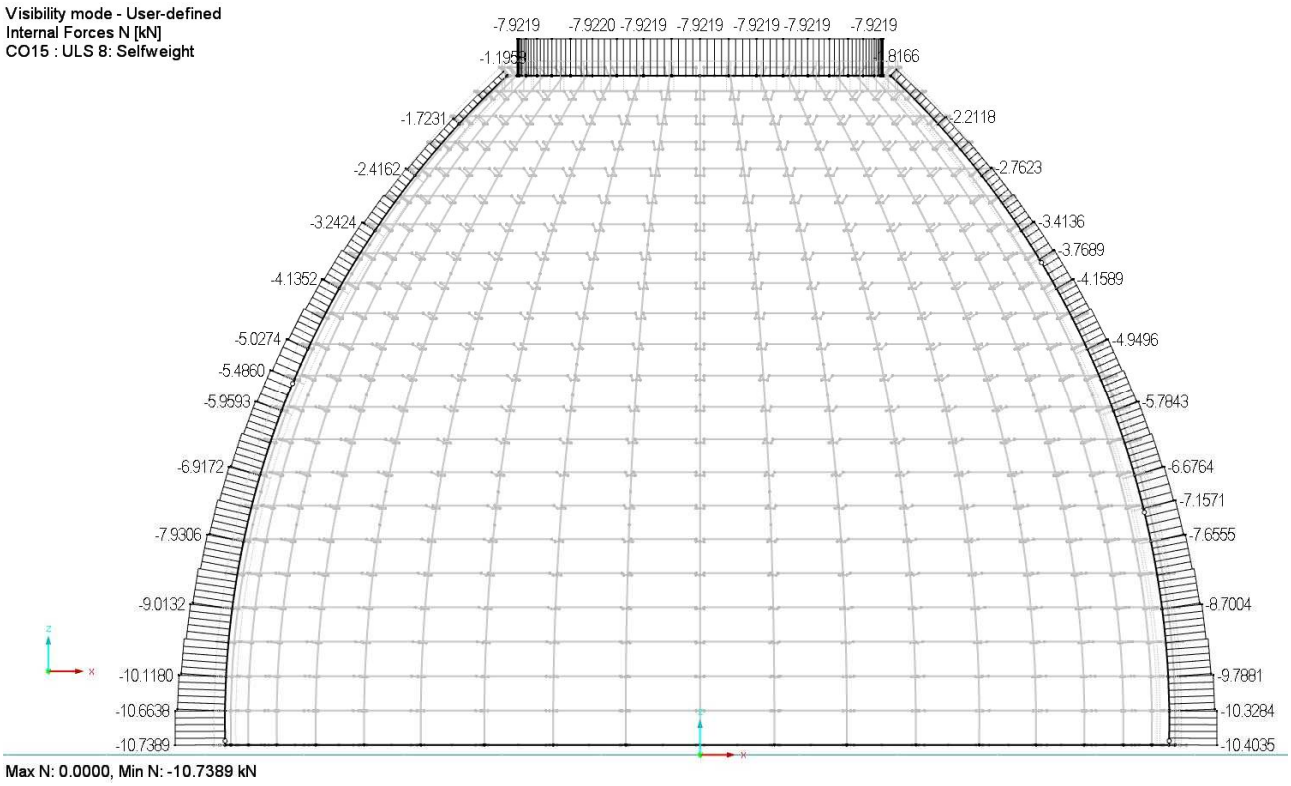

Figure 9-16 – CO15: 1.35 · LC1. Normal forces N [kN]

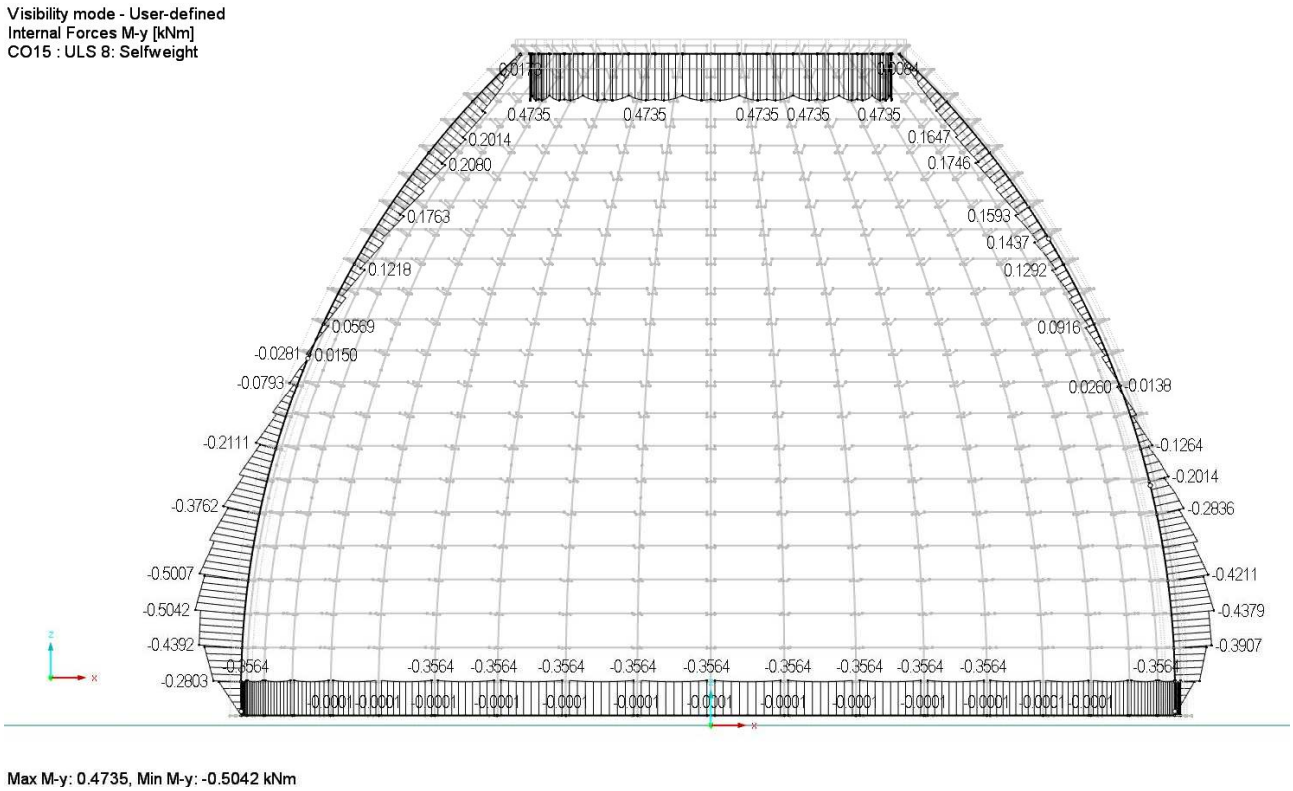

Figure 9-17 – CO15: : 1.35 · LC1. Moment M_y [kN · m]

Observations on the LC1 results

The moment is not uniform along the length of the rib, a jump in correspondence of the dummy rigid elements is present. This behaviour (also in the no-self-weight pre-calculation) is justified by the presence of a certain amount of N force along the axis of the planking, eccentric respect to the axis of the rib.

In the Figure 9-18 the scheme of the point of joining between the dummy rigid element and the rib is presented. Taking into account the local reference system *x,y,z* of a board, the surface laying on the *xy* plane is always tangent to the axis of the curved rib in correspondence with the connection with the board. Depending on the circle the planking are part of, the angle between the main axis of the beam and the main axis of the rib (in *xy*) is changing. The bigger the circumference formed by the planks, the smaller is the angle, decreasing from the bottom to the top of the dome.

Considering the CO15 – dead loads, on the generic node n° 22 of the rib, N is the normal force along the element, *e* is the eccentricity between the axis of the plank and the axis of the rib, and ϕ_{xy} the angle in the xy

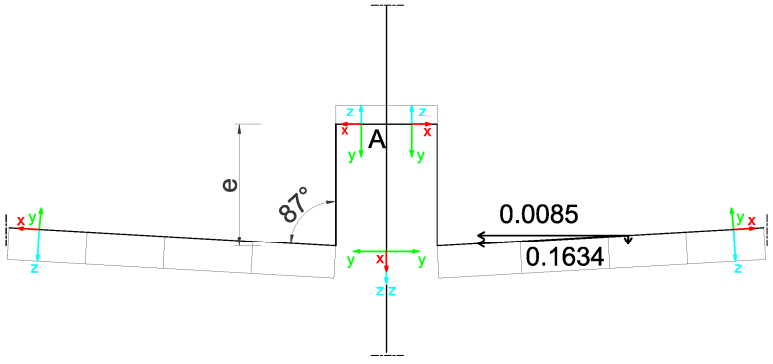

Figure 9-18 – LC1: N. Joint point between the dummy-rigid element and the rib (point n° 22)

plane between the axis of the plank, and the axis of the beam. When N is split into components, *Ny*, the vertical component, has a strong influence on the resulting bending diagram of the rib.

$$N = 0.1634kN$$

$$e = 0.10 + 0.015 = 0.115m$$

$$\phi_{xy} = 87°$$

$$N_y = 0.1634 \cdot \cos(87°) = 0.0085kN$$

$$e \cdot N_y = 0.015 \cdot 0.0085 = 0.00013kN \cdot m \quad \text{9-36}$$

This result, must be correspondent to the half (the other half is due by the adjacent plank) of the value of the "jump" moment in the rib in A and also corresponds to the value of the torsional moment Mt in the dummy rigid element in A.

$M_{t,dummy} \cdot 2 = M_{y,rib}$ 9-37

Is demonstrated in the

M_y (of the rib, in A) = 0.002 kNm 9-38

Mt (of the dummy, in A)= 0.001 kNm 9-39

NAILS VERIFICATION

The load-carrying capacity for the nails (eq. 9-41) is verified according eq. 9-35 for permanent loads

$$N_{\max,d} = \left|N_{board,\max,d}\right| / 2 = 1.14 / 2 = 0.57 \text{ (Normal force on the single nail)} \quad \text{9-40}$$

$$N_{\max,d} \le F_{v,d,p}$$

$$0.57kN < 1.06kN \quad \text{9-41}$$

DEAD LOADS + WIND (CO4 and CO11)

The results of the structural analysis' simulation are contained in the Table 9-14. Rotations and displacement in the structure are in the CO4 very significant. The maximum rotation contained in the eq. 9-42 is 8 times the reference value contained in the eq. 9-19.

$$\gamma_{x,\max} = 34.48mrad = 0.0345rad \quad \text{9-42}$$

The maximum displacement value at the top of the ribs is recorded in the y direction (eq. 9-43), while the maximum global displacement is the one in the eq. 9-44. The value of displacement, in absolute values (eq. 9-45), is three times the reference value contained in the eq. 9-27.

$$u_{top,y,m\max} = 81.24mm \quad \text{9-43}$$

$$u_{top,\max} = 95.15mm \quad \text{9-44}$$

$$\frac{u_{top}[mm]}{h_{dome}[mm]} = \frac{95}{6750} = 0.014 \quad \text{9-45}$$

In accordance with the Table 9-16, on one side, the stress is generally very low in the 3p joints (among 5% and 15% of the capability of the halved cross section), on the other side, the level of stress is very relevant in the 2p-rib joint. Here, both in the verification 1 and in verification 2 the maximum level of stress in the *Jupiter joint* reaches the 50-75% of the capability. The most stressed cross section has also lower level of stress.

Table 9-16 – Results of the stresses in the CO11

		PERFECT STRUCTURE + wind (short term load)															
		Results				Analysis											
		Moment			Normal force	geometry		max. stresses in the cross section			verification 1			verification 2			members
		$\lvert M_{T,max,d}\rvert$ [N·mm]	$\lvert M_{y,max,d}\rvert$ [N·mm]	$\lvert M_{z,max,d}\rvert$ [N·mm]	$\lvert N_{max,d}\rvert$ [N]	b [mm]	h [mm]	$\sigma_{c,0,d}$ [N/mm²]	$\sigma_{m,y,d}$ [N/mm²]	$\sigma_{m,z,d}$ [N/mm²]							
dead	CO11	33500	220300	126000	5838.3	180	100	0.32	0.73	0.23	0.05	≤	1	0.05	≤	1	3p-1
loads		16900	713100	92900	8519	180	100	0.47	2.38	0.17	0.15	≤	1	0.11	≤	1	3p-2
wind		0	3596000	100	28875	180	100	1.60	11.99	0.00	0.73	≤	1	0.52	≤	1	2p
		0	3789100	200	28450	180	200	0.79	3.16	0.00	0.19	≤	1	0.14	≤	1	c-s

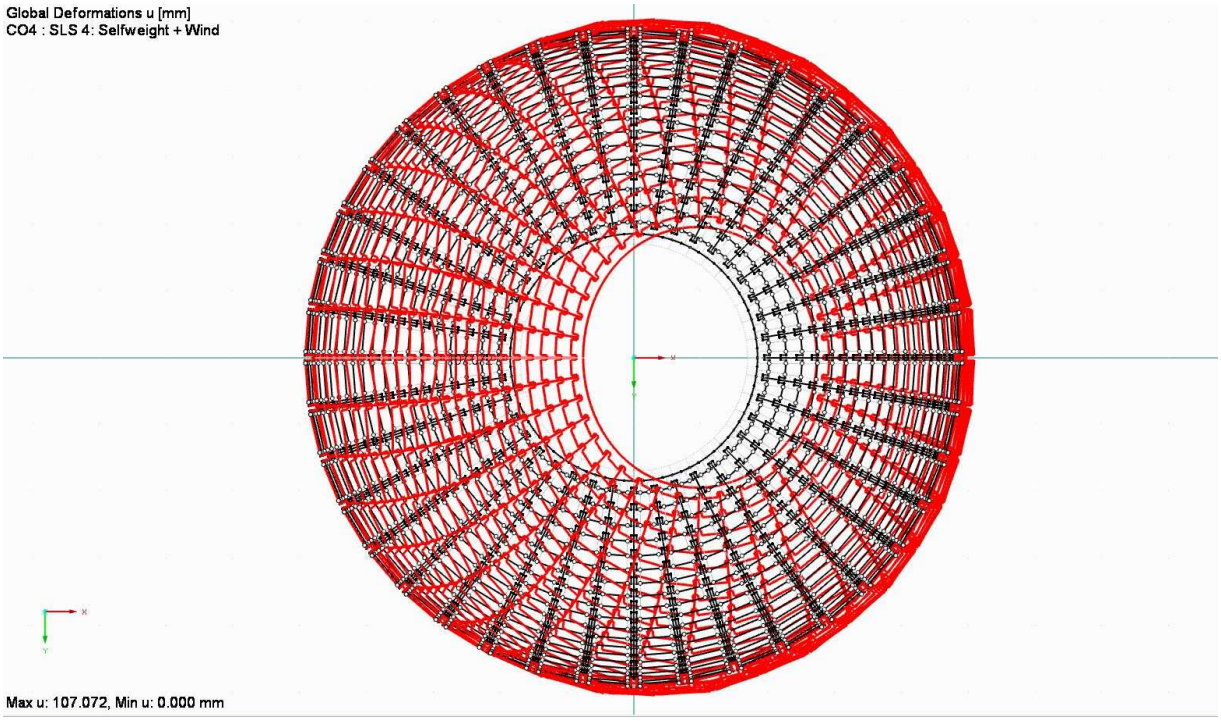

Figure 9-19 – CO4: 1.00 · LC1 + 1.00 · LC2. Global deformations *u* [mm] (top)

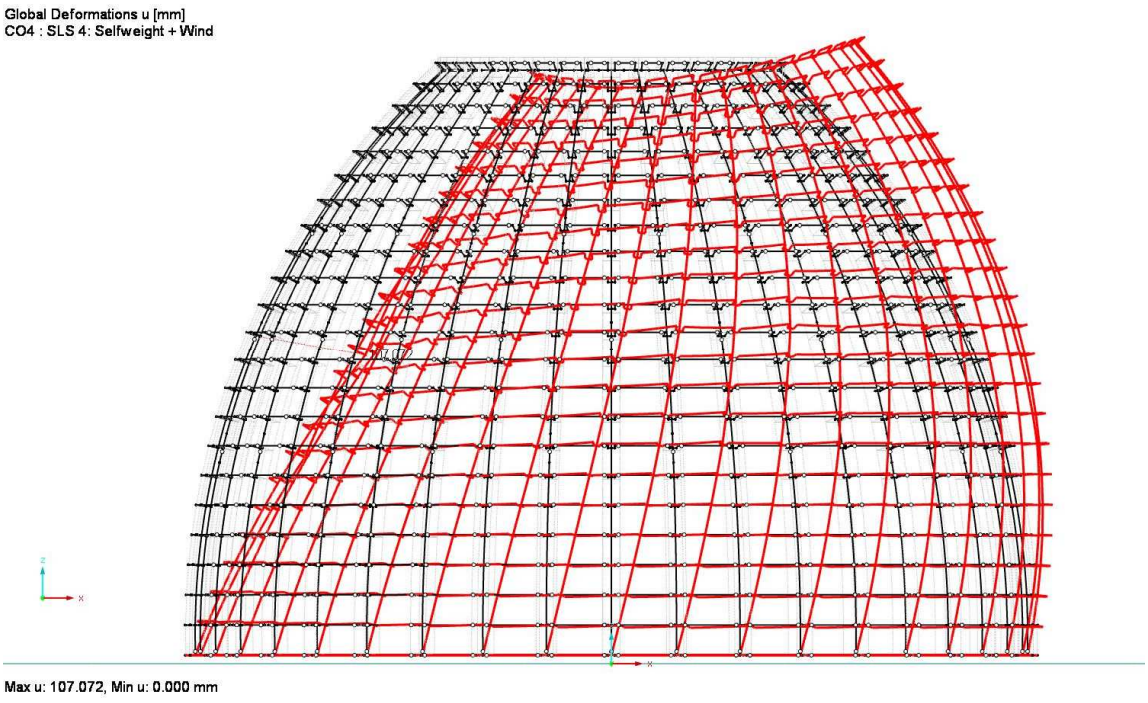

Figure 9-20 – CO4: 1.00 · LC1 + 1.00 · LC2. Global deformations *u* [mm] (front)

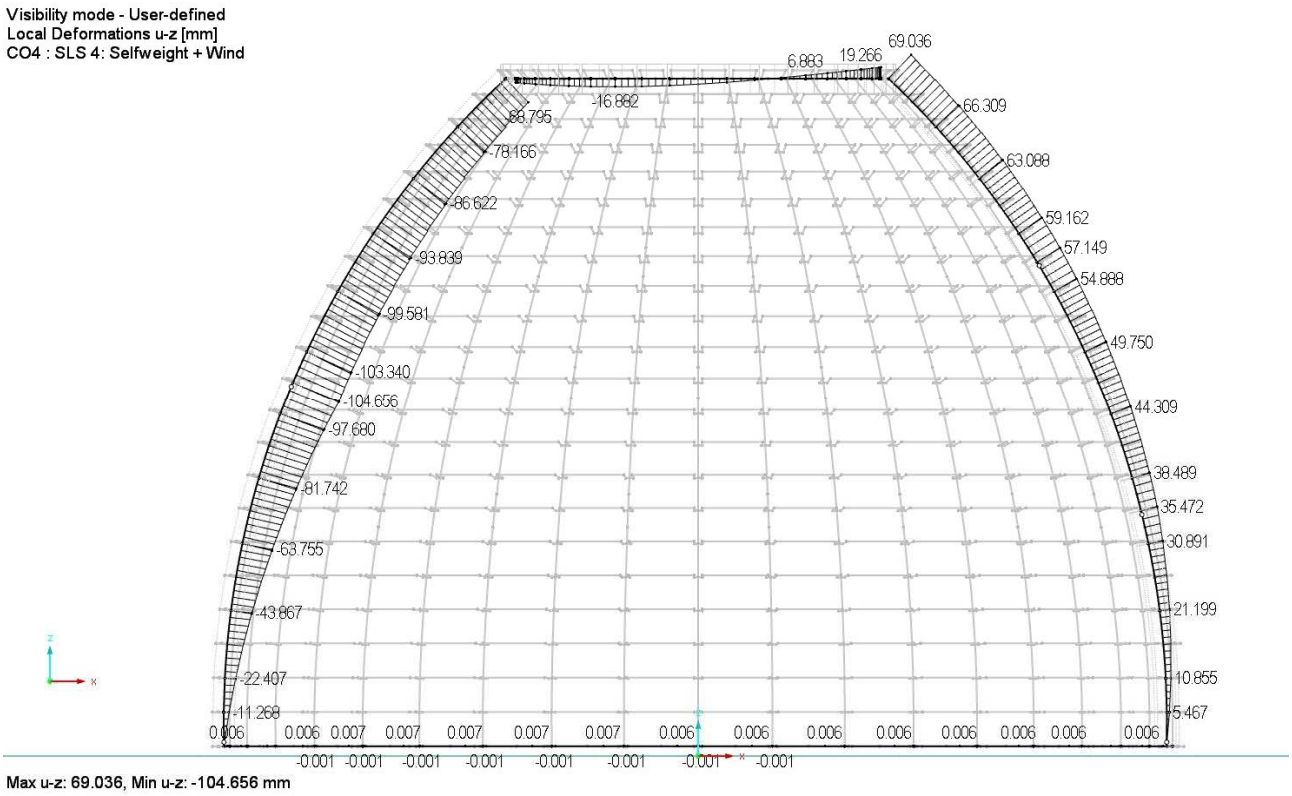

Figure 9-21 – CO4: 1.00 · LC1 + 1.00 · LC2.

Local deformations u_z [mm] in the 2 (left) and 3 -pieces ribs (right)

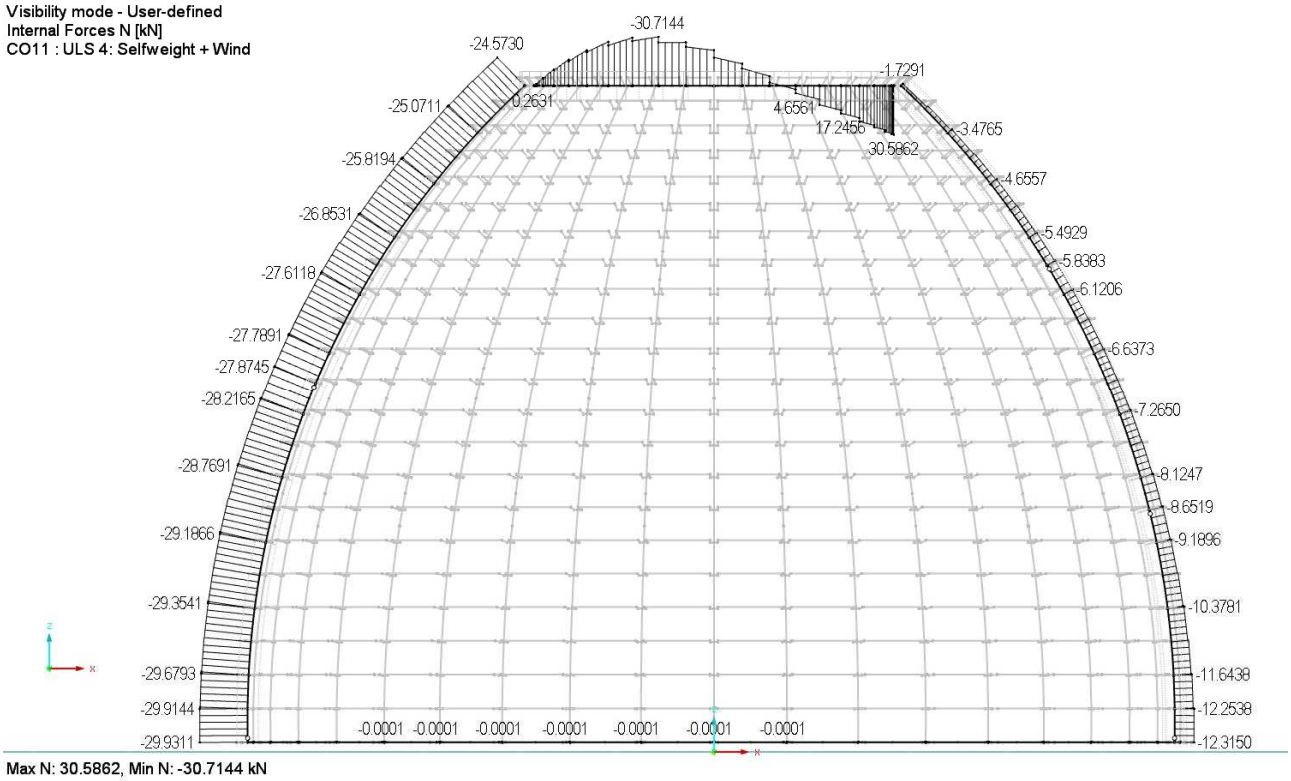

Figure 9-22 – CO11: 1.35 · LC1 + 1.50 · LC2. Normal force *N* [kN]

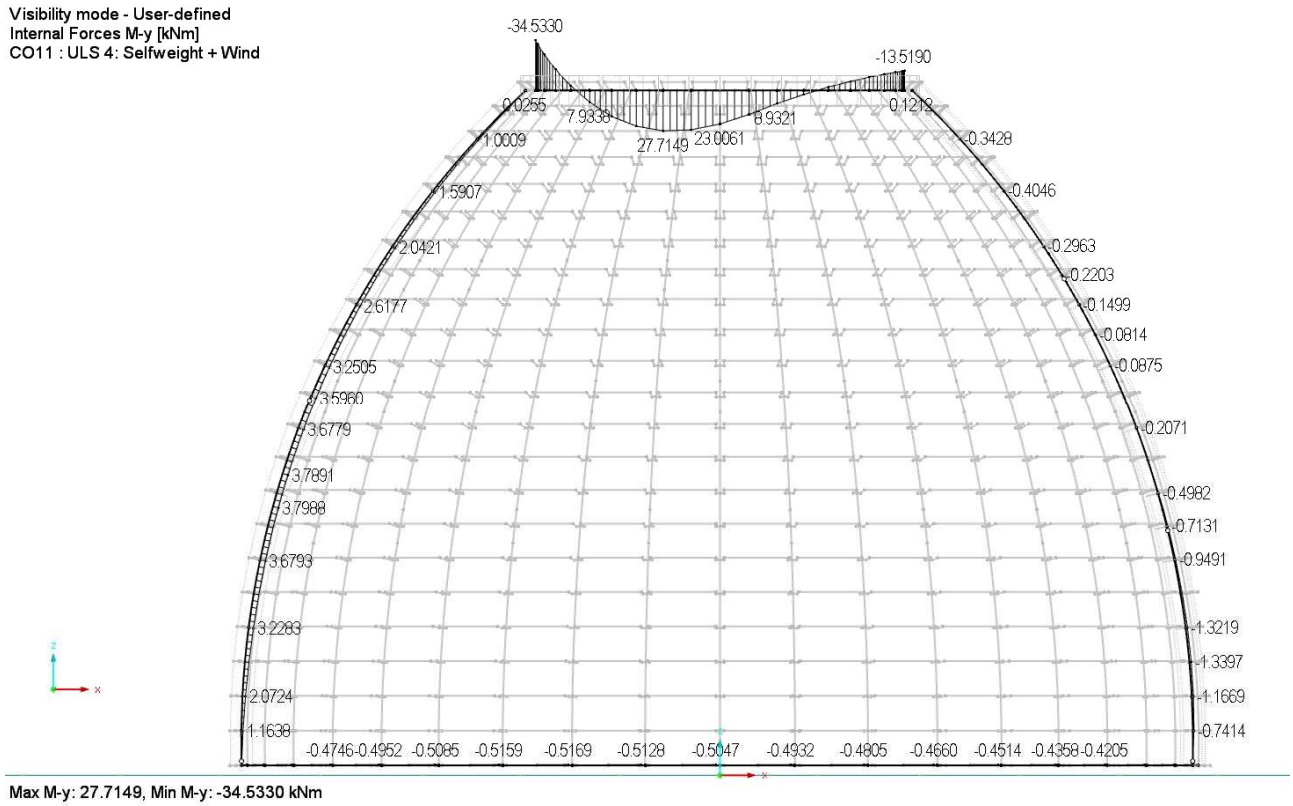

Figure 9-23 – CO11: 1.35 · LC1 + 1.50 · LC2. Moment M_y [kN · m]

NAILS VERIFICATION

For what concerns the load-carrying capacity of the nail, the value of normal force in the beam varies from the top to the bottom of the dome. The verification follows:

$$N_{board,\max} = \begin{cases} -4.14kN \\ 7.11kN \end{cases} \qquad 9\text{-}46$$

$$N_{\max,d} = \left|N_{board,\max}\right| / 2 = 7.11/2 = 3.56kN \quad \text{(Normal force on the single nail)} \qquad 9\text{-}47$$

Considering the verification in the eq. 9-35 for the short-term combination value's of $F_{v,d}$, the load-carrying capacity for the nails is not verified in the eq. 9-48.

$$N_{\max,d} \le F_{v,d,s}$$
$$3.56kN > 1.69kN \qquad 9\text{-}48$$

CONCLUSIONS

The verification on the nails is not satisfied.

In case of perfect structure, loaded in self weight, with the minimum values of rotational stiffness in the joint, the structure is still isostatic, and does not need any further stiffening effect of the planking. However, for the structure loaded under horizontal loads, i.e. wind loads, the presence of the planking is crucial as stiffening element.

9.5.2 Imperfect structure

The results of the structural analysis' simulation are contained in the Table 9-14. The imperfect structure is the one considered in the three following pair of combinations: CO1, CO8 (dead loads + imperfection 0); CO2, CO9 (dead loads + imperfection 1) and CO3, CO10 (Dead loads + imperfection 0 + imperfection 1).

Deformations: among the three imperfect models, the one that has the biggest global displacements $u_{\max}$ are in the CO3. The contribution of different imperfections to the result is very significant. In fact, from the comparison of both the combinations CO1 and CO2 with the combination CO3, it is inferred that the dominant and most significant contribution to the deformations is due by LC4 (imperfection 0) (eq. 9-49).

$$u_{\max,LC1+LC4} \cong u_{\max,LC1+LC3+LC4} \cong 36.5mm \qquad 9\text{-}49$$

Being the CO3 the relevant imperfect combination, the following analysis refers to the CO3.

The maximum rotation contained in the eq. 9-50 is the 45% more than the reference value contained in the eq. 9-19. Considering that the CO3 includes the pre-imposed imperfection that is already a 20% more than the reference value, the rotation can be defined not very significant.

$$\gamma_{z,\max} = 6.89mrad = 0.0069rad \qquad 9\text{-}50$$

The maximum displacement value at the top of the ribs is recorded in the y direction (eq. 9-51), while the maximum global displacement is the one in the eq. 9-52. The value of displacement, in absolute values (eq. 9-53), is equal to the reference value (eq. 9-27) plus the 20% of pre-imposed increment.

$$u_{top,y,m\max} = -36.60mm \qquad 9\text{-}51$$

$$u_{top,\max} = 36.60mm \qquad 9\text{-}52$$

$$\frac{u_{top}[mm]}{h_{dome}[mm]} = \frac{36.6}{6750} = 0.0054 \qquad 9\text{-}53$$

As a conclusion, the rotations and displacement in the structure are not very significant, but correspond to the pre-imposed deformation intrinsic in the load cases "imperfection".

Table 9-17 – Elaboration of the structural analysis' results in the imperfect structure.

		IMPERFECT STRUCTURE (permanent load)															
		Results				**geometry**		**Analysis**									
		Moment			**Normal force**			**max. stresses in the cross section**			**verification 1**			**verification 2**			**mem-bers**
		|MT,max,d| [N·mm]	**|My,max,d|** [N·mm]	**|Mz,max,d|** [N·mm]	**|Nmax,d|** [N]	**b** [mm]	**h** [mm]	**σc,0,d** [N/mm²]	**σm,y,d** [N/mm²]	**σm,z,d** [N/mm²]							
dead	CO8	107500	142500	236800	3765.3	180	100	0.21	0.48	0.44	0.07	≤	1	0.07	≤	1	3p-1
loads		92500	201800	206600	7155.2	180	100	0.40	0.67	0.38	0.09	≤	1	0.08	≤	1	3p-2
imp 0		95200	29700	210600	5484.3	180	100	0.30	0.10	0.39	0.03	≤	1	0.04	≤	1	2p
		6500	504200	0	9560	180	200	0.27	0.42	0.00	0.04	≤	1	0.03	≤	1	c-s
dead	CO9	9100	143800	6900	3769.4	180	100	0.21	0.48	0.01	0.04	≤	1	0.03	≤	1	3p-1
loads		30800	201500	400	7157.8	180	100	0.40	0.67	0.00	0.06	≤	1	0.04	≤	1	3p-2
imp 1		26300	28100	4500	5485.7	180	100	0.30	0.09	0.01	0.01	≤	1	0.01	≤	1	2p
		27700	504100	0	9565.3	180	200	0.27	0.42	0.00	0.04	≤	1	0.03	≤	1	c-s
dead	CO10	116600	142200	229700	3762.1	180	100	0.21	0.47	0.43	0.07	≤	1	0.07	≤	1	3p-1
loads		123200	202400	206100	7154.5	180	100	0.40	0.67	0.38	0.09	≤	1	0.08	≤	1	3p-2
imp 0		121400	30600	205900	5481.6	180	100	0.30	0.10	0.38	0.03	≤	1	0.04	≤	1	2p
imp 1		28300	504300	264900	9560	180	200	0.27	0.42	0.25	0.05	≤	1	0.05	≤	1	c-s

From the observation of the Table 9-17, the single imperfection 0 or imperfection 1 do not affect significantly the level of stress of the structure; therefore, the combination of imperfections 0 + 1 is taken into account; therefore, the stress analysis is conducted on the CO10.

The level of stress in the *Jupiter joint* is generally very low. In the 2p-rib joint the stress is smaller than the one in the 3p-rib joint; here, the maximum level of stress is in the 3p-2, that reaches the 9% of the capability of the halved cross section.

NAILS VERIFICATION

The maximum values of normal force in the beam $N_{boards,\max}$ is reported in the eq. 9-54. Follows the verification of the nails.

$$N_{board,\max} = \begin{cases} -1.03kN \\ \\ 1.63kN \end{cases} \qquad 9\text{-}54$$

$$N_{\max,d} = \left|N_{board,\max}\right| / 2 = 1.63/2 = 0.82kN \quad \text{(Normal force on the single nail)} \qquad 9\text{-}55$$

The load-carrying capacity for the nails is verified in the eq. 9-56 considering permanent combination's value of $F_{v,d}$.

$$N_{\max,d} < F_{v,d,p}$$

$$0.82kN < 1.06kN \qquad 9\text{-}56$$

The following figures represent the deformations and stresses in the imperfect structure.

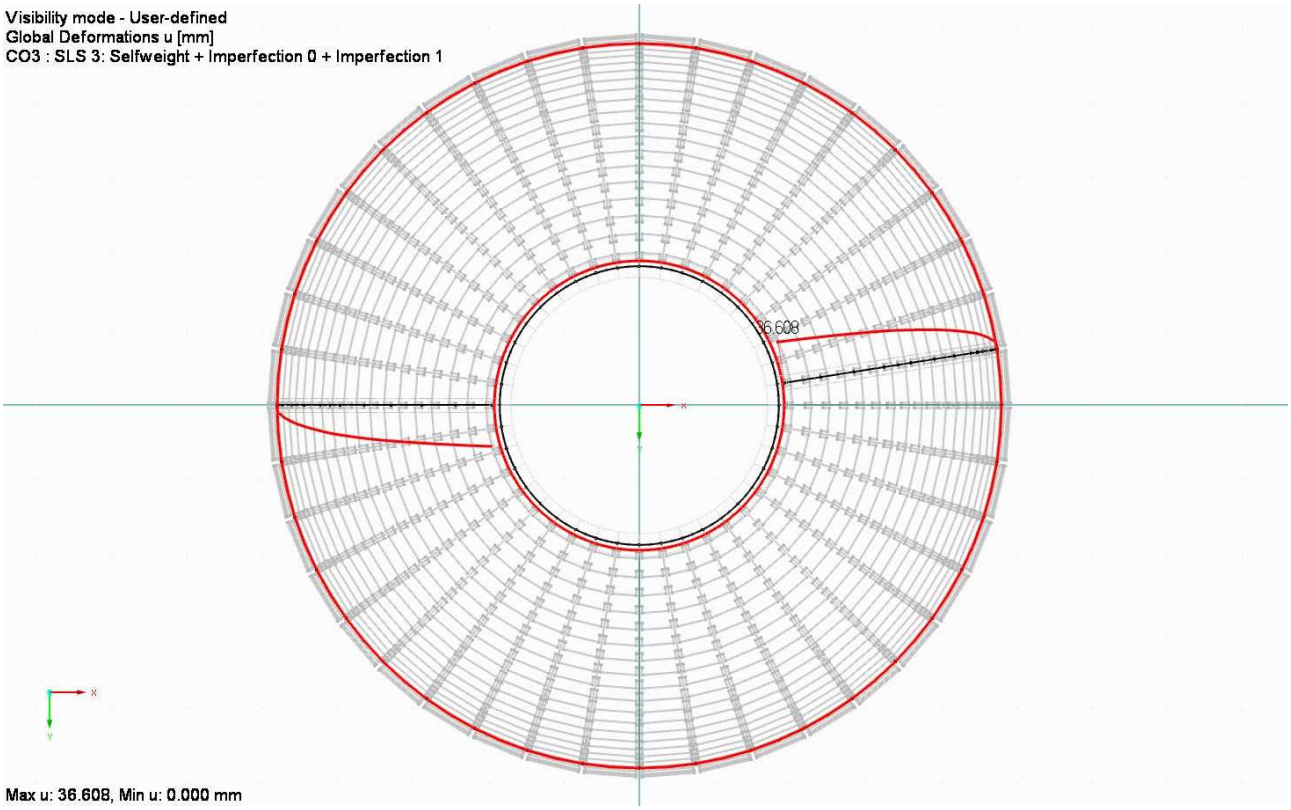

Figure 9-24 – CO3: 1.00 · LC1 + 1.00 · LC3 +1.00 · LC4. Global deformations *u* [mm] (top)

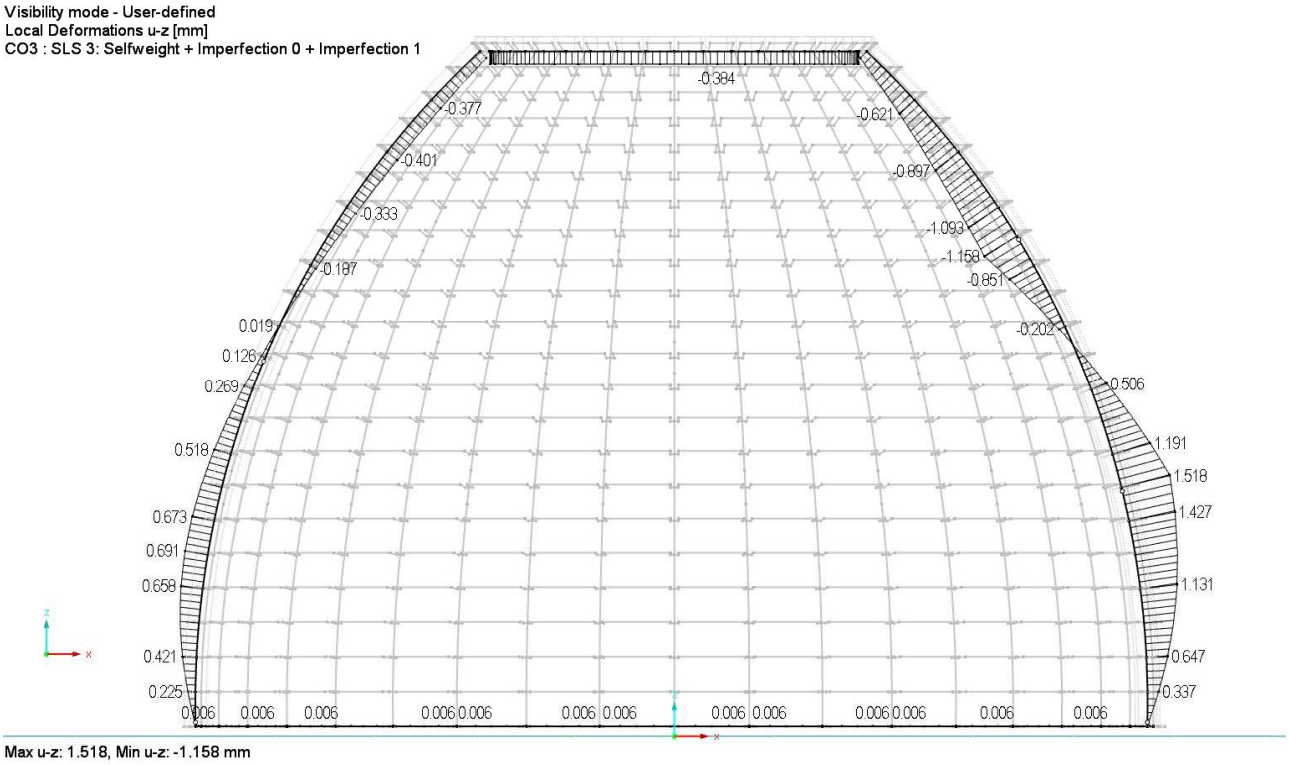

Figure 9-25 – CO3: 1.00 · LC1 + 1.00 · LC3 +1.00 · LC4.

Local deformations u_z [mm] in the 2 (left) and 3 -pieces ribs (right)

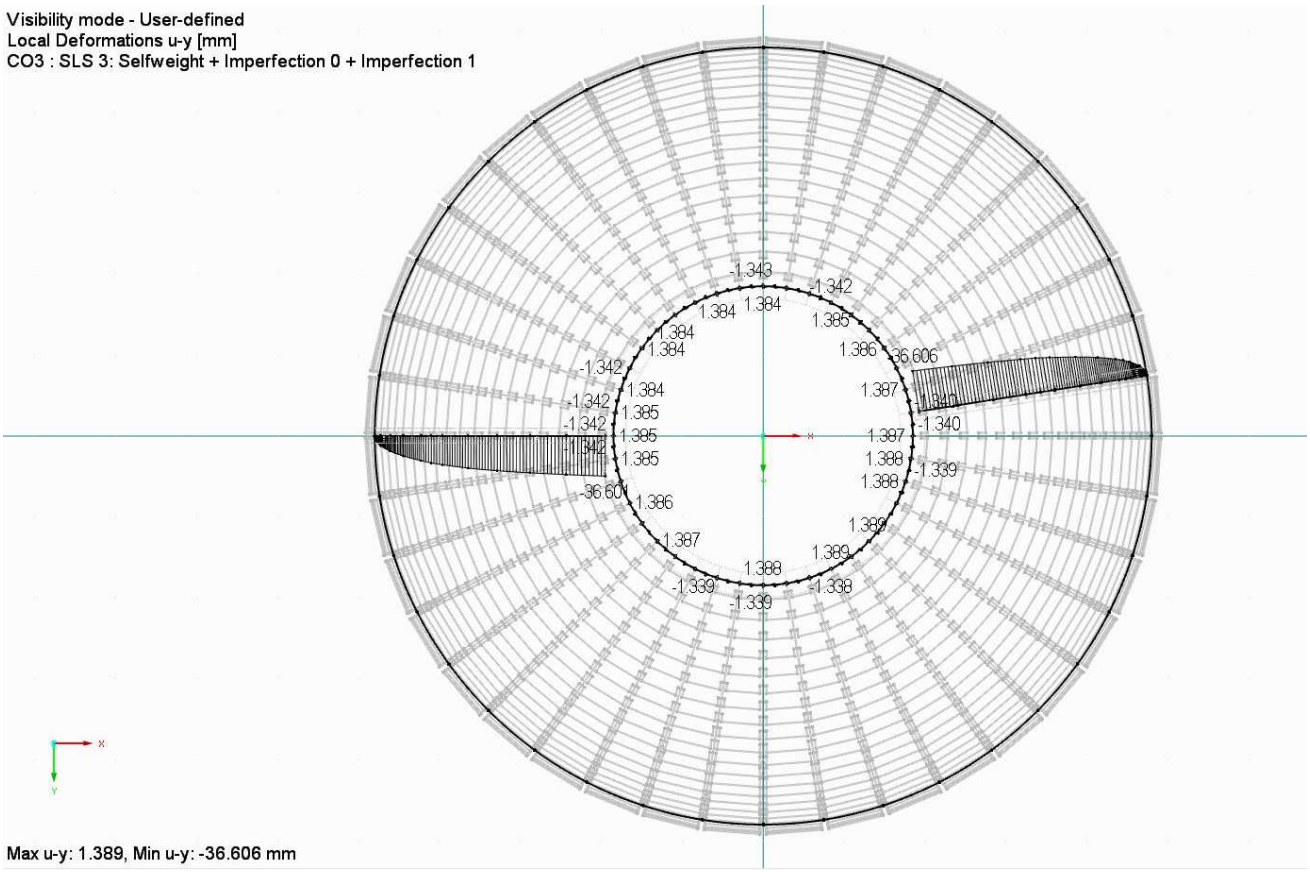

Figure 9-26 – CO3: 1.00 · LC1 + 1.00 · LC3 +1.00 · LC4.

Local deformations u_y [mm] in the 2 (left) and 3 -pieces ribs (right)

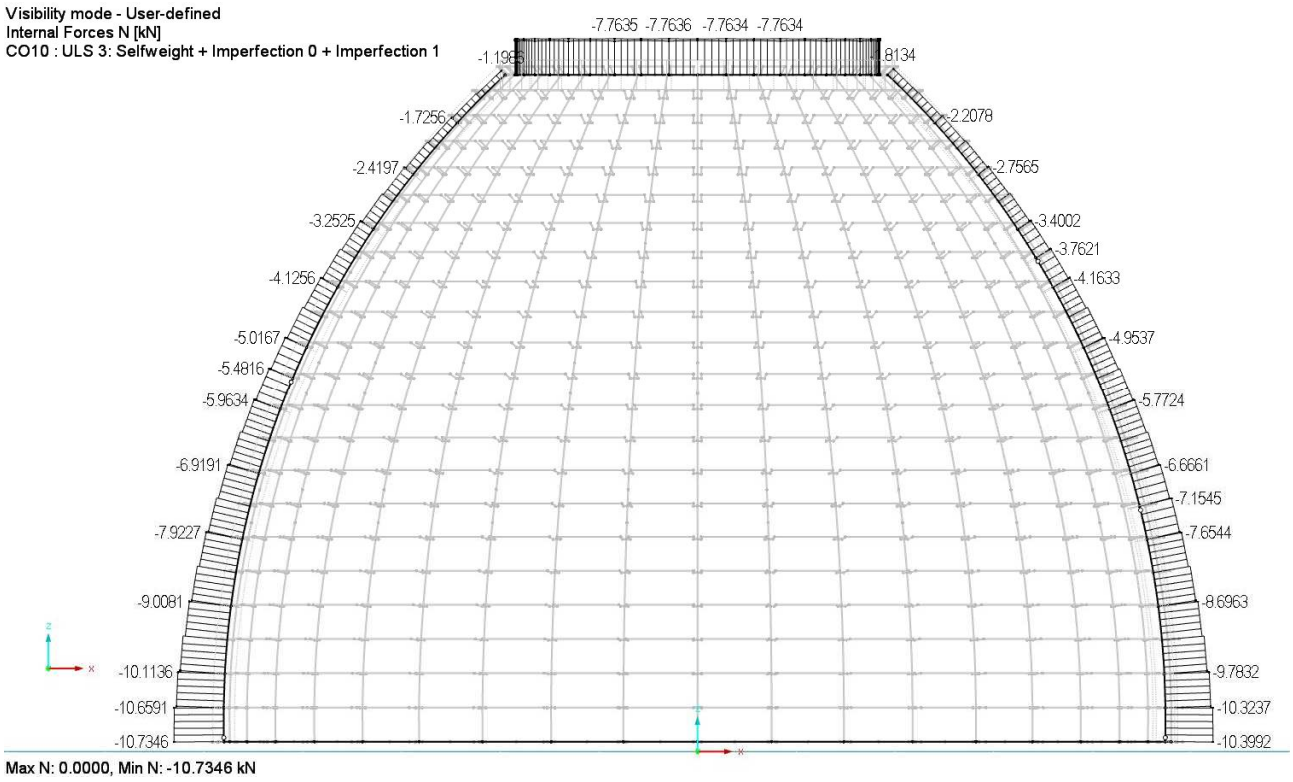

Figure 9-27 – CO10: 1.35 · LC1 + 1.00 · LC3 +1.00 · LC4. Normal force *N* [kN]

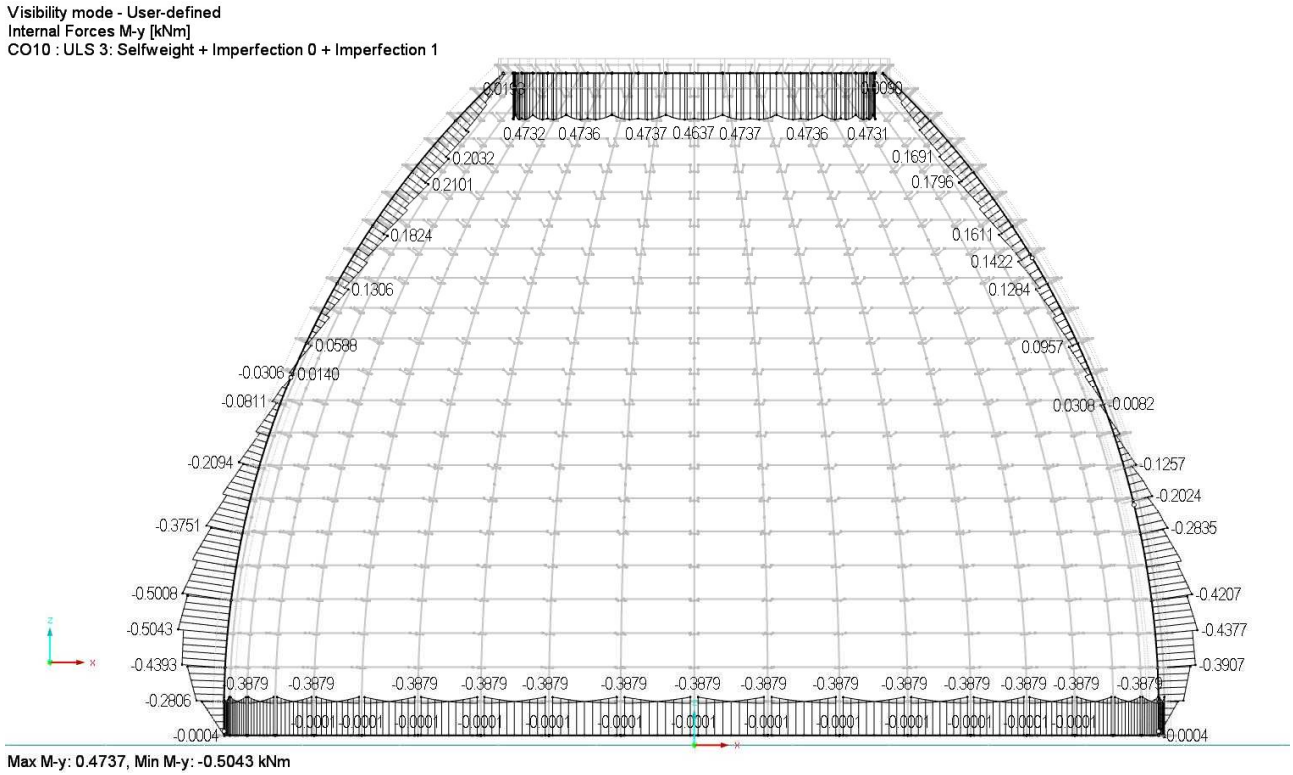

Figure 9-28 – CO10: 1.35 · LC1 + 1.00 · LC3 +1.00 · LC4. Moment M_y [kN · m]

CONCLUSIONS

In general, the imperfections stress the torsional axis of the joint/beam. The imperfection 1 has small influence on the results. The imperfection 0 has also a small influence on the general stresses, but more

influence in terms of local deformations in the *Jupiter Joint*. Therefore, the combination of both the imperfections (CO10) is considered for the stress verification in the imperfect structure + wind, as in the next paragraph..

9.5.3 Imperfect structure + wind

The results of the structural analysis' simulation are contained in the Table 9-18. In this paragraph the imperfect structure + wind is the one considered in the three following pair of combinations: CO5, CO12 (dead loads + imperfection 0 + wind); CO6, CO13 (dead loads + imperfection 1 + wind) and CO7, CO14 (Dead loads + imperfection 0 + imperfection 1 + wind).

Among the three imperfect + wind models, the same situation on the previous analysed load cases is encountered. The biggest global displacements $u_{\max}$ are in the combination CO7. Here, the most significant contribution to the results is from the imperfection 0. In fact, from the comparison of both the combinations CO6 and CO5 with the combination CO7 it is inferred that the dominant and most significant contribution to the deformations is due by LC4 (imperfection 0); in fact the

$$u_{\max,LC1+LC2+LC4} \cong u_{\max,LC1+LC2+LC3+LC4} \cong 115.8mm \qquad 9\text{-}57$$

Being the CO7 the relevant imperfect combination, the following analysis refers to the CO7.

Rotations and displacement in the structure are very significant.

The maximum rotation contained in the eq. 9-42 is 8 times the reference value contained in the eq. 9-19.

$$\gamma_{x,\max} = 32.83mrad = 0.0328rad \qquad 9\text{-}58$$

The maximum displacement value at the top of the ribs is recorded in the y direction (eq. 9-59), while the maximum global displacement is the one in the eq. 9-60. The value of displacement, in absolute values (eq. 9-61), is four times the reference value contained in the eq. 9-27.

$$u_{top,y,m\max} = -116.72mm \qquad 9\text{-}59$$

$$u_{top,\max} = 116.72mm \qquad 9\text{-}60$$

$$\frac{u_{top}[mm]}{h_{dome}[mm]} = \frac{116.72}{6750} = 0.017 \qquad 9\text{-}61$$

Table 9-18 – Elaboration of the structural analysis' results in the imperfect structure + wind.

		IMPERFECT + wind (short term load)															
		Results				geometry		Analysis									mem-bers
		Moment			Normal force			max. stresses in the cross section			verification 1			verification 2			
		|MT,max,d| [N·mm]	|My,max,d| [N·mm]	|Mz,max,d| [N·mm]	|Nmax,d| [N]	b [mm]	h [mm]	σc,0,d [N/mm²]	σm,y,d [N/mm²]	σm,z,d [N/mm²]							
dead loads	CO12	57600	221600	106000	5936.2	180	100	0.33	0.74	0.20	0.05	≤	1	0.04	≤	1	3p-1
		60900	714500	104900	8650.9	180	100	0.48	2.38	0.19	0.15	≤	1	0.11	≤	1	3p-2
imp 0		105000	3594900	201900	27870	180	100	1.55	11.98	0.37	0.75	≤	1	0.54	≤	1	2p
wind		82830	3732900	162800	28493	180	200	0.79	3.11	0.15	0.20	≤	1	0.14	≤	1	c-s
dead loads	CO13	23400	219300	135600	5844.8	180	100	0.32	0.73	0.25	0.06	≤	1	0.05	≤	1	3p-1
		19600	713900	93900	8656.7	180	100	0.48	2.38	0.17	0.15	≤	1	0.11	≤	1	3p-2
imp 1		65800	3595300	18100	27858	180	100	1.55	11.98	0.03	0.73	≤	1	0.52	≤	1	2p
wind		22700	3789400	206200	28350	180	200	0.79	3.16	0.19	0.20	≤	1	0.15	≤	1	c-s
dead loads	CO14	97700	221700	96100	5846.1	180	100	0.32	0.74	0.18	0.05	≤	1	0.04	≤	1	3p-1
		97200	716300	103800	8661	180	100	0.48	2.39	0.19	0.15	≤	1	0.11	≤	1	3p-2
imp 0+1		170800	3593700	273000	27854	180	100	1.55	11.98	0.51	0.75	≤	1	0.55	≤	1	2p
wind		97200	3790900	668200	28477	180	200	0.79	3.16	0.62	0.22	≤	1	0.17	≤	1	c-s

As counterpart of the CO7 for the deformations, the combination CO14 is considered for the calculation of the stresses.

According to the Table 9-18 the stress level in the *Jupiter joint* is generally low along in the 3p-1 rib joint (maximum 5% of the capability of the halved cross-section), it increases in the lower part of the 3p-2 (maximum 15% of the capability of the halved cross-section), while is very relevant in the 2p joint. According to the verification 1, the joint reaches the 75% of the capability of the halved cross section.

Observing the most stressed full cross-section, it is the one in the lower segment of the 2-p rib, and reaches the 22% of the total capability.

NAILS VERIFICATION

The maximum values of normal force in the beam $N_{boards,\max}$ is reported in the eq. 9-62.

$$N_{boards,\max} \begin{cases} -4.43kN \\ \\ 7.56kN \end{cases} \qquad 9\text{-}62$$

$$N_{\max,d} = \left| N_{board,\max} \right| / 2 = 7.56 / 2 = 3.78kN \quad \text{(Normal force on the single nail)} \qquad 9\text{-}63$$

Considering the verification in the eq. 9-35 for short-term combination value's of $F_{v,d}$, the load-carrying capacity for the nails is not verified in the following eq. 9-64.

$$N_{\max,d} \le F_{v,d,s}$$

$$3.78kN > 1.59kN \qquad 9\text{-}64$$

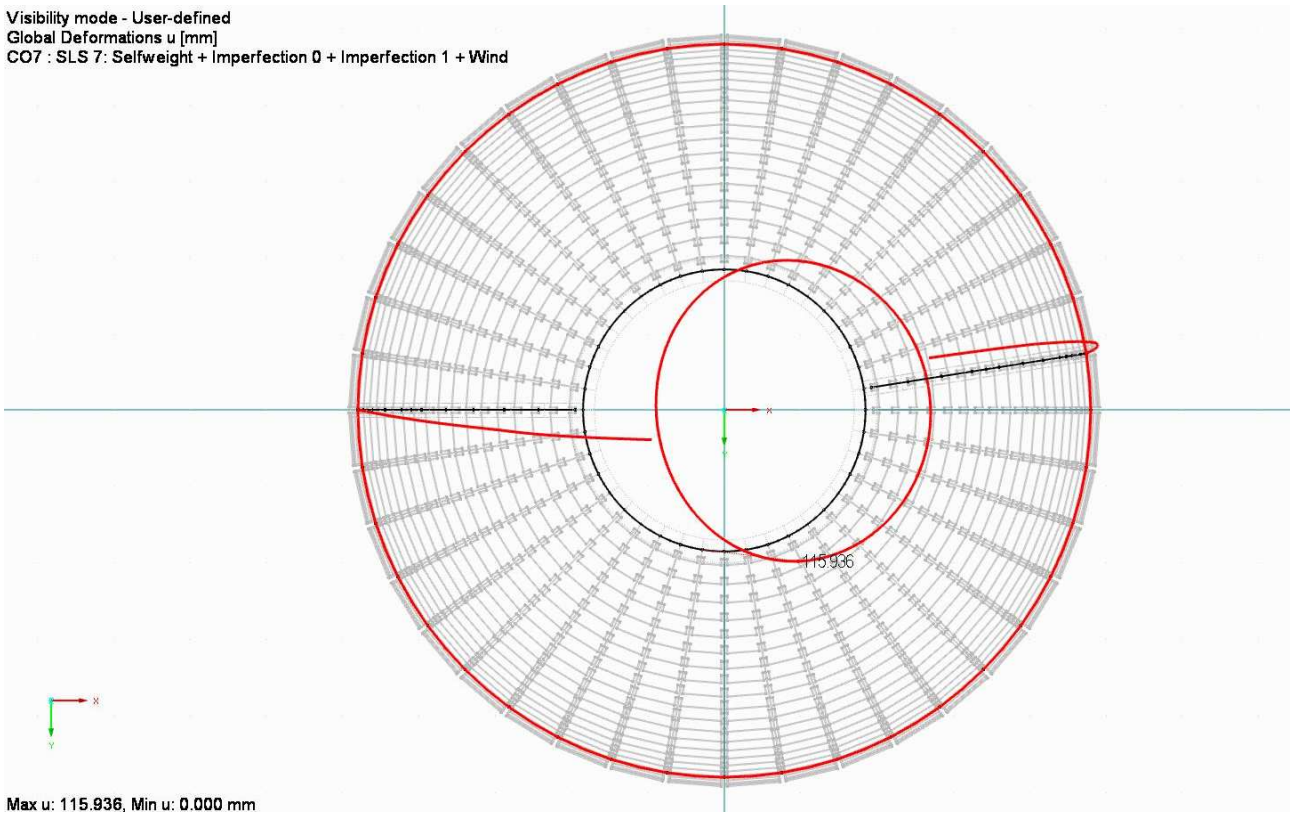

Figure 9-29 – CO7: 1.00 · LC1 + 1.00 · LC2 + 1.00 · LC3 + 1.00 · LC4.
Global deformations *u* [mm] (top)

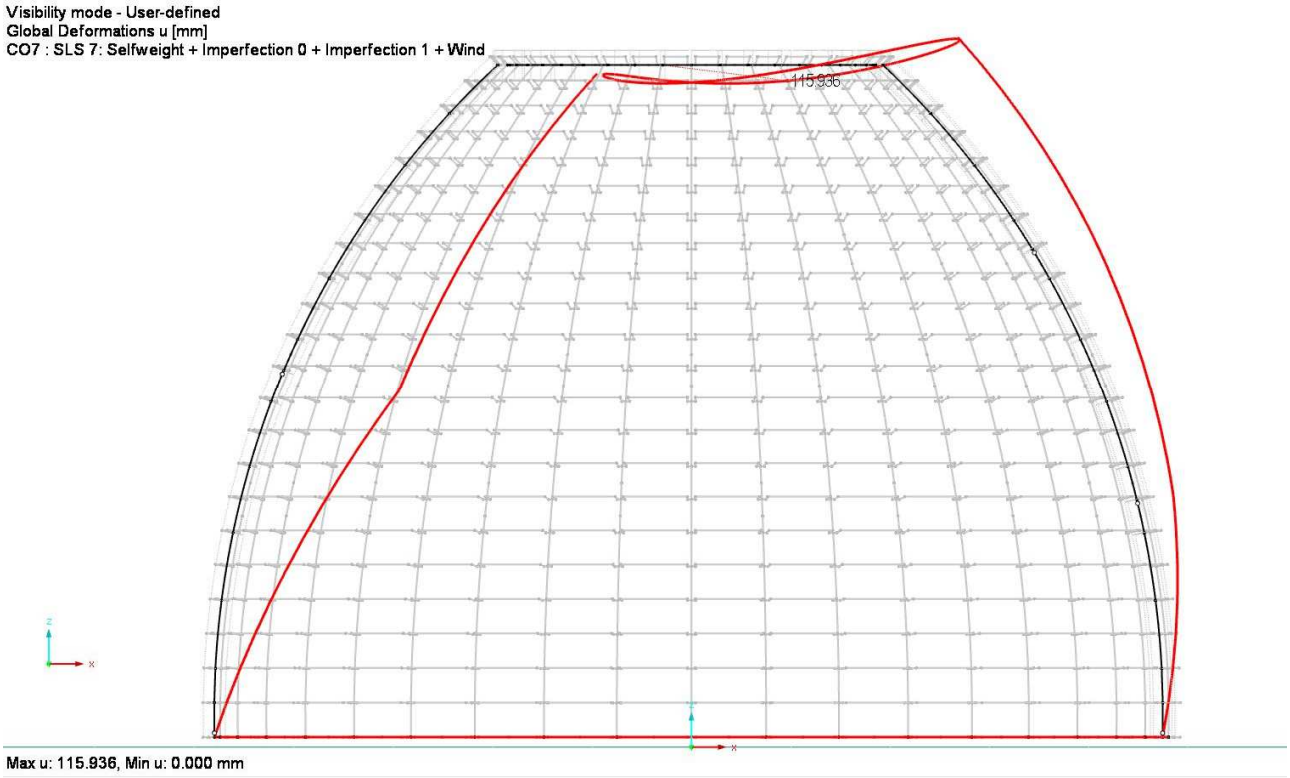

Figure 9-30 – CO7: 1.00 · LC1 + 1.00 · LC2 + 1.00 · LC3 + 1.00 · LC4.
Global deformations *u* [mm] (front)

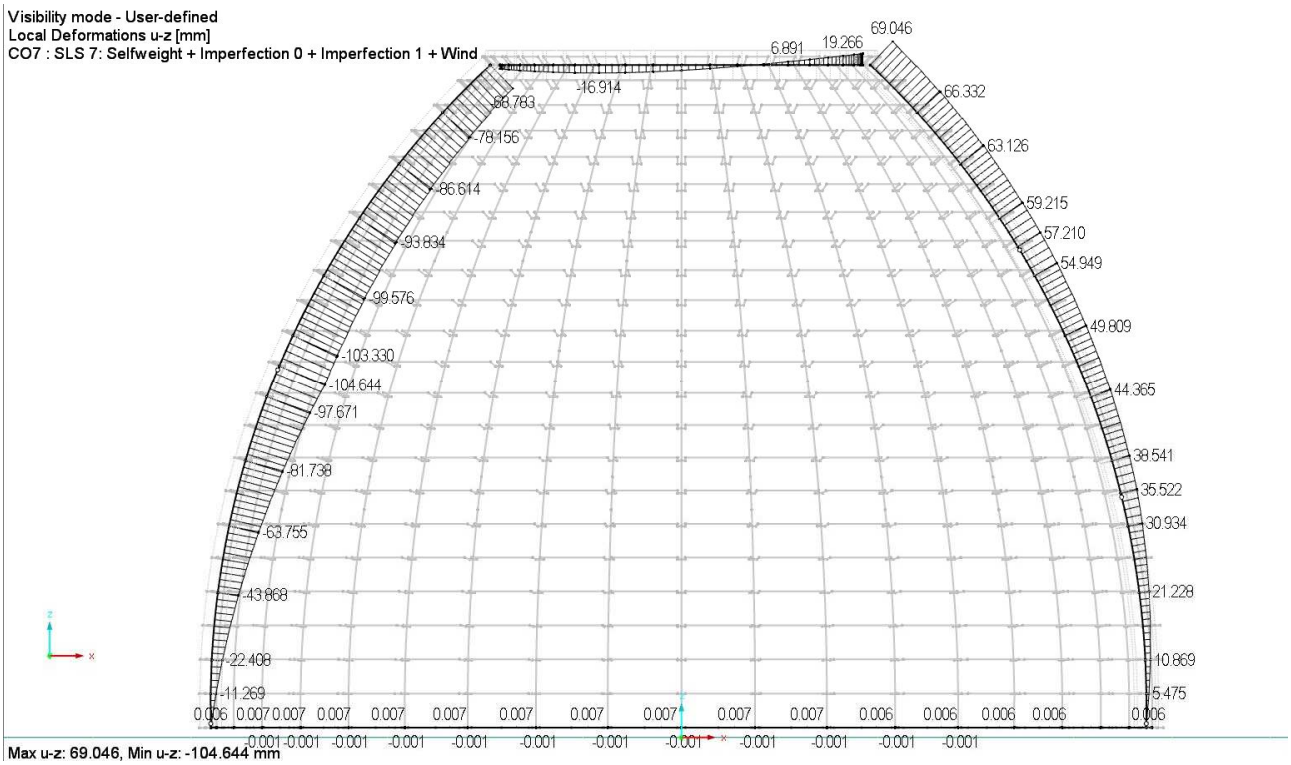

Figure 9-31 – CO7: 1.00 · LC1 + 1.00 · LC2 + 1.00 · LC3 + 1.00 · LC4.
Local deformations u_z [mm] in the 2 (left) and 3 -pieces ribs (right)

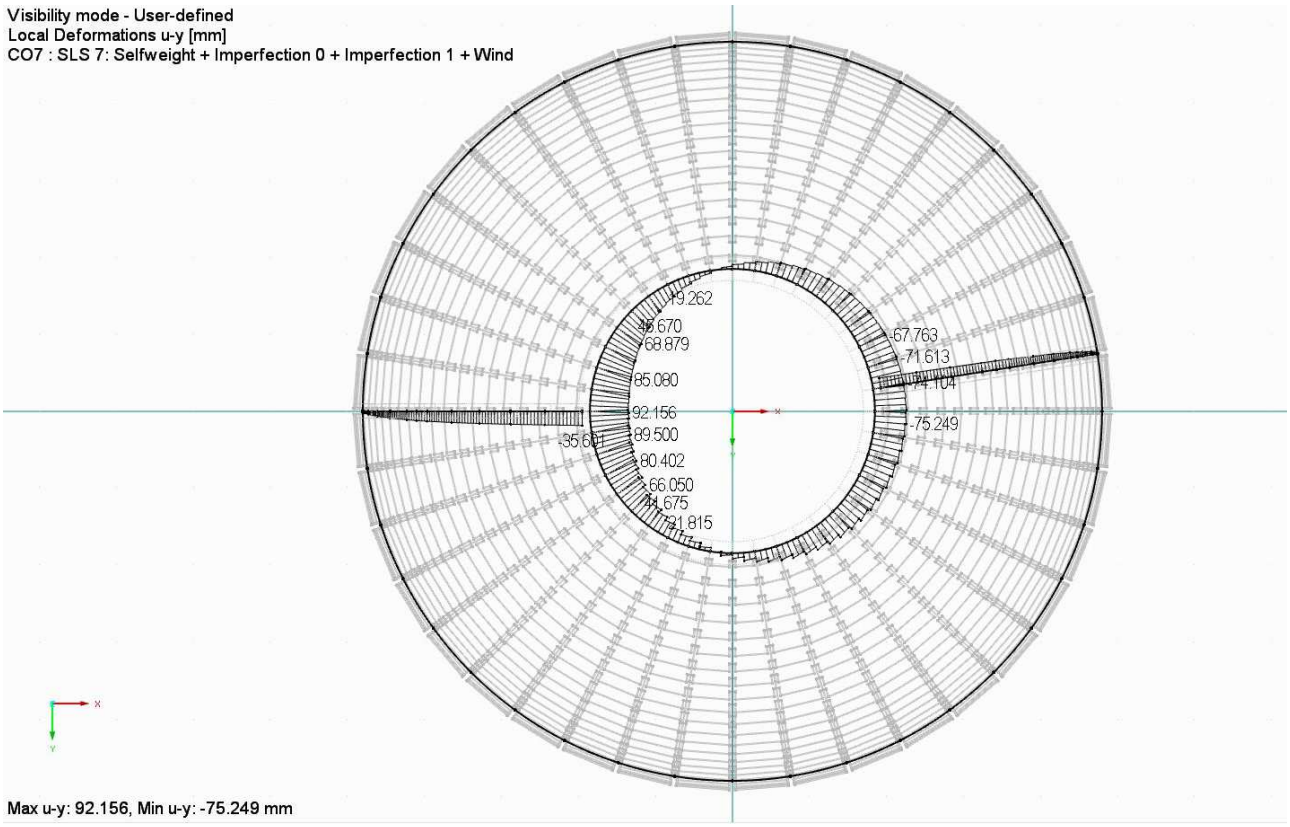

Figure 9-32 – CO7: 1.00 · LC1 + 1.00 · LC2 + 1.00 · LC3 + 1.00 · LC4.
Local deformations u_y [mm] in the 2 (left) and 3 -pieces ribs (right)

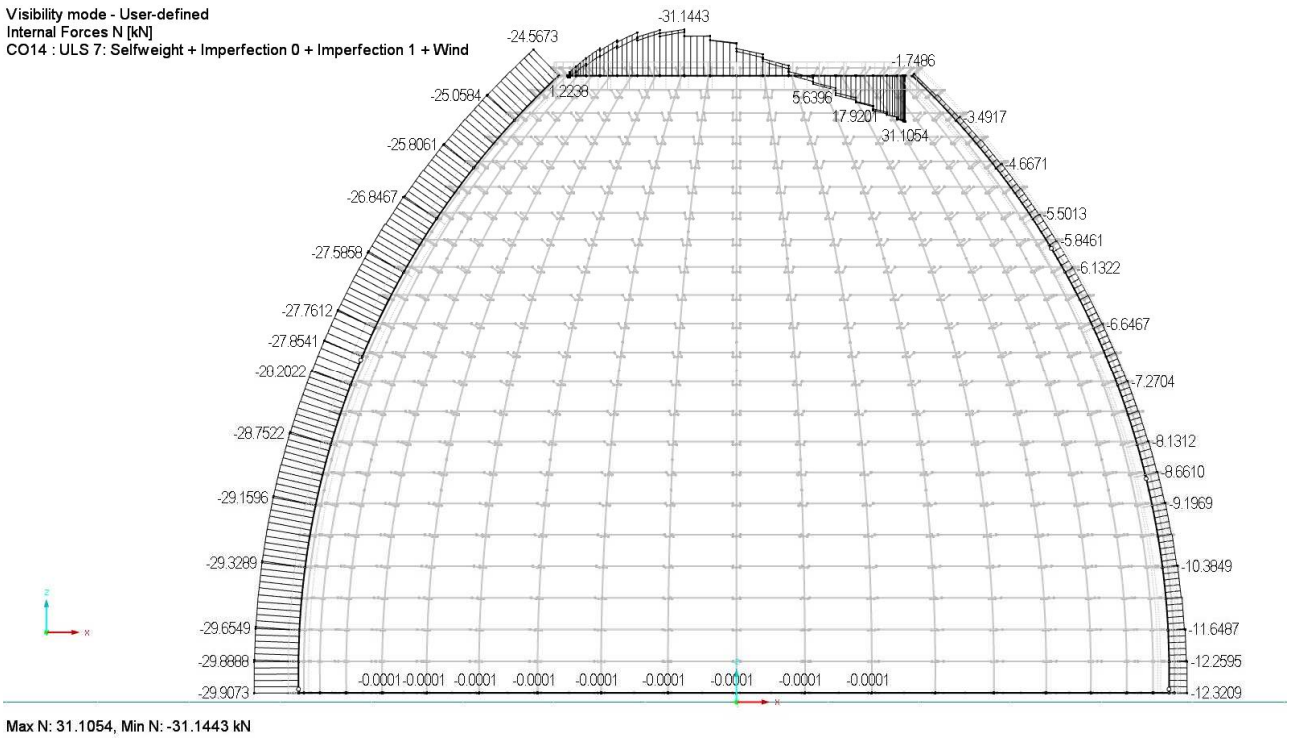

Figure 9-33 – CO14: 1.35 · LC1 + 1.50 · LC2 + 1.00 · LC3 + 1.00 · LC4. Normal force N [kN]

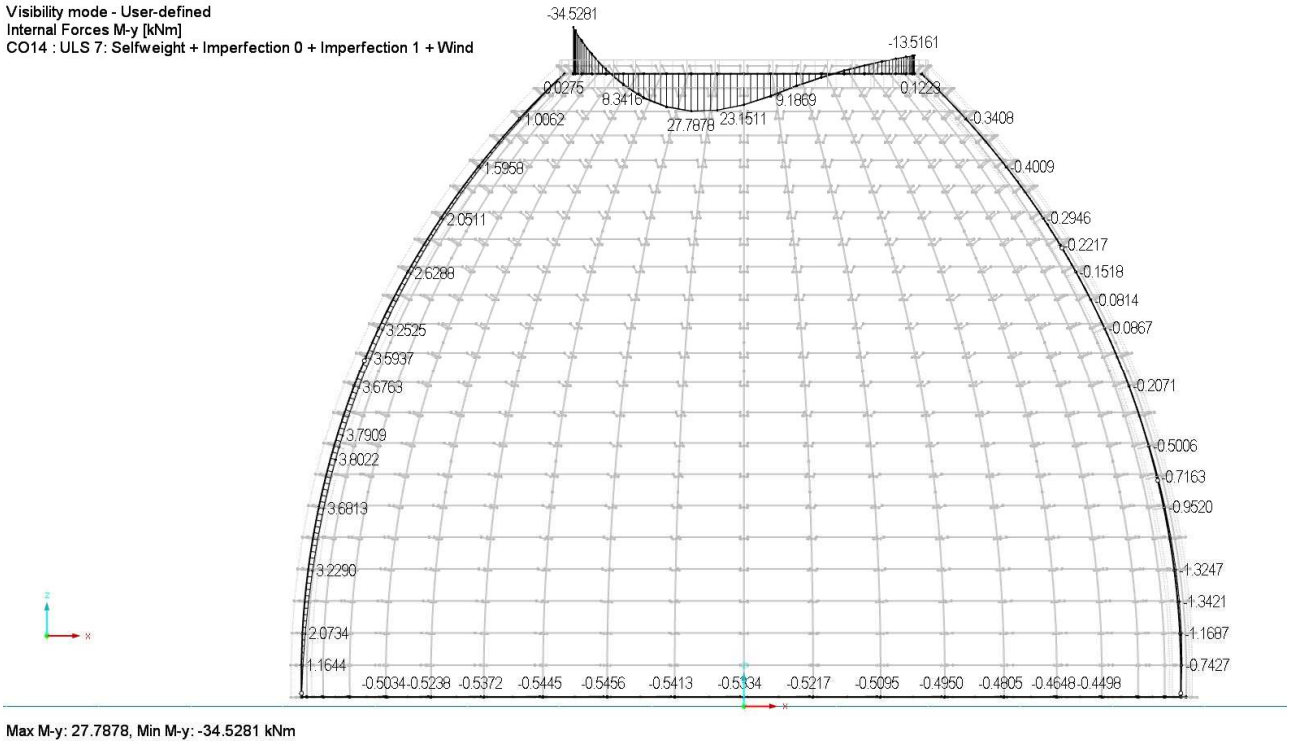

Figure 9-34 – CO14: 1.35 · LC1 + 1.50 · LC2 + 1.00 · LC3 + 1.00 · LC4. Moment M_y [kN · m]

CONCLUSIONS

The wind is the most influent load on the structure.

The section with the biggest flectional moment is always the one in the lower segment of the 2-p rib. Under the effect of wind, the flectional moment moves from the middle of the lower segment of the 2-p rib to the first upper third of the same rib. The highest stressed section get closer to the joint. Hence, the *Jupiter joint* is stressed by higher flectional moment My and normal force N.

9.5.4 Conclusions

The general conclusions are following in short reported.

- From a comparison between the imperfect and the perfect structure, loaded by the wind, the following observations are inferred. In the imperfect structure, the global displacements are 10% bigger than the one in the perfect structures. Nevertheless, the local displacements in the *Jupiter joint* are almost the same, except a bigger deformation (+25%) along the $u_{y,max}$. The local displacements at the top of the ribs are in the CO7 the 20% bigger than in the CO4. This increase is equal to the pre-imposed displacement from the imperfection. The imperfections affect the rotations at the base of the beam in the 3p beam along the torsional axis, and increases of approx. 10% along the two other axis. In conclusion, the presence of imperfections does not further affect the displacements in the wind-stressed structure.
- In the load combinations with wind, the nails are not verified. Nevertheless, the verification was done in accordance with the Eurocode 5 and correspondent standard resistance values for nails, without any particular knowledge about the real resistance of the same.
- The *Jupiter joint*, as modelled in the structural model, is a hinge with value of rotational stiffness different from zero along the y axis. Nevertheless, from an accurate lecture of the test results, the

value of torsional moment, is on one side, not equal to zero in the imperfect load cases and combinations, on the other side, it is equal to zero in the perfect structure. As a conclusion, the imperfections affect the torsional response along the beam's axis. The present work does not deal with torsional resistance in the *Jupiter joint*, therefore, more research is needed.

9.6 Comparison among the experimental and numerical results.

The experimental testing of the *Jupiter Joint* has been performed in order to find out a verification under compressive and bending force. As in the methodology contained in the Chapter 1.2, the comparison among the experimental and numerical results should be done as in the eq. 1-1 and eq. 1-4. Nevertheless, the response of the numerical investigation contained in this chapter, brought to the result that is not possible to define in detail the distribution of the stresses in the joint. Therefore, the comparison between the experimental and numerical values was not possible.

The verification of the structure under compressive and bending force was done with the verification of the stresses in the effective cross section and the *Jupiter joint* as if it were a cross section, but considering the half of the effective height on the safe side.

Chapter 10 CONCLUSIONS

10.1 Introduction

The understanding of the mechanical behaviour and the vulnerabilities of the connections is the first requirement for a correct structural analysis. Since they govern the whole strength and stiffness of the structure, the carpentry connections represent a further challenge for the correct understanding of old timber structures. Therefore, the formulation of appropriate assumptions about the purpose and behaviour of the joints is of basic importance.

The aim of the thesis is the description of the mechanical properties of the *halved undersquinted scarf* joint and *stop-splayed undersquinted and tabled with key scarf* joint (*Jupiter joint*). This thesis focuses mainly on experimental results aiming to the description of important aspects like the friction coefficient, the geometry of the joint and inclination of the faces, rotational stiffness, failure modes and in-plane and out-of-plane behaviour. The goal is pursued with analytic description of the behaviour of the *halved undersquinted* joint, experimental campaigns on the load-carrying capacity under combined compressive and bending action for both the connections, and the numerical analysis of a case study. The numerical simulations are to confirm the behaviour and to give an example for the simulation of the *Jupiter joint*, in sight of future developments in the field of reinforcement of old timber structures.

The important conclusion for each topic are contained in the chapters; here, an overview about the most important topics in reference to the chapters is done. The work is concluded with some outlooks about more topics to be investigated in the future.

10.2 Analytical models for the halved undersquinted scarf joint

In the present work, the behaviour of the *halved undersquinted scarf* joint under combined compressive and bending action is described through four main analytical models represented in the Figure 5-1. The analytical models (i) (ii) (iii) and (vii) represent the *equilibrium configurations* for the performed linear-elastic analysis. The value of the resultant force, boundary conditions and limit states for the models are resumed in the Chapter 4.7. The model (i) represents the particular case of (ii) under pure bending action. The model (ii) gives a description of the behaviour of the connection under pure bending and combined compressive and bending force; in this models the friction is considered as a very important parameter for the characterization of the load-bearing behaviour of the connection. The friction coefficient (μ_α) assumes for the generic angle α values contained in the Diagram 4-4 and in the eq. 4-65. The single values of the friction coefficient along the loading

process are expressed in the eq. 4-44. The model (iii) is a unique configuration, particular case of the model (ii) where the friction coefficient assumes null value. The model (vii) describes the connection under external compression action. The friction force μ_α is negligible because very high values of axial compression (F = N). The load-carrying capacity of the connection depends both on geometric and material conditions. The load-carrying capacity of the connection is zero for selected geometric configurations expressed in the GC(ii)1 in eq. 4-54 and Diagram 4-2; GC(vii)2 in eq. 4-94 and Diagram 4-5; GC(vii)3 in eq. 4-97.

The material conditions determine the fracture criteria that is expressed by the Gustafsson's energy of crack G_f. The action that is necessary to start the propagation of the crack (F_f) for the specimen is a function of the generally G_f calculated in the eq. 3-48 and eq. 3-50. The equations do not take into account the contemporary action of the two different and opposite internal resultant forces in the fibre in B; therefore, such equations cannot be used for the anticipation of the joint's resistance. In fact, it has been demonstrated that the geometry (i.e. the direction of the force with respect to the grains' direction) influences the characteristic resistance of the connection.

For the evaluation of the joint's behaviour, the external action has to be considered. The load-carrying capacity of the connection depends on the external action. The behaviour under pure bending and combined compressive and bending action can be described a posteriori from the experimental tests, while the connection capacity in pure compression can be (partially) anticipated. The description of the procedure to follow for both load conditions is following resumed. The a) describes the FM II shear / tension perpendicular to the grains in B, while the b) describes the FM III shear / tension perpendicular to the grains in B and C.

a) The ultimate value of the action F_u for specimens under pure bending and combined compressive and bending action is described according to the following procedure:

1. Individuation of the friction coefficient for the μ_α evaluated according to the eq. 4-44
2. Verification of the equilibrium state LS1(ii) (eq. 4-71) considering the experimental results F_u, M_u values of epsilon parameters contained in the Table 10-1 for the model (ii) and the fixed value of μ_α calculated in the passage 1.
3. Calculation of the (experimental) action that is necessary to start the propagation of the crack $F_{f,\exp}$ according to LS2(ii) (eq. 4-73)
4. The F_u is given by the LS3(ii).

(ii)	(vii)
$\begin{cases}\varepsilon_1=\frac{3}{4}\\ \varepsilon_2=\frac{1}{4}\end{cases}$	$\begin{cases}\varepsilon_1=\frac{1}{2}\\ \varepsilon_2=\frac{1}{2}\\ \varepsilon_3=\frac{1}{2}\end{cases}$

Table 10-1 – position for the ε_i in the model (ii), (vii) at the failure

b) The $F_{f,C}$ for specimens under pure compression force can be evaluated through the eq. 4-112 of the LS4(vii) and used for the anticipation of the load-carrying capacity of the joint in pure compression with squint $\alpha = 30°$.

For the angle $\alpha = 30°$ the failure of the fibre in C can be evaluated considering a value of $G_f = 11000 J/m^2$ (eq. 3-40 and eq. 4-117). That value of G_f is chosen from the Table 3-1 for the mixed mode angle 90°.
For the angle $\alpha = 60°$, the LS4(vii) describes the test results but does not express the characteristic resistance of the joint. The specimen was, in fact, loaded in pure compression up to the arbitrary value of $F_{u,e}$, without reaching the failure of the specimen (for test installation security). To describe the real value of F_f for the angle $\alpha = 60°$ and, as a consequence, for the correct evaluation of G_f for big angles, more tests in pure compression until the failure are necessary.
Once these experimental evaluation will be done, the evaluation of the F_f has to be done according to the eq. 4-113 to find the value of $F_{f,\exp}$; then, the evaluation of the ultimate F_u is done inserting that value of experimental $F_{f,\exp}$ in the eq. 4-112. For the evaluation of the correspondent value of G_f for the squint $\alpha = 60°$, the eq. 3-48 has to be used.

10.3 Experimental campaign

The in–plane and out-of-plane performed tests remarked the important influence of the geometry of the joint on the load-carrying capacity and failure mode. Another factor that really influences the joint's behavior is the orientation of the joint in the structural elements. In fact, the performed tests with the specimen in horizontal position brought always to smaller values of load-carrying capacity and rotational stiffness' values. In the Figure 10-1 the behaviour of the tested joints (with vertical orientation) is reported in a schematic N-M diagram. The behaviour of the *halved undersquinted & tabled scarf* joint and the *halved undersquinted scarf* with horizontal orientation are reported in the Annex A. For a global overview about the tested geometries, see Annex C, failure modes.

10.3.1 The *halved undersquinted scarf* joint

For the *halved undersquinted scarf* joint the most influencing geometry factor is the inclination of the lower squint. The biggest the angle of the lower squint, the lower the pure bending capacity. For practical purposes, the pure bending capacity can be approximated as zero for angles of lower squint $\alpha > 35°$ (according to horizontal orientation, the unfavourable case). This last behaviour is determined by the value of the friction force. The friction assumes "active" values for angles up to $\alpha \leq 45°$ and is considered null for angles $\alpha > 45°$.
The friction is influent for squint angles $\alpha < 35°$; here, the load-carrying capacity in pure bending can reach significant values. For the load-carrying capacity in pure bending and combined small compression and bending the relevant surface is the lower squint, while the contact among the two pieces of the upper squint can also be neglected (see above Chapter 6.3.2, TEST 2, 6.3.3 TEST 3 and 6.4.3.1, TEST 9). Thanks to the compression component on the surface 2 and the presence of friction, an internal resultant force parallel to the surface generates in the lower squint and guarantees the load-carrying capacity of the joint. The value of friction, according to the analytic solution, varies according to the eq. 4-65 and reaches the maximum value of $\mu_\alpha = \tan(\alpha)$.

The biggest the angle of the lower squint, the biggest the load-carrying capacity in combined compression and bending action and pure compression. The real load-carrying capacity in pure compression for big angles has not be evaluated because of security problems during the tests. For inclination of the squint $45° \le \alpha < 75°$ degrees good properties under both load conditions are registered. For angles of squint $\alpha \ge 75°$ and in general big angles, the combined compression and bending load-carrying capacity can be considered as null (see Annex C, failure modes), and the pure compression load-carrying capacity has been evaluated as $R_{c(\alpha=big)} > 90kN$ (to be evaluated case for case, in accordance with the angle). In average, the best performances in terms of load-carrying capacity under the generic external action are the one of the *halved undersquinted* with squint $\alpha = 60°$ (see Diagram 7-1, -diagram 7-2, with overview of Figure 7-2).

The *halved undersquinted* with any inclination of the squint does not show any out-of-plane resistance.

The failure mode depends on the external load conditions and the angle. The most significant and prevalent failure mode is the shear / tension perpendicular to the grain failure in the point B. Another relevant failure mode is the buckling registered for big angles loaded in pure bending.

10.3.2 Intermediate joint's geometries

In case of the *stop-splayed* connection. With same inclination of α and same length of the joint $l_j = 2 \cdot h$, the increasing of β brings to a reduction of the length of the lower squint (or rather the surface 2). This, causes a further reduction of the load-carrying capacity of the joint in pure bending and in pure compression with increasing probability of buckling failure for low amounts of pure bending (see Diagram 7-14). Therefore, the only increasing of the inclination β of the surface 1 does not bring any enhancement of the performances in the joint. The pure bending resistance is in fact equal to zero.

On the other side, in case of *halved undersquinted and tabled scarf* joint, the pure bending tests (see Annex A) show that the addiction of the *table* improves the load-carrying capacity in pure bending of the joint respect to the *halved undersquinted* with correspondent inclination α of the squint . For this connection, the shear failure of the block B'C'C has to be taken into account as relevant failure mode.

10.3.3 *Stop – splayed undersquinted and tabled with key scarf* joint (*Jupiter joint*)

IN-PLANE BEHAVIOUR.

The in–plane tests performed on the *stop-splayed undersquinted and tabled with key scarf* joint (*Jupiter joint)* remarked the important influence of the inclination of the *splayed* surface and the key pre-compression.

The inclination β of the *splayed* surface in association with the presence of a key confers an improvement in the load-carrying capacity in the lower branch of the diagram (low compression and bending action).

The table and key are important components that increase the load-bearing behaviour of the general *stop-splayed* form. On one side, they increase the general performances of the joint; on the other side, depending on the given pre-compression, they can also influence the failure mode. The pre-compression conferred by the key depends on the key's angle. The optimal ratio between the length and the height of the key (two wedges key, square-cut key) has been found in 1:6. The key also confers the joint stability (no buckling failure)

under pure bending or low compression and bending loads (see above the *halved undersquinted scarf* with equivalent squint α = 60° and external load conditions R60_M0).

The 'cut' of the key also has an effect on the joint performances. The *square-cut* key installation causes the joint to be loaded in compression perpendicular to grain during the pre-compression phase. This effect is disadvantageous for the capacity of the connection in bending. An attempt to improve the *Jupiter joint* and avoid that pre-compression negative effect has been studied by Sangree and Schafer (2009). It has been proven that in a tensile-stressed *Jupiter joint*, the *oblique-cut* improves the joint axial stiffness, because during the key-installation phase avoids the compression perpendicular to the grains (see Figure 2.9 and Annex D).

The combined compression and bending load-bearing capacity is comparable to the one of the *halved undersquinted*, but the pure compression load-bearing capacity is lower.

The failure modes depends on the external load conditions (Figure 7-15). The main failure mode in combined compressive and bending force up to $N = 0.2 \cdot F_u$ is the shear failure (FM V); with the increasing of the load $N > 0.2 \cdot F_u$ the main failure mode is the shear / tension perpendicular to the grains in the point B (FM II) or points B and C (FM III). In pure bending, prevalent is the shear failure (FM V) and in pure compression the FM II or FM III. The solution to increase the shear resistance, or rather the pure compression / bending load-carrying capacity of the *Jupiter joint* is to increase the length of the joint / height of the beam ratio (in the present investigation is equal to 2).

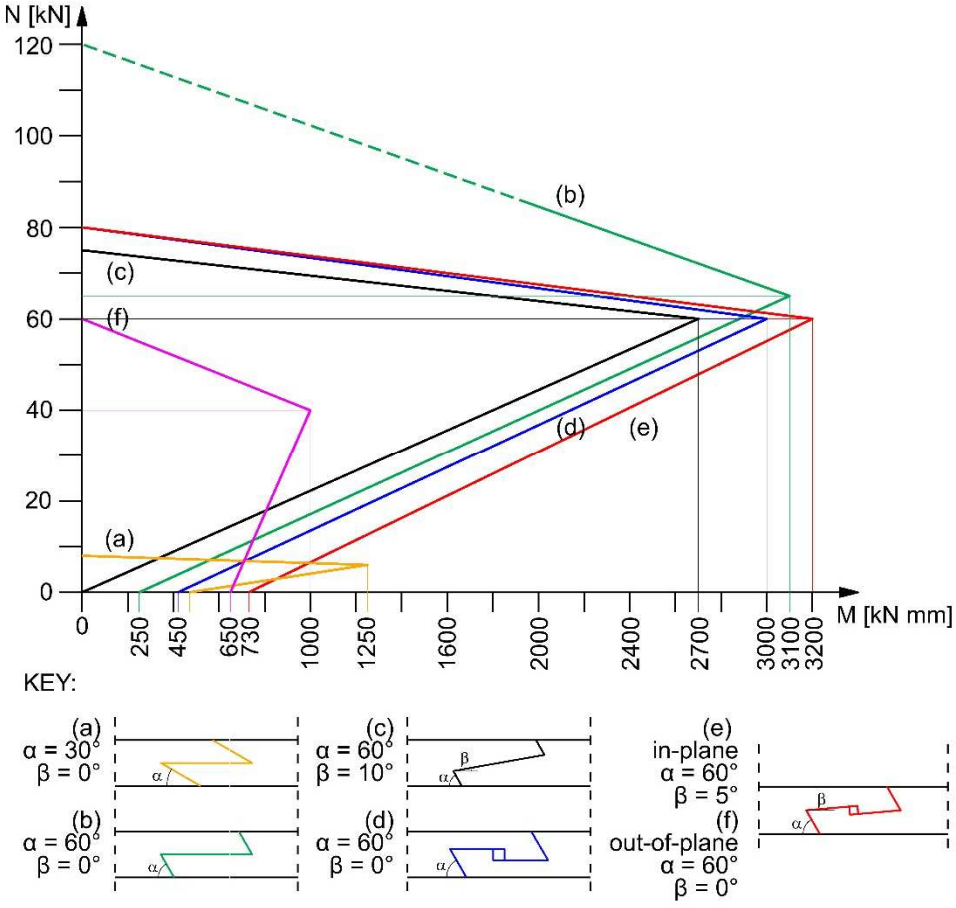

Figure 10-1 – Simplification of the load-bearing behaviour of the (a) *halved undersquinted scarf* α = 30°; (b) *halved undersquinted scarf* α = 60°; (c) *stop-splayed and undersquinted scarf*, (d) *halved undersquinted and tabled scarf with key*; (e) in-plane and (f) out-of-plane *stop of the splayed undersquinted and tabled with key scarf* joint (*Jupiter joint*) .

OUT-OF PLANE BEHAVIOR.

The out-of–plane tests performed on the *stop-splayed undersquinted and tabled with key scarf* joint (*Jupiter joint)* remarked the important influence of the key. The presence of the pre-compression of the key, in fact, guarantees the load-carrying capacity of the *Jupiter joint* along the weak axis.

The failure modes of the *Jupiter joint* in case of out-of-plane tests have to be divided in tensile stressed side and compression stressed side (Figure 7-18 and Figure 7-19). For joints loaded with small amounts of compression and prevalence of bending force, the general prevalent failure mode is the shear failure (FM V); vice versa, the joints loaded with bigger amounts of compression, the prevalent failure mode are the (FM II) and (FM III) shear / tension perpendicular to the grains failure in B (and C).

10.4 Stiffness evaluation

10.4.1 Stiffness in the experimental tests

In the present work, the experimental evaluation of in-plane rotational stiffness values of the *halved undersquinted scarf* joint, *halved undersquinted and tabled scarf joint* (tests reported in the Annex A), *stop – splayed and undersquinted scaf joint, halved undersquinted and tabled with key* and *stop – splayed undersquinted and tabled with key scarf* joint (*Jupiter joint*) is done. For the *halved undersquinted scarf* joint and *Jupiter joint*, the evaluation is also done for out-of-plane behaviour.

The tests demonstrate that for the evaluation of the rotational stiffness of a wood-wood joint, not only the geometry, but also the orientation of the element that contains the joint has to be considered. In fact, the variation of the rotational stiffness has an influence on the load-bearing behaviour of the structural element. The final experimental values of rotational stiffness for all the tested joints in pure bending are resumed in the Table 7-14. Here, both the orientations horizontal and vertical of the specimen are considered, when available.

IN-PLANE BEHAVIOUR.

Considering the most unfavourable situation (horizontal orientation) the bigger is the angle α in the *halved undersquinted* the lower the rotational stiffness. For angles $\alpha > 45°$ the joint shows null rotational stiffness.

The presence of the *table* in the *halved undersquinted and tabled* confers rotational stiffness also to the angles with squint $\alpha > 45°$ (see Annex A). As a conclusion, the table confers the rotational stiffness to the joint.

Finally, the rotational stiffness of the *Jupiter joint* in comparison with the one of the *halved undersquinted* (*and tabled*) *scarf* joint. In the *Jupiter joint* the presence of both the *table*, wedges, and also the inclination of the surface 2 ($\beta \neq 0°$) further increases the rotational stiffness along the strong axis.

OUT-OF-PLANE BEHAVIOUR.

The out-of-plane rotational stiffness of the *halved undersquinted scarf* is considered equal to zero, while the *Jupiter joint* shows a minimum amount of rotational stiffness due to the presence of the key that pre-stress the connection.

10.4.2 Stiffness in the numerical tests (*Jupiter joint*)

In the numerical tests, the stiffness of the hinges and the structure are described in the Table 9-3. The *rib inner connection n° 11*, the *Jupiter joint*, is set with equal to zero *torsional rotational stiffness* ($k\varphi x = 0$) and *rotational stiffness along the weak axis* ($k\varphi z = 0$), while along the strong axis the rotational stiffness is $k\varphi y = 100$, set with a smaller value than in the results, on the safe side.

From an accurate lecture of the table of results Table 9-14, on one side, the value of torsional moment M_T is equal to zero in the perfect structure (CO15, CO11); on the other side, it is not equal to zero in both the imperfect load cases (LC3, LC4) and combinations (CO8, CO9, CO10, CO12, CO13, CO14). The same is valid for the M_z value of moment along the *z* axis (*weak* axis), for both the imperfect and perfect structure. As a conclusion, the imperfections affect the torsional and weak axis' responses along the beam's axis.

In all the load cases and combinations, the response, in terms of load capability in the *Jupiter joint* and in the general cross section is acceptable. The resultant stresses in compression are very low respect to the cross-section capability, and verified. On the other side, in the CO14 the load capability of the *Jupiter joint* reaches the 75% in correspondence of the exposed side, much more than in all the other combinations. Therefore, can be concluded that the horizontal wind load is the most relevant effect in the performed analysis. On the other side, the imperfections do not affect significantly the stress in both the *Jupiter joint* and the cross-section.

According to the performed experimental tests, both the strong and weak axis have a value of rotational stiffness different from zero $k\varphi y = k\varphi z \neq 0$. Therefore, the increase of the rotational stiffness along the weak axis ($k\varphi z > 0$) of the hinge, may avoid the presence of traction stresses in the connection (FEM response; CO14) as a consequence of the lateral wind loads.

In conclusion, the present work does not deal with torsional resistance in the *Jupiter joint*, and therefore the rotational stiffness along the weak, and torsional axis were considered as zero, on the safe side. For an implementation of the FEM model, more experimental tests are required.

10.5 Case study

At the time of the dome's erection, the carpenters chose the *Jupiter joint* for practical reasons and "structural feeling" more than because of a scientific point of view. Nevertheless, the reason why the *Jupiter joint* was the right choice, according to the master experience, lies in the structural efficiency of such wood-wood connection. In the present work, the scientific explanation for the use of the joint has been done.

The different factors that can influence the choice of the *Jupiter joint* (among other wood-wood connections) for the erection of the dome, are either geometry and material factors, or constructive factors. As is following resumed, the constructive factor, i.e. the mechanical behaviour and assembly of the structure are the most determinant factors for the choice of the *Jupiter joint* connection among others.

10.5.1 Mechanical behaviour

As already concluded in the Chapter 10.3, the *Jupiter joint's* mechanical properties can be defined an improvement of the most basic *halved undersquinted scarf* joint. To understand the reason of the choice of the *Jupiter joint* as main structural connection, a comparison is following done.

1. On one side, the *Jupiter joint* has less compression capacity along the strong axis than the *halved undersquinted* scarf joint; on the other side, the *Jupiter joint* has similar bending capacity with the *halved undersquinted* scarf joint.
2. The *Jupiter joint* has been shown shear failure, while the *halved undersquinted* buckling instability. The shear failure of the *Jupiter joint* can be solved by using a bigger ratio joint length / height of the beam without drop of load-carrying capacity but an improvement; while, the buckling instability in the *halved undersquinted* can be avoid by using lower inclination of the squint α with significant decreasing of the load-carrying capacity in pure compression of the connection.
3. In the *Jupiter joint*, the pre-compression conferred by the wedges can accelerate the shear failure. On the other side, the *Jupiter joint*, thanks to the presence of the wedges, shows out-of-plane load-carrying capacity, while the *halved undersquinted* does not.

As a conclusion, the behaviour under compressive loads is of primary concern, but when looking at the curvature of the dome's beams and the overall behaviour of the frame, also the bending moment and the behaviour along the weak axis play important roles. In accordance with the FEM analysis, the beam (and the connection) is mainly stressed in tension because of the lateral wind loads, while the stresses in compression are very few respect to the real compression capacity of the connection. Therefore, the required capability of the joint, according to the case study, has not to be high in compression, but in tension and effective along all the directions because of the structural shape (see geometry factors in the Chapter 8.6.1).

10.5.2 Assembly reason

The connection, because of the presence of the wedges, offers the possibility to hold the structure in position during the construction process (see Chapter 8.6.4, Figures 8-33, Figure 8-34, and Figure 8-35); therefore, is very probable that this connection was chosen among others for its very high practical efficiency.

As a conclusion, the *Jupiter joint* was mainly chosen for its good level of load-carrying capacity along both the strong and weak axis and some amount of tension capacity (with attention to the shear failure), among the practical constructive reasons.

10.6 OUTLOOKS

The present research sets the stage for a new field of research about the characterization of old wood-wood *scarf joints*, in order to implement their use and / or for a better understanding in phase of restoration of old structure where that connections are present. The systematic approach to old structures is not possible, therefore, for a good understanding of them, more research is needed.

- More experimental information about the real rotational stiffness along the torsional axis and weak axis of the *halved undersquinted* and *Jupiter joint* is required.
- The global approach to the mechanical behaviour, the fundamental geometric parameter and the vulnerability of the *scarf* joints given by the present work have to be resumed in an all-encompassing model.
- More numerical information about the internal distribution of stresses in the joint is required for the comparison with the experimental data.

- An implementation *application-oriented* of the model with characteristics values of load-carrying capacity for the connections is required for both the practice of use and the application in numerical models of old timber structures.
- More information about the influence of the geometry on the material failure is needed for the evaluation of F_f, the action that is necessary to start the propagation of the crack ($F_{f,B}$ in B and $F_{f,C}$ in C) This information is useful for the evaluation in advance of the load-carrying capacity of the joint with the generic inclination of the squint.
- Some research about the effect of the contemporary action of two forces with different verse acting on a single fibre (for the evaluation of the action that is necessary to start the propagation of the crack) has to be done in order to implement the analytical model.

REFERENCES

1.1 BOOKS AND CONFERENCE PROCEEDINGS

Adam J. P. (1988), *L'arte di costruire presso i Romani*. Longanesi, Milano.

Aira J. R., Arriaga F., Íñiguez-González G., Guaita M. (2015). Failure modes in halved and tabled tennoned timber scarf joint by tension test. In: *Construction and Building materials.* 96 pages 360-367.

Ashurst, J. and N. (2012). *English heritage. Practical building conservation: TIMBER*. Ashgate. ISBN: 9780754645542.

Avrami E. edited by (2010). *Preserving Haiti's Gingerbread Houses 2010 Earthquake Mission Report*, World Monuments Fund, New York.

Bizzeti F. (2015) *Analisi sperimentale di pannelli in adobe e bambù: un esempio di recupero di antiche tecniche costruttive latinoamericane*. Unpublished master thesis. Università degli studi di Firenze, Italia.

Blass H. J., Aune P. et alii. (1995). Timber Engineering, *STEP 1 (STEP 2)*, *Basis of design, material properties, structural components and joints*, Centrum Hout, The Netherlands.

Böttcher D. (2008). *Sanierung von Holz- und Steinkonstruktionen*, Bauwerk, Berlin, Germany.

Branco J. M., Descamps T. (2015) Analysis and strengthening of carpentry joints. In: *Construction and Building Materials,* 97 (2015) 34–47.

Cardoso R., Lopes M., Bento R. (2004). *Earthquake resistant structures of portuguese old 'pombalino' buildings*, 13th World Conference on Earthquake Engineering, Vancouver, B.C., Canada, August 1-6, Paper No. 918.

Cóias V. (2007). *Structural rehabilitation of ancient buildings* (in Portuguese). Lisbon: Argumentum, GECoPRA.

Collings G. (1992). *Circular Work in Carpentry and Joinery*, illustrated by Karl Shumaker, Roger Holmes, Canada.

Dederich L., Koch J., Fischer M. (2004). *Erneuerung von Fachwerkbauten*, INFORMATIONSDIENST - HOLZ. Holzbau handbuch, Reihe 7, Teil 3, Folge 1: 12/2004. Retrieved from http://informationsdienst-holz.de/home/ . ISSN-Nr. 0466-2114

Fairham W., Roberts G. R. (1920). *Woodwork Joints: Carpentry, Joinery, Cabinet-Making: The Woodworker Series*, Ewan –Bros., London. ISBN: 978-1519715173.

Fairham, W. (1921). *Woodwork joints; how they are set out, how made and where used; with four hundred and thirty illustrations and a complete index of eleven hundred references.* Philadelphia and London: J. B. Lippincott company.

Gatzelu L., D., (1899). *Carpinteria de armar*, Madrid.

Gerner M. (1990). *Historische Häuser erhalten und instandsetzen*, Augustus Verlag, 2. Aufl. S.131-132.

Gerner, M. (1983). *Fachwerk: Entwicklung, Gefüge, Instandsetzung*, Deutsche Verlags-Antstalt, Stuttgard. ISBN: 3-421-02475-8.

Giordano G. et alii. (2010). *Tecnica delle costruzioni in legno*, V edizione, Hoepli, Milano.

Görlacher R. (1996). *Hölzerne Tragwerke. Untersuchen und Beurteilen*, Sonderforschungsbereich 315, Universität Karlsruhe (TH)

Graubner W. (2004), *Holzverbindungen - Gegenüberstellungen japanischer und europäischer Lösungen*, Deutsche Verlags-Anstalt, München Stuttgard 2004.

Grezel J., (1950), *Manuel de la charpente en bois, n° 9 les assemblages*. ICOMOS Document, Annales de l'Institut Technique du Bâtiment et des Travaux Publics, Centre d'études supérieure, Paris.

Gulkan P., Langenbach R. (2004), *The earthquake resistance of traditional timber and masonry dwellings in Turkey*, In 13th World Conference on Earthquake Engineering Vancouver, B.C., Canada, August 1-6, 2004, Paper No. 2297. PHOTO

Gustafsson J., (ca. 1990). *A study of strenght of notched beams.* Division of Structural Mechanics, Lund Institute of Technology. Lund, Sweden

Gustafsson P. (2003). *Fracture perpendicular to Grain – Structural applications*. In: Thelandersson and Larsen H., J., Timber Engineering, Wiley.

Gustafsson, P. J. (1988). A study of strength of notched beams. In: *Proc. of CIB-W18A Meeting 21*, Parksville, Canada. Paper No. CIB-W18/21-10-1.

Hewett C. A. (1980). *English Historic Carpentry*. London and Chichester: Phillimore and Co., Ltd.

Hirst, E., Brett, A., Thomson, A., Walker, P. and Harris, R. (2008). *The structural performance of traditional oak tension and scarf joints*. In: 10th World Conference on Timber Engineering, 2008-06-02 - 2008-06-05.

Holzer S. (2015). *Statische Beurteilung historischer Tragwerke Band 2, Holzkonstruktionen*, Ernst & Sohn, Berlin, Germany.

Jackson A.W. (1921). *The Half Timber House*. McBride, Nast & Company. Retrieved from http://archive.org/stream/halftimberhouse005929mbp/halftimberhouse005929mbp_djvu.txt

Kessel M. H., Augustin R. (1991). *Lateral stability of roofs*, International Timber engineering conference London, volume 4., pp.362-369.

Kessel M., Augustin R. (1995). Load behaviour of Connections with Pegs, *Timber Framing*. 38 (12/1995). 6-9.

Kessel M., Augustin R. (1996). Load behaviour of Connections with Pegs II, *Timber Framing*. 39 (3/1996). 8-11.

Kessel M., Speich M., Hinkes F. J. (1989). The reconstruction of an eight-floor timber frame house at Hildesheim (FRG). In: *Il restauro del legno, Atti del 2° Congresso Nazionale Restauro del Legno* (by Tampone G.), Firenze, 8-11 November. Firenze: Nardini. 217-222.

Krauth, T.. Meyer, F. S. (1985). *Die Bau- und Kunstzimmerei: mit besonderer Berücksichtigung der äußeren Form*, Seemann, Leipzig.

Lagenbach, (2013). *Timber Frames and Solid Walls: Earthquake Resilient Construction from Roman Times to the Origins of the Modern Skyscraper*, Hearth 2013 Proceedings

Langenbach R. (2006). *Saga of the Half-timbered Skyscraper: What Does Half-Timbered Construction have to do with the Chicago Frame?* In: Proceedings of the Second International Congress on Construction History, Cambridge University.

Larsen, H. J. and Gustafsson, P. J. (1990). *The fracture energy of wood in tension perpendicular to the grain – results from a testing project*. In: Proc. of CIB-W18A Meeting 23, Lisbon, Portugal. Paper No. CIBW18/23-19-2.

Lopez de Arenas, D., (1912). *Carpinteria de lo blanco*, Madrid.

Luxner H. (2005). *Fachwerk-Häuser*, Reinhard Welz Vermittler Verlag e.K.. ISBN: 3-938622-o7-5.

Madsen B. (2000). *Behaviour of Timber Connections*. Vancouver, Canada: Timber engineering Ltd.

Madsen B. (2000). Structural b*ehaviour of Timber*. Vancouver, Canada: Timber engineering Ltd.

Matauco E. N., (2003). *La carpinteria de armar española*, Munillaleria.

McGuire, J. (1995). *Notes on Semi-Rigid Connections. Finite Element Modeling Continuous Improvement*. Retrieved from http://femci.gsfc.nasa.gov/semirigid/index.html

Orozco Melgar M. E., El quatier français de Santiago de Cuba, in *Revolución y Cultura* 1 (2004): 11-18.

Otten, J. B.. (2016) *Experimentelle und analytische Untersuchung auf Tragfähigkeit und Gebrauchstauglichkeit des beidseitig schräg eingeschnittenen Geraden Blattes*. Unpublished bachelor. Hochschule HAWK Hildesheim.

Paradiso M, Milani P et al. (2011). *Atlas del patrimonio arquitectónico y cultural del casco històrico de Santiago de Cuba*. Edición Medina, Borgo San Lorenzo.

Paradiso M, Perria E et al. (2013). *La Catedral de Santiago de Cuba como ejemplo emblemático de la difusión de saberes entre Europa y Latino-América*, CNHC 2013 Proc. Vol. 2, Congreso Nacional de la Historia de la Construcción, Ed. Instituto Juan de Herrera, Madrid, Spain.

Paradiso M, Tempesta G et al. (2012), *Degradation and consolidation of the Cathedral of Santiago de Cuba*, SAHC 2012 Proc., Int. Con. on Structural Analysis of Historical Construction, Jerzy Jasienko Ed., Breslavia, Poland, 2012, pp. 508-516.

Paradiso M, Tempesta G et al. (2012). Static and antiseismic behaviour of the Cathedral of Santiago de Cuba, SISMOS 2012 Proc., IV Int. Conf. on Danger, Geologic Risk and Seismic Disasters, Ediciones UO, Stgo de Cuba, Cuba, 2012, cd-rom.

Paradiso M, Tempesta G et al. (2012). *The dome of the Cathedral of Santiago de Cuba: degradation and consolidation*, Proc. vol 1, Int. Conf. Domes in the world, Nardini editore, Firenze, Italy. pp. 215-228.

Perria E., Sinicropi D., Paradiso M. (2013), *La Catedral de Santiago de Cuba cómo ejemplo emblemático de la difusión de saberes entre Europa y Latinoamérica*. In: Huerta, Santiago y Fabián López Ulloa (eds.). Actas del Octavo Congreso Nacional de Historia de la Construcción. Madrid, 9-12 de octubre de 2013. Madrid: Instituto Juan de Herrera.

Perria, E., Paradiso M., Kessel M., Sieder, M.. (2016). *Characterization of the halved and undersquinted scarf carpentry connection*. In: Proc. of WCTE 2016, World conference on Timber engineering, Vienna university of technology, Grafisches zentrum HTU, Austria.

Perria, E., Paradiso M., Kessel M.. (2016). *Experimental verification of the static model for the characterization of the halved and undersquinted scarf connection*. In: Proc. of 10th International Conference on Structural Analysis of Historical Constructions, in press, Leuven, Belgium.

Poletti E. (2013). *Characterization of the seismic behaviour of traditional timber frame walls*, Tese de Doutoramento, Universida do Minho.

Porteous J., Kermani A. (2013) *Structural Timber Design to Eurocode 5*, Blackwell Science Ltd, Oxford, UK.

Ruggieri N. (2013). *Il sistema antisismico borbonico muratura con intelaiatura lignea genesi e sviluppo in Calabria alla fine del '700*. Bollettino ingegneri N. 10 – 2013, pp. 3-14.

Sánchez, F. ,De Julián, J. J.,Ordoñez, A., (2010). *Tipologías Constructivas En una Ciudad Patrimonio de la Humanidad: Trinidad, Cuba - Constructive Typologies in a Patrimony City: Trinidad*, Cuba Revista de la Construcción Vol. 9 Nº 1 – 2010, Santiago de Cuba, pag. 89 – 97.

Sangree R. H., Schafer B.W. (2009). Experimental and numerical analysis of a stop-splayed traditional timber scarf joint with key. In: *Construction and Building materials.* 23 pages 376-385.

Schneider K. (1997). *Fassadenentwicklungen im städtischen niederdeutschen Fachwerk,* (unedited Diplomarbeit, Gottfried Wilhelm Leibniz Universität Hannover). Retrieved from http://www.diplom.de/e-book/216175/fassadenentwicklungen-im-staedtischen-niederdeutschen-fachwerk

Schübler, J., J., (1749). *Zimmermann Kunst*, Nürberg.

Sobon J. A. (2002). *Historic American Timber Joinery: A Graphic Guide*, Pub. By Timber Framers Guild, Ed. by Kenneth Rower. Retrived from https://www.ncptt.nps.gov/wp-content/uploads/2004-08.pdf.

Stade F., (1904). *Die Holzkonstruktionen*, Moritz Schäfer, Leipzig.

TEMTIS (2008). *Handbook 1 – timber structures*, Educational Materials for Designing and Testing of Timber Structures – TEMTIS, Leonardo da Vinci Pilot Project.

TEMTIS (2008). *Handbook 2 - design of timber structures according to ec 5*, Educational Materials for Designing and Testing of Timber Structures – TEMTIS, Leonardo da Vinci Pilot Project.

TEMTIS (2008). *Instruction handbook to elaborated case studies Guide to case studies for lectures*, Educational Materials for Designing and Testing of Timber Structures , Leonardo da Vinci Pilot Project.

Thelandersson S., Larsen H. J. (2003). *Timber Engineering*. Chichester : Wiley.

Touliatos P. (2004). Evaluation and drafting of recommendations for interventions in buildings of the historical settlement of Lefkas (in Greek). *Organization for seismic design and protection*, NTUA, Public Library of Lefkas Editions, Athens, Greece.

Traditional Timber Framing: a Brief Introduction, University of the West of England, Bristol, 2008. Retrieved from http://fet.uwe.ac.uk/conweb/house_ages/timber/print.htm

Tregold, T., (1858). *Elementary principles of carpentry*, John Weale, London.

Van Ravenswaay C., Schroeder A. E. (2006). *The Arts and Architecture of German Settlements in Missouri. A Survey of a Vanishing Culture.* University of Missouri press.

Warth O., (1900). *Konstruktionen in Holz*, Derlag, Leipzig.

Yeomans D. T. (2008). Repairs to Historic timber structures: Changing attitudes and knowledge. In: *Structural analysis of historic construction* (eds D'ayala & Fodde), Taylor and Francis, London.

Zan B. (2015). *Calcolo e verifica delle strutture di legno*, Dario Flaccovio editore, Palermo.

1.2 CODES AND NORMS

C.T.E., Documento Básico SEM (2006). *Seguridad estructural – Estructuras de madera*. In Código técnico de la edificación, ministerio de vivienda, Spain.

CNR-DT 206/2007 (2008). Istruzioni per la Progettazione, l'Esecuzione ed il Controllo delle Strutture di Legno. Consiglio Nazionale delle Ricerche, Roma.

DIN 1052 (2004). Entwurf, Berechnung und Bemessung von Holzbauwerk. Allgemeine bemessungsregeln und bemessungsregeln fur den hochbau. CEN European Committee for Standardization, Brussels.

DIN 1052 Zimmermannsmäßige Verbindungen. *TP_II-Holz-Holz-Verbindungen.pdf,* Holzbau-Kompetenzzentren. Bundesbildungszentrum Des Zimmerer- und Ausbaugewerbes, Kassel. Retrieved from http://www.holzbau-kompetenzzentren.de/bundesbildungszentrum-kassel/t-ii-normungswesen.html

DIN 1052: 2004-08, CEN European Committee for Standardization, Brussels. Part 15 (p.156-158).

DIN EN 1912:2012-06 (German version); EN 1912:2012 (English version). Structural timber strength classes Assignment of visual grades and species. Normenauschuss bauwesen (NABau im DIN). Juni 2012.

DIN EN 1995-1:2005, NCI NA 6.8.3. (2005). *National German Annex to Eurocode 5: design of timber structures. Part 1–1. Common rules and rules for buildings*. Brussels: CEN, European Committee for Standardization.

DIN EN 26891:1991-07, *Holzbauwerke; Verbindungen mit mechanischen Verbindungsmitteln; Allgemeine Grundsätze für die Ermittlung der Tragfähigkeit und des Verformungsverhaltens* (ISO 6891:1983); Deutsche Fassung

EN 1991-1-4 (2005). *Eurocode 1: Actions on structures - Part 1-4: General actions - Wind actions*. CEN European Committee for Standardization, Brussels.

Eurocode 1990 (2002). Annex D (informative) *Design assisted by testing*

Eurocode 1990 (2002). *Eurocode - Basis of structural design*. CEN European Committee for Standardization, Brussels.

Eurocode 5. (2005). *Eurocode - Design of timber structures* - Part 1-1: General – Common rules and rules for buildings. EN 1995-1-1:2004. CEN European Committee for Standardization, Brussels.

UNI – EN1995 1 / CNR DT 206:2007

UNI EN 14081-1 *Legno strutturale con sezione rettangolare classificato secondo la resistenza – requisiti generali*, Dicembre 2011.

UNI EN 338 Structural timber - Strength classes

ANNEX A COMPARISON AMONG THE PURE BENDING PERFORMANCES OF THE *HALVED UNDERSQUINTED* AND *HALVED UNDERSQUINTED AND TABLED SCARF* JOINTS

A.1 Introduction

The following tests show the flexural behaviour of the *halved undersquinted* and *halved undersquinted & table scarf* joints.

In the first part of the Annex, tests on the *halved undersquinted scarf* with horizontal position are presented. The tests were performed with the Machine 1 and horizontal orientation (Figure A-1). In order to compare the load-carrying capacity of the joint depending on its position in a structure, the tests with the horizontal orientation are compared with the tests performed with vertical orientation presented in the Chapter 7.2.

In the second part of this Annex the *halved undersquinted & table scarf* joint's flexural behaviour is analysed. This connection, not analysed in the main work, is provided with a *tabled* shape. The main focus of this tests is to understand the increase of load-carrying capacity of the joint conferred by the table, respect to the simple *halved undersquinted* connection.

At the end of this Annex, the comparison between the flexural behaviour of the two different geometries is given. Different squint's inclinations are also taken into account.

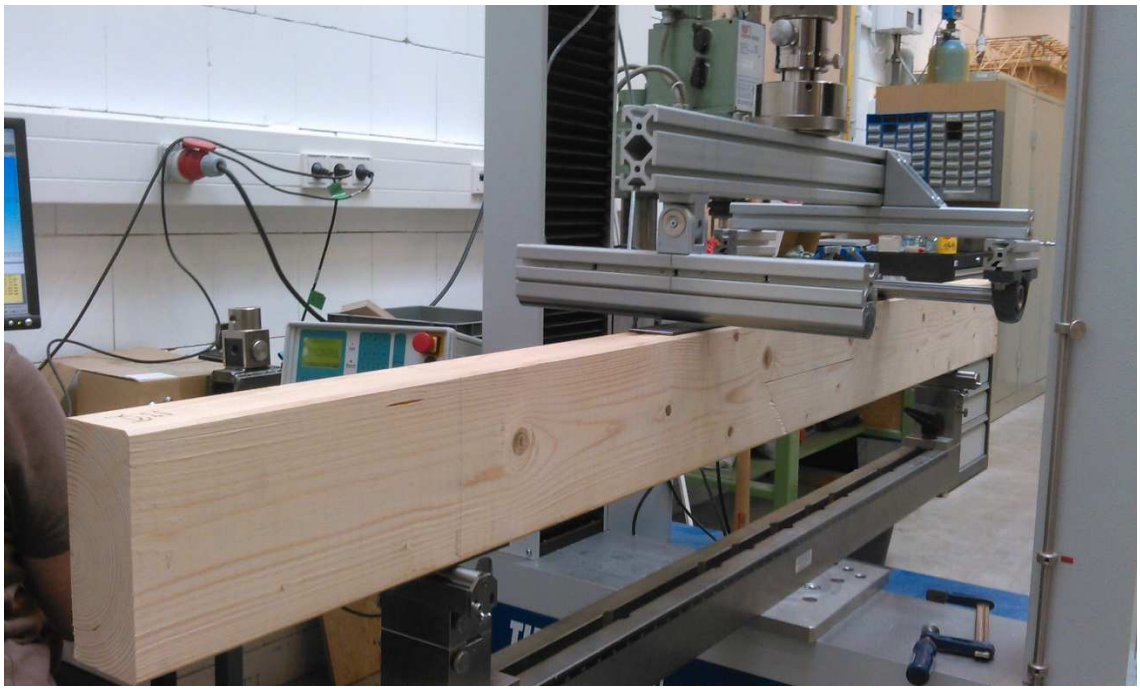

Figure A-1 - Test machine 1 with the specimen, four point bending test asset.

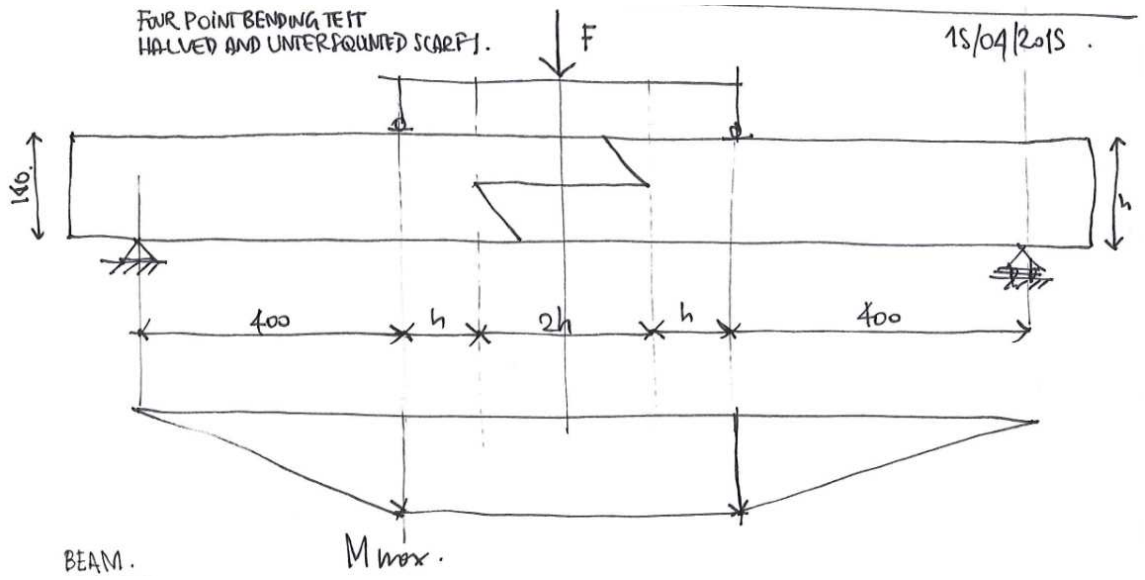

Figure A-2 – *Halved undersquinted scarf* joint. Beam and static asset schema

A.2 Halved undersquinted scarf joint – strong axis' horizontal-oriented bending tests

A.2.1 Tests description

Date: 15/04/2015; Specimen: S1; Procedure: P0 + a.

Connection properties:

$$l_{BC} = l_j = 2h = 280mm$$

$$b = 60mm \qquad \text{A-1}$$

$$a = 400mm$$

External load conditions: M (Figure A-2)

In the following Table A-1 the resume of tests is done. F_u is the ultimate load applied by the machine, when the specimen fails. The relationship between the applied force (F) and the bending action (M), and the normal force (N) are the one in the eq. 5-4. The displacements (u) refers to the displacement of the hydraulic piston. In the Figure A-3 to Figure A-8 the single test specimens in the unloaded and failure configuration are reported.

SPECIMEN	Date	Specimen	Procedure	α [°]	Fu [kN]	u [mm]	Mu [kN·mm]	Observations
0415_01	**15-16.04.2015**	S1	P0 + a	45	2.55	10.07	510	
0415_02	**15-16.04.2015**	S1	P0 + a	60	0	∞	0	No load-carrying capacity
0415_03	**15-16.04.2015**	S1	P0 + a	30	3.56	13.34	712	Last tested F. Than unloading even not reaching the loose of loading capacity of the section (but also failed in B).

Table A-1 – *Halved and undersquinted scarf* joint horizontal-oriented bending tests

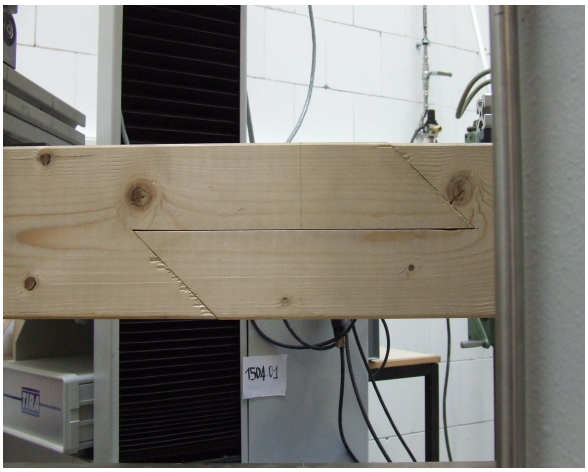

Figure A-3 - TEST 0415_01 (0415_01_1_1,5kN)

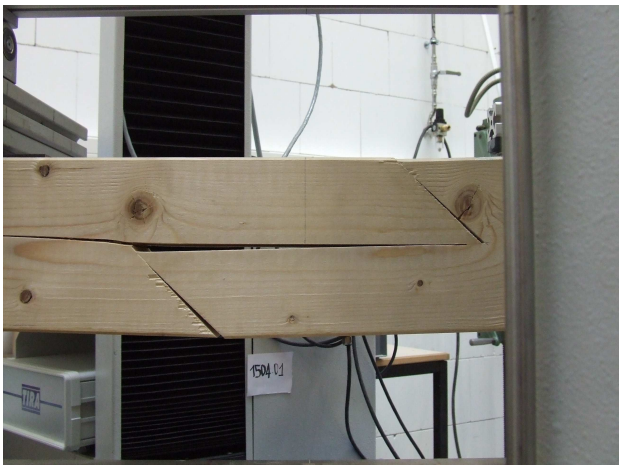

Figure A-4 - TEST 0415_01 . Failure. (0415_01_5_2,7kN_Fu)

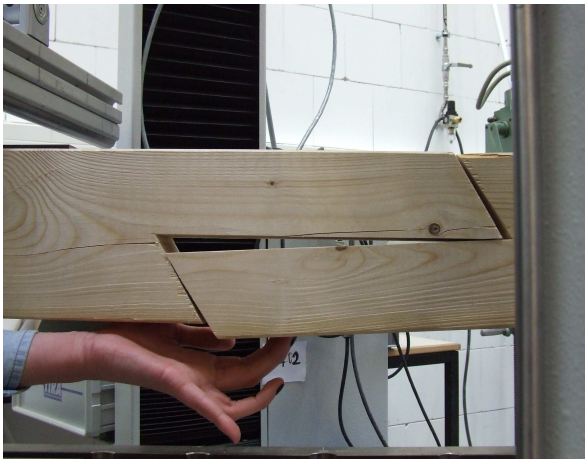

Figure A-5 - TEST 0415_02 - *α=60°*. (0415_02_0kN_def) Deformation with only self weight.

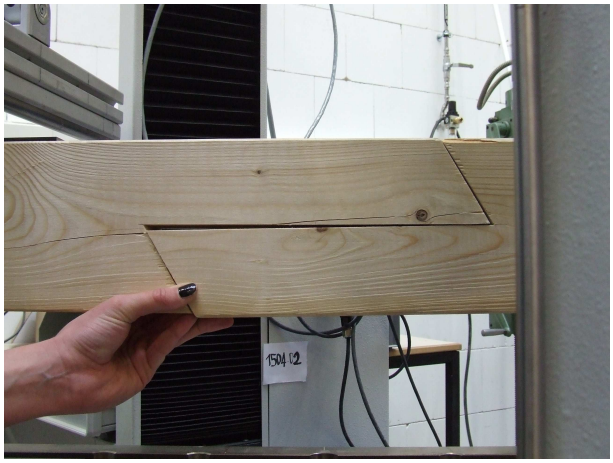

Figure A-6 - TEST 0415_02 - *α=60°*. (0415_02_0kN_Mu) Deformation with only self weight

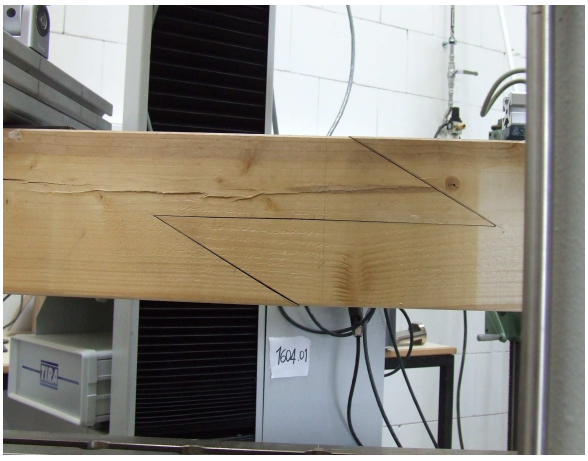

Figure A-7 - TEST 0415_03 - *α=30°* (DSCF6905)

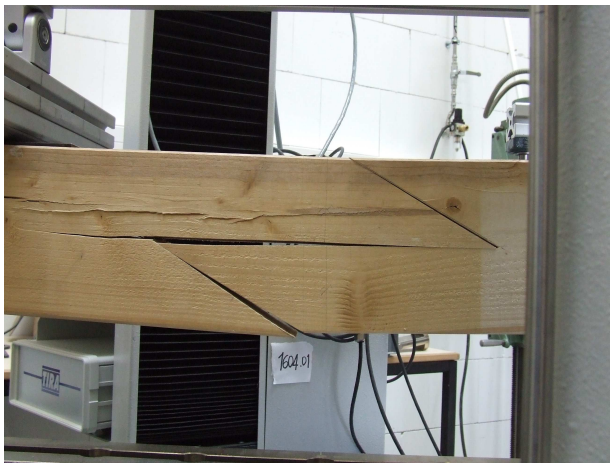

Figure A-8 - TEST 0415_03 - *α=30°*. Failure (DSCF6912)

A.3 Halved undersquinted & tabled scarf joint – strong axis' horizontal-oriented bending tests

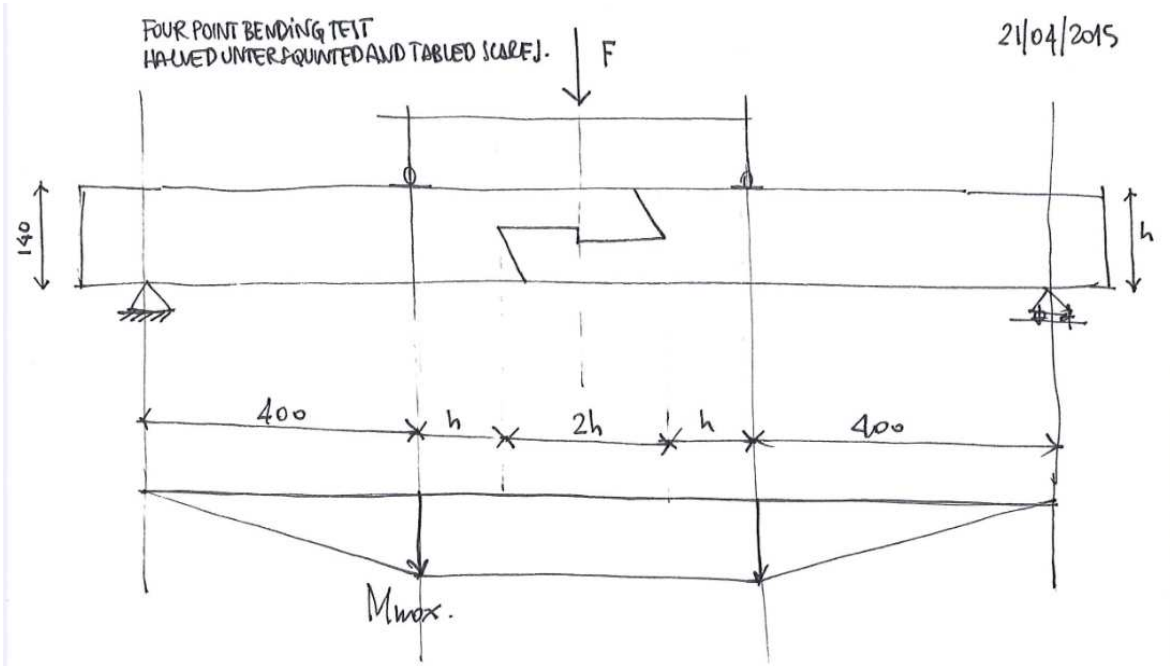

Figure A-9 – *Halved undersquinted & tabled scarf* joint. Beam and static asset schema

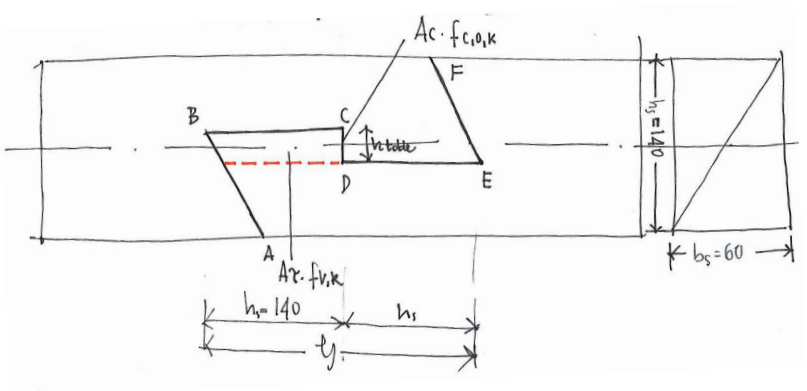

Figure A-10 – *Halved undersquinted & tabled scarf* joint's specimen.
The red dashed line indicate the failure line of the specimen.

Date: 21/04/2015; Specimen: Represented in the Figure A-10; Procedure: P0 + a.

Connection properties:

$h = 140mm$

$l_{BC} = l_j = 2h = 280mm$ A-2

$b = 60mm$

$a = 400mm$

External load conditions: M (Figure A-9).

The dimension of the geometric surfaces of the joint are the ones illustrates in the Figure A-10. The height of the table have been chosen depending on the right aproximation between table's dimensions in existing joints and according to the following analytical aproximation:

$$A_\tau \cdot f_{v,k} = A_c \cdot f_{c,o,k} \qquad \text{A-3}$$

$$A_c = \frac{A_\tau \cdot f_{v,k}}{f_{c,o,k}} = 1600mm^2 \qquad \text{A-4}$$

$$h_{table} = \frac{1600mm^2}{60mm} = 26.6mm \cong 25mm \qquad \text{A-5}$$

In the following Table A-2 the tests are resumed. F_u is the ultimate load applied by the machine, when the specimen fails. The relationship between the applied force (F) and the bending action (M), and the normal force (N) are the one in the eq. 5-4. The displacements (u) refers to the displacement of the hydraulic piston. In the Figure A-11 to Figure A-14 the single test specimens in the unloaded and failure configuration are reported.

Table A-2 – *Halved undersquinted & tabled scarf* joint horizontal-oriented bending tests

SPECIMEN	Date	Specimen	Procedure	α [°]	Fu [kN]	u [mm]	Mu [kN·mm]	Observations
0421_01	**21.04.2015**	S1	P0 + a	60	3.58	9.81	716	Unloading and separation of the piece XBCD
0421_02	**21.04.2015**	S1	P0 + a	45	3.59	13.98	718	Unloading and back in the same shape

Figure A-11 - TEST 0421_01 - *α = 60°* (DSCF6971)

Figure A-12 - TEST 0421_01 - *α = 60°*. Failure. (DSCF6978)

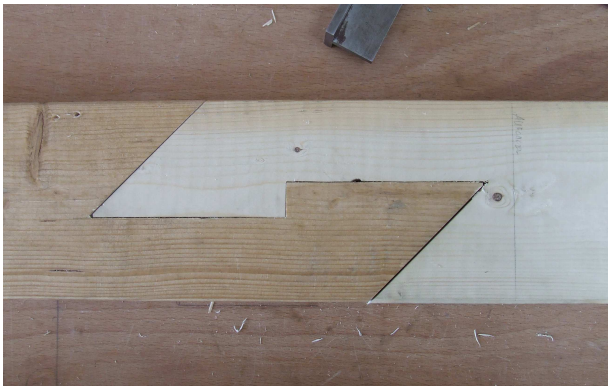

Figure A-13 - TEST 0421_02 (DSCF6969)

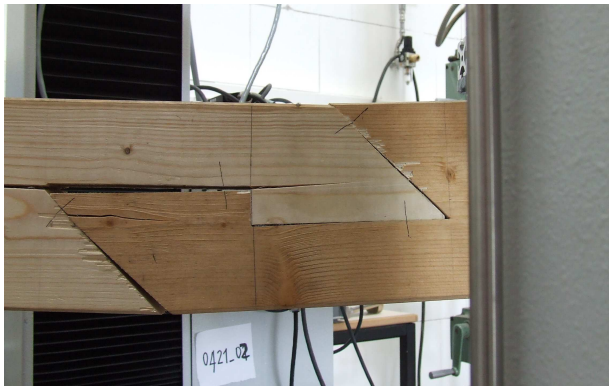

Figure A-14 - TEST 0421_02. Failure. (DSCF6988)

A.4 General observations

In the following Diagram A-1 the force-displacement (F-u) diagram of the *halved undersquinted* and *halved undersquinted & table scarf* joint is illustrated.

On one hand, the *halved and untersquinted joint*'s load-carrying capacity depends on the squint's angle. In fact, specimen 0415_01 (α = *45°*) resisted until a maximum bending force of M_u = 510 kN · mm, while specimen 0415_01 (α = *60°*) did not have any bending resistance (M_u = 0 kN · mm). On the other hand, the specimens of *halved undersquinted & tabled scarf* joint, demonstrated load-carrying capacity for any inclination of the squint. For example, specimen 0421_01 with α = *60°* and 0421_02 with α = *45°* have similar load-carrying capacity up to M_u = 716 kN · m. While specimen 0421_01 (α = *60°*) stopped bearing forces after the first failure at F = 3.6 kN, the 0421_02 (α = *45°*) kept bearing load after the failure at F_u = 3.6kN.

A.5 Conclusions

As a conclusion, it is demonstrated that the shaping of the table in the connection increases the load-carrying capacity of the joint.

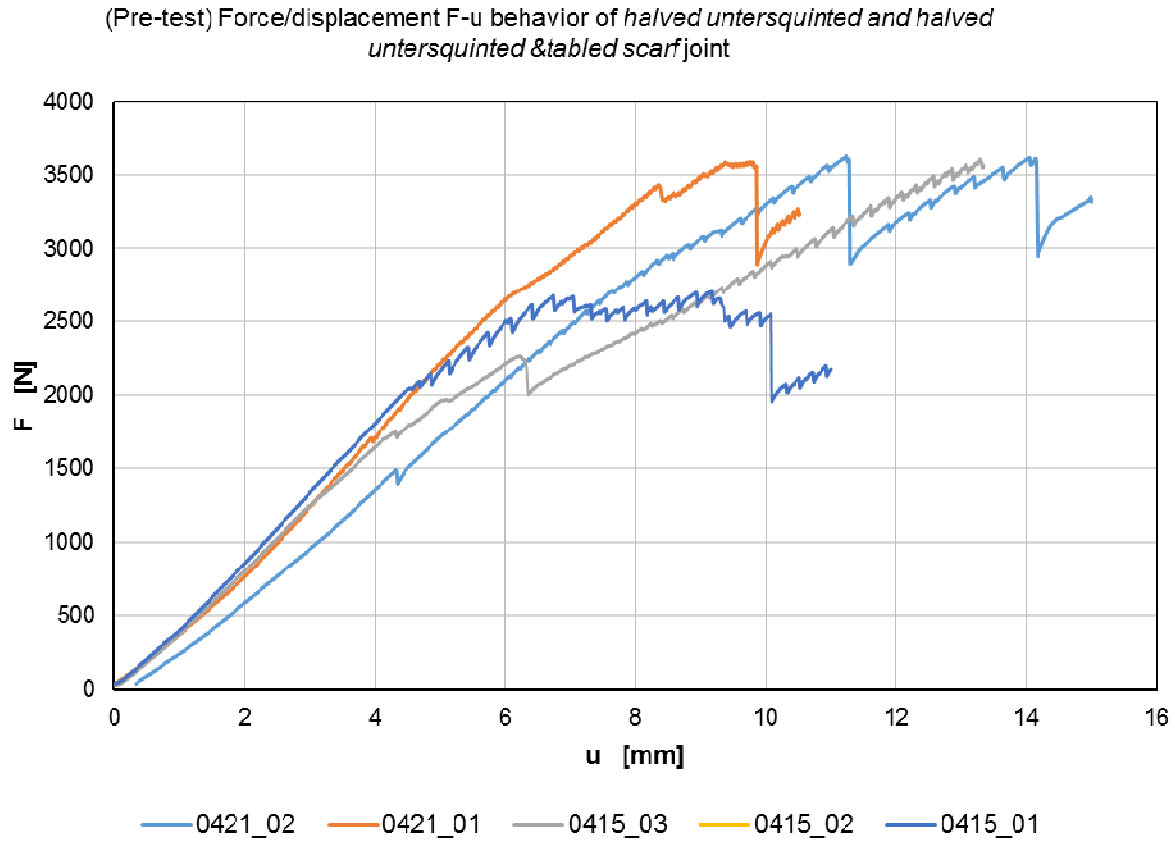

Diagram A-1 – Force displacement behaviour of the *halved undersquinted* and *halved undersquinted & table scarf* joint

ANNEX B EXPERIMENTAL CAMPAIGNS

B.1 Introduction

The present annex contains the tests developed for the *halved undersquinted scarf* with squint *α = 30°* and *α = 60°* given in detail. Furthermore, the analytical models are verified (demonstrated) through the performed tests on the joint.

B.1.1 TESTS: *halved undersquinted scarf* joint

In the following Diagram B-1 and Diagram B-2 the N-M interaction diagram respectively for the *halved undersquinted scarf* with squint *α = 30°* and *α = 60°* are given.

The Table B-1 contains the description of the test results of the mentioned diagrams, performed with both the procedure P1 and P2, where the comparable data are highlighted.

Table B-1 – Description of the test results.

procedure	M_u [kN mm]	F_u [kN]	F_{target} [kN]	Date	specimen	note
α = 30°						
P1 - a	470.61	0.00	-	20/01/2016	R30_F0	FM II
P1 - a	679.19	0.00	-	20/01/2016	R30_F0_2	FM II. Same specimen F_M_2; F_M_3; F_M_4
P1 - c	1345.80	6.41	-	20/01/2016	R30_F0_bis	FM II
P1 - c	879.46	7.87	-	20/01/2016	R30_F0_bis2	FM II
P1 - b	0.00	8.40	-	20/01/2016	R30_M0	FM III
P1 - c	992.66	6.17	-	20/01/2016	R30_F_M	FM II
P1- -d	4.78 (s)	5.48 (s)	1.00	20/01/2016	R30_F_M_2	Stopped, first crack. Same specimen F_M_3; F_M_4; F0_2
P1 - d	4.78 (s)	5.48 (s)	0.50	20/01/2016	R30_F_M_3	Stop, first crack. Same specimen as F_M_2; F_M_4; F0_2
P1 - d	4.78 (s)	5.48 (s)	0.25	20/01/2016	R30_F_M_4	Stop, first crack. Same specimen as F_M_2; F_M_3; F0_2
P2 - c	580.37	1.98	2.00	01/02/2016	R30_N2_Ma	FM II
P2 - c	516.98	1.98	5.00	01/02/2016	R30_N5_M	FM II
α = 60°						
P2 - a	247.65	-0.00	-	01/02/2016	R60_F0	FM IV
P2 - b	-15.99	42.00 (s)	-	01/02/2016	R60_M0	Stopped, instability
P1 - b	-15.39	84.51 (s)	-	01/02/2016	R60_M0_2	Stopped, instability . It can bear more and more load.
P2 - c	1244.16	16.00	16.00	01/02/2016	R60_N16_M	FM II
P2 - c	2069.34	32.06	32.00	01/02/2016	R60_N32_Ma	FM II
P2 - c	2601.72	47.96	48.00	01/02/2016	R60_N48_M	FM II, critic crack points also ε1=1/4 and ε3=1/4
P2 - c	3063.82	63.97	64.00	01/02/2016	R60_N64_M	Test interrupted, danger instab.. Upper plate bent.

Comparable procedures

(s) Stopped test (not up to break)

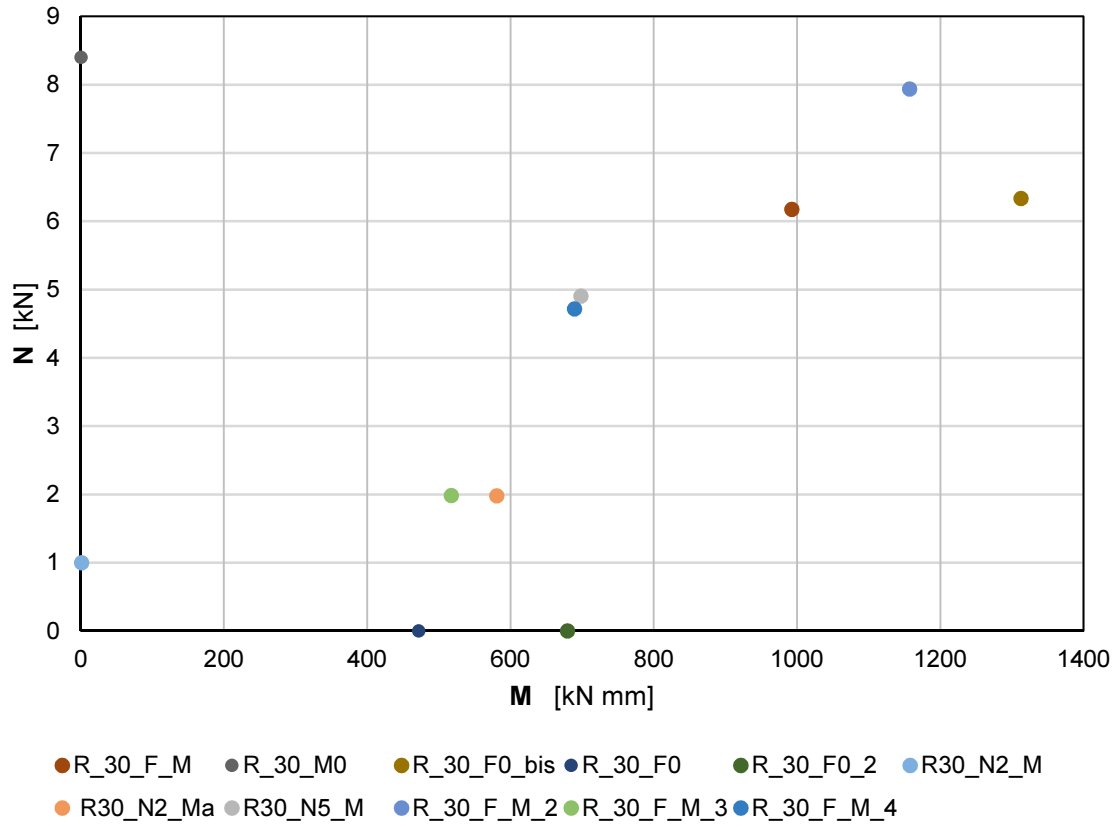

Diagram B-1 – M-N interaction curve for *α=30°*.
Tests performed with P1 and P2 procedures (See Table B-1 for a better legibility)

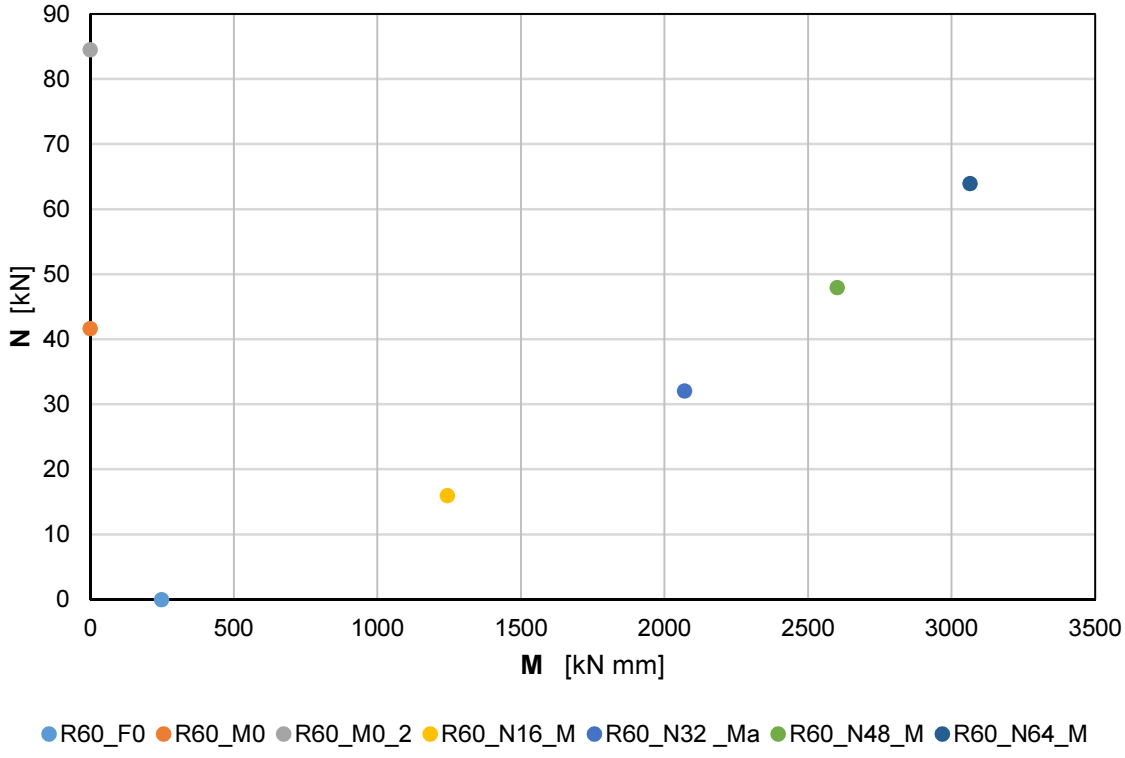

Diagram B-2 – M-N interaction curve for *α=60°* performed with P2.

B.2 Comparison between the analytic and experimental results for the halved undersquinted scarf joint

For both the inclination of the squints *α = 30°* and *α = 60°* the evaluation of the experimental results on the *halved undersquinted scarf* joint through the analytical model of the Chapter 4 is performed.

B.2.1 Test results for the *halved undersquinted scarf* with squint *α* = 30°

LS1 (ii) – equilibrium state

In the following diagrams some of the test results for the *α = 30°* are described according to the parameters evaluated for the analytical models.

In the Diagram B-3 the straight lines describe: the limit state or equilibrium state LS1(ii) for the model (ii) (eq. 4-52) considering failure values F_u and M_u contained in the Table B-2, the constant values of μ_α , and constant values of $\varepsilon_1(F_u, M_u)$ and $\varepsilon_2(F_u, M_u)$ as in the eq. B-1 .

$$\begin{cases} \varepsilon_1(F_u, M_u) = 0.75 \\ \varepsilon_2(F_u, M_u) = 0.25 \end{cases} \qquad \text{B-1}$$

The parameter μ_α variates as described in the Diagram 7-3 according to:

$$\text{Where} \begin{cases} \mu_\alpha = \tan(\alpha) & (i) \\ -\dfrac{1}{\tan\alpha} \le \mu_\alpha < \tan\alpha & (ii) \\ \mu_\alpha = 0 & (iii) \end{cases} \qquad \text{B-2}$$

The value of μ_α for the single specimen is evaluated according to the eq. 4-44:

$$\mu_\alpha = \frac{F_{1,\perp} \cdot \sin\alpha - F \cdot \cos\alpha}{F_{1,\perp} \cdot \cos\alpha + F \cdot \sin\alpha}$$

and eq. 4-52:

$$\text{LS1(ii):} \quad F = \frac{\dfrac{M}{h}}{\left[2 \cdot \left(\varepsilon_1 - \dfrac{\varepsilon_2}{4 \cdot \tan\alpha}\right) \cdot \left(\dfrac{\cos\alpha + \mu_\alpha \sin\alpha}{\sin\alpha - \mu_\alpha \cos\alpha}\right) - \dfrac{(\varepsilon_F - \varepsilon_2)}{2}\right]}$$

With $\mu_\alpha = 0$ we obtain the:

$$\text{LS1 (iii):} \quad 2 \cdot F \cdot \left[-\frac{(\varepsilon_F - \varepsilon_2)}{4} \cdot \frac{1}{\tan\alpha} \cdot \left(\varepsilon_1 - \frac{\varepsilon_2}{4\tan\alpha}\right)\right] = \frac{M}{h} \qquad \text{B-3}$$

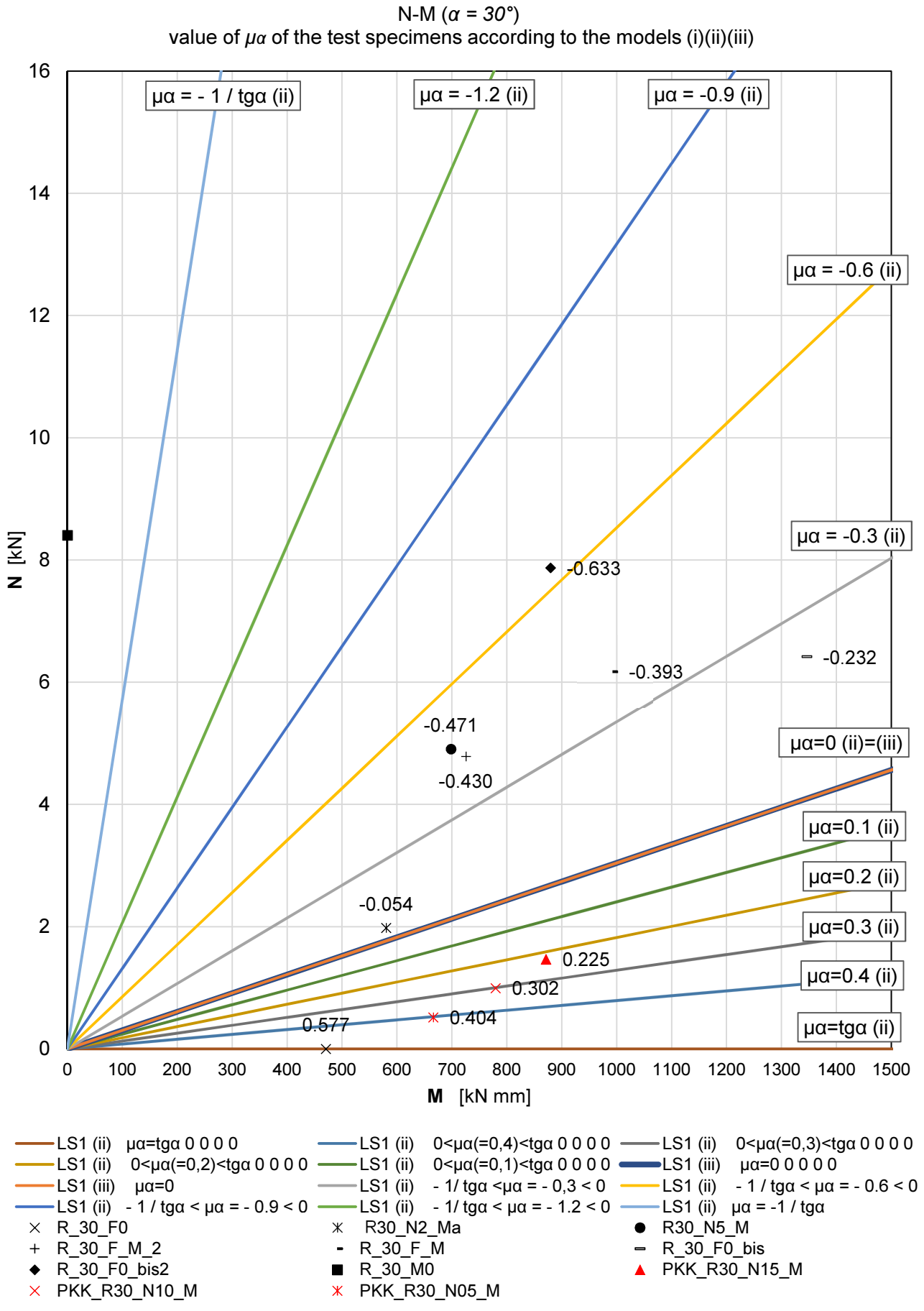

Diagram B-3 - N-M (*α = 30°*) – LS1 (ii) according to (i)(ii)(iii). Data description: *μα*

Table B-2 – Test specimen *α = 30°*: test results and analytic evaluation according to (ii)

model	α [°]	h [mm]	ε1	ε2	ε3	εF	test results				analytic results					
							P II			P I.	F2,⊥ [kN]	F2,// [kN]	F1,⊥ [kN]	F3,⊥ [kN]	Ff [kN] LS2(ii)	μα LS1(ii)
							lever arm [mm]	FII [kN]	M [kN mm]	F [kN]						
(ii)																
R_30_F0	30	140	0.75	0.25	-	0	405	2.32	470.61	0.00	2.27	1.31	2.62	-	2.62	0.58
PKK_R30_N05_M	30	140	0.75	0.25	-	0	405	3.29	666.02	0.51	3.42	1.38	3.66	-	3.66	0.40
PKK_R30_N10_M	30	140	0.75	0.25	-	0	405	3.85	779.42	0.99	4.17	1.26	4.24	-	4.24	0.30
PKK_R30_N15_M	30	140	0.75	0.25	-	0	405	4.30	871.36	1.47	4.81	1.08	4.71	-	4.71	0.23
PKK_R30_N30_M	30	140	0.75	0.25	-	0	405	4.76	962.89	3.03	5.90	-0.10	5.06	-	5.06	-0.02
PKK_R30_N40_M	30	140	0.75	0.25	-	0	405	5.18	1048.55	3.93	6.69	-0.68	5.45	-	5.45	-0.10
PKK_R30_N5_M	30	140	0.75	0.25	-	0	405	5.34	1080.34	5.01	7.29	-1.58	5.52	-	5.52	-0.22
R_30_F_M	30	140	0.75	0.25	-	0	405	4.90	992.66	6.18	7.35	-2.89	4.92	-	4.92	-0.39
R_30_F0_bis	30	140	0.75	0.25	-	0	405	6.65	1345.82	6.42	9.15	-2.13	6.87	-	6.86	-0.23
R_30_F0_bis2	30	140	0.75	0.25	-	0	405	4.34	879.46	7.87	7.51	-4.75	4.13	-	4.13	-0.63
R_30_M0	30	140	0.75	0.25	-	0	405	0.00	0.00	8.40	3.49	-7.69	-0.82	-	-0.82	-2.20
R30_N2_M	30	140	0.75	0.25	-	0	405	2.55	516.98	1.99	3.31	-0.38	2.68	-	2.68	-0.11
R30_N2_Ma	30	140	0.75	0.25	-	0	405	2.87	580.37	1.98	3.62	-0.20	3.04	-	3.04	-0.05
R30_N5_M	30	140	0.75	0.25	-	0	405	3.45	698.22	4.91	5.40	-2.54	3.41	-	3.41	-0.47
PKK_R30_N8_M	30	140	0.75	0.25	-	0	405	7.15	1447.27	8.03	10.31	-3.31	7.27	-	7.27	-0.32
PKK_R30_N8_M2	30	140	0.75	0.25	-	0	405	5.71	1156.68	7.94	8.88	-4.04	5.66	-	5.66	-0.46
R_30_F_M_2	30	140	0.75	0.25	-	0	405	3.58	725.36	4.79	5.49	-2.36	3.57	-	3.57	-0.43

LS2(ii) - FM II

In the Diagram B-4, the values of F_f for the single specimen are calculated starting from the experimental values of F_u and M_u contained in the Table B-2, with constant values of $\varepsilon_1(F_u, M_u)$ and $\varepsilon_2(F_u, M_u)$ as in the eq. B-1 . In the diagram, the straight lines represent constant values of $F_f = F_{f,2}$ for the FM II, valid for specimens under pure bending and combined compression and bending actions (eq. 4-31 and eq. 4-72).

LS2 (i): $$\frac{M}{2 \cdot h \cdot \left(\varepsilon_1 - \frac{\varepsilon_2}{4 \cdot \tan \alpha} \right)} = F_f$$

LS2 (ii): $$\frac{M + F \cdot \left[\frac{h}{2} \left(\varepsilon_F - \varepsilon_2 \right) \right]}{\left[2 \cdot h \cdot \left(\varepsilon_1 - \frac{\varepsilon_2}{4 \cdot \tan \alpha} \right) \right]} = F_f$$

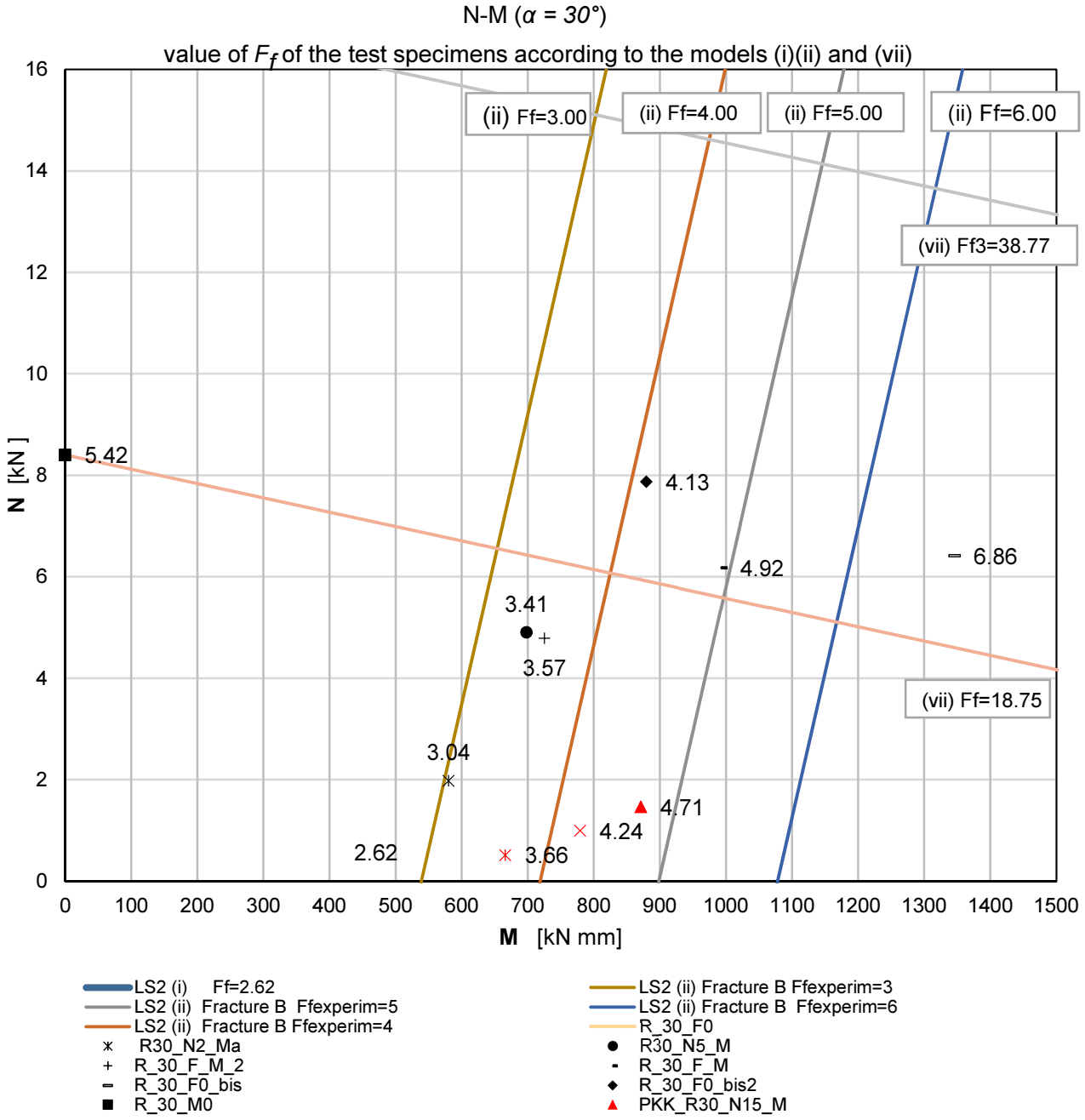

Diagram B-4 – N-M (α = 30°) - LS2(ii). Data description: $F_{f,experimental}$, according to LS2(ii). The F_f from the test specimen F30_M0 is calculated according to (vii)

LS3 (ii) - Fu

In the Diagram B-5 the fixed value of $F_{f,\exp} = 5$ (calculated from eq. 4-75 for R30_F_M) for the values of $\tan\alpha \le \mu_\alpha \le -1/\tan\alpha$ are used for the calculation of the straight line that are defined for the LS3(ii) (iv).

LS3(ii): $F_u = \dfrac{\sin\alpha - \mu_\alpha \cos\alpha}{\cos\alpha + \mu_\alpha \sin\alpha} F_f$ B-4

The specimens are described with the individual value of F_u. For the specimens loaded under pure bending and combined compression and bending action considering the LS3 (ii) (eq. B-4). For the specimens loaded in pure compression, the ultimate value F_u is calculated according to the Gustafsson formula (see next paragraph).

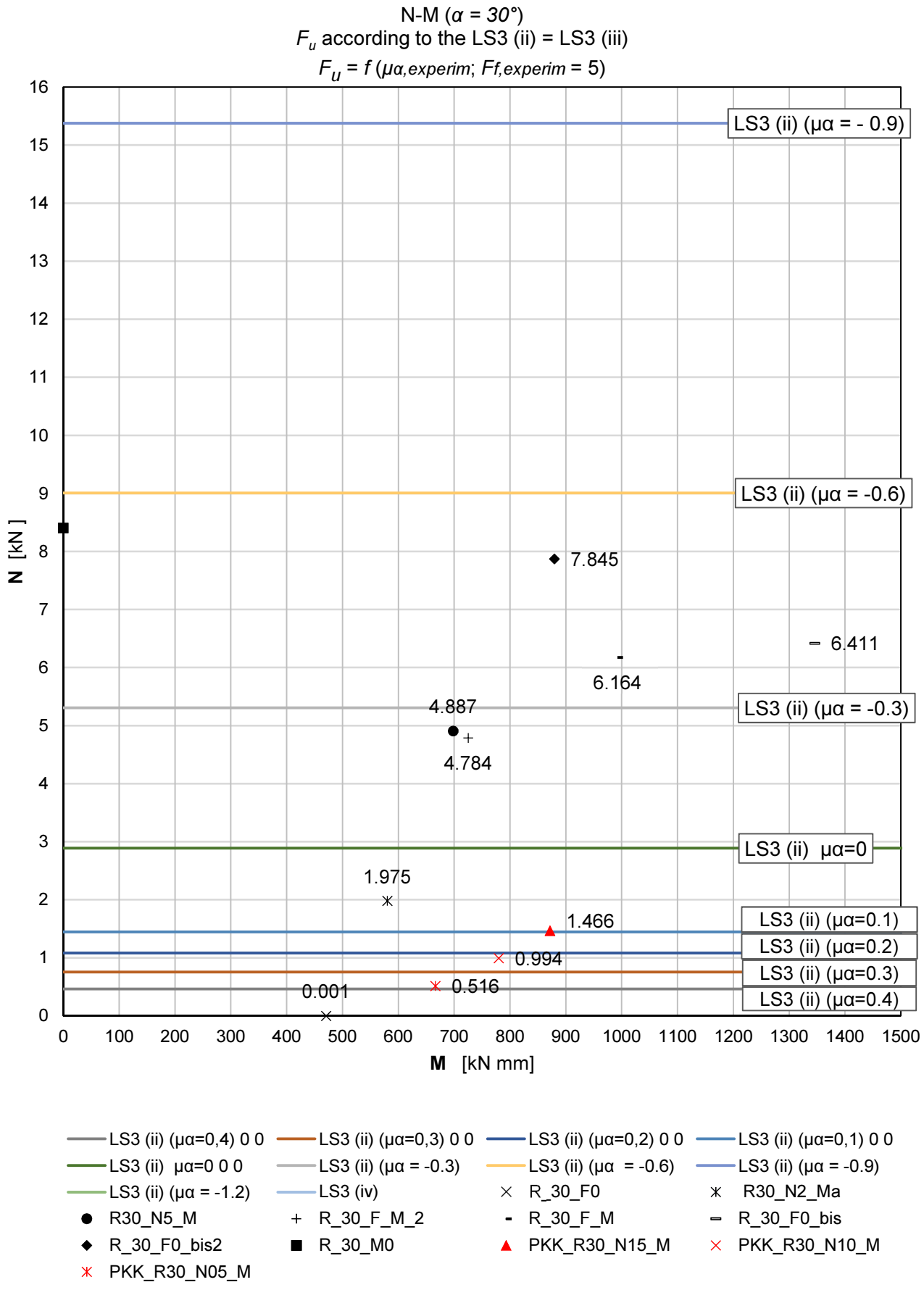

Diagram B-5 - N-M (*α = 30°*) - LS2(ii). Data description: Fu according to the LS3 (ii) = *f (μα; Ff)*

LS4 (vii) - FM III

The Table B-5 shows the values of F_f calculated according to the LS4 (vii) for the failure in B and in C.

The analytic evaluation of the FM III (specimen R_30_M0, pure compression) is done according to the Gustafsson formula of the energy of failure starting from the experimental results contained in the Table B-3.

$$a_2 = e_2 \cdot \cos\alpha = \varepsilon_2 \cdot l_{AB} \cdot \cos\alpha = \frac{1}{2} \cdot \frac{140}{2 \cdot \tan(30)} = 60.62mm \quad \text{B-5}$$

$$a_3 = e_3 \cdot \cos\alpha = \varepsilon_3 \cdot l_{CD} \cdot \cos\alpha = \frac{1}{2} \cdot \frac{140}{2 \cdot \tan(30)} = 60.62mm \quad \text{B-6}$$

therefore

$$F_{f,\mathbf{B},analy} = F_{f,C,analy} \sqrt{G_f \cdot b \cdot \left(\frac{b \cdot h_{eff}^3}{12} \right) E_0 \cdot \frac{1}{a_2{}^2}} = \sqrt{0.0012 \cdot \left(\frac{60^2 \cdot 70^3}{12} \right) \cdot 11 \cdot \frac{1}{60^2}} = 19.38 \quad \text{B-7}$$

The Diagram B-6 shows the analytical evaluation of the LS4 (vii) according to different values of F_f. The experimental value of $F_{f,\exp}$ of the specimen R_30_M0 (eq. B-8) is compared with the $F_{f,B,analy}$ and $F_{f,C,analy}$ (eq. 4-114 for the fracture in B and eq. 4-117 for fracture in C). On one side, the calculation with $F_{f,B}$ is not reflecting the experimental results, on the other side the one with $F_{f,C}$ is in the range of the experimental results. Therefore, the FM III fracture in C is evaluated with the LS4(vii) for $F_{f,C,analy}$ (eq. 4-117 and eq. 3-40).

$$F\left\{ \frac{1}{\tan\alpha} - \cos\alpha \cdot \frac{\left[\frac{(\varepsilon_2 - \varepsilon_F)}{4} + \frac{1}{\tan\alpha} \cdot \left(\varepsilon_1 - \frac{\varepsilon_2}{4 \cdot \tan\alpha} \right) \right]}{\left(\cos\alpha - \frac{\varepsilon_2 + \varepsilon_3}{4 \cdot \sin\alpha} \right)} \right\} + M \left[\frac{1}{2 \cdot h} \cdot \frac{\cos\alpha}{\left(\cos\alpha - \frac{\varepsilon_2 + \varepsilon_3}{4 \cdot \sin\alpha} \right)} \right] = F_f \quad \text{B-8}$$

$$F_{f,\exp} = 18.75 \quad \text{B-9}$$

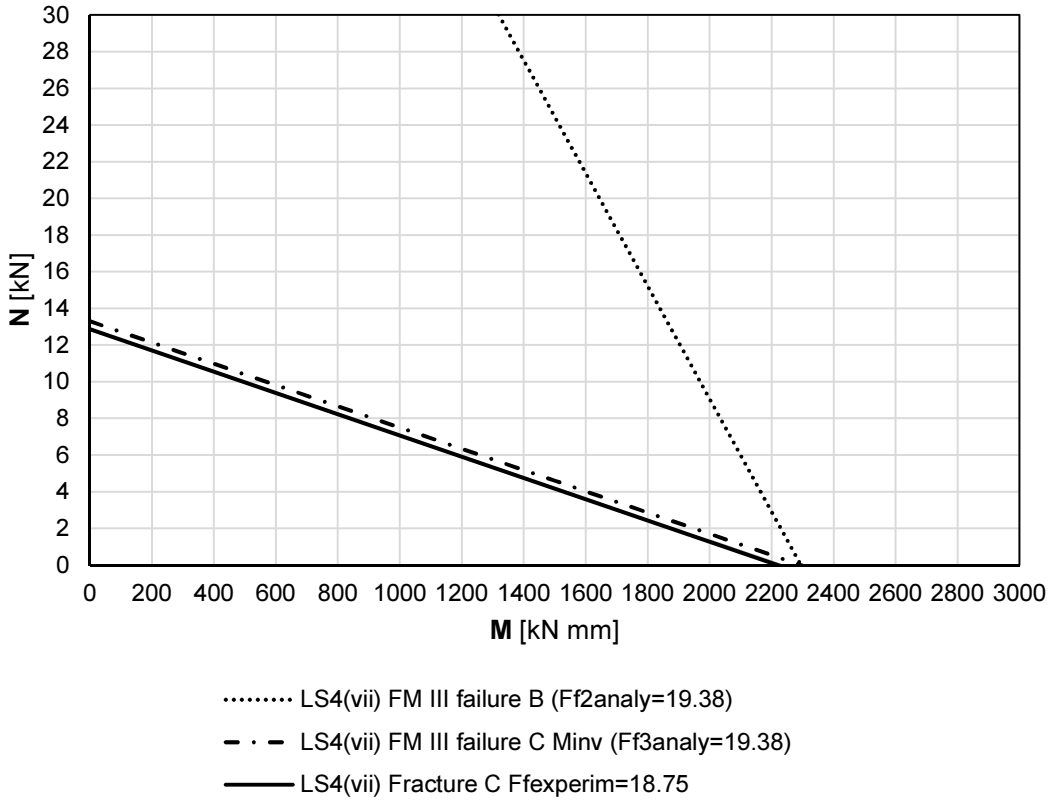

Diagram B-6 – Comparison among the LS4 (vii) calculated through the experimental value of the pure-compression loaded test *α = 30°* and the analytical values from the Gustafsson formula.

Table B-3 – Test specimen *α = 30°*: test results and analytic evaluation according to (vii)

model	α [°]	h [mm]	ε1	ε2	ε3	ε_F	test results				analytic results					
							P II			P I.	F2,⊥ [kN]	F2,// [kN]	F1,⊥ [kN]	F3,⊥ [kN]	Ff,C expm [kN] LS4(vii)	Ff,B expm [kN] LS4(vii)
							lever arm [mm]	FII [kN]	M [kN mm]	F [kN]						
(vii)																
R_30_F0	30	140	0.88	0.5	0.25	0	405	2.32	470.61	0	3.42	-	0.00	-3.42	2.96	2.96
R_30_M0	30	140	0.88	0.5	0.25	0	405	0.00	0.00	8.40	-4.85	-	14.55	21.65	18.75	-4.20
R_30_F_M	30	140	0.88	0.5	0.25	0	405	4.90	992.66	6.18	3.65	-	10.70	8.70	20.04	3.16
R_30_F0_bis	30	140	0.88	0.5	0.25	0	405	6.65	1345.82	6.48	6.08	-	11.11	6.75	22.80	5.27
R_30_F0_bis2	30	140	0.88	0.5	0.25	0	405	4.34	879.46	7.88	1.85	-	13.64	13.89	23.11	1.60
R30_N2_M	30	140	0.88	0.5	0.25	0	405	2.55	516.98	1.99	2.61	-	3.44	1.36	7.69	2.26
R30_N2_Ma	30	140	0.88	0.5	0.25	0	405	2.87	580.37	1.98	3.08	-	3.43	0.88	8.08	2.67
R30_N5_M	30	140	0.88	0.5	0.25	0	405	3.45	698.22	4.91	2.25	-	8.50	7.56	15.35	1.95
R_30_F_M_2	30	140	0.88	0.5	0.25	0	405	3.58	725.36	4.79	2.51	-	8.29	7.06	15.25	2.18
PKK_R30_N05_M	30	140	0.88	0.5	0.25	0	405	3.29	666.02	0.52	4.55	-	0.89	-3.52	5.34	3.94
PKK_R30_N10_M	30	140	0.88	0.5	0.25	0	405	3.85	779.42	0.99	5.10	-	1.72	-3.11	7.13	4.41
PKK_R30_N15_M	30	140	0.88	0.5	0.25	0	405	4.30	871.36	1.47	5.49	-	2.54	-2.56	8.76	4.76
PKK_R30_N30_M	30	140	0.88	0.5	0.25	0	405	4.76	962.89	3.03	5.25	-	5.26	0.82	12.84	4.55
PKK_R30_N40_M	30	140	0.88	0.5	0.25	0	405	5.18	1048.55	3.93	5.36	-	6.81	2.51	15.38	4.64
PKK_R30_N5_M	30	140	0.88	0.5	0.25	0	405	5.34	1080.34	5.01	4.97	-	8.68	5.05	17.99	4.30
PKK_R30_N8_M	30	140	0.88	0.5	0.25	0	405	7.15	1447.27	8.03	5.89	-	13.90	10.16	27.03	5.10
PKK_R30_N8_M2	30	140	0.88	0.5	0.25	0	405	5.71	1156.68	7.94	3.83	-	13.75	12.05	25.01	3.32

B.2.2 Test results for the *halved undersquinted scarf* with squint *α = 60°*

For the verification of the *halved undersquinted scarf* with squint *α = 60°* is followed the same procedure used for the one *α = 30°*.

LS1 (ii) – equilibrium state

Considering the test results contained in the Table B-4 the evaluation of the parameter μ_α is done according to LS1 (ii) and the F_f is calculated according to the LS2 (ii).

In the Diagram B-7, the straight lines represent the lines of constant value of LS1 (μ_α). The specimens are ordered along the correspondent straight line's values.

LS2 (ii) - FM II

The experimental evaluation of the $F_{f,2}$ for the FM II is done starting from the experimental results contained in the Table B-4 in the LS2 formulas from LS2 (i) (eq.4-31) and LS2 (ii) (eq.4-72). In the Diagram B-8 the results are illustrated.

Table B-4 – Test specimen *α = 60°*: test results and analytic evaluation according to (i),(ii)

model	α [°]	h [mm]	ε1	ε2	ε3	εF	test results				analytic results					
							P II			P I	F2,⊥ [kN]	F2,// [kN]	F1,⊥ [kN]	F3,⊥ [kN]	Ff [kN] LS2(ii)	μα LS1(ii)
							lever arm [mm]	FII [kN]	M [kN mm]	F [kN]						
(i)																
R60_F0	60	140	0.75	0.25	-	0	405	1.22	247.66	-0.00	0.62	1.07	1.24	-	1.24	1.73
(ii)																
R60_F0	60	140	0.75	0.25	-	0	405	1.22	247.66	-0.00	0.62	1.07	1.24	-	1.24	1.74
R60_M0	60	140	0.75	0.25	-	0	405	-0.08	-16.00	42.01	34.50	-24.26	-3.76	-	-3.76	-0.70
R60_M0_2	60	140	0.75	0.25	-	0	405	-0.08	-15.39	84.52	69.46	-48.73	-7.48	-	-7.48	-0.70
R60_N16_M	60	140	0.75	0.25	-	0	405	6.14	1244.16	16.01	16.27	-3.83	4.82	-	4.82	-0.24
R60_N32_Ma	60	140	0.75	0.25	-	0	405	10.22	2069.35	32.07	31.54	-9.50	7.54	-	7.54	-0.30
R60_N48_M	60	140	0.75	0.25	-	0	405	12.85	2601.72	47.97	45.95	-16.35	8.82	-	8.82	-0.36
R60_N64_M	60	140	0.75	0.25	-	0	405	15.13	3063.83	63.98	60.27	-23.57	9.73	-	9.73	-0.39

Table B-5 – Test specimen *α = 60°:* test results and analytic evaluation according to (vii)

model	α [°]	h [mm]	ε1	ε2	ε3	εF	test results				analytic results					
							P II			P I	F2,⊥ [kN]	F2,// [kN]	F1,⊥ [kN]	F3,⊥ [kN]	Ff,C expm. [kN] LS4(vii)	Ff,B expm [kN] LS4(vii)
							lever arm [mm]	FII [kN]	M [kN mm]	F [kN]						
(vii)																
R60_F0	60	140	0.75	0.25	0.25	0	405	1.22	247.66	-0.01	2.49	-	0.00	-2.49	1.24	1.24
R60_M0	60	140	0.75	0.25	0.25	0	405	-0.08	-16.00	42.01	-7.72	-	24.25	56.22	27.95	-3.86
R60_M0_2	60	140	0.75	0.25	0.25	0	405	-0.08	-15.39	84.52	-15.36	-	48.80	112.95	56.32	-7.68
R60_N16_M	60	140	0.75	0.25	0.25	0	405	6.14	1244.16	16.01	9.61	-	9.24	8.87	16.93	4.81
R60_N32_Ma	60	140	0.75	0.25	0.25	0	405	10.22	2069.35	32.07	15.01	-	18.52	22.02	31.79	7.50
R60_N48_M	60	140	0.75	0.25	0.25	0	405	12.85	2601.72	47.97	17.49	-	27.69	37.89	45.07	8.75
R60_N64_M	60	140	0.75	0.25	0.25	0	405	15.13	3063.83	63.98	19.25	-	36.94	54.62	58.08	9.63

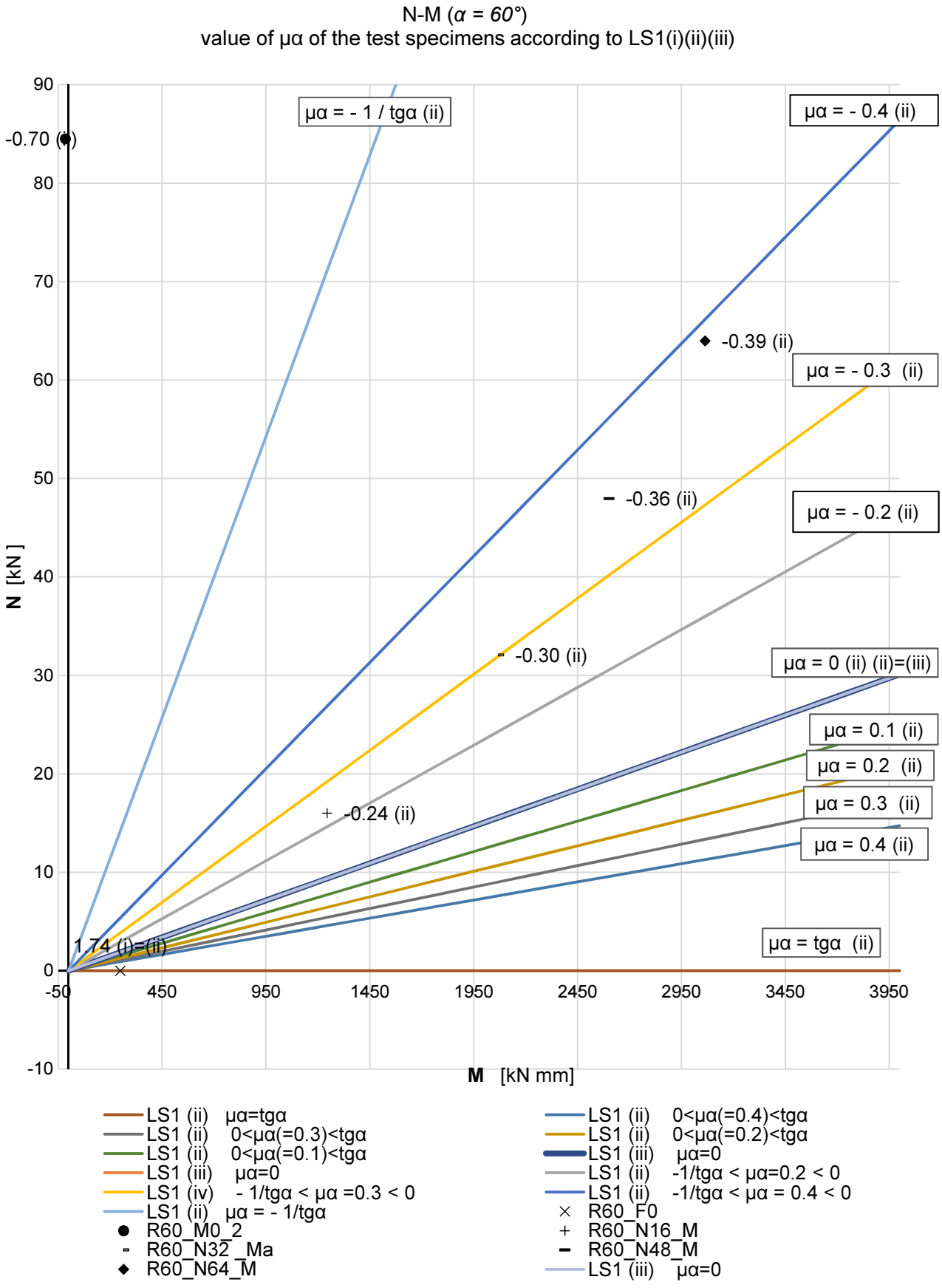

Diagram B-7 – N –M ($\alpha = 60°$) – LS1 (ii) according to (i)(ii)(iii). Data description: $\mu\alpha$

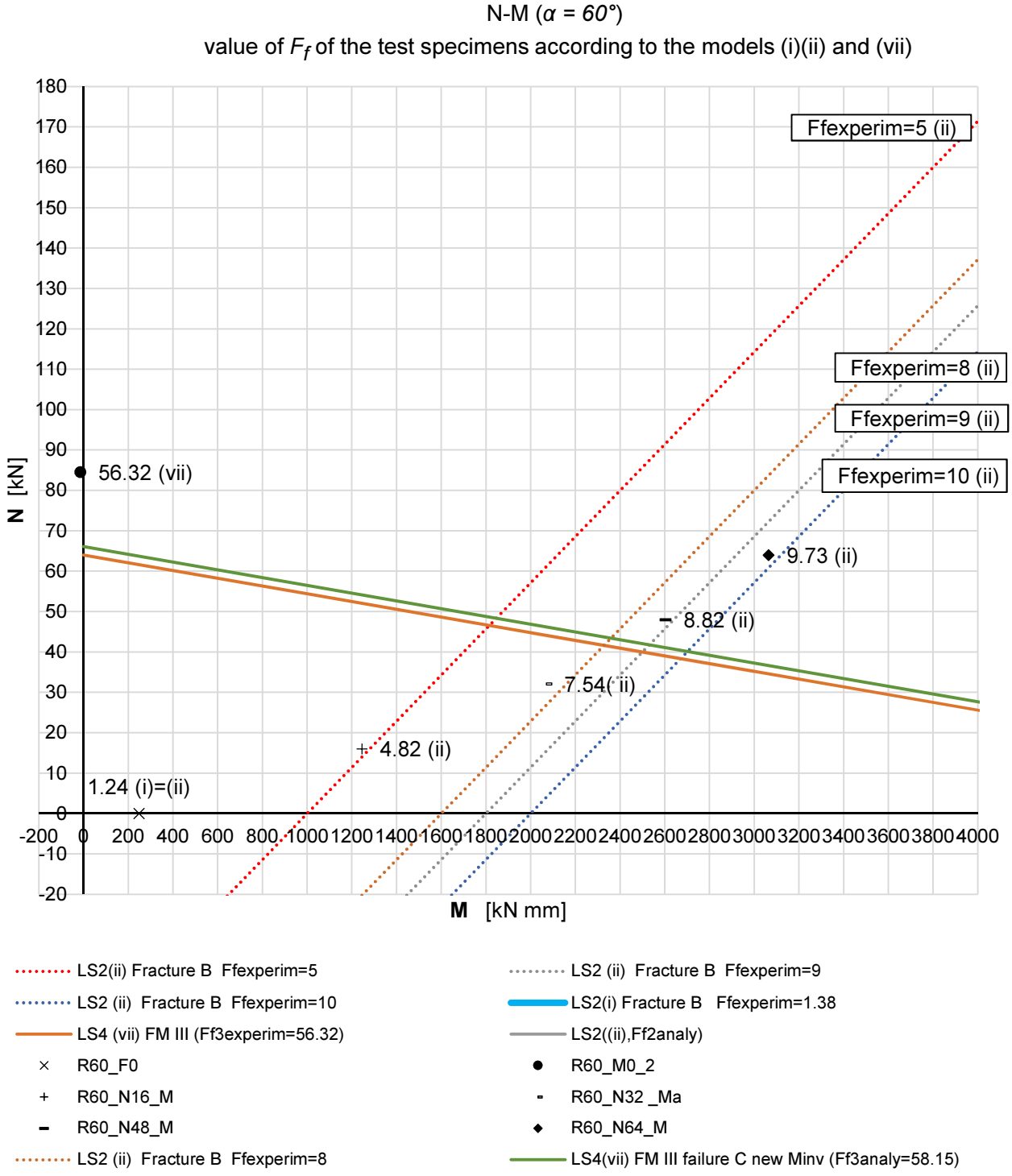

Diagram B-8 -- N-M (*α = 60°*) – LS2 (ii), data description: *Ff* - LS4 (vii).

B.2.2.1 LS4 (vii) – FM III

The Table B-5 contains the values of F_f calculated according to LS4 (vii) for the failure in B and in C.

In the Diagram B-9 the F_f for the LS4 (vii) is calculated from the experimental value of $F_{f,\exp}$ (eq. B-8) and compared with the $F_{f,B,analy}$ and $F_{f,C,analy}$ (eq. 4-114 for the fracture in B and eq. 4-117 for fracture in C).

The value of $F_{f,\exp}$ consider the position of the forces as in the eq. B-10

$$\varepsilon_{1,u} = \varepsilon_{2,u} = \varepsilon_{3,u} = \frac{1}{2} \qquad \text{B-10}$$

The analytic evaluation of the FM II and FM III is done in accordance with the Gustafsson formula of the energy of failure.

$$a_3 = a_2 = \varepsilon_3 \cdot \frac{h}{2 \cdot \tan\alpha} = \frac{1}{2} \cdot \frac{h}{2 \cdot \tan\alpha} = 20.20mm \qquad \text{B-11}$$

The F_f for both the failure in B and C is evaluated as:

$$F_{f,B,analy} \cong F_{f,C,analy} = \sqrt{G_f \cdot b \cdot \left(\frac{b \cdot h_{eff}^3}{12}\right) E_0 \cdot \frac{1}{{a_3}^2}} = \sqrt{0.0012 \cdot \left(\frac{60^2 \cdot 70^3}{12}\right) \cdot 11 \cdot \frac{1}{20^2}} = 58.15kN \qquad \text{B-12}$$

In the following Diagram B-9 the comparison among the LS4 (vii) calculated through the experimental value of the pure-compression tests *α =60°* and the analytical values from the Gustafsson formula is done.

The $F_{f,B} = F_{f,C}$ from the Gustafsson formula corresponds to the $F_{f,\exp}$ calculated back from the test results, nevertheless, the considered ultimate value of F is not the real load-carrying capacity of the joint F_u, but the chosen value of $F_{u,e}$. More tests have to be performed.

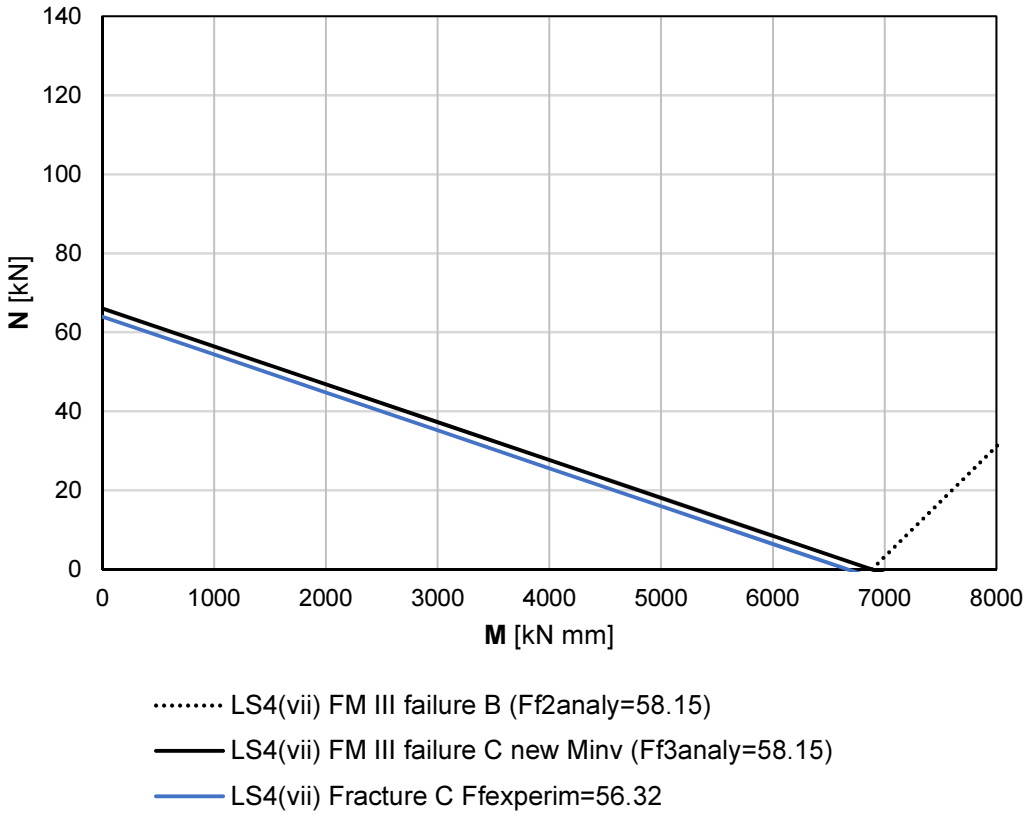

Diagram B-9 – Comparison among the LS4 (vii) calculated through the experimental value of the pure-compression loaded test *α = 60°* and the analytical values from the Gustafsson formula.

B.2.3 General conclusions

In the following Diagram B-11 and Diagram B-12 the lecture of the test results according to the analytical models respectively for the *α = 30°* and *α = 60°* is given. The value of μ_α is calculated according to the eq.4-44 and the F_f is calculated with the eq. 4-75.

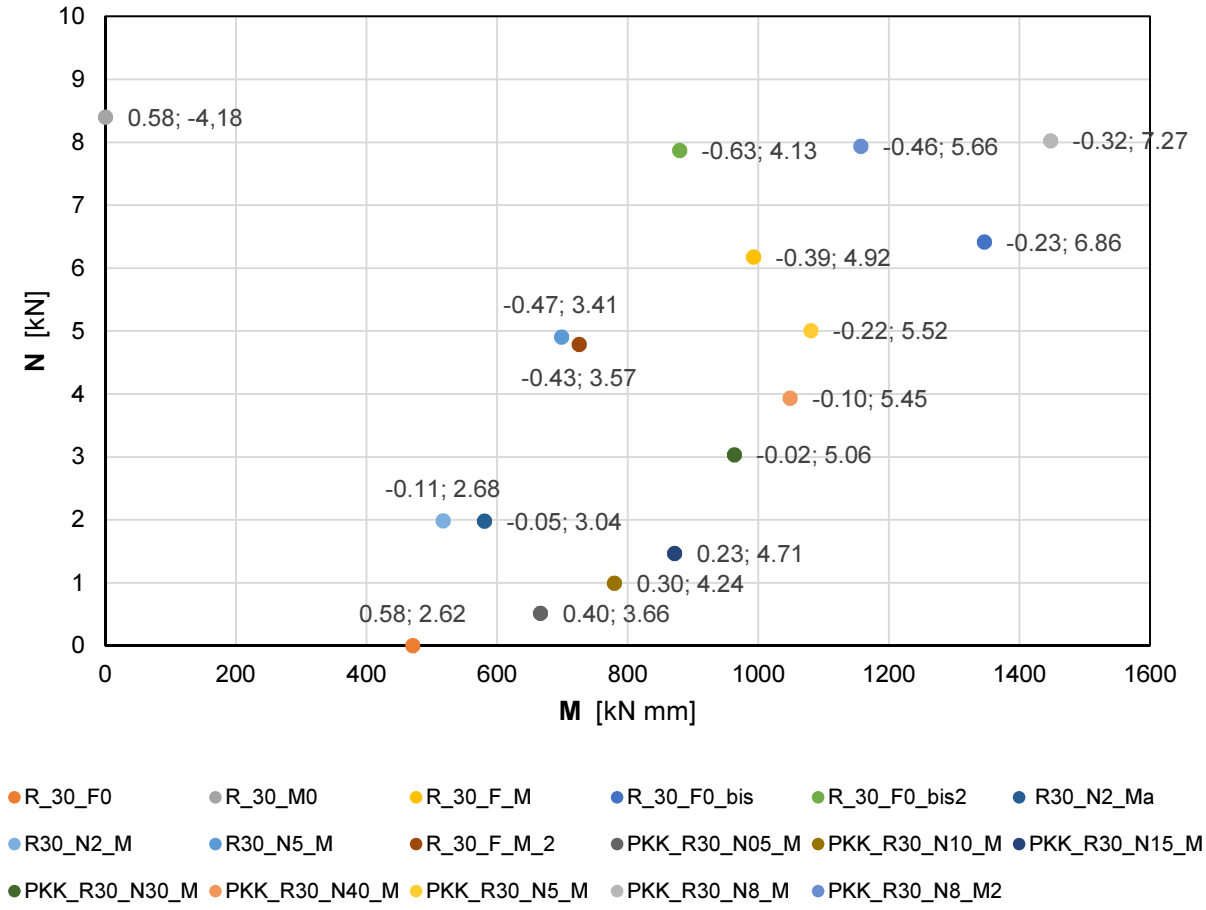

Diagram B-10 - N-M diagram $\alpha = 30°$ with ($\mu\alpha$; Ff) (ii)

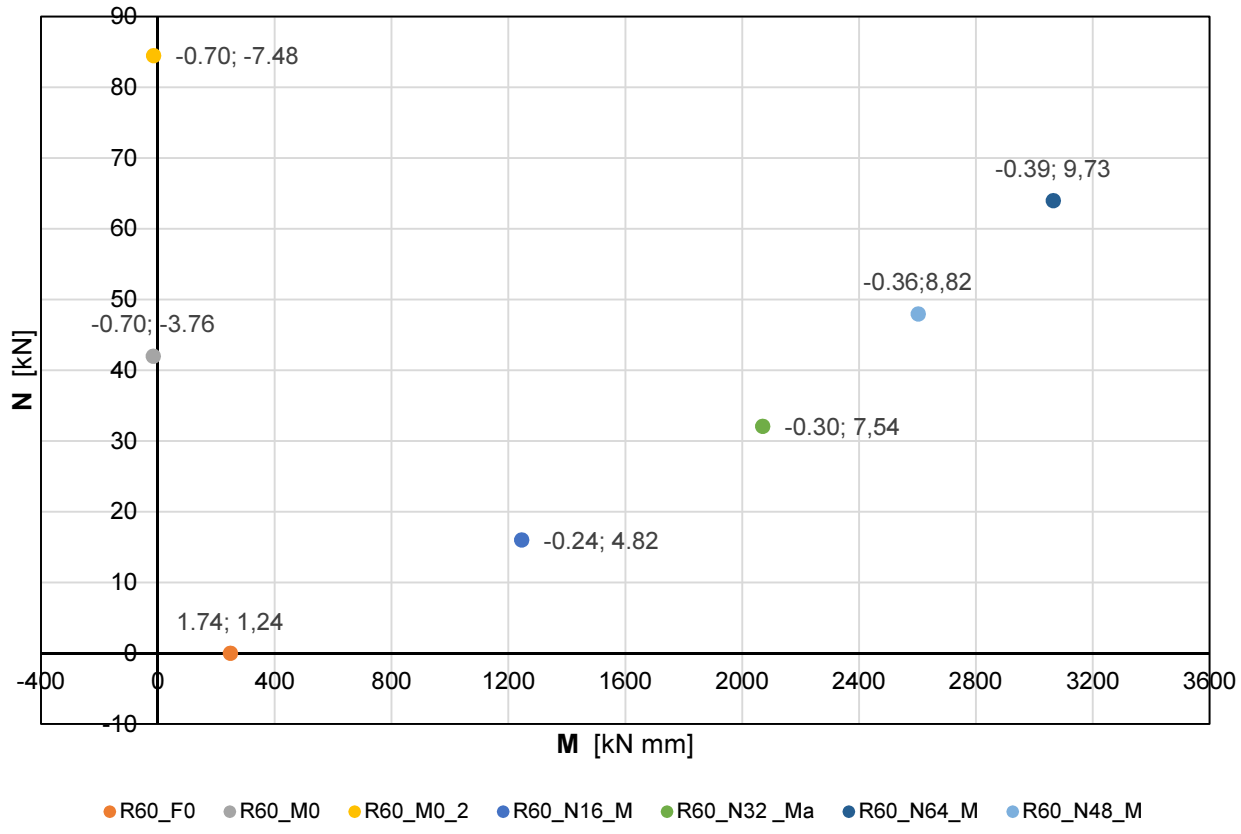

Diagram B-11 - N-M diagram $\alpha = 60°$ with ($\mu\alpha$; $F_{f,exp}$) (ii)

Example for the R30_F_M

In the following Diagram B-12 the description of the test specimen F30_F_M is described in detail. For all the specimen the respective values of $\mu_\alpha ; F_{f,\exp}$ are given.

Concluding, the procedure is the following:

- the value of μ_α is described by the eq. 4-52 (equilibrium equation LS1 (ii), Diagram B-3);
- the value of F_f from the eq. 4-72 (equilibrium equation LS2 (ii), Diagram B-4);
- finally, the ultimate value of $F_u(\mu_\alpha ; F_{f,\exp})$ from the eq. 4-75, eq. 7-10 (equilibrium equation LS3 (ii)) is described for the each of the test results.

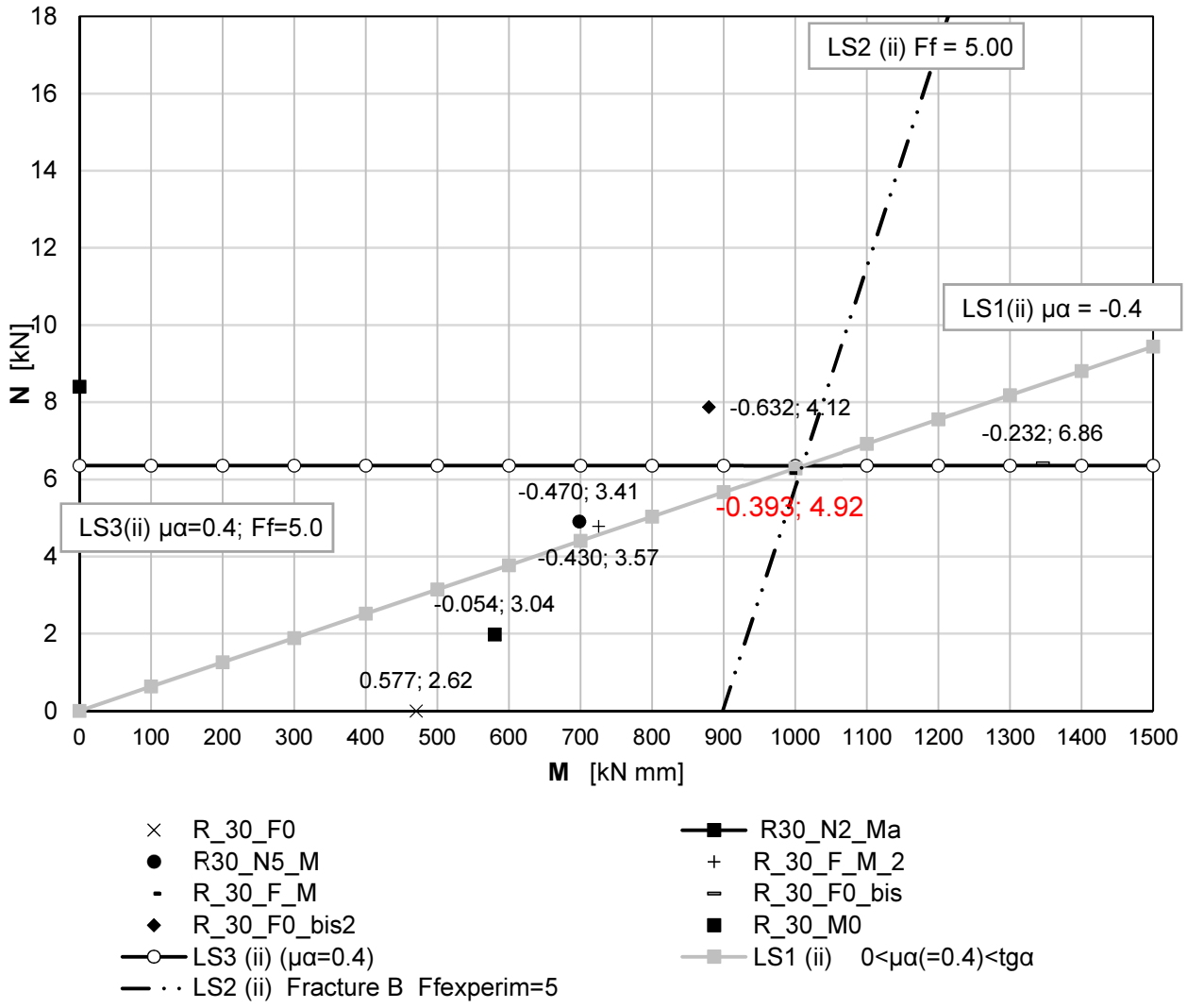

Diagram B-12 - N-M (α = *30°*) – Example of description of the test specimen F30_F_M. Data description: μ_α *; Ff.*

ANNEX C DIAGRAMS OF THE EXPERIMENTAL CAMPAIGNS

C.1 *Halved undersquinted scarf joint (α = 30°) – strong axis tests*

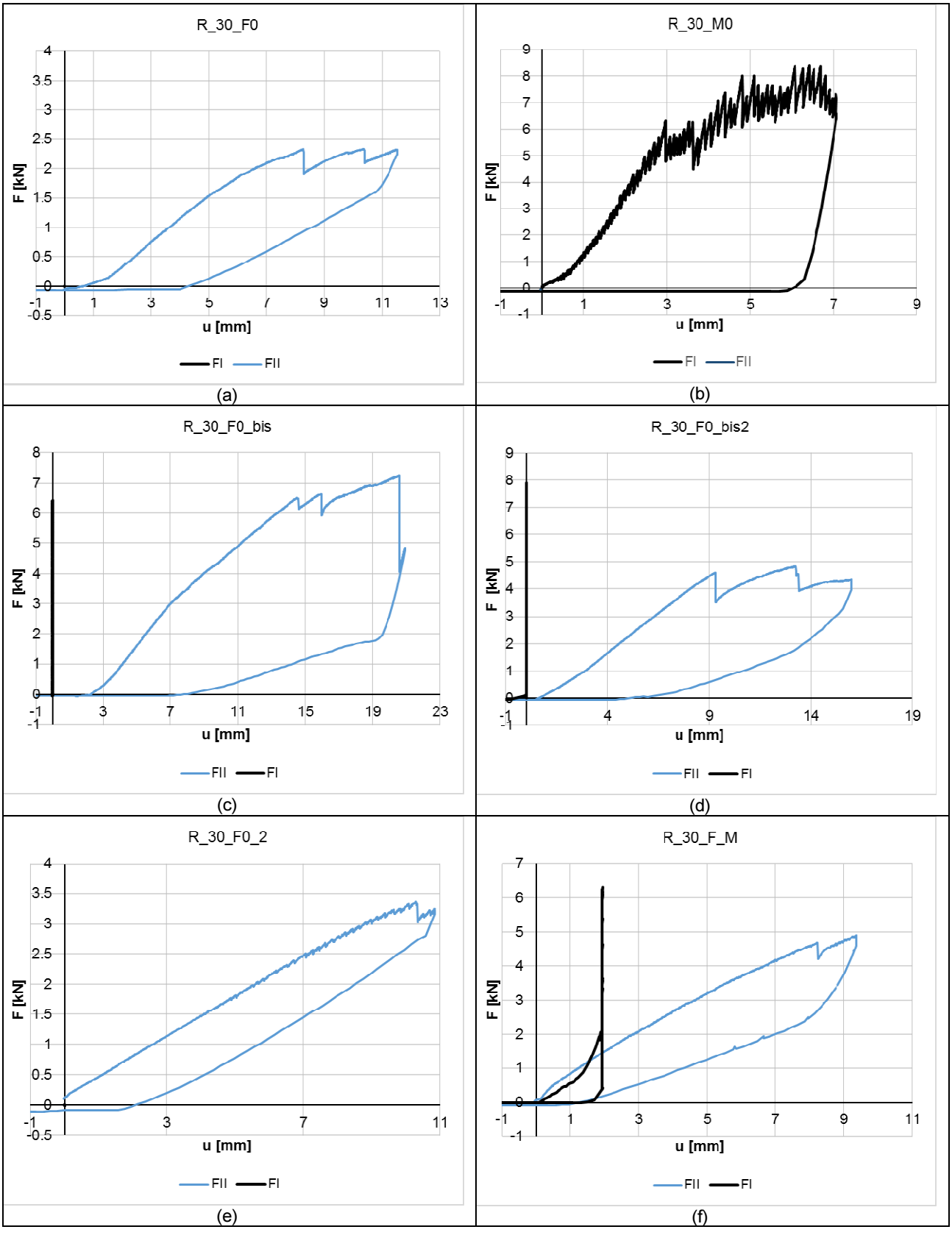

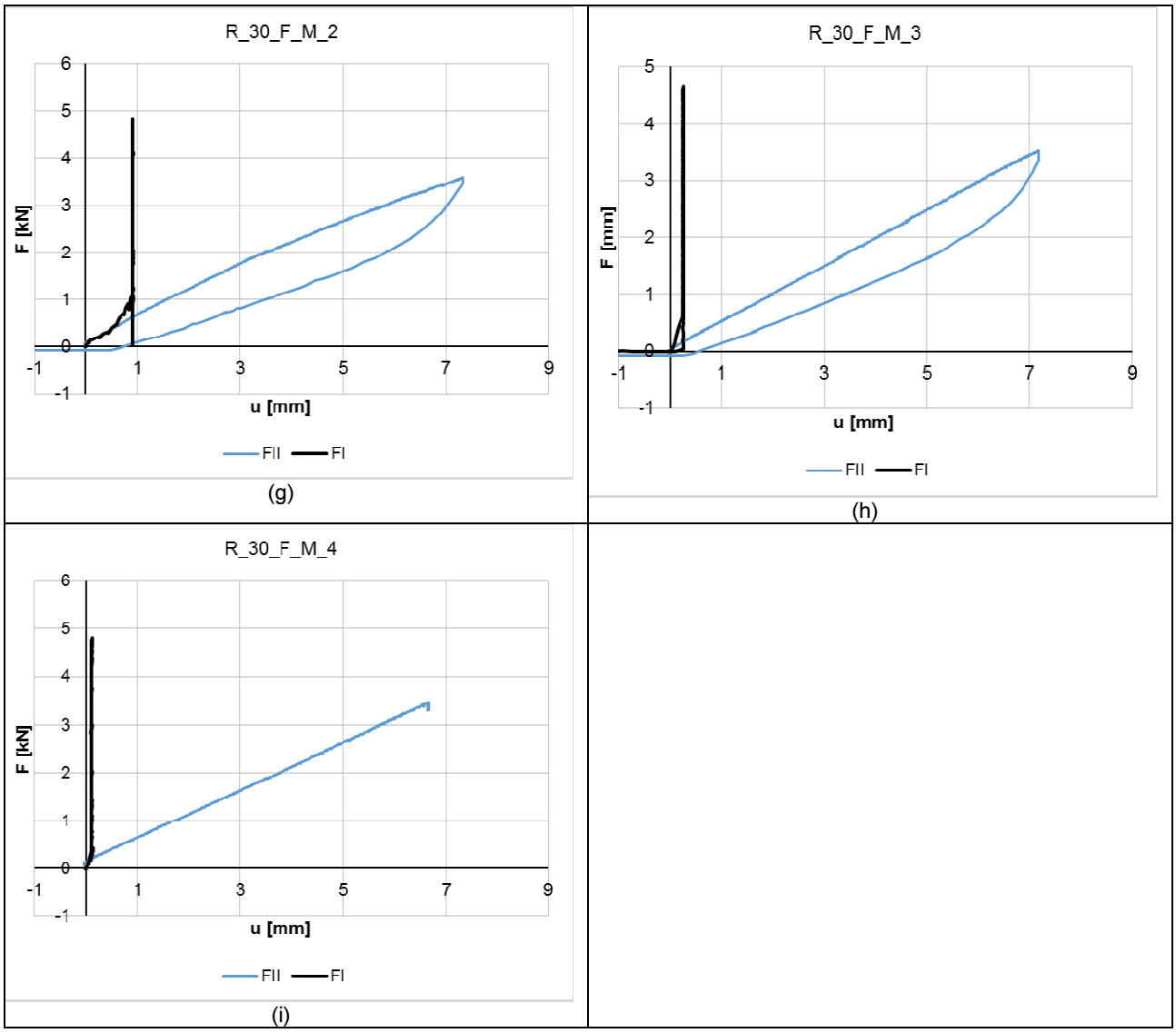

Table C-1 – *Halved undersquinted scarf* joint. Specimens *α = 30°*: (a) R30_F0 ; (b) R30_M0 ; (c) R30_F0_bis ; (d) R30_F0_bis2 ; (e) R30_F0_2 ; (f) R30_F_M ; (g) R30_F_M_2; (h) R30_F_M_3 ; (i) R30_F_M_4 .

C.2 Halved undersquinted scarf joint (α = 60°) – strong axis tests

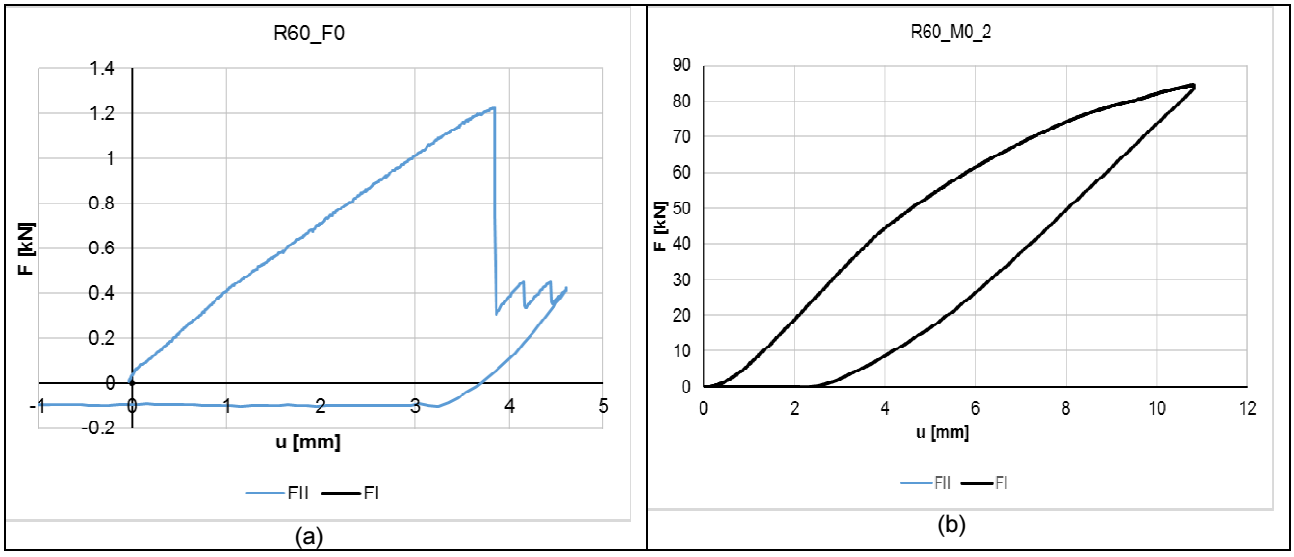

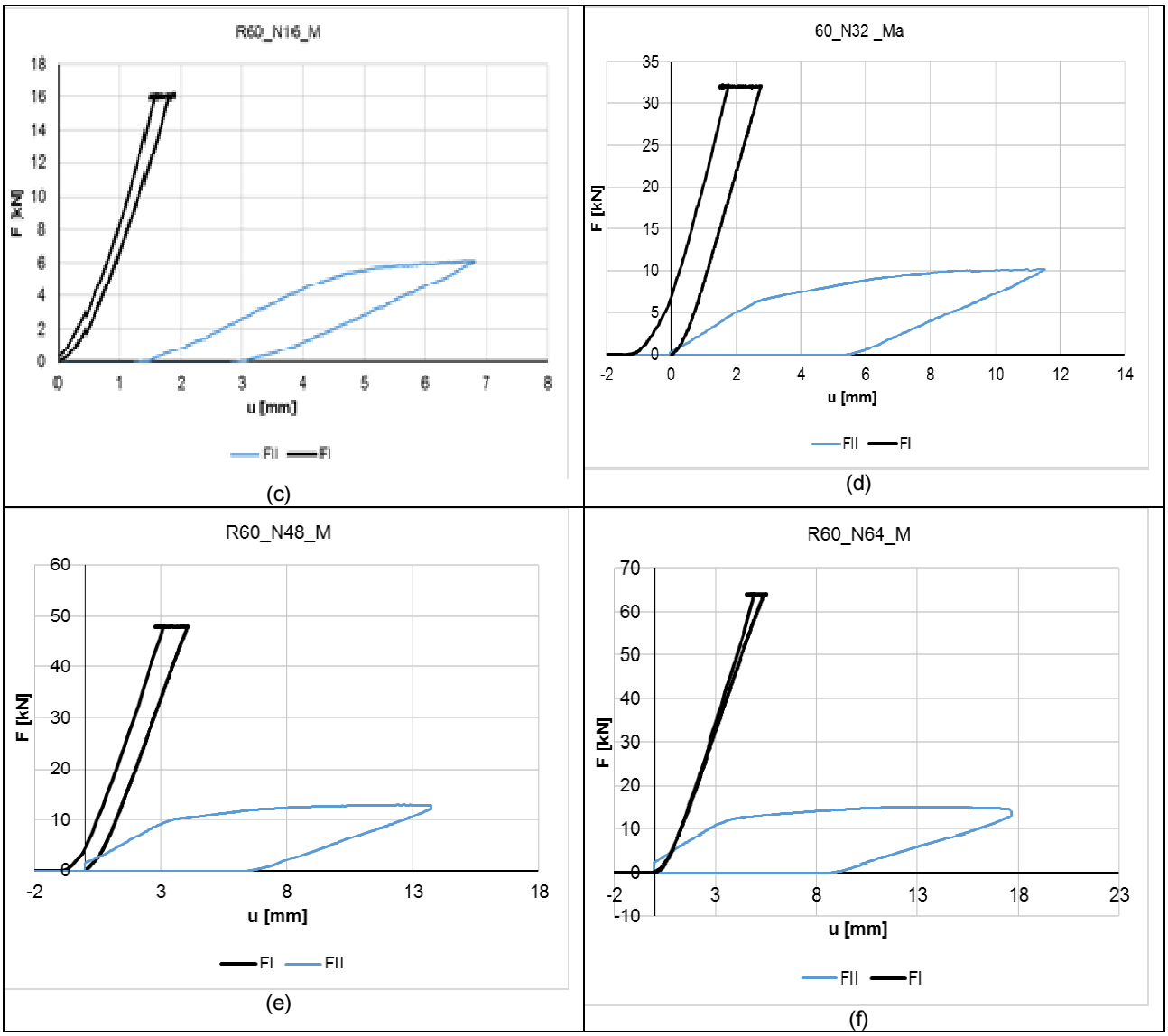

Table C-2 – *Halved undersquinted scarf* joint. Specimens *α = 60°*: (a) R60_F0 ; (b) R60_M0_2 ; (c) R60_N16_M ; (d) R60_N32_M ; (e) R60_N48_M ; (f) R60_N64_M .

C.3 Stop – splayed and undersquinted (α = 60°; β = 10°) – strong axis tests

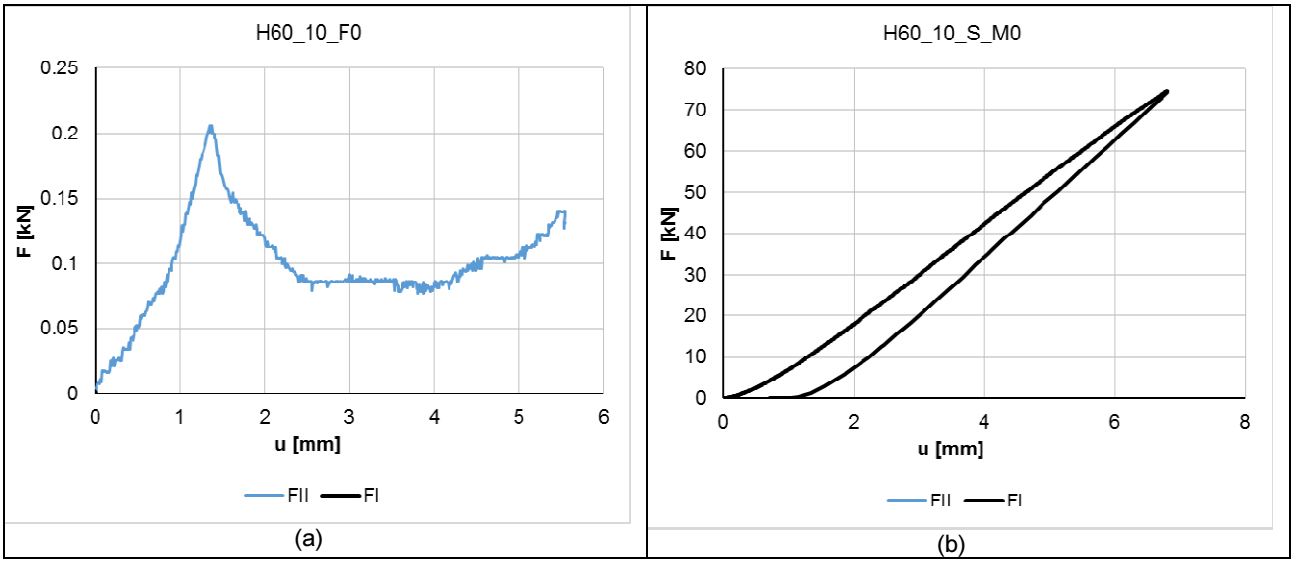

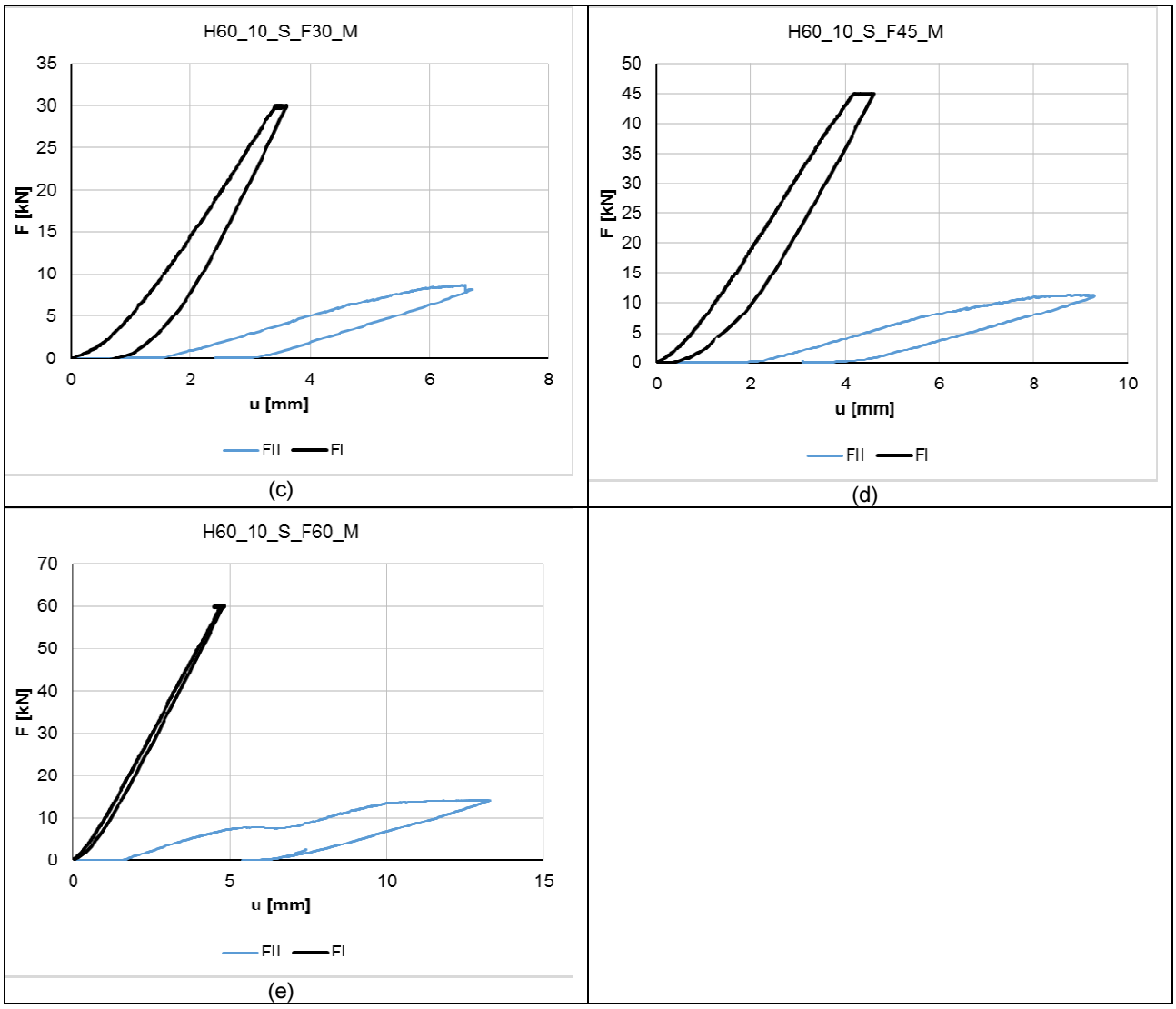

Table C-3 – *Stop – splayed and undersquinted.* Specimens *α = 60; β = 10°*: (a) H60_10_F0 ; (b) H60_10_M0 ; (c) H60_10_s_F30_M ; (d) H60_10_s_F45_M ; (e) H60_10_s_F60_M.

C.4 Halved undersquinted and tabled with key (α = 60°) – strong axis tests

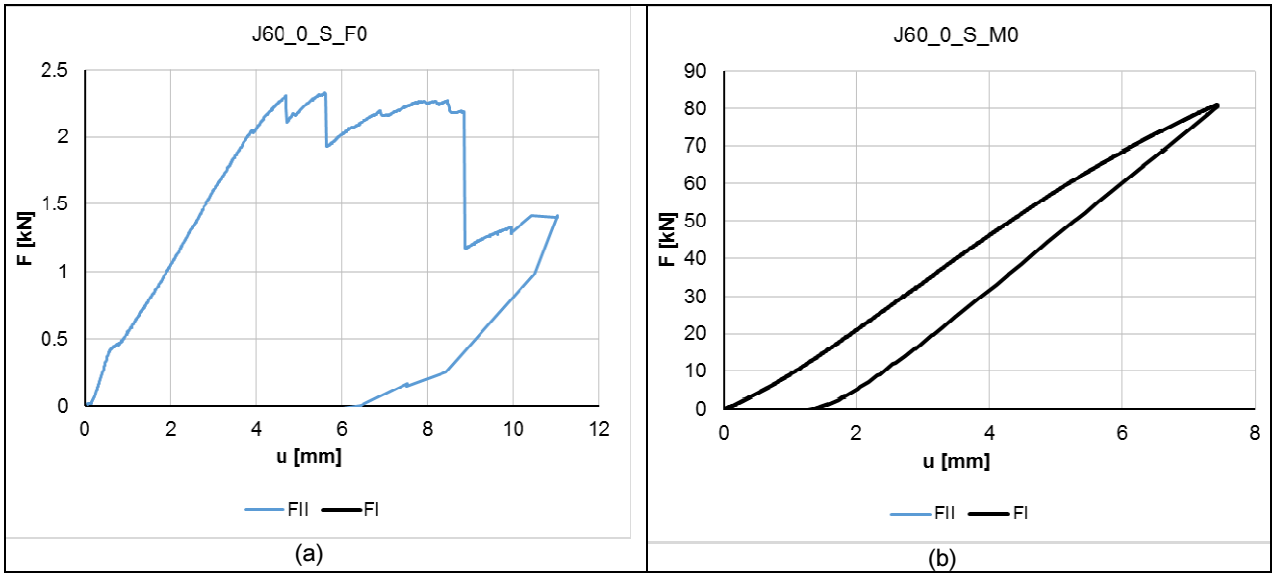

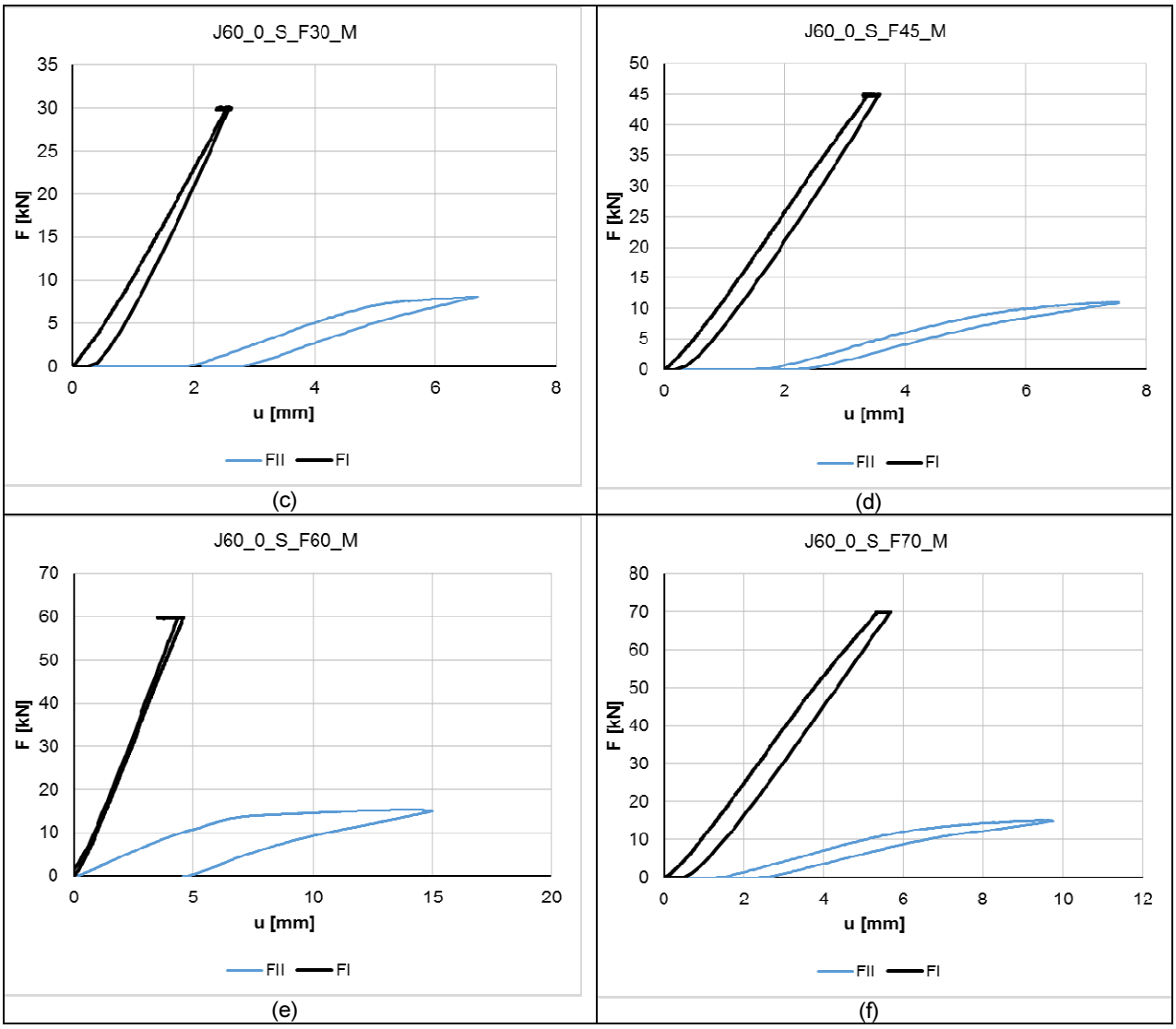

Table C-4 – *Halved undersquinted and tabled with key*. Specimens *α = 60*: (a) J60_0_s_F0 ; (b) J60_0_s_M0; (c) J60_0_s_F30_M ; (d) J60_0_s_F45_M ; (e) J60_0_s_F60_M; (f) J60_0_s_F70_M.

C.5 Stop – splayed undersquinted and tabled with key – strong axis tests

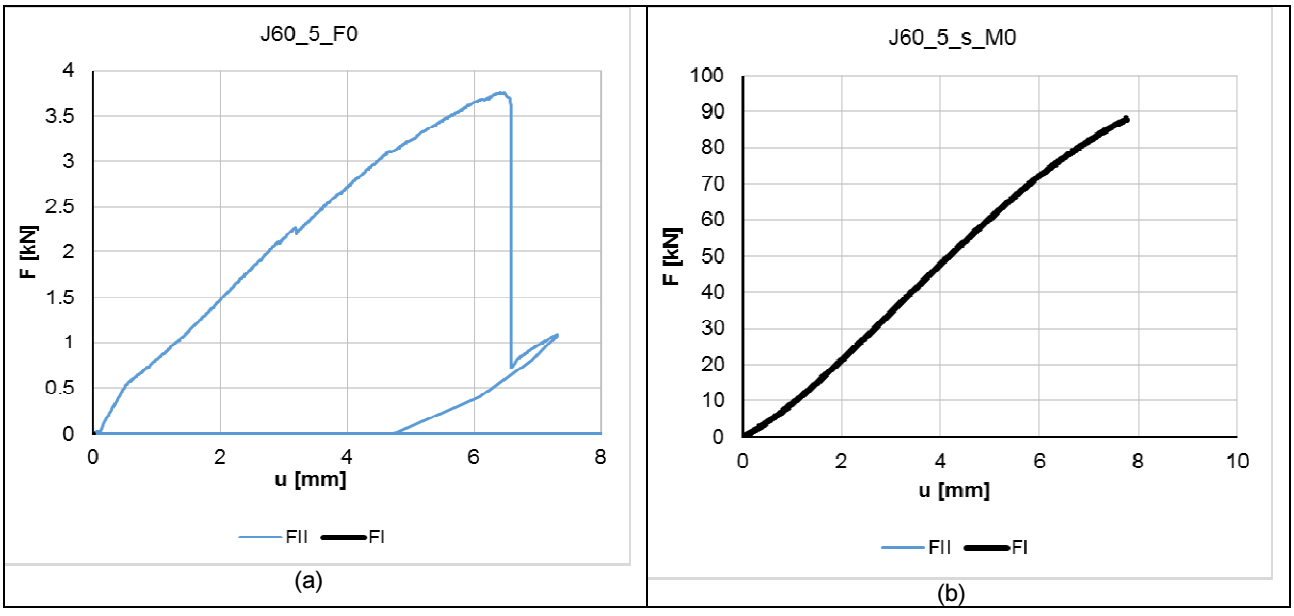

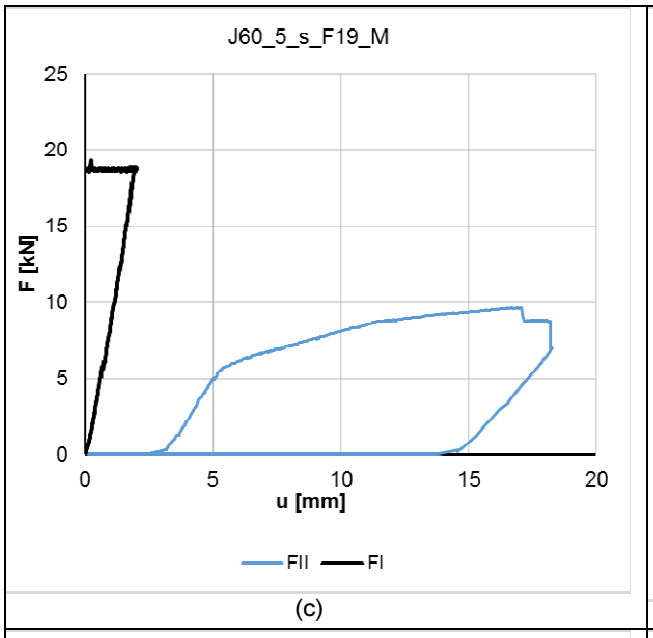
J60_5_s_F19_M
F [kN]
u [mm]
FII
FI

(c)

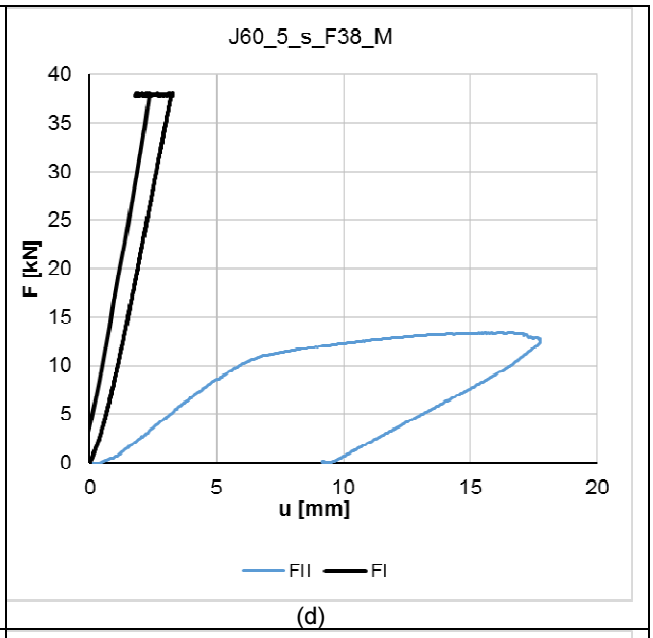
J60_5_s_F38_M
F [kN]
u [mm]
FII
FI

(d)

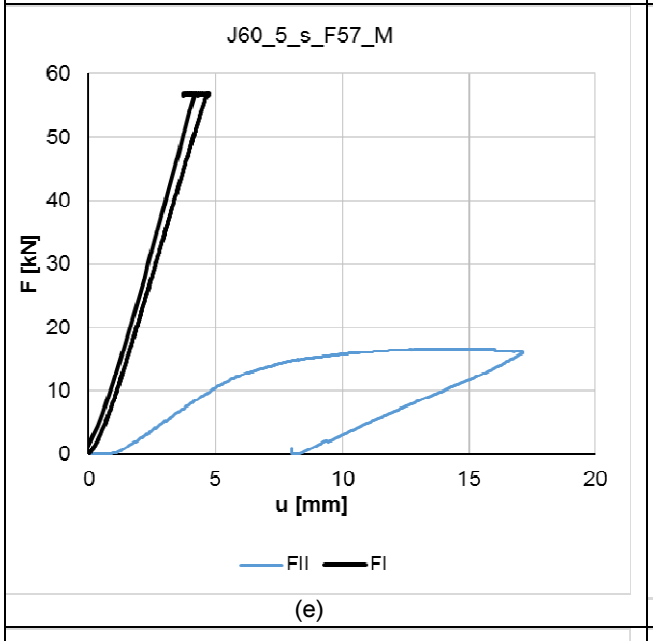
J60_5_s_F57_M
F [kN]
u [mm]
FII
FI

(e)

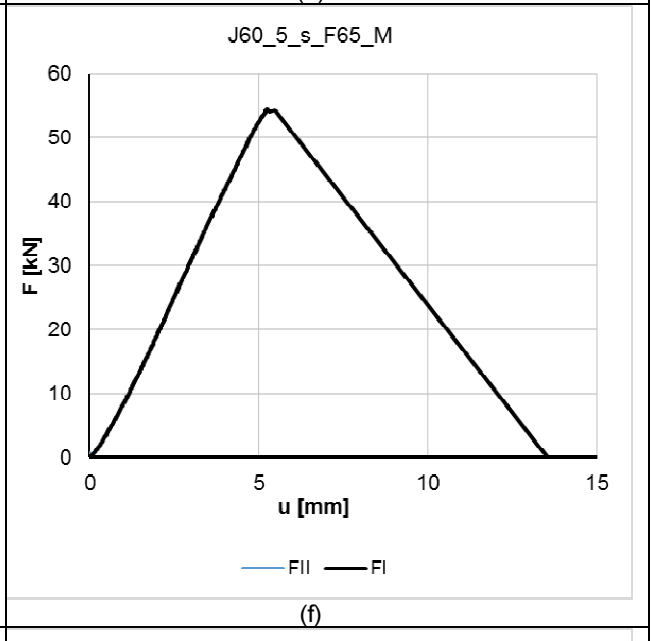
J60_5_s_F65_M
F [kN]
u [mm]
FII
FI

(f)

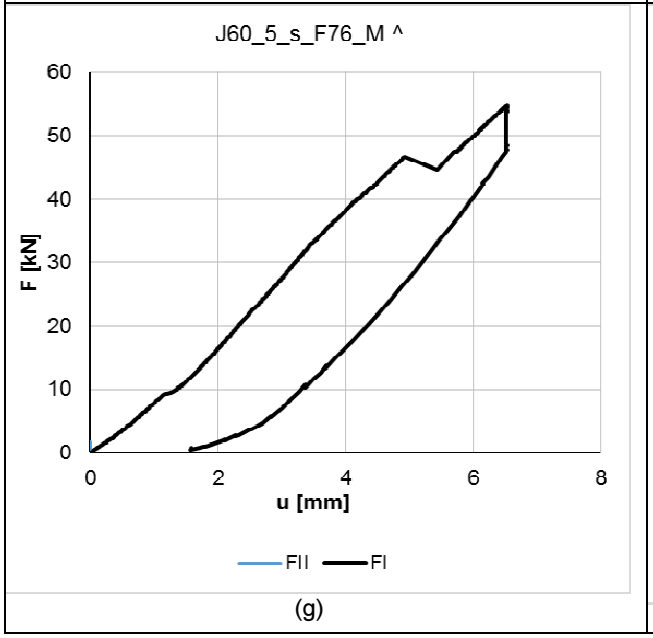
J60_5_s_F76_M ^
F [kN]
u [mm]
FII
FI

(g)

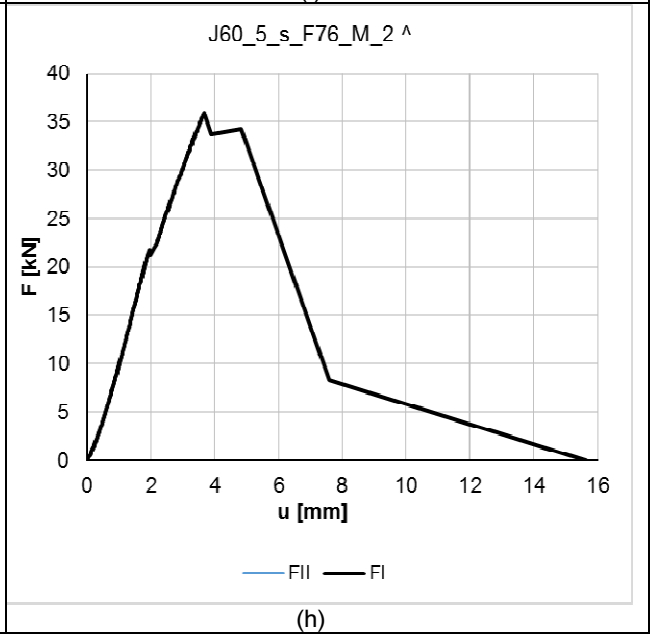
J60_5_s_F76_M_2 ^
F [kN]
u [mm]
FII
FI

(h)

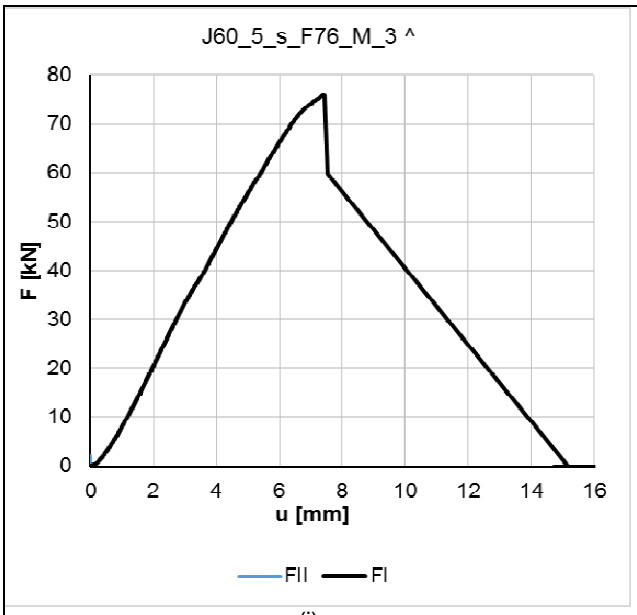
J60_5_s_F76_M_3 ^
F [kN]
u [mm]
FII
FI

(i)

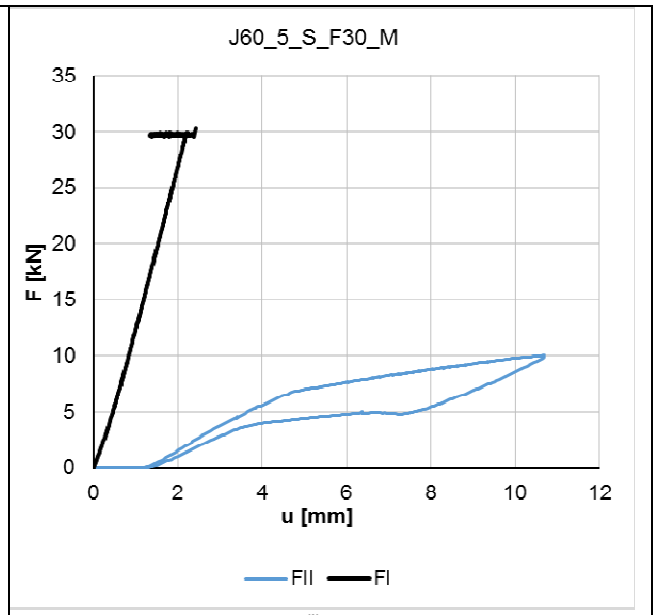
J60_5_S_F30_M
F [kN]
u [mm]
FII
FI

(j)

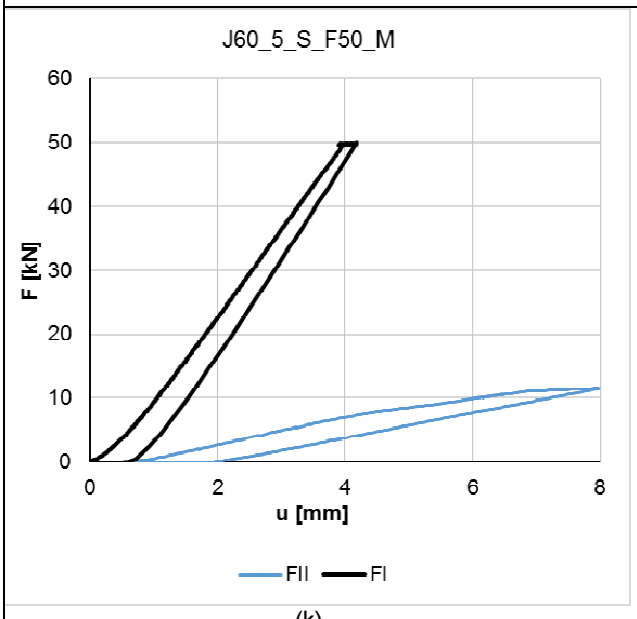
J60_5_S_F50_M
F [kN]
u [mm]
FII
FI

(k)

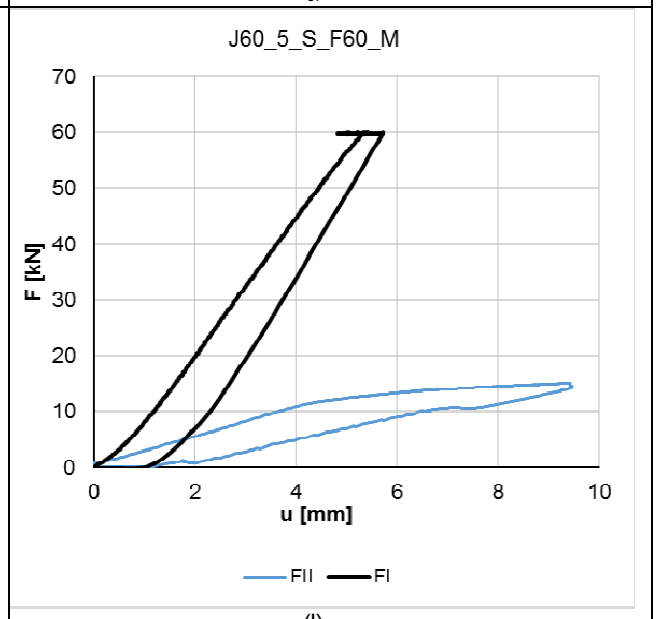
J60_5_S_F60_M
F [kN]
u [mm]
FII
FI

(l)

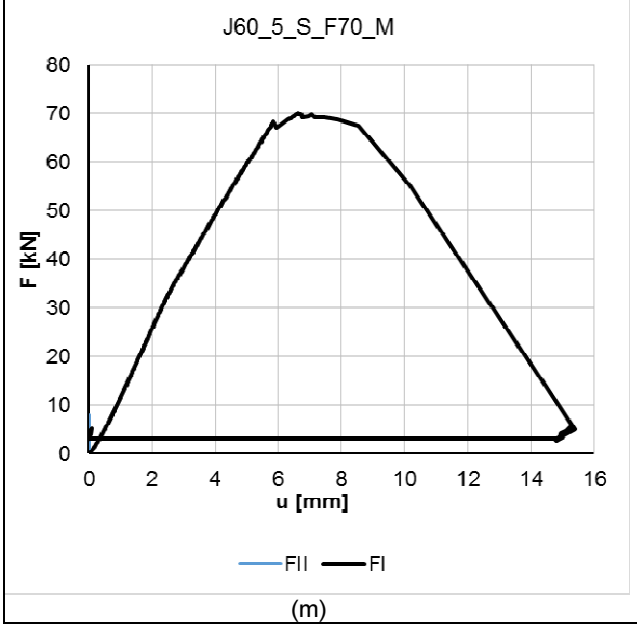
J60_5_S_F70_M
F [kN]
u [mm]
FII
FI

(m)

Table C-5 – *Stop – splayed undersquinted and tabled with key.* Specimens *α = 60; β = 5°* - strong axis tests: (a) J60_5_s_F0 ; (b) J60_5_s_M0 ; (c) J60_5_s_F19_M ; (d) J60_5_s_F38_M ; (e) J60_5_s_F57_M ; (f) 60_5_s_F65_M; (g) J60_5_s_F76_M ; (h) J60_5_s_F76_M_2 ; (i) J60_5_s_F76_M_3 ; (j) J60_5_s_F30_M ; (k) J60_5_s_F50_M ; (l) J60_5_s_F60_M ; (m) J60_5_s_F70_M.

C.6 Stop – splayed undersquinted and tabled with key – weak axis tests

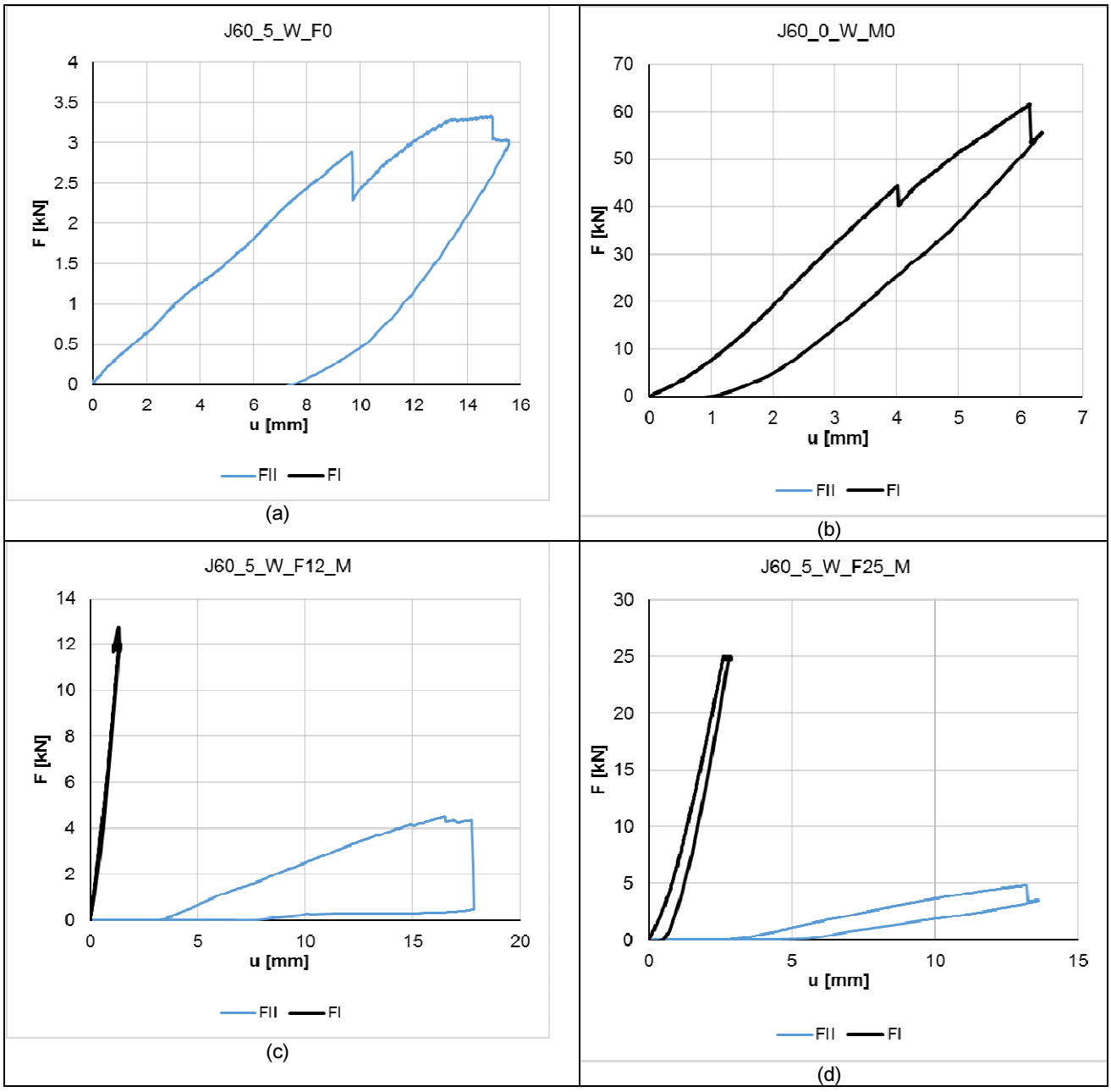

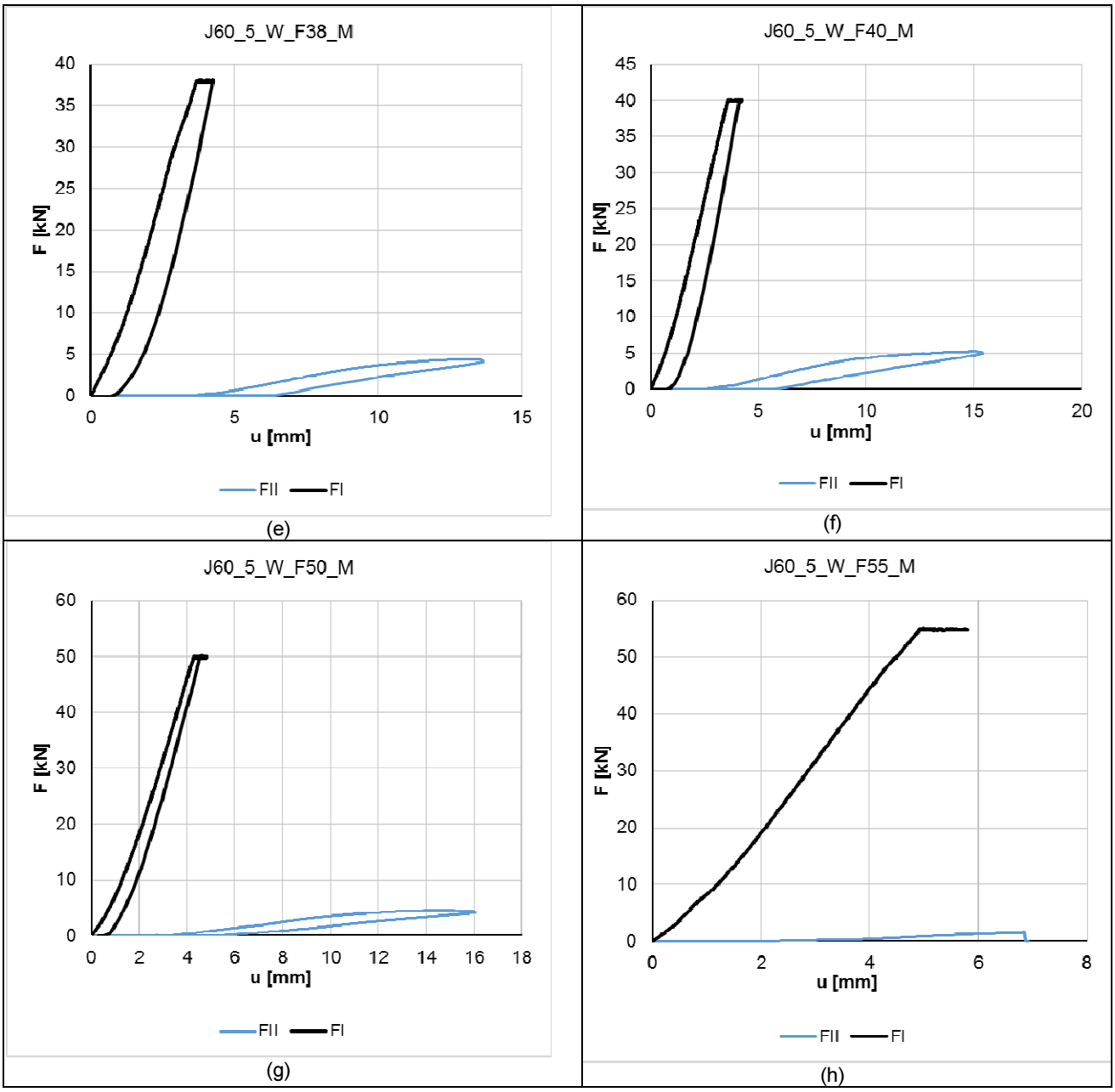

Table C-6 – *Stop – splayed undersquinted and tabled with key*. Specimens *α = 60; β = 5°* – weak axis tests: (a) J60_5_w_F0 ; (b) J60_5_w_M0 ; (c) J60_5_w_F12_M ; (d) J60_5_w_F25_M ; (e) J60_5_w_F38_M ; (f) 60_5_w_F40_M; (g) J60_5_w_F50_M ; (h) J60_5_w_F55_M

ANNEX D FAILURE MODES OF THE SPECIMENS

D.1 Investigation on the influence of the surfaces in the failure modes of the halved undersquinted scarf joint – experimental pre-campaign

Specimen	angle	date	specimen	Procedure	test type	FII [kN]	FI [kN]	a [mm]	Mu [kN mm]	Fu [kN]	photo number	photo failure	failure mode
1	30	16/04/2015	S1	P0 + a	pure bending	3.60	-	400	720.00	-	DSCF6912	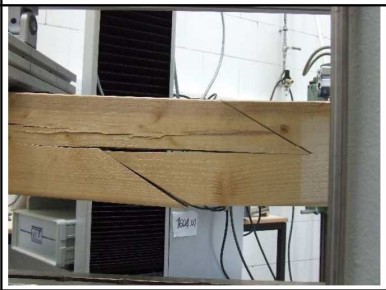	shear / tension perpendi-cular grain B
2	30	28/04/2015	S0	manual	μα test: pure bending - Self weight	self weight	-	-	self weight	-	100-7015	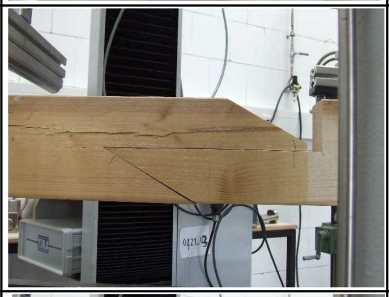	in equili-brium (no applied load)
3	30	28/04/2015	S0	manual	μα test: pure bending - ROLLER surf 1	-	-	-	-	-	100-7017	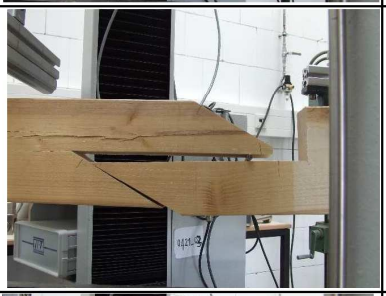	in equili-brium (no applied load)
4	30	28/04/2015	S0	manual	μα test: pure bending - ROLLER surf 2	-	-	-	-	-	100-7019	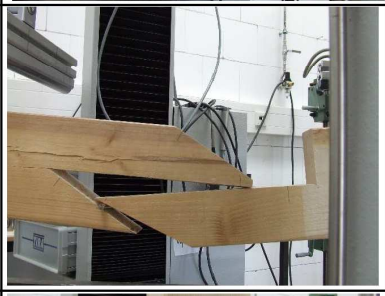	in equili-brium + big deforma-tions (no applied load)
5	35	05/05/2015	S1	P0 + b	pure compression a=0	-	-	-	-	-	DSCF7127		shear / tension perpendi-cular grain B and C

Table D-1 – Failure modes in the *halved undersquinted scarf* joint – First series of test – Influence of the surfaces_1

Specimen	angle	date	specimen	Procedure	test type	FII [kN]	FI [kN]	a [mm]	Mu [kN mm]	Fu [kN]	photo number	photo failure	failure mode
6	35	08/05/2015	S1	P0 + b	pure compression a=0	-	-	-	-	-	DSCF7166		shear / tension perpendi-cular grain B and C
7	35	16/05/2015	S1	P0 + b	pure compression a=0	-	13.00	-	-	13.00	DSCF7247	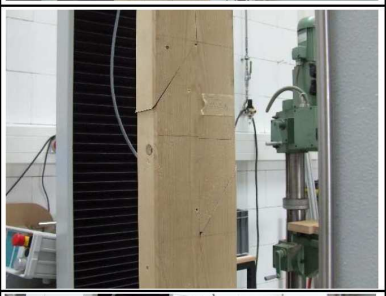	shear / tension perpendi-cular grain B and C
8	35	28/04/2015	S0	manual	μα test: pure bending - Self weight	self weight	-	-	self weight	-	100-7021	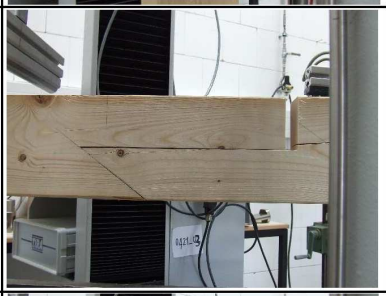	in equili-brium (no applied load)
9	35	28/04/2015	S0	manual	μα test: pure bending - ROLLER surf 1	0.00	-	-	0.00	-	100-7023	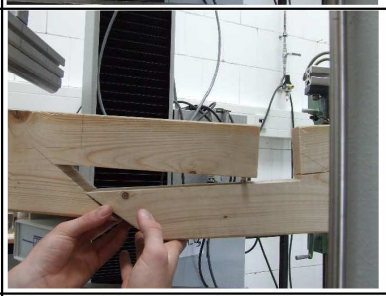	kinematic
10	35	28/04/2015	S0	manual	μα test: compression (manual) + bending (self weight)	self weight	-	-	self weight	-	100-7024	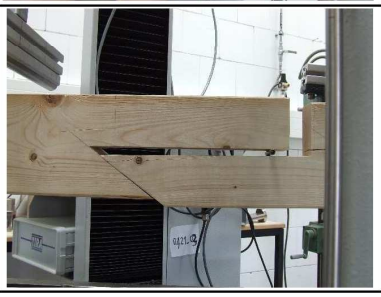	in equili-brium (no applied load)

Table D-2 – Failure modes in the *halved undersquinted scarf* joint – First series of test – Influence of the surfaces_2

Specimen	angle	date	specimen	Procedure	test type	FII [kN]	FI [kN]	a [mm]	Mu [kN mm]	Fu [kN]	photo number	photo failure	failure mode
11	35	29/05/2015	S1	P0 + a	pure bending, 1	2.79	-	400	558.00	-	DSCF7454	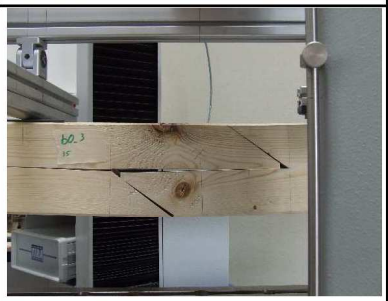	shear / tension perpendi-cular grain B
					pure bending, 2	2.48	-	400	496.00	-			
					pure bending, 3	2.65	-	400	530.00	-			
12	35	21/05/2015	S1	P0 + c	compression + bending a=40mm	-	17.85	40	714.00	17.85	DSCF7369		shear / tension perpendi-cular grain B and C
13	35	08/06/2015	S1	P0 + c	compression + bending a=40mm_1	-	11.85	40	474.00	11.85	DSCF7578		shear / tension perpendi-cular grain B and C
					compression + bending a=40mm_2	-	9.82	40	392.80	9.82			
14	35	02/06/2015	S1	P0 + c	compression + bending a=75mm_1	-	8.89	75	666.75	8.89	DSCF7492		shear / tension perpendi-cular grain B and C
					compression + bending a=75mm_2	-	7.72	75	579.00	7.72			
					compression + bending a=75mm_3	-	70.76	75	5307.00	70.76			
15	35	04/06/2015	S1	P0 + c	compression + bending a=95_1	-	11.50	95	1092.50	11.50	DSCF7531	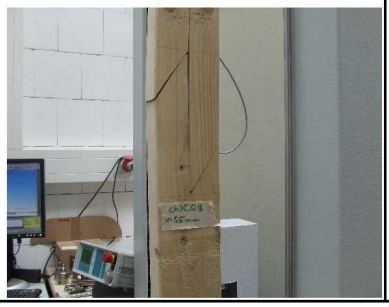	shear / tension perpendi-cular grain B and C
					compression + bending a=95_2	-	10.67	95	1013.65	10.67			

Table D-3 – Failure modes in the *halved undersquinted scarf* joint – First series of test – Influence of the surfaces_3

Specimen	angle	date	specimen	Procedure	test type	FII [kN]	FI [kN]	a [mm]	Mu [kN mm]	Fu [kN]	photo number	photo failure	failure mode
16	35		S1	P0 + c	compression + bending a=95 (record of the reaction forces' eccentricities in the surfaces)							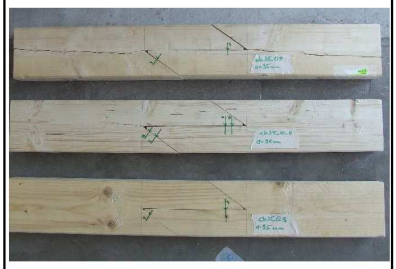	
17	35	10/06/2015	S1	P0 + c	compression + bending a=185_1	-	3.25	185	601.25	3.25	DSC_0873		shear / tension perpendi-cular grain B and C
					compression + bending a=185_2	-	3.45	185	638.25	3.45			
18	45	28/04/2015	S0	manual	µα test: pure bending - Self weight	self weight	-	-	self weight	-	100-7008	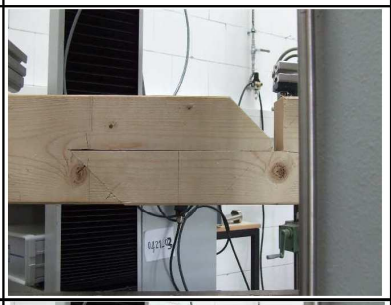	in equili-brium (no applied load)
19	45	28/04/2015	S0	manual	µα test: pure bending - ROLLER surf 1	0.00	0.00	-	0.00	0.00	100-7009	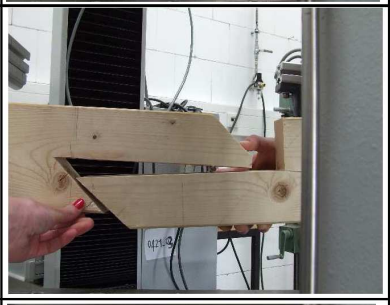	kinematic
19b	45	15/04/2015	S1	P0 + a	pure bending	27.00	-	400	5400.00	-	DSCF6901	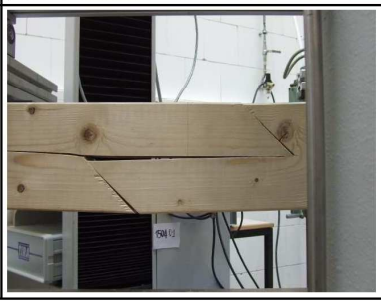	shear / tension perpendi-cular to the grains in B

Table D-4 – Failure modes in the *halved undersquinted scarf* joint – First series of test – Influence of the surfaces_4

Specimen	angle	date	specimen	Procedure	test type	FII [kN]	FI [kN]	a [mm]	Mu [kN mm]	Fu [kN]	photo number	photo failure	failure mode
20	45	28/04/2015	S0	manual	μα test: compression (manual) + bending (self weight)	-	-	-	-	-	100-7010		in equilibrium (no applied load)
21	45	29/05/2015	S1	P0 + a	pure bending	-	-	-	-	-	DSCF6901	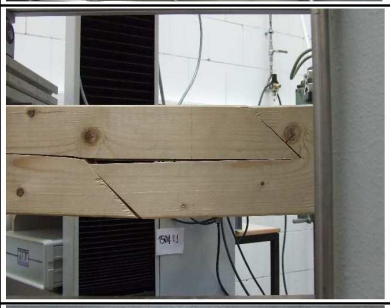	shear / tension perpendicular grain B
22	45	07/05/2015	S1	P0 + b	pure compression a=0	-	-	-	-	-	DSCF7154		shear / tension perpendicular grain B and C
23	45	16/05/2015	S1	P0 + b	pure compression a=0 _1	-	26.97	0	-	26.97	DSCF7236		shear/tension perpendicular grain B and C
					pure compression a=0 _2	-	49.81	0	-	49.81			(stopped)
24	45	18/05/2015	S1	P0 + b	pure compression a=0	-	39.07	0	-	39.07	DSCF7252	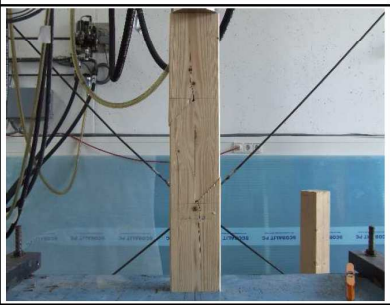	shear / tension perpendicular grain B and C

Table D-5 – Failure modes in the *halved undersquinted scarf* joint – First series of test – Influence of the surfaces_5

Specimen	angle	date	specimen	Procedure	test type	FII [kN]	FI [kN]	a [mm]	Mu [kN mm]	Fu [kN]	photo number	photo failure	failure mode
25	45	21/05/2015	S1	P0 + b	compression + bending a=40mm	-	19.63	40	785.20	19.63	DSCF7359		shear / tension perpendi-cular grain B and C
26	55	15/04/2015	S1	manual	pure bending (self weight)	-	-	-	-	-	DSCF6903	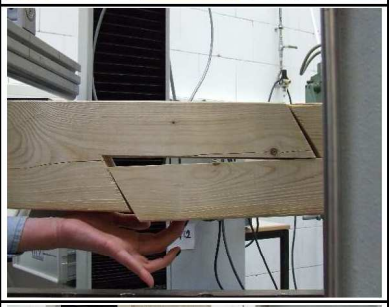	kinematic (it not bears the self weight)
27	55	08/05/2015	S1	P0 + b	pure compression a=0 (small machine)	-	-	-	-	-	DSCF7172		not broken
28	55	11/05/2015	S1	P0 + b	pure compression a=0 (big machine)	-	-	-	-	-	DSCF7188		shear / tension perpendi-cular grain B
29	55	18/05/2015	S1	P0 + b	pure compression a=0 (big machine)_1	-	46.71	0	-	46.71	DSCF7266	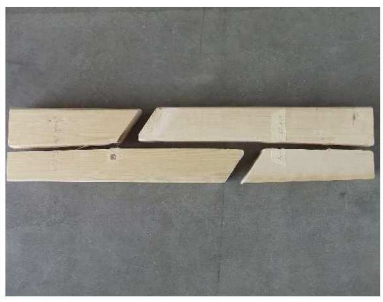	shear / tension perpendi-cular grain B and C
					pure compression a=0 (big machine)_2	-	33.73	0	-	33.73			
					pure compression a=0 (big machine)_3	-	38.57	0	-	38.57			

Table D-6 – Failure modes in the *halved undersquinted scarf* joint – First series of test – Influence of the surfaces_6

Specimen	angle	date	specimen	Procedure	test type	FII [kN]	FI [kN]	a [mm]	Mu [kN mm]	Fu [kN]	photo number	photo failure	failure mode
30	55	21/05/2015	S1	P0 + c	compression + bending a=40mm	-	27.70	40	1108.00	27.70	DSCF7383		shear / tension perpendi-cular grain B and C
30a	60	15/04/2015	S1	P0 + a	pure bending	0.00	0.00	-	0.00	0.00	DSCF6903	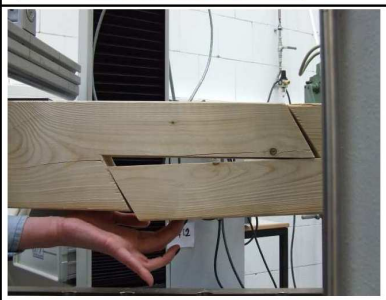	kinematic
31	70	04/05/2015	S0	P0 + b	compression - ROLLERS	0.00	>>0	0	0.00	>>0	DSCF7037		not broken
32	70	04/05/2015	S1	P0 + b	compression - GAP	0.00	>>0	0	0.00	>>0	DSCF7080	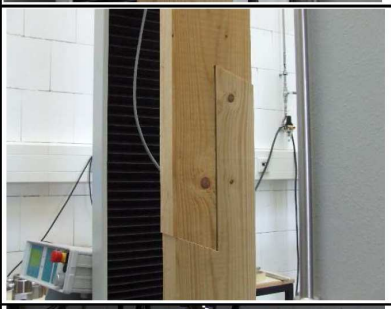	not broken
33	70	11/05/2015	S1	P0 + b	compression a=0	0.00	85.13	0	0.00	85.13	DSCF7199	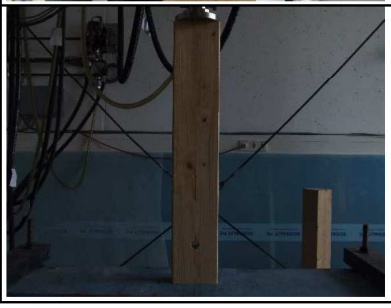	not broken (stopped)

Table D-7 – Failure modes in the *halved undersquinted scarf* joint – First series of test – Influence of the surfaces_7

Specimen	angle	date	specimen	Procedure	test type	FII [kN]	FI [kN]	a [mm]	Mu [kN mm]	Fu [kN]	photo number	photo failure	failure mode
34	75	24/04/2015	S0	manual	manual compression + bending with string - ROLLERS	0.00	>0	0	0.00	>0	DSCF7006 - DSCF6999	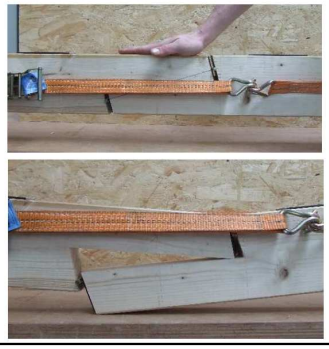	Zero load-carrying capacity for the connection with alignment of the ε1 - ε2 - ε3 (GC2 (vii) TEST 4 Chapter 6.3.4)
35	75	07/06/2015	S0	P0 + c	compression + bending a=58,3 - GAP_1	-	20.85	58.3	1215.56	20.85	DSCF7563		instability
					compression + bending a=58,3 - GAP_2	-	16.78	58.3	978.45	16.78			instability
36	75	05/06/2015	S1	P0+c	compression + bending a=58,3	-	-	58.3	-	-	DSCF7549		instability
37	90	05/06/2015	S1	P0 + c	compression + bending a=95	self weight	self weight	95	self weight	self weight	DSCF7536		kinematic
37a	90	05/06/2015	S1	P0+ + c	compression + bending a=46,7	-	17.69	46	813.74	17.69			not broken

Table D-8 – Failure modes in the *halved undersquinted scarf* joint – First series of test – Influence of the surfaces_8

Specimen	angle	date	specimen	Procedure	test type	FII [kN]	FI [kN]	a [mm]	Mu [kN mm]	Fu [kN]	photo number	photo failure	failure mode
38	90	05/06/2015	S1	P0 + c	compression + bending a=58,3	-	>>	58.3	>>	>>	DSCF7548	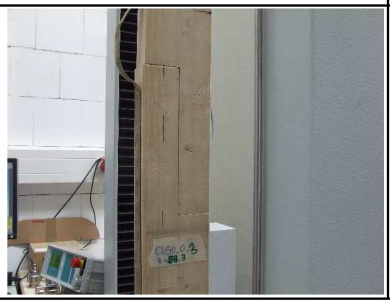	not broken

Table D-9 – Failure modes in the *halved undersquinted scarf* joint – First series of test – Influence of the surfaces_9

D.2 Failure modes of the halved undersquinted scarf joint, in-plane

D.2.1 *Halved undersquinted* with *α = 30°,* in-plane

Specimen	Date	Specimen	Procedure	FI,target [kN]	FII [kN]	FI [kN]	a [mm]	Mu [kN·mm]	Fu [kN]	Observations + FM Failure foto	FM
R30_F0	20/01/2016	S3	P1 - a	-	2.32	0	405	470.61	0	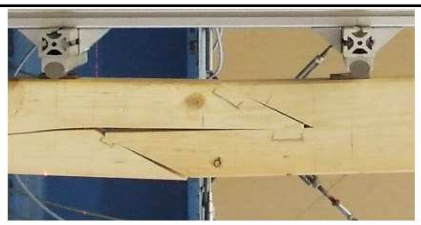	FM II
R30_F0_2	20/01/2016	S3	P1 - a	-	3.35	0	405	679.19	0	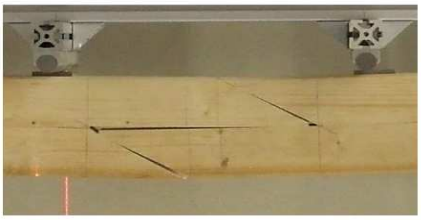	FM II. Same specimen F_M_2; F_M_3; F_M_4
R30_F0_bis	20/01/2016	S3	P1 - c	-	6.65	6.41	405	1345.8	6.41	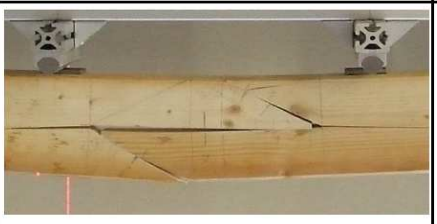	FM II
R30_F0_bis2	20/01/2016	S3	P1 - c	-	4.34	7.87	405	879.46	7.87	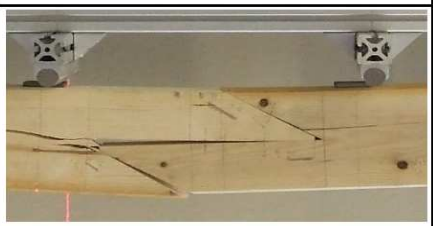	FM II
R30_M0	20/01/2016	S3	P1 - b	-	0.00	8.4	405	0	8.4	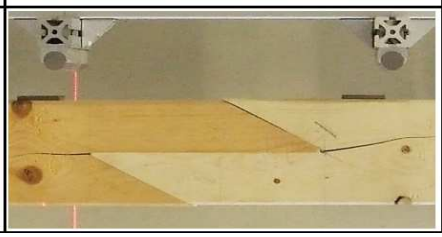	FM III

Table D-10 – Failure modes in the *halved undersquinted scarf* joint, in-plane – α = 30°_1

Specimen	Date	Specimen	Procedure	Fl,target [kN]	FII [kN]	Fl [kN]	a [mm]	Mu [kN·mm]	Fu [kN]	Observations + FM Failure foto	FM
R30_F_M	20/01/2016	S3	P1 - c	-	4.90	6.17	405	992.66	6.17	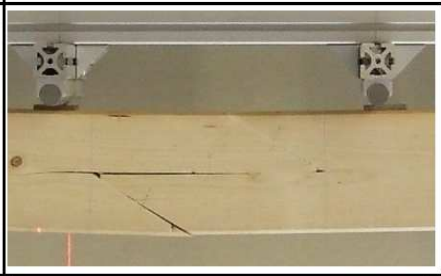	FM II
R30_F_M_2	20/01/2016	S3	P1- -d	1	0.02	5.48	405	4.78	5.48	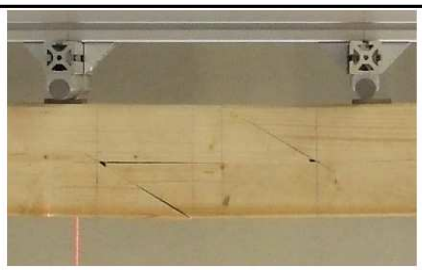	Stopped, first crack. Same specimen F_M_3; F_M_4; F0_2
R30_F_M_3	20/01/2016	S3	P1 - d	0.5	0.02	5.48	405	4.78	5.48	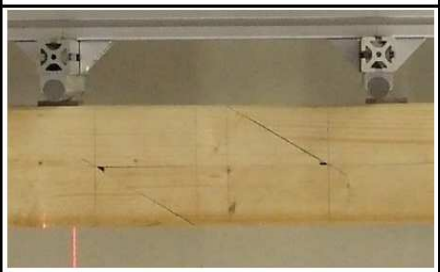	Stop, first crack. Same specimen as F_M_2; F_M_4; F0_2
R30_F_M_4	20/01/2016	S3	P1 - d	0.25	0.02	5.48	405	4.78	5.48	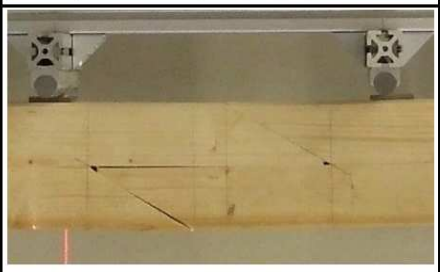	Stop, first crack. Same specimen as F_M_2; F_M_3; F0_2
R30_N2_Ma	01/02/2016	S3	P2 - c	2	2.87	1.98	405	580.37	1.98	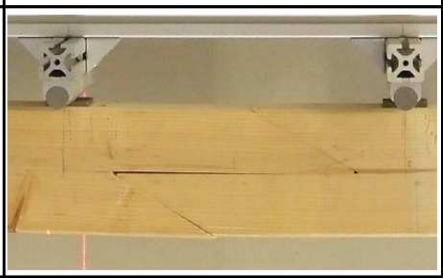	FM II
R30_N5_M	01/02/2016	S3	P2 - c	5	2.55	1.98	405	516.98	1.98	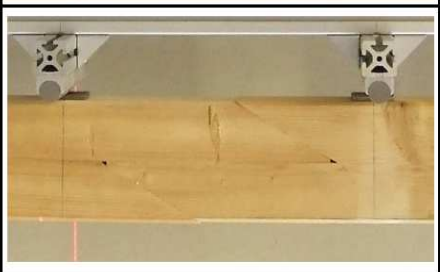	FM II

Table D-11 – Failure modes in the *halved undersquinted scarf* joint, in-plane – α = 30°_2

D.2.2 Halved undersquinted with *α = 60°,* in-plane

Specimen	Date	Specimen	Procedure	Fl,target [kN]	Fll [kN]	Fl [kN]	a [mm]	Mu [kN·mm]	Fu [kN]	Observations + FM Failure foto	FM
R60_F0	01/02/2016	S3	P2 - a	-	1.22	-0.01	405	247.1	0	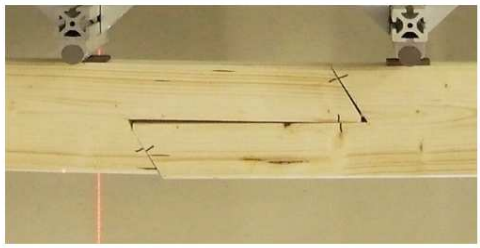	FM IV
R60_M0	01/02/2016	S3	P2 - b	-	-0.08	42.01	405	-16	42	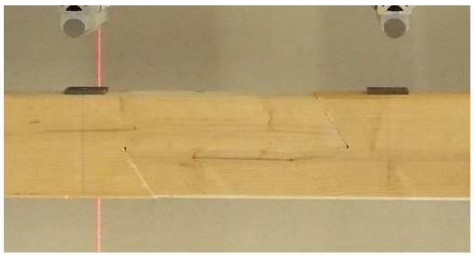	Stopped, instability
R60_M0_2	01/02/2016	S3	P1 - b	-	-0.08	84.52	405	-15.4	84.51	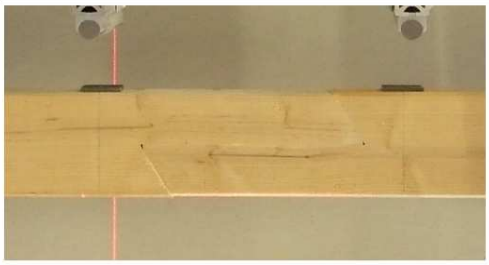	Stopped, instability. It can bear more and more load.
R60_N16_M	01/02/2016	S3	P2 - c	16	6.14	16.01	405	1244	16	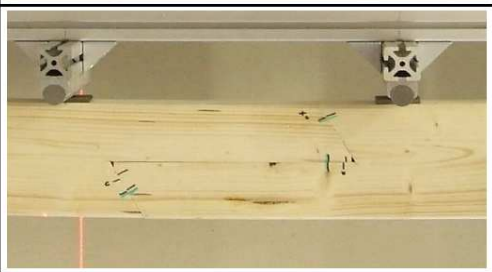	FM II
R60_N32_Ma	01/02/2016	S3	P2 - c	32	10.22	32.07	405	2069	32.06	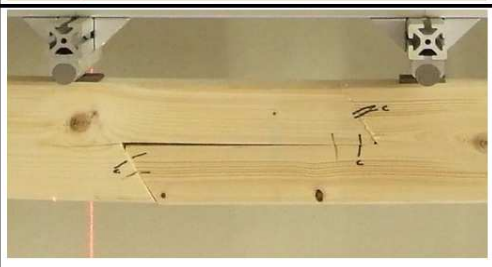	FM II
R60_N48_M	01/02/2016	S3	P2 - c	48	12.85	47.97	405	2602	47.96	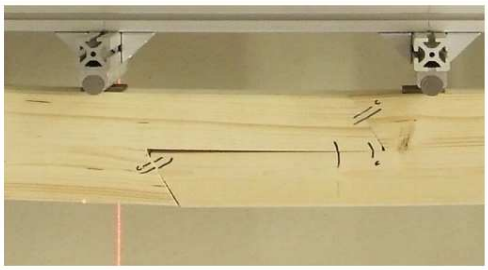	FM II, critic crack points also ε1=1/4 and ε3=1/4

Table D-12 – Failure modes in the *halved undersquinted scarf* joint, in-plane – α = 60° _1

R60_N64_M	01/02/2016	S3	P2 - c	64	15.13	63.98	405	3064	63.97	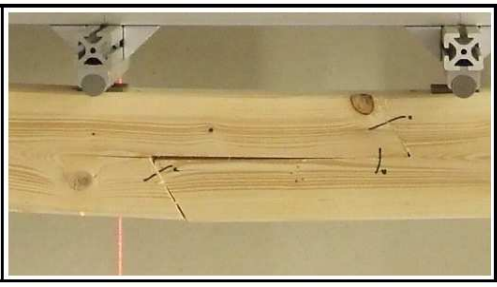	Test interrupt danger instab. Upper plate bent.

Table D-13 – Failure modes in the *halved undersquinted scarf* joint, in-plane – α = 60° _2

D.3 Failure modes of the stop-splayed and undersquinted scarf joint, in-plane

Specimen	Date	Specimen	Procedure	Fl,target [kN]	Fll [kN]	Fl [kN]	a [mm]	Mu [kN·mm]	Fu [kN]	Observations + FM Failure foto	FM
H60_10_S_F0	20/07/2016	S4	P2 + a	-	0.20	0.00	390.00	39.2	0.00		FM IV
H60_10_S_F30_M	20/07/2016	S4	P2 + c	30	8.61	29.67	390.00	1678	29.67	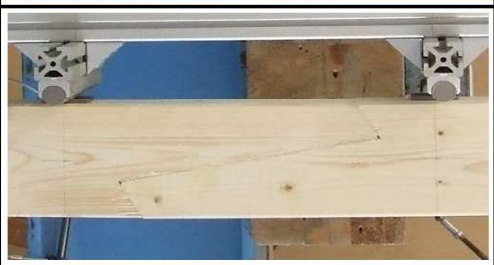	FM II
H60_10_S_F45_M	20/07/2016	S4	P2 + c	45	11.14	44.96	390.00	2172	44.96		FM II
H60_10_S_F60_M	20/07/2016	S4	P2 + c	60	14.03	59.93	390.00	2735	59.93		FM II. Same specimen H60_10_S_F0.
H60_10_S_M0	20/07/2016	S4	P2 + b	-	0.00	74.76	390.00	0	74.76		NO FM. Stopped. can bear aprox. up to Fl= 80-90kN. Same specimen H60_10_S_F0.

Table D-14 – H60_10_s specimens failure modes, in-plane

D.4 Failure modes of the halved undersquinted and tabled with key, in-plane

Specimen	Date	Specimen	Procedure	Fl,target [kN]	Fll [kN]	Fl [kN]	a [mm]	Mu [kN·mm]	Fu [kN]	Observations + FM Failure foto	FM
J60_0_S_F30_M	20/07/2016	S5	P2 + c	30	8.03	29.78	390.00	1565	29.78	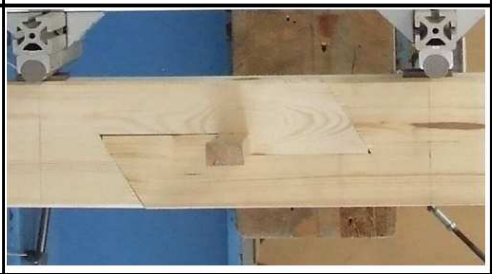	FM II + FM V. Stopped first crack B'. Same specimen upper J60_0_S_M0.
J60_0_S_F45_M	20/07/2016	S5	P2 + c	45	11.03	44.83	390.00	2151	44.83	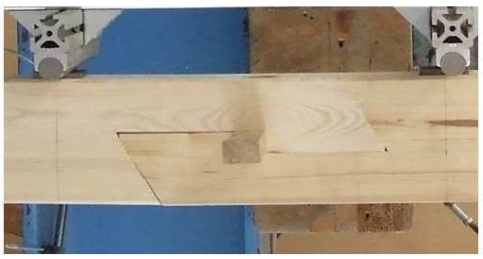	FM II + FM V. Stopped first crack B'. Same specimen upper J60_0_S_M0.
J60_0_S_F60_M	19/07/2016	S5	P2 + c	60	15.20	59.73	390.00	2964	59.73	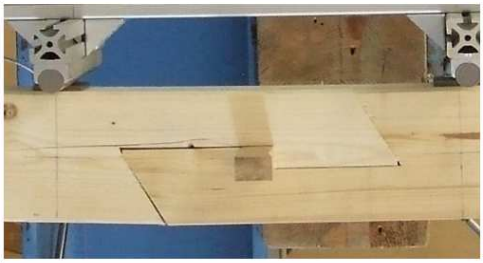	FM II. Stopped first crack B. Same specimen upper J60_0_S_M0.
J60_0_S_F70_M	20/07/2016	S5	P2 + c	70	14.07	67.54	390.00	2744	67.54	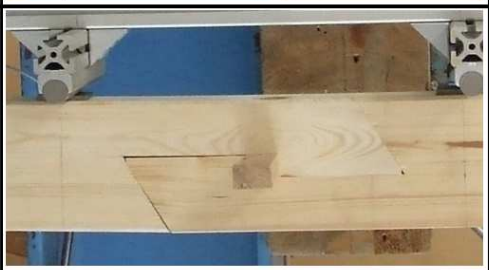	FM II + FM V. Stopped first crack B'. Same specimen upper J60_0_S_M0.
J60_0_S_M0	19/07/2016	S5	P2 + b	-	0.00	81.03	390.00	0	81.03	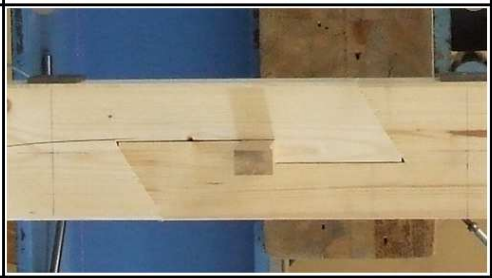	FM II. Stopped. It can bear more and more N.
J60_0_S_F0	19/07/2016	S5	P2 + a	-	2.30	0.00	390.00	448.1	0.00	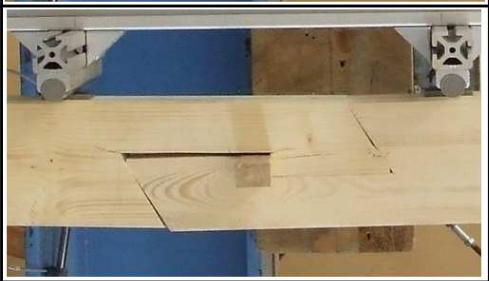	FM V

Table D-15 – J60_0_s specimens failure modes, in-plane

D.5 Failure modes of the Jupiter joint

D.5.1 *Jupiter joint*, in plane

Specimen	Data	Specimen	Procedure	$F_{I,target}$ [kN]	F_{II} [kN]	F_I [kN]	a [mm]	Mu [kN·mm]	Nu [kN]	FM	Observations +FM Failure foto
J60_5_F0	18/07/2016	S6	P2 - a	-	3.75	0.00	390	731.25	0.00	FM V	
J60_5_s_M0	18/07/2016	S6	P2 - b	-	0.00	87.95	390	0	87.95	FM II	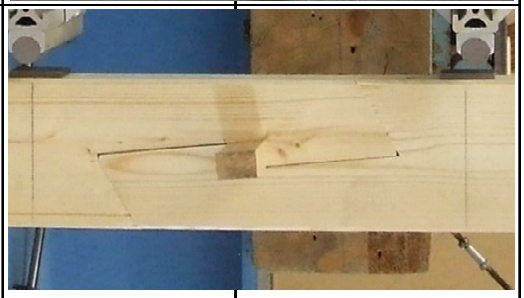
J60_5_s_F19_M	19/07/2016	S6	P2 - c	19	9.62	18.73	390	1876.095	18.73	FM II + FM V	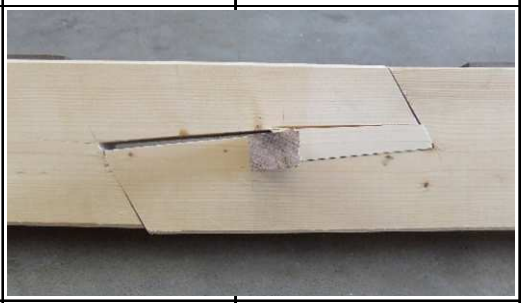
J60_5_s_F38_M	19/07/2016	S6	P2 - c	38	13.34	37.77	390	2601.3	37.77	FM II + FM V	
J60_5_s_F57_M	19/07/2016	S6	P2 - c	57	16.55	56.80	390	3226.86	56.80	FM II + FM V	

Table D-16 – J60_5_s specimens failure modes – in-plane tests_1

Specimen	Data	Specimen	Procedure	$F_{I,target}$ [kN]	F_{II} [kN]	F_I [kN]	a [mm]	Mu [kN·mm]	Nu [kN]	FM	Observations +FM Failure foto
J60_5_s_F65_M	19/07/2016	S6	P2 - c	65	0.00	54.30	390	0	54.30	FM II + FM III	 brittle failure, loaded in only pure compression Fi
J60_5_s_F76_M ^	19/07/2016	S6	P2 - c	76	0.00	54.47	390	0	54.47	FM II	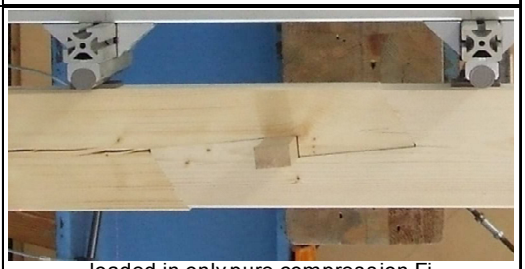 loaded in only pure compression Fi
J60_5_s_F76_M_2 ^	19/07/2016	S6	P2 - c	76	0.00	35.94	390	0	35.94	FM II + FM III	 brittle failure, loaded in only pure compression Fi
J60_5_s_F76_M_3 ^	19/07/2016	S6	P2 - c	76	0.00	75.87	390	0	75.87	FM II + FM III	 brittle failure, loaded in only pure compression Fi
J60_5_s_F60_M	20/07/2016	S6	P2 - c	60	15.03	59.84	390	2931.045	59.84	FM II	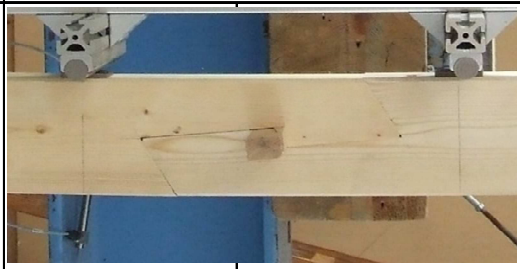
J60_5_s_F50_M	20/07/2016	S6	P2 - c	50	11.53	49.71	390	2248.545	49.71	FM II	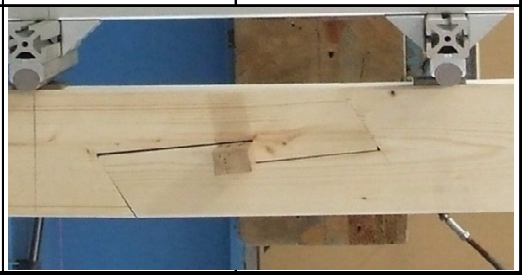

Table D-17 – J60_5_s specimens failure modes – in-plane tests_2

Specimen	Data	Specimen	Procedure	$F_{I,target}$ [kN]	F_{II} [kN]	F_I [kN]	a [mm]	Mu [kN·mm]	Nu [kN]	FM	Observations +FM Failure foto
J60_5_s_F30_M	20/07/2016	S6	P2 - c	30	10.00	29.60	390	1950	29.60	FM II	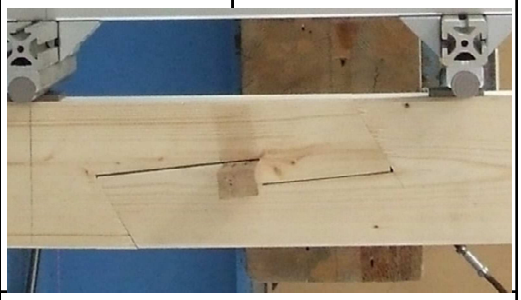
J60_5_s_F70_M	20/07/2016	S6	P2 - c	70	7.83	70.09	390	1527.24	70.09	FM II	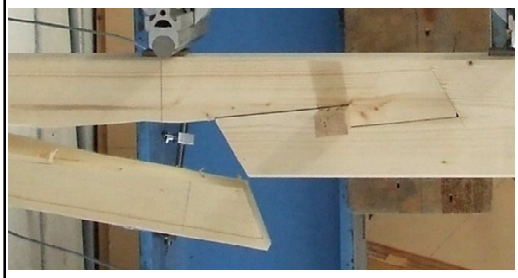 brittle failure

Table D-18 – J60_5_s specimens failure modes – in-plane tests_3

D.5.2 *Jupiter joint*, out-of-plane

Specimen	Date	Specimen	Procedure	$F_{I,target}$ [kN]	F_{II} [kN]	F_I [kN]	a [mm]	M [kN·mm]	N [kN]	FM		observations	FOTO FM	
										Comp. side	Tension side		Compression side	Tension side
J60_5_w_M0	21/07/2016	S6	P2 - b	-	0	61.53	390	0.00	61.53	C, C', B	B	(stopped)	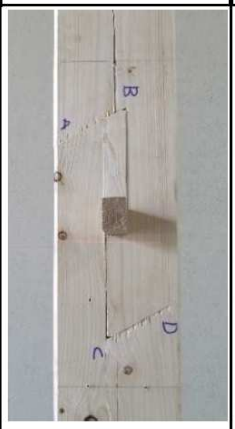	
J60_5_w_F0	21/07/2016	S6	P2 - a	-	3.338	0.00	390	650.91	0.00	B, K	B			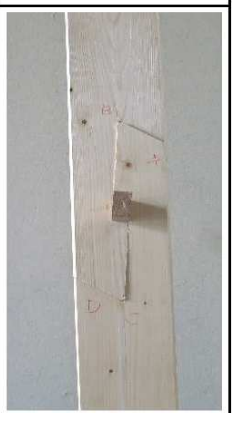

Table D-19 – J60_5_s specimens failure modes – out-of-plane tests_1

Specimen	Date	Specimen	Procedure	$F_{I,target}$ [kN]	F_{II} [kN]	F_I [kN]	a [mm]	M [kN·mm]	N [kN]	FM		observations	FOTO FM	
										Comp. side	Tension side		Compression side	Tension side
J60_5_w_F50_M	21/07/2016	S6	P2 - c	50	4.57	49.75	390	891.15	49.75	B	B (FM II)			
J60_5_w_F38_M	21/07/2016	S6	P2 - c	38	4.359	37.97	390	850.01	37.97	B, C', C	B, B', C', C		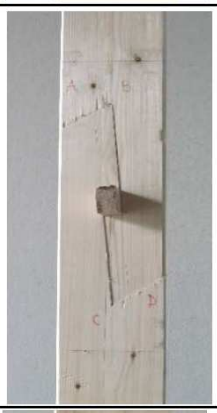	
J60_5_w_F25_M	21/07/2016	S6	P2 - c	25	4.83	24.89	390	941.85	24.89	-	C', B (FM V)	il provino ha nodi nel centro della cross-section, su entrambi i lati, quello compresso e quello teso.		
J60_5_w_12_M	21/07/2016	S6	P2 - c	12	4.342	12.77	390	846.69	12.77	H, B	K, C, B', B	the specimen is bent respect to the vertical. Once loaded with FII, the lower contact with external support later respect to the upper one.		

Table D-20 – J60_5_s specimens failure modes – out-of-plane tests_2

Specimen	Date	Specimen	Procedure	Fl,target [kN]	Fll [kN]	Fl [kN]	a [mm]	M [kN·mm]	N [kN]	FM		observations	FOTO FM	
										Comp. side	Tension side		Compression side	Tension side
J60_5_w_40_M	21/07/2016	S6	P2 - c	40	5.281	39.91	390	1029.80	39.91	B, C'	B			
J60_5_w_55_M	21/07/2016	S6	P2 - c	55	1.63	54.85	390	317.85	54.85	B, C	B, C	brittle failure. Used specimen. Upper part in good conditions from w_F50_M, lower part from s_F60_M with some cracks.	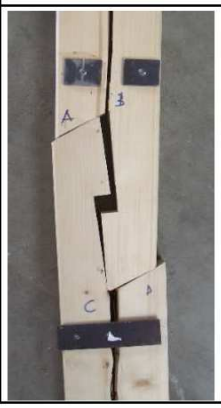	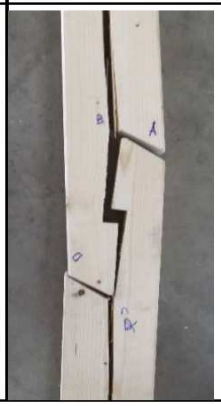

Table D-21 – J60_5_s specimens failure modes – out-of-plane tests_3

ANNEX E KEY INSTALLATION

E.1 Key length

The capacity of the key depends on the key's angle; therefore, during the preparation of the test specimens, the dimension of the key's wedges was a focus point for the carpenter. In the 1:1 beams (see Chapter 8.2), the key is fully contained in the width of the beam (180 x 200 mm^2). The specimen used for the experimental campaigns are in-scale beams and the key should consequently be scaled to be contained in the width *b* of the beam.

The first key (Figure E-1) with proportion 1:2.3, gave an angle of θ = 25°. During the installation of the wedges, the provided pre-compression was not enough. In fact, during the installation it came out with the minimum movement. The key was remodelled with the angle present in the original case study's beams with ratio between the length and the height of the key 1:6. The new key (Figure D-2) is therefore bigger than the width of the beam, but it confers the correct pre-compression to the joint.

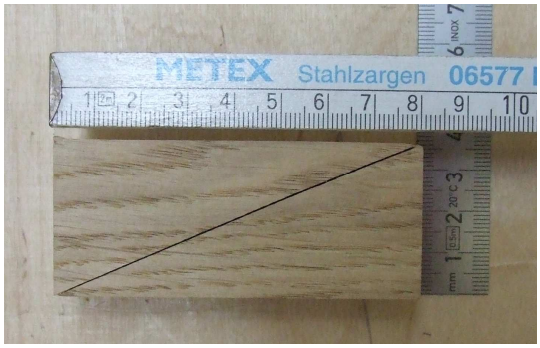

Figure E-1 – First key

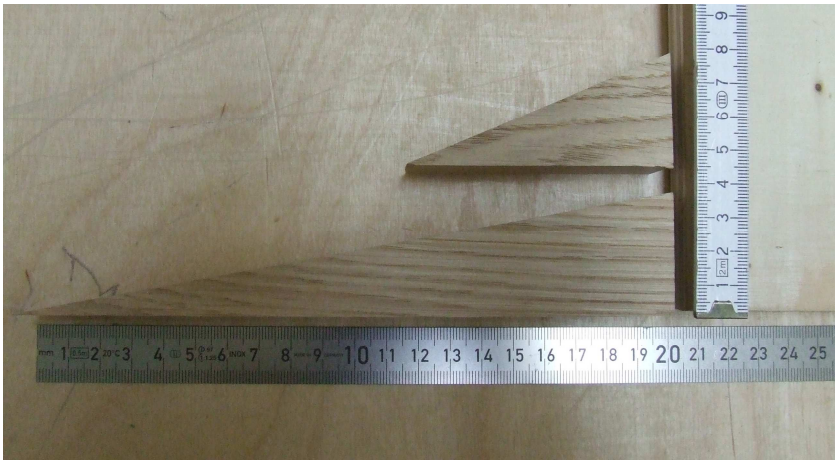

Figure E-2 – Comparison among the discarded key with proportion 1:2.3 and the selected key 1:6

E.2 Key installation

The geometry of the *Jupiter joint* is provided with a *square-cut* key geometry. This particular cut of the key is the most diffused in carpentry jointry. The pre-compression conferred by this geometry has particular consequences on the joint.

During the installation, the force applied from the carpenter to the wedges is transmitted to the two internal walls of the beams in correspondence with the segments $\overline{B'C''}$ and $\overline{B''C'}$. The horizontal force applied on these faces $F_{pc,1} = F_{pc,2}$, inclined of an angle β = 5° respect to the fibres, decomposes in two components $F_{pc,90}$ and $F_{pc,0}$. The $F_{pc,0}$ is the horizontal force that confers pre-compression to the connection, and $F_{pc,90}$ is the vertical component that separates the two $\overline{BB'}$ and $\overline{CC'}$ adjacent surfaces.

The *square-cut* key installation causes the joint to be loaded in compression perpendicular to grain during the pre-compression phase. This effect is disadvantageous for the capacity of the connection in bending. The bigger the angle β the bigger the vertical component that induces the opening of the adjacent $\overline{BB'}$ and $\overline{CC'}$ surfaces.

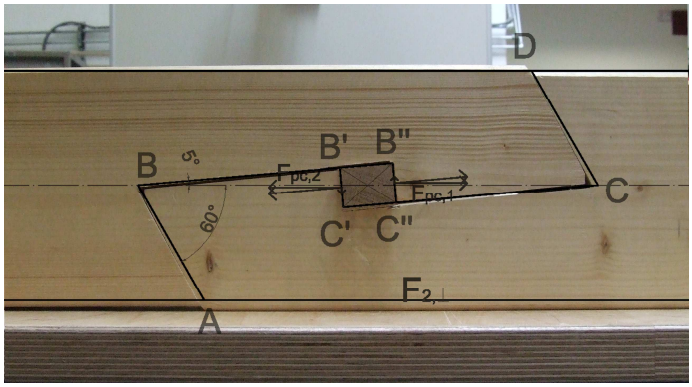

Figure E-3 –Forces due to the key installation.

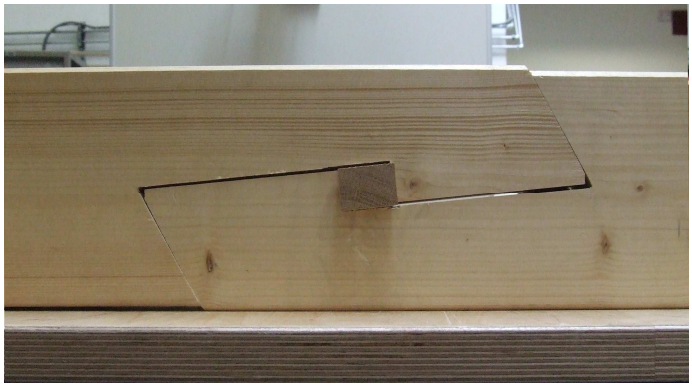

Figure E-4 – Gap on the surface $\overline{CC'}$ due to the key installation.

An attempt to improve the *Jupiter joint* and avoid that pre-compression negative effect has been studied by Sangree and Schafer (2009). It has been proofed that in a tensile-stressed *Jupiter joint*, the oblique-cut key (Figure 2-29 – b) influences the joint axial stiffness. Such key orientation has also an improving effect in the key-installation phase, because avoids the compression perpendicular to the grains; therefore, the absence of the angle β in the *oblique-cut key* avoids the opening-effect of the key along the BB' and CC' surfaces.

Nevertheless, the constructional praxis, due to the easiness to fashion of the *square-cut key* respect to the *oblique-cut key* rendered more common the use of the first one.

ANNEX F CALIBRATION OF THE STRUCTURAL MODEL

F.1 Introduction

The aim of the calibration of the structural model is obtain a functioning model for the structural analysis, in which the stiffness properties of the materials and structural elements are well defined and in accordance with the real structure. In order to get this result, a step-by-step process is performed.

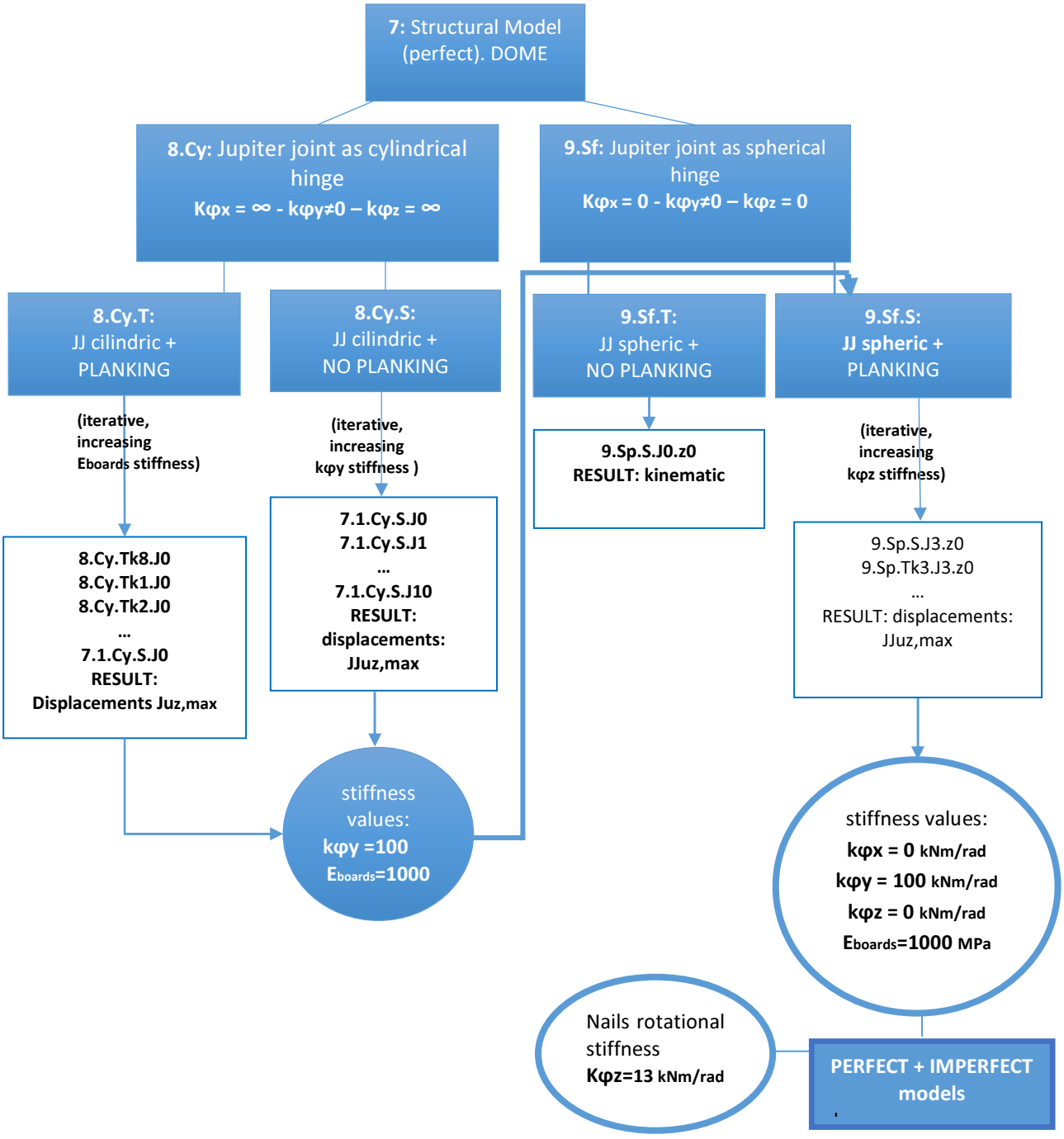

Figure F-1 – Scheme of the calculation process

In the Figure F-1 the whole step-by-step process for the calibration of the model is summarized. The main definition for the understanding present chapter follows in the Table F-1, key of the structural calculation. A short description of the main properties analysed in the used models follows. The summary of the properties, for each step, is contained in the Table F-2.

Table F-1 – Key of the structural calculations

8_	**Cy /Sf_**	**Tk8_**	**x0_**	**J0_**	**z10**
|	|	|	|	|	|
Model	Cylindrical/ sferical jupiter joint	Stiffness of the boarding	Jupiter joint torsional stiffness (**JJ kϕ*x***)	Jupiter joint stiffness along the strong axis (**JJ kϕ*y***)	Jupiter joint stiffness along the weak axis (**JJ kϕ*z***)

E_{boards}

The Young modulus (E) of the planking's timber is considered as an important parameter to model the stiffness of the planking system. The E_{boards} (modulus of elasticity assigned to the planking's elements) is defined as the stiffness of the "nail + (aged) board + nail", that would correspond to the static system "spring + plate + spring" in the structural model.

Cylindric model (Cy)

The cylindrical model is defined as a model whose *Jupiter joints*, represented as hinges in the structural model, have the properties in the equation eq. F-1

$$\begin{cases} k_{\varphi,x} = \infty \\ k_{\varphi,y} \neq 0 \\ k_{\varphi,z} = \infty \end{cases} \qquad \text{F-1}$$

Spheric model (Sf)

On the other side, the spherical model is defined as a model, whose *Jupiter joints* have the properties in the eq. F-2

$$\begin{cases} k_{\varphi,x} \neq 0 \\ k_{\varphi,y} \neq 0 \\ k_{\varphi,z} \neq 0 \end{cases} \qquad \text{F-2}$$

F.2 Step 1

First, the stiffness of the *Jupiter joint* is calibrated considering the variation of stiffness of the boards E_{boards} in both a cylindrical and a spherical model. In the Table F-3, decreasing values of elasticity modulus are assigned to the boards (E_{boards}) in order to simulate a drop of stiffness in the "spring + boards + spring" system. In the Diagram F-1 is to observe that when the E_{boards} increases, the displacement in the *Jupiter joint* ($JJu_{z,max}$) tends to zero. In the case of E_{boards} = 8000 MPa (model Cy.T.k8) of the deformation are almost null; while in the models with null-boards (model Cy.S) the deformations are infinite, and the model is kinematic.

Reducing the E_{boards} from $E_{boards,(k8)}$ = 8000 MPa to $E_{boards,(k3)}$ = 1000 MPa, the deformations are still in the range of acceptable deformations.

With same board stiffness, what is significant for the global stiffness of the (perfect) structure is the rotational stiffness of the *Jupiter joint* along the strong axis. In the area of the diagram from the E_{boards} > 1000 MPa, the deformation are sensitively reduced by the passage from JJkϕy = 0 kN·m / rad to JJkϕy= 100 kN·m / rad (with JJkϕy= JJkϕz = ∞). More, is important to remark that with the E_{boards} = 8000 MPa the contribution of the *Jupiter joint* to the general stiffness is not relevant.

Table F-2 – Stiffness values assigned to the cylindrical and spherical models (calibration).

MODEL 8.Cy.S (Cylindrical hinge)							
	PLANKING			**RIB with UPPER RING**	**RIB with LOWER RING**	**RIB INNER CONNECTION**	**UPPER - LOWER RING**
	n° 10 (START)	**n°5 (END)**	**E_{boards}**	**n° 13**	**n° 6**	**n° 11**	**n° 9**
ux	0	0	(global planking + nails stiffness) **k0 (= 0 MPa)**	0	0	0	0
uy	0	0		0	0	0	0
uz	0	0		0	0	0	0
ϕx [kN m / rad]	-	-		∞	∞	0	0
ϕy [kN m / rad]	-	-		∞	∞	≥0	0
ϕz [kN m / rad]	-	-		∞	0	0	0
MODEL 8.Cy.T (Cylindrical hinge)							
	PLANKING			**RIB with UPPER RING**	**RIB with LOWER RING**	**RIB INNER CONNECTION**	**UPPER - LOWER RING**
	n° 10 (START)	**n°5 (END)**	**E_{boards}**	**n° 13**	**n° 6**	**n° 11**	**n° 9**
ux	0	0	(global planking + nails stiffness) **kvariable**	0	0	0	0
uy	0	0		0	0	0	0
uz	0	0		0	0	0	0
ϕx [kN m / rad]	∞	0		∞	∞	0	0
ϕy [kN m / rad]	∞	∞		∞	∞	0	0
ϕz [kN m / rad]	∞	∞		∞	0	0	0
MODEL Sf (Spherical hinge)							
	PLANKING			**RIB with UPPER RING**	**RIB with LOWER RING**	**RIB INNER CONNECTION**	**UPPER - LOWER RING**
	n° 10 (START)	**n°5 (END)**	**E_{boards}**	**n° 13**	**n° 6**	**n° 11**	**n° 9**
ux	0	0	(global planking + nails stiffness) **k3 (= 1000 MPa)**	0	0	0	0
uy	0	0		0	0	0	0
uz	0	0		0	0	0	0
ϕx [kN m / rad]	∞	0		∞	∞	≥0	0
ϕy [kN m / rad]	∞	∞		∞	∞	100	0
ϕz [kN m / rad]	∞	∞		∞	0	≥0	0

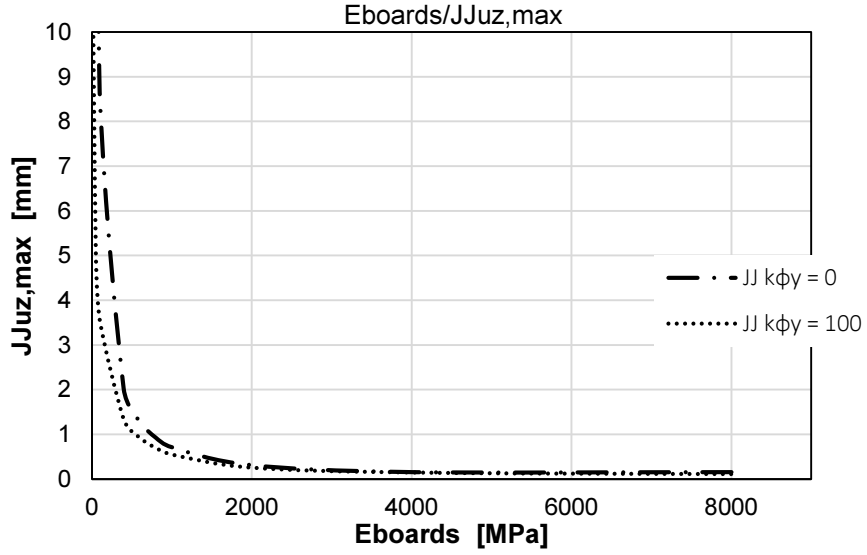

Diagram F-1 - Decrease of stiffness of the boards

Table F-3 - Decrease of the stiffness of the boards.

Cy.T												
	boards stiffness						jupiter joint stiffness			LC1 - dead loads results		
	board stiff.	Eboards [mPa]	n°5 kϕx [kN·m /rad]	n°5 kϕy [kN·m /rad]	n°5 kϕz [kN·m /rad]	n°10 kϕx,y,z [kN·m /rad]	JJ kϕx [kN·m /rad]	JJ kϕy [kN·m /rad]	JJ kϕz [kN·m /rad]	JJ uz,max [mm]	JJ uz,min [mm]	JJ |uz,max| [mm]
Cy.Tk8.J0	k8	8000	∞	0	0	0	∞	0	∞	0.064	-0.112	0.112
Cy.Tk1.J0	k1	4000	∞	0	0	0	∞	0	∞	0.130	-0.155	0.155
Cy.Tk2.J0	k2	2000	∞	0	0	0	∞	0	∞	0.290	-0.307	0.307
Cy.Tk3.J0	k3	1000	∞	0	0	0	∞	0	∞	0.708	-0.653	0.708
Cy.Tk4.J0	k4	800	∞	0	0	0	∞	0	∞	0.924	-0.833	0.924
Cy.Tk5.J0	k5	600	∞	0	0	0	∞	0	∞	1.287	-1.138	1.287
Cy.Tk6.J0	k6	400	∞	0	0	0	∞	0	∞	2.020	-1.756	2.020
Cy.Tk7.J0	k7	100	∞	0	0	0	∞	0	∞	8.649	-7.393	8.649
Cy.Tk9.J0	k9	50	∞	0	0	0	∞	0	∞	17.503	-14.930	17.503
Cy.S.J0	k0	0	∞	0	0	0	∞	0	∞	1E+12	∞	1E+12
Sf.Tk8.J6.z0	k8	8000	∞	0	0	0	0	100	0	0.064	-0.111	0.111
Sf.Tk1.J6.z0	k1	4000	∞	0	0	0	0	100	0	0.126	-0.148	0.148
Sf.Tk2.J6.z0	k2	2000	∞	0	0	0	0	100	0	0.257	-0.258	0.258
Sf.Tk3.J6.z0	k3	1000	∞	0	0	0	0	100	0	0.552	-0.492	0.552
Sf.Tk4.J6.z0	k4	800	∞	0	0	0	0	100	0	0.698	-0.602	0.698
Sf.Tk5.J6.z0	k5	600	∞	0	0	0	0	100	0	0.927	-0.722	0.927
Sf.Tk6.J6.z0	k6	400	∞	0	0	0	0	100	0	1.339	-1.066	1.339
Sf.Tk7.J6.z0	k7	100	∞	0	0	0	0	100	0	3.569	-2.255	3.569
Sf.Tk9.J6.z0	k9	50	∞	0	0	0	0	100	0	5.084	-2.491	5.084
Sf.S.J6.z0	k0	0	∞	0	0	0	0	100	0	13.221	-5.339	13.211

As a conclusion, the rotational stiffness of the *Jupiter Joint* along the strong axis (without the contribution of the torsional and weak axis, cylindrical model) is very important in case of deficiency of the stiffening effect of the planking. In case of new (perfect) structure, the contribution of the stiffness of the *Jupiter joint* along the strong axis is not relevant.

F.3 Step 2

The second step is to determinate the value of rotational stiffness for the *Jupiter joint*. The analysis is conducted under the hypothesis of perfect structure

The increasing of the stiffness of the local *Jupiter joint*'s stiffness $JJk\phi_y \neq 0\ kN{\cdot}m\ /rad$ was considered. The contribution of the boards (model Cy.S, eq. F-1) is here null.

The Diagram F-2 represents the ratio $JJk\phi_y - u_{z,max}$, with stiffness of the planking equal to zero (S).

The diagram illustrates how the deformations in the *Jupiter joint* along the *z* axis $JJu_{z,max}$, decrease with the increasing of the stiffness $JJk\phi_y$.

According to EC5, section 5.4.4, the maximum acceptable deflection of a curved frame as

$$e_0 = 0.0025 \cdot l \qquad \text{F-3}$$

In the hypothesis of perfect structure and *Jupiter joint* as a cylindrical hinge, in order to stay in the field of acceptable deformations it is assumed the *Jupiter joint* has a value of rotational stiffness along the strong axis as described in the following F-4.

JJkϕy,min = 100 kN · m / rad (minimum amount of stiffness along the strong axis) F-4

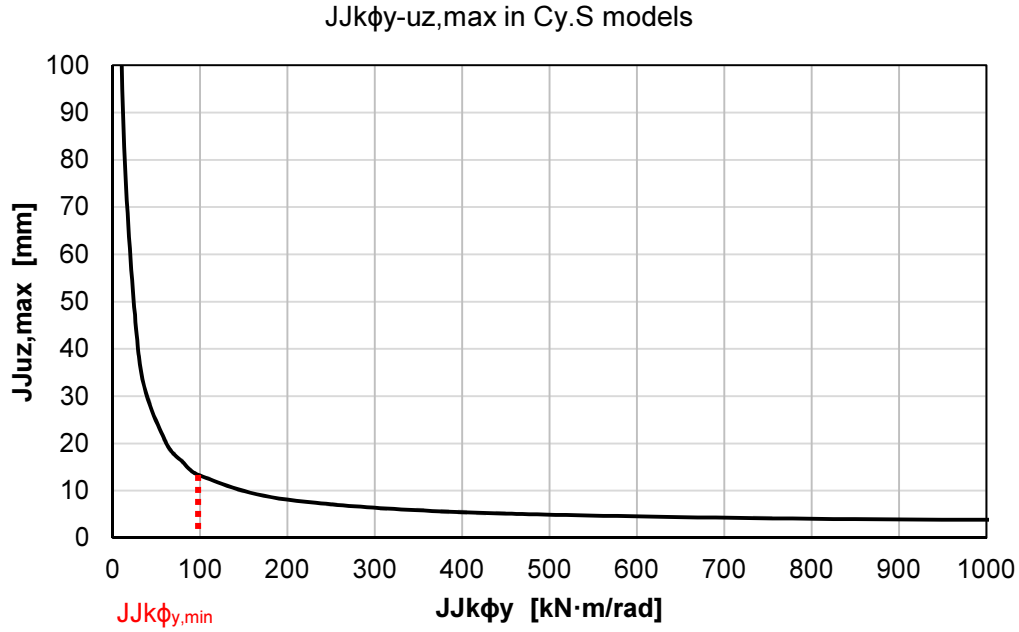

Diagram F-2 - JJkϕy-uz,max in the Cy.S models

Table F-4 - Increment of the JJkϕy and consequent uz,max in the Cy.S models

Cy.S					
Model	**boards stiffness**	**JJ kϕx** [kN·m /rad]	**JJ kϕy** [kN·m /rad]	**JJ kϕz** [kN·m /rad]	**JJ uz,max** [mm]
8.Cy.S.J0	0.00	∞	0	∞	∞
8.Cy.S.J1	0.00	∞	0.001	∞	1176226
8.Cy.S.J2	0.00	∞	0.01	∞	104432.00
8.Cy.S.J3	0.00	∞	0.1	∞	10540
8.Cy.S.J4	0.00	∞	1	∞	1053
8.Cy.S.J5	0.00	∞	10	∞	107.78
7.1.Cy.S.J5	0.00	∞	30	∞	38.49
	0.00	∞	60	∞	20.62
	0.00	∞	80	∞	16.16
8.Cy.S.J6	0.00	∞	100	∞	13.21
	0.00	∞	200	∞	8.12
	0.00	∞	450	∞	5.15
7.1.Cy.S.J8	0.00	∞	1000	∞	3.85
7.1.Cy.S.J9	0.00	∞	10000	∞	2.93
7.1.Cy.S.J10	0.00	∞	100000	∞	2.84
7.1.Cy.S.J11	0.00	∞	1000000	∞	2.83

F.4 Step 3

Once fixed the values of *kϕy* and E_{boards}, the *Jupiter joint* was modelled as a spherical hinge (eq. F-2) (*JJkϕx* = *JJkϕz* ≠ ∞). In the Table F-5 the results are presented.

Table F-5 - Increment of the *JJkϕy* and E_{boards}, consequent $JJu_{z,max}$ in the *Sf* models

9.Sf.									
		Assigned stiffness values				Results			
		E_{boards}	*Jupiter joint*			Displacements			
			kϕx [kN·m /rad]	kϕy [kN·m /rad]	kϕz [kN·m /rad]	u_{max} [mm]	$U_{x,\|max\|}$ [mm]	$U_{y,\|max\|}$ [mm]	$U_{z,\|max\|}$ [mm]
9.Sp.S.J0.z0		0.00	0	0	0	(kinematic)			
9.Sp.S.x8.J9.z0	b	0.00	0	100	0	13.60	0.23	0.01	13.22
9.Sp.S.x0.J9.z0	a	0.00	∞	100	0	13.56	0.03	0.01	13.22
9.Sp.Tk3.x8.J9.z0	a	1000	∞	100	0	0.55			-0.56
9.Sp.Tk3.x8.J9.z0	b	1000	0	100	0	0.55			-0.49

From the Table F-5 is desumed that:

- with some amount of stiffness *jjKϕy*, indipendently from the entity of *jjKϕx* and *jjKϕz* , the boarding are not crucial (in load case LC1) for the equilibrium of the structure. The u_{max} are in the acceptable range.
- The *JJkϕx* (torsional axis) does not crucially influences the behaviour of the structure, thus the displacement are very similar for the models 9.Sp.S.x8.J9.z0 and 9.Sp.S.x0.J9.z0, and 9.Sp.Tk3.J3.z0 a & b.
- In case of perfect structure, the reduced value of E_{boards} = *400 MPa* is considered acceptable.

F.5 Stiffness of the nails

Once established the value of stiffness for both the boarding and the *Jupiter joint* in the perfect structure, also the rotational stiffness $K_{\varphi,z}$ of the nails of the planking was established as described in the eq. F-5.

$$K_{\varphi,z} = \frac{1}{2} \cdot K_{ser} \cdot a^2 \qquad \text{F-5}$$

Where:

a distance between the two nails, and according to EC5 section 7.1 joint slip, the value of the slip modulus K_{ser} is the one in the eq. F-6.

$$K_{ser} = \frac{(\rho_m)^{1.5} \cdot (d)^{0.8}}{30} = \frac{(450)^{1.5} \cdot (5)^{0.8}}{30} = 1153 N \cdot mm \cong 1150 N \cdot mm \qquad \text{F-6}$$

Where

ρ_m Density of the wood contained in the Table 8-3 in [kg / m^3]

$d = 5mm$ Diameter of the nail (squared).

The value of rotational stiffness of the nails is thus

$$K_M = \frac{1}{2} \cdot K_{ser} \cdot a^2 = \frac{1}{2} \cdot 1150 \cdot (150)^2 = \quad 12937500 \quad N \cdot mm \quad \cong \quad 13\, kN \cdot m \qquad \text{F-7}$$

The EC5 meant the value of rotational stiffness has an implicit non-dimensional reference to the angle of rotation θ [*rad*] that defines the rotational stiffness (see eq. 2-1). For this reason, in the structural analysis program the unity of measure of the inserted value to define the K_M is (eq. F-8).

$$K_M = 13 \qquad \frac{kN \cdot m}{rad} \qquad \text{F-8}$$

F.6 Stiffness of the mortise-and-tennon joint (hinge n° 6)

For what concerns the *mortise and tennon* at the base of the ribs (n° 6), in the first tests was assigned a value of rotational stiffness equal to infinite $k\phi z = \infty$ [kN m / rad], while in the second tests the arbitrary value of $k\phi z$ = 10 [kN m / rad] was assigned to the joint. The value was chosen as different from infinite but not zero (because a shape factor).

The two analysed models have the properties listed in the Table F-6. The two cases with the hinge n° 6 normally hinged $k\phi z = 0$ [kN m / rad] (a) and fully hinged $k\phi z = 10$ [kN m / rad] (b) are presented. The value of E_{boards} = 400 MPa is considered the elasticity modulus that represents the (reduced) value of stiffness of the system boards + nails.

The results concerning the CO3: Dead loads + Imperfection 0 + Imperfection 1 follow.

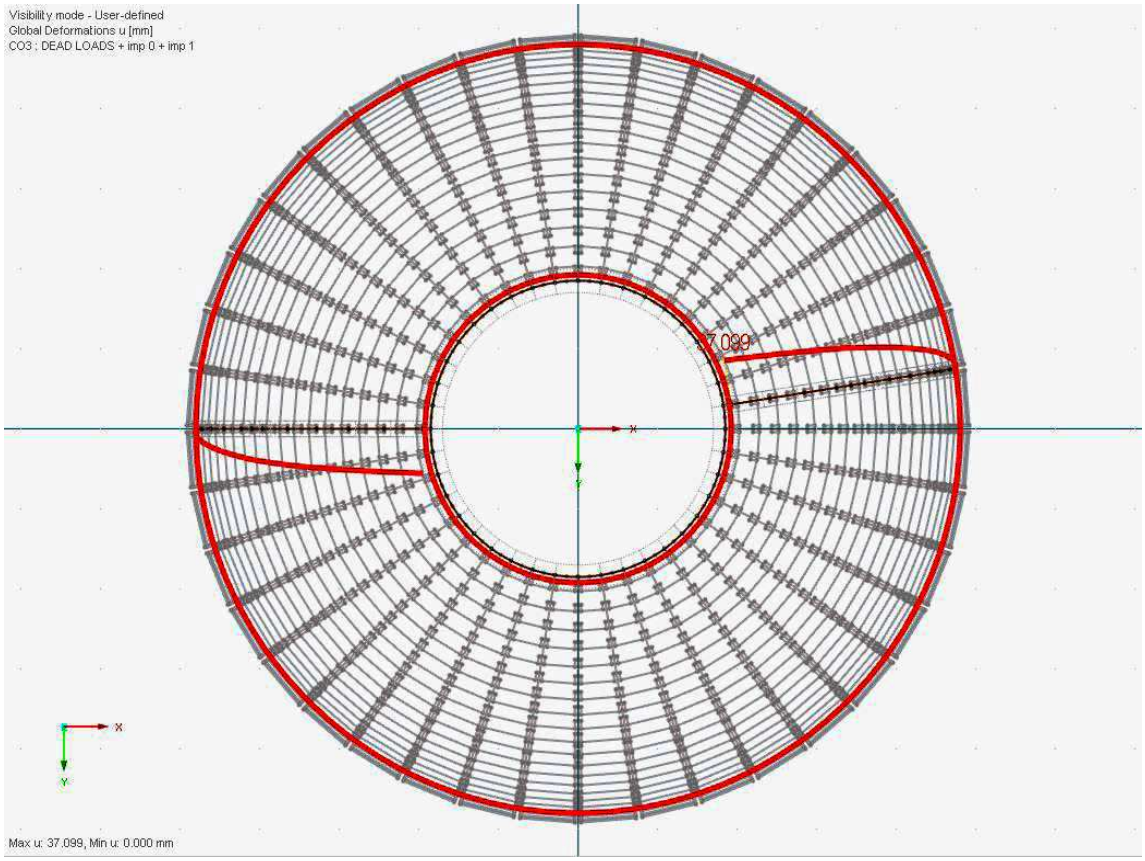

Figure F-2 – CO3: Global deformations *u* (top)

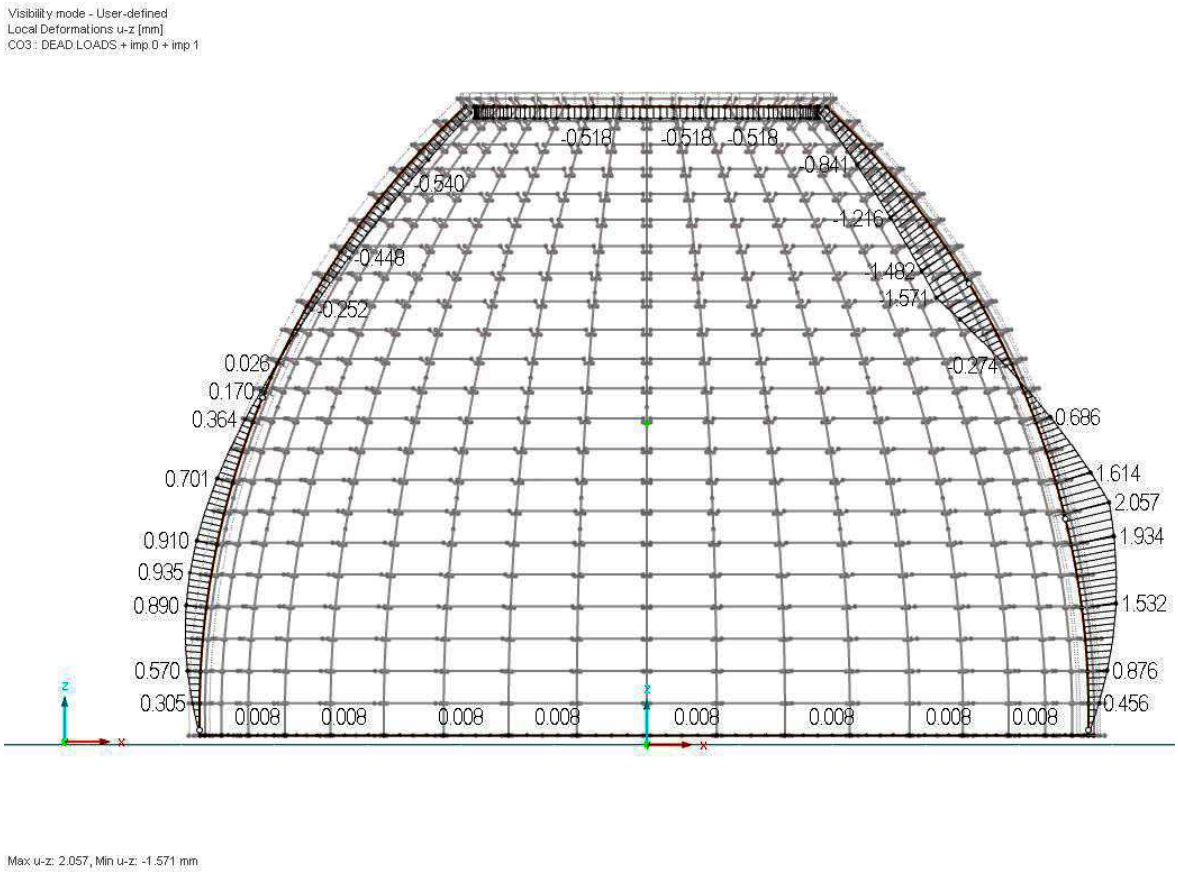

Figure F-3 – CO3: Local deformations u_z (in the 2 and 3 -pieces ribs)

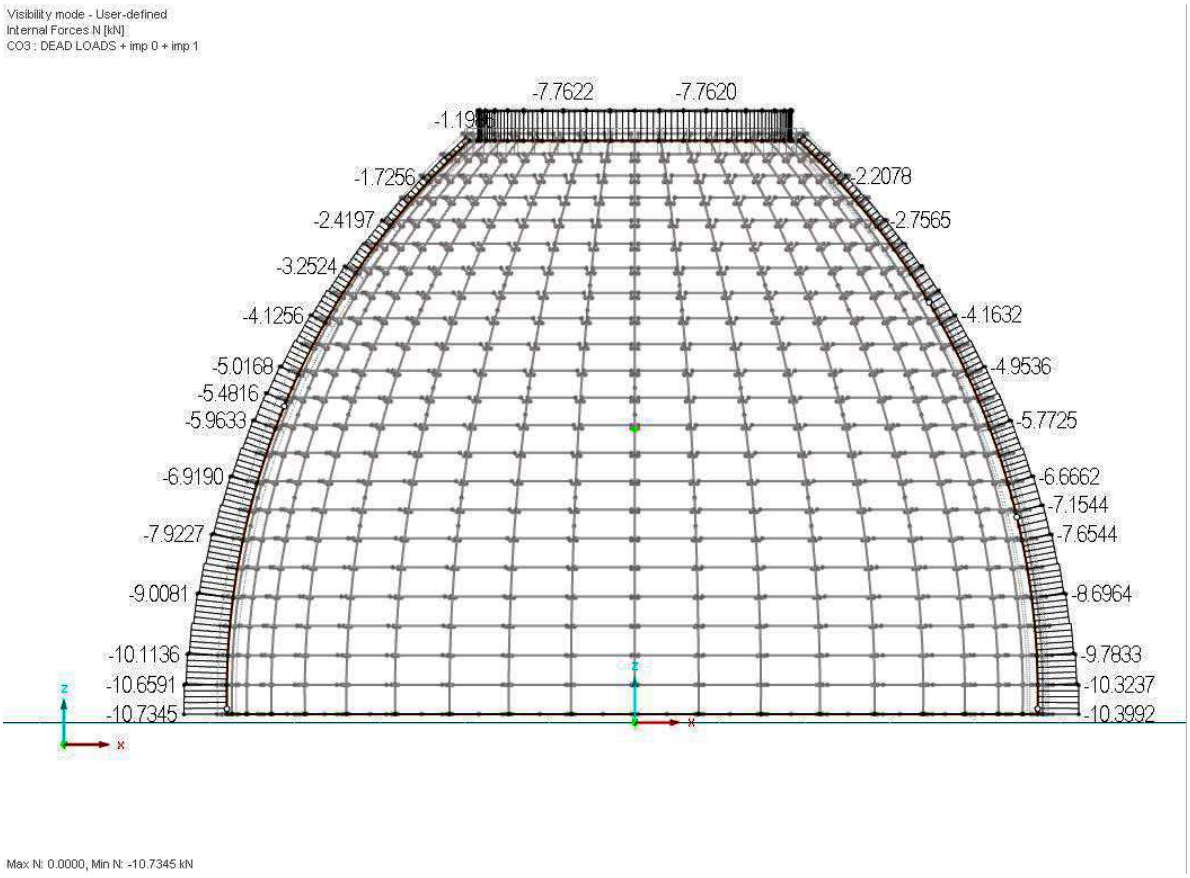

Figure F-4 – CO3: Normal forces N

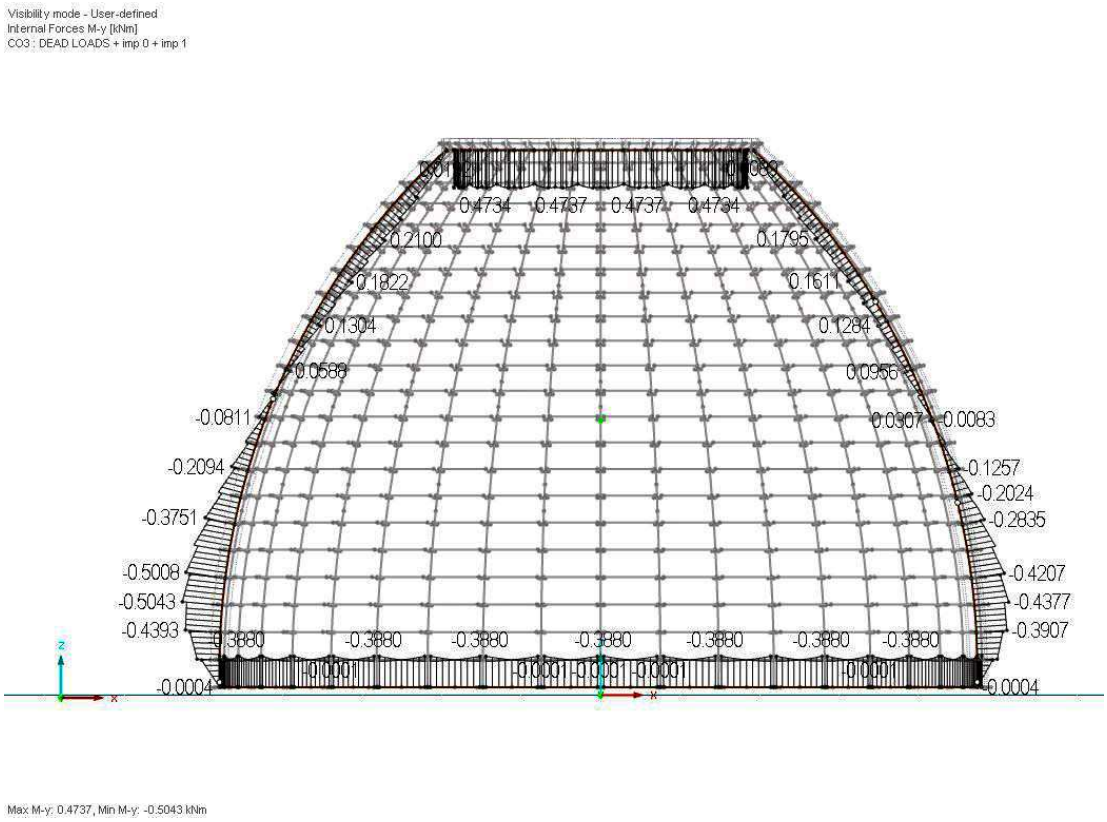

Figure F-5 – CO3: Moment M_y

Table F-6 – values of stiffness assumed for the elements in the model *10.Sp.Tk6.J3.z0 - IMPERFECT*

	PLANKING			RIB with UPPER RING	RIB with LOWER RING	RIB INNER CONNECTION	UPPER - LOWER RING
	n° 10 (START)	n°5 (END)	Eboards	n° 13	n° 6	n° 11	n° 9
(a) MODEL 10.Sp.Tk6.J12.z0 (n°6 normally hinged) (imperfect)							
ux [mm]	0	0	(global planking + nails stiffness) k6 (= 400 MPa)	0	0	0	0
uy [mm]	0	0		0	0	0	0
uz [mm]	0	0		0	0	0	0
ϕx [kN m / rad]	0	∞		0	0	0	∞
ϕy [kN m / rad]	0	0		0	0	100	∞
ϕz [kN m / rad]	13	13		0	∞	0	∞
(b) MODEL 10.Sp.Tk6.J12.z0 (n°6 fully hinged) (imperfect)							
ux [mm]	0	0	(global planking + nails stiffness) k6 (= 400 MPa)	0	0	0	0
Uy [mm]	0	0		0	0	0	0
Uz [mm]	0	0		0	0	0	0
ϕx [kN m / rad]	0	∞		0	0	0	∞
ϕy [kN m / rad]	0	0		0	0	100	∞
ϕz [kN m / rad]	13	13		0	10	0	∞

DISPLACEMENTS:

According to Table F-7, the maximal global u and local u_y displacements in the fully (n° 6) hinge model are bigger than in the (n° 6) clamped-hinge version.

ROTATIONS:

In contrast with the results on the displacements, the maximum absolute rotation $|\varphi_{jj,max}|$ of the *Jupiter joint* hinge is bigger in the clamped-hinged model than in the n° 6 fully-hinged model. The maximum rotations at the base of the rib 3-pieces rib are, in the clamped-hinged model equal to $\varphi_{z,max}$ = *15.60 mrad*, while, in the fully-hinged model, the maximal rotation is $\varphi_{x,max}$ = *7.21 mrad*. The meaning of that results is that in the first

case the beam (and the *Jupiter joint*) is stressed along the weak axis of the beam, in the second case, the inward-directed force, stresses the beam along the torsional axis.

In order to remain on the safe side, the second option (fully hinge) was chosen.

Table F-7 – Results for the CO3 in the model *10.Sp.Tk6.J3.z0 - IMPERFECT*

	Assigned stiffness values				imperfection			Results													
	E_{board} [Mpa]	jupiter joint			assigned imperfection			displacements				rotation at the base			moment				normal force		
		$k\phi x$ [kN·m/rad]	$k\phi y$ [kN·m/rad]	$k\phi z$ [kN·m/rad]	imp 0 [rad]	imp1 [mm]	imp 2 [mm]	u_{max} [mm]	$u_{x,max}$ [mm]	$u_{y,max}$ [mm]	$u_{z,max}$ [mm]	$\phi_{x,max}$ [mrad]	$\phi_{y,max}$ [mrad]	$\phi_{z,max}$ [mrad]	$M_{T,max}$ [kN·m]	$M_{y,max}$ [kN·m]	$M_{y,min}$ [kN·m]	$M_{z,max}$ [kN·m]	N_{max} [kN]	N_{min} [kN]	
10.Sp.Tk6.J12.z0 (n°6 normally hinged)	400	0	100	0	1/0.00427 (Utop = 30mm)	1/400 · l		32.82	-4.37	**-21.01**	-1.30	0.80	1.29	**15.60**	0.00	0.14	0.10	0.21	-3.47	-3.76	(3p-1)
									1.48	-6.87	0.08				-0.12	-0.16	-0.20	0.13	-6.76	-7.16	(3p-2)
									-0.40	14.33	-0.30	-1.47	-0.89	15.55	-0.20	0.01	-0.03	0.16	-5.09	-5.49	(2p)
10.Sp.Tk6.J12.z0 (n°6 fully hinged)	400	0	100	0	1/0.00427 (Utop = 30mm)	1/400 · l		37.10	-5.95	**-30.98**	-1.31	**7.21**	0.21	2.59	0.00	0.14	0.11	0.23	-3.47	-3.78	(3p-1)
									-0.61	-17.25	0.08				0.13	-0.16	-0.20	0.21	-6.75	-7.15	(3p-2)
									-0.47	25.52	-0.31	-7.10	-0.89	2.64	-0.12	0.01	-0.03	0.21	-5.48	-5.10	(2p)

KEY of the results:

(3p - 1) : Upper *Jupiter joint* in the 3-pieces rib;

(3p - 2) : Lower *Jupiter joint* in the 3-pieces rib;

(2p) : *Jupiter joint* in the 2-pieces rib.

F.7 Conclusions

As a conclusion the stiffness parameters for the *Jupiter joint*, the boarding system E_{boards} and the nails is determined as (Table F-8).

Table F-8 – Stiffnesses of the elements used for the structural analysis model.

	PLANKING			RIB with UPPER RING	RIB with LOWER RING	RIB INNER CONNECTION	UPPER - LOWER RING
	n° 10 (START)	n° 5 (END)	Eboards	n° 13	n° 6	n° 11	n° 9
ux [mm]	0	0	(global planking + nails stiffness) k6 (= 400 MPa)	0	0	0	0
Uy [mm]	0	0		0	0	0	0
Uz [mm]	0	0		0	0	0	0
ϕx [kN m / rad]	0	∞		0	0	0	∞
ϕy [kN m / rad]	0	0		0	0	100	∞
ϕz [kN m / rad]	13	13		0	10	0	∞

ANNEX G IDENTIFICATION OF THE SANTIAGO DE CUBA'S CATHEDRAL WOODEN SPECIES

G.1 Introduction

The present annex contains the document that identifies the wooden species used for the construction of the Santiago de Cuba Cathedral's timber frame. The CNR IVALSA Trees and Timber Institute in Sesto Fiorentino, Florence, Italy, conducted the recognition on February 2013. We thank the colleague Dott. Nicola Macchioni and the IVALSA technical staff for the support.

G.2 Document

Consiglio Nazionale delle Ricerche

IVALSA TREES AND TIMBER INSTITUTE

CATEDRAL DE NUESTRA SEÑORA DE LA ASUNCION DE SANTIAGO DE CUBA

Identificazione Delle Specie Costituenti Le Strutture Lignee Di Copertura

Relazione finale

Nicola Macchioni, Simona Lazzeri, Lorena Sozzi

Il giorno 21 gennaio 2013 ci sono stati recapitati 8 campioni lignei prelevati dalle strutture lignee che compongono la struttura lignea di sostegno della copertura della Cattedrale di Santiago di Cuba.

La tabella che segue elenca la denominazione di ciascuno dei campioni.

1	S01/2010
2	S02/2010
3	S03/2010
4	S04/2010
5	S05/2010 - trave
6	S05/2010 – pilastro
7	Imposta Tamburo 3
8	Legno lanterna 1

Da ciascun campione è stato prelevato un piccolo cuboide di circa 5 mm di lato, orientato secondo le tre direzioni anatomiche del legno (trasversale, longitudinale radiale e longitudinale tangenziale), posto successivamente a bollire in acqua in modo da poterlo rendere più morbido. Questa operazione consente un taglio più agevole delle sezioni sottili da osservare al microscopio.
Le sezioni tagliate a mano libera per mezzo di lametta sono state poste su vetrino portaoggetto, coperte con vetrino coprioggetto e osservate per mezzo di microscopio ottico Leica DM LB2.

L'identificazione per mezzo della caratterizzazione anatomica del legno consente, attraverso l'osservazione ad alti ingrandimenti, di osservare la distribuzione degli elementi

CNR IVALSA
ISTITUTO PER LA VALORIZZAZIONE
DEL LEGNO E DELLE SPECIE ARBOREE
www.ivalsa.cnr.it
P.IVA 02118311006
C.F. 80054330586

Firenze
Via Madonna del Piano 10
50019 Sesto Fiorentino
T +39 055 52251
F +39 055 5225507

Trento
Via Biasi 75
38010 S. Michele all'Adige
T +39 0461 660111
F +39 0461 650045

Grosseto
Via Aurelia 49
58022 Follonica
T +39 056 652356
F +39 056 652356

cellulari che compongono il tessuto legnoso, la loro distribuzione e i loro collegamenti reciproci lungo le tre direzioni principali del legno.
Si tratta di caratteristiche che consentono di distinguere tra di loro i legnami. In numerosi casi è possibile conseguire le caratteristiche specifiche di una specie legnosa, ma più frequentemente è possibile raggiungere il livello di genere o di gruppo di specie all'interno della tassonomia botanica, vista la grande somiglianza e sovrapposizione di caratteristiche anatomiche tra specie tassonomicamente contigue.

Le caratteristiche osservate vengono confrontate con quelle disponibili nella raccolta di specie legnose dell'Istituto e con quelle messe a disposizione nei vari atlanti del legno che costituiscono la letteratura di settore.

Queste operazioni hanno consentito di conseguire i risultati elencati nella tabella che segue.

S01/2010	*Cedrela* sp.
S02/2010	*Calophyllum* cfr. *brasiliense*
S03/2010	*Millettia* sp.
S04/2010	*Calophyllum* cfr. *brasiliense*
S05/2010 – trave	*Millettia* sp.
S05/2010 – pilastro	*Millettia* sp.
Imposta Tamburo 3	*Cedrela* sp.
Legno lanterna 1	*Cedrela* sp.

Caratteristiche anatomiche dei legnami identificati:

Cedrela

Anelli di incremento visibili per linee concentriche di parenchima terminale. Vasi piuttosto numerosi nel legno primaticcio, rotondeggianti, irregolarmente distribuiti, solitari o in gruppi radiali di 2-6, da medi a grandi, con lume spesso occupato da inclusioni gommose rossastre; semplicemente perforati e con punteggiature areolate, a disposizione alternata sulle pareti longitudinali. Fibre libriformi, raramente settate, a parete piuttosto sottile e lume ampio, disposte in serie radiali alquanto irregolari e con piccole punteggiature semplici. Parenchima assiale abbondante, sia di tipo paratracheale diffuso, più spesso vasicentrico, aliforme e confluente in larghe bande a riunire diversi vasi, sia terminale. Parenchima radiale in raggi ad andamento leggermente sinuoso a fianco dei vasi

CNR IVALSA
ISTITUTO PER LA VALORIZZAZIONE
DEL LEGNO E DELLE SPECIE ARBOREE
www.ivalsa.cnr.it

più grandi, subomogenei, raramente monoseriati, più spesso bi-triseriati, alti 7-25 assise di cellule, quelle procombenti ellittico-tondeggianti in sezione tangenziale, quelle apicali poco più grandi e triangolari a ferro di lancia, semplicemente punteggiate, con lume spesso occupato da inclusi gommosi rossastri.

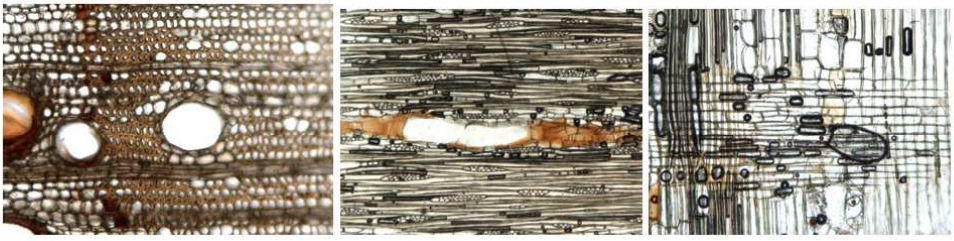

Figura 1 – da sinistra verso destra, sezione trasversale, tangenziale e radiale del campione S01 2010

Sotto la denominazione pilota di Cedrela, si raggruppano le seguenti specie legnose: *Cedrela odorata, C. guianensis, C. fissilis, C. mexicana* della famiglia delle Meliaceae.

Questo gruppo di specie cresce spontaneo nelle foreste primarie e secondarie dell'intera fascia tropicale comprendente America Centrale e Meridionale, ad esclusione del Cile.
Le denominazioni locali più usate sono CEDRO e RED CEDAR.

Calophyllum

Anelli di incremento indistinti. Vasi poco numerosi, non uniformemente distribuiti, ellittico-tondeggianti, per lo più solitari, di media grandezza, con lume spesso occupato da tille e inclusi gommosi rossastri; semplicemente perforati e con punteggiature areolate a disposizione alternata sulle pareti longitudinali. Fibre di tipo fibrotrachedidi a parete piuttosto sottile e lume ampio, disposte in serie radiali più o meno regolari e con piccole punteggiature lievemente bordeggiate. Parenchima assiale di tipo apotracheale e bande talvolta discontinue di 3-6 file di cellule, piuttosto ampie e con lume occupato da inclusi gommosi rossastri e qualche cristallo. Parenchima radiale in raggi leggermente sinuosi a fianco di vasi più grandi, eterogenei, mono e pluriseriati, generalmente biseriati, alti 4-25 assise di cellule; quelle procombenti pressoché rotondeggianti in sezione tangenziale, quelle erette e apicali più grandi e triangolari a ferro di lancia, semplicemente punteggiate e con lume spesso occupato da inclusi gommosi rossastri.

CNR IVALSA
ISTITUTO PER LA VALORIZZAZIONE
DEL LEGNO E DELLE SPECIE ARBOREE
www.ivalsa.cnr.it

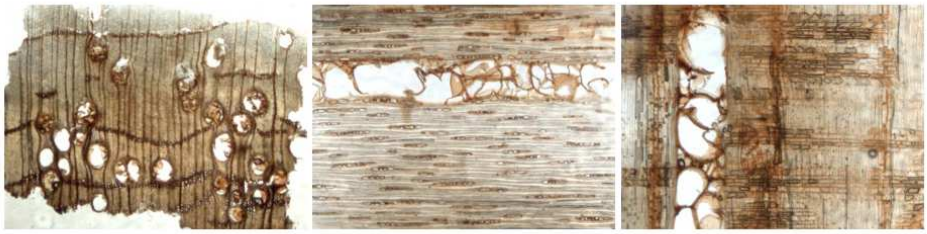

Figura 2 - da sinistra verso destra, sezione trasversale, tangenziale e radiale del campione S02 2010

La denominazione pilota di Santa Maria comprende il legname prodotto dalla specie *Calophyllum brasiliense*, della famiglia delle Guttiferae, che cresce nelle formazioni pluviali di latifoglie mi ste di tutta la fascia tropicale Centro e SudAmericana.

Millettia

Anelli di incremento indistinti. Vasi non molto numerosi, uniformemente distribuiti, ellittico rotondeggianti, solitari od in gruppi radiali di 2-4, piuttosto grandi, con lume occluso talvolta da sostanze gommose bruno-nerastre; semplicemente perforati e con punteggiature areolate, a disposizione alternata sulle pareti longitudinali. Fibre libriformi a pareti molto ispessite e lume ridottissimo, fittamente cementate l'una accanto all'altra a guisa di mosaico, e con punteggiature semplici. Parenchima assiale molto abbondante, di tipo paratracheale vasicentrico, ampio 1-3 file di cellule, ma per lo più confluente in larghe bande parenchimatiche di 12 – 20 file di cellule, ripiene di inclusi scuri e qualche cristallo, oppure apotracheale in strette bande continue di cellule, in certe zone somiglianti a parenchima terminale, piuttosto ampie, semplicemente punteggiate e con lume occluso da sostanze gommose rossastre e qualche cristallo. Parenchima radiale in raggi leggermente sinuosi a fianco di vasi maggiori, a disposizione seriata regolarissima, omogenei, raramente monoseriati, per lo più 2-5 seriati a forma di fuso piccolo e tozzo, alti 8-15 assise di cellule, pressoché rotondoggianti in sezione tangenziale e semplicemente punteggiate.

La denominazione Wenge riunisce le specie *Millettia laurentii e M. stuhlmannii* della famiglia delle Leguminosae Papillionaceae. Nel commercio internazionale è ugualmente diffusa la denominazione Panga panga.

CNR IVALSA
ISTITUTO PER LA VALORIZZAZIONE
DEL LEGNO E DELLE SPECIE ARBOREE
www.ivalsa.cnr.it

Si tratta di piante che crescono nelle foreste sempreverdi equatoriali primarie del medio bacino del Congo (*M. laurentii*) e nelle zone umide delle foreste tropicali del Mozambico e regioni circostanti (*M. stuhlmannii*).

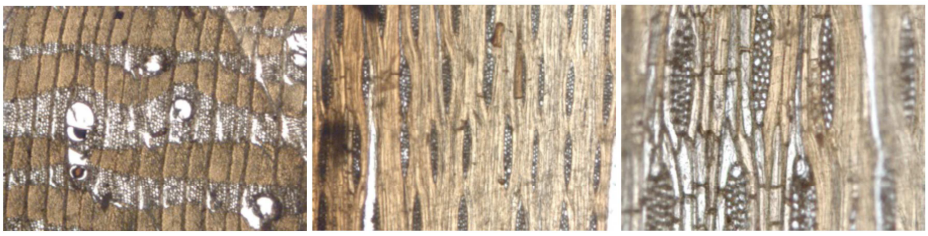

Figura 3 – a sinistra sezione trasversale del campione S03 2010; al centro ed a sinistra due immagini a diverso ingrandimento di sezioni tangenziali dello stesso campione.

Sesto Fiorentino, 4 febbraio 2013

dott. Nicola Macchioni

CNR IVALSA
ISTITUTO PER LA VALORIZZAZIONE
DEL LEGNO E DELLE SPECIE ARBOREE
www.ivalsa.cnr.it